EFFECT OF COPPER ADDITIONS ON DEFORMATION PROCESSING OF ALUMINIUM ALLOYS

BY

RICHARD PAUL VIEROD, B.Sc (ENG), A.R.S.M.

A Thesis submitted for the
Degree of Doctor of Philosophy
of the University of London

John Percy Research Group,
Department of Metallurgy
and Material Science,
Royal School of Mines,
Imperial College,
London, SW7 2BP

May 1983

ABSTRACT

The effect of an increase in copper content from 1 wt% Cu to 5 wt% Cu on the hot working characteristics of a 2000 series alloy based on AA2014 have been investigated, as well as a binary 4 wt% Cu alloy. The torque twist data generated from the hot torsion tests has been analysed using a graphical and mathematical minimisation technique, the temperature during testing being allowed for in the latter technique. The development of a strain dependent constitutive equation used in the temperature rise model has been investigated.

The dependence of the direct extrusion peak pressure and peak height on extrusion ratio, billet temperature and Zp the temperature compensated strain rate has been investigated in the 2000 series alloys and for direct and indirect extrusion of the 2014 alloy. The effect of container temperature and billet length on the peak pressure has also been investigated. The development of a general pressure equation applicable over a wide range of extrusion conditions and to a complete alloy system is investigated in the 2000 series alloys and a non heat treatable 5052 alloy. A solution preheat treatment determined from hot torsion tests has been used on the 2014 alloy to investigate whether surface cracking can be reduced during direct extrusion.

The structures in the 2000 series alloys have been investigated at all stages of processing from the as cast to the steady state quenched extrusion and torsion specimens using optical and transmission electron microscopy. The effect of process conditions on the hot worked substructure and the variation of structure within the direct and indirect deformation zones and across and along the extrudes has been investigated. The effects of direct and indirect extrusion, and the solution soak treatment on the structures of the solution treated (T6) and press quenched and aged (T5) 2014 alloy have been investigated.

The mechanical properties of the T1, T6 and T5 2014 alloy have been evaluated using hardness, tensile, fracture toughness and stress corrosion cracking tests. The effect of Cu content on the T1 and T6 tensile properties has also been established.

Limit diagrams for all the alloys and extrusion modes are presented.

CONTENTS

	Page
ABSTRACT	1
CONTENTS	2
LIST OF PLATES	6
LIST OF TABLES	7
LIST OF FIGURES	10
INTRODUCTION	16
CHAPTER 1 LITERATURE SURVEY	
1.0 Introduction	18
1.1 Commercial Aluminium - Copper - Magnesium System	18
1.2 Effect of Alloying Elements	19
1.3 Heat Treatments Applied to the Al-Cu System	21
1.3.1 Ageing Mechanism	21
1.3.2 The Effects of Ageing and Second Phase Particles on the Room Temperature Properties	24
1.4 Hot Working	26
1.4.1 Empirical Relationships	27
1.4.2 Structural Aspects of Hot Working	30
1.4.3 Restoration Processes	30
1.5 Substructure Strengthening	35
CHAPTER 2 THEORY	
2.1 Introduction	37
2.2 Torsion Analysis	37
2.2.1 Temperature Rise During Torsion Testing	37
2.2.2 Evaluation of the Hot Working Constants	42
2.2.2.1 Mathematical Minimisation	42
2.2.2.2 Graphical Analysis	45
2.3 Extrusion Analysis	48
2.3.1 Temperature Rise at Peak Load	48
2.3.2 Temperature Rise During Extrusion	49
2.3.3 Strain Rate Evaluation	50
2.3.4 Evaluation of the Billet Container Friction	50
CHAPTER 3 EXPERIMENTAL	
3.1 Introduction	53
3.2 The Extrusion Press	53
3.2.1 Container Heating	54

		Page
3.2.2	Billet Preheat	54
3.2.3	Extrusion Data Recording	56
3.2.4	Direct Extrusion Tooling	57
3.2.5	Indirect Extrusion Tooling	58
3.2.6	Water Quench	59
3.2.7	Experimental Procedure	59
3.2.8	Direct Extrusion	59
3.2.9	Indirect Extrusion	60
3.3	Materials	61
3.4	Partially Extruded Billets	63
3.5	Heat Treatment of Extrudes	63
3.6	Examination of Extrudes	64
3.6.1	Hardness Tests	64
3.6.2	Tensile Tests	65
3.6.3	Fracture Tests	65
3.6.4	Optical Microscopy	66
3.6.5	Electron Microscopy	66
3.6.6	Surface Quality	67
3.6.7	Stress Corrosion Testing	67
3.7	Torsion Tests	68

CHAPTER 4 RESULTS AND DISCUSSION

4.1	Torsion Data Analysis	71
4.1.1	Torque Twist Curves	71
4.1.2	Temperature Rise During Testing	73
4.1.3	Flow Stress Characteristics	78
4.1.3.1	Graphical Analysis	80
4.1.3.2	Mathematical Minimisation	86
4.1.4	Strain Dependency of the Hot Working Characteristics	99
4.1.5	Torsion Ductility	107
4.2	Extrusion Data Analysis	111
4.2.1	Extrusion Parameter Measurement	111
4.2.2	Load Displacement Curves	112
4.2.3	Variation of Peak Pressure With Extrusion Ratio	115
4.2.4	Variation of Peak Pressure With Initial Billet Temperature	117
4.2.5	Effect of Container Temperature on the Peak Pressure	121
4.2.6	Evaluation of the Friction Conditions	126
4.2.7	The Variation in Peak Pressure with Z_p	132
4.2.8	The Variation of ΔP with Z_p	137
4.2.9	General Pressure Equation	140
4.2.10	Extrude Surface Condition	153
4.2.10.1	Evaluation of the Presolution Soak Flow Stress and Extrusion Characteristics	155
4.2.10.2	Evaluation of the Surface Condition	164

Page

4.3 Structural Investigation 170
4.3.1 Introduction 170
4.3.2 As Cast Structure 170
4.3.3 Homogenised Structure 173
4.3.4 Extrusion Structures 174
4.3.5 The Variation in Steady State Substructures in Extrusion and Torsion 178
4.3.5.1 Extrude Substructures 178
4.3.5.2 Torsion Substructures 181
4.3.5.3 The Effect of Process Conditions on the Steady State Substructure 183
4.3.6 Material Flow During Steady State Extrusion 196
4.3.6.1 Flow Characteristics During Steady State Direct and Indirect Extrusion 196
4.3.6.2 Substructural Variations Within the Deformation Zones 198
4.3.6.3 Variation in Substructure Across and Along the Direct and Indirect Extrude of the 2014 Alloy 206
4.3.7 Heat Treated Structures 210
4.3.7.1 Solution Treated Structures 210
4.3.7.2 Aged Microstructures 220

4.4 Room Temperature Properties 226
4.4.1 Introduction 226
4.4.2 Effect of Extrusion Condition on the Hardness Properties 226
4.4.3 Ageing Characteristics 228
4.4.4 Tensile Tests 232
4.4.5 Stress Strain Curves 232
4.4.6 Tensile Properties of the 2014 Alloy 234
4.4.6.1 T1 Temper 234
4.4.6.2 T6 Temper 238
4.4.6.3 T5 Temper 244
4.4.7 The Effect of Cu Content on the Tensile Properties 249
4.4.8 Fracture Toughness Properties of the 2014 Alloy 254
4.4.9 Stress Corrosion Resistance of the 2014 Alloy 264
4.4.10 Limit Diagrams 267
4.4.11 Process Conditions vs Properties 276

CHAPTER 5

5.1 Conclusions 279

5.2 Recommendations for Further Work 284

APPENDICES

I Torsion Data 287

II Extrusion Data 290

III Room Temperature Mechanical Properties 298

IV Grain Size Measurements 303

		Page
V	Calibration Curves and Experimental Errors	304
VI	Computer Programmes	306
NOMENCLATURE		315
REFERENCES		317
ACKNOWLEDGEMENTS		319

List of Plates

Plate No	Title
I	General Layout of the Extrusion Press
II	Direct and Indirect Tooling
III	Surface Cracking of 2014 Alloy
IV	As Cast Microstructures of 1% Cu and 5% Cu Alloys
V	Homogenised Microstructures
VI	Typical Microstructures of the Press Quenched Extrudes - 2% Cu
VII	Substructures Observed in the Longitudinal Plane of the Press Quenched Direct Extrudes of the 1% Cu, 3% Cu and 5% Cu Alloys
VIII	Substructures Observed in the Longitudinal Plane in the Periphery of the as-Quenched Torsion Specimens of the 1% Cu, 3% Cu and 5% Cu Alloys
VIII b)	Presolution soak steady state torsion substructures - 2014 alloy
IX	Macrosections of Partially Extruded Billets of the 1% Cu Alloy
X	Development of Substructure along the Flowline during Steady State Direct Extrusion of the 1% Cu Alloy
XI	Development of Substructure along the Flowline during Steady State Indirect Extrusion of the 1% Cu Alloy
XII	Substructures Observed in the Longitudinal Plane of the Press Quenched Direct and Indirect Extrudes of the 2014 Alloy
XIII	Solution Treated and Aged Structures of the 2014 Alloy
XIV	T6 Solution Treated and Aged Microstructures of the Direct and Indirect 2014 Alloy - Longitudinal Plane
XV	T5 and T6 Microstructures of the 2014 Alloy CH Direct, Indirect and SS Direct Extrudes
XVI	Fracture Surfaces of T6 and T5 Extrudes of 2014 Alloy just below the Fatigue Crack
XVII	Stress Corrosion Structures in the Longitudinal Plane of the Indirect Extrudes of 2014 Alloy - Unetched

List of Tables

Table No	Title
1.1	Composition Limits for 2014
3.1	Alloy Compositions
3.2	Classification of Heat Treatments Used
4.1	Initial and Temperature Corrected Hot Working Constants at Homologous Strains of 1.0, 0.75 and 0.5
4.2	Area Average Temperature Rises, Flow Stress Data and Hot Working Constants in the 1% Cu and 3% Cu Alloys
4.3	Comparison of the Evaluated Temperature Rises in Torsion
4.4	Empirical Constants Derived from the Graphical Analysis
4.5	Hot Working Constants Derived from the Graphical Analysis
4.6	Hot Working Characteristics of the 4% Cu 2014 Alloy
4.7	Quoted Values of the Hot Working Constants
4.8	Empirical peak pressure-process parameter relationships for direct extrusion of the 2000 series alloys.
4.9	Temperature dependency of the flow stress - 2000 series alloys.
4.10	The dependence of peak and minimum pressure on container temperature T_I = 400°C — 3% Cu alloy.
4.11	Peak pressure vs billet length regression data for direct extrusion of 2% Cu and 5% Cu alloys.
4.12	Coefficient of friction μ established from direct and indirect extrusion data - 2014 alloy.
4.13	The dependence of peak pressure on Ln(Zp) and Ln(Zp/A) for direct extrusion of the 2000 series alloys.

4.14	Peak height ΔP vs $Ln(Z_p)$ regression data for direct extrusion of the 2000 series alloys.
4.15	Extrusion constants in the general pressure equation 4.12
4.16	Extrusion constants in the general pressure equation 4.14
4.17	Extrusion constants in the general pressure equation 4.16
4.17b)	Peak pressure vs billet length regression data - 5052 alloy
4.18	Constants in the flow stress equation 4.17
4.19	Hot working constants for the presolution soak (SS) and conventionally heated (CH) 2014 alloy.
4.20	CH and SS 2014 peak pressure and flow stress equations
4.21	The mean temperatures evaluated by the integral profile model at which cracking occurs during CH and SS direct extrusion of 2014 alloy.
4.22	The variation in % recrystallization during direct and indirect extrusion of CH and SS 2014 alloy in the T1 temper.
4.23	Misorientation measurements between subgrains 1% Cu, 3% Cu and 5% Cu extrudes.
4.24	Subgrain size measurements and relationships derived from extrusion and torsion specimens for the 1% Cu, 3% Cu and 5% Cu alloys.
4.25	$\sigma - \sigma_y$ vs subgrain size relationships evaluated from 1% Cu, 3% Cu and 5% Cu torsion specimens
4.26	Presolution soak torsion subgrain misorientation and subgrain size relationships.
4.27 a),b)	Variation in subgrain size within the steady state direct and indirect deformation zones of 1% Cu alloy T_I = 325°C.
4.28	Subgrain size measurements across and along the direct and indirect extrudes of 2014 alloy.
4.29	Predicted subgrain size and temperatures for direct and indirect extrusion of 2014 alloy.

4.30 The variation in % recrystallization after solution treating and ageing direct and indirect extrudes of 2014 alloy.

4.31 The variation in % recrystallization with container temperature - solution treated 3% Cu alloy.

4.32 Subgrain size measurement from T6 and T5 direct and indirect CH and SS 2014 extrudes.

4.33 Comparison between T1 and T5, T6 subgrain dimensions 2014 alloy.

4.34 Strain hardening exponents-2014 alloy.

4.35 Reported tensile properties of 2014 alloy from ref. 32, 33 and 35.

4.36 Percentage increase in P.S. from high Z_I to low Z_I extrudes in T1 and T6 temper of the 2000 series alloys.

4.37 Values of K_c determined by the off set procedure - T6 indirect extrudes of 2014 alloy.

List of Figures

Figure No	Title
1.1	Aluminium-Copper Phase Diagram
3.1	Torsion Specimen
4.1-3	Torque Twist Curves
4.4	Area Average Temperature Profiles at Homologous strains of 1.0, 0.75 and 0.5
4.5	The Variation of 1/n' with Initial Test Temperature
4.6	The Variation of α with Initial Test Temperature in the 1% Cu and 5% Cu 2000 Series Alloys
4.7-10	The Variation of the Steady State Hot Working Constants with Alloy Content
4.11-13	Flow Stress Characteristics of the 1% Cu to 5% Cu 2000 Series Alloys
4.14	Microhardness vs $\mathrm{Ln}Z_p$ in the 1% Cu and 5% Cu Torsion Specimens
4.15	Flow Stress Characteristics of the 2014 and 3.8% Cu Binary Alloy
4.16	The Variation of αn with Alloy Content
4.17-19	The Variation of ΔH, α and n with Homologous Strain
4.20	Incremental Increase in Flow Stress from $0.5\,\varepsilon_H$ to $1.0\,\varepsilon_H$ at $\dot{\varepsilon} = 26.0\ \mathrm{sec}^{-1}$
4.21	$\mathrm{Ln}\,\sigma_p$ vs $\mathrm{Ln}\,\varepsilon_p$ in the 2% Cu Alloy
4.22	The Variation in Torsion Ductility with Temperature and Alloy Content at $\dot{\varepsilon} = 26.0\ \mathrm{sec}^{-1}$
4.23	The Variation in Torsion Ductility with Flow Stress at $\dot{\varepsilon} = 26.0\ \mathrm{sec}^{-1}$ below 350°C
4.24	Direct Load Displacement Loci - 1% Cu, 3% Cu and 5% Cu 2000 Series Alloys
4.25	Direct and Indirect Load Displacement Loci - 4% Cu 2014 Alloy $T_I = 480^{\circ}C$

4.26 Direct and indirect load displacement loci - 4% Cu 2014 alloy T_I = 300°C

4.27 Peak pressure vs Ln(R) T_I = 350°C direct extrusion of 2000 series alloys

4.28 Peak pressure vs Ln(R) T_I = 450°C direct extrusion of 2000 series alloys

4.29 Peak pressure vs initial billet temperature ER = 30:1 direct extrusion of 2000 series alloys

4.30 Peak pressure vs initial billet temperature ER = 50:1 direct extrusion of 2000 series alloys

4.31 Peak pressure vs container temperature - direct extrusion of 3% Cu alloy T_I = 400°C

4.32 Minimum pressure vs container temperature - direct extrusion of 3% Cu alloy T_I = 400°C

4.33 Change in billet cooling rate with container temperature T_I = 400°C

4.34 Peak pressure vs billet length direct extrusion of 5% Cu alloy

4.35 Peak pressure vs billet length direct extrusion of 2% Cu alloy

4.36 Peak pressure vs initial billet temperature direct and indirect extrusion of 2014 alloy ER = 20:1

4.37 Peak pressure vs $\ln Z_p$ direct extrusion of 2000 series alloys ER = 20:1

4.38 Peak pressure vs $\ln Z_p$ direct extrusion of 2000 series alloys ER = 50:1

4.39 Peak pressure vs $\ln(Z_p/A)$ direct extrusion of 2000 series alloys

4.40 Peak height ΔP tangential construction

4.41 ΔP vs $\ln Z_p$ direct extrusion of 2000 series alloys

4.42 ΔP vs wt % Cu direct extrusion of 2000 series alloys

4.43 ΔP vs $Ln Z_p$ direct and indirect extrusion of 4% Cu 2014 alloy

4.44 Peak pressure vs predicted pressure calculated using equation 4.12 3% Cu alloy

4.45 Peak pressure vs predicted pressure calculated using equation 4.12 3% Cu alloy

4.46 Peak pressure vs billet length - 5052 alloy

4.47 Peak pressure vs predicted pressure calculated using equation 4.16 - 5052 alloy

4.48 Cooling curves for the presolution soak torsion specimens and extrusion billets - 2014 alloy

4.49 The variation of peak torque with soak time 2014 alloy

4.50 Flow stress characteristics of the CH and SS 2014 alloy

4.51 Torsion ductility vs initial test temperature at $\dot{\epsilon} = 26\ sec^{-1}$ CH 3% Cu, 5% Cu and SS 2014 alloy

4.52 Peak pressure vs initial billet temperature for direct extrusion of CH and SS 2014 alloy ER = 20:1

4.53 Peak height ΔP vs initial billet temperature for direct extrusion CH and SS 2014 alloy ER = 20:1

4.54 $Ln Z_I$ vs T_I - Dependence of surface cracking on the initial process conditions during direct extrusion of CH and SS 2014 alloy

4.55 Strain rate required for surface cracking vs T_I for direct extrusion of CH and SS 2014 alloy

4.56 Al - 4Cu and Al - 4Cu - 0.6Mg binary phase diagrams ref. 33,35,38

4.57 Quaternary phase diagram of Al - Cu - Mg for 0.6% Si at 460°C isothermal ref. 36

4.58 Volume % recryn vs initial billet temperature in the T1 temper for 2% Cu and 3% Cu alloys

Figure	4.59-61	d^{-1} vs LnZ_c 1% Cu, 3% Cu and 5% Cu alloys
Figure	4.62-64	Flow stress vs d 1% Cu, 3% Cu and 5% Cu alloys
Figure	4.65	Flow stress vs wt % Cu at constant subgrain sizes
Figure	4.66	$\sigma - \sigma_y$ vs d 3% Cu alloy
Figure	4.67	d^{-1} vs LnZ_c presolution soak torsion tests 2014 alloy
Figure	4.68	$\sigma - \sigma_y$ vs d presolution soak torsion tests 2014 alloy
Figure	4.69	Location of T.E.M. specimens within the steady state direct and indirect deformation zones 1% Cu alloy
Figure	4.70-71	Volume % recryn vs initial billet temperature in the T6 temper – 1% Cu and 3% Cu alloys
Figure	4.72	Volume % recryn vs initial flow stress for direct extrusion of the 1% Cu - 5% Cu alloys
Figure	4.73	Volume % recryn vs solution soak time at 500°C-direct extrusion of the 5% Cu alloy ER = 30:1
Figure	4.74-76	Recrystallised grain size (t) vs initial billet temperature for the CH direct, indirect and SS direct 2014 alloy
Figure	4.77	Recrystallised grain size vs subgrain size direct and indirect extrusion of 2014 alloy
Figure	4.78	Hv_{10} vs initial billet temperature T1 temper-1% Cu and 5% Cu alloys
Figure	4.79	Hv_{10} vs preheat temperature TF, T1 tempers-1% Cu and 5% Cu alloys
Figure	4.80-82	Ageing characteristics at 120°C, 160°C and 180°C solution treated 1% Cu - 5% Cu alloys
Figure	4.83-84	Room temperature stress strain curves 2014 alloy T1 and T6 temper
Figure	4.85	Tensile properties vs LnZ_I – T1 temper – CH direct extrusion of 2014 alloy
Figure	4.86	Tensile properties vs LnZ_I – T1 temper – SS direct extrusion of 2014 alloy

4.87 Tensile properties vs LnZ_I - T6 and T5 temper-CH direct extrusion of 2014 alloy

4.88 Tensile properties vs LnZ_I - T6 and T5 temper-CH indirect extrusion of 2014 alloy

4.89 Tensile properties vs LnZ_I - T6 temper-SS direct extrusion of 2014 alloy

4.90-91 Ageing characteristics at 160°C and 180°C press quenched extrudes of CH 2014 alloy

4.92-93 Ageing characteristics at 160°C and 180°C press quenched extrudes of SS 2014 alloy

4.94 Tensile properties vs LnZ_I -T5 temper - SS direct extrusion of 2014 alloy

4.95 Tensile properties vs wt % Cu - T1 temper- T_I = 300°C ER = 30:1

4.96 Tensile properties vs wt % Cu - T1 temper- T_I = 450°C ER = 30:1

4.97 Tensile properties vs wt % Cu - T6 temper- T_I = 300°C ER = 30:1

4.98 Tensile properties vs wt % Cu -T6 temper- T_I = 450°C ER = 30:1

4.99-100 Applied load vs clip gauge displacement - T6 and T5 temper-indirect extrusion of 2014 alloy

4.101 Plane stress fracture toughness K_c vs LnZ_I-T6 and T5 temper-CH direct extrusion of 2014 alloy

4.102 Plane stress fracture toughness K_c vs LnZ_I-T6 and T5 temper-CH indirect extrusion of 2014 alloy

4.103 Plane stress fracture toughness vs LnZ_I-T6 and T5 temper-SS direct extrusion of 2014 alloy

4.104-5 Limit diagram for CH direct, indirect and SS direct extrusion of 2014 alloy v = 3mm/s and v = 13mm/s

4.106-7 LnZ_I vs T_I - dependence of surface cracking on the initial process conditions. Indirect extrusion of 2014 alloy and direct extrusion of 5% Cu alloy

4.108-9 Limit diagram showing T6 and T5 % recrystallisation lines CH direct and indirect extrusion of 2014 alloy v = 3mm/s and v = 13mm/s

4.110 Limit diagram for direct extrusion of 1% Cu - 5% Cu alloys v = 13mm/s

4.111-2 Process conditions vs properties - direct and indirect extrusion of the 2014 alloy - T6 temper extrudes ER = 20:1

INTRODUCTION

The success or failure of any fabrication process relies on whether the final product is produced with the correct geometric, mechanical and cosmetic properties via the most economical route. The principle advantage of the extrusion process lies in the relative ease and efficiency in which complex sections can be manufactured in one operation. In some instances extrusion represents the only production route that is commercially viable. From the very first extrusion press developed by Joseph Bramah[1] in 1797 the extrusion process has grown to become one of the major fabrication industries for the processing of a wide range of metals, from lead and aluminium and it's alloys to high strength steels and nimonic alloys.

The earliest research work[1] on the extrusion process dealt primarily with the empirical relationships relating pressure to the extrusion parameters and material. Although these results were useful in establishing the more fundamental aspects of extrusion, the relationships were limited by the experimental facilities and the limited range of conditions considered.

In the early 1950's the application of plasticity theory led to the development of theoretical slip-line field and load bounding solutions[2,3]. The original models assumed plain strain conditions and a rigid perfectly plastic material, but these have been superseded by more complex axisymetric solutions which also consider strain hardening

materials.[4,5] In recent years the rapid improvement in computer technology has enabled finite difference techniques to be used to increase the flexibility of these solutions, to allow for the complex variation of strain rate and temperature within the deforming billet.[6]

The importance of temperature changes throughout the process has long been recognized and both experimental and theoretical investigations have been carried out.[7-19] The results have shown that temperature rises when extruding close to the incipient melting temperature or a phase change boundary can markedly effect the cosmetic and mechanical properties of the extrudate.

More recently the application of hot working theory to the extrusion process[17,20-24] has emphasized the importance of establishing meaningful values of temperature, strain rate and flow stress for use in any calculation.

Although in the past many industrialists have often doubted the applicability of extrusion research to the more complex extrusion processes, this view point has gradually changed in recent years with the realisation that the final structure and properties of the extrudate may be related to the process conditions and material characteristics.

It is in this area of research that present thesis was initiated to investigate the effect of alloy content on the hot working characteristics of a commercial Al-Cu-Mg alloy AA2014 and to establish the effects of process conditions and extrusion mode on the as extruded and heat treated product.

CHAPTER 1

LITERATURE SURVEY

1. INTRODUCTION

The literature relating to the general aspects of direct and indirect extrusion has been extensively reviewed by several authors in recent works[25-29] and will therefore not be considered in the present review.

1.1. COMMERCIAL ALUMINIUM-COPPER-MAGNESIUM SYSTEM

Aluminium-Copper-Magnesium alloys have been used for well over half a century since their first discovery by Wilm[30] in 1911. In 1919 Merica[31] associated the increase in hardness with the decomposition of a super saturated solid solution, and since then further improvements in the age hardening response have been brought about by alloying additions and thermal treatments so that today a range of commercial aluminium-copper alloys are available, collectively known as the 2000 series, of which 2014 and 2024 are the most widely used.

The development of the 2014 alloy utilised the effect of silicon to produce an Al-Cu-Mg more susceptible to artificial ageing than the original Duralumin alloy (now designated 2017), whilst 2024 was introduced in the 1930's as a higher strength natural ageing alloy to replace 2017. The alloys are normally used in the naturally aged and artificially aged conditions, where specific wrought products are also available in a number of worked and aged tempers designed to improve fatigue and toughness properties[32].

The 2014 alloy is mainly used in the aircraft industry where high strength to weight ratios are required, but is also used in bridges, truck frames, rivets and structural fittings.

The composition limits for 2014 are shown in table 1.1.

Alloys with low Cu contents of 2% to 3% Cu are used with higher magnesium 1.5% to 3% Mg and silicon 1% to 2% Si for rivets, because of their slow ageing response, and are also finding increasing use because of their high fabricability and fracture toughness[33].

Al	Cu	Mg	Mn	Si	Fe	Zn	
Rem	5.0	0.80	1.20	1.20	1.00	0.25	Max
	3.9	0.20	0.40	0.50	-	-	Min

Table 1.1 Composition Limits for 2014 Weight %

1.2. EFFECT OF ALLOYING ELEMENTS

The equilibrium compounds in the Al-Cu-Mg system are $CuAl_2$ (θ phase) and $CuMgAl_2$ (S phase)[33-35]. Both are soluble in the matrix during solution treatment where the proportion of S phase increases with decreasing Cu content as Mg:Cu ratio increases[33-36].

Addition of silicon improves the artificial ageing in 2014 and has some strengthing effect especially at higher temperatures but at the expense of ductility[37]. Silicon tends to combine preferentially with Mg as Mg_2Si but will also form compounds such as $Cu_2Mg_8Si_6Al_5$ (Q phase) and $(CuFeMn)_3Si_2Al_{15}$.[33,38]

The presence of iron up to 1% has a beneficial strengthening effect especially at high temperatures[39]. It forms such compounds as $(CuFe)Al_6$ and Cu_2FeAl_7 which crystallizes as long needles and thus has a considerable embrittling effect on the alloy[40].

The addition of Mn has a marked strengthening effect partly because of its solubility and partly because of the formation of intermetallic compounds[34,37]. Manganese additions remain in solution during casting but combine with iron during homogenization to form small intermetallic particles such as $(CuFeMn)_3Si_2Al_{15}$ and $(CuFeMn)Al_6$.[33,41,42] This reduces the embrittling effect of Cu_2FeAl_7 and increases the available copper since the Cu content of Mn bearing compounds is less. The manganese in solution can retard the onset of recrystallization[35,42] whilst the manganese-rich intermetallics, which tend to be associated with the sub-boundary dislocation network, inhibit grain growth[41]. The size and spacing of these particles therefore have an important effect on the mechanical properties of the material.

Small amounts of titanium and boron are added to form compounds such as $TiAl_3$ and AlB_2 which act as extremely effective grain refiners[35].

Phragmen's[38] comprehensive study of the Al-Cu-Mn-Mn-Si-Fe senary system indicates that no other equilibrium phases exist apart from those in the subsidiary systems reported above. The principal effect of a reduction in the copper content is therefore likely to reduce the amount of θ phase ($CuAl_2$) in each alloy, in the low copper alloys θ may be entirely replaced by either S or Q.

1.3. HEAT TREATMENTS APPLIED TO THE Al-Cu SYSTEM

Nearly all heat treatable aluminium alloys are subjected to a series of heat treatment cycles prior to and after fabrication to attain the optimum mechanical properties. A typical processing route for a 2000 series alloy would consist of an initial homogenization treatment to modify the usually brittle as cast structure, followed by preheating to the processing temperature and finally a solution treating and ageing cycle to produce the required properties. The characteristics of the as cast, homogenized and solution treated structures have all been extensively reviewed by previous workers[28,29,43] and therefore the structure and properties of the final age hardened material will be considered.

1.3.1. AGEING MECHANISM

Age hardening is a relatively well known phenomena in Al-Cu alloys and is associated with one or more of the transition phases formed during the decomposition of the super saturated solid solution (SSSS) produced after solution treating and quenching. In the binary Al-Cu system the nature and structure of the intermediate phases and their effects on the mechanical properties have been reviewed by several workers[44-46]. Before considering the commercial Al-Cu alloys it may be useful to briefly outline the ageing characteristics in the binary system.

The transformation from a SSSS to the equilibrium θ ($CuAl_2$) phase occurs by the following sequence of precipitates:

SSSS → GP1 → GP2(θ") → θ' → θ

The GP1 phase is a zone structure and forms immediately at room temperature as plate like copper rich regions on the (100) planes of the matrix[47]. They are 30 - 50 Å in diameter and can exist below 200 deg.C, but rapidly vanish above 130 deg.C. The θ" precipitates, which form spontaneously below 200 deg.C can exist at temperatures up to 270 deg.C and also lie on the (100) planes and are coherent with the matrix[44,48]. They form as thin platelets 20 Å thick and 400 Å in diameter. The semi-coherent, intermediate θ' precipitates nucleate and grow at the expense of θ" and lie parallel to the (100) planes[49]. The final equilibrium precipitate θ can nucleate directly from the θ' precipitate or from the matrix with slightly different orientation relationships and is incoherent with the matrix[33,50]. All three precipitate phases are reported to have a tetragonal structure[51].

The effect of Cu content on the solvus temperature for each of the transition phases is shown in figure 1.1.

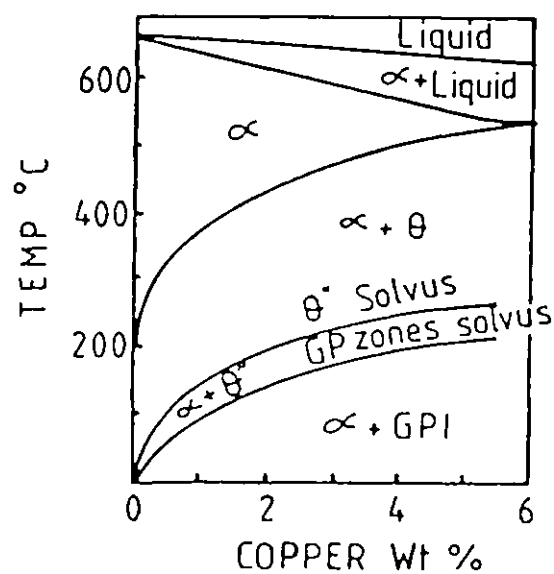


Figure 1.1 Al - Cu binary phase diagram

In the commercial alloys the presence of Mg and Si results in a modification of the precipitation sequence depending on the Mg:Cu and Mg:Si ratio[33]. The iron and manganese do not affect the ageing sequence directly, but affect the overall age hardening response by tying up the hardening solute via compound formation[52]. In the Al-Cu-Mg system Silcock[53] investigated alloys with Cu:Mg ratios of 2.2:1 and 7:1. At a ratio of 2.2:1 the ageing sequence changes to:

$$SSSS \rightarrow GPB \rightarrow S'' \rightarrow S' \rightarrow S$$

Details of GPB (Al-Cu-Mg) zone formation are not fully understood[13,53,55,56]. The zones are known to be stable at temperatures up to 260 deg.C with smaller lattice strains than the GP1 zones and lie on the (100) planes of the matrix. The transition phase S" is analogous to θ" of the Al-Cu system, and the semicoherent S' ($CuMgAl_2$) consists of platelets coherent on the (021) matrix planes. The equilibrium S phase is orthorhombic and incoherent with the matrix. For a Mg:Cu ratio 7:1 both precipitation sequences are reported to occur simultaneously resulting in θ and S as the final equilibrium precipitates.

In the 2014 alloy the presence of silicon is reported to result[55-57] in the formation of complex GPB type zones (Al-Cu-Mg-Si), as well as GP1 zones, during the initial stage of ageing at temperatures above 150 deg.C. Further ageing results in the transformation of GP1 zones to θ" and θ', whilst the GPB type zones persist throughout the ageing cycle. Ageing at room temperature results in the formation of GPB types zones only[57].

A change in the ageing sequence may also be brought about by preferential precipitation of one or more of the transition phases. This is the basis of the T3 and T8

tempers used for 2000 series alloys in which dislocations introduced by either cold or warm working prior to artificial ageing act as nucleation sites for θ' or S' precipitates. The precipitates are reported to be finer than those formed in the absence of dislocations, resulting in an increase in peak hardness and decrease in ageing time[58,59].

1.3.2. THE EFFECTS OF AGEING AND SECOND PHASE PARTICLES ON THE ROOM TEMPERATURE PROPERTIES

The basic mechanisms associated with age hardening in Al-Cu alloys have been reviewed by several authors[44,45] and may be classified thus:

(i) Strain hardening: The strain field produced by the precipitation of coherent particles with slightly different lattice parameters from that of the matrix oppose the motion of dislocations and so increase the flow stress.

(ii) Chemical Hardening: The presence of solute rich zones increases the number of solute-solvent bonds and consequently a higher stress is required to force a dislocation through the zones than through a super-saturated matrix.

(iii) Dispersion Hardening: Non-deformable particles acting as obstacles to dislocation motion, increase the stress required for dislocations to by-pass the obstacles. The flow stress increasing as the distance between the particles decreases.

In the 2014 alloy the first two mechanisms will be associated with zone formation, the first and third with the intermediate precipitates and the third with the equilibrium precipitates. The maximum hardness and strength in the

binary system is obtained when the amount of θ" is at a maximum although some contribution will be provided by θ'. As the amount of θ' increases, particle growth causes a loss of coherency together with a decrease in θ" resulting in overageing and a loss of strength. In 2014 peak hardness after artificial ageing is reported[56,57] to be associated with the partially coherent θ' in the presence of GPB zones and subsequent overageing is controlled by the slow growth of θ'.

The presence of the second phase particles discussed in section 1.2. will have a marked influence on the mechanical properties of extrudes whether in the as extruded or aged conditions. Previous workers[41,61] have reviewed the effect of these particles according to their size, of which there are three types:

(i) Coarse particles formed during casting or subsequent processing: 1 to 10 μm in diameter.

(ii) Intermediate particles formed during homogenization: 0.05 to 0.5 μm in size.

(iii) Ageing precipitates: 0.01 to 0.05 μm.

Other microstructural features may be important, such as precipitate free zones, but are often difficult to dissociate from other effects[62].

Coarse particles are deleterious to fracture toughness since they crack easily promoting void growth and coalescence ahead of the crack tip[61]. Preferred orientation of the particles in the extrusion direction further reduces fracture toughness in the short transverse direction due to the presence of aligned weak particles[61].

Intermediate sized particles affect the properties indirectly by retarding recrystallization and grain growth, thus controlling the grain size. Toughness and strength are improved by a reduction in grain size[41,61].

The fracture toughness decreases with increase in strength with ageing[63], which has been attributed to the reduction in the work needed to link voids prior to fracture[61]. A decrease in toughness is also observed between the naturally aged and artificially aged conditions. This is partly due to the increase in yield strength, and the detrimental effects of the coarser S' and θ' precipitates[41].

Ageing has a significant effect on the corrosion resistance[33]. During ageing those areas of the structure which are in a more advanced state of ageing are electronegative to the rest of the matrix and so corrosion concentrates there. Susceptibility to stress corrosion cracking, intergranular corrosion and exfoliation are all greatest in the underaged condition, and least in the overaged condition[64-67].

Clearly the optimum structure and properties and hence the process conditions and heat treatment chosen, will depend on the particular service conditions. However the overall situation is not helped by the fact that although the effects of heat treatment on age hardening aluminium alloys is well known, the mechanisms operating are not fully understood.

1.4. HOT WORKING

The use of high temperatures above 0.6 Tm (Tm is the melting point in deg. K) for the extrusion of aluminium and it's alloys is necessary as the stress to deform a metal at

low temperatures increases markedly with strain due to the work hardening caused by the complex generation and interaction of dislocation within the material. At elevated temperatures strain hardening is reduced by dynamic softening processes to the extent that the deformation stress or flow stress becomes strain independent under isothermal conditions. It is these softening or restoration processes that have been studied in investigations into hot working[68,69]. An important feature of the flow stress is it's temperature and strain rate dependency, where the higher the strain rate at a given temperature, the greater the flow stress[68,70-73]. This is an important consideration in the metal working processes where high strain rates in the region of 0.5 to 500 sec^{-1} are used to deform materials to large strains at high temperatures. This has resulted in the subject of hot working becoming an important aspect of metallurgical research with respect to the empirical relationships, structural characteristics and deformation mechanisms involved.

1.4.1. EMPIRICAL RELATIONSHIPS

In order to establish the flow stress characteristics of a material during hot working a testing technique must be chosen which can simulate the high temperatures and strain rates associated with hot working operations. The most common methods are tensile, compression and torsion testing which have recently been reviewed by several authors[27,29,74]. The following relationships have been determined using data derived from all three testing techniques.[68,70,72,73,76]

At low stress levels and constant temperatures the steady state flow stress can be described by:-

$$\dot{\varepsilon} = A_1 \sigma^{n'} \qquad 1.1.$$

when n' and A_1 are assumed to be temperature independent constants. At high stress levels and constant temperature:-

$$\dot{\varepsilon} = A_2 \exp(\beta\sigma) \qquad 1.2.$$

where A_2 and β are assumed to be temperature independent constants.

The relationships are comparable to those found to describe steady state creep experiments indicating the similarity between creep and hot working data. Garafalo[77] has shown by creep experiments that these two relationships may be combined to give:-

$$\dot{\varepsilon} = A(\mathrm{Sinh}(\alpha\sigma))^n \qquad 1.3.$$

where $$\alpha = \beta/n' \qquad 1.4.$$

At low stress levels equation 1.3. reduces to a power form and at high stresses to an exponential form. This relationship has also been fitted to hot working data[78,79] with A, α and n being temperature independent.

The similarity between steady state creep and steady state hot working led Sellars and Tegart[80] to propose a relationship of the form:-

$$\dot{\varepsilon} = A(\mathrm{Sinh}(\alpha\sigma))^n \exp\left[-\frac{\Delta H}{RT}\right] \qquad 1.5.$$

where A, α and n were described as temperature independent constants, and ΔH as the activation energy of the hot working process. At low stress levels ($\alpha\sigma < 0.8$) this

equation reduces to a power relationship and at high stress levels ($\alpha\sigma > 1.2$) to an exponential relationship. Equation 1.5. can also be written in the form:-

$$Z = \dot{\varepsilon} \exp\left[\frac{\Delta H}{RT}\right] = A(\mathrm{Sinh}(\alpha\sigma))^n \qquad 1.6.$$

where Z is the Zener-Holloman parameter[81]. Z was originally proposed for low temperature tests but was shown to apply to hot working data[80] and has been used to correlate data over a wide range of strain rates and temperatures[68,78-80].

The dependence of temperature through an Arhenius term indicates that hot working is a thermally activated process with ΔH equal to the activation energy of the rate controlling process. Values of activation energy for different materials have been determined by many workers[68] and can generally be divided into two groups, depending on the stacking fault energy (S.F.E.) of the material[68,75]. For high S.F.E. materials such as aluminium and it's alloys[68,82,83] the activation energy for hot working is similar to that for bulk self-diffusion, which is attributed to the fact that the rate controlling mechanism in the deformation of these materials is climb aided by cross slip[68,84]. Since climb requires the diffusion of vacancies, the activation energy will be more or less equal to that for self-diffusion depending on the influence of cross-slip. For low to medium S.F.E. materials which includes copper, nickel and austenitic steels, the activation energy for hot working is reported[68] to be much higher than that for self diffusion owing to the difficulty of dislocation climb.

The physical interpretation of the empirical constants A, α and n have yet to be properly established. Jonas et al[68] deduced by comparison with rate theory that at high

stress levels ($\propto\sigma > 1.2$) A is a structure factor and $\propto nKT$ an apparent activation volume. The constant $\propto$ has been defined[68] as the reciprocal stress at which Z changes from a power to an exponential relationship where n may be considered as a measure of the temperature compensated strain rate sensitivity of the flow stress.

1.4.2. STRUCTURAL ASPECTS OF HOT WORKING

The change in activation energy for hot working from high S.F.E. materials to low S.F.E. materials is also reflected in the structural characteristics of the hot worked structures. In high S.F.E. materials the steady state structures are characterised by subgrains of low misorientation[68,78,85] whilst in low S.F.E. materials a steady state structure comprising of recrystallized grains is found[69]. The difference in activation energy and structure have been associated with two separate restoration mechanisms.

1.4.3. RESTORATION PROCESSES

The predominant restoration mechanism in high S.F.E. materials is dynamic recovery. Luton and Jonas[86] have described how in the initial stages of substructure development the stress strain curves may be divided into three stages. The first stage is that of microstrain deformation during which the strain rate in the sample increases from zero to the test value. During this stage the stress rises rapidly and dislocations are generated to accomodate the plastic strain, increasing in density from 10^{10} - 10^{11} m^{-2} (annealed state) to 10^{11} - 10^{12} m^{-2}.[69] The end of the microstrain interval is signified by a decrease in the slope of the loading curve and the dislocation density continues to rise with strain till a steady state region is attained in which the dislocation density remains

constant at 10^{14} - 10^{15} m^{-2} depending on the prevailing temperature and strain rate[69]. During this stage of strain hardening before the attainment of steady state the dislocations become entangled and begin to form a cellular structure by clustering into cell walls separating relatively dislocation free regions. Clustering is energetically favourable as the inter-action energy between positive and negative dislocations decreases with decreasing dislocation spacing[87]. With further deformation, more dislocations are generated, and attracted to the existing sub-boundaries, where they can be annihilated by interacting with dislocations of the opposite sign. The rate of annihilation depending on the dislocation density and on the ease of operation of the recovery mechanisms such as climb and cross-slip.

In face centred cubic metals the dislocations lying in the close packed planes can dissociate into partial dislocations with a stacking fault ribbon between them[87]. The higher the stacking fault energy of the metal the stronger is the binding energy and the closer together are the partial dislocations. Before dislocations can climb or cross slip, the partials must come together under the action of the applied force, so that in aluminium and it's alloys climb and cross-slip take place easily, leading to rapid subgrain formation.

The effect of alloying additions such as copper will largely be dependent on whether the solute is in solution or as a precipitate distribution. In general an increase in alloying additions increases the strain and stress required to establish the steady state substructure which is generally less recovered than the unalloyed metal[68]. In solution an increase in the solute content is reported[88] to decrease the S.F.E. in low S.F.E. materials, although there is no evidence to suggest that this is the case for high

S.F.E. materials[75]. Solid solution additions can also hamper climb through the binding energies that tie vacancies to solute atoms[90]. The presence of second phase particles which are not cut by dislocations at the temperature of deformation can help to build up and stabilise the substructure by acting as obstacles to dislocation motion[69,88,89]. Under such conditions the subgrain diameter may be reduced to the interparticle spacing.

The onset of steady state deformation occurs at strains between 0.1. to 0.5. depending on the temperature and strain rate[69]. During steady state deformation the subgrain size and the dislocation density remain constant[68]. The mean subgrain size increases with increase in temperature and decrease in strain rate[75,91-94]. As the size increases the subgrains contain fewer dislocations and have boundaries in which there are less dislocations arranged in more orderly arrays[92]. These substructural variations can be explained by the decrease in the equilibrium dislocation density. The generation rate decreases because the effective stress decreases with strain rate and temperature. The annihilation rate is not so sensitive and does not decrease at the same level.

In aluminium alloys the subgrains are reported to consist of very sharp boundaries with an equilibrium dislocation network within the subgrains. The misorientation between them is small ranging from $<1^{o}$ to 7^{o} [68,85,91-94]. Smaller cells have been observed within these subgrains[82,91,95], which have been attributed to the formation of subgrains during deformation[69] and the remnants of subgrains that have annealed out by rotation at the end of deformation. Although other evidence suggests that this structure occurs by subgrain coalescence in the time between

deformation and quenching[96].

For extrudes processed below 0.5 Tm the subgrains tend to be elongated in the extrusion direction whilst above this temperature the subgrains are equiaxed although the grains in which they are embedded are elongated in accordance with the imposed macroscopic strain[25-29]. This indicates that the subgrains are continuously migrating and reforming at an equilibrium spacing depending on Z[97-98]. The process of continuous substructure regeneration during hot working has been termed repolygonization[98].

In materials of low S.F.E. where the rate of dynamic recovery is low, steady state deformation is the result of dynamic recrystallization[75]. The process of dynamic recrystallization has recently been reviewed by McQueen and Jonas[69]. Essentially its occurrence does not result in the elimination of the substructure as does static recrystallization, although the dynamic restoration mechanism does involve the movement of high angled boundaries through the matrix during deformation[69]. Evidence of dynamic recrystallization has been reported in Al-Mg alloys[88,99] although its occurrence in Al-Cu alloys has yet to be found, dynamic recovery being the only reported mechanism.[25,26,29,100]

The basic assumption made when examining the as quenched hot worked structures is that little or no change in the structure occurs before or during quenching. As soon as deformation is completed or interrupted the release of stored energy in the form of the substructure introduced during working, acts as the driving force for static restoration processes to be initiated after deformation. These processes can proceed either by static recovery, which involves annihilation in individual events or static recrystallization in which dislocations are

simultaneously eliminated in large numbers as a result of the motion of high angled boundaries.

If the critical strain for recrystallization[69] is not reached or the deformation temperature is not high enough for static recrystallization, then static recovery will be the only softening process after deformation. However it should be noted that full softening cannot be produced by static recovery alone[101,102]. The effect of alloying additions on the occurrence of static recovery is not fully understood. However, it is generally considered that the presence of solutes or precipitates tend to pin dislocations thereby making static recovery more difficult[103].

It is well known that the static recrystallization process is one of nucleation and growth[104] although the exact mechanism of nucleation is still uncertain. The more recent theories have considered nucleation to occur either by subgrain coalescence in which growth of the subgrains proceeds by the gradual disappearance of the sub-boundaries[105,106] or by a mechanism of rapid sub-boundary migration[107,108]. As the subgrains grow the boundary misorientation increases until it becomes sufficiently large, for migration by high angle boundary processes to become dominant[95]. In recrystallization this may be strain induced in a direction away from the centre of curvature of the boundary[109].

The presence of second phase particles may either accelerate or retard recrystallization. Particles > 0.5 μm can accelerate the nucleation process due to the large lattice rotations in the vicinity of the particles[107], where as fine particles < 0.1 μm tend to reduce the mean misorientation between subgrains[110] and reduce the rate of subgrain growth and hence nucleation by pinning the sub boundaries[95]. An increase in the solute content can also

indirectly increase the rate of nucleation by reducing the preceeding recovery processes[68]. Indeed the recrystallization temperature is reported[33] to be lowered by copper additions, where the rate of recrystallization is maximum when the excess copper is in the form of coarse particles, less when in solution and least when as a fine precipitate.

The deformation mechanisms proposed for dynamic recovery and dynamic recrystallization have been extensively reviewed in several recent works.[27-29,68,112]

1.5. SUBSTRUCTURE STRENGTHENING

Many workers[68,98] have observed that the steady state flow stress and the subgrain size (d) under creep and hot working conditions can be related via an equation of the form:

$$\sigma = \sigma_o + kd^{-m} \qquad 1.7.$$

where σ_o, k and m are constants. During high temperature deformation $\sigma_o \simeq 0$ whilst m ranges in value from 1 to 1.5.[85,113]. The exact effect of the subgrain structure on the flow stress characteristics are not fully understood, although it is generally thought that the strengthening arises because the sub-boundaries are the principle source of internal stress opposing dislocation motion[69,114]. Alternative relationships have been suggested by Jonas et al[68].

$$d^{-1} = a + b\ \mathrm{Ln}(\mathrm{Sinh}(\propto\sigma)) \qquad 1.8.$$

and $$d^{-1} = p\ (\mathrm{Sinh}(\propto\sigma))^q \qquad 1.9.$$

where a, b, p and q are constants. Since the temperature compensated strain rate is also a function of the hyperbolic

stress, many workers[20,23,76,98,115-117] have shown the subgrain size can be related to Z by a relationship of the form:-

$$d^{-m} = a + b \text{ Ln } Z \qquad 1.10.$$

The hot worked substructure retained by rapid cooling can also have a marked influence on the room temperature mechanical properties. Several workers[118,119] have observed that the yield strength σ_y can be related to the subgrain size through a modified Hall Petch equation:-

$$\sigma_y = \sigma_A + kd^{-m} \qquad 1.11.$$

where σ_A is the yield strength of the annealed material, m is a constant, and k a constant relating to the subgrain boundary strengthening[119]. In heat treatable alloys solution treating and ageing is likely to remove all traces of the substructure due to the occurrence of static recrystallization. Therefore, substructure strengthening is generally regarded to be more important in the production of non heat treatable alloys such as the 1000, 3000 and 5000 series alloys. However, recent work[120,121] has shown that the presence of a retained substructure can improve creep resistance, whilst the effect on fatigue, fracture toughness and corrosion properties are currently being investigated in the field of thermomechanical processing.[41,58,69]

The dependence of the subgrain size on the temperature compensated strain rate and their relationship with the room temperature mechanical properties is an important consideration in extrusion, since it should enable the final properties of the extrudate to be related to the process variables of temperature and strain rate.

CHAPTER 2

THEORY

2.1. Introduction

In this chapter the analyses used to establish the flow characteristics from hot torsion test data are discussed. The temperature change and strain rate analyses for torsion testing and extrusion are also presented.

2.2. Torsion Analysis

2.2.1 Temperature Rise During Torsion Testing

The adiabatic temperature rise during testing can be calculated using the following relationship:-

$$\Delta T = \frac{\eta}{\varrho c} \int_{o}^{\varepsilon max} \sigma \, d\, \varepsilon \qquad 2.1.$$

where ϱ is the density, c the specific heat, η the fraction of work converted into heat, σ the stress and strain ε .

Adiabatic conditions are only likely to occur at high strain rates, while at low strain rates heat loss by convection and conduction may be considerable. To allow for these heat losses the finite difference model developed by Wright [122] has been used. The specimen is divided into 20 radial and 40 axial elements giving them equal length and width for the specimen geometry. Heat losses by radial and axial conduction, and convection from the surface are considered. For aluminium alloys the radiation

heat losses are negligible, but can be significant for other materials where the hot working temperature may be in excess of 1000 deg. K. Circumferencial conduction is ignored since the circumferencial elements will be deformed equally during testing and can therefore be expected to have a uniform temperature. Details of the mathematical analysis and the computer programme can be found in reference 122.

The model assumes that strain and strain rate vary linearly across the radius, so that in order to evaluate the stress at any point, the variation of stress and strain rate with strain must be known. Previous workers [27-29] have used a relationship of the form

$$\sigma = A \dot{\varepsilon}^n$$

where A and n are temperature independent constants, the equation being solved at several constant values of strain. A number of disadvantages are associated with this analysis, the principle one being the use of equivalent stress-strain rate data. A Fields and Backoffen[126] type analysis was used, which apart from being very laborious, is inherently incorrect as it assumes that the torque is a unique function of the amount of twist Θ and twist rate $\dot{\Theta}$, and independent of the detailed history of the test. It therefore makes no allowance for the temperature rise during testing. Canova[127] et al have described an alternative method which is reported to be history independent i.e. it is independent of the strain rates and temperatures at which the previous strains were applied. However the analysis requires at least five specimens of differing radii in order to establish one

stress strain curve.

An alternative method has therefore been developed in the present work which uses raw torque twist data to evaluate the stress as a function of strain. The strain to peak arises from the operation of thermally activated mechanisms and therefore the controlling equation is likely to be in the form of equation 1.5. the general hot working equation

The absolute values of the constants ΔH, α, n and A may either be a function of the strain to peak or similar to those at peak. The strain to peak will be dependent upon both the strain rate and temperature for each alloy therefore to correlate data at equivalent values of strain, an homologous strain can be defined such that

$$\varepsilon_H = \frac{\varepsilon}{\varepsilon_p} \qquad 2.3.$$

where ε_p is the strain to peak and ε the relevant value of strain. At equivalent values of ε_H the deformation mechanism might be expected to be consistent. Assuming that

$$\frac{\varepsilon}{\varepsilon_p} = \frac{\Theta}{\Theta_p} \qquad 2.4$$

it is then possible to digitize the torque twist curves in terms of homologous strain.

Minimization of the torque twist rate temperature data at each ε_H provides a set of hot working constants that are strain dependent. The use of these constants and equation 2.5

below enables a value of the flow stress to be calculated at each interval of strain in the temperature rise model.

$$\sigma = \frac{1}{\alpha} \ln \left[\left(Z/A \right)^{1/n} + \sqrt{\left(Z/A \right)^{2/n} + 1} \right] \qquad 2.5.$$

The original program TORTEMP from reference[122] has been modified to read in the separate sets of constants and evaluate the stress to the required strain. A listing of the new programme THTEMP is shown in appendix VI . At each interval of strain the program evaluates a volume average temperature using the equation defined by Wright[122]

$$T_V = \frac{1}{\pi R^2 L} \int_0^R T_r V_r dr \qquad 2.6$$

where Tr is the temperature of volume Vr at radius r. This allows for the fact that a greater volume of material is at a higher temperature in the outer elements. A value of stress at each strain increment is therefore calculated with reference to the actual temperature at that strain and not the initial temperature. The final volume average temperatures are used in a further minimization at each ε_H, the new set of constants being used to evaluate a new temperature rise, the minimization being repeated till no further change in the constants is recorded. Repeating the minimization enables a more realistic evaluation of the temperature rise, since the first set of constants are based upon the initial temperatures and are therefore likely to give temperature rises no better than the original stress-strain rate analysis.

A futher development in the above analysis would be to define the stress dependency on strain in one equation-i.e.

$$\sigma = f\ (\alpha(\varepsilon),\ A(\varepsilon),\ n(\varepsilon),\ \Delta H(\varepsilon))$$

Such a relationship could be used in any deformation process where the strain associated with steady state is not achieved. Instances of this can be found in e.g. rolling for material adjacent to the roll gap or in extrusion for elements of the material adjacent to the shear zones or near the back of the deformation zone. The main problem here is that the present analysis uses a value of homologous strain and not the actual strain. Therefore for such an equation to be of any practical use, the relationship between ε_p and strain rate and temperature must first be established.

Although numerous equations have been reported[75] to predict the stress/strain behaviour, nearly all are limited to the specific temperatures and strain rates considered. Alternative constitutive equations have been proposed by several workers[75], which claim to be able to predict the stress/strain behaviour for any combination of strain rate and temperature within the experimental range. However the variety of empirical equations proposed indicates that such equations are only relevant to the precise conditions and testing techniques used and a more general relationship which includes the strain dependency of the flow stress at different temperatures and strain rates has yet to be established.

The temperature rise analysis described above represents a quicker and less tedious route for estimating the temperature rise during testing, and provides a set of hot working constants

at constant values of homologous strain up to and including the steady state.

2.2.2. Evaluation of the Hot Working Constants

Two methods have been utilized in the present work to evaluate the hot working constants ΔH, α , n and A in equation 1.5. The first method is used in conjunction with the temperature rise analysis described in the previous section and is based on a mathematical minimization technique used to establish the least best squares fit to the equation. The second technique is based on a simpler graphical analysis and makes no allowance for a temperature change during testing.

The conversion of shear stresses and strains from torsion into equivalent tensile stresses and strains is accomplished using Von Mises criterion:-

$$\begin{aligned} \sigma &= \sqrt{3}\ \tau \\ \varepsilon &= \frac{\gamma}{\sqrt{3}} \\ \dot{\varepsilon} &= \frac{\dot{\gamma}}{\sqrt{3}} \end{aligned} \qquad 2.7$$

2.2.2.1. Mathematical Minimization

The general hot working equation described in section 1.4.1 may be written as:-

$$Z = \dot{\varepsilon} \exp \frac{\Delta H}{RT} = A\ [\ \mathrm{Sinh}\ (\alpha\sigma)]^n \qquad 2.8$$

which can be re-arranged to give:-

$$\alpha\sigma = \mathrm{Sinh}^{-1}\ [Z/A]^{1/n} \qquad 2.9.$$

The sinh term can be expanded using:-

$$\text{Sinh}^{-1}\ x = \ln[x + (1 + x^2)^{\frac{1}{2}}] \qquad 2.10$$

To give:-

$$\dot{\sigma} = \frac{1}{\alpha} \ln \left[\left(Z/A\right)^{1/n} \left[\left(Z/A\right)^{2/n} + 1 \right]^{\frac{1}{2}} \right] \qquad 2.11$$

The surface strain rate during testing can be expressed in terms of the equivalent strain rate using :-

$$\dot{\varepsilon} = \frac{2\pi r \dot{\Theta}}{\sqrt{3L}} \qquad 2.12$$

where r is the specimen gauge radius, $\dot{\Theta}$ is the twist rate in revolutions per second and L the specimen length.

The torque generated during testing may be related to the flow stress in a simple manner through:-

$$M = \frac{2\pi}{\sqrt{3}} \int_{r_1}^{r_2} \sigma \dot{r}^2 \ dr \qquad 2.13$$

where M is the torque and r_1 and r_2 the inner and outer radii of the gauge length respectively. (r = 0 for a solid specimen).

Expanding the Z parameter in equation 2.11 and substituting for the flow stress and strain rate using equations 2.11 and 2.12, equation 2.13 can be re-written:-

$$M = \frac{2\pi}{\alpha\sqrt{3}} \int_{r_1}^{r_2} \ln \left[\left(\frac{2\pi r \dot{\Theta} \exp \Delta H/RT}{\sqrt{3}\ L\ A} \right)^{1/n} + \left[\left(\frac{2\pi r \dot{\Theta} \exp \Delta H/RT}{\sqrt{3}\ L\ A} \right)^{2/n} + 1 \right]^{\frac{1}{2}} \right] r^2 \ dr \qquad 2.14$$

which now relates the torque, twist rate and temperature through the four constants ΔH, α , n and A.

The solution to equation 2.14 is obtained by first defining a parameter C such that

$$C = \left[\frac{2\pi \dot{\Theta} \exp \Delta H/RT}{\sqrt{3}\ L\ A} \right]^{1/n} \qquad 2.15$$

which allows equation 2.14 to be re-written:-

$$M = \frac{2\pi}{\alpha\sqrt{3}} \int_{r_1}^{r_2} [\ln (Cr^{1/n}) + \ln (1 + (Cr^{1/n})^{-2})]^{\frac{1}{2}}]\ r^2\ dr \qquad 2.16$$

Equation 2.16 may be re-written as the sum of three integrals:-

$$M = \frac{2\pi}{\alpha\sqrt{3}} (J_1 + J_2 + J_3) \qquad 2.17$$

where

$$J_1 = \ln C \int_{r}^{r_2} r^2\ dr$$

$$J_2 = \frac{1}{n} \int_{r_1}^{r_2} r^2 r^{2^{-1}} \ln r\ dr \qquad 2.18$$

$$J_3 = \int_{r_1}^{r_2} r^2 \ln [1 + (1 + (Cr^{1/n})^{-2}]\ dr$$

The solution to the three integrals can be found in references [27,29]. A computer programme has been written to perform the calculations and is listed in the above references. The programme reads in the complete matrix of torque, twist rate and temperature data and iterates the values of ΔH, α, n and A to obtain the least squares regression between the calculated and experimental values. Initial estimates of ΔH, n and A were obtained from the following graphical analysis.

2.2.2.2. Graphical Analysis

At high stress levels the relationship between strain rate and stress may be written as:-

$$\dot{\varepsilon} = A_2 \exp(\beta\sigma) \qquad 2.20$$

where β is a temperature independent constant. Also at high stress levels ($\alpha\sigma > 1.2$) and constant temperature equation 2.8 reduces to:-

$$\dot{\varepsilon} = A \, \text{Sinh} (\alpha\sigma)^n \qquad 2.21$$

Expanding the Sinh term gives

$$\dot{\varepsilon} = \frac{A}{2^n} \exp(n\alpha\sigma) \qquad 2.22$$

At low stress levels:-

$$\dot{\varepsilon} = A_1 \sigma^{n'} \quad \text{i.e. } (\alpha\sigma < 0.8) \qquad 2.23$$

where n' is also assumed to be temperature independent .

comparing equations 2.20 and 2.22 gives:-

$$\beta = n\alpha \qquad 2.24$$

given that[23] $n \simeq n'$

$$\alpha = \beta/n' \qquad 2.25$$

where β is obtained from plotting $\ln \dot{\varepsilon}$ vs σ at high stress levels i.e. low temperatures, n' by plotting $\ln \dot{\varepsilon}$ vs $\ln\sigma$ at low stress levels i.e. high temperatures.

The analysis is however limited to the use of equivalent stress/strain rate data. This can be overcome by using the same substitutions used in the minimization analysis shown in equations

2.12 and 2.13 for the strain rate and stress.

The power relationship can be re-written as:-

$$\sigma = \left[\frac{\dot{\varepsilon}}{A_1}\right]^{1/n'} \qquad 2.26$$

substituting for the stress and strain rate using equation 2.13 and 2.12 gives:-

$$M = \frac{2\pi}{\sqrt{3}} \int_{r_1}^{r_2} \left[\frac{2\pi r \dot{\Theta}}{\sqrt{3}\, L\, A_1}\right]^{1/n'} r^2\, dr \qquad 2.27$$

which can be integrated to give:-

$$M = \frac{2\pi}{\sqrt{3}} \left(\frac{2\pi \dot{\Theta}}{\sqrt{3}\, A_1 l}\right)^{1/n'} \cdot \left[\left(\frac{n'}{n'+1}\right)\left(r_1^{(3n'+1)/n'} + r_2^{(3n'+1)/2}\right)\right] \qquad 2.28$$

such that for a solid specimen ln M vs ln $\dot{\Theta}$ gives:-

$$\text{slope} = {}^{1}/_{n'}$$

$$\text{intercept} = \frac{\ln 2\pi}{\sqrt{3}} + \frac{1}{n'}\left[\ln\left(\frac{2\pi}{\sqrt{3}\, lA_1}\right)\right] + \ln\left(\frac{n'}{3n'+1}\right) + \left(\frac{3n'+1}{n'}\right) \ln r_2$$

A similar analysis for the exponential equation 2.20 gives:-

$$M = \frac{2\pi}{\beta\sqrt{3}}\left[\left(\frac{r_2^3 - r_1^3}{3}\right) \cdot \left(\frac{4\pi \dot{\Theta}}{3\sqrt{3} LA_1}\right) + \frac{r_2^3}{3}\left(\ln r_2 - {}^{1}/_{3}\right) - \frac{r_1^3}{3}\left(\ln r_1 - {}^{1}/_{3}\right)\right] \qquad 2.29$$

for a solid specimen M vs ln $\dot{\Theta}$ gives:-

$$\text{slope} = \frac{2\pi}{3\sqrt{3}\,\beta} \cdot r_2^3$$

$$\text{intercept} = \frac{2\pi}{\sqrt{3}\beta}\left[\frac{r_2^3}{3} \cdot \ln\left(\frac{2\pi}{\sqrt{3} LA_1}\right) + \frac{r_2^3}{3}\left(\ln r_2 - {}^{1}/_{3}\right)\right]$$

Therefore values of A_1, β, A_2 and n' can now be derived from raw torque-twist data.

To find the activation energy equation 2.8 is re-arranged to give:-

$$\ln \dot{\varepsilon} = n \ln [A \sinh (\alpha\sigma)] - \frac{\Delta H}{RT} \qquad 2.30$$

at constant flow stress:-

$$-R \frac{\partial \ln \dot{\varepsilon}}{\partial {}^{1}/_{T}} = \Delta H \qquad 2.40$$

This may be expanded to give[23]:-

$$R \left[\frac{\partial \ln \dot{\varepsilon}}{\ln \sinh (\alpha\sigma)}\right]_T \cdot \left[\frac{\ln \sinh (\alpha\sigma)}{\partial {}^{1}/_{T}}\right]_{\dot{\varepsilon}} = \Delta H \qquad 2.41$$

Substituting for stress and strain rate using equations 2.12 and 2.13 plots of:-

$$\ln \left[\frac{2\pi r \dot{\theta}}{\sqrt{3}\, L}\right] \text{ vs } \ln \sinh \left[\frac{\alpha 3M\sqrt{3}}{2\pi r^3}\right] \text{ at constant temperature}$$

and

$$\ln \sinh \left[\frac{\alpha 3M\sqrt{3}}{2\pi r^3}\right] \text{ vs } {}^{1}/_{T} \text{ at constant strain rate.}$$

enables values of ΔH to be obtained as a function of temperature at constant strain rate or vice-versa.

Finally values of A and n can be obtained by using equation 2.8 in the form:-

$$Z = A [\sinh (\alpha\sigma)]^n$$

taking natural logarithms:-

$$\ln Z = \ln A + n \ln \sinh (\alpha\sigma) \qquad 2.42$$

Substituting for stress and strain rate using equations 2.12 and 2.13, and using the values of α and ΔH already obtained, A and n can be derived from a plot of

$$\ln \left[\left(\frac{2\pi r \dot{\Theta}}{\sqrt{3}\ 1}\right)\right] \exp \frac{\Delta H}{RT} \quad \text{vs} \quad \ln \operatorname{Sinh} \left(\frac{\alpha\, 3M\sqrt{3}}{2\pi r^3}\right)$$

where intercept = ln A and slope = n.

A computer programme has been written to evaluate the values of ΔH, α, n and A using the raw torque-twist data and is listed in appendix VI.

2.3. Extrusion Analysis

2.3.1. Temperature Rise at Peak Load

A characteristic of both direct and indirect extrusion is the more or less linear rise in load to a peak value at the start of extrusion. Since this represents a net energy input and hence heat into the system, an estimate of the temperature at peak load must be made. Assuming that the rise in load is linear for all extrusions, the work done can be approximated by:-

$$\text{Work done} = \frac{Lp \times dp}{2} \qquad 2.43$$

where Lp is the peak load and dp the ram displacement to peak. As the peak load is reached in a relatively short time, heat losses will be minimal so that the approximate heat gain may be written as:

$$V_B\ \rho_{AL}\ C_{AL}\ \Delta T$$

giving

$$\Delta T = \frac{Lp\ \ dp}{2V_B \rho_{AL} C_{AL}} \qquad 2.44$$

For a maximum load of 5MN, the adiabatic temperature rise is approximately 30 deg C., the heat losses to the container therefore are likely to be negligible in the short time required to develop the peak load. In the present work this heat loss is further reduced by container temperatures of 50 deg. C below the billet temperature so that the assumption of an adiabatic temperature rise may be justified.

2.3.2. Temperature Rise During Extrusion

The temperature rise during extrusion has been estimated using an integral profile model first developed by Sheppard and Wood[128] and later modified for use with indirect extrusion[29]. The model places two control volumes over the billet, one around the deformation zone which is assumed to be a cone and the other around the undeformed billet. The heat leaving the two control volumes is equated to the heat generated in the deformation zone, the size of which is determined from the single triangle upper bound solutions[27-29]. It is assumed that 90%[125] of the work is converted into heat and that conduction of heat between the two control volumes does not occur i.e. there are no heat losses due to back conduction as shown by Tanner and Johnson[7].

The only modification to the model described by Paterson[29] has been made to the temperature differential term allowing for heat loss to the tooling during extrusion, since the original model assumes a constant liner temperature of 300 deg C. as opposed to the variable temperature used in the present work. The modified programme EXTRUDE is shown listed in appendix VI.

2.3.3. Strain Rate Evaluation

During direct and indirect extrusion the values of strain rate will differ from point to point throughout the deformation zone. It is therefore necessary to define a mean value representative of the extrusion conditions.

In the present work a mean strain rate for direct and indirect extrusion has been derived from single triangle axisymmetric upper bound solutions[28,29,129]. Using a mesh size of 10 x 5 within the deforming triangle, the mean strain rate can be calculated by piecewise integration and time averaging of the strain rates acting along the five streamlines, coupled with area averaging over the 10 areas within the deformation zone. For direct extrusion the mean strain rate is comparable to the modified Felthams strain rate evaluated by Tutcher and Sheppard[100], whilst the indirect strain rate is higher at equivalent extrusion ratios and ram speeds due to the smaller deformation zone size involved.

2.3.4. Evaluation of the Billet Container Friction

During direct extrusion the force required to overcome the friction between the billet and container results in a marked increase in the overall pressure to extrude. The friction may be defined in one of two ways:-

1) the friction coefficient μ where:

$$\tau = \mu P \qquad 2.45$$

τ is the tangential stress acting opposite to the motion and P is the pressure between the bodies[1].

ii) a constant friction factor m; where

$$\tau = m \left(\frac{\sigma_o}{\sqrt{3}} \right) \qquad 2.46$$

σ_o is the flow stress of the plastic material and ranges in value $0 < m < 1$.

The coefficient of friction μ can be experimentally evaluated by one of 2 methods:

i) Measuring the pressure to extrude two billets of different lengths L_1 and L_2 under otherwise identical extrusion conditions, where μ is given by[111]:

$$\mu = \frac{D_B}{4\,(L_1 - L_2)} \ln \left(\frac{P_1}{P_2} \right) \qquad 2.47$$

where D_B is the billet diameter.

ii) The rate of change of pressure with billet length can be used to evaluate μ using the relationship[1,79]:-

$$\mu = \frac{D_B}{4P} \frac{dP}{dx} \qquad 2.48$$

where P is the ram pressure and x the axial distance along the container.

The friction factor m can be calculated using the following relationship derived from the single triangle upper bound analysis[28,29]:-

$$m = \frac{\sqrt{3}\ (P_1 - P_2)\ R_B}{2\,\sigma\,(L_1 - L_2)} \qquad 2.49$$

where R_B is the billet radius. The accuracy of the friction factor m is largely dependent upon the value of stress σ chosen to represent the material billet at the container interface, where theoretically the strain rate is zero. A mean strain rate derived from the adjacent layers must therefore be used to determine a value of flow stress, so that m can only be considered as an approximate guide to the friction conditions.

CHAPTER THREE

EXPERIMENTAL

3.1 INTRODUCTION

The experimental procedures used to investigate the hot working characteristics, microstructural variations and mechanical properties of the aluminium-copper alloys are briefly outlined in the following section. The techniques are common to all the alloys considered unless otherwise stated.

3.2 THE EXTRUSION PRESS

The extrusion press used in the experimental work was a 5MN fast action ENEFCO hydraulic press mounted vertically over an accessible pit (depth 3 metres). The press tooling was supported by a backing plate and the container could be raised or lowered hydraulically. The press layout is shown in Plate I with the operating controls, load indicating dial on the right, whilst the induction heater can be seen on the left.

The container dimensions allowed the extrusion of a maximum billet length of 158 mm and the different size container liners were available for the extrusion of 57 or 75 mm diameter billets. In order to minimize the effect of friction on the load, the length of the billet was usually 95mm for 75mm diameter.

An auxiliary pump enabled a fast approach by the ram prior to the commencement of extrusion. This reduced the time for heat loss from the billet while the ram was being

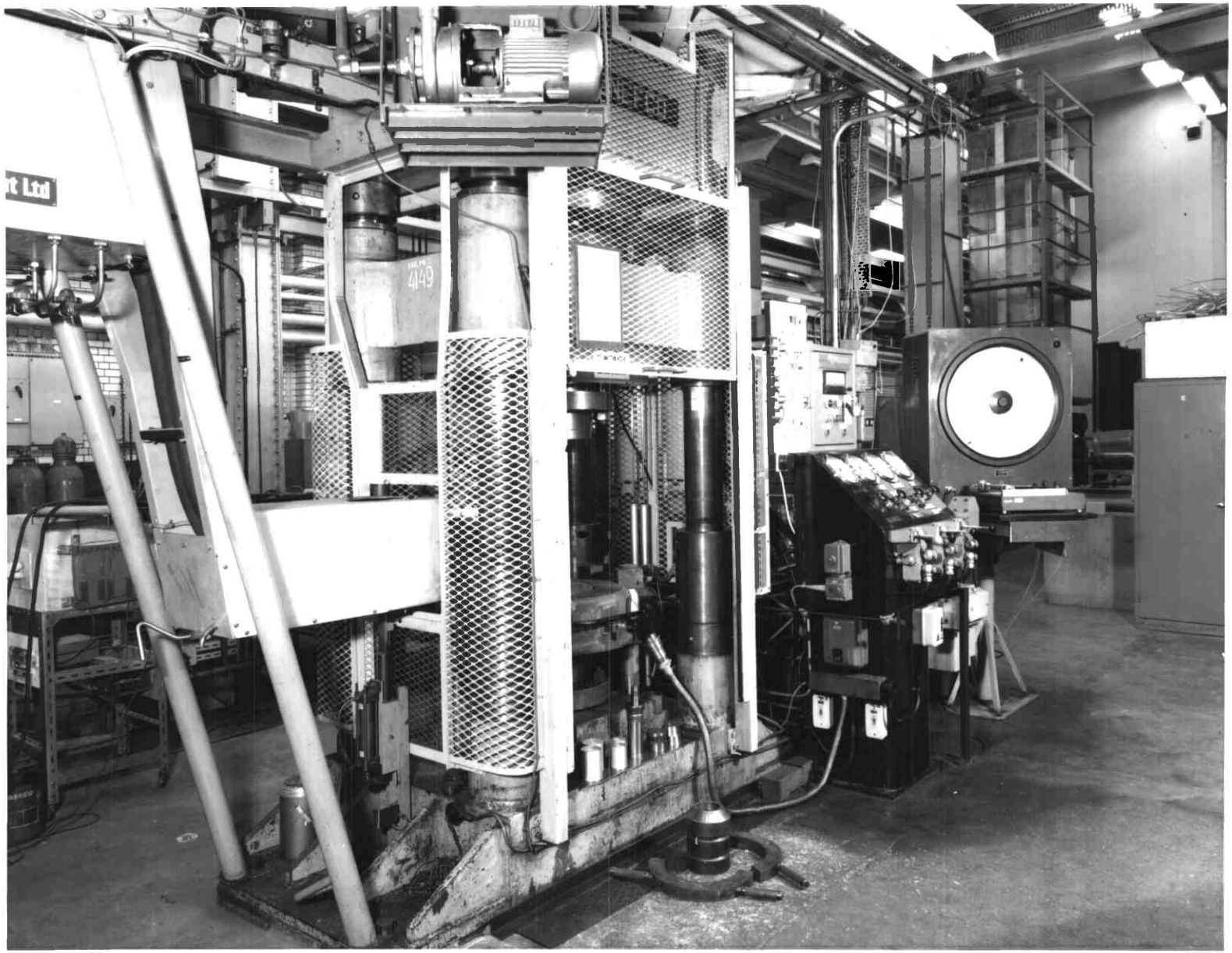


Plate I. General Layout of the Extrusion Press

lowered. When the ram hit the pressure pad and the load exceeded 0.2 MN the pump was automatically bypassed and the ram moved at the pre-set speed during extrusion. The ram speed was controlled by adjusting the oil flow from the hydraulic pumps to give a range of speeds varying from 2 mm/sec to 13 mm/sec. Higher speeds of the order of 100 mm/sec to 600 mm/sec could be obtained by accumulator drive, that is by discharging nitrogen filled bottles to increase the rate of delivery of oil to the main ram.

3.2.1. CONTAINER HEATING

The container assembly was heated by two separate sets of inconel heating elements positioned in the container holder casting (8 elements) and the inner container liner (12 elements) giving a combined power rating of 16 kilowats. The temperature of each container was controlled by two Eurotherms attached to thermocouples brazed onto each element. The temperature profile of the liner was measured by attaching thermocouples at various positions on the surface of the liner and was found to vary within + 5 deg.C of the set temperature. The liner temperature was set 50 deg.C below the billet temperature for direct and indirect extrusion. The maximum temperature is limited by the tempering temperature of the steel, which is 530 deg.C.

3.2.2. BILLET PREHEAT

For direct extrusion of the 1,2,3 and 5% Cu alloys billets were preheated in a Banyard Metalheat induction furnace attached to the press. The furnace operated at mains frequency, the design enabling 75mm diameter billets of lengths up to 150mm to be heated to temperatures of 600 deg.C at a rate of $\sim$125 deg.C/min. depending on the billet length. The billet temperature was continually monitored by a thermocouple placed in a 15mm deep hole in

the centre of the billet which also acted as the temperature controller for the induction heater. The induction heater was suspended from two rails and could be moved over the container by means of a pneumatic system operated by controls on the main press control panel. When the heater was above the container the hot billet was transferred manually by removing a rod that supported the billet in the coil. Extrusion could then be started as soon as the heater had returned to its initial position. The billets were allowed to soak for twenty minutes prior to extrusion to remove the possibility of any temperature gradients within the billet.

The tooling for indirect extrusion prevented the use of the induction heater. In order to keep conditions for direct and indirect extrusion as similar as possible, all the billets for the 4% Cu 2014 alloy were preheated in an air circulating furnace adjacent to the press and transferred manually to the container immediately prior to extrusion. Each billet was drilled with a single central hole to monitor the temperature. With the furnace at temperature a heating rate of $\sim$35 deg.C/min. could be achieved depending on the temperature set. As for induction heating, billets were soaked for twenty minutes.

Both furnaces were calibrated using a billet with five 15mm deep holes drilled axially across the radius from the centre, with the five Ni/Cr thermocouples connected to a multiple channel digital thermometer.

Heat losses during transfer from the furnace to the press were allowed for by noting the transfer time and calculating the temperature drop from the cooling curves shown in appendix V

3.2.3. EXTRUSION DATA RECORDING

The data for all the extrusions was recorded on a Datalab DL2800 transient recorder consisting of a control module and four memory modules. This recorder which was designed to capture single-shot and low repetition events and present them for continuous oscilloscope display, is also ideal for high speed data acquisition. The recorder can sample at very fast rates, store the data, and then output it at an acceptable rate in analogue or digital form.

The control module contains the timebase, delay control and output circuitry and is independent of the number of memory modules used. It permits recording cycles in single, delayed or continuous modes with manual or automatic triggers. The sampling rate varies from 0.5 ms to 200 ms per sample and records each channel simultaneously. The data for each channel is stored in the corresponding memory modules at 4096 x 10-bit words. A memory module consists of a pre-amplifier, a track and hold circuit, an analogue-to-digital converter and a digital memory. The pre-amplifier has switchable and continuously variable gain to allow for a wider range of input signals, and a d.c. offset control to bring biased inputs within the rate of the instrument.

For the recording of the extrusion data the transient recorder was operated in the single mode with a manual trigger. The sample rate was generally 2 ms or 5 ms which gave recording times of 8 or 20 seconds respectively.

The load was measured by a Mayes load cell, situated directly above the ram, the output of which increased from 1.5 mV to 500 mV as the actual load and the indicated load rose from 0-500 Tons. These figures were confirmed by a calibration done by the National Physical Laboratory in

March 1980. The output was recorded directly by the transient recorder with an input setting of 2 V full scale and an offset value of 5.0 (centre of the scale).

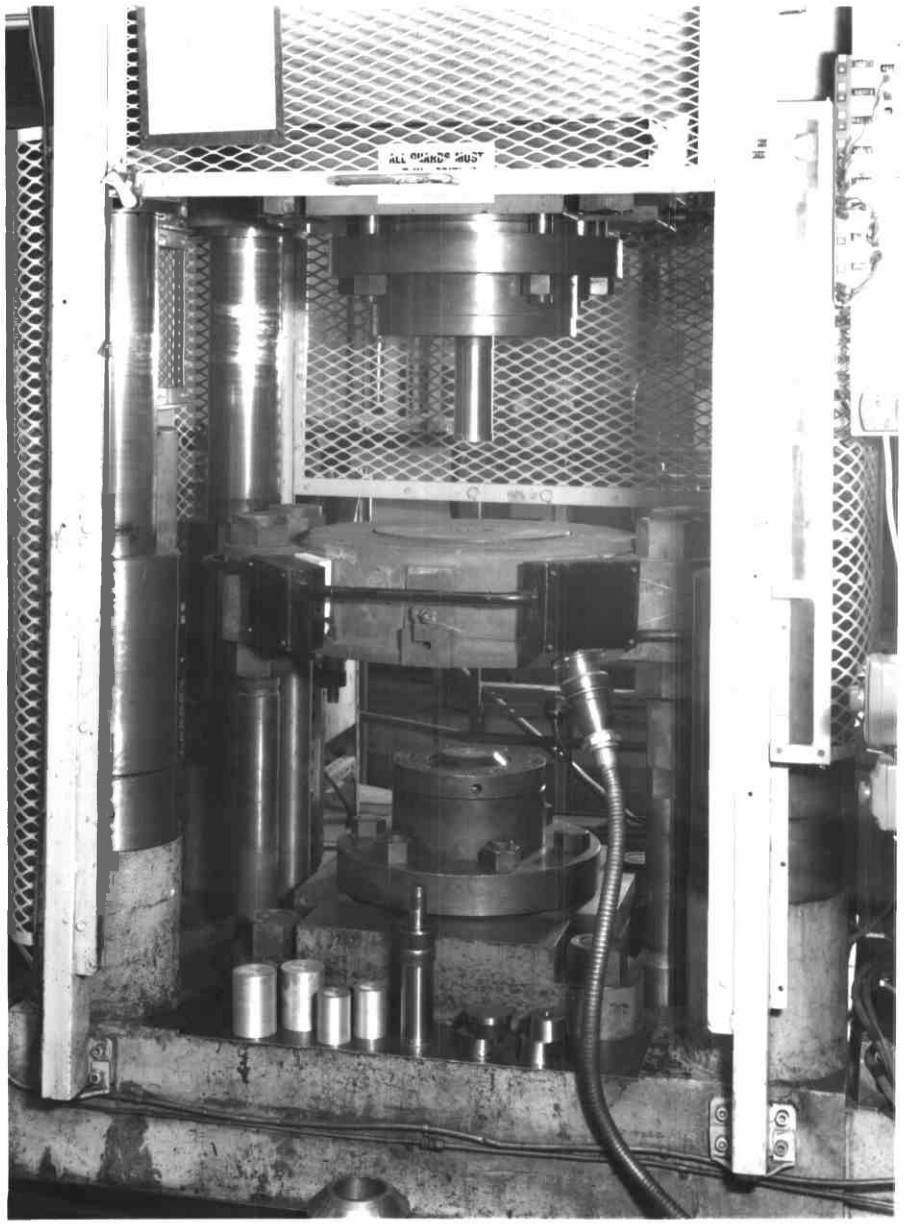
The ram displacement was measured by a rectilinear potentiometer with a 0.6m stroke which was fixed between the main ram and the base of the press. The output from the displacement transducer varied by 1.75 V per 100mm movement of the ram and was recorded by the transient recorder with an input setting of 10 V full scale. The offset values used were 2.0 for direct extrusion and 3.5 for indirect extrusion.

The hydraulic pressure of the press was measured with a pressure transducer situated at the inlet to the main cylinder. The output from this transducer increased from 0-30 mV as the hydraulic pressure increased from 0-3500 p.s.i. (0-24 MN/sq.m). The diameter of the main cylinder was 22.75" which gave pressure recording ranges of 0-1300 MN/sq.m for a 75mm ram and 0-2265 MN/sq.m for a 57mm ram. This output was recorded by the transient with an input setting of 0.1 V full scale and an offset value of 5.0.

The first 4000 words of each memory channel were individually displayed in analogue form on an oscilloscope. For a more permanent record each channel was plotted on an X-Y recorder which was linked to the transient.

3.2.4. DIRECT EXTRUSION TOOLING

Plate IIa) shows the direct extrusion tooling for 75mm diameter billets. The ram, container and die assembly are in the background with 95 x 75mm dia. billets, pressure pad, scraper pad and dies in the foreground. Also shown are 72 x 57mm dia. billets and ram.



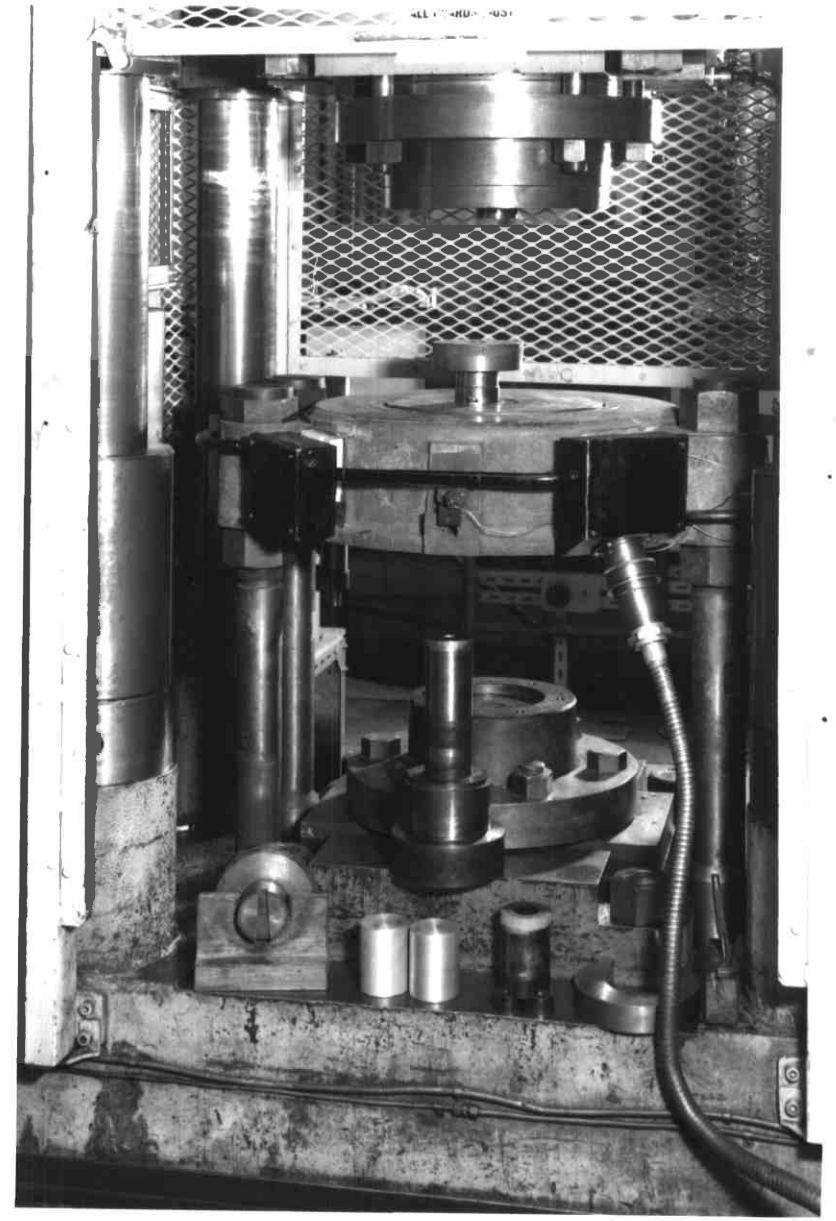


Plate II. a) Direct Tooling

b) Indirect Tooling

The ram, container liner, dies, pressure and scraper pads were all machined from KEA 5% Cr-V steel.

Changing the die was effected by taking off the retaining ring, lifting out the die assembly and removing the die backer and die. The dies used for direct extrusion were for rod shaped extrudes with reduction ratios of 10, 20, 30, 40, 50, 80, 100:1 and 150:1, the dimensions of which have been described elsewhere.

3.2.5. INDIRECT EXTRUSION TOOLING

The indirect tooling is shown in Plate IIb). The ram and pressure pad have been replaced by a dummy block with a tapered notch for the removal of the discard after extrusion. This is shown in the left foreground in the discard removal postion. The die assembly is located at the top of a mandrel, the dimensions of which allow the container to pass over it. The mandrel and die assembly are shown in the centre of the plate, slightly out of position. A spare die holder, die backer and die are shown in the foreground with two 95 x 75mm dia. billets. The horseshoe piece on the right is to facilitate the removal of the discard from the container. All components were machined from KEA 145 5% Cr-V steel.

Changing the die is effected by lifting the container, unscrewing the die holder and removing the die backer and die. The dies used for indirect extrusion were also for rod shaped extrudes with reduction ratios of 20, 30 and 40:1.

The dimensional arrangement of the tooling for indirect extrusion is such that only 75mm dia. extrusions are possible with a minimum reduction ratio of 20:1 and a maximum billet length of 120mm. Detailed drawings of the tooling can be found in references 124, 129.

3.2.6. WATER QUENCH

In order that the structure of the material should reflect that due to the hot working process the extruded product was passed through a water quench immediately upon exit from the die assembly.

The quench consisted of two concentric cylinders, the inner one containing holes of 1.2mm dia. drilled radially, 532 of which were contained in the initial 26cm, the remainder in groups of 28 holes placed at 10cm intervals along the 1.37m length. Water was delivered at approximately 60 gallons/minute by a centrifugal pump.

3.2.7. EXPERIMENTAL PROCEDURE

Certain procedures were common to direct and indirect extrusion to ensure the tooling was at the optimum temperature . The containers were left at the required temperature for at least one hour before extrusion to allow the die and bolster to attain a similar temperature. The pressure pad, or the dummy block used in the indirect extrusion, were preheated on the container for at least 20 minutes prior to extrusion. No lubrication was used in either direct or indirect extrusion.

3.2.8. DIRECT EXTRUSION

At the start of the extrusion cycle the container was hydraulically lowered onto the die assembly to obtain a pressure seal and two semi-circular rings were placed on top of the container to prevent any damage to the main ram. Upon transferring the preheated billet to the container, the pressure pad was dropped onto the billet and the water quench, recording instruments and the fast ram approach were

then initiated. Extrusion was continued at the predetermined speed until the main ram touched the rings whereupon the pumps were reversed and the ram raised. In order to assess the heat losses from the billet the extrusion cycle was timed from when the furnace door was opened until the ram hit the pressure pad.

The container was then raised and the extrude cut with a hacksaw, before being punched through the die into the pit below. The discard (average length of 12.5mm) was removed by placing three circular rings between the bottom of the container and the die assembly, and using the ram to push a tight fitting scraper pad through the container. This also had the effect of cleaning the liner to produce similar starting conditions for each extrusion.

The overall procedure is the same for the induction heated and furnace heated billets.

3.2.9. INDIRECT EXTRUSION

The procedure for indirect extrusion was essentially the same except that the 75mm ram was removed from the main ram and immediately prior to extrusion the container was raised such that the die assembly at the top of the mandrel was positioned in the bottom 50mm of the container. Upon transferring the preheated billet the dummy block was placed in the container and the extrusion cycle was initiated as for direct extrusion. When the main ram hit the dummy block both the billet and container were pushed down onto the mandrel and moved simultaneously at the predetermined speed during extrusion.

At the end of extrusion, after the main ram had been raised, the container was hydraulically lowered to break the container/billet linkage. The container was then raised so

that the dummy block lifted off the die face, enabling the extrude to be cut. Following this the container was again lowered and the discard, the length of which was approximately 14mm including a diametrical allowance of 1.8mm for the notch, was separated from the dummy block by punching it at the tapered notch. The ease of this operation was improved by lubricating the face of the dummy block with DAG 580 prior to extrusion. The container was then raised and lowered again to clean the container liner.

It should be noted that the removal of the discard relies entirely on the hydraulic force exerted by the container. Since this is only 0.5 MN for the downward stroke and 0.75 MN for the upward stroke, large discards of the stronger alloys can remain stuck in the container. The only method of removal is then to heat the containers to high enough temperature to facilitate the removal of the 'sticker'.

3.3. MATERIALS

The material was supplied by Alcan International Laboratories, Banbury, in the form of semi-continuously cast logs of 86mm diameter. The quoted compositions of the various casts used are given in Table 3.1.

The as cast logs were homogenized at 500 deg.C for 24 hours and furnace cooled. The homogenized material was turned to a diameter of 73.5mm, which allowed for expansion on preheating, and cut into billets of the required length.

ALLOY %Cu	CAST No	Al	Cu	Fe	Mg	Mn	Si	Ti	Zn	B ppm
1	D679/681	REM	0.90	0.20	0.50	0.71	0.82	0.014	0.02	7
2	D935	REM	1.97	0.15	0.40	0.70	0.79	0.011	0.02	18
3	D936	REM	2.88	0.18	0.42	0.70	0.81	0.014	0.02	22
4	D677	REM	3.90	0.20	0.47	0.78	0.78	0.013	0.02	10
5	D680/683	REM	4.8	0.21	0.45	0.75	0.86	0.012	0.02	12
4	D685	REM	3.8	0.20	0.001	0.01	0.07	0.013	0.02	14

TABLE 3.1 Alloy Compositions in Weight Percent

3.4. PARTIALLY EXTRUDED BILLETS

In order to examine the flow patterns during steady state direct and indirect extrusion billets were extruded to half their length, and the discards quenched in water. The nature of the extrusion process makes a fast quench almost impossible, a quench delay of ~ 60 seconds was common. The billets were sectioned along the longitudinal axis using a Metaserv cut off wheel, which was continuously lubricated to avoid excessive heat generation. The face of one half of the billet was ground and polished in a similar manner to that of the extrudes and overetched in a modified Kellers reagant to reveal the grain structure and flow lines.

The remaining half had a slice 3mm thick removed parellel to the section face using the cut off wheel, and specimens were taken from the desired positions using a fine piercing saw. Disc specimens were prepared for transmission electron microscopy as described in section 3.6.5.

3.5. HEAT TREATMENT OF EXTRUDES

The typical heat treatment given to extrudes of the 2014 alloy was a solution treatment at 500 deg.C for 1/2 hour in an air circulating furnace, followed by water quenching to room temperature and subsequent age hardening in an air circulating oven. Hardening versus time characteristics were determined for solution treated and press quenched extrudes by artificially ageing at temperatures of 120 deg.C, 160 deg.C and 180 deg.C for up to 1000 hours. A standard treatment of 18 hours at 160 deg.C was adopted for most applications. The classification of the various heat treatments is given in Table 3.2.

DESCRIPTION OF HEAT TREATMENTS	TEMPER DESIGNATION	
	A.A.	B.S.
- As-extruded, quenched	F	M
- As-extruded, quenched, natural age	T1	
- Solution-treated, quenched, natural age	T4	TB
- As-extruded, quenched, artificial age	T5	TE
- Solution-treated, quenched, artificial age	T6	TF

B.S. : British Standards B.S. 1470-1477 and 1490
A.A. : Aluminium Association, U.S.A.

TABLE 3.2. Classification of Heat Treatments Used

3.6. EXAMINATION OF EXTRUDES

Specimens for mechanical testing, for heat treating and for optical and electron microscopy were cut from a position of one third along the extrude length in order to ensure steady state conditions. Specimens were also taken from positions along the length of given extrudes to determine the change in structure.

3.6.1. HARDNESS TESTS

Hardness tests were carried out on a number of torsion specimens and extrudes in the as-extruded, solution treated, naturally aged and artificially aged conditions. Transverse specimens cut from the extrudes were tested at the edge, mid-radius and centre using a standard Vickers Hardness machine fitted with a 10 Kg weight. Microhardness results

were obtained using a 50 gm weight on a Reichert microhardness indenter attached to a Reichert optical microscope.

3.6.2. TENSILE TESTS

Standard No. 12 Hounsfield specimens were machined from the extrudes and tested on an Instron Universal Testing machine. The crosshead speed remained constant during each test and the approximate strain rate was calculated using the initial gauge length. Tests were conducted at room temperature with a strain rate of 5.2×10^{-3} sec^{-1}. Tests were performed on as-extruded, naturally aged and artificially aged extrudes.

3.6.3. FRACTURE TESTS

Fracture toughness tests were carried out on the 2014 alloy extrudes in the artificially aged condition. This was done using the crack opening displacement method (COD) specified in British Standard B.S. 5762:1979. Specimens of dimensions (10 x 10 x 52) mm with a 2.5mm deep notch were machined from 16.77mm diameter extrudes, and 1mm thick knife edges were glued adjacent to the notch prior to testing. A fatigue crack of approximately 2.5mm was developed in each specimen, the length being determined, as specified, subsequent to testing. The testing was done on an Instron Universal Testing machine using a three-point bending system. The load and the crack displacement, which was measured with a clip gauge specified in B.S. 5762:1979, were output directly to an X-Y recorder. The maximum applied force and the plastic component of the clip gauge opening displacement were used in the analysis described in B.S. 5762:1979 to obtain values of the critical crack opening displacement from which fracture toughness can be estimated.

3.6.4. OPTICAL MICROSCOPY

Both longitudinal and transverse sections were cut from the extrude, heat treated if required, and prepared for optical examination. The sections were mounted in Metaserv S.W., a slow hardening resin which has the advantage of setting without any temperature rise. The mounted specimens were ground on 200 and 800 grade silicon carbide papers and polished using 6 μm and 1 μm diamond paste. Final polishing was achieved using 0.3. um alumina powder.

After much trial and error with caustic, nitrate and nitric acids etches it was found that a modified Kellers Reagent recommended for 24S alloys by Alcan was suitable for all the alloys:-

$$2ml HF \quad 3ml HCl \quad 5ml HNO_3 \quad 190ml H_2O$$

The etching time depended on the state of the extrude i.e. as extruded or heat treated and on the Cu content, varying from 30-40 secs for the 1% Cu alloy to 10-15 secs for the 5% Cu alloy. The specimens were cleaned with concentrated nitric acid before and after etching, and then washed in a stream of water and blow dried.

3.6.5. ELECTRON MICROSCOPY

Transverse and longitudinal sections 2-3mm thick were carefully cut from the torsion specimens and extrudes using a fine piercing saw and ground to a thickness of 0.25-0.3mm, from which 3mm discs were punched using a simple hand press.

The discs were electropolished in a commercial Struers jet thinner using a solution of 30% nitric acid - methanol. Good results were obtained for all the alloys using a potential of 13 volts at a temperature of -30 deg.C. It was sometimes necessary to use the window technique in which case specimens were carefully ground to a thickness of less than 0.15mm and eletropolished using the same solution and conditions as above.

The specimens were examined in a high resolution Phillips EM 301 100 kV transmission electron microscope.

Specimens for scanning electron microscopy needed no special preparation apart from the simple mounting procedure. The samples were examined using a Cambridge Streoscan and Jeol T-200 scanning electron microscope.

3.6.6. SURFACE QUALITY

The surface quality is of prime importance in many industrial extrusion processes. Extrudes were assessed for quality and categorized as follows:-

A - Good surface finish along the whole extrude length.
B - Surface cracking along part of the extrude length.
C - Surface cracking along the whole extrude with some hot shortness.

A series of extrusion runs were made to determine the effect on the surface of different billet preheating conditions.

3.6.7. STRESS CORROSION TESTING

The stress corrosion resistance has been tested using the alternate immersion constant strain Alcoa Test. Three 1/8 inch diameter tensile specimens were machined from 50:1

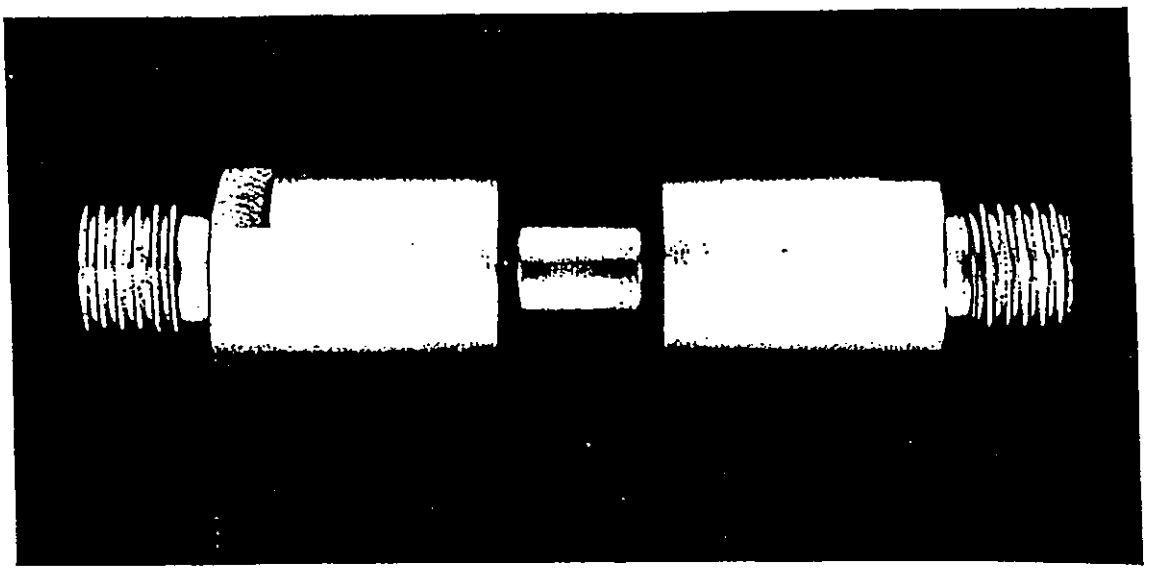
extrudes for each test condition and loaded into individual wedge-type stressing frames. The tensile specimens were pre-strained to 75% of their proof stress under a constant uniaxial tensile stress. The stress was measured to a standard error of 0.5% using a type F Huggenburger Tensometer. In general stresses are not applied to 75% of the proof stress to avoid significant stress relaxation during the exposure test. The stressing frame and shoulder area of the specimen were coated with molten Maskcoat to leave the 1/2 inch gauge length exposed. The exposed section was cleaned with acetone before placing in an alternate immersion tank containing 3% NaCl at a constant room temperature of 25 deg.C. The specimens were immersed for 10 minutes on every hour and checked daily for any signs of cracking. Details of the specimen dimensions and apparatus can be found in references.[132,133]

3.7. TORSION TESTS

Specimens for torsion testing were machined from extruded rod (extrusion ratio 10:1) which had been heat treated at 500 deg.C for 24 hours and furnace cooled. The specimens were machined to the specifications in Figure 3.1.

The testing machine, details of which are given by Tweedale[140], was capable of twisting at 1000 r.p.m. maximum which is equivalent to a surface shear strain rate of 50 sec for the specimen geometry used. Tests were carried out over a range of shear strain rates from 0.05 sec^{-1} to 50 sec^{-1} and over a temperature range of 280 - 483 deg.C.

The specimens were clamped in the machine and heated in situ by an induction coil, the temperature being controlled by a mineral insulated NiCr/NiAl thermocouple inserted in one end of the specimen and connected to a Eurotherm controller. The temperatures along the gauge length and the



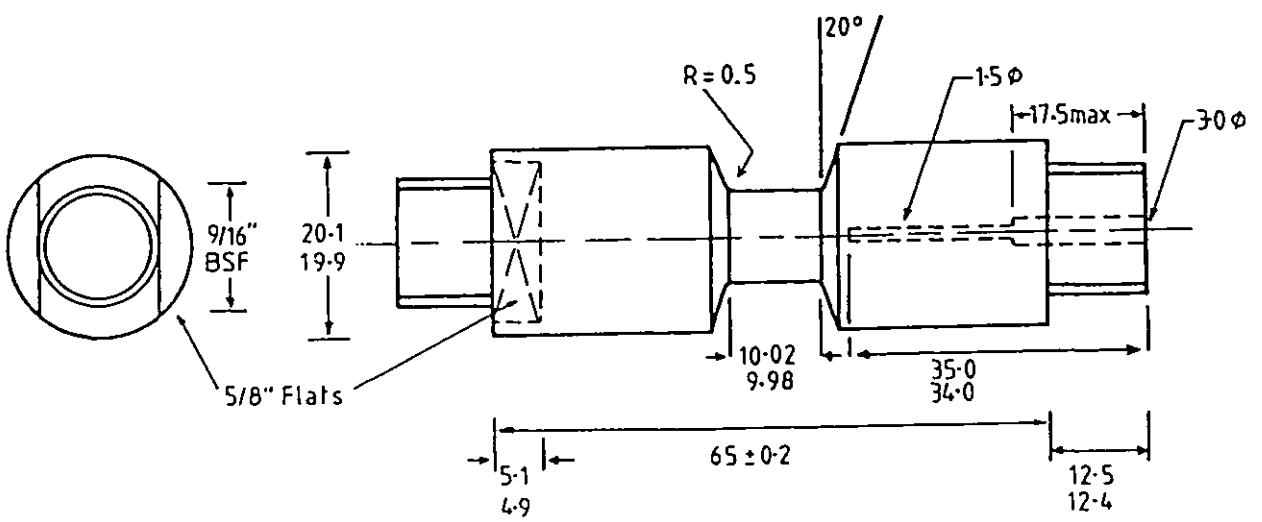


Figure 3.1 Torsion Specimen

settings of the Eurotherm controller were calibrated with another thermocouple connected to a Cormark digital thermometer. This indicated that after a five minute soaking period the Eurotherm controlled and maintained the temperature along the gauge length to within ± 2 deg.C, i.e. less than 1% error.

Upon twisting, the torque generated was measured by a load cell situated at the end of a lever arm and connected to a high speed U.V. recorder. The load cell was regularly calibrated by the application of known moments about the shaft. The twist data was measured with a light source and a photoelectric cell separated by a wheel containing radial gaps positioned evenly around the circumference. The gaps triggered a voltage drop which was recorded on the U.V. recorder. The load cell output was displayed simultaneously with the trigger marks produced at every 1/10 revolution of the specimen. Since the paper speed from the recorder was known, the twist rate could be calculated. When the peak torque coincided with steady state flow the test was stopped and automatically quenched in water to retain the hot worked structure.

CHAPTER 4

RESULTS AND DISCUSSION

4.1. TORSION DATA ANALYSIS

The hot torsion test has been used to evaluate the hot working characteristics of the alloys listed in table 3.1. A temperature range of 480 deg.C to 280 deg.C and a strain rate range of 26 sec^{-1} to 0.03 sec^{-1} has been tested, as described in section 3.7. Specimens were tested to peak torque, stopped and water quenched at a rate of $\sim$ 60 deg.C per sec.

4.1.1. TORQUE TWIST CURVES

The torque twist curves from all the tests produced three characteristic sets of curves. Those at high temperatures and low strain rates, i.e. low Z (Fig. 4.1), showed an initial rapid rise in torque corresponding to the interval of microstrain deformation, where the strain rate rises from zero to that applicable to the test. A decrease in the slope of torque twist curve indicates that this stage has been left and work hardening has commenced. As the work hardening decreases with increasing strain, the slope of the load curve decreases. This continues until a steady state is achieved where the rate of dislocation generation is equal to the rate of annihilation.

The second type of curve (Fig. 4.2) corresponds to tests carried out between 330-400 deg.C and strain rates of 1 to $5s.^{-1}$ Once again there is a rapid rise in torque, followed by a more prominent interval of work hardening, where the degree of work hardening tended to increase with alloy content. The final type of curve (Fig. 4.3)

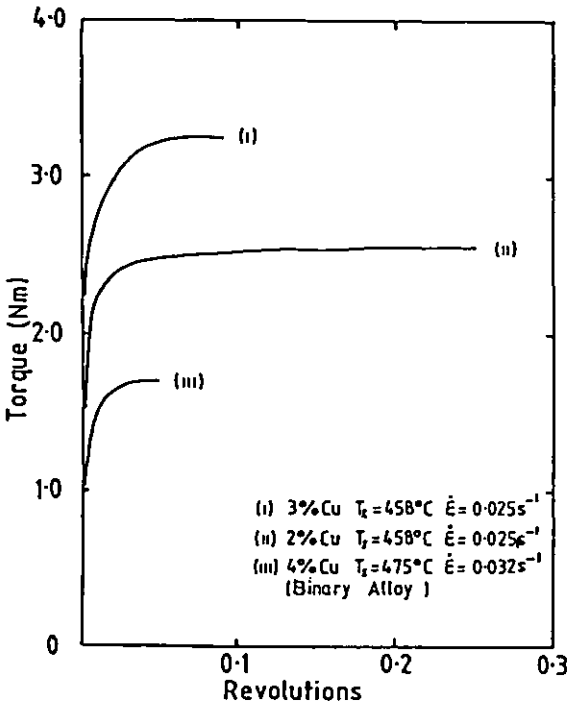


Figure 4.1 Low Z_I

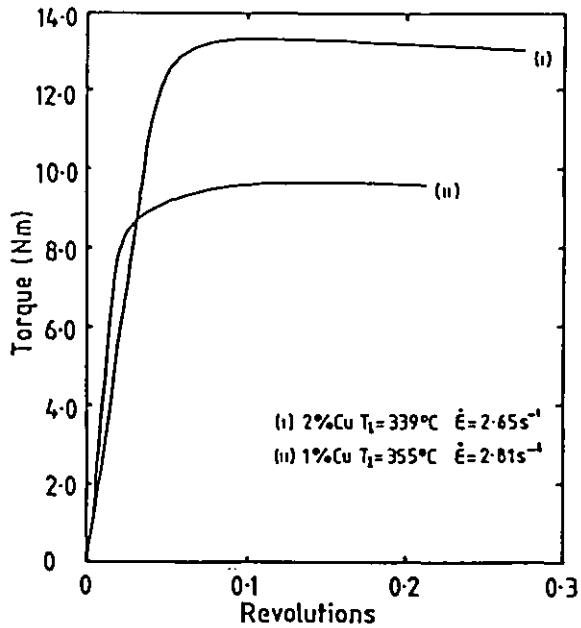


Figure 4.2 Mid Z_I

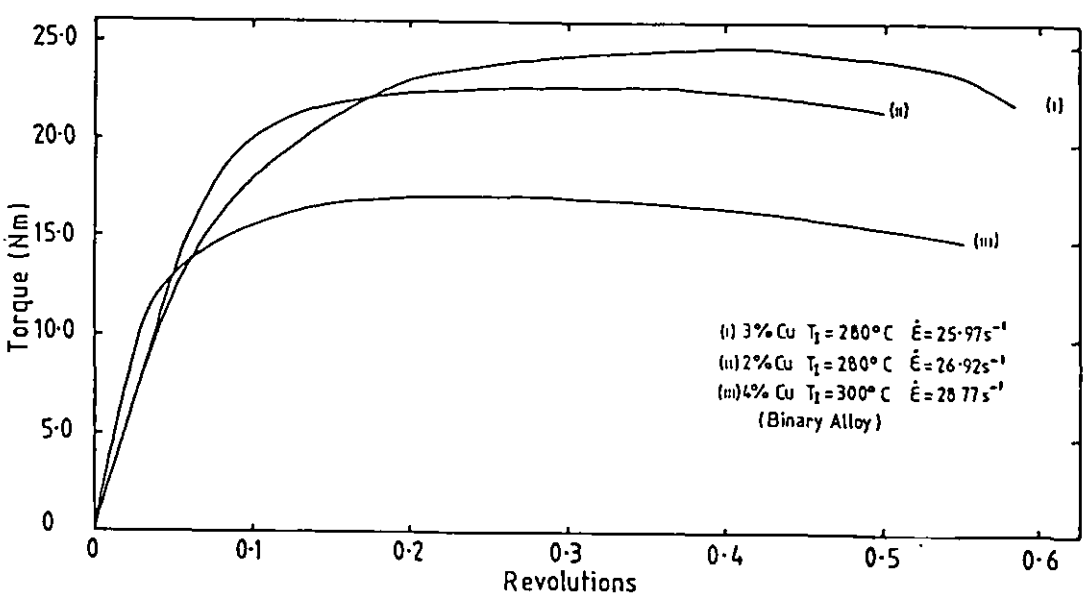


Figure 4.3 High Z_I

Torque Twist Curves

corresponds to tests at high Z values, i.e. low temperatures and high strain rates. The initial stage of microstrain deformation is followed by a decreasing work hardening rate prior to a fall in torque and in most tests failure. The steady decrease in torque after peak is due to the conversion of energy input to heat, resulting in a reduced flow stress.

The effect of alloy content on the nature of the torque twist curves was noticeable in the second and third type of curve due to the effects of increased work hardening in the higher Cu alloys.

4.1.2. TEMPERATURE RISE DURING TESTING

The temperature rise during testing has been evaluated using the analysis described in section 2.2.1. a complete listing of the results is shown in appendix I. It is apparent from these results that the strain to peak torque is relatively small in all the alloys and it was therefore decided to analyse the curves at 0.5, 0.75 and 1.0 homologous strains, where for all the tests a linear increase in torque with strain occurs below 0.5 ε_H as shown in figures 4.1 to 4.3. The initial and temperature corrected values of the hot working constants are shown in table 4.1.

The results in appendix I show that in general the temperature rise increases with decreasing initial temperature and increasing strain rate as the flow stress increases and the heat losses decrease. The hot working constants in table 4.1. show that inclusion of the temperature rise reduces the absolute values of ΔH, α and A, the difference increasing with strain as the temperature rise increases, whilst n shows no significant change. Previous workers[27-29, 122] have reported similar trends for

INITIAL TEMPERATURE

	ε_H	ΔH J/mole	$\propto$ m^2/MN	n	A s^{-1}	cc
	1.00	157907	0.0207	5.69	6.24×10^{11}	0.9834
1% Cu	0.75	161012	0.0235	5.38	5.22×10^{11}	0.9814
	0.50	168755	0.0274	5.32	8.18×10^{11}	0.9795
	1.00	162323	0.0192	4.90	1.60×10^{12}	0.9889
2% Cu	0.75	163139	0.0202	4.80	1.42×10^{12}	0.9890
	0.50	166915	0.0219	4.69	2.07×10^{12}	0.9886
	1.00	157515	0.0171	5.07	7.11×10^{11}	0.9705
3% Cu	0.75	157679	0.0181	5.01	5.71×10^{11}	0.9717
	0.50	161394	0.0255	4.53	1.90×10^{11}	0.9606
	1.00	138245	0.0159	5.04	4.42×10^{9}	0.9924
5% Cu	0.75	138641	0.0162	5.02	4.74×10^{9}	0.9891
	0.50	139743	0.0193	4.58	1.19×10^{9}	0.9836
	1.00	130780	0.0249	3.96	4.17×10^{9}	0.9876
4% Cu Binary	0.75	132478	0.0278	3.87	3.73×10^{9}	0.9827
	0.50	135305	0.0362	3.62	2.26×10^{9}	0.9668

ACTUAL TEMPERATURE

	ε_H	ΔH J/mole	$\propto$ m^2/MN	n	A s^{-1}	cc
	1.00	147950	0.0167	5.65	4.23×10^{11}	0.9778
1% Cu	0.75	153706	0.0200	5.40	3.75×10^{11}	0.9761
	0.50	163099	0.0241	5.39	6.97×10^{11}	0.9762
	1.00	152817	0.0144	5.13	1.60×10^{12}	0.9893
2% Cu	0.75	155860	0.0165	4.93	1.26×10^{12}	0.9889
	0.50	161526	0.0191	4.80	1.82×10^{12}	0.9884
	1.00	145964	0.0133	5.15	4.02×10^{11}	0.9688
3% Cu	0.75	149083	0.0155	4.99	3.39×10^{11}	0.9700
	0.50	154293	0.0220	4.62	1.25×10^{11}	0.9583
	1.00	130309	0.0128	5.13	4.51×10^{9}	0.9910
5% Cu	0.75	132504	0.0137	5.11	4.74×10^{9}	0.9883
	0.50	134579	0.0173	4.67	1.21×10^{9}	0.9845
	1.00	127629	0.0229	3.91	3.51×10^{9}	0.9885
4% Cu Binary	0.75	130197	0.0259	3.86	3.55×10^{9}	0.9835
	0.50	133374	0.0345	3.63	2.05×10^{9}	0.9878

Table 4.1 Initial and temperature corrected hot working working constants at homologous strains of 1.0, 0.75 and 0.5

1000, 2000, 5000 and 7000 series alloys. The similarity suggests that if the temperature rise during testing is ignored, then the flow stress characteristics described by equation 1.5 are likely to be inaccurate due to the temperature dependency of the torque and hence flow stress.

In the analysis described in section 2.2.1. an average temperature rise was evaluated by integrating over the volume elements in the gauge section using equation 2.6 below:

$$T_v = \frac{1}{\pi R^2 L} \int_{r=o}^{R} T_r V_r dr \qquad 2.6.$$

The temperature rise model predicts that heat flow to the end pieces during testing will result in a higher temperature in the centre of the gauge. This is to some extent proved by the fact that all the specimens which failed during testing, failed in the centre. Therefore an alternative average temperature has been evaluated by integrating the temperature at each central axial point over the cross sectional area of the specimen using the following relationship:

$$T_{AV} = \frac{1}{\pi R^2} \int_{r=o}^{R} T_r 2\pi r dr \qquad 4.1.$$

where Tr is the temperature at the radial position r.

This effectively gives an area average temperature T_{AV} at each axial point along the gauge section. Examples of

the predicted temperature profiles in high and low strain rate tests are shown in figure 4.4. The figure shows that a more or less uniform temperature profile exists for a short time after the start of the test i.e. at $\varepsilon_H = 0.5$. This is caused by the ends of the gauge length being fixed at the initial test temperature, so providing a constant heat sink. At high strain rates the heat generation rate is large, but the conduction rate is smaller which results in a uniform gauge temperature profile,until high strains are reached. At slower strain rates the lower heat generation rate and longer testing time allows conduction towards the ends to produce a distinct temperature profile.

Precise experimental verification of temperature profiles during testing have yet to be made. However Castle[25] observed when testing specimens of a longer gauge length, that the onset of hot shortness always occurred in the centre of the gauge length and decreased towards the ends as predicted by the temperature profiles in figure 4.4.

Since the peak torque will be a function of the maximum temperature during testing, the area average temperature at the centre of the gauge length has been used as the actual temperature in a trial run on the 1%Cu and 3%Cu alloys. A full listing of the temperature rises, flow stresses and temperature corrected hot working constants are shown in Table 4.2. and can be compared with the volume average temperature results in appendix I and table 4.1. The new constants predict slightly higher values of flow stress at equivalent strain rates and temperatures, although the maximum difference at high strain rates and low temperatures is less than 1.5%. This therefore suggests that the inclusion of an area average temperature produces no real change in the overall correlation, and results in predicted flow stresses similar to those produced assuming a volume average temperature.

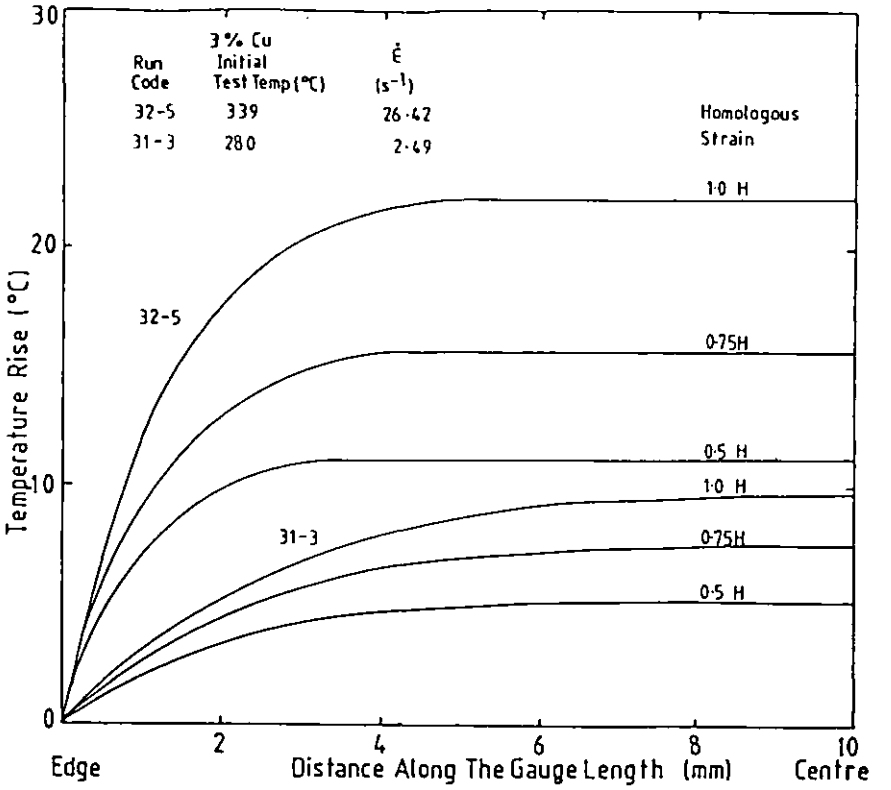


Figure 4.4 Area average temperature profiles at homologous strains of 1.0, 0.75 and 0.5

1 % Cu

CODE	STRESS MN/M2	HOMOLOGOUS STRAINS 1.00H TEMP DEG.C	0.75H TEMP DEG.C	0.05H TEMP DEG.C
11-1	61.10	295.0	295.0	295.0
11-2	80.59	298.0	298.0	298.0
11-3	88.82	324.0	320.0	316.0
11-4	105.44	313.0	308.0	305.0
11-5	114.27	318.0	312.0	308.0
12-1	38.65	357.0	355.0	355.0
12-2	55.22	357.0	357.0	357.0
12-31	71.89	363.0	361.0	359.0
12-32	71.05	365.0	363.0	360.0
12-5	91.23	367.0	364.0	361.0
13-1	26.04	415.0	415.0	415.0
13-2	38.04	417.0	417.0	416.0
13-3	52.16	422.0	421.0	419.0
13-4	60.15	425.0	423.0	421.0
13-5	63.11	447.0	440.0	432.0
14-11	18.15	475.0	475.0	475.0
14-12	18.15	475.0	475.0	475.0
14-2	27.20	476.0	476.0	476.0
14-3	39.00	477.0	477.0	476.0
14-4	45.14	483.0	481.0	479.0
14-51	52.66	487.0	484.0	481.0

3% Cu

CODE	STRESS MN/M2	HOMOLOGOUS STRAINS 1.00H TEMP DEG.C	0.75H TEMP DEG.C	0.05H TEMP DEG.C
31-1	79.53	280.0	280.0	280.0
31-21	109.84	283.0	282.0	282.0
31-22	109.08	284.0	283.0	283.0
31-3	133.94	290.0	288.0	285.0
31-41	150.08	291.0	288.0	286.0
31-42	148.66	293.0	290.0	287.0
31-5	151.80	311.0	303.0	297.0
32-1	49.21	339.0	339.0	339.0
32-2	72.42	342.0	341.0	341.0
32-31	97.55	344.0	343.0	342.0
32-32	98.15	343.0	342.0	341.0
32-33	94.81	349.0	346.0	344.0
32-4	111.92	346.0	344.0	343.0
32-5	117.41	363.0	357.0	353.0
33-1	31.22	398.0	398.0	398.0
33-21	49.03	398.0	399.0	398.0
33-22	48.70	399.0	399.0	399.0
33-3	68.73	402.0	401.0	400.0
33-41	81.18	404.0	402.0	401.0
33-42	79.62	408.0	406.0	403.0
34-11	20.79	458.0	458.0	458.0
34-12	20.79	458.0	458.0	458.0
34-2	33.49	458.0	458.0	458.0
34-3	49.03	460.0	459.0	459.0
34-4	58.57	464.0	463.0	461.0
34-5	68.12	472.0	469.0	465.0
35-1	17.84	483.0	483.0	483.0
35-3	43.11	484.0	483.0	484.0
35-5	61.16	496.0	493.0	490.0

1 % Cu

ε_H	ΔH	α	n	A	cc
1.00	147649	0.0171	5.48	3.36×10^{11}	0.9735
0.75	152416	0.0199	5.30	2.92×10^{11}	0.9720
0.50	162608	0.0240	5.32	6.97×10^{11}	0.9728

3 % Cu

ε_H	ΔH	α	n	A	cc
1.00	144311	0.0131	5.03	3.36×10^{11}	0.9666
0.75	147633	0.0146	5.06	3.36×10^{11}	0.9696
0.50	154006	0.0215	4.74	1.33×10^{11}	0.9576

Table 4.2 Area average temperature rises, flow stress data and hot working constants in the 1% Cu and 3% Cu alloys

Before leaving this subject it may be useful to compare the adiabatic temperature rises at low and high strain rates with the two average temperature rises. The results in table 4.3. show that the volume average temperature rises are lower at high and low strain rates, although one might have expected a similar temperature rise to the adiabatic case at high strain rates. The area average temperature rises are $\sim$ 10% lower at both strain rates. The question arises as to whether at high strain rates an area average temperature rise is more applicable and at low strain rates a volume average temperature rise. The answer to the question could be obtained from accurate temperature measurements during testing, which was not possible in the present work. However, the results in tables 4.1. and 4.2. suggest that such an exercise may not significantly alter the flow stress characteristics, due to the small difference in temperature rise shown in table 4.3.

	T_I = 280°C $\dot{\varepsilon}$ = 26.0 ε_H			T_I = 339°C $\dot{\varepsilon}$ = 2.6 ε_H		
Trise(°C)	0.5	0.75	1.0	0.5	0.75	1.0
Vol Ave	15	19	25	4	5	7
Area Ave	17	23	31	5.0	7	10
Adiabatic	17	25	34	5.5	8	11

Table 4.3 Comparison between the evaluated temperature rises during torsion testing.

4.1.3. FLOW STRESS CHARACTERISTICS

There are several factors which affect the ease of dynamic recovery during deformation and therefore the flow

stress characteristics. The two most obvious factors are the process parameters of temperature and strain rate. There effects have been well documented[68,69] where the relationship between them and the flow stress can be accurately described by either the general hot working equation or the individual stress strain rate relationships shown in section 1.4.1. An increase in temperature reduces the flow stress as thermally activated cross slip and climb increases the rate of recovery. An increase in strain rate increases the dislocation generation rate and effectively reduces the time for the recovery processes resulting in a less recovered substructure and higher flow stress. The two conflicting parameters can be combined into a single parameter Z, the temperature compensated strain rate, which previous workers[23,27-29,69] have shown can be used to predict a specific substructure or flow stress for any combination of temperature and strain rate.

Perhaps the other most important factor is the material itself. The rate of dynamic recovery will be dependent upon the nature of the material e.g. pure metal, solid solution, the nature of the precipitate and particle distribution etc. and as such will ultimately determine the flow stress characteristics described by the temperature - strain rate relationships.

In the present work the effect of an increase in copper content on the flow stress characteristics of the 1% Cu to 5% Cu 2000 series alloys has been investigated, whilst the effect of the second phase particles associated with the Mg, Mn and Si has also been investigated using the binary Al-4% Cu alloy listed in table 3.1. The flow stress characteristics have been established using the graphical analysis described in section 2.2.2.2. and the mathematical minimization technique described in section 2.2.2.1. using

the temperature corrected data discussed in the previous section.

4.1.3.1. GRAPHICAL ANALYSIS

With aid of the computer programme TRQGRAF listed in appendix VI, the graphical analysis has been carried out for each of the alloys, the results shown in table 4.4.

$$\dot{\varepsilon} = A_2 \exp(\beta\sigma) \qquad 2.20.$$

$$\dot{\varepsilon} = A_1 \sigma^{n'} \qquad 2.23.$$

The applicability of equations 2.20. and 2.23. to the high and low stress data is shown by the high correlation coefficients which exist at all temperatures. Only the 1% Cu and binary alloy show a reduction in correlation when the exponential equation is applied to data above 350 deg.C, the correlation decreasing with increasing temperature. The power relation results in a good correlation at all temperatures. The constants n' and β are clearly temperature dependent β increasing with temperature whilst n' decreases. Since 1/n' is a direct measure of the strain rate sensitivity at constant temperature, the results in figure 4.5. clearly show that for all the alloys the strain rate sensitivity increases with temperature as the rate of dynamic recovery increases. The applied stress at higher temperatures may therefore be regarded as more effective in aiding dislocation motion and so more dependent on the strain rate. This is also reflected in the higher strain rate sensitivity of the binary alloy due to the reduction in the number of second phase particles which inhibit dislocation motion. The effect of copper content on the strain rate sensitivity is masked by the scatter in the values of 1/n', which can be attributed to the limited number of results available at each temperature and the

	T_I °C	β	cc	n′	cc	Ln($\dot{\varepsilon}$) v Ln(Sinh($\alpha\sigma$)) gradient	cc	Ln(1/T) v Ln(Sinh($\alpha\sigma$)) gradient	cc	ΔH J/mole	n	LnA	cc
1% Cu	295.0	.1259	.9967	10.552	.9961	5.422	.9971	3496.6	.9889	155706.	5.422	24.595	.9971
	355.0	.1361	.9971	7.385	.9985	5.107	.9998	3546.4	.9938	146654.	5.107	25.734	.9998
	415.0	.1597	.9789	6.810	.9902	5.298	.9874	3642.3	.9942	152127.	5.298	25.308	.9874
	475.0	.1751	.9799	5.720	.9966	4.875	.9945	3310.4	.9849	140000.	4.875	24.893	.9945
2% Cu	280.0	.0915	.9993	9.812	.9975	5.088	.9997	3758.2	.9931	153857.	5.088	28.455	.9997
	339.0	.1146	.9988	7.479	.9893	5.385	.9963	3460.6	.9977	162860.	5.385	28.938	.9963
	398.0	.1506	.9977	7.271	.9917	5.956	.9955	3636.1	.9938	180111.	5.956	28.459	.9955
	458.0	.1575	.9952	5.386	.9905	4.829	.9942	3567.8	.9945	146036.	4.829	28.092	.9942
3% Cu	280.0	.0898	.9953	10.599	.9947	5.030	.9958	3969.8	.9947	156535.	5.030	26.933	.9958
	339.0	.1135	.9974	8.126	.9976	5.531	.9992	3828.4	.9871	172126.	5.531	27.843	.9992
	398.0	.1194	.9860	6.827	.9995	5.207	.9963	3561.1	.9848	162033.	5.207	27.283	.9963
	458.0	.1376	.9980	5.228	.9930	4.564	.9972	3580.6	.9878	142024.	4.564	26.912	.9972
5% Cu	295.0	.0807	.9935	10.280	.9987	5.799	.9954	3061.3	.9987	138292.	5.799	23.290	.9954
	355.0	.0913	.9968	8.345	.9992	5.834	.9989	2861.4	.9984	139138.	5.834	23.465	.9989
	415.0	.1080	.9999	7.449	.9958	5.929	.9985	2751.4	.9959	141389.	5.929	23.207	.9985
	475.0	.1211	.9976	6.285	.9981	5.464	.9993	2647.9	.9999	130305.	5.464	23.340	.9993
4% Cu (Binary)	300.0	.1049	.9994	7.842	.9938	3.868	.9995	4070.6	.9923	129824.	3.868	21.749	.9995
	350.0	.1288	.9888	7.390	.9985	4.461	.9938	4513.1	.9981	149711.	4.461	21.469	.9938
	390.0	.1207	.9786	5.306	.9997	3.754	.9930	4127.2	.9929	125976.	3.754	22.185	.9930
	430.0	.1392	.9690	5.154	.9950	3.963	.9881	3799.1	.9861	132996.	3.963	21.865	.9881
	475.0	.1399	.9688	4.061	.9978	3.402	.9943	3674.1	.9944	114175.	3.402	21.602	.9943

Table 4.4 Empirical constants derived from the graphical analysis

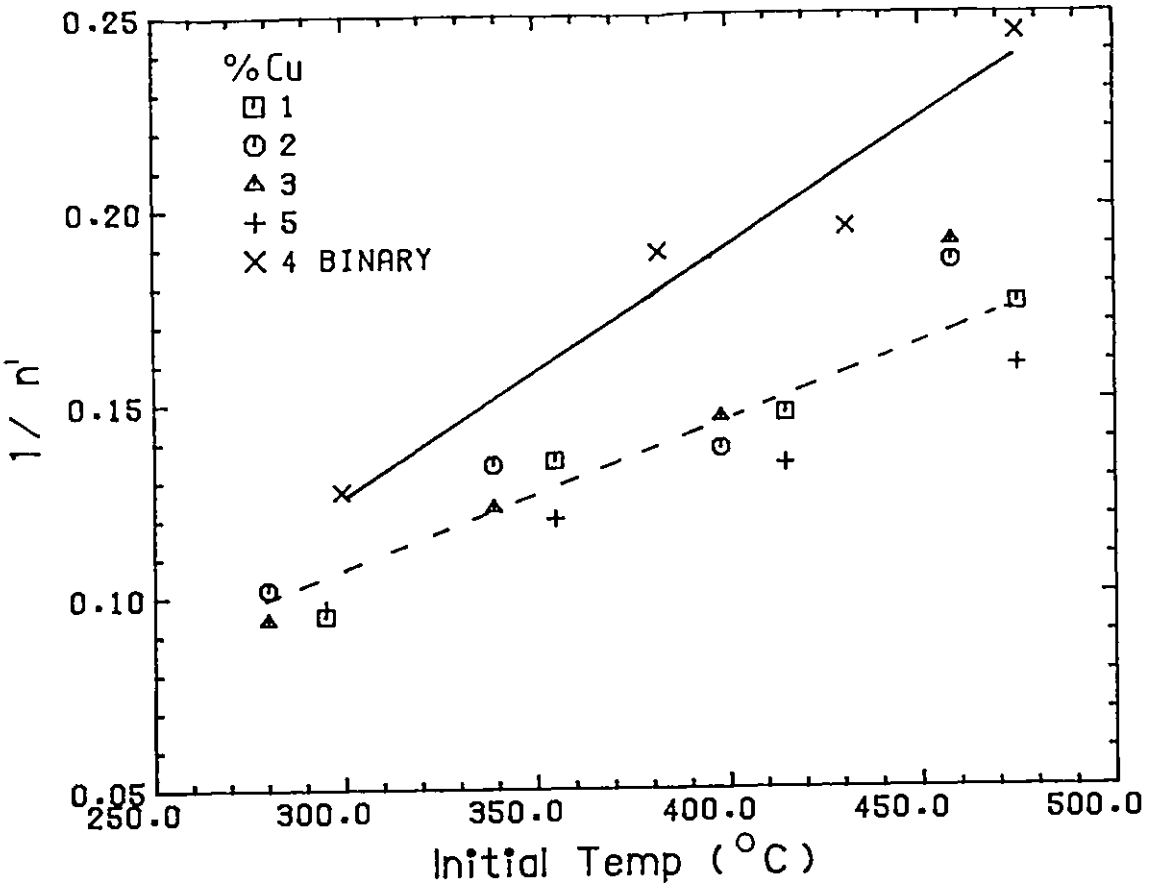


Figure 4.5 The variation of $1/n'$ with initial test temperature

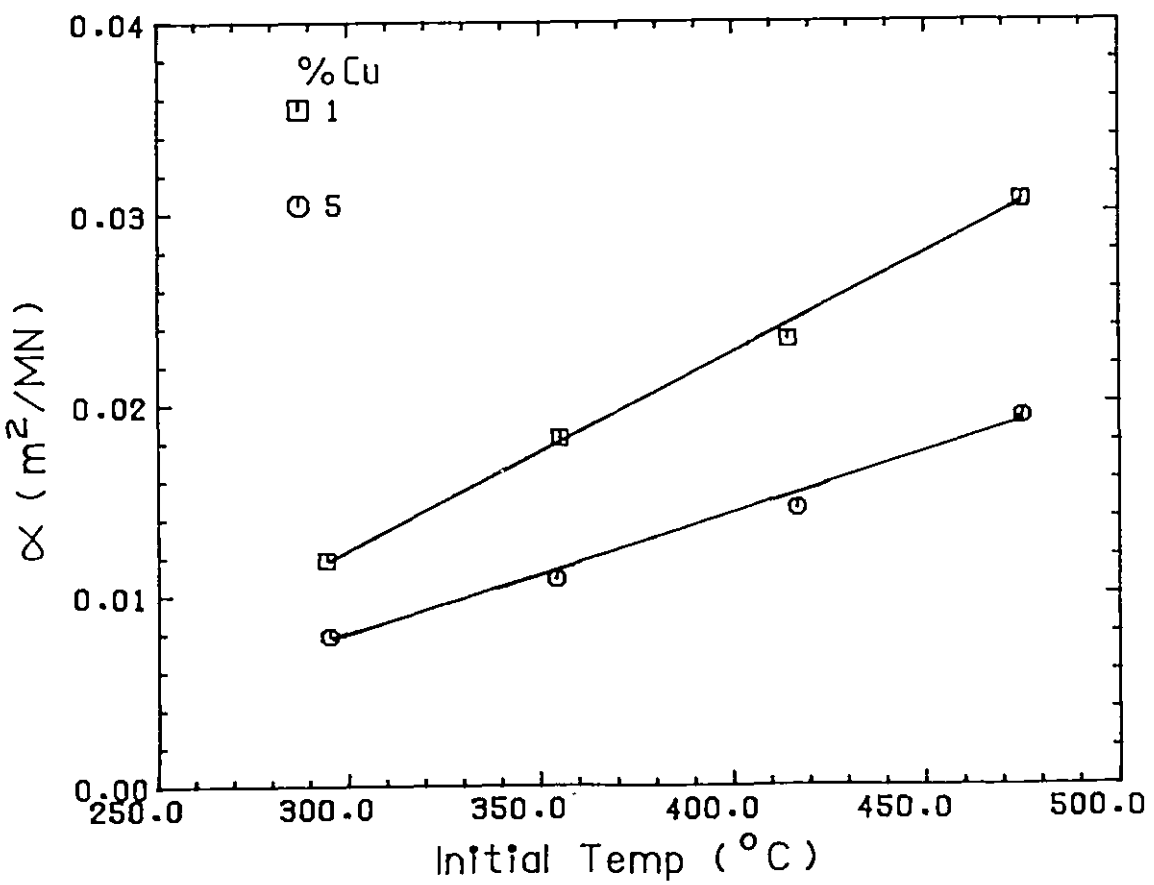


Figure 4.6 The variation of $\propto$ with initial test temperature in the 1% Cu and 5% Cu 2000 series alloys

temperature rise during testing.

In section 2.2.2.2. it was shown that values of α could be obtained using the relationship $\alpha = \beta/n'$ where β and n correspond to the low and high stress values respectively. Using this data values of α were calculated for each alloy, the results are shown in table 4.5. The description of α as being reciprocal stress at which Z changes from a power to an exponential relationship means that in the 1% Cu and binary alloy at stresses below 45 MN/m^2 the exponential relationship no longer holds. This stress level coincides with tests carried out above 350 deg.C and below $\dot{\varepsilon}$ of 1 to $25s^{-1}$ depending on the temperature. The fact that both equations apply at all temperatures in the other alloys is perhaps indicative of the higher stresses associated with these alloys. Previous workers[26,150] have also shown that a linear temperature dependency for α can be established by using the individual values of β and n' at each temperature. Figure 4.6. shows a similar linear increase can be established in the present series of alloys. It is doubtful whether any physical significance can be attached to this since $\alpha = \beta/n'$ is strictly only correct when $n \simeq n'$, which coincides with the high temperature values of n' only as shown in table 4.1. The temperature dependency shown in figure 4.6. is perhaps not surprising since both β and n are related to the strain rate sensitivity. This fact was recognised by Garofalo[77] who points out that the increase in alpha with temperature is due to the decrease in n' not being sufficient to compensate for the increase in β with temperature.

Using the regression data from the plots on Ln $\dot{\varepsilon}$ v Ln sinh ($\alpha\sigma$) and Ln sinh ($\alpha\sigma$)vs 1/T, values of the activation energy ΔH have been calculated at each test temperature the results shown in table 4.4. No consistent

variation in ΔH with temperature was found, although all the alloys exhibit a lower than average value at the highest test temperatures.

Values of n and A have been established at each temperature from the regression of LnZ vs Ln sinh ($\alpha \sigma$), the results shown in table 4.4. No apparent trend was found for either of the constants with temperature, where the mean values in table 4.5. show no consistent variation of n with copper content, whilst A decreases with copper content above 2% Cu. The mean values of n and A are lowest in the binary alloy.

In order to establish the overall correlation of the constants, the steady state flow stress was calculated for each test condition using equation 2.5. and the average values of ΔH, n and A shown in table 4.5. and compared with the corresponding peak torque data in appendix I. Table 4.5. shows that a good correlation exists for all the alloys, even though the temperature rise has not been allowed for and only average values ΔH, n and A were considered.

The usefulness of the graphical analysis as a means of obtaining realistic values of the hot working constants is somewhat limited due to the original assumptions made in the analysis and the use of initial temperature torque-twist data and hence no allowance for the temperature rises predicted in section 4.1.2. However the analysis is a useful guide as to the nature of the individual temperature and strain rate dependencies of the torque-twist data and provides a quick method, with the aid of TRQGRAF, to estimate initial values of the hot working constants for use in the minimization analysis described in section 2.2.2.1. The values of the constants in table 4.5. have been used for this purpose in the present work.

%Cu	ΔH	α	n	A	cc
1	148622	0.0220	5.09	8.71×10^{10}	0.9882
2	161461	0.0168	5.28	2.94×10^{12}	0.9895
3	153240	0.0181	4.72	2.12×10^{11}	0.9717
5	137281	0.0128	5.75	1.34×10^{10}	0.9825
4B	128913	0.0283	3.49	1.44×10^{9}	0.9843

Table 4.5 Hot working constants derived from the graphical analysis

FORTRAN HIGH SPEED MINIMISATION.(RPV-2.7.82-VERS2.2)
FLOW STRESS DATA ANALYSIS FOR THE TORSION TEST
TABLE OF RESIDUALS FOR 2014
THE SPECIMEN DIMENSIONS ARE
INNER RADIUS = 0
OUTER RADIUS = 5.00
LENGTH = 10.00
THE PARAMETER VALUES ARE
ALPHA= .01523
DELTA H = 144408.
N = 5.27
LN A = 24.11

POINT NUMBER	TWIST RATE (RPS)	TEMPER -ATURE (C)	OBSRVD TORQUE (N-MM)	ESTIM. TORQUE	RESI-DUAL
1	3.180	359.	15710.	16353.	-643.
2	7.300	360.	17000.	17744.	-744.
3	15.270	368.	18670.	18451.	219.
4	.030	400.	7520.	6896.	624.
5	.150	400.	8670.	8887.	-217.
6	3.210	406.	12550.	13139.	-589.
7	7.280	408.	14030.	14374.	-344.
8	15.270	407.	15420.	15705.	-285.
9	.017	350.	8890.	8747.	143.
10	.017	400.	6630.	6277.	353.
11	.017	450.	4310.	4614.	-304.
12	.170	351.	12060.	12044.	16.
13	.170	401.	9310.	9004.	306.
14	.170	450.	6370.	6838.	-468.
15	1.580	357.	15630.	15291.	339.
16	1.620	406.	11360.	12041.	-681.
17	1.660	454.	9520.	9554.	-34.
18	4.880	368.	16500.	16426.	74.
19	4.950	411.	13500.	13544.	-44.
20	4.950	458.	10950.	10955.	-5.
21	15.050	380.	18860.	17535.	1325.
22	15.410	423.	14900.	14713.	187.
23	15.410	468.	12990.	12217.	773.

RESIDUAL SUM OF SQUARES = 5525254.
R-SQUARED = .9849

Temperature Range (^{o}C)	ΔH J/mole	α m^2/MN	n	A s^{-1}	cc
350-500	134403	0.0247	3.80	3.45×10^{8}	0.983
350-450	144408	0.0152	5.27	2.96×10^{10}	0.985

Table 4.6 Hot working characteristics of the 4% Cu 2014 alloy

4.1.3.2. TORQUE MINIMIZATION

The temperature corrected steady state hot working constants established using the minimization analysis described in section 2.2.2.1. are listed in table 4.1. A rapid convergence to the final solution was found in all the alloys due to the use of the initial estimates of the hot working constants derived from the graphical analysis. The hot working characteristics of the 4% Cu 2014 alloy have been established using the torque twist data from a recent work by Paterson[29]. The alloy tested contained 4.2. weight % Cu with identical Mg, Mn, Fe and Si contents to those shown in table 3.1. However the original constants shown in table 4.6. did not correlate with the hot working constants in table 4.1. due to the higher temperature range of 350 deg.C to 500 deg.C considered. Reducing this range to 350 deg.C to 450 deg.C and repeating the temperature analysis resulted in the constants shown in table 4.6. the output from the minimization programme is also listed in table 4.6. The output contains the evaluated constants, the test conditions, the estimated and actual torque and an estimation of the accuracy of the solution R^2 the correlation coefficient. However it should be noted that the maximum difference in flow stress predicted by the corrected constants was less than 4%, the difference increasing with Z. The corrected constants have been used for the 2014 alloy in the rest of this thesis.

The effect of alloy content on the steady state temperature corrected hot working constants are shown plotted in figures 4.7. to 4.10. Examples of steady state constants established by previous workers for heat treatable and non heat treatable aluminium alloys are shown in table 4.7. Before considering the significance of each figure it may be useful to establish the variation in flow stress with

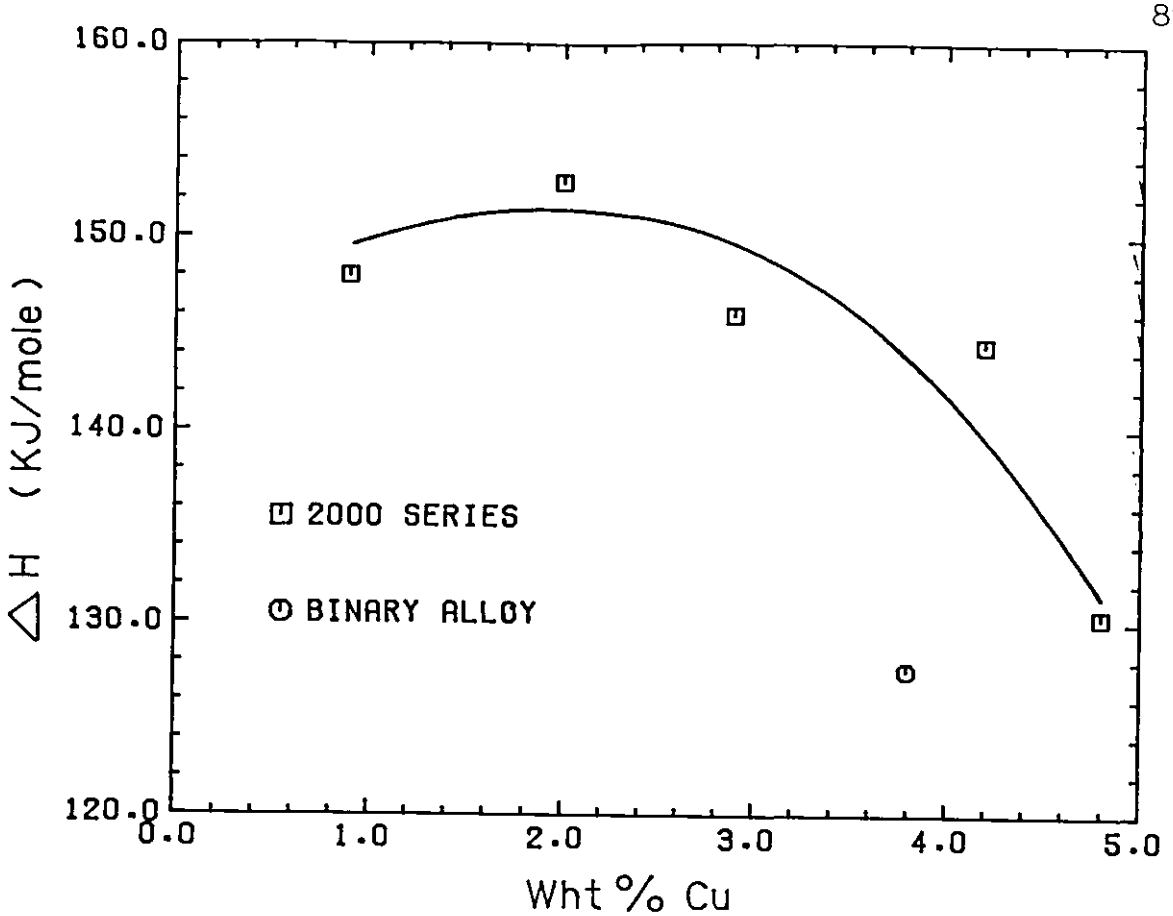


Figure 4.7 Variation of ΔH with alloy content

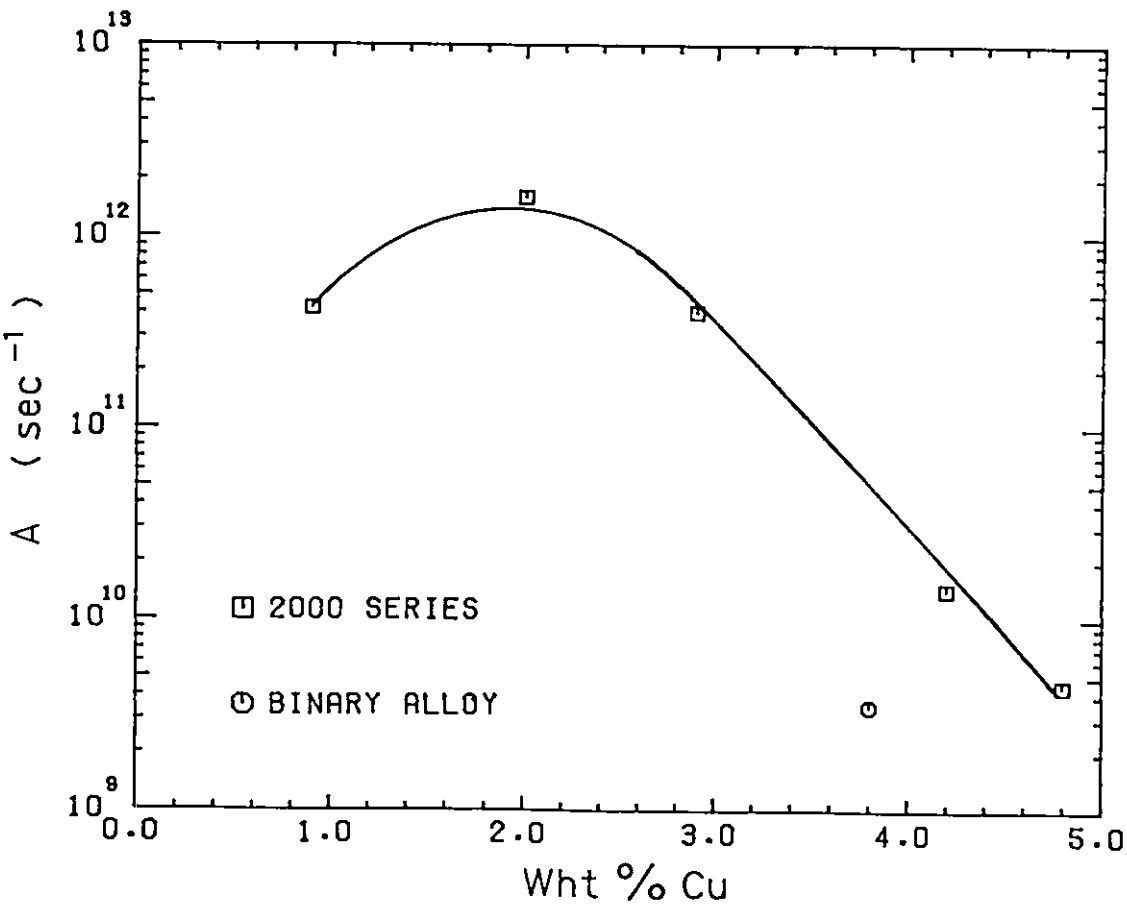


Figure 4.8 Variation of A with alloy content

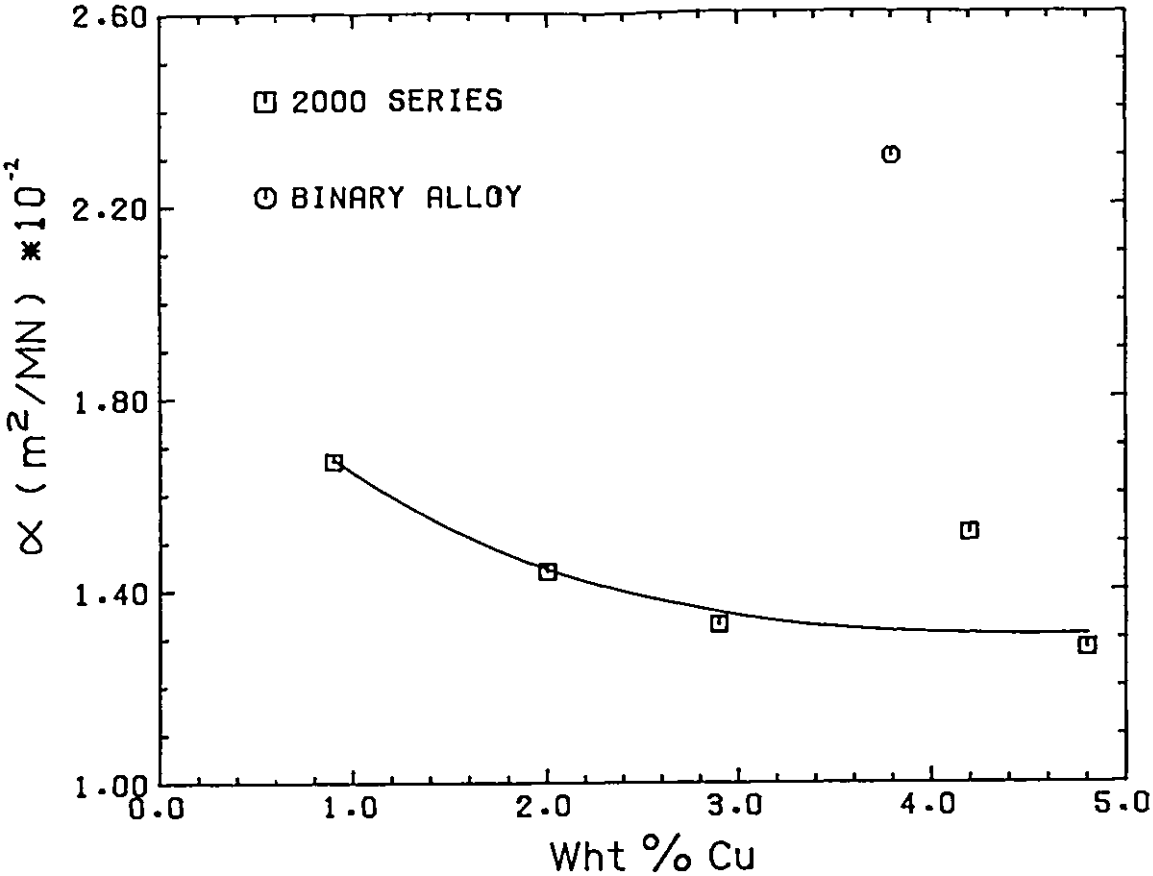


Figure 4.9 Variation of ∝ with alloy content

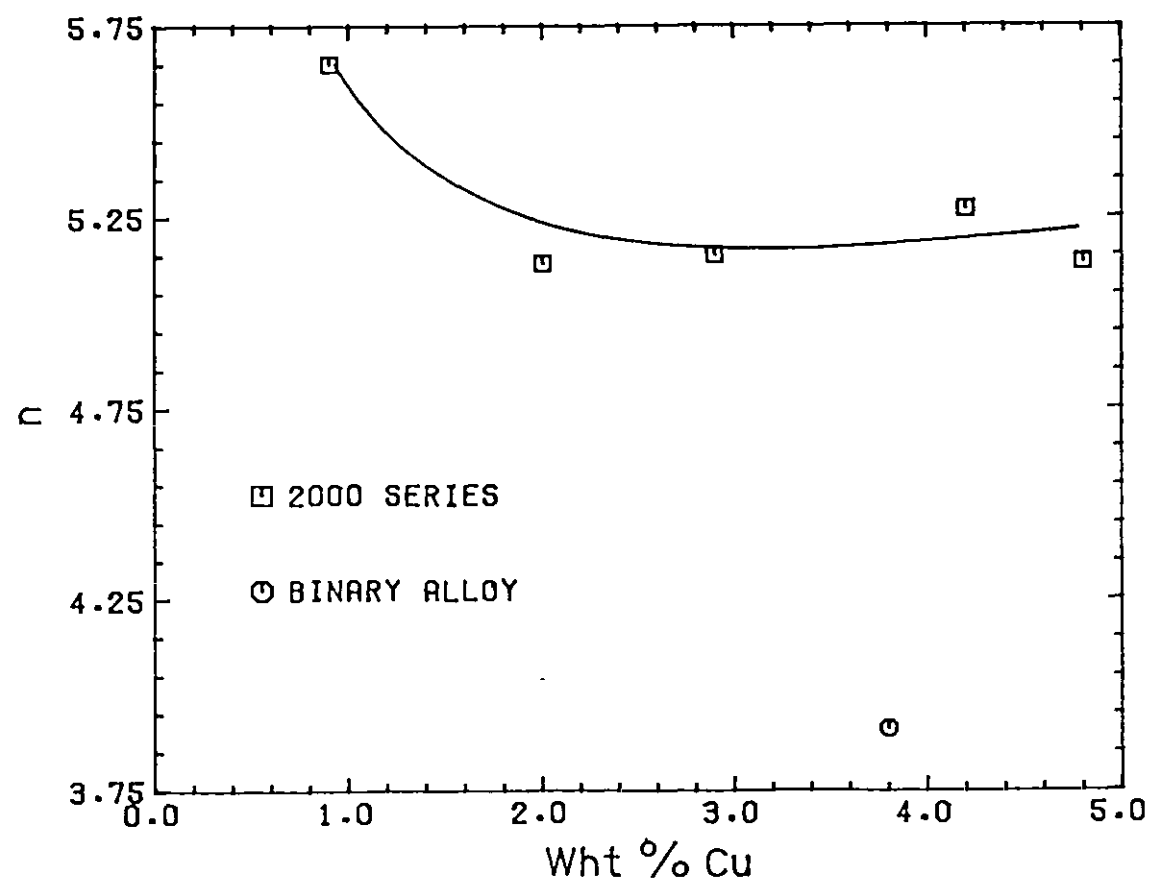


Figure 4.10 Variation of n with alloy content

copper content predicted by the constants in figures 4.7. to 4.13. The results in figures 4.11. to 4.13. show that over the entire range of temperatures and strain rates tested, the flow stress increases with copper content, the difference increasing with decreasing temperature and increasing strain rate i.e. increasing Z, a similar trend can also be established from the torque twist characteristics.

Ref No.	ΔH (KJ/mole)	α (m^2/MN)	n	A (s^{-1})	Material + Method
60	159.3	0.029	6.40	6.70×10^{10}	Al-1Mg-2 Cu Si AA6066 : Hot Torsion
60	159.7	0.016	5.33	3.30×10^{11}	Al-4 Cu - Mn AA2017 : Hot Torsion
26	151.5	0.016	4.17	1.90×10^{11}	Al-4 Cu - Mn : Hot Torsion
28	134.6	0.012	5.30	2.01×10^{10}	Al-Zn-Mg-Cu AA7075 : Hot Torsion
147	114.2	0.039	1.20	5.31×10^{6}	Al-7Zn-3Mg Extrusion
27	106.4	0.014	2.61	3.30×10^{9}	Al-4Mg-Mn AA5456 Hot Torsion
122	154.5	0.017	5.11	3.25×10^{10}	Al-2Mg AA5052 Hot Torsion
80	153.5	0.045	4.80	1.40×10^{12}	Al AA1100 Hot Torsion
29	162.8	0.052	3.69	2.70×10^{11}	Al AA1100 Hot Torsion

Table 4.7 Quoted Values of the Hot Working Constants

The presence of the Arhenius term in equation 1.5. below implies that hot working is a thermally activated process where ΔH is equal to the activation energy of the rate controlling mechanism.

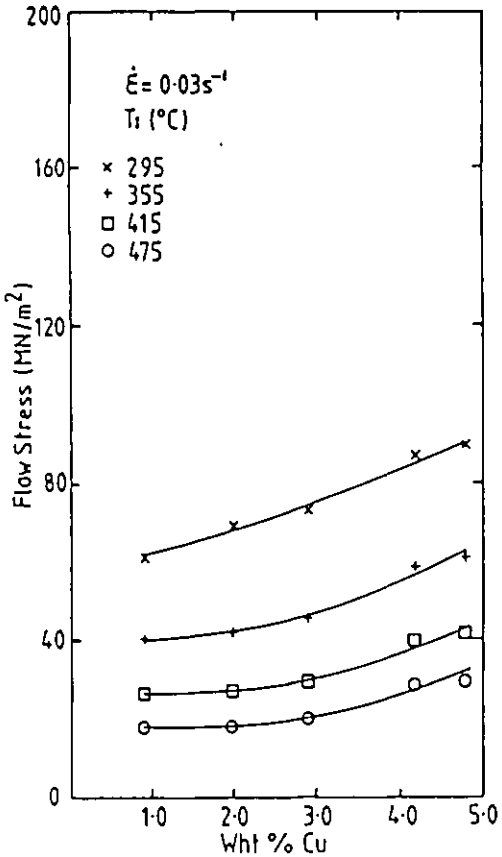


Figure 4.11

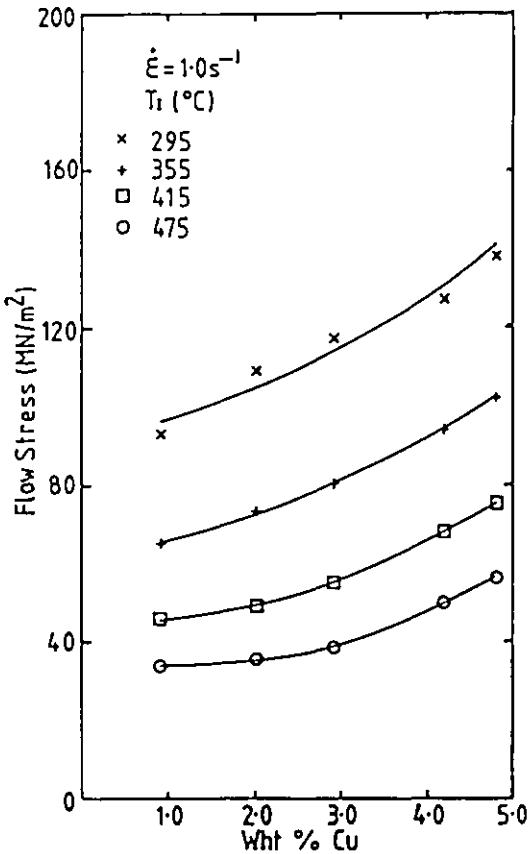


Figure 4.12

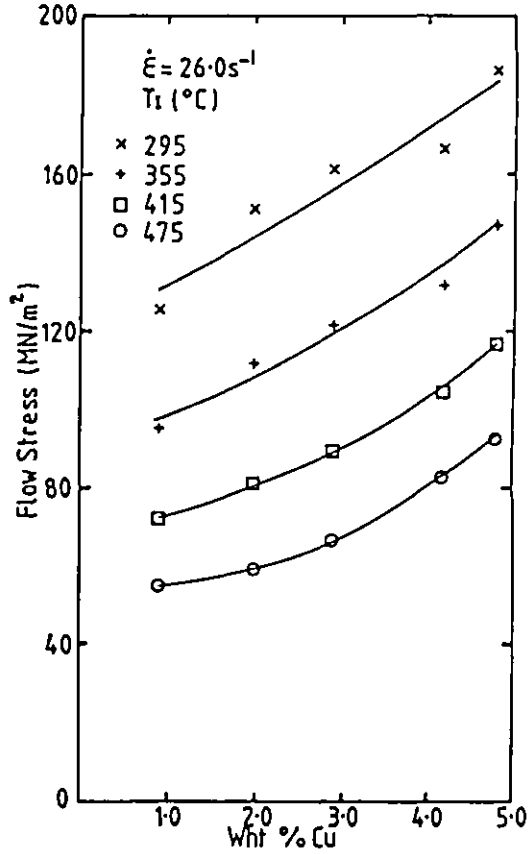


Figure 4.13

Flow stress characteristics of the 1% Cu to 5% Cu 2000 series alloys

$$Z = \dot{\varepsilon} \exp\left[\frac{\Delta H}{RT}\right] = A \, \mathrm{Sinh}\,(\alpha\sigma)^n \qquad 1.5.$$

ΔH represents the size of energy barrier preventing the atomic rearrangements involved in the mechanism and the ease of overcoming this barrier depends on the temperature and the applied strain rate. Although it must also be remembered that other processes may be occurring whose energy barriers are lower than ΔH.

The values of ΔH of 152 KJ/mole to 144 KJ/mole shown for figure 4.7., for the 1% Cu to 4% Cu alloys are close to the reported[68] values for high temperature creep and vacancy self diffusion in aluminium of 150 KJ/mole and 142 KJ/mole respectively. The values are therefore consistent with the observation that plastic flow may be regarded as a mass transfer process[100] where the rate controlling thermally activated mechanism is diffusion controlled. The rate controlling step may be considered to be the climb of edge dislocations and the motion of jogged screw dislocations by the migration of vacancies[68,79]. Above 4% Cu figure 4.7. shows ΔH decreases to a value of 130.3 KJ/mole in the 4.8.% Cu alloy, whilst the 3.8% binary alloy shows the lowest value 127.6 KJ/mole. A decrease in the activation energy below that for self diffusion in aluminium implies a change in the rate controlling step although the relatively small decrease does not suggest a change in the restoration process to eg dynamic recrystallization, which is confirmed by the recovered substructures observed in similar Al-Cu alloys over the entire hot working range.[25,26,29] The results from the graphical analysis in Table 4.4. also show that a lower than average value of ΔH is obtained at the highest test temperature in all the alloys, whilst the results for the 2014 alloy, show that inclusion

of the 500 deg.C data lowers the activation energy by approximately 10 KJ/mole but does not significantly alter the flow stress characteristics.

A feature of virtually all heat treatable alloys is that the solid solution content increases with temperature. This is perhaps best shown in the present series of alloys by the microhardness vs Ln Zp data plotted in figure 4.14. from the 1% Cu and 5% Cu alloys in the naturally aged condition. Microhardness measurements were taken in the periphery of the specimens and in the centre of the gauge length, the position corresponding to the nominal flow conditions and highest temperatures. It is evident that during the presoak period of five minutes and during testing sufficient solute is taken into solution above 400 deg.C in the 5% Cu alloy and $\sim$430 deg.C in the 1% Cu alloy to result in an appreciable age hardening reaction. Below these temperatures the hardness increases with Ln Zp as the subgrain size decreases and the substructure strengthening increases.

During creep testing of binary aluminium solid solution alloys previous workers[151] have also observed that a change in the rate controlling recovery mechanisms to viscous glide can occur. During glide controlled creep the interaction of solute atom atmospheres with moving dislocations acts as the rate controlling process. The activation energy for diffusion of the solute species determines the activation energy for creep, where the stress exponent n is normally found to be in the range of 3-4 as opposed to 4-5 in pure metals. The reported[33] activation energy for diffusion of Cu in Al of 135 $\pm$ 11KJ/mole and a stress exponent n = 3.9. in the binary alloy indicates that at the low stress levels associated with the binary alloy viscous glide may still be involved in the rate controlling mechanism in the hot working range. In the 2000 series alloys although the

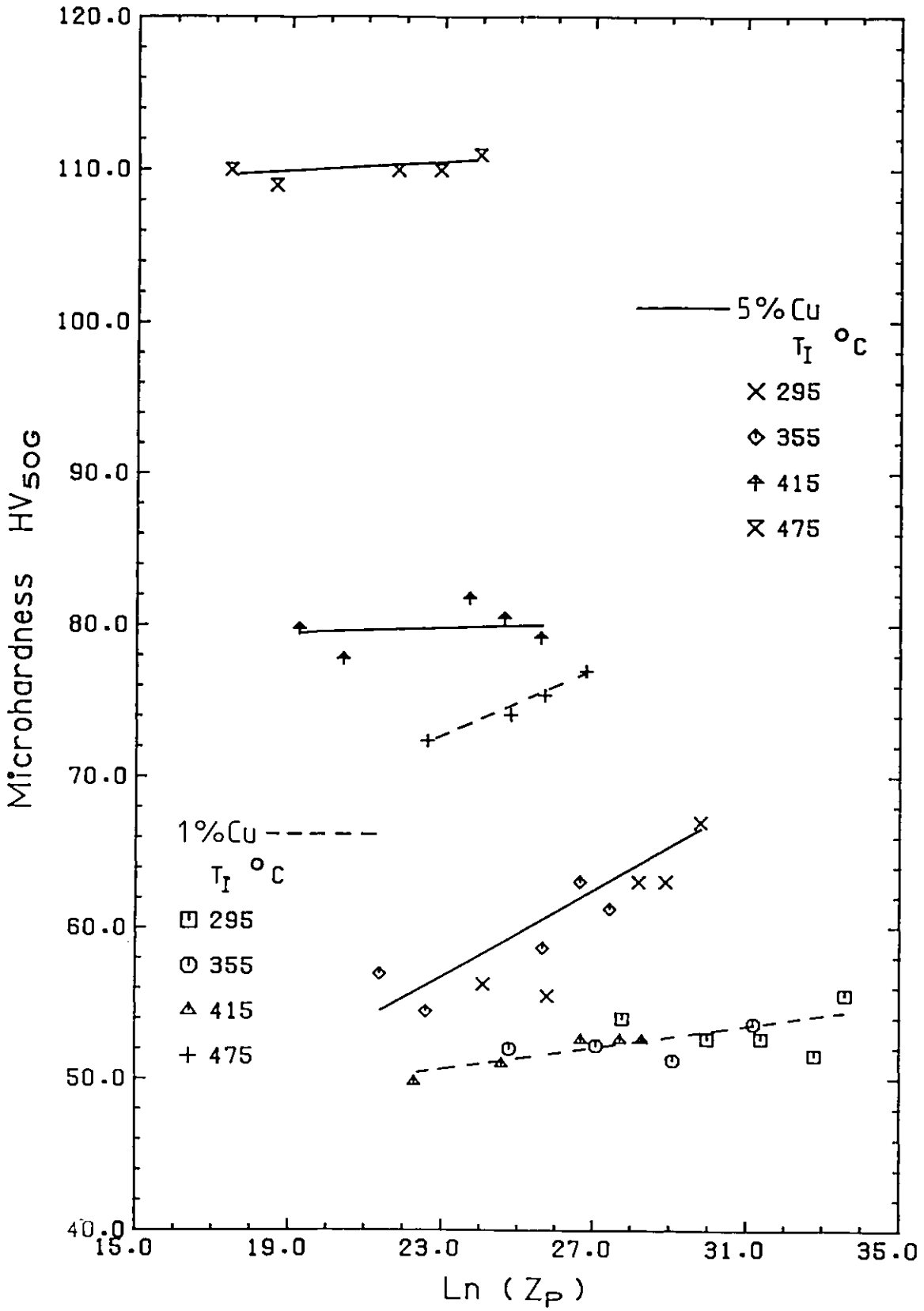


Figure 4.14 Microhardness vs LnZ_p in the 1% Cu and 5% Cu torsion specimens

increase in solid solution content with temperature and initial copper content can be related to the decrease in ΔH shown in graphical analysis and by the 2014 alloy, the total flow stress and hence flow stress characteristics are as much dependent on the minor alloying additions, which is reflected in the large differences in α and n between the binary and 2014 alloy. The difference in flow stress between the binary alloy and the equivalent 2000 series alloy extrapolated from figures 4.11. and 4.13 is shown more clearly in figure 4.15. Since the solid solubility of Cu in Al is reported[35] to be little changed by the presence of Mg, Mn or Si in the 2014 alloy, the marked increase in flow stress can be associated with the intermetallic particles formed by the above elements noted in section 1.2. The presence of a second phase particle distribution can increase the flow stress by reducing the subgrain diameter to the interparticle spacing and so increase the substructure strengthening according to equation 1.7. The greater increase in hardness at high Zp in the 5% Cu alloy in figure 4.14. may well be associated with a decrease in interparticle spacing with an increase in θ or S phase present at low temperatures. Other workers[118] have also considered that the geometrically necessary dislocations generated to maintain the continuity between the deforming matrix and the coarser particles can also act as sources of internal stress, which suggests the flow stress should be a function of the total dislocation density and hence the particle distribution, rather than simply the subgrain size as equation 1.7 implies. The relationship between the hot worked structure and flow stress will be discussed in further detail in section 4.3.5.3. It should of course be noted that these phenomena will also apply to the binary alloy especially at high Z due to the presence of θ precipitated out of solution during cooling from the homogenization temperature. However the presence of the intermetallic particles in the 2000 series alloys are as

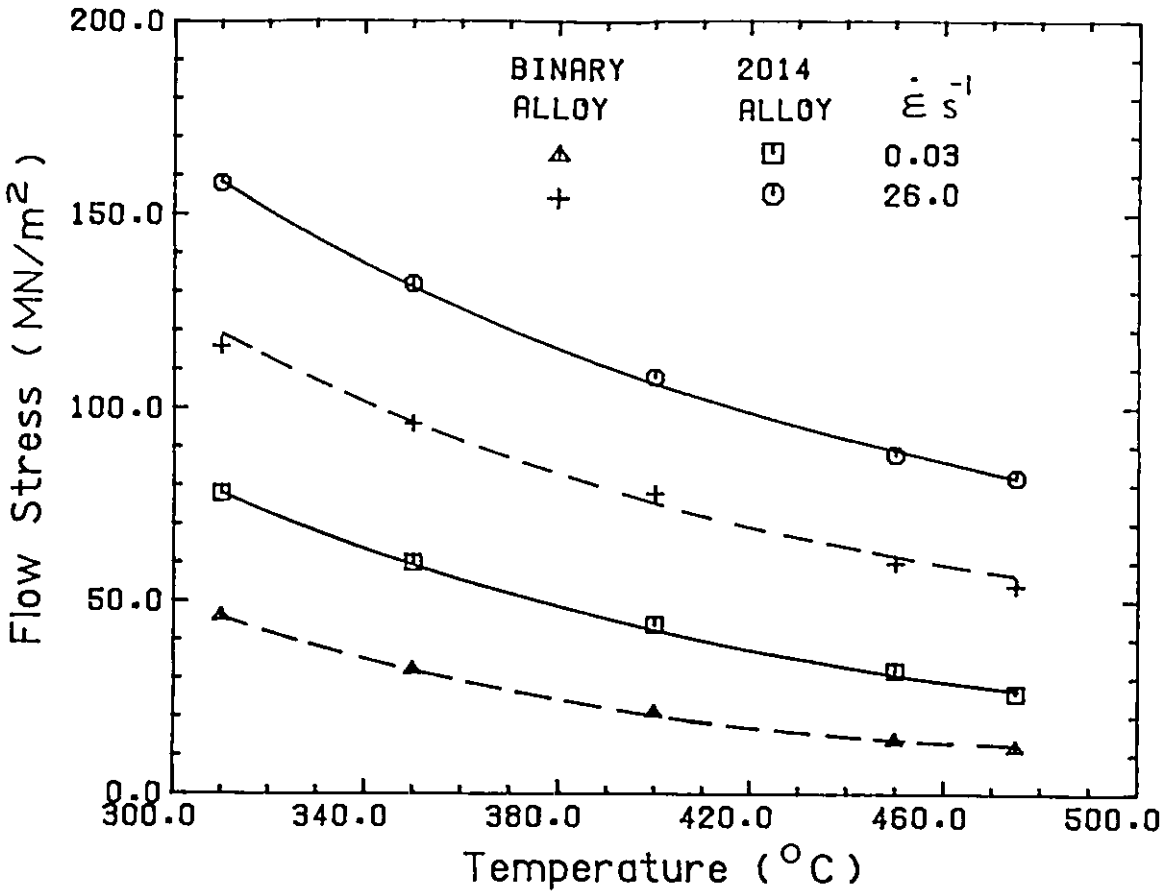


Figure 4.15 Flow stress characteristics of the 2014 and 3.8% Cu binary alloy

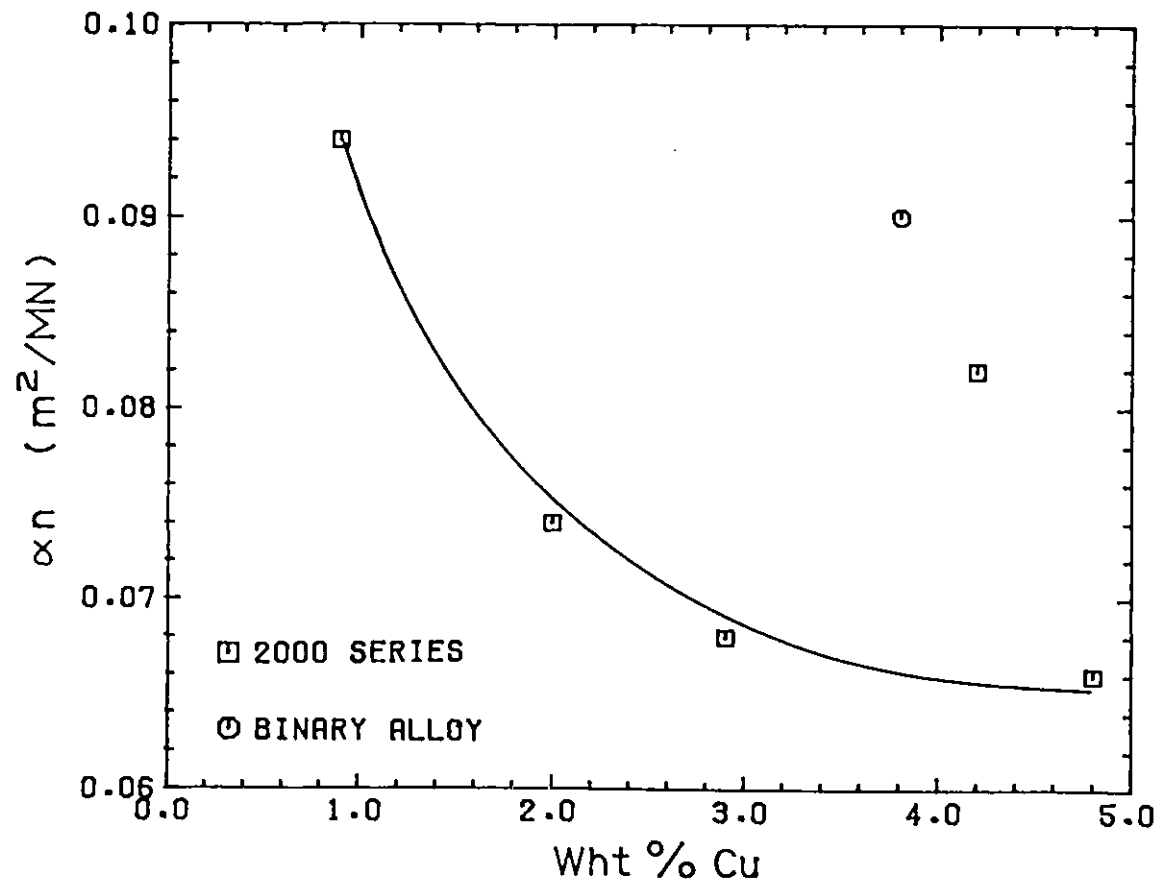


Figure 4.16 The variation of ∝n with alloy content

effective in increasing the flow stress as the total weight percent copper in the binary alloy since the flow stresses extrapolated at 0% Cu are similar to the flow stresses in the binary alloy.

The difficulty in interpreting the rate controlling mechanism from the values of ΔH is that the remaining empirical constants A, α and n do not have a simple physical interpretation. Jonas et al[68] established from a comparison between rate theory and the general hot working equation that at high stress levels $\alpha\sigma > 1.2$. A may be regarded as a structure factor related to the frequency with which events occur and $\propto nkT$ an apparent activation volume. An increase in the structure factor with stress has been related to an increase in the mobile dislocation density or in the density of activatable sites[68]. Whilst an increase in stress results in a decrease in activation volume since the activation volume represents the size of the obstacle opposing dislocation motion and may also be regarded as a measure of the effectiveness with which the applied stress aids dislocations to overcome the barrier. However the rate theory utilized by Jonas assumes there to be only one type of obstacle of constant size and hence activation energy which is extremely unlikely considering the complexity of the work hardening mechanisms involved and the change in ΔH with temperature range shown by results for the 2014 alloy. Therefore the physical interpretations based on such a comparison for hot working constants obtained over a wide range of temperatures and strain rates can only be regarded as approximate especially in relation to complex alloy systems such as the commercial 2000 series alloys.

The variation of A with weight % copper is shown in figure 4.8. It is apparent that A shows an identical variation with alloy content as ΔH in figure 4.7. which is perhaps not surprising considering the form of the stress equation derived from the general hot working equation:-

$$\sigma = \frac{1}{\alpha n} \text{Ln} \left[(Z/A)^{1/n} + \sqrt{(Z/A)^{2/n} + 1} \right] \qquad 2.5.$$

The hot working constants listed in table 4.7. show a similar trend, A decreasing with ΔH. The results in figure 4.8. show that A decreases with Cu content in the 2000 series alloys and hence increase in stress, whilst A decreases with decrease in stress in the binary alloy. Clearly the absolute value of A is not a function of the flow stress characteristics, but as the results in figures 4.7. and 4.8. indicate,the physical significance of the constant is related to the rate controlling mechanism during deformation. Assuming that the rate controlling process is diffusion controlled, then the values of A of 10^{11} to $10^{12} s^{-1}$ in the low Cu alloys below 3% Cu and the alloys listed in table 4.7. with similar values of ΔH and A may be related to the self diffusion of vacancies, whilst an increase in solid solution content with temperature in the high Cu alloys reduces A to 10^{9} to 10^{10} in a similar manner to the heat treatable alloys 7075 and 5456 listed in table 4.7.

The variation of α with copper content in figure 4.9. shows that α decreases with Cu content in 2000 series alloys and increases in the binary alloy consistent with it's relationship to the flow stress in equation 2.5. Figure 4.10. shows only a small variation in n from the 2% Cu to 5% Cu alloys but an increase in the 1% Cu alloy and a large decrease in the binary alloy. The strain rate and temperature dependencies of the flow stress are clearly not a simple function of the copper content and as the results from the 2014 alloy show are also temperature dependant or perhaps more precisely stress dependent, α and n increasing with the decrease in stress range considered. The presence of the intermetallic particles in the 2000 series alloys

results in a decrease in the temperature compensated strain rate sensitivity represented by 1/n, consistent with the decrease in strain rate sensitivity shown in figure 4.5. The results in figure 4.16. show that the description of $\propto n$ as the activation volume is consistent with the values in the 1% Cu and binary alloy which exhibit a similar stress range whilst a small decrease from the 3% Cu to the 5% Cu alloy indicates that above 3% Cu an increase in Cu content results in only a small increase in the size of the obstacles opposing dislocation motion. Again it is apparent from the value for the 2014 alloy that $\propto n$ is stress dependent and as expected increases with decreasing stress.

It is evident from the results in figures 4.7. to 4.10 that there are basic differences in the interpretation of the constants due to their relationships to the flow stress shown in equation 2.5. ΔH and A may be regarded as material constants related to the diffusion characteristics of the matrix and hence the rate controlling mechanism, whilst $\propto$ and n describe the flow stress characteristics in terms of the strain rate and temperature dependencies and as such are highly dependent on the stress range considered due to the large variation in strain rate dependency shown in the graphical analysis. The fact that all the constants may be regarded as temperature dependent raises the question as to whether a single set of hot working constants can be used to adequately describe the complex variation in stress over a wide range of strain rates and temperatures, since as already noted in the 2014 alloy slightly different flow stress characteristics were predicted by the change in hot working constants. Tutcher[27] investigated this phenomena in an Al-Mg alloy 5456 by defining an equation of the form:-

$$\exp \dot{\varepsilon} \left[\frac{\Delta Hf(T)}{RT}\right] = Af(T)\ \mathrm{Sinh}(\propto f(T)\sigma)^{n f(T)} \qquad 4.2.$$

The accuracy of the equation was found to be largely dependent on the individual temperature dependencies established from the graphical analysis, where it was found that the overall correlation was no better than that assuming temperature independent constants.

In conclusion therefore the dependence of flow stress on copper content and particle distribution shown in figures 4.11. to 4.13. and 4.16. is not a simple function of an increase in flow stress with Cu content over a wide range of temperatures and strain rates due to the complex change in the work hardening mechanisms associated with the nature of the particle size, distribution and solid solution content which change with initial Cu content, and temperature. The overall situation is not helped by the fact that although the general form of the empirical equations are well known and relatively easy to establish, the recovery mechanisms and dislocation dynamics involved during hot working are not fully understood.

4.1.4. STRAIN DEPENDENCY OF THE HOT WORKING CHARACTERISTICS

The question of stress strain dependency is often ignored in most hot working studies since the high strains involved mean that steady state conditions are normally achieved where the flow stress is effectively strain independent. However the stress strain characteristics of the material prior to the onset of steady state flow must influence the initial load characteristics and the size and shape of the extrusion deformation zone and hence the temperature and strain rate distribution within it. During extrusion previous workers[76,115] have shown that the quasi static deformation zone is not fully established at peak load and hence the dependence of the extrusion load on the stress strain characteristics may even be greater, such that any realistic model of the total extrusion pressure may also

require constitutive equations describing the stress strain temperature and strain rate dependency.

In the present work the stress strain-rate temperature relationships have been established at homologous strains of 1.0, 0.75 and 0.5 using the general hot working equation as described in section 2.2.1., the resulting hot working constants are shown in table 4.1. and plotted in figures 4.17 to 4.19. The constant A has not been plotted since it shows no consistent variation with strain in any of the alloys.

An average correlation coefficient of greater than 0.98 to some extent justifies the assumption made in section 2.2.1. that prior to steady state deformation the rate controlling processes are still thermally activated and can therefore be described by the Sinh relationship, although as figure 4.17 shows the activation energy associated with the rate controlling process decreases with strain, the strain dependency decreasing with copper content. The decrease in ΔH can be associated with a decrease in thermal activation required to overcome the short range obstacles opposing dislocation motion, as the dislocation density within the developing subgrains decreases with strain. The greater decrease in ΔH with strain in the low copper 2000 series alloys can be related to the decrease in work hardening shown in figures 4.1. to 4.3. and hence an increase in the stress strain dependency. The change in stress strain characteristics with copper content is shown more clearly in figure 4.20. which shows the incremental increase in stress from $0.5\ \varepsilon_H$ to $1.0\ \varepsilon_H$ predicted by the hot working constants at a strain rate of 26 sec^{-1}, the difference decreasing with Z in all the alloys. However it is evident from this figure that the binary 4% Cu alloy shows the greatest stress strain dependency, although as figure 4.17. shows the strain dependency of ΔH is similar to the 5% Cu

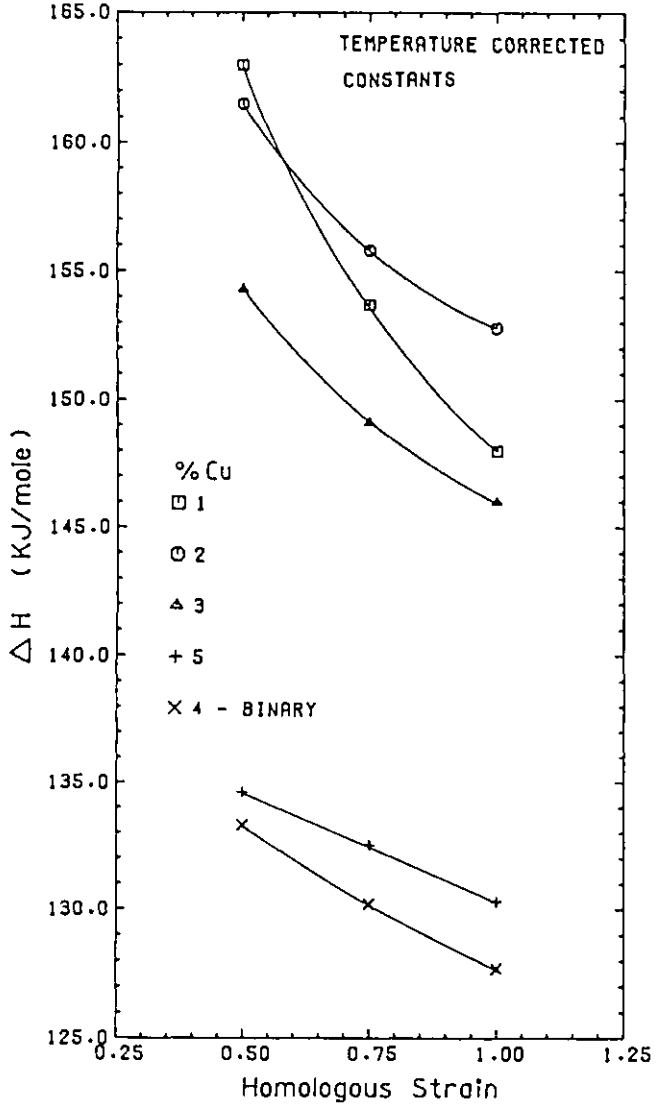


Figure 4.17 ΔH vs ε_H

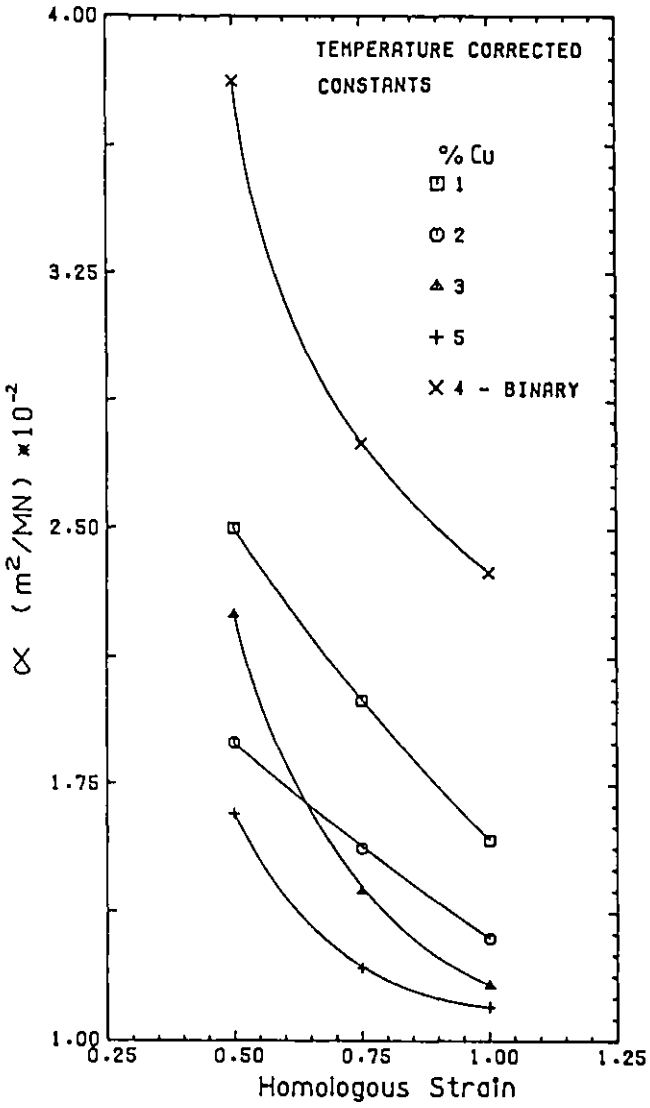


Figure 4.18 $\propto$ vs ε_H

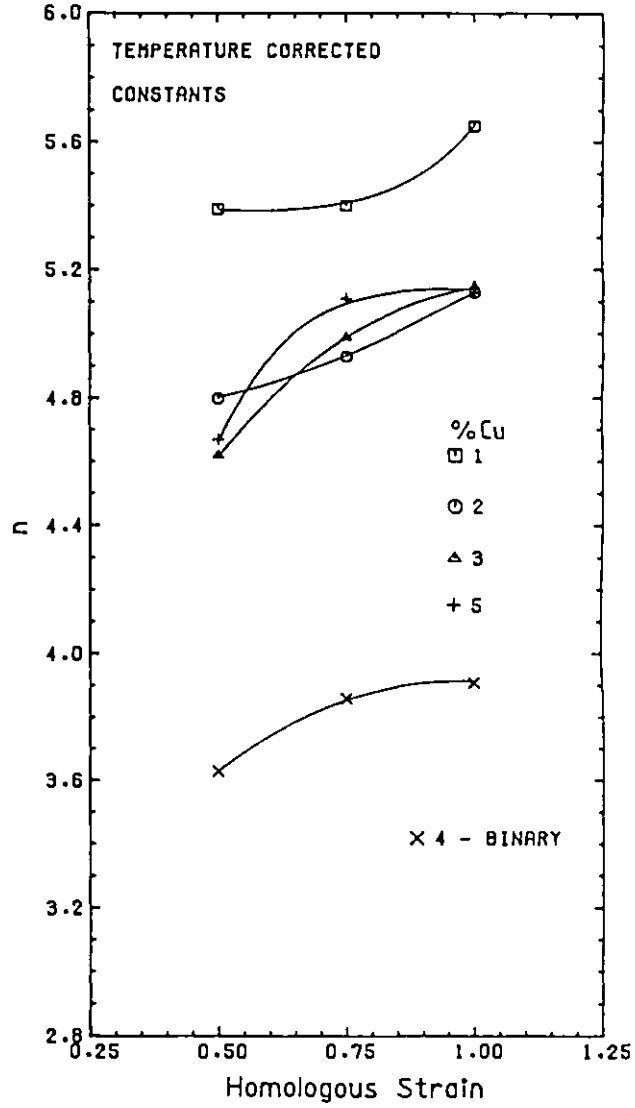


Figure 4.19 n vs ε_H

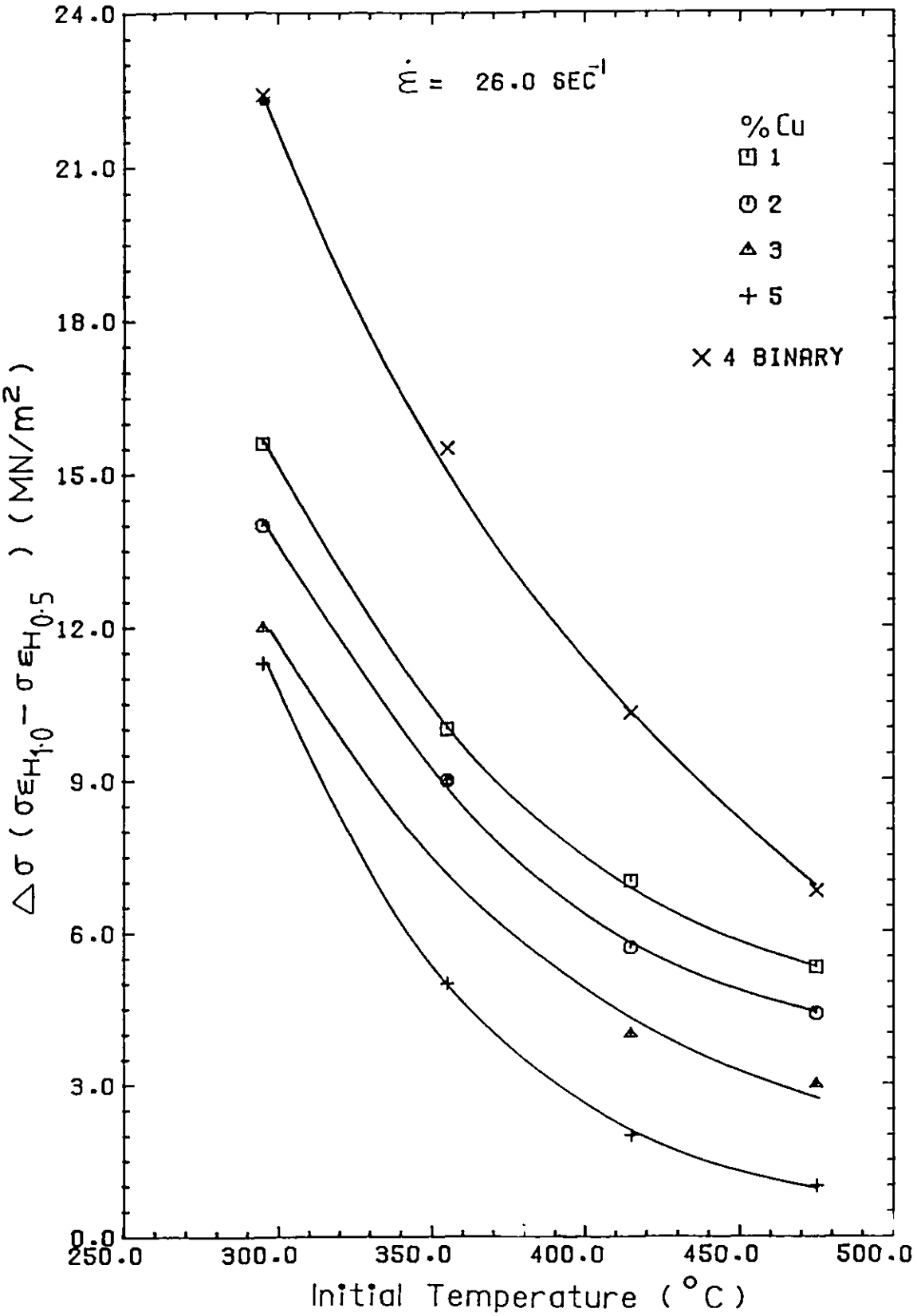


Figure 4.20 Incremental increase in flow stress from 0.5 ε_H to 1.0 ε_H at $\dot{\varepsilon}$ = 26.0 sec^{-1}

2000 series alloy. This therefore implies that alloys containing an appreciable solid solution content the rate controlling mechanism prior to steady state is similar to that operating during steady state deformation, although the stress-strain characteristics are dependent on the second phase particle distribution, the increase in particle content increasing the degree of strain hardening and hence reducing the stress strain dependence above 0.5 ε_H. What is perhaps an encouraging feature of figure 4.20. is the relatively high correlation between $\Delta\sigma$ and temperature considering the change in torque twist characteristics with Z shown in figures 4.1. to 4.3., and tends to confirm the assumption made in the original analysis that the deformation mechanism may be considered to be consistent at equivalent values of homologous strain. This is of course an important point to note since any consideration of the physical significance of the variation of the hot working constants with strain must be made on the basis of this assumption.

The decrease in α with ε_H shown in figure 4.18. can be directly related to the decrease in stress with strain, which as figure 4.20. shows decreases from the 1% Cu to 5% Cu alloy and is greatest in the binary alloy. The high value of α in the 3% Cu alloy at $\varepsilon_H = 0.5$ is probably related to the lower than average correlation of 0.96. Figure 4.19. shows that n increases with strain in all the alloys, the rate of increase at low strains increasing with Cu content. Since n is inversely proportional to the temperature compensated strain rate sensitivity, the above trends can be associated with an increase in the dislocation annihilation rate and substructural development with strain, which reduces the effect of the dislocation generation rate on the applied stress and hence the strain rate dependency whilst in the low Cu alloys the large decrease in ΔH shown in figure 4.17. results in only a small change in n.

The random variation of the constant A with ε_H shown in table 4.1. prevents any conclusion from being drawn as to its dependency on strain, although the fact that it shows no consistent variation is surprising due to its dependence on ΔH during steady state deformation shown in the previous section and its description from rate theory as a frequency term, where one would have expected a more consistent variation with strain as the frequency with which events occur changes in line with the change in dislocation generation and annihilation rate.

It should of course be noted that for all the alloys the increase in temperature with strain will also be instrumental in changing the absolute values of the constants which as table 4.1. shows results in a decrease in ΔH and A and an increase α .

The results in figures 4.17. to 4.19. do show that it is possible, perhaps with a constant value of A, to define a constitutive equation based on the Sinh relationship in the form:

$$\sigma = f(\alpha, n, A, \Delta H, \varepsilon_H) \qquad 4.3.$$

However as noted in section 2.2.1. the present analysis relates to the homologous strain and not the true strain in each individual test. Therefore the relationship between the strain to peak and the process conditions must be established for the above relationship to be of any practical use. Several relationships have been considered based on the individual temperature and strain rate dependencies and the Zp values but with no real success. The stress strain relationships reviewed by Sellars[74] were also utilised but again no consistent correlation was found. The highest correlation that could be achieved in any of the alloys was established in the 2% Cu alloy using an equation

of the form:

$$\varepsilon_p = 0.85.10^{-3} \quad \sigma^{1.34} \qquad \dot{\varepsilon}_{cc}^{0.684} \qquad 4.4.$$

The results in figure 4.21. show the extent of the correlation and the standard error associated with the repeat tests. The above equation if applicable to other alloy systems could be used to evaluate the peak strain corresponding to a specific strain rate and temperature, and thus determine whether the steady state has been achieved and if not the relevant value of homologous strain.

The principal limitation in the present analysis is made in the assumption that during testing of a solid torsion specimen:

$$\frac{\varepsilon}{\varepsilon_p} \simeq \frac{\theta}{\theta_p} \qquad 2.4.$$

At θp the surface of material will be strain independent, but due to the radial variation in strain the inner elements must be strain dependent, and therefore the location of the exact element corresponding to εp will be at an intermediate value of θ and as such the above relationship can only be regarded as approximate. The problem is therefore to evaluate the true value of εp. One solution would be to obtain values of θp from a separate set of torsion tests using thin walled specimens, since the radial variation in strain is far less, where the value of θp should be lower than those obtained from solid specimens at equivalent strain rates and temperatures.

In conclusion therefore although the stress strain characteristics can be described at increments of homologous strain above $\varepsilon_H = 0.5$ using the general hot working

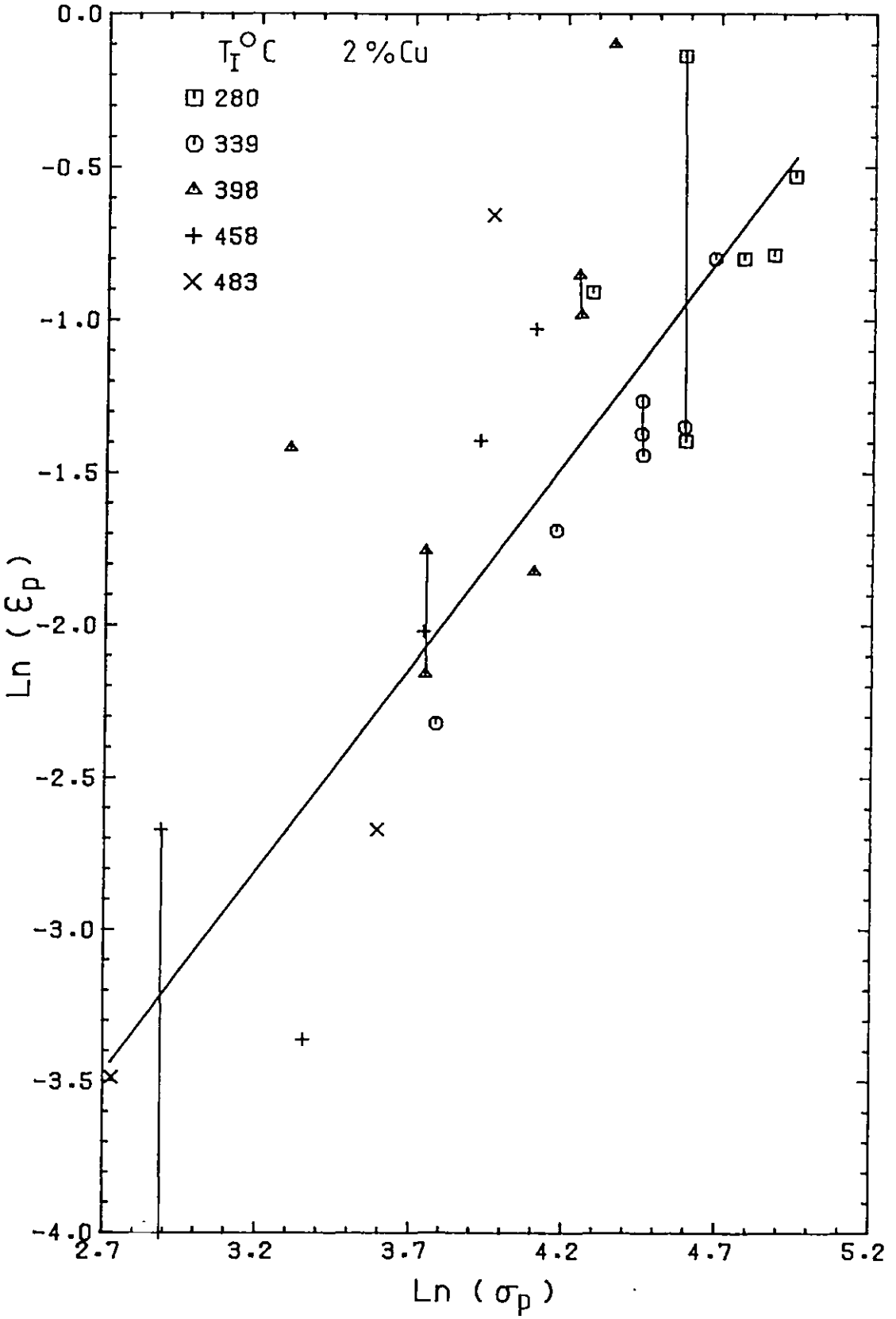


Figure 4.21 $Ln\sigma_p$ vs $Ln\varepsilon_p$ in the 2% Cu alloy

equation, the true strain corresponding to the attainment of steady state flow is unlikely to equate to θp due to the radial variation in strain associated with a solid torsion specimen. It should of course be noted that the temperature rise model also assumes $\theta p = \varepsilon p$, which may therefore result in a slight underestimation of the temperature rise during testing since the measured $\theta p \geqslant \varepsilon p$, although this is unlikely to have a significant effect due to the small strains to peak shown in appendix I.

4.1.5. THE EFFECT OF ALLOY CONTENT ON THE TORSION DUCTILITY

During high temperature torsion testing the normal mode of failure involves the formation of pores by grain boundary sliding, where propagation by pore coalescence and tearing is promoted by the high shear stresses which exist during testing[69]. The formation of subgrain boundaries during dynamic recovery is reported[69,74,75] to reduce grain identity, so that fracture tends to occur via nucleation at grain boundary junctions or as the result of the linking of internal voids nucleated at inclusions.

In the present work the only specimens which failed were those tested at the highest strain rate of 26 s^{-1} since it was not possible to stop the tests at peak torque, the average time to failure being less than 0.2 seconds. The effect of alloy content and test temperature on the torsion ductility measured by the revolutions to failure is shown plotted in figure 4.22. It is evident that below 350 deg.C the ductility decreases with temperature as the flow stress decreases, and decreases with Cu content as the particle content increases. Figure 4.23. shows that in the 2000 series alloys below an initial temperature of 350 deg.C the revolutions to failure can be directly related to the flow stress at peak via an equation of the form:

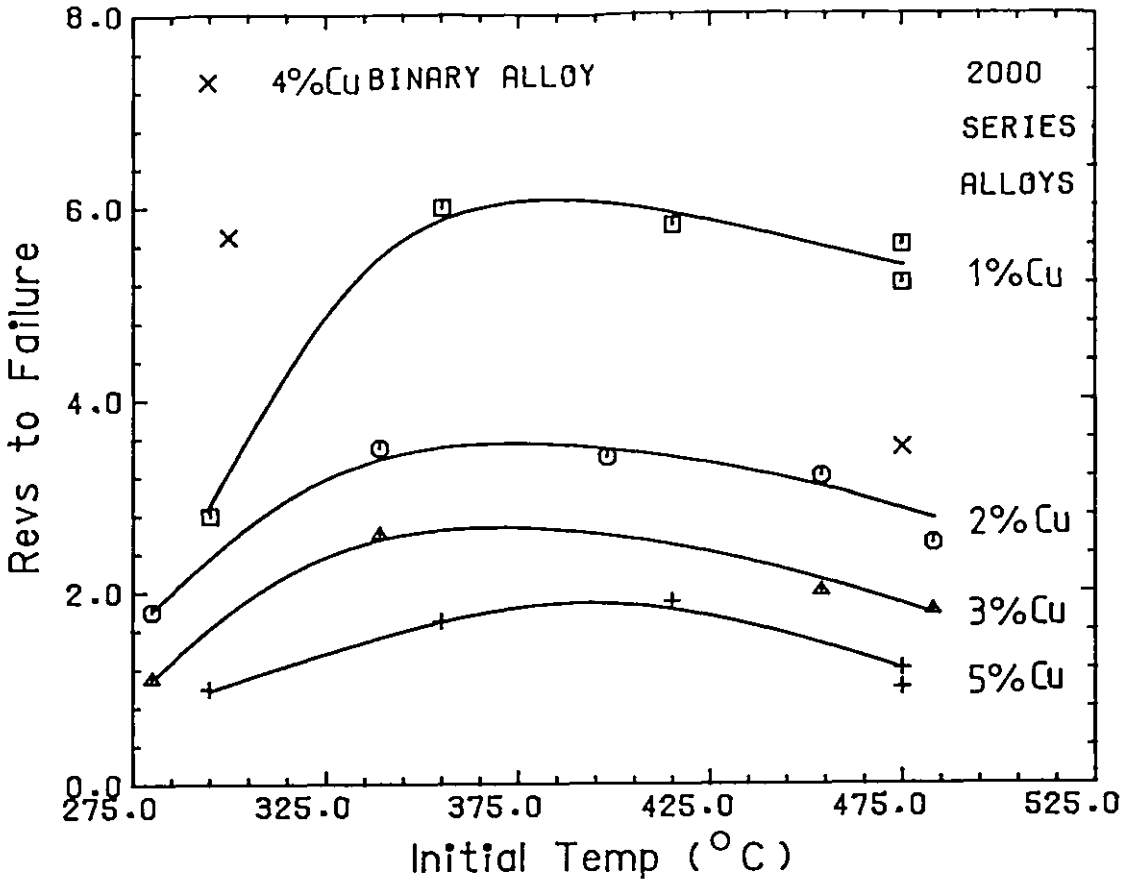


Figure 4.22 The variation in torsion ductility with temperature and alloy content at $\dot{\varepsilon} = 26.0\ sec^{-1}$

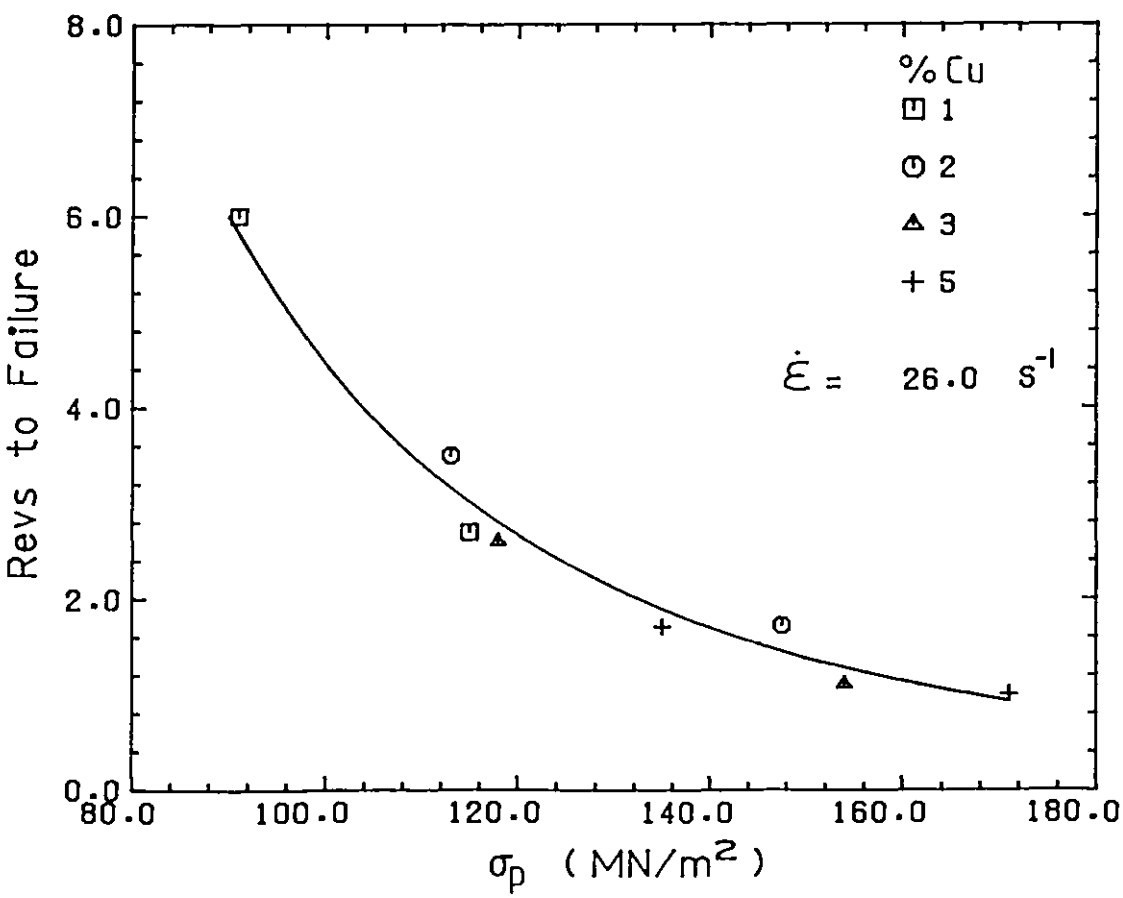


Figure 4.23 The variation in torsion ductility with flow stress at $\dot{\varepsilon} = 26.0\ sec^{-1}$ below 350°C

$$Rev_f = 2.589.106\,\sigma^{-2.88} \quad cc\ 0.976 \qquad 4.5.$$

The high correlation is perhaps surprising considering the variation in copper content and may be explained by the fact that although crack initiation is normally considered[69] to be enhanced by an increase in particle size and distribution and therefore Cu content, crack propagation and hence the total ductility is also dependent on the intermediate sized particle distribution associated with the Mg, Mn, Si and Fe.

Above 350 deg.C all the alloys show a decrease in ductility with temperature and Cu content, a similar decrease in ductility with temperature has also been reported in heat treatable Al-Cu, Al-Mg and Al-Zn-Mg alloys[27-29,75]. It is evident that the decrease in ductility at high temperatures coincides with the increase in solid solution content predicted by the microhardness data in figure 4.14. An increase in solid solution content is generally considered[69] to result in a decrease in ductility due to the increase in flow stress, and the retarding affects on the grain boundary migration due to segregation of the solute atom atmospheres at the grain boundaries. The latter effect is likely to be more significant in the present series of alloys since the ductility decreases with decreasing flow stress in the high temperature range.

The temperature rise during testing at initial temperatures close to the eutectic temperature has also been shown[28] to result in extensive eutectic melting and a subsequent decrease in ductility, although this phenomena was not observed in the present work.

The pronounced effect of the particle distribution associated with the Mg, Mn and Si in the 2000 series alloys

is shown in figure 4.22. by the 70% increase in ductility in the binary alloy at an equivalent flow stress at 300 deg.C, and a higher ductility than the 2% Cu Alloy at 475 deg.C, whilst between 330 deg.C and 430 deg.C failure does not occur after 10 revolutions. It therefore seems likely that the presence of the intermetallic particles and the subsequent decrease in the interparticle spacing may enhance both crack initiation and propagation via the linking of internal voids nucleated at such particles[75].

Despite the differences between the stress states and hence failure mode in torsion testing and those found in most hot working processes, the torsional ductility is often used as a measure of the formability[74] and as such the results in figure 4.22. indicate that the formability of the 2000 series alloys decreases markedly below 1% Cu and with the addition of the minor alloying elements Mg, Mn and Si.

4.2. EXTRUSION DATA ANALYSIS

A total of eight separate extrusion matrices have been carried out to investigate the effect of Cu content and process conditions on the direct load characteristics of the 2000 series alloys and the effect of extrusion mode and billet preheat treatment on the load characteristics of the 2014 alloy. A temperature range of 500 deg.C to 300 deg.C, ram speeds of 14 mm/s to 4 mm/s and extrusion ratios from 150:1 to 10:1 have been used. The strain rate and temperature rise during extrusion have been calculated using the theory outlined in section 2.3., the relevant values of flow stress and LnZ have been evaluated using the steady state temperature corrected hot working constants shown in table 4.1.

4.2.1. EXTRUSION PARAMETER MEASUREMENT

Before each extrusion run the following parameters were noted:-

Furnace Temperature, Extrusion Ratio
Billet Dimensions, Container Temperature

The load, oil pressure, ram displacement curves and the billet transfer time enabled the following data to be measured:-

Maximum Load, Minimum Load, Initial Billet Temperature, Ram Speed, Distance to Peak Load, Size of Peak, Maximum Oil Pressure, Minimum Oil Pressure

A full listing of the above data and the relevant calibration curves are shown in appendix II and appendix V. Values of initial, peak and final Z and the corresponding

flow stress data are also listed in appendix II.

It should be noted that the oil pressure data has not been used in the extrusion data analysis since the use of by pass valves at low ram speeds greatly reduces the oil pressure at constant loads. However, by calibrating the press at constant ram speeds it was found that the ram pressures were approximately 10% lower than the oil pressures and could therefore be used as a useful check on the accuracy of the load displacement curves.

4.2.2. LOAD DISPLACEMENT CURVES

Examples of the load displacement curves for direct extrusion of the 1% Cu, 3% Cu and 5% Cu alloys at high and low Z conditions are shown in figure 4.24. All the curves show that the initial stage of extrusion is characterised by a rapid increase in load as the billet is upset to fill the container. It should however be noted that some extrusion does occur during this stage[76]. The load gradually decreases after the peak load as the billet length decreases and hence the friction is reduced. At high Z conditions i.e. low extrusion temperatures and high strain rates the decrease in load is accentuated by the larger temperature rises associated with the work done during extrusion, which increases with increasing Cu content. At low Z conditions the temperature rises are not as significant and therefore a smaller decrease in load results. The above observations are confirmed by the final temperature rises predicted by the integral profile model which increase with Cu content from 140 deg.C to 170 deg.C, and 70 deg.C to 90 deg.C in the high Z and low Z extrudes shown in figure 4.24.

It is evident from figure 4.24. that all the alloys show a peak in the load displacement curves at the maximum load which tends to increase with increasing Z and

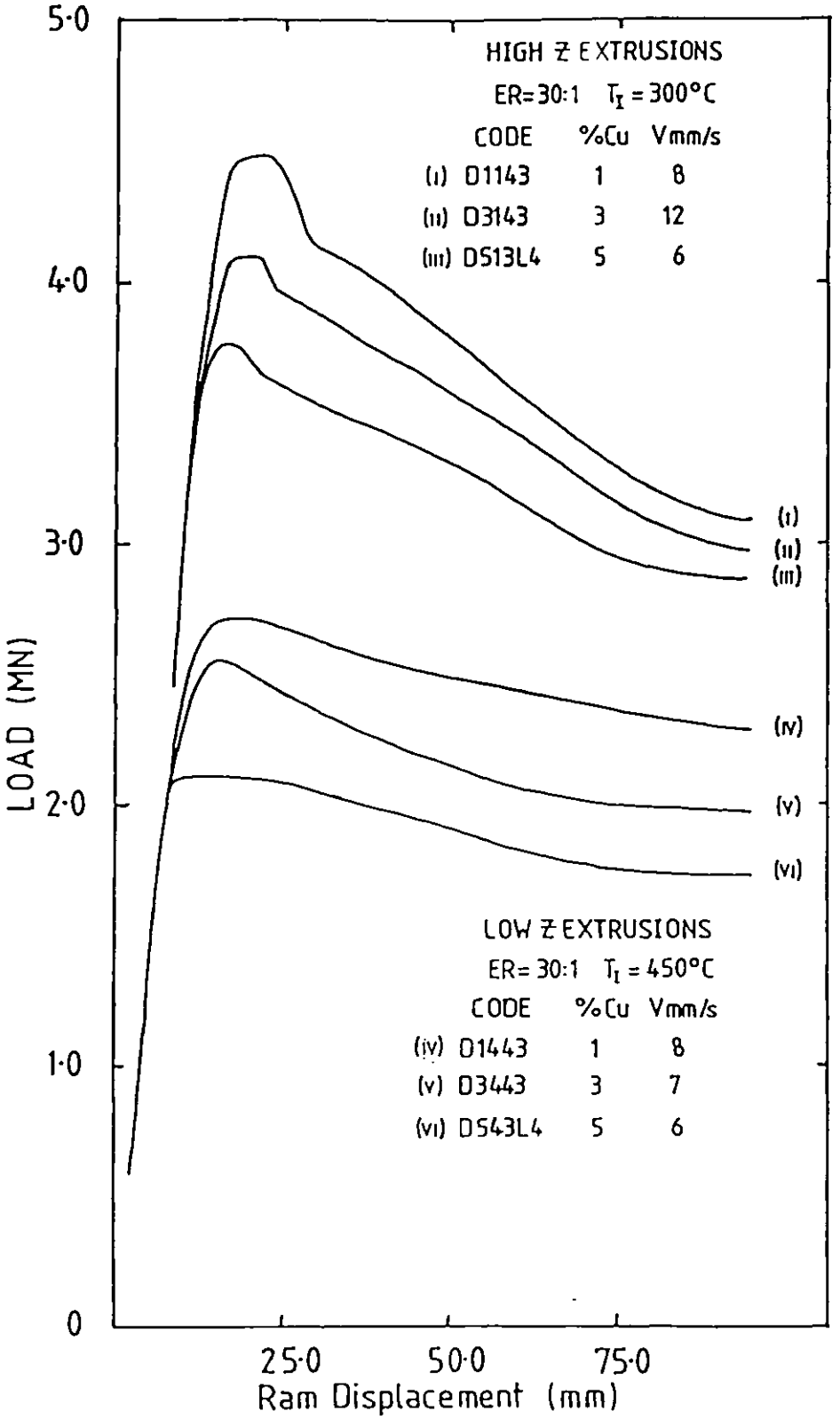


Figure 4.24 Direct load displacement loci - 1% Cu, 3% Cu and 5% Cu 2000 series alloys

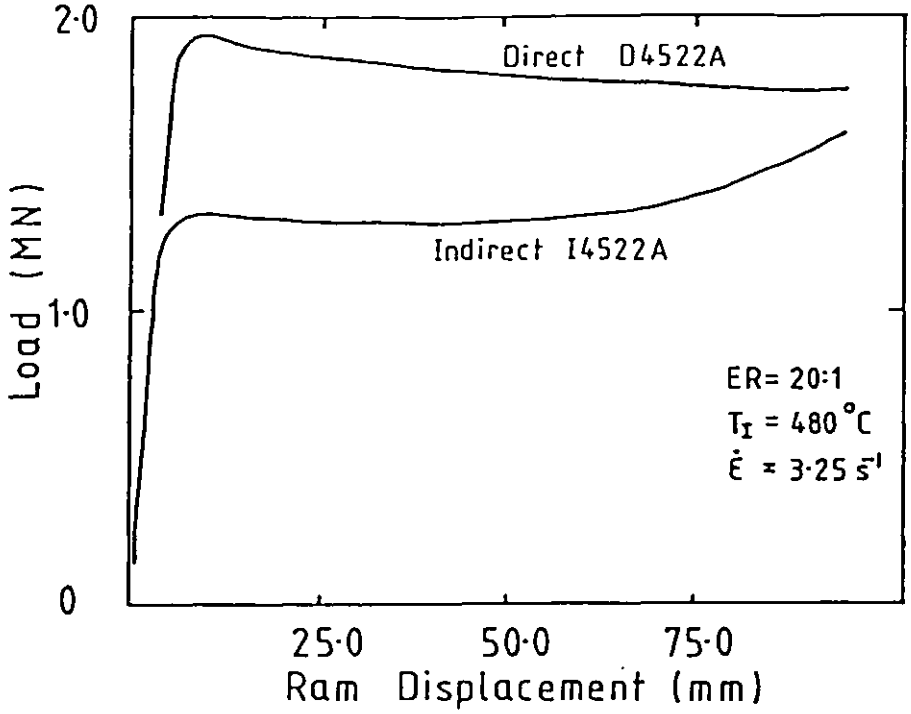


Figure 4.25 Direct and indirect load displacement loci - 4% Cu 2014 alloy T_I = 480°C

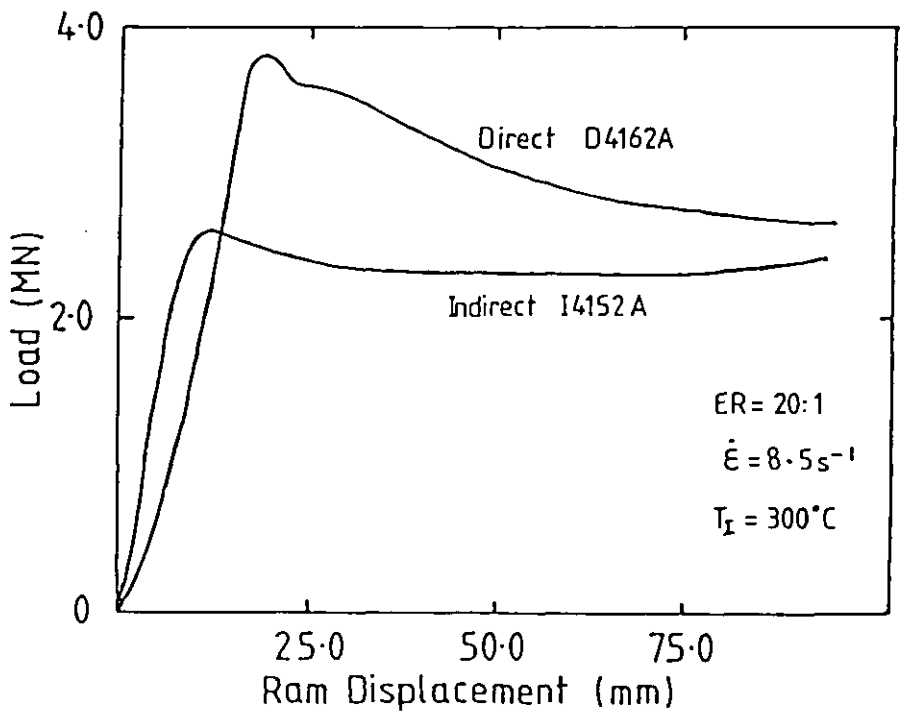


Figure 4.26 Direct and indirect load displacement loci - 4% Cu 2014 alloy T_I = 300°C

increasing Cu content. The size of the peak is an important factor with respect to the available press capacity and its characteristics will be discussed in further detail in section 4.2.8.

The effect of extrusion mode is shown in figures 4.25. and 4.26.for the direct and indirect extrusion of the 4%Cu 2014 alloy at high Z and low Z conditions. It is clear that the loads developed during indirect extrusion are lower due to the removal of the billet container friction which also results in a small variation in load with ram displacement. It is also noticeable that the size of the peak decreases. At high extrusion temperatures previous workers[25-29] have reported that heat losses during direct and indirect extrusion can result in an increase in load when the container temperature was maintained at 300 deg.C. This effect has largely been eliminated in the present work by the use of a container temperature 50 deg.C below the billet temperature, although figures 4.25. and 4.26. do show a slight increase in load during indirect extrusion.

4.2.3. VARIATION OF PEAK PRESSURE WITH EXTRUSION RATIO

The effect of Cu content on the peak pressure versus Ln extrusion ratio relationships is shown in figures 4.27. and 4.28. for extrusion temperatures of 350 deg.C and 450 deg.C, with ram speeds between 7-11 mm/s. A constant temperature has been assumed for each curve, which may not be strictly true due to the heat losses during transfer. However, with the container 50 deg.C below the billet temperature the heat losses will be relatively small as shown by the initial billet temperatures in appendix II.

The results in figures 4.27. and 4.28. show that for each alloy and temperature the increase in peak pressure with Ln ER is more or less linear which is confirmed by the

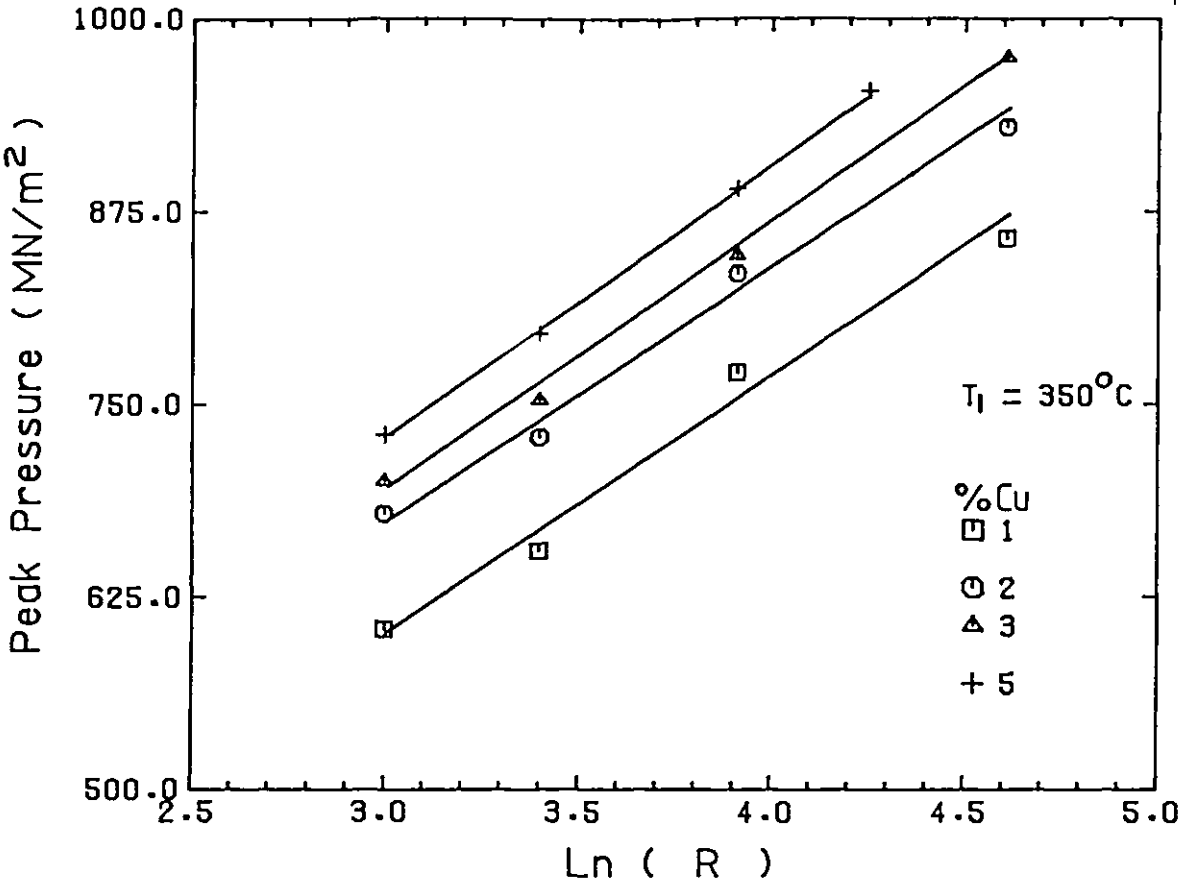


Figure 4.27 Peak pressure vs Ln(R) T_I = 350°C direct extrusion of 2000 series alloys

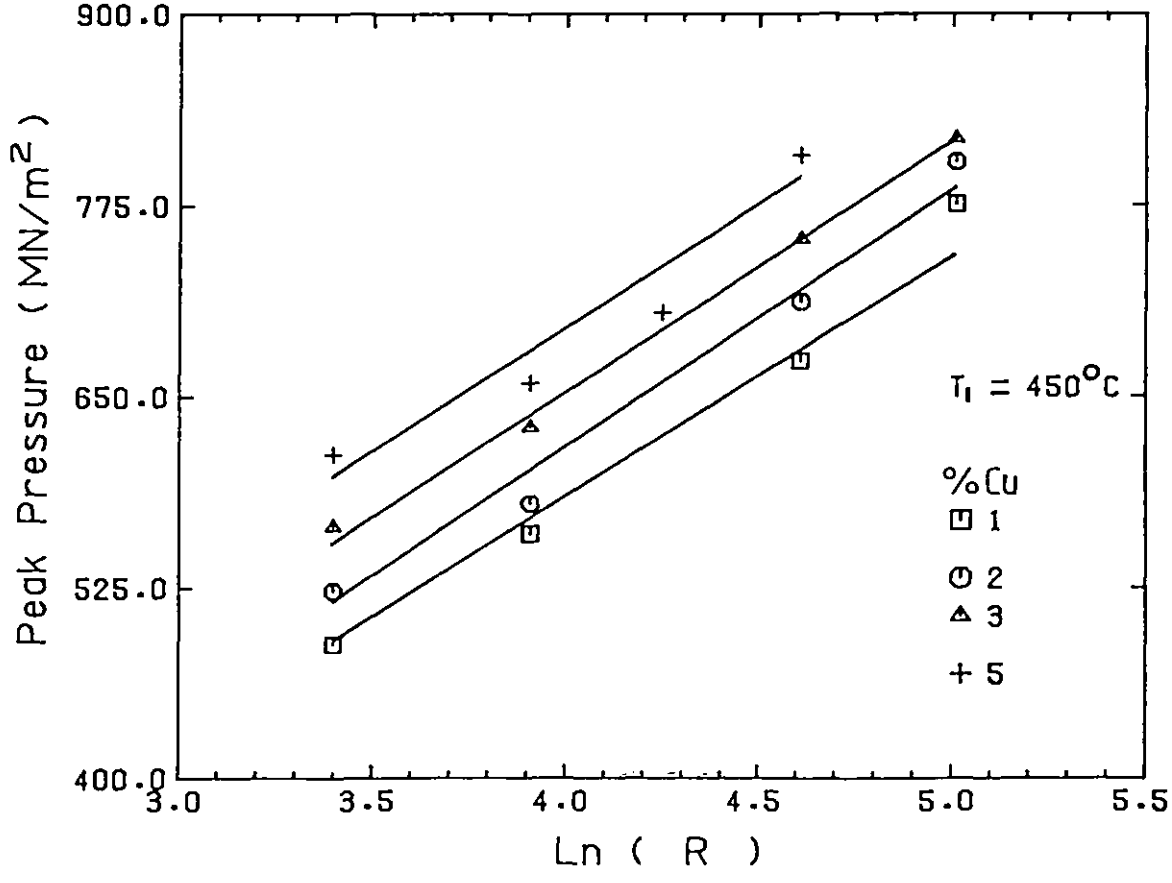


Figure 4.28 Peak pressure vs Ln(R) T_I = 450°C direct extrusion of 2000 series alloys

high correlation coefficients shown in table 4.8. Similar relationships have been found by previous workers[25-29] for heat treatable and non heat treatable aluminium alloys. The equations in table 4.8. show that at both temperatures the rate of increase in pressure with $Ln\dot{R}$, i.e. the value of B, increases with Cu content and decreasing temperature. Both trends are consistent with an increase in the flow stress dependency with Cu content, which increases with decreasing temperatures.

4.2.4. VARIATION OF PEAK PRESSURE WITH INITIAL BILLET TEMPERATURE

The dependence of peak pressure on the initial billet temperature is shown in figures 4.29. and 4.30. for direct extrusion of the 1, 2, and 3 and 5% Cu alloys at extrusion ratios of 30:1 and 50:1, with ram speeds between 7-11 mm/s. The figures show that for each alloy the peak pressure decreases with billet temperature as the flow stress decreases, the pressure decreasing with copper content at equivalent temperatures. A power relationship of the form:

$$P = A\,T^{n}$$

was found to give the best fit, where T is in degrees kelvin, the regression data is shown in table 4.9. Previous workers[1,23,25-28] have reported linear, reciprocal and exponential relationships although in most of these works the extrusion conditions were not kept constant by the use of a constant container temperature, which will be shown in section 4.2.5. to have a significant affect on the peak pressure.

It is apparent from the results in table 4.8. that the dependence of peak pressure on the initial billet temperature shows no

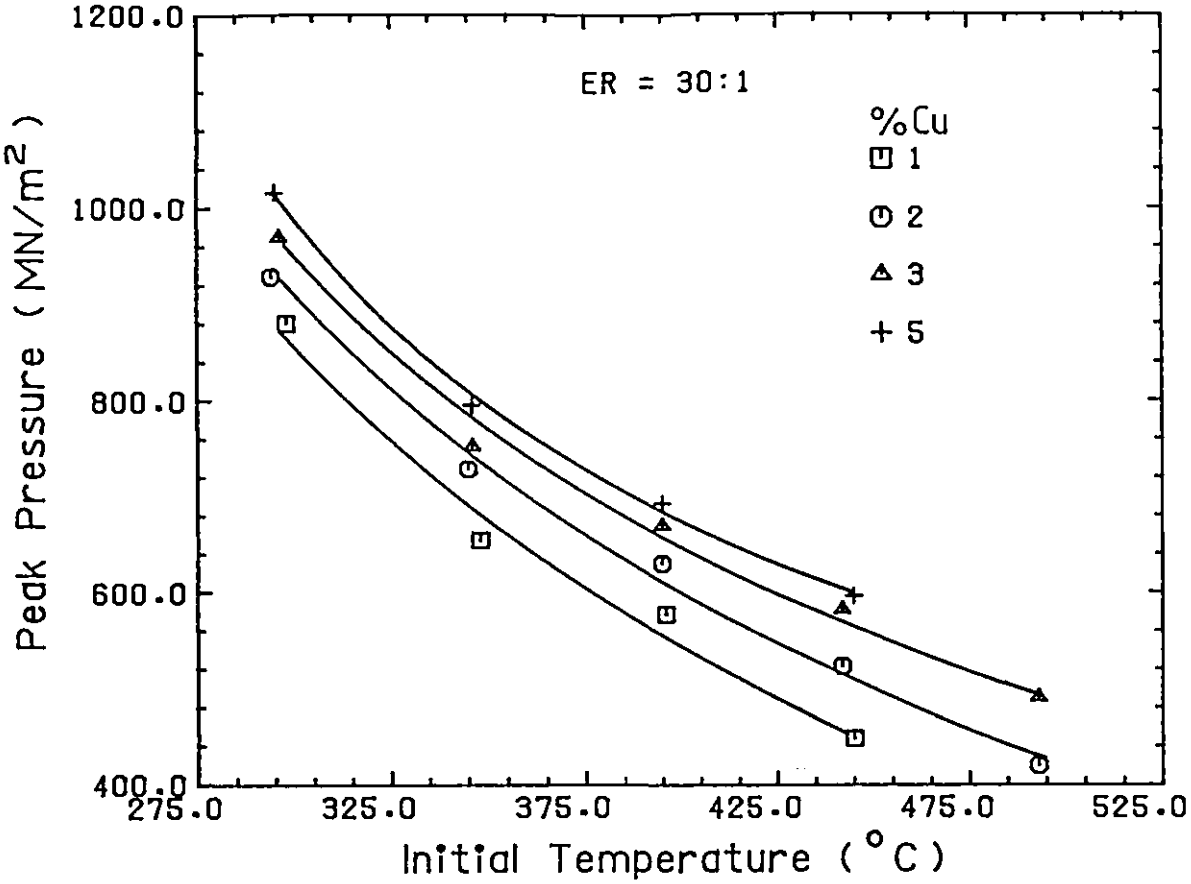


Figure 4.29 Peak pressure vs initial billet temperature ER = 30:1 direct extrusion of 2000 series alloys

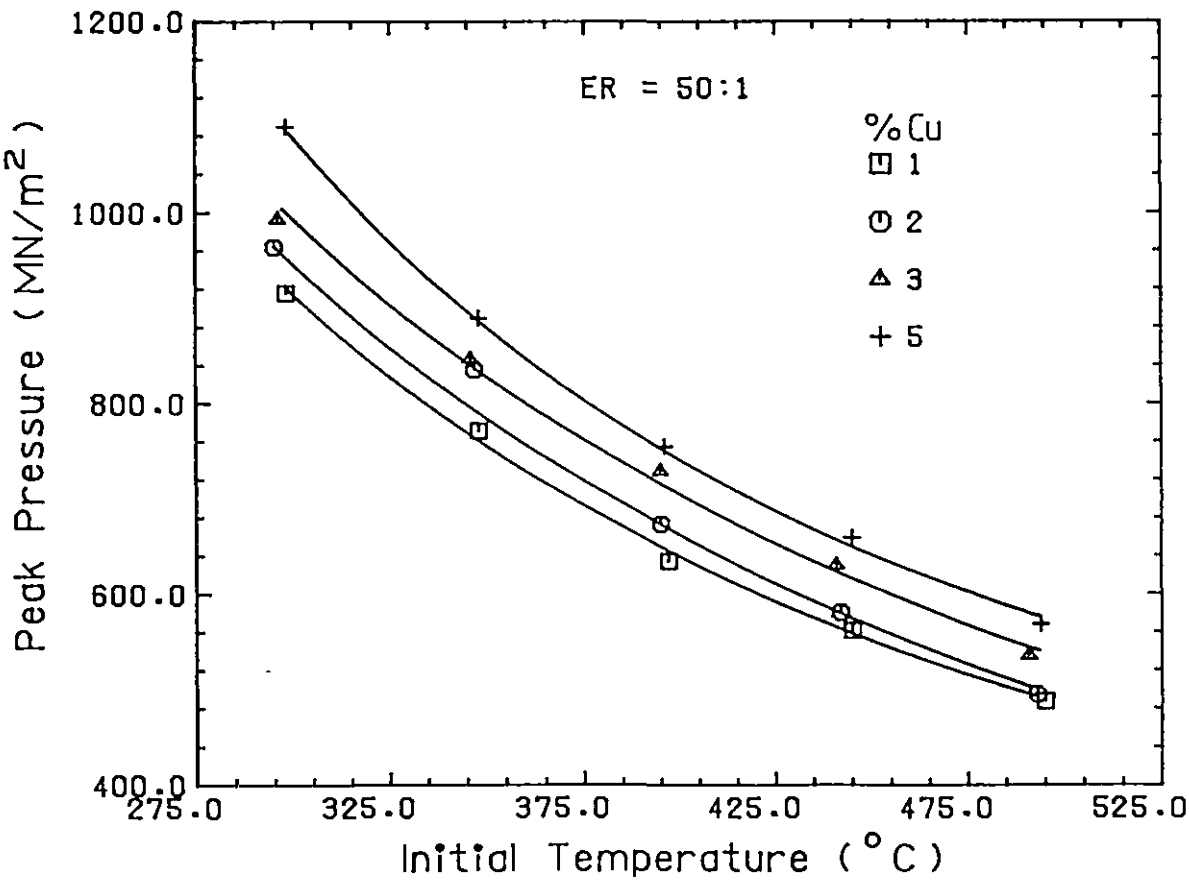


Figure 4.30 Peak pressure vs initial billet temperature ER = 50:1 direct extrusion of 2000 series alloys

$P = A + B \ln R$

$T_I = 350^{\circ}C$

%Cu	A	B	cc
1	110.6	164.0	0.985
2	175.8	165.0	0.993
3	170.8	173.8	0.998
5	192.6	179.2	0.999

$T_I = 450^{\circ}C$

%Cu	A	B	cc
1	-38.2	154.0	0.999
2	-25.6	158.8	0.991
3	10.1	161.0	0.998
5	35.0	165.7	0.979

$P = a T_I^{\ n}$

Initial billet temperature ($^{\circ}K$)

ER = 30:1

% Cu	a	n	cc
1	5.956×10^{9}	-2.480	0.987
2	9.601×10^{9}	-2.548	0.996
3	1.188×10^{9}	-2.213	0.993
5	1.315×10^{9}	-2.223	0.995

ER = 50:1

% Cu	a	n	cc
1	7.141×10^{8}	-2.138	0.998
2	2.182×10^{9}	-2.304	0.996
3	5.193×10^{8}	-2.074	0.997
5	8.514×10^{8}	-2.139	0.998

$P = a T_p^{\ n}$

Peak billet temperature ($^{\circ}K$)

ER = 30:1

% Cu	a	n	cc
1	3.368×10^{10}	-2.746	0.987
2	3.901×10^{10}	-2.757	0.997
3	2.189×10^{9}	-2.303	0.993
5	2.210×10^{9}	-2.202	0.996

ER = 50:1

% Cu	a	n	cc
1	1.589×10^{9}	-2.257	0.998
2	4.107×10^{9}	-2.397	0.994
3	6.770×10^{8}	-2.111	0.996
5	2.592×10^{9}	-2.306	0.999

Table 4.8 Empirical peak pressure-process parameter relationships for direct extrusion of the 2000 series alloys.

$\sigma = a T^{n}$

ER = 30:1

% Cu	a	n	cc
1	4.500×10^{10}	-3.120	0.998
2	5.531×10^{11}	-3.491	0.997
3	1.281×10^{12}	-3.612	0.998
5	1.435×10^{11}	-2.883	0.999

$\sigma = a T^{n}$

ER = 50:1

% Cu	a	n	cc
1	8.081×10^{10}	-3.211	0.996
2	1.723×10^{11}	-3.312	0.997
3	3.910×10^{11}	-3.421	0.995
5	3.750×10^{9}	-2.660	0.997

Table 4.9 Temperature dependency of the flow stress - 2000 series alloys.

consistent variation with copper content at either extrusion ratio. Perhaps the first point to note is that the extrusion conditions are not identical due to the slight variation in ramspeed, although this is unlikely to have a significant effect, since the flow stress is dependent on Ln ($\dot{\varepsilon}$). Secondly the use of the initial billet temperature ignores the temperature rise at peak load, which increases with load and hence copper content. However the results in table 4.8. show that the peak pressure peak temperature dependencies show a similar random variation. If one considers the dependence of flow stress on temperature for identical Z_I conditions, the regression data in table 4.9. shows that similar power relationships can be established, although clearly the temperature dependencies for each alloy at each extrusion ratio is not identical to the pressure relationships shown in table 4.8.

The results in tables 4.8. and 4.9. therefore imply that although the pressure can be described in a similar manner to the flow stress characteristics which is consistent with the basic hypothesis that extrusion is a thermally activated hot working process similar to hot torsion testing, the total peak pressure is not a simple function of the steady state flow stress. The absence of a direct correlation clearly demonstrates the difficulty in predicting the peak pressure from the flow stress characteristics and, may be partly explained by the non homogeneous nature of deformation during extrusion which necessitates defining a mean temperature and strain rate and the fact that the total peak pressure is also a function of the work done against friction and the incremental increase in pressure associated with the development of the steady state deformation zone. The pressure dependencies shown in table 4.8. will therefore also be dependent on the effect of process conditions on the friction pressure and peak height, which will be considered in the following sections.

Finally it should be noted that a presoak time of 5 minutes during torsion testing and 20 minutes during extrusion may contribute towards a slight change in flow stress characteristics due to the increase in solid solution content with temperature and time, although the results in figure 4.14. clearly show a significant age hardening reaction occurs in the torsion specimens above 400 deg.C. It may therefore be concluded that with due consideration to the above phenomena the similarity of the peak pressure and flow stress dependencies in tables 4.8. and 4.9. confirm the basic assumption that extrusion is a thermally activated hot working process similar to torsion testing.

4.2.5. EFFECT OF CONTAINER TEMPERATURE ON THE PEAK PRESSURE

The container heaters described in section 3.2.1. allow a container temperature of up to 500 deg.C to be maintained during extrusion. Previous workers[25-29] have been limited to using a constant container temperature of 300 deg.C since only one set of heating elements in the outer cast container block was available. In order to establish the effect of container temperature on the peak and minimum pressures the 3%Cu alloy was extruded at a constant billet temperature of 400 deg.C at ram speeds of 3 mm/s and 13 mm/s with a reduction ratio of 50:1, the container temperature being varied between 500 deg.C and 200 deg.C. The variation of peak and minimum pressure with container temperature are shown plotted in figures 4.31. and 4.32. For both ram speeds the peak and minimum pressure increase with decreasing container temperature below the initial billet temperature and decrease with container temperature above the billet temperature. The relationships are considered to be linear which is confirmed by the high correlation coefficients in table 4.10.

The first point to note is that for each container temperature the mean initial billet temperature and hence peak temperature will be different due to the change in cooling or heating rates shown in figure 4.33. If the change in peak pressure is solely due to a change in the

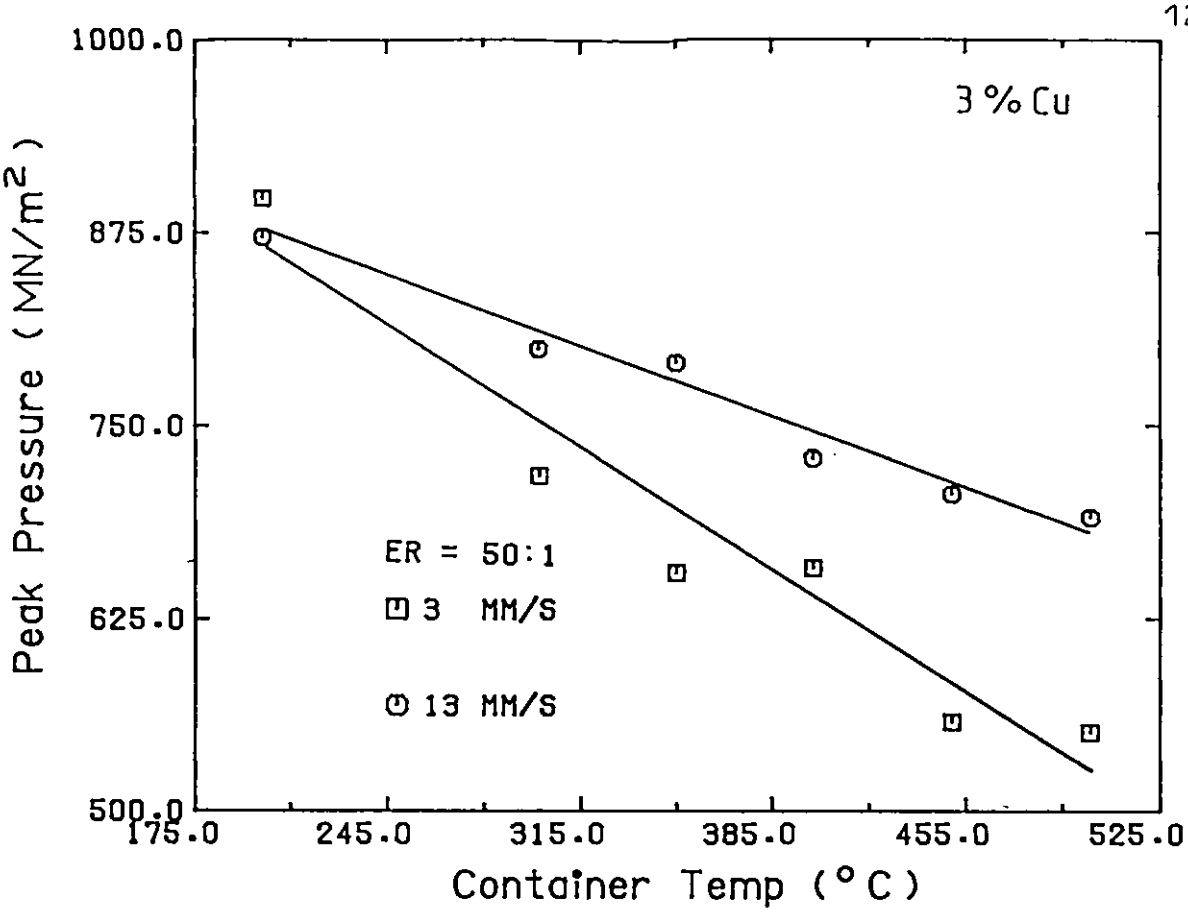


Figure 4.31 Peak pressure vs container temperature - direct extrusion of 3% Cu alloy T_I = 400°C

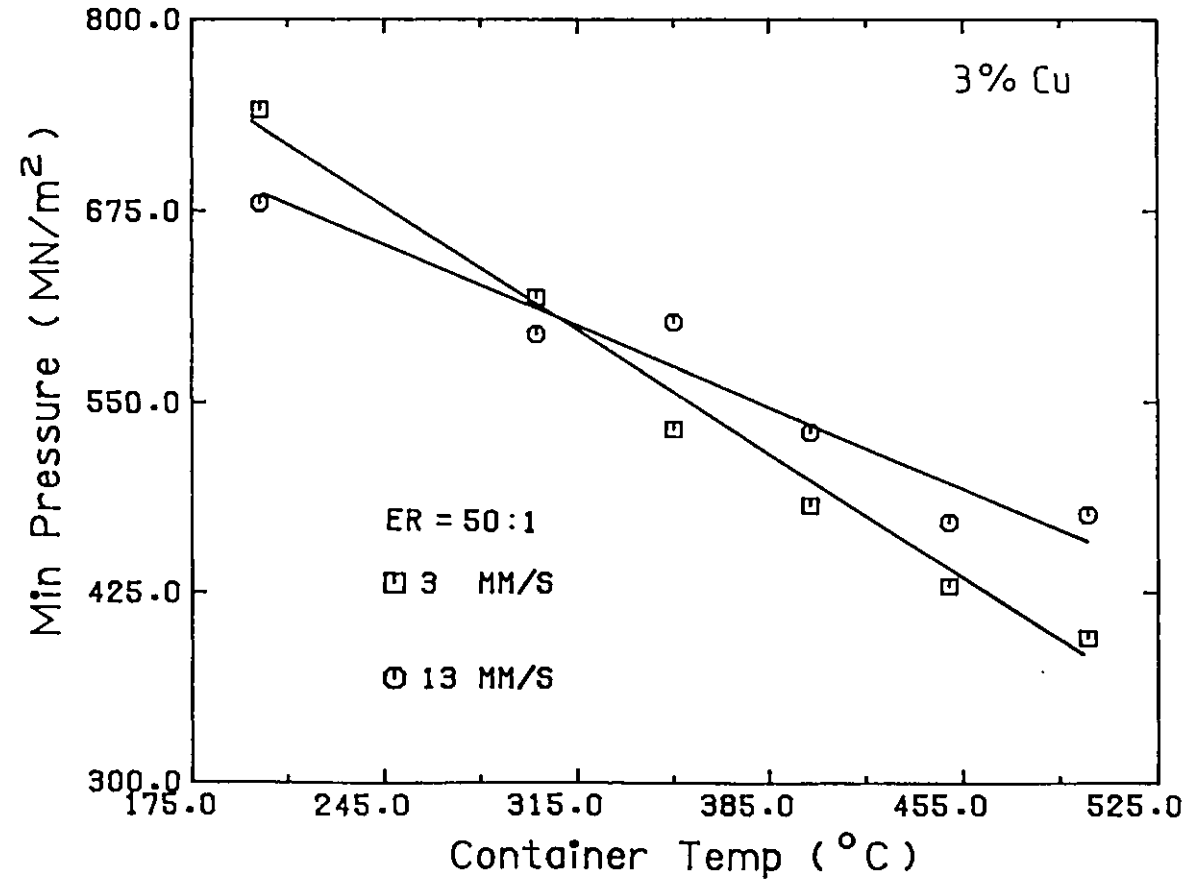


Figure 4.32 Minimum pressure vs container temperature - direct extrusion of 3% Cu alloy T_I = 400°C

$P = a + bC_t$

v	Peak Pressure			v	Minimum Pressure		
mm/s	a	b	cc	mm/s	a	b	cc
3	1090.7	-1.14	0.967	3	966.4	-1.18	0.994
13	994.4	-0.63	0.986	13	825.1	-0.73	0.967

C_t - container temperature °C

Table 4.10 The dependence of peak and minimum pressure on container temperature T_I = 400°C — 3% Cu alloy.

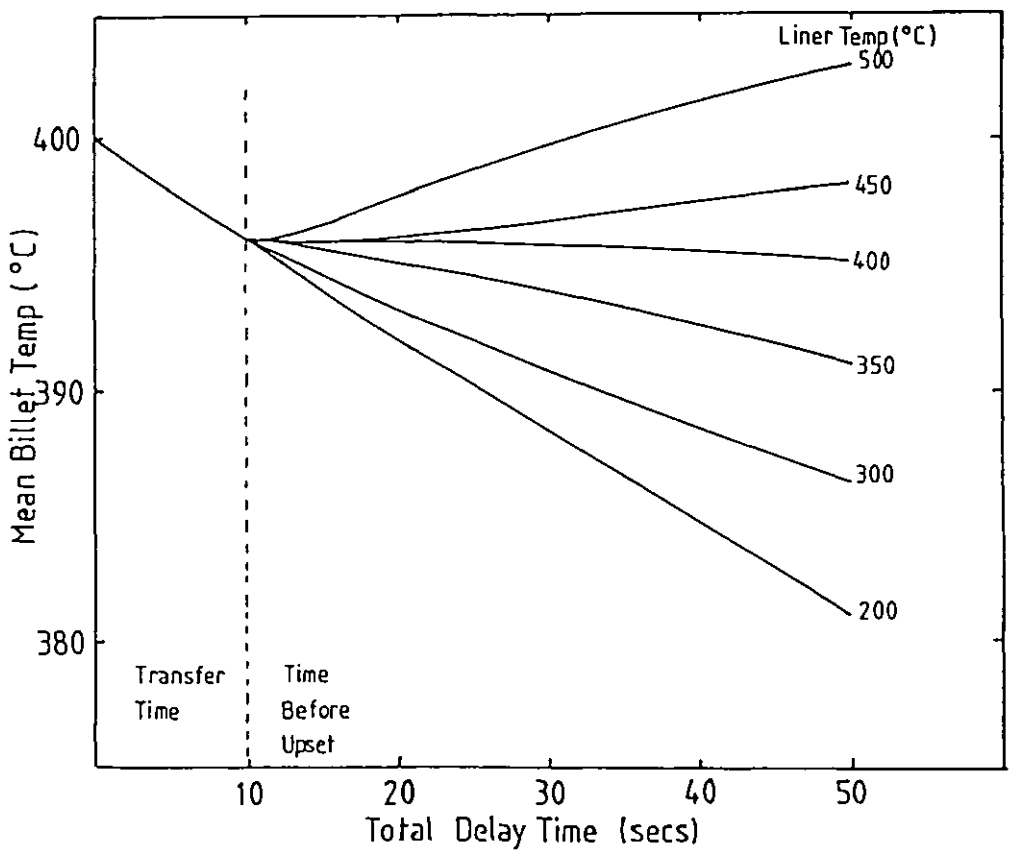


Figure 4.33 Change in billet cooling rate with container temperature T_I = 400°C

mean peak temperature then it should be possible, using the empirical peak pressure temperature relationships derived in section 4.2.4. and the peak temperatures listed in appendix II, to predict the peak pressures for each container temperature. However, for a container temperature of 200 deg.C and a peak temperature of 404 deg.C the predicted pressure of 540 MN/m^2 is well below the peak pressure of 880 MN/m^2 shown in figure 4.31. For a peak pressure of 880 MN/m^2 the empirical relationship predicts a mean peak temperature of 330 deg.C which would require billet cooling rates of 70 deg.C/sec and 23 deg.C/sec at ram speeds of 13 mm/s and 3 mm/s respectively, neither of which corresponds to the cooling rates shown in figure 4.33.

Previous workers[76,115] have shown that during the rise to peak pressure the friction due to the relative motion between the billet and container is sufficient to establish a shear zone within the billet adjacent to the billet container interface during unlubricated direct aluminium alloy extrusion. The overall pressure will therefore be a function of the shear stress of the material within this shear zone. As the cooling rate and temperature gradient within the shear zone increase with decreasing container temperature, which are also reported[141] to increase after upsetting, the shear stress of the material increases and hence the peak pressure increases. An opposite trend results from an increase in the container temperature. Since the effective cooling times associated with peak and minimum pressure at a ram speed of 3 mm/s are 3 secs and 26 secs, and at 13 mm/s 1 sec and 8 secs, then the increase in pressure due to the increase in shear stress within these shear zones will be more pronounced at low ram speeds as shown in figures 4.31. and 4.32. However it should be noted that a change in the friction conditions defined by μ the friction coeficient may also contribute towards the change in pressure seen in figures 4.31. and 4.32., where previous

workers[23,28,79] have reported a temperature dependency for μ, μ increasing with decreasing billet temperature. This topic will be discussed in further detail in section 4.2.6.

The results in figure 4.31. indicate that empirical relationships relating the peak pressure to the billet temperature, extrusion ratio, ram speeds, etc. will be dependent on the container temperature used. If such relationships are to be of any use in estimating the peak pressure for presses with fixed or variable container temperatures then the relationships between the container temperature and the peak pressure of the type shown in table 4.10. must first be established. However, this would require a large number of experimental measurements and may only be applicable to individual alloys if the increase in pressure is a function of the flow stress characteristics. Ideally it should be possible from a knowledge of the cooling rates and the flow stress characteristics, preferably as a function of strain, to introduce the correct values of stress into the terms which allow for energy dissipation due to friction in eg a transient thermally coupled finite element or difference solution. However, although the flow stress data is relatively easy to obtain, the theoretical solutions are not yet available.

Finally it should be noted that although an increase in container temperature can effectively extend the extrusion range for a given press capacity, it was found that at the low ram speed of 3 mm/s severe pick up occurred along the entire length of the extrudes processed with a container temperature above 400 deg.C, the pick up increasing in severity with container temperature. At 13 mm/s pick up was only noticeable towards the rear of the extrudes at a container temperatures higher than 450 deg.C. This phenomena has been associated with oxide from the

surface of the billet being extruded over the die bearing[171], which implies a change in flow pattern with container temperature and ram speed. A change in flow pattern with billet/container temperature differential has also been observed[28,149] during direct extrusion of gridded billets, with a constant container temperature of 300 deg.C. The resistance of the material to withstand the imposed strain gradients, at low Z conditions i.e. low flow stress results in a larger deformation zone extending to the rear of the billet whilst at high Z conditions the high flow stress restricts the deformation zone to the die mouth region. A similar change in flow pattern was observed at low Z conditions with the container only 50 deg.C below the billet temperature. The effect this has on the temperature and strain rate distribution within the deformation zone and hence the final product structure has yet to be properly established, and may well be an important factor during direct extrusion if a more uniform product structure can be produced via careful control of the biller/container temperature differential. The effect of container temperature on the solution treated structures will be considered in section 4.3.7.1.

4.2.6. EVALUATION OF THE FRICTION CONDITIONS

In section 2.3.4. two methods were considered for determining μ the coefficient of friction between the billet and container. The first method based on equation 2.47. requires extruding billets of different lengths under identical conditions which from an experimental point of view is often difficult to achieve. The second method using equation 2.48. needs no separate experimental programme since it is based upon the load displacement traces of individual extrusions, the decrease in pressure with ram stroke being directly related to the decrease in billet length and hence friction. However, at low Z conditions the

change in pressure with displacement dp/dx is often small and difficult to measure and therefore unreliable, whilst at high Z conditions although the values of dp/dx are larger the change in pressure after peak is also a function of the temperature rise during extrusion, which increases with increasing Z. Both of these features can be seen in figure 4.24. The values of μ calculated using this method are therefore likely to show an increase with increasing strain rate and decreasing temperature which indeed several workers have reported. [23,28,79]

In the present work values of μ have been estimated using equation 2.47. The variation of peak pressure with billet length is shown in figures 4.34. and 4.35. for the 2%Cu and 5%Cu alloys extruded at identical strain rates over a temperature range of 500 deg.C to 300 deg.C. Both alloys show a linear increase in peak pressure with billet length, which is confirmed by the regression data shown in table 4.11. Previous workers[23,28] have reported similar linear relationships above a minimum billet length equal to the size of the deformation zone below which the pressure increases. The results in figures 4.34. and 4.35. do not show this feature indicating that the deformation zone and flow conditions are similar for all the billet lengths considered. Values of the friction coefficient μ evaluated using equation 2.47. and from a regression analysis of Ln pressure on the billet length, are shown in table 4.11. The absolute values are similar to those reported by other workers [23,28,79,124] for unlubricated aluminium alloy extrusion, although neither alloy shows a consistent increase or decrease in μ with billet temperature as reported in the above references. However, references 23 and 79 are based upon values of μ calculated using equation 2.48. and therefore a temperature dependency is to be

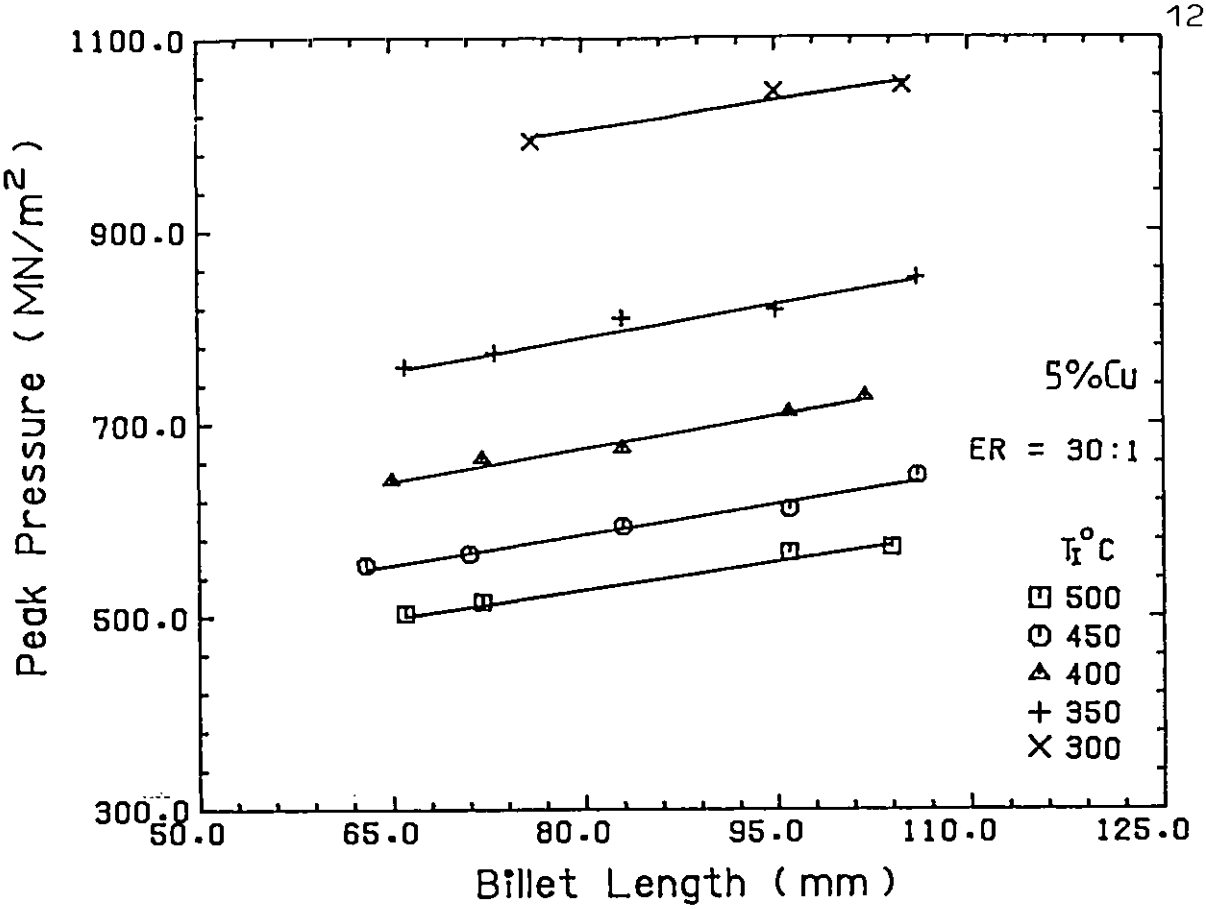


Figure 4.34 Peak pressure vs billet length direct extrusion of 5% Cu alloy

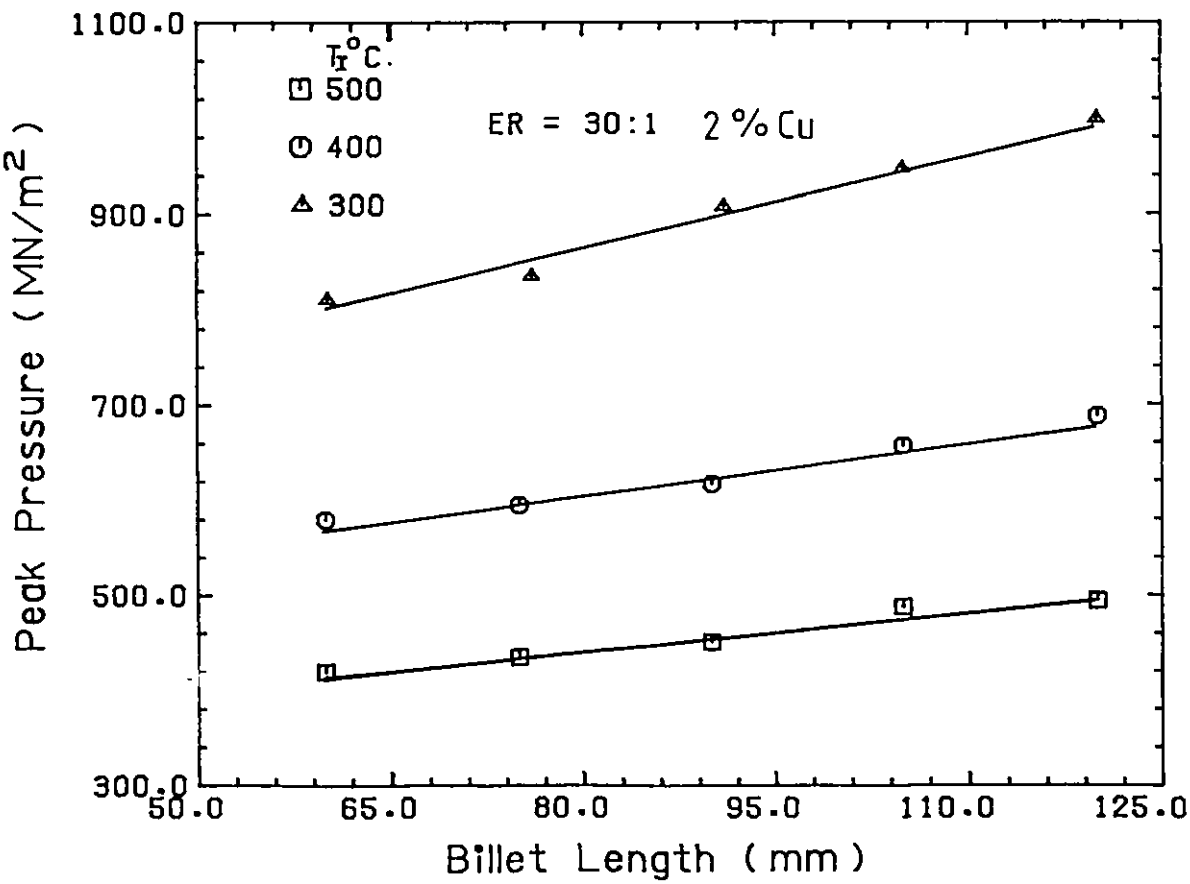


Figure 4.35 Peak pressure vs billet length direct extrusion of 2% Cu alloy

expected. References 28 and 124 have used equation 2.47. but report opposite trends in the temperature dependency of μ. However, in these two works a constant container temperature of 300 deg.C was used which, as shown in section 4.2.5., can result in an increase in pressure especially at high billet temperatures, so that the extrusion conditions can no longer be considered to be identical over a range of billet temperatures. For the 5%Cu alloy the lower than average value of μ at 300 deg.C may be misleading due to the limited number of results available, which is also reflected in the lower correlation for the linear regression.

Since the pressure to overcome friction Pf is defined by equation 4.6. below, a constant value of μ implies that Pf increases with decreasing temperature as Pt the total pressure increases.

$$Pf = Pt\left[\exp\left(\frac{4\mu L}{D}\right) - 1\right] \qquad 4.6.$$

L = Length of the billet-container shear zone
D = billet diameter

An alternative method for evaluating μ can be derived from the difference between the direct and indirect extrusion pressure for identical conditions. Assuming that the decrease in pressure associated with indirect extrusion can be related to the removal of the billet container friction i.e.

$$Pf = Pe - Pi \qquad 4.7.$$

where Pi is the indirect extrusion pressure and Pe the direct pressure. The substituting equation 4.7. into 4.6. gives:

$$\mu = Ln\left[\frac{2Pe - Pi}{Pe}\right].\frac{D}{4L} \qquad 4.8.$$

$P = aL + c$

2% Cu R = 30:1 v = 6mm/s

T_I °C	a	c	cc	μ	m
500	1.34	337	0.979	0.055	1.02
400	1.85	460.6	0.986	0.055	0.80
300	3.28	603.4	0.991	0.069	0.86

5% Cu R = 30:1 v = 6mm/s

T_I °C	a	c	cc	μ	m
500	1.86	382.7	0.991	0.064	0.88
450	2.07	420.9	0.990	0.066	0.82
400	2.22	498.5	0.988	0.060	0.72
350	2.19	617.6	0.982	0.051	0.57
300	2.06	839.5	0.968	0.038	0.44

Table 4.11 Peak pressure vs billet length regression data for direct extrusion of 2% Cu and 5% Cu alloys.

2014

$$\mu = \text{Ln}\left[\frac{2P_e - P_i}{P_i}\right] \cdot \frac{D}{4L}$$

R = 30:1		R = 20:1	
T_I (°C)	μ	T_I (°C)	μ
475	0.058	480	0.061
450	0.063	450	0.066
300	0.066	400	0.060
		350	0.062
		300	0.064

Table 4.12 Coefficient of friction μ established from direct and indirect extrusion data - 2014 alloy.

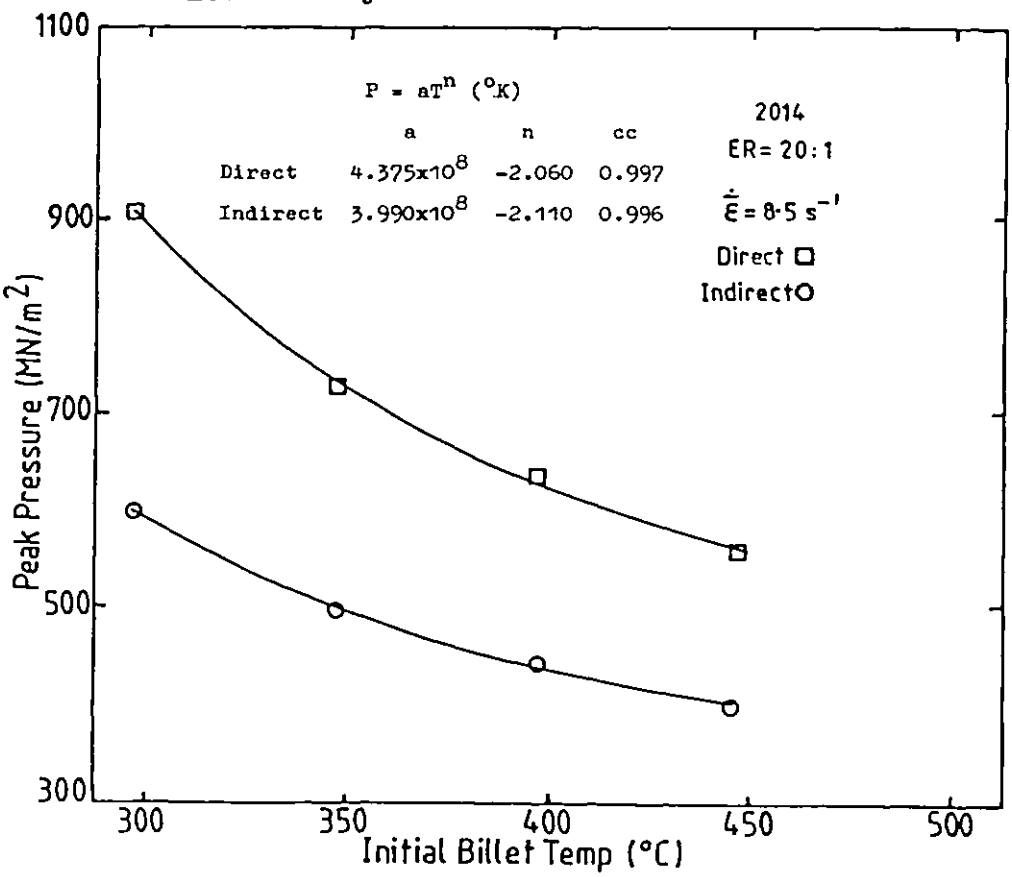


Figure 4.36 Peak pressure vs initial billet temperature direct and indirect extrusion of 2014 alloy ER = 20:1

The values of L can be obtained from the size of the dead metal zone predicted by the upper bound solutions. The results of this analysis are shown in table 4.12. for the 4%Cu 2014 alloy extruded at the same mean equivalent strain rates with reduction ratios of 20:1 and 30:1. The results show that for both reduction ratios and at all temperatures a more or less constant value of μ is obtained similar to the values shown in table 4.11. Assuming that equations 4.6. and 4.7. are correct then the results show that the difference in pressure between direct and indirect extrusion increases with decreasing temperature due to the increase in pressure required to overcome friction during direct extrusion. This is shown more clearly in figure 4.36. which shows the variation of peak pressure with initial billet temperature for direct and indirect extrusion of the 4%Cu alloy at 20:1. A similar trend has been reported by Paterson[124] and indicates that the benefit to be gained from indirect extrusion in terms of the reduction in peak load increases with decreasing initial billet temperature.

Since the above equations have been derived by making several simplifying assumptions, the value of μ can only be regarded as a qualitative measure of the friction conditions. The alternative method of defining the friction conditions is to evaluate the friction factor m used in the upper bound solutions described in section 2.3.4. The values of m are shown in table 4.11. and have been calculated using the regression data in table 4.11. and equation 2.48., the flow stress being determined from equation 2.5. with the strain rate predicted from theory. An average value of 0.8 is close to full sticking friction conditions coinciding with m = 1.0. and is similar to the values reported by previous workers[124,129] for the same billet/container temperature differential and has therefore been used in the present work to calculate the values of

strain rate from the upper bound solutions. However, although the friction factor m is a more quantitative measure of the friction conditions than μ, it can still only be regarded as an approximate value due to the difficulty in establishing the true value of flow stress representative of the temperature and strain rate conditions within the shear zone at the billet container interface, which is reflected in the value of $m>1$ at 500 deg.C for the 2%Cu alloy.

In conclusion it should also be noted that since the work done in overcoming friction is a function of the shear stress within the shear zone, then the friction pressure must also be a function of the billet/container temperature differential. This is reflected in the abnormally high value of $\mu = 0.098$ reported by Paterson[124] for an initial billet temperature of 475 deg.C and container temperature of 300 deg.C. Therefore although a coefficient of friction $\mu = 0.06$ can be used to predict the increase in pressure with billet length and decrease in pressure during indirect extrusion, a constant value of μ can only be assumed for a specific billet/container temperature differential.

4.2.7. VARIATION OF PEAK PRESSURE WITH Ln Zp

The assumption that extrusion is a thermally activated hot working process similar to torsion testing is to some extent confirmed by the many excellent correlations obtained between the peak pressure and Ln Zp[25-29]. Since Ln Zp effectively combines both the temperature and strain rate parameters, it has been found that a single line relationship can be obtained over a range of temperatures and strain rates for a constant reduction ratio. The results from the present work are shown plotted in figures 4.37. and 4.38. for reduction ratios of 20:1 and 50:1, the regression data shown in table 4.13. The high correlation coefficients indicate that each relationship is applicable

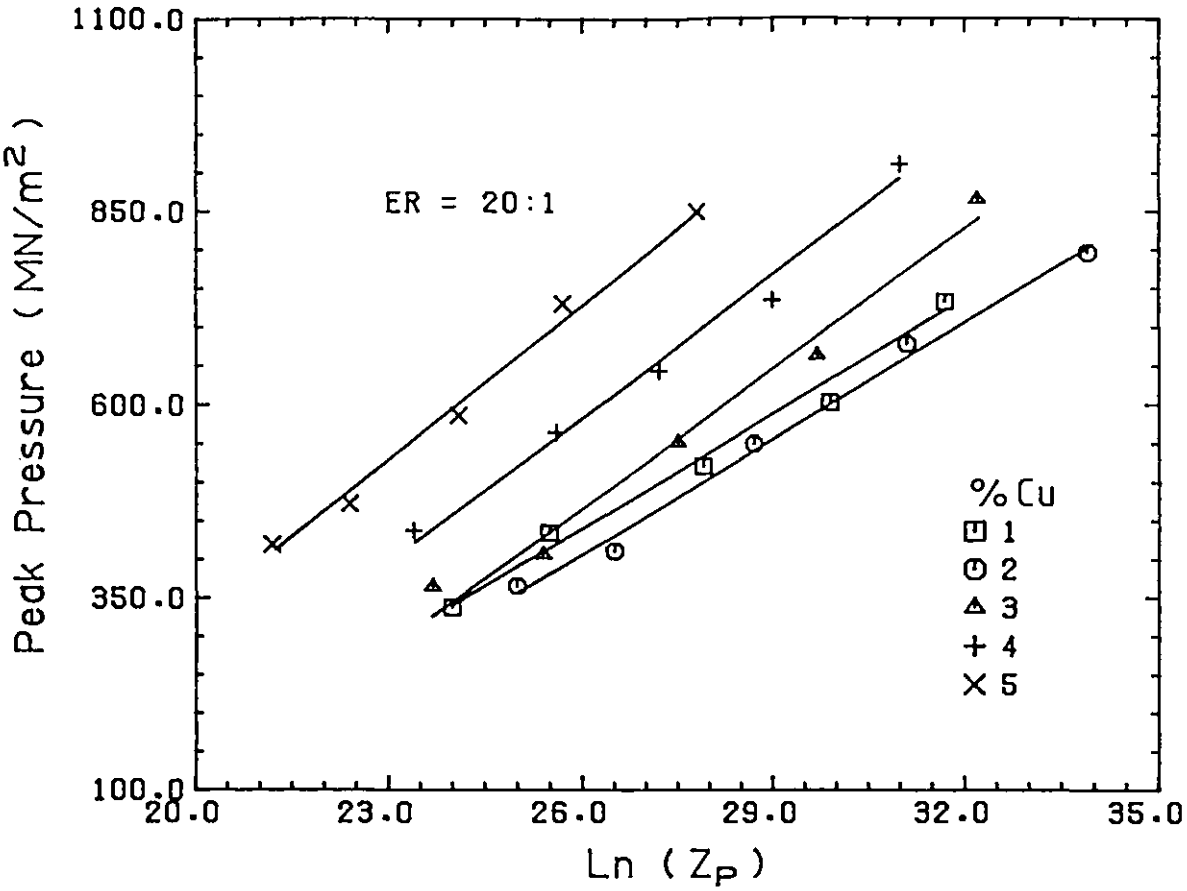


Figure 4.37 Peak pressure vs LnZ_p direct extrusion of 2000 series alloys ER = 20:1

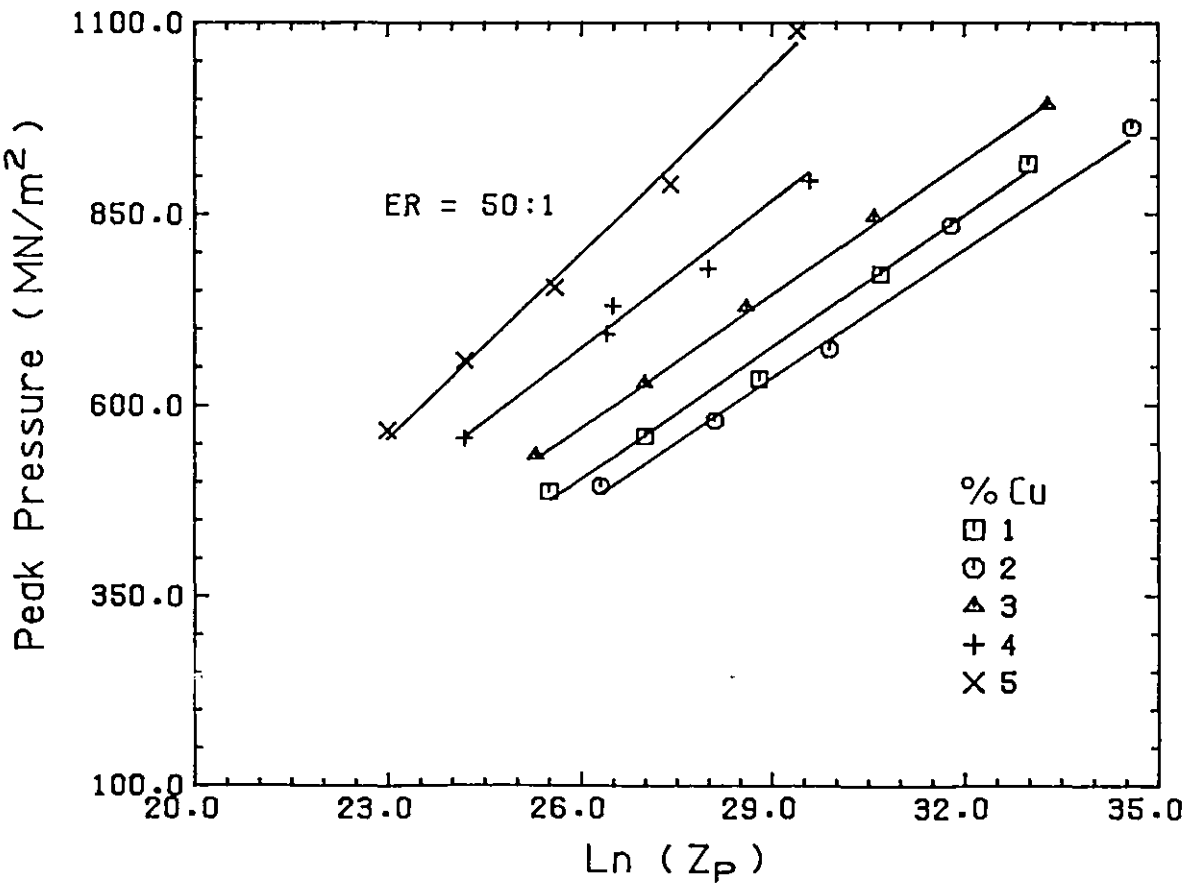


Figure 4.38 Peak pressure vs LnZ_p direct extrusion of 2000 series alloys ER = 50:1

$P = A + B\ln Z_p$

	20:1			50:1		
%Cu	A	B	cc	A	B	cc
1%	-836.6	49.0	0.983	-1011.9	58.1	0.990
2%	-923.0	51.1	0.993	-1079.6	59.3	0.989
3%	-1101.4	60.3	0.982	-927.2	57.8	0.999
4%	-1017.3	61.9	0.992	-925.5	61.5	0.982
5%	-1030.6	67.7	0.996	-1280.3	79.9	0.996

$P = A + B\ln Z_p$

%Cu	A	B	cc
1%	-1149	61.4	0.940
2%	-1107	58.8	0.946
3%	-1089	61.7	0.934
4%	-1041	63.8	0.912
5%	-1291	76.0	0.966

$P = a + b\ln(Z_p/A)$

ER	a	b	cc
20:1	490.5	53.98	0.982
50:1	560.3	59.30	0.973

Table 4.13 The dependence of peak pressure on Ln(Zp) and Ln(Zp/A) for direct extrusion of the 2000 series alloys.

$\Delta P = a\ln Z_p + b$

%Cu	a	b	cc
1	6.48	-162.3	0.903
2	7.56	-181.8	0.976
3	9.29	-224.2	0.959
4	9.94	-225.4	0.960
5	10.91	-242.6	0.969

Table 4.14 Peak height ΔP vs $\ln(Z_p)$ regression data for direct extrusion of the 2000 series alloys.

to all the temperatures and strain rates considered. The gradient of each line shown by the values of a in table 4.13. increase with alloy content and reduction ratio consistent with the increase in temperature and strain rate dependency with Cu content shown in figures 4.11. to 4.13.

In order to establish whether a single line relationship could be established for each alloy over a range of extrusion ratios, the extrusion runs were analysed together, the regression data shown in table 4.13. The relationships are similar to those for the individual extrusion ratios, although a marked decrease in the correlation coefficients indicates that inclusion of a factor for the reduction ratio may be required to produce a single line relationship.

Since the above relationships are limited to the individual alloys considered, the peak pressure has also been plotted as a function of Ln (Zp/A) to determine whether the separate dependencies shown in figures 4.3 7. and 4.3 8. can be amalgamated in a single relationship independent of alloy content. The results are shown plotted in figure 4.39. and the regression data is shown in table 4.13. for reduction ratios of 20:1 and 50:1. It is apparent that the use of Ln (Zp/A) is effective in compensating for the difference in peak pressure dependencies with alloy content, although the decrease in correlation shown in table 4.13. indicates that a more realistic alloy dependent term must also include the constants α and n to compensate for the marked difference in temperature and strain rate dependencies discussed in section 4.1.3.2.

It may therefore be concluded that the inclusion of the two factors to allow for the variation of peak pressure with reduction ratio and alloy content may result in an equation applicable to a complete alloy system over a wide

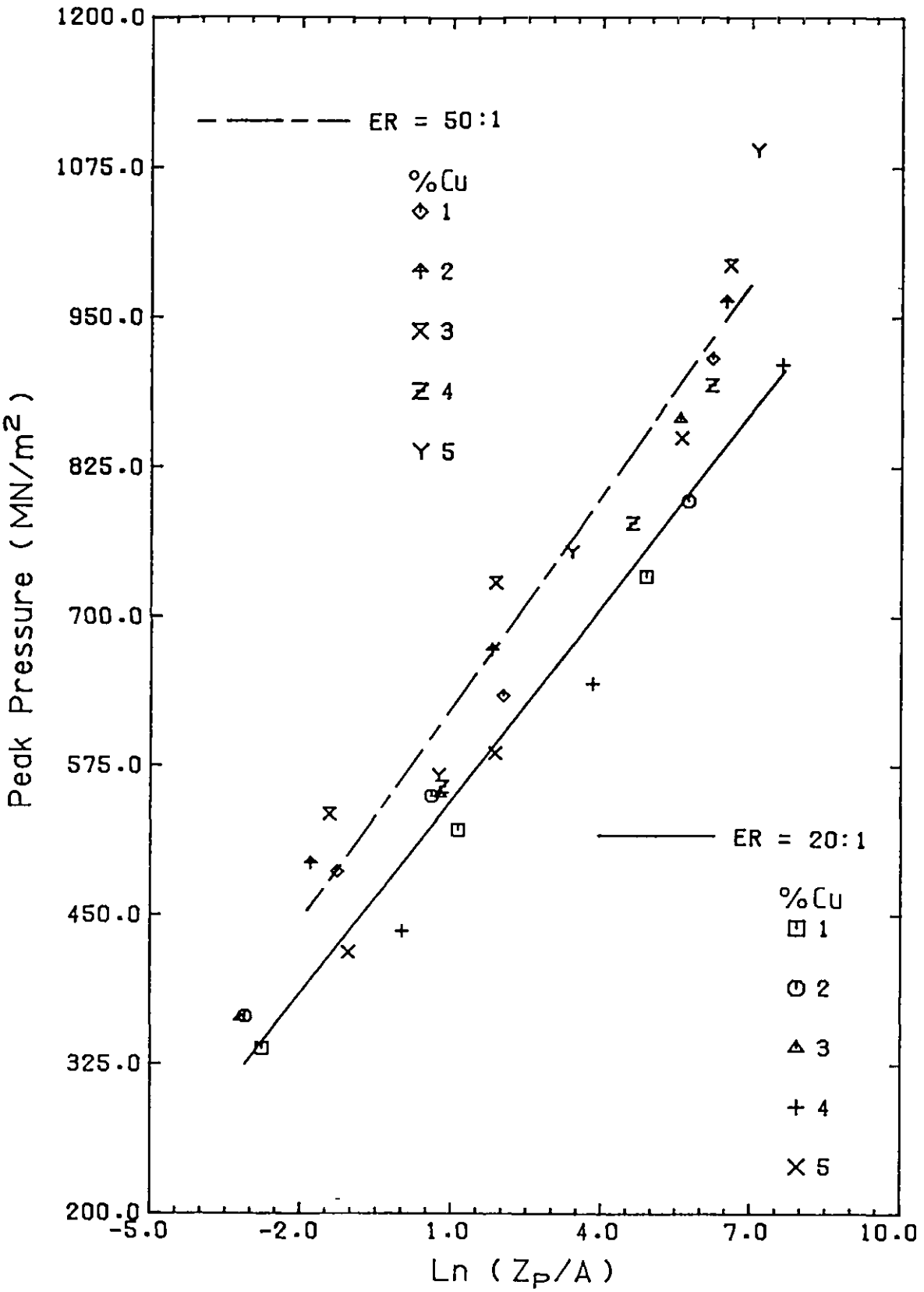


Figure 4.39 Peak pressure vs Ln(Z_p/A) direct extrusion of 2000 series alloys

range of extrusion conditions. The development of such a relationship will be discussed in more detail in section 4.2.9.

4.2.8. THE VARIATION OF ΔP WITH Zp AND ALLOY CONTENT

It was shown in section 4.4.2. that a peak in the load displacement locus occurs at the maximum or break-through pressure in all the alloys. The existence of the excess pressure ΔP was first recognised by Castle + Sheppard[76] to be associated with the energy required to establish the quasi-static deformation zone. They suggested that the formation of the zone involved considerable dislocation generation and movement, and therefore the incremental pressure associated with its formation could be expected to vary with temperature, strain rate, reduction ratio and alloy content. If the above theory is correct then the values of ΔP for identical extrusions should increase with Cu content as the flow stress increases.

The values of ΔP have been measured using the tangential construction shown in figure 4.40. Previous workers[76,100,124] have shown that the size of ΔP can be directly related to Ln Z at peak in a similar manner to the peak pressure in the previous section. The results of using this relationship are shown in table 4.14. and plotted in figure 4.41. For all the alloys ΔP increases with Ln Zp consistent with a decrease in the thermal activation and increase in the dislocation generation rate. The results also show that for constant values of Ln Zp ΔP increases with Cu content, as does the rate of increase shown by the increase in the values of a in table 4.14., similar to the peak pressure relationships shown in table 4.13. The effect of Cu content on the size of ΔP for identical extrusion conditions is shown more clearly in figure 4.42.

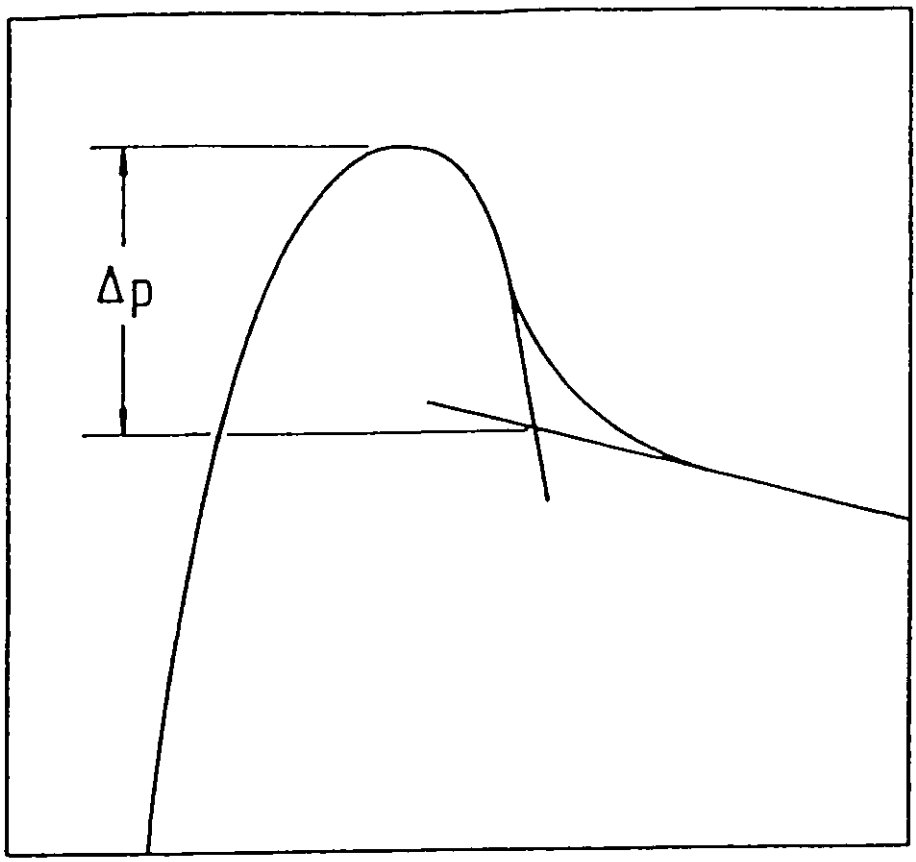


Figure 4.40 Peak height ΔP tangential construction

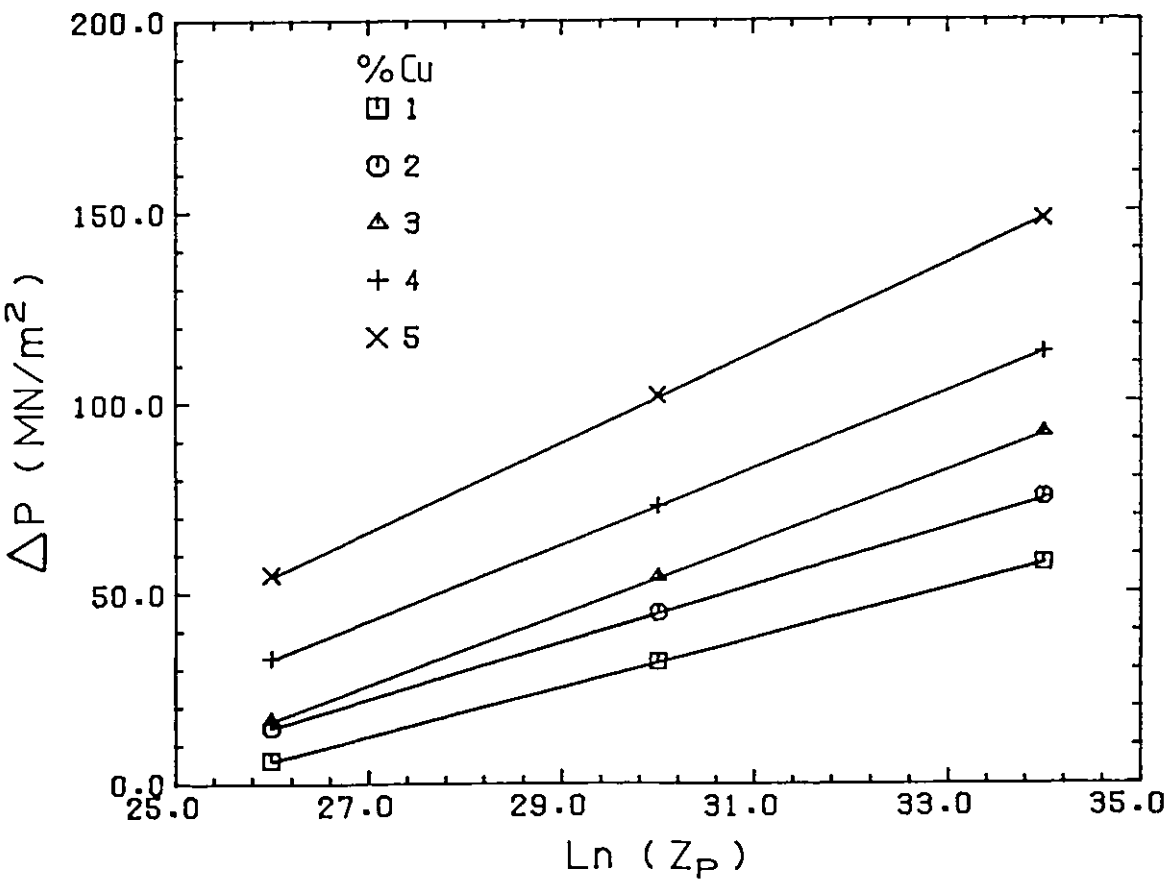


Figure 4.41 ΔP vs LnZp-direct extrusion of 2000 series alloys

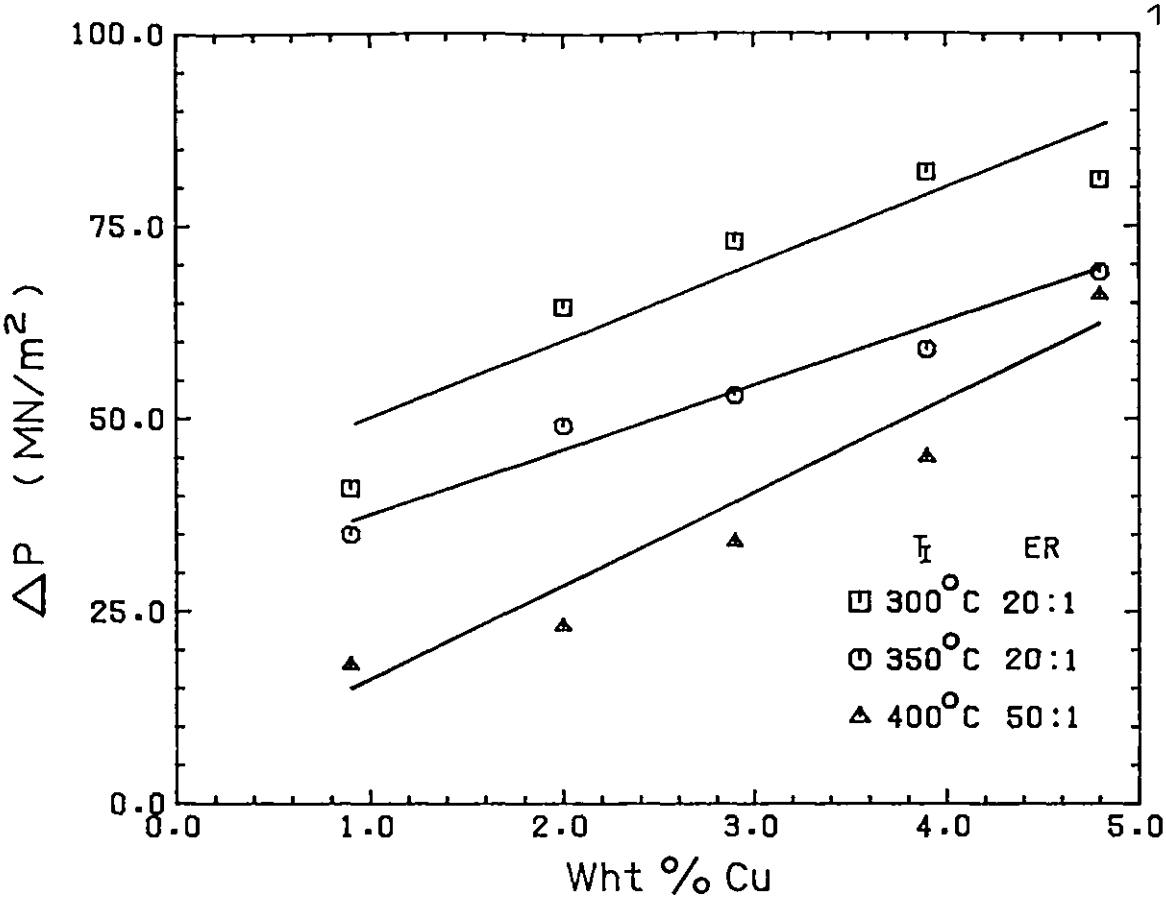


Figure 4.42 ΔP vs wt % Cu direct extrusion of 2000 series alloys

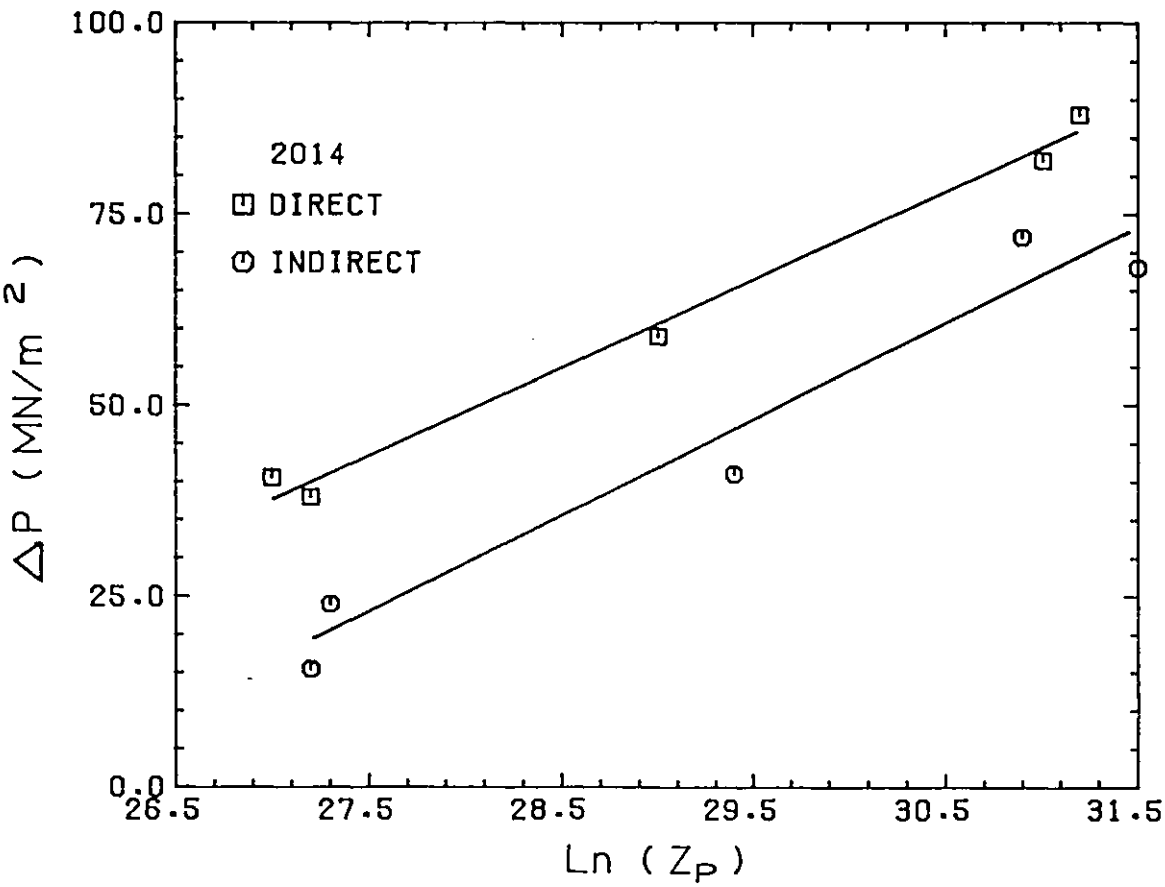


Figure 4.43 ΔP vs $\ln Z_p$ direct and indirect extrusion of 4% Cu 2014 alloy

It is evident that ΔP increases with Cu content for identical strain rates and temperatures, whilst the ratio of peak height to the total peak pressure also increases, in a similar manner. The above results are therefore consistent with the hypothesis that the energy required to establish the deformation zone increases with the decrease in the dislocation mobility associated with the increase in flow stress with Cu content shown in figures 4.11. to 4.13.

The existence of an incremental peak during indirect extrusion shown in figures 4.25. and 4.26. implies that ΔP is not associated with the work done in overcoming the billet/container friction, where the results in figure 4.43. clearly show that ΔP is 15-20 MN/m^2 smaller during indirect extrusion for extrudes processed with the same mean equivalent strain rates. Since both modes of extrusion effectively correspond to the same mean flow stresses then a smaller ΔP for the indirect mode can be explained in terms of the geometrically smaller deformation zone which requires fewer dislocations to accommodate the imposed strain gradients and hence the energy required to establish the deformation zone is smaller. The characteristics of the steady state direct and indirect deformation zone will be considered in further detail in section 4.3.6.

It may therefore be concluded from the dependence of peak height on alloy content and extrusion mode that the ΔP pressure can be associated with the formation of the steady state deformation zone during direct and indirect extrusion.

4.2.9. GENERAL PRESSURE EQUATION

The results in the previous sections have shown that the total extrusion pressure is dependent on the strain rate, extrusion ratio and extrusion temperature. Mathematical models based on slip line field theory and upper bound solutions predict[154] that a general pressure equation relating the above extrusion parameters will be in the form:

$$P/\sigma = A + B \text{ Ln } R \qquad 4.9.$$

where P is the extrusion pressure, σ is the mean equivalent

flow stress, R the extrusion ratio and A and B extrusion constants. If we assume that the value of σ equates to the steady state flow stress given by the general hot working equation:

$$\sigma = \frac{1}{\alpha} \text{Ln} \left[(Z/A)^{1/n} + \sqrt{(Z/A)^{2/n} + 1} \right] \qquad 2.5.$$

then, since the two terms within the brackets are approximately equal this equation reduces to:

$$\sigma \simeq \frac{0.7}{\alpha} + \frac{1}{\alpha n} \text{Ln} \left[\frac{Z}{A} \right] \qquad 4.10.$$

such that combining equations 4.9. and 4.10. gives:

$$P = \left[\frac{0.7}{\alpha} + \frac{1}{\alpha n} \text{Ln} \left(\frac{Z}{A} \right) \right] \left[A + B \text{ LnR} \right] \qquad 4.11.$$

The similarity between this equation and the empirical relationships established in sections 4.2.3., 4.2.7. and 4.2.8. indicates that the total pressure including the initial peak may be more conveniently described by an equation of the form:

$$P = \frac{1}{\alpha n} \left[a + b \text{ Ln } R + c \text{ Ln } \left(\frac{Zp}{A} \right) \right] \qquad 4.12.$$

where a, b and c are extrusion constants. In order to establish the validity of this equation to the individual alloys and the alloys combined, a multiple regression analysis has been carried out with the aid of a standard computer statistics package[156]. The results are presented in table 4.15. along with the standard error for each constant a, b and c and the overall correlation coefficients.

$P = 1/\alpha n \left[a + bLnR + cLn(Z_p/A) \right]$

Alloy	a	±	b	±	c	±	cc
1% Cu	24.72	8.67	6.55	2.53	5.66	0.34	0.962
2% Cu	16.77	3.28	7.11	0.98	4.16	0.15	0.986
3% Cu	13.12	3.23	7.62	0.97	3.94	0.15	0.985
4% Cu	13.10	3.97	7.25	1.15	5.06	0.24	0.975
5% Cu	12.46	3.74	5.77	1.04	4.86	0.27	0.976
1 - 5% Cu	18.83	3.47	6.48	0.98	4.68	0.19	0.891
5052	4.21	3.25	9.04	1.01	5.58	0.20	0.991
1 - 5% Cu + 5052	20.86	3.59	5.56	1.04	4.49	0.18	0.839
4% Cu (Indirect)	-34.70	10.39	19.12	3.32	3.30	0.24	0.975
4% Cu (ref 124) (Direct C_t=300°C)	-2.32	——	14.39	——	3.79	——	0.973

Table 4.15 Extrusion constants in the general pressure equation 4.12

$P = 1/\alpha n \left[a + bLnR + cLn(Z_p/A) + d(L/D_B) \right]$

Alloy	a	±	b	±	c	±	d	±	cc
2% Cu	7.29	5.64	6.39	1.48	4.27	0.12	10.27	2.02	0.979
5% Cu	14.22	4.31	2.81	1.10	4.78	0.17	8.12	2.22	0.969
5052	-11.32	4.01	8.55	1.02	5.84	0.12	13.14	2.00	0.991

Table 4.16 Extrusion constants in the general pressure equation 4.14

$P = 1/\alpha n \left[a + bLnR + cLn(Z_p/A) + dLn(Z_p/A)(\exp 4uL/D_B - 1) \right]$

Alloy	a	±	b	±	c	±	d	±	cc
2% Cu	20.23	6.06	6.31	1.77	2.14	0.56	8.52	2.27	0.969
5% Cu	26.35	3.96	2.09	1.16	2.84	0.60	8.38	2.41	0.968
5052	6.37	2.81	8.41	0.84	3.36	0.29	9.66	1.12	0.994

Table 4.17 Extrusion constants in the general pressure equation 4.16

The high correlation of greater than 0.96 for each alloy indicates that the derived equation is applicable over the range of extrusion conditions considered. An example of the correlation is shown in figure 4.44. which shows the experimental pressure vs the predicted pressure for the 3% Cu alloy. The lower than average correlation coefficient of the combined equation is still considered to be good considering the large number of experimental points regressed (104 points) and demonstrates that inclusion of the $1/\alpha n$ term in equation 4.12. results in a higher correlation coefficient compared to the results in figure 4.39. The decrease in correlation associated with the combined equation is shown more clearly in figure 4.45. which shows the same results from the 3% Cu alloy in figure 4.44. However the principal limitation of equation 4.12. is that it applies to billets of specific dimensions and is therefore of little use as a general pressure equation. The following discussion will therefore consider the inclusion of a billet dimension term and the relationship of the individual constants to the extrusion process.

It has been shown[134] that equation 4.9. can be written in the form:

$$\frac{P}{\sigma} = a' + b' \, Ln \, R + c'L \qquad 4.13.$$

where L is the billet length remaining in the container and a', b' and c' are constants. This therefore suggests that equation 4.12. may also be written in the form:

$$P = \frac{1}{\alpha n}\left[a + bLnR + cLn\left(\frac{Zp}{A}\right) + d\left(\frac{L}{D_B}\right)\right] \qquad 4.14.$$

where L represents the length of the shear zone in contact with the container wall used in equation 4.8. and D_B the

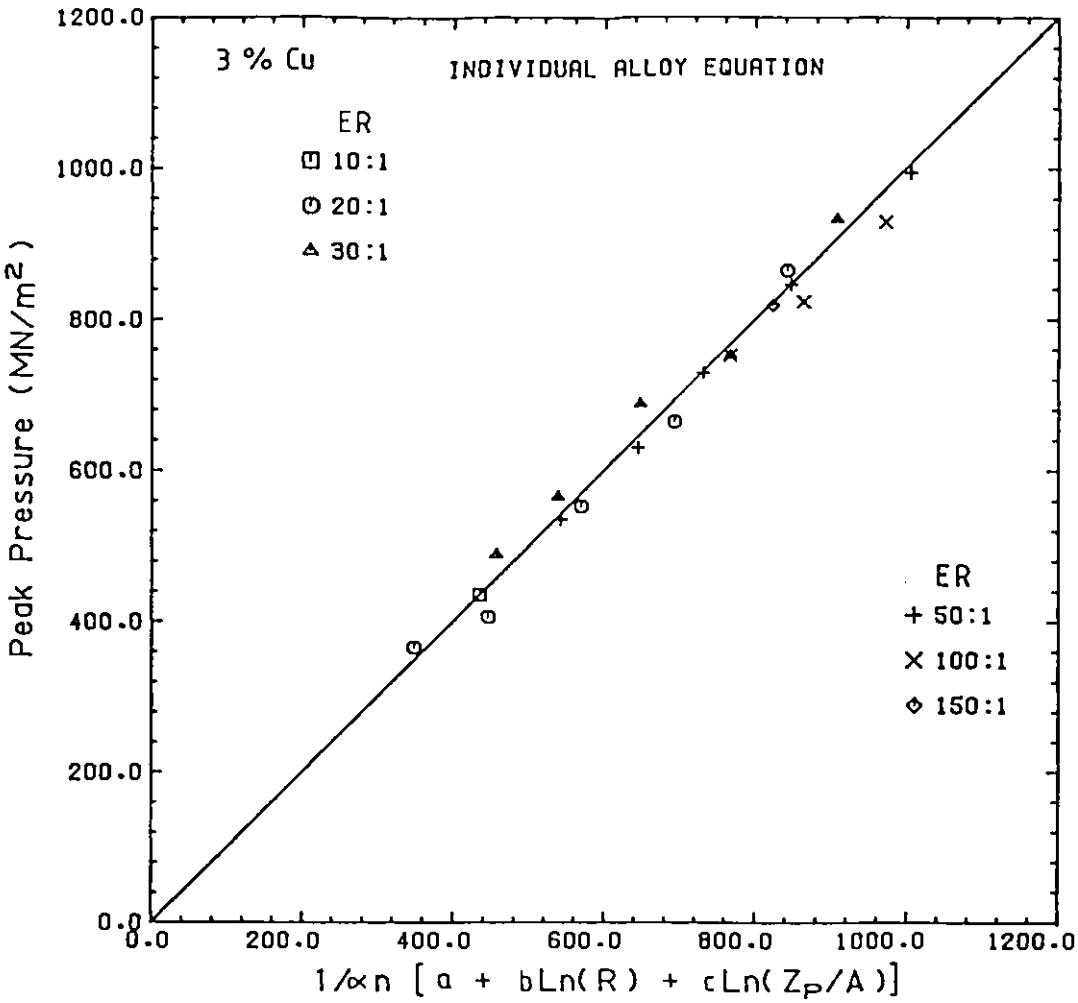


Figure 4.44 Peak pressure vs predicted pressure calculated using equation 4.12 — 3% Cu alloy

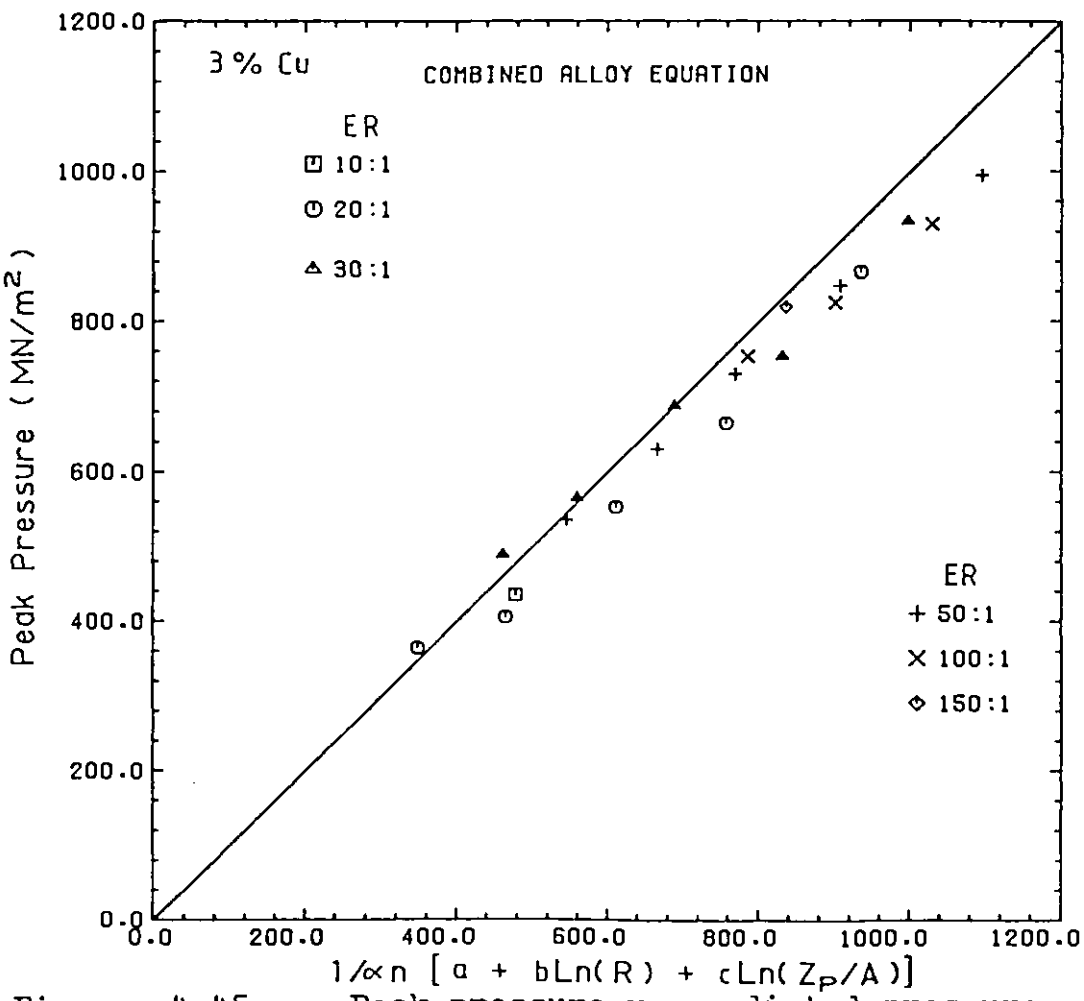


Figure 4.45 Peak pressure vs predicted pressure calculated using equation 4.12 — 3% Cu alloy

billet diameter. The above equation has been used to regress the constant and variable billet length data of the 2% Cu and 5% Cu alloys, the results shown in table 4.16. The correlation coefficients of the individual equations are again >0.96 although both alloys show a slight decrease in correlation due to the inclusion of a billet length term.

The question arises as to whether the linear increase in pressure with billet length shown in figures 4.34. and 4.35. can be simply allowed for by introducing the separate d L/D_B term. In section 4.2.6. it was shown that a friction pressure P_f may be related to the total extrusion pressure Pt by:

$$P_f = Pt \left[\exp\left(\frac{4\mu L}{D}\right) - 1 \right] \qquad 4.6.$$

which can also be written as:

$$P_f = \left[A + B\mathrm{Ln}^{Z}/_{A} \right] \left[\exp\left(\frac{4\mu L}{D}\right) - 1 \right] \qquad 4.15.$$

which implies that the friction pressure is a function of the process conditions and may therefore be incorporated into equation 4.12. by:

$$P = \frac{1}{\alpha n} \left[a + b\ \mathrm{Ln}\ R + c\ \mathrm{Ln}\ ({}^{Z}/_{A}) + d\ \mathrm{Ln}\ ({}^{Z}/_{A}) . \exp\left(\frac{4\mu L}{D}\right) - 1 \right] 4.16.$$

The results in section 4.2.6 indicate that a constant value of $\mu = 0.06$ can be assumed. The regression data in table 4.17. again shows a decrease in correlation in comparison to equation 4.12, where the correlation coefficients are similar to those established using equation 4.14.

The decrease in correlation in equation 4.14. and 4.16. may be partly explained by the experimental error associated with the relatively small increase in peak pressure with billet length and the fact that for both alloys the affect of billet length has been considered for one extrusion ratio only and assumed to apply to all other ratios and billet diameters, a correlation which has yet to be established. However the main problem is in defining the correct billet dimension term to incorporate into equation 4.12. It is of course possible to regress numerous variations of equations 4.14. and 4.16. to find the highest correlation for a specific set of data, although such an analysis reduces to guess work and is likely to result in a number of empirical relationships applicable to specific alloys and extrusion conditions. The affect of container temperature on peak pressure shown in section 4.2.5. emphasizes the problem in defining the friction term and hence billet dimension term since the friction pressure is ultimately related to the shear stress of the material within the shear zone, and hence the process conditions and material characteristics. If one compares the results for direct extrusion of 2014 processed with a constant container of 300 deg.C, the regression results obtained using equation 4.12. in table 4.15. clearly show a marked change in the constants, especially in 'a' and 'b'. This therefore suggests that a friction factor term similar to equation 2.49. used in the upper bound analysis is required, although as already noted in section 4.2.6. the friction factor can only be regarded as an approximate measure of the true friction conditions due to the difficulty in defining a single value of stress for use in the relationship.

In order to establish whether the above trends are specific to the heat treatable Al-Cu system a commercial non heat treatable Al-Mg alloy AA 5052 has also been extruded over a temperature range of 550 deg.C to 325 deg.C, with

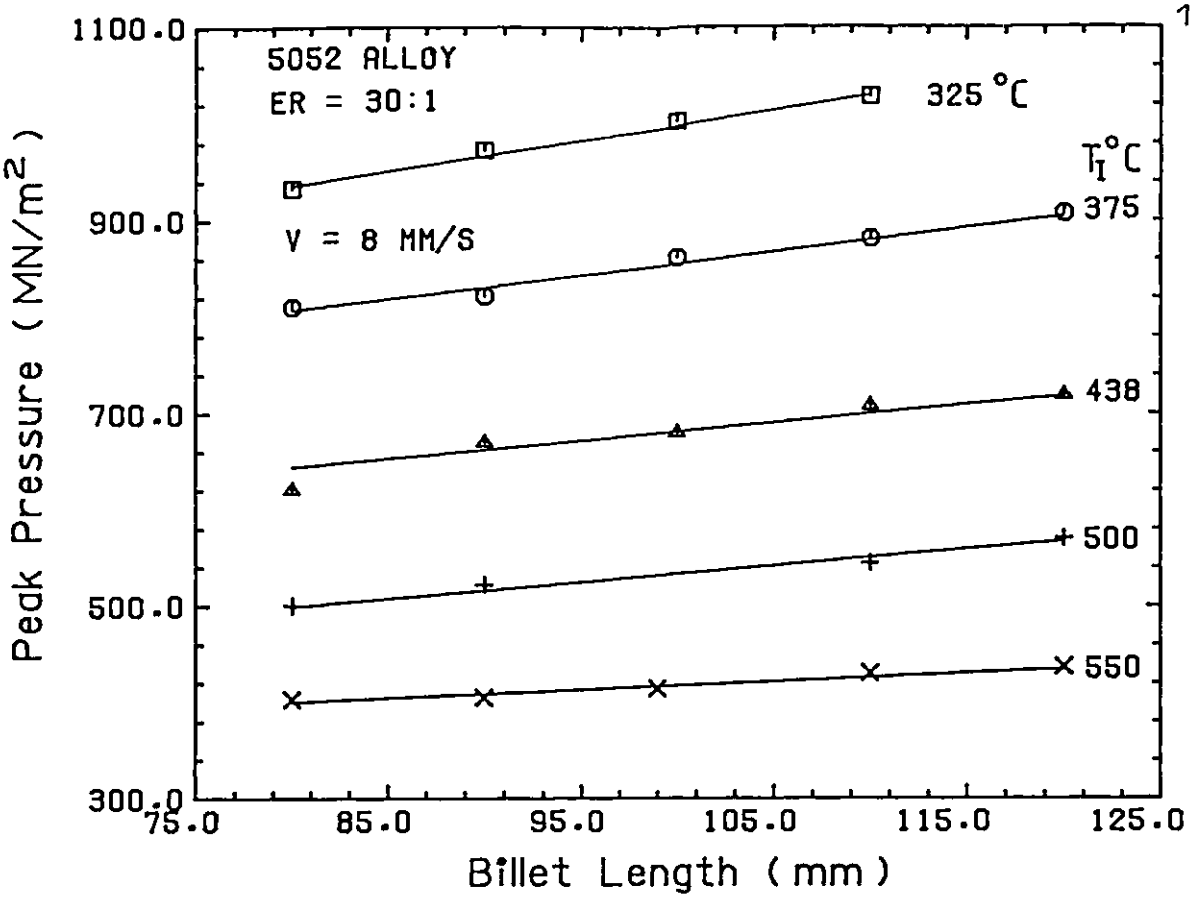


Figure 4.46 Peak pressure vs billet length - 5052 alloy

P = aL + c
5052 - Alloy

T_I (°C)	a	c	cc	μ
550	0.93	324.7	0.976	0.043
500	1.62	372.0	0.986	0.056
438	2.33	445.8	0.962	0.065
375	2.53	603.0	0.990	0.056
325	3.15	685.0	0.994	0.060

Table 4.17b) Peak pressure vs billet length regression data - 5052 alloy

extrusion ratios from 10:1 to 80:1 and billet lengths from 120mm to 80mm at a constant extrusion ratio of 30:1 and ram speed of 8mm/s. A full listing of the results, alloy composition and the hot working constants used (from ref. 122) are shown in appendix II.

The dependence of peak pressure on billet length is shown in figure 4.46., the regression data and friction coefficients are shown in table 4.17.b). The results in table 4.17.b) show that as for the 2% Cu and 5% Cu alloys a constant value of $\mu = 0.06$ can be assumed below 500 deg.C which has been used in the multiple regression analysis. The results in tables 4.15. to 4.17. show that all the relationships have a remarkably high correlation of greater than 0.99, where equation 4.16. now shows the highest correlation of 0.994 as opposed to the lowest in the 2000 series alloys, the extent of the correlation is shown in figure 4.47.

Clearly each term in equation 4.12., 4.14 and 4.16. has its own significance in relation to the extrusion pressure. For direct extrusion previous workers[1,154] have pointed out that the right hand side of equation 4.13. may be regarded as being made up of three contributions to the total work of deformation. The term 'b'LnR' is proportional to the useful work, since LnR is simply a measure of the logarithmic or true strain suffered by the material,'a'' represents the redundant work, whilst 'c'L' represents the work done against friction. Introduction of the hot working constants into equations 4.12. to 4.16. effectively introduces the material properties or flow stress characteristics into the equation , so that the individual terms may no longer be solely a function of the extrusion process.

In order to establish the relationship between the

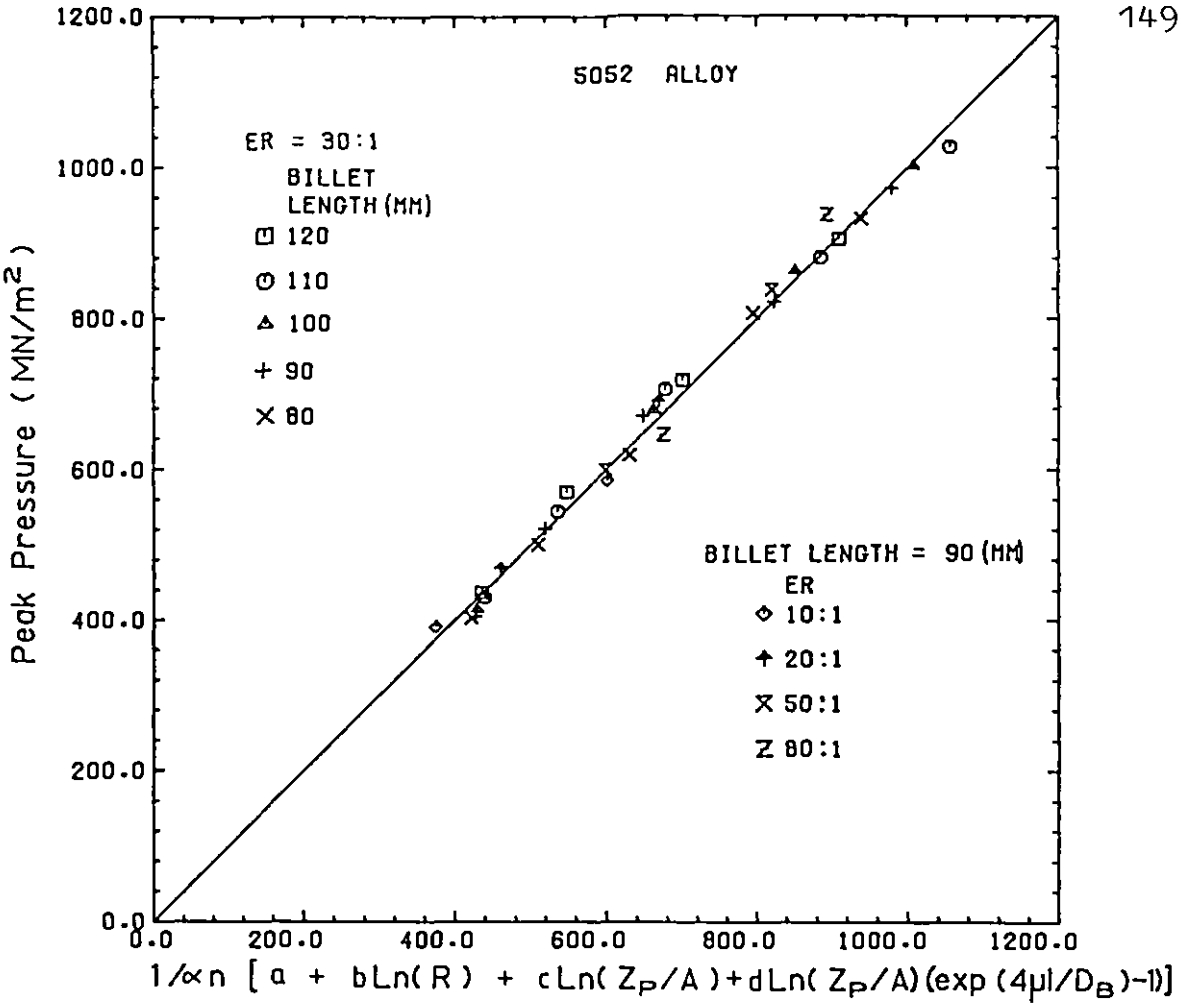


Figure 4.47 Peak pressure vs predicted pressure calculated using equation 4.16 - 5052 alloy

Flow Stress Equations

$$\sigma = \frac{1}{\alpha n}\ a'' + b''Ln(Z_p/A)$$

Alloy	a"	a"/∝n	b"	b"/∝n	cc
1% Cu	5.027	53.479	0.829	8.823	0.994
2% Cu	4.683	63.284	0.811	10.953	0.993
3% Cu	4.568	67.176	0.825	12.138	0.990
4% Cu	4.437	54.110	0.894	10.897	0.999
5% Cu	4.416	66.909	0.866	13.124	0.997
1 - 5% Cu	4.646	——	0.837	——	0.988
5052	4.287	49.360	0.907	10.441	0.998

Table 4.18 Constants in the flow stress equation 4.17

individual constants and flow stress characteristics, the flow stress data has also been regressed using an equation of the form:

$$\sigma = \frac{1}{\alpha n}\left[a'' + b'' \, Ln\left(\frac{Zp}{A}\right)\right] \qquad 4.17.$$

The results in table 4.18. shows that the individual alloy equations exhibit a high correlation of > 0.99 confirming the applicability of equation 4.17. in describing the flow stress characteristics. The constant $b''/\alpha n$ may be regarded as a measure of the temperature compensated strain rate sensitivity, which the flow stress data in figures 4.11. to 4.13. show increases with copper content, whilst $a''/\alpha n$ corresponds to the value of flow stress when LnZ = LnA. It is however evident that a" and b" are similar in the 2000 series alloys, which is confirmed by the high correlation of 0.988 obtained in the combined alloy equation. Inclusion of the 5052 data results in a further decrease in correlation to 0.980due to the difference flow stress characteristics reflected in a" and b".

It is apparent that the absolute values of a" and b" are not directly related to the extrusion constants a,b, c and d but certain trends are clearly similar. Considering equation 4.12. first the value of a" shows the same variation with Cu content as 'a' in the 2000 series alloys and is remarkably similar to the value of 'a' in the 5052 alloy. b" and the equivalent constant 'c' shows the same variation with alloy content in all three equations in the 2% Cu to 5% Cu and 5052 alloys, but not in the 1% Cu alloy which may be related to the lower than average correlation obtained in the regression analysis. The values of 'b' are similar in the 2000 series alloys but higher in the 5052 alloy which may be related to the change in flow stress characteristics associated with the non heat treatable

alloy. It is however evident that within the standard error of estimate the extrusion constants are similar in the 2000 series alloys, which is confirmed by the relatively high correlation obtained in the combined equation shown in figures 4.44. and 4.45., whilst inclusion of the 5052 data results in a further decrease in correlation consistent with the results for the flow stress equation.

Inclusion of the billet length term d L/D_B in equation 4.14. results in a decrease in 'a' equal to the value of 'd' and a slight increase in 'b' in the 2% Cu and 5052 alloy, whilst in the 5% Cu alloy 'a' increases and 'b' decreases, the values of 'c' in all the alloys showing no significant change. The results from the 2% Cu and 5052 alloy suggest that 'a' in equation 4.12. may be regarded as a measure of the friction and redundant work, whilst 'a' in equation 4.14. is a measure of the redundant work and 'd' the friction work. In the 5% Cu alloy a higher value of 'a' is consistent with higher extrusion pressures, whilst the decrease in 'b' implies a reduction in dependence of pressure on extrusion ratio. The reason for this is not clear and may be partly related to the low correlation obtained and the assumption of a friction term independent of the process conditions.

The regression results for equation 4.16. in table 4.17. show that in comparison to equation 4.12. 'a' increases,and 'b' and 'c' decrease in the 2% Cu and 5052 alloy. The 5% Cu alloy exhibits virtually indentical values of 'a' and 'b' to equation 4.14., but a lower value of 'c' consistent with the 2% Cu and 5052 alloy, the value of 'd' is similar in all the alloys. The reduction in 'c' is consistent with the observation that the friction pressure can be regarded as a function of the process conditions, whilst the constant value of 'd' implies that 'd' may be regarded as a function of the extrusion process

i.e. the work done against friction during unlubricated direct extrusion.

It should be noted that the combined alloy equations resulted in a decrease in correlation for both relationships, the largest decrease in correlation resulting when the 5052 data was included.

The regression data for indirect extrusion in table 4.15. shows that in comparison to the equivalent 2014 direct equation a large increase in 'b' and decrease in 'a' and slight decrease in 'c' results. The decrease in 'a' may be related to the lower extrusion pressures observed, whilst the increase in 'b' is indicative of the more homogeneous work done during extrusion in the absence of friction and the slight decrease in 'c' is consistent with the smaller peaks observed during indirect extrusion.

It is therefore evident that although certain trends are consistent with the change in flow stress characteristics and extrusion process, these are not consistent in all the alloys. This may be related to the assumptions made in the present analysis. Firstly that the flow stress evaluated from a mean strain rate and temperature predicted by theory is an accurate representation of the complex variation in stress, strain rate and temperature within the non steady state deformation zone at peak. Secondly, that the work required to overcome friction during direct extrusion is a simple function of the contact area and steady state flow stress and not the shear stress within the shear zone. However the theoretical analysis required to define more accurately the above phenomena is not yet available, where it is likely that a more realistic pressure equation could be established from a comprehensive experimental extrusion matrix which considers the effect of billet length and billet diameter at different

extrusion ratios and Z conditions.

4.2.10. EXTRUDE SURFACE CONDITION

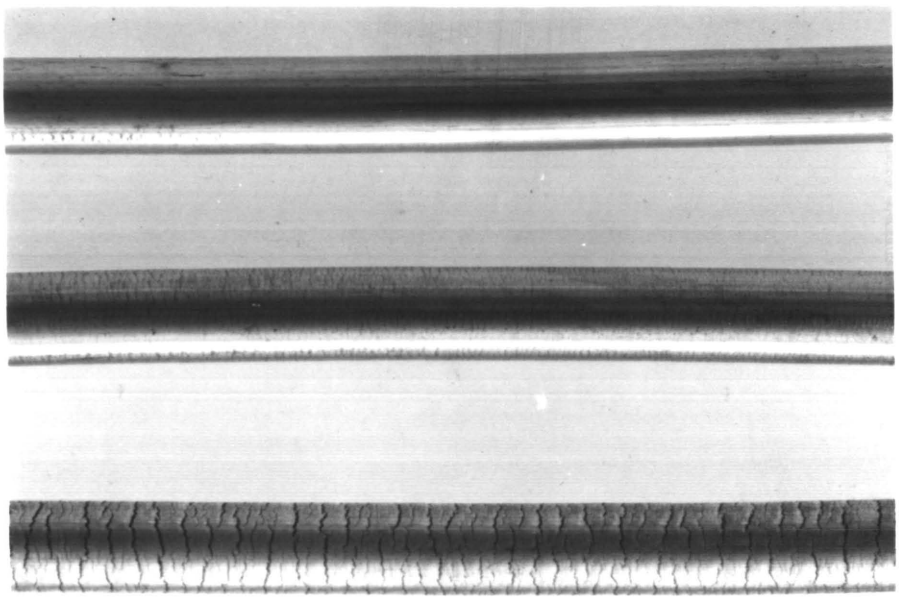
There are numerous surface defects associated with aluminium alloy extrusion which have been extensively reviewed by several authors.[1,25,169,171] For the present work defects deriving from the as cast surface have been eliminated by scalping of the billets before extrusion, as have the defects associated with lubrication, since all extrusions were carried out unlubricated. Surface defects common to all the alloys were die lines and die pick up. The appearance of these defects showed no significant dependence on either strain rate or temperature and tended to increase in severity if the dies were not cleaned between extrusions. This was not always possible due to the time required for the dies to attain a uniform temperature. For the 4% Cu and 5% Cu alloys surface cracking was also a major problem especially at high temperatures and strain rates. Since the product must be scrapped due to the poor surface quality and the inferior mechanical properties, both the occurrence and prevention of surface cracking has been investigated in the 4%Cu 2014 alloy.

In order to evaluate the surface cracking the extrudes have been placed into one of three categories:-

A - No evidence of cracking.
B - Cracking commences at some distance along the extrude.
C - Cracking occurs along the entire length of the extrude increasing in severity as extrusion proceeds.

Typical examples of these three categories are shown in the top three extrudes in plate III which were taken from the same position along the extrude length corresponding to

a) Direct Extrudes ER = 30:1 (x 0.89)



b) Direct Extrude D4543A T_I = 475°C

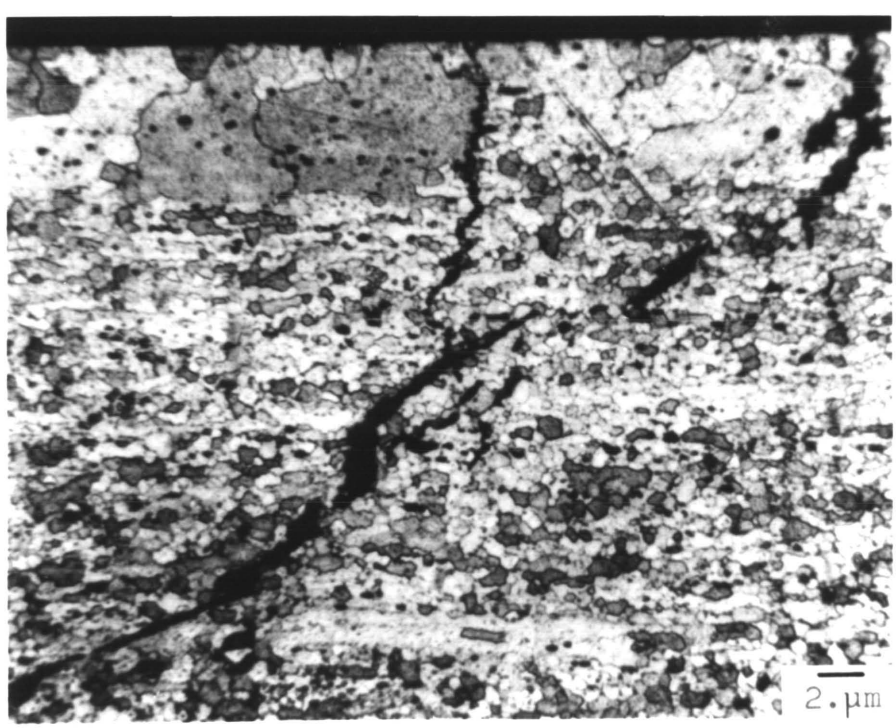


Plate III. Surface Cracking of 2014 Alloy.

a position at 0.5L, i.e. halfway along the extrude length.

Category A extrudes were usually achieved by extruding at low temperatures and low ram speeds. Category B extrudes were normally associated with the medium temperatures and high ram speeds, where the temperature rise during extrusion resulted in hot tearing due to plastic instability or at higher extrusion temperatures incipient melting leading to hot shortness. Category C occurred at high temperatures and high strain rates and often resulted in complete disintegration of the product at the end of the ram stroke.

An example of the microstructure associated with surface cracking is shown in plate III b). The extrusion direction is from left to right and the crack extends backwards at an angle of 45 degrees and is clearly associated with an overheated structure comprising of fine grains surrounded by a continuous intergranular network. The temperature rise during extrusion results in incipient melting of the second phase particles which form an intergranular network when rapidly quenched, resulting in a brittle product of poor mechanical properties. However, incipient melting is not a prerequisite for surface cracking in the 2014 alloy since it is reported[29] to occur well below the eutectic temperature of 517 deg.C. For such extrudes the absence of hydrostatic stresses in the die land area reduces the duclility whilst a reductionmflow stress caused by the temperature rise during extrusion increases the likelihood of tearing in the weakened outer regions of the extrude.

Recent work[29] has shown that it may be possible to reduce the onset of surface cracking by effectively increasing the strength of the material at the edge of the extrude through solid solution strengthening. This was

achieved by solution soaking the extrusion billets at 500 deg.C for 30 minutes before furnace cooling to the extrusion temperature. It was summized that sufficient solute had been retained in solution to increase the peak pressure by 5% and reduce the surface cracking at an extrusion temperature of 400 deg.C. Following this lead a more extensive experimental programme has been carried out in order to determine the optimum soak time and change in hot working characteristics for the 4%Cu 2014 alloy. The effect of a press-solution soak on the mechanical properties of press quenched T1, T5 and T6 extrudes has also been investigated and the results are presented in section 4.4.

4.2.10.1. EVALUATION OF THE PRESOLUTION SOAK FLOW STRESS AND EXTRUSION CHARACTERISTICS

To evaluate the optimum soak time corresponding to the maximum increase in flow stress torsion specimens were heated at 500 deg.C for varying times up to 8 hours and allowed to air cool to a typical extrusion temperature of 425 deg.C. The specimens were held for two minutes to attain a uniform temperature and tested in a similar manner to that described in section 3.7. The air cooling rate is shown in figure 4.48. The resuts are plotted in figure 4.49. which shows that no significant increase in torque occurs after two hours heating. It is interesting to note that Reti et al[148] have also reported that during solution treating of an as cast and wrought Al-4.5% Cu alloy no substantial decrease in the number of second phase particles was found after two hours heating. Which indicates that the maximum increase in torque may be related to the complete solid solution of all the soluble second phase particles.

In order to establish the change in hot working characteristics a torsion matrix was tested using a presolution soak time of two hours at 500 deg.C. The

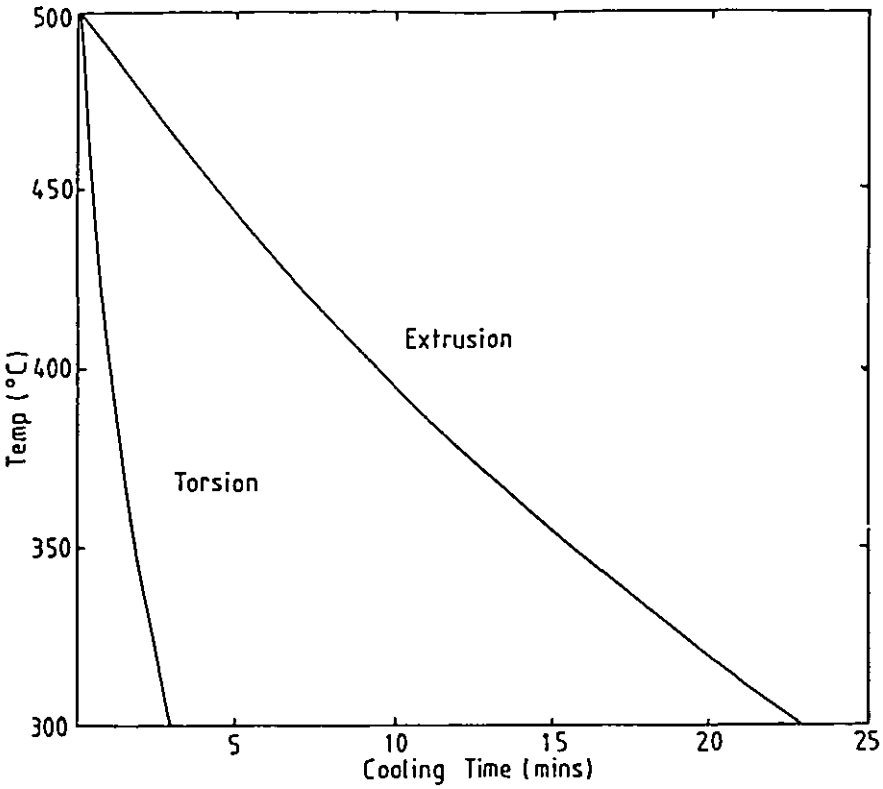


Figure 4.48 Cooling curves for the presolution soak torsion specimens and extrusion billets - 2014 alloy

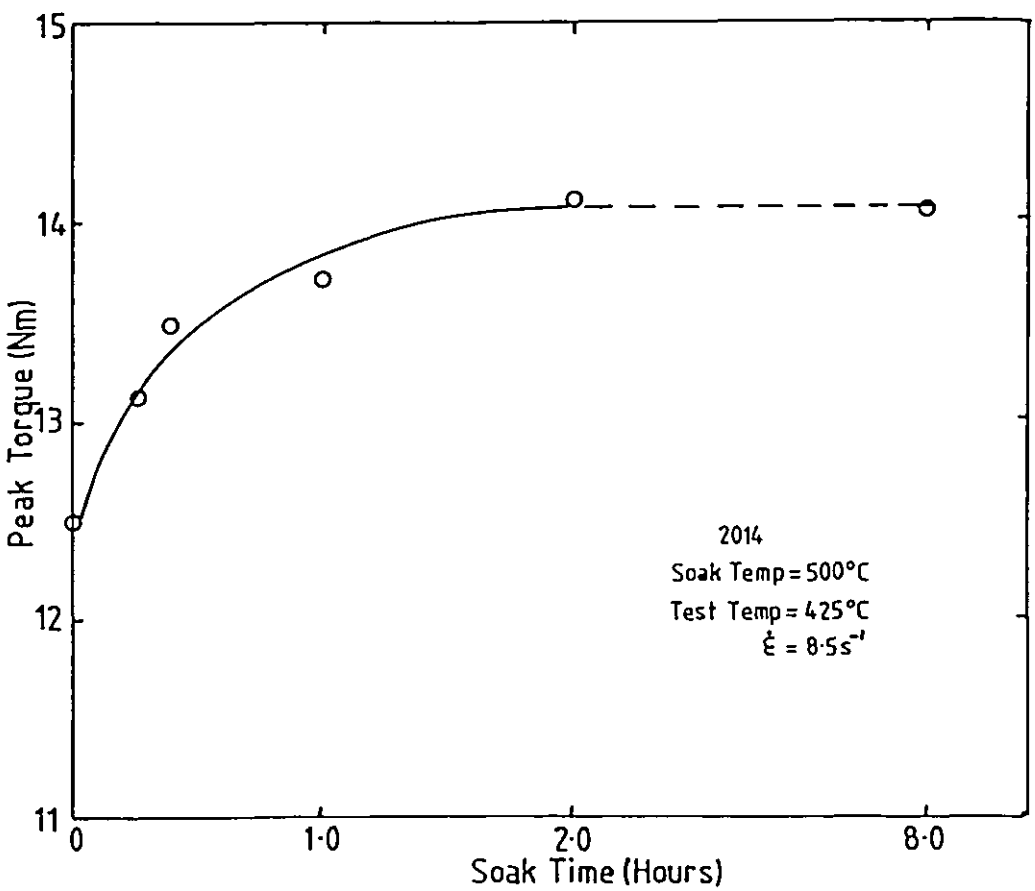


Figure 4.49 The variation of peak torque with soak time 2014 alloy

specimens were air cooled and tested using the same procedure as above at temperatures in the range of 450 deg.C to 275 deg.C with strain rates from 0.03 to 25s^{-1}. The values of peak torque and flow stress are shown in appendix I along with data derived from the temperature rise analysis described in section 2.2.1. The torque twist curves exhibited similar characteristics to those shown in figures 4.1. to 4.3. and showed no pronounced yield point or serrated yielding over the entire range of temperatures and strain rates considered. The degree of strain hardening reflected in the values of strain to peak shown in appendix I are similar to the 3% Cu and 5% Cu alloys and no significant correlation could be established between the strain to peak and process conditions.

The temperature corrected hot working constants of the presolution soak (SS) material as a function of strain are shown in table 4.19., as well as those of the conventionally heated (CH) material at $\varepsilon_H = 1.0$ used in section 4.1.4. The high correlation coefficients demonstrate the applicability of the general hot working equation in describing the flow stress characteristics of the presolution soak material, although a higher value of ΔH and an accompanying increase in A imply a change in the rate controlling process during deformation. The change in flow stress at equivalent temperatures and strain rates is shown in figure 4.50. which clearly shows that a uniform increase in flow stress does not occur, but increases with decreasing temperature and increasing strain rate. This therefore implies that at low Z conditions the high rate of recovery, particle hardening and the increase in solid solution content in both the CH and SS material results in similar flow stress characteristics, whilst the rapid cooling shown in figure 4.48. and the slow precipitation kinetics[51] retain a high solid solution content prior to testing in the SS material, the increase in flow stress resulting from the

Presolution Soak Matrix

2014

ε_H	ΔH J/mole	$\propto$ m^2/MN	n	A s^{-1}	cc
1.00	176867	0.0118	5.86	4.466×10^{13}	0.9840
0.75	182353	0.0115	6.06	1.190×10^{14}	0.9813
0.50	203317	0.0112	7.01	1.160×10^{16}	0.9557

Conventionally Heated Matrix

2014

ε_H	ΔH J/mole	$\propto$ m^2/MN	n	A s^{-1}	cc
1.00	144408	0.0152	5.27	2.957×10^{10}	0.9849

Table 4.19 Hot working constants for the presolution soak (SS) and conventionally heated (CH) 2014 alloy.

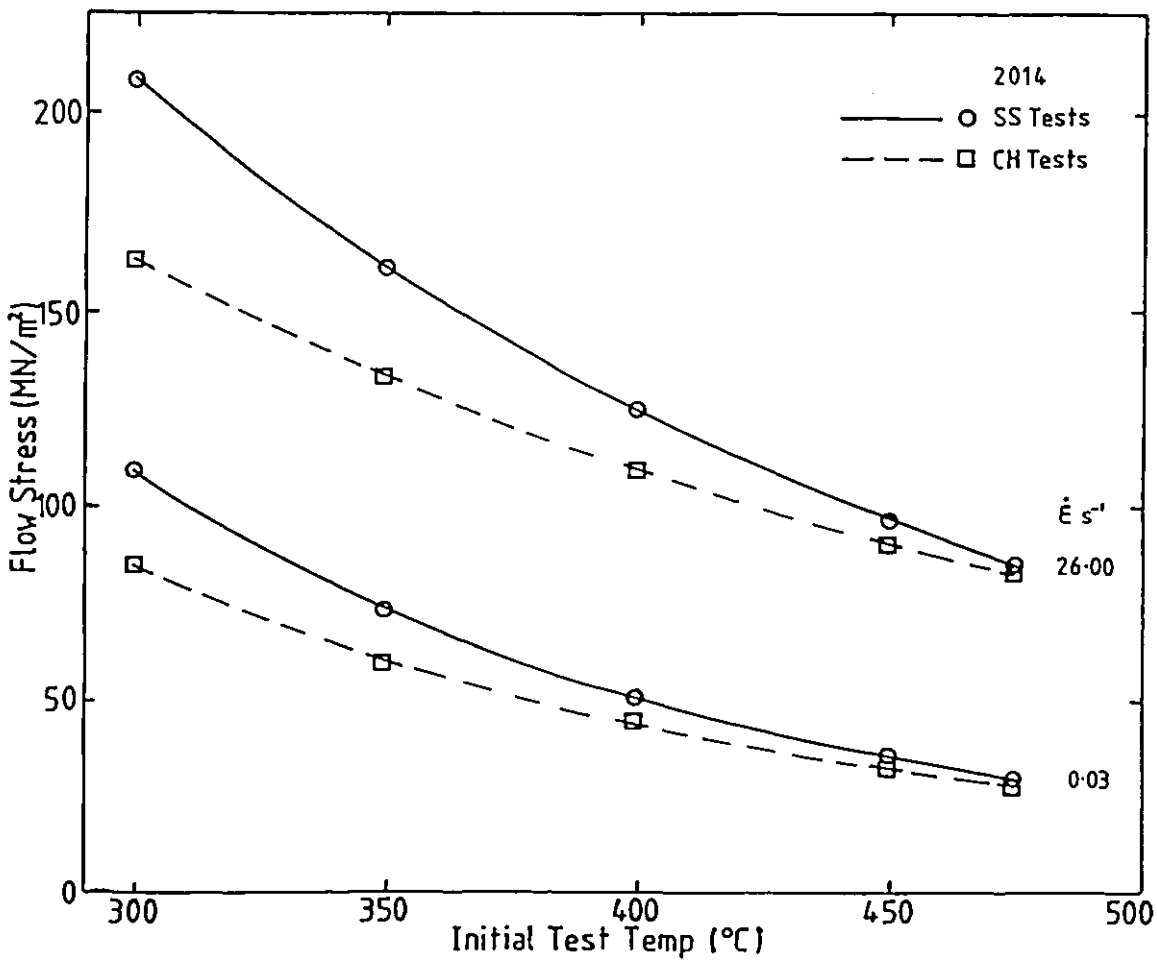


Figure 4.50 Flow stress characteristics of the CH and SS 2014 alloy

solution hardening which increases with decreasing Z.

Solid solution hardening can be defined as an increase in the flow stress of the metal as foreign atoms are dissolved in it. A number of mechanisms have been proposed to explain solution hardening and these have been extensively reviewed in a number of recent works[152-154]. Essentially the mechanisms consider one of two dislocation solute atom interactions:

i) Stationary dislocations can be pinned by solute atoms providing that diffusion of the solute atoms to the dislocations is possible. An extra stress $\Delta\tau$ is then required to free the dislocations from their energetically favourable position which is often observed as a yield point at the beginning of deformation.

ii) A dislocation moving through a solid solution encounters friction and the effect of this friction stress is to raise the stress strain curve to higher stress levels.

Both mechanisms can be expected to increase ΔH due to the increase in thermal activation energy required to overcome the respective obstacles. However since the flow stress characteristics from high strain rate tests are being considered, this tends to rule out dislocation unpinning as the predominent mechanism since this is a yield phenomena normally associated with body centred cubic material tested at low strain rates[153]. If an increase in the friction stress or back stress is the only solution hardening mechanism, then the increase in flow stress will be dependent on a number of factors the principal ones being the solute concentration, the difference in atomic size (d) and the difference in elastic properties between the solute and solvent. In a multicomponent alloy such as 2014 the situation is further complicated by the fact that the

incremental increase in flow stress will be a function of three separate hardening solutes Cu, Mg and Si and hence three different solute concentrations, atomic size factors (d solute/d solvent) of 0.89, 1.12 and 0.95 respectively and elastic interactions. The incremental increase in flow stress shown in figure 4.50. results in a lower value of α whilst a high value of n implies a decrease in the temperature compensated strain rate sensitivity, which may be related to the decrease in dislocation mobility associated with the friction stress and hence decrease in strain rate sensitivity, whilst the high value of ΔH effectively increases the temperature sensitivity.

In a more recent review[155] solution hardening during creep testing has also been associated with a decrease in the rate of recovery and an increase in dislocation multiplication. During high strain rate deformation a decrease in recovery with Z may be attributed to the high solute atom vacancy binding energy which effectively reduces the number of vacancies available for dislocation climb, whilst an increase in dislocation density may result from part of the misfit strain between the substitutional solute atoms and solvent matrix being taken up by dislocations, the misfit strain increasing with decreasing temperature. The effect of the solution soak treatment on the hot worked structure will be considered in section 4.3.5.3.

The effect of the presolution soak treatment on the torsion ductility is shown in figure 4.51. at the highest strain rate of 26 sec^{-1}. The figure shows that in comparison to the 3% Cu and 5% Cu alloys the ductility is lower, especially in the mid-temperature range, but increases in a linear fashion with temperature as the flow stress decreases. The decrease in ductility is consistent with an increase in solid solution content and hence solute atom segregation at grain boundaries prior to testing, which

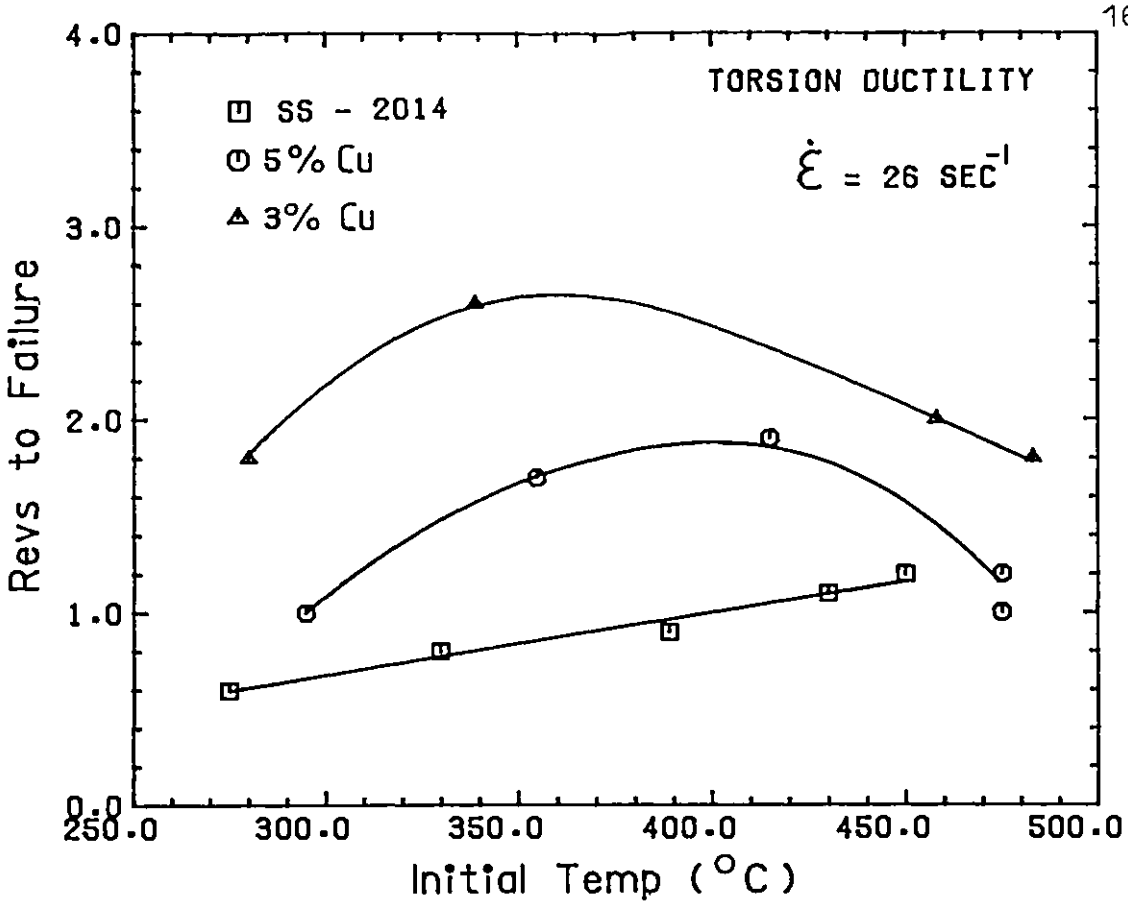


Figure 4.51 Torsion ductility vs initial test temperature at $\dot{\epsilon}$ = 26 sec^{-1} CH 3% Cu, 5% Cu and SS 2014 alloy

$P = 1/\alpha n [a + bLnR + cLn(Z_p/A)]$

Preheat treatment	a	±	b	±	c	±	cc
SS	14.45	6.01	8.25	1.71	4.32	0.23	0.962
CH	13.10	3.97	7.25	1.15	5.06	0.24	0.975

$\sigma = 1/\alpha n [a" + b"Ln(Z_p/A)]$

Preheat treatment	a"	a"/ n	b"	b"/ n	cc
SS	5.217	82.810	0.801	12.715	0.994
CH	4.437	54.110	0.894	10.897	0.999

Table 4.20 CH and SS 2014 peak pressure and flow stress equations

is associated with the decrease in ductility in the CH material above approximately 350 deg.C. Although a decrease in ductility during hot working implies an increase in susceptibility to surface cracking associated with hot tearing, the results in figure 4.51. are relevant to the shear mode of failure discussed in section 4.1.5., which is unlikely to be equivalent to the complex stress state existing at the die exit.

It is therefore apparent that the incremental increase in flow stress shown in figure 4.50. may be a function of a number of mechanisms although in terms of the original objective i.e. to increase the tensile strength of the material during hot working the presolution soak treatment will be more beneficial to high Z extrudes where surface cracking is more likely to be associated with surface tearing in the absence of incipient melting.

An extrusion matrix based upon the above results has been tested using the same presolution soak treatment of two hours at the 500 deg.C. The extrusion billets were heated in the air circulating furnace and furnace cooled to the extrusion temperature and held for two minutes before extruding, the extrusion results are listed in appendix II. The fastest cooling rate that could be achieved using this furnace is also shown in figure 4.48. The cooling rate is clearly slower and results in a maximum cooling time of 20 minutes at 300 deg.C as opposed to 3 minutes for the torsion specimen. The effect of an increase in time for precipitation during cooling on the solution strengthening and hence the flow stress characteristics described by the hot working constants in table 4.19. has been established by comparing the peak pressure and peak height with those of the conventionally heated billets, in a similar manner to the flow stress data in figure 4.50. The results in figures 4.52. and 4.53. clearly show that the presolution soak

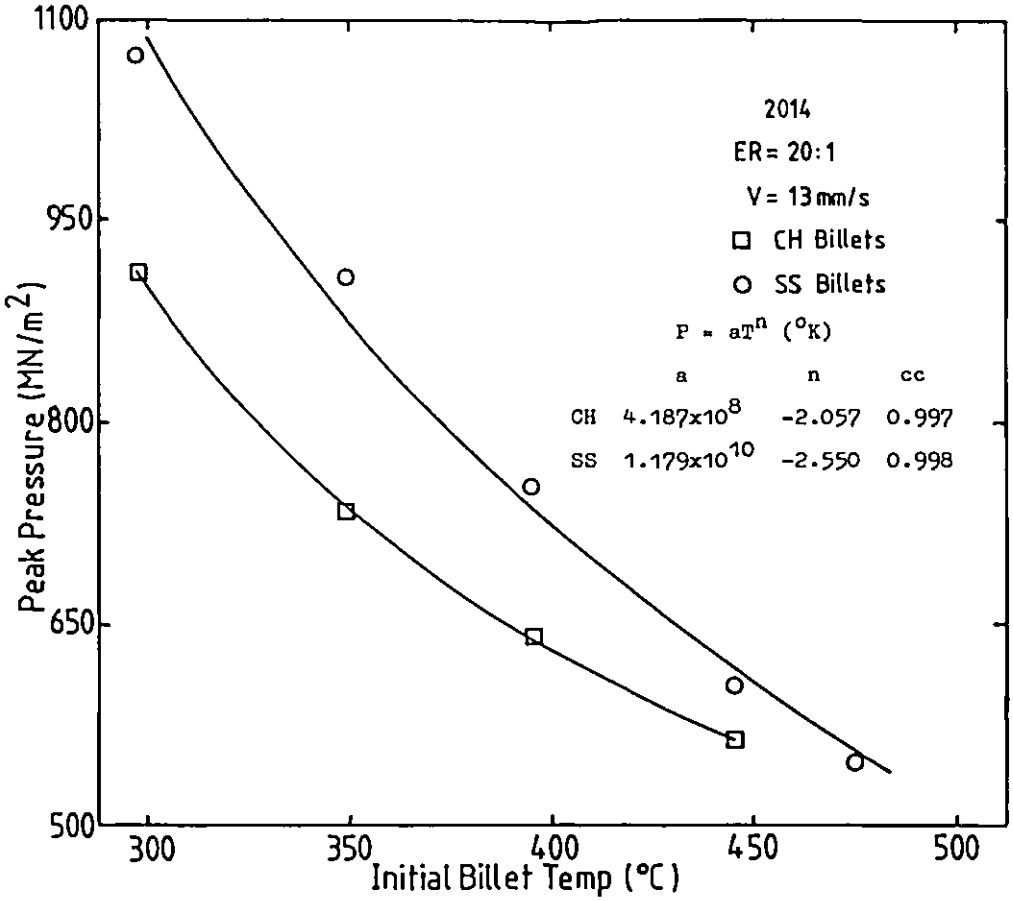


Figure 4.52 Peak pressure vs initial billet temperature for direct extrusion of CH and SS 2014 alloy ER = 20:1

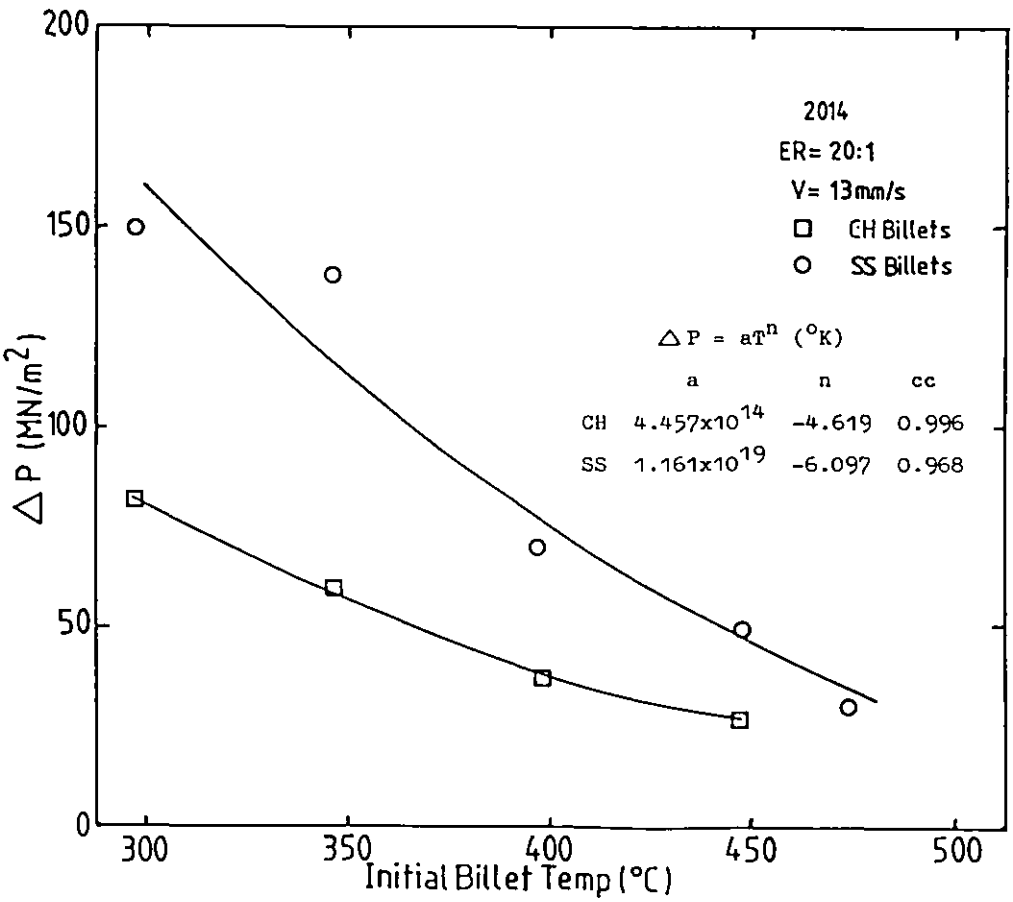


Figure 4.53 Peak height ΔP vs initial billet temperature for direct extrusion CH and SS 2014 alloy ER = 20:1

treatment increases the peak and ΔP pressure, the difference increasing with decreasing temperature, as predicted by the flow stress data. The extrusion data and flow stress data have also been regressed using the general pressure equation 4.12. and flow stress equation 4.17. and compared with the CH 2014 data. The results in table 4.20. show that the values of 'a' and 'c' show the same trend as the values of 'a"' and 'b"' in the flow stress equations, and 'b' is similar in both pressure equations, consistent the trends observed in the 2000 series alloys discussed in section 4.2.9.

It may therefore be concluded that although a slower cooling rate is necessary for extrusion, which is likely to be the case for the larger extrusion billets used in industry, the slow precipitation kinetics of the transition phases and equilibrium precipitate results in an appreciable solid solution content prior to extrusion and hence similar flow stress characteristics to the material cooled at a faster cooling rate.

4.2.10.2. EVALUATION OF SURFACE CRACKING

Previous workers[124,149] have shown that it is possible to correlate the surface quality with respect to the categories A,B and C using the initial billet temperature and the corresponding values of LnZ_I. These relationships are shown plotted in figure 4.54. for the two different initial heat treatments using the steady state constants in table 4.19. The defining lines between a good (A) and bad (B,C) surface finish have been established using the following power relationships, so that for a good surface finish:

			Correlation	
Conventional Heating (CH)	$\ln Z_I <$	$\frac{67954}{T1.199}$	0.998	4.18.
Presolution Soak (SS)	$\ln Z_I <$	$\frac{97955}{T1.223}$	0.999	4.19.

where T is in degrees Kelvin.

Due to the large difference in ΔH shown in table 4.19. the strain rates at which cracking occurs have also been evaluated using equations 4.18. and 4.19. and plotted as a function of the initial temperature in figure 4.55. The figure shows that surface cracking is effectively reduced in the SS extrudes below an initial billet temperature of 450 deg.C, the increase in strain rate increasing with decreasing temperature as the flow stress increases, which implies that surface cracking may well be reduced by the increase in tensile strength in the weakened outer regions of the extrude. Above 450 deg.C the increase in flow stress and hence tensile strength in the SS extrudes is only marginal and surface cracking is therefore not significantly reduced by a presolution soak treatment.

Although equations 4.18. and 4.19. are useful in determining the initial extrusion conditions resulting in surface cracking, the exact conditions cannot be properly defined by these equations due to the temperature change during extrusion. The effect of the presolution soak has therefore also been considered by calculating the temperatures, using the integral profile model, at which cracking commences along the length of the extrude. The results in table 4.21. show that for identical extrusion conditions cracking commences further along the length of the extrude for all the presolution soak billets, which

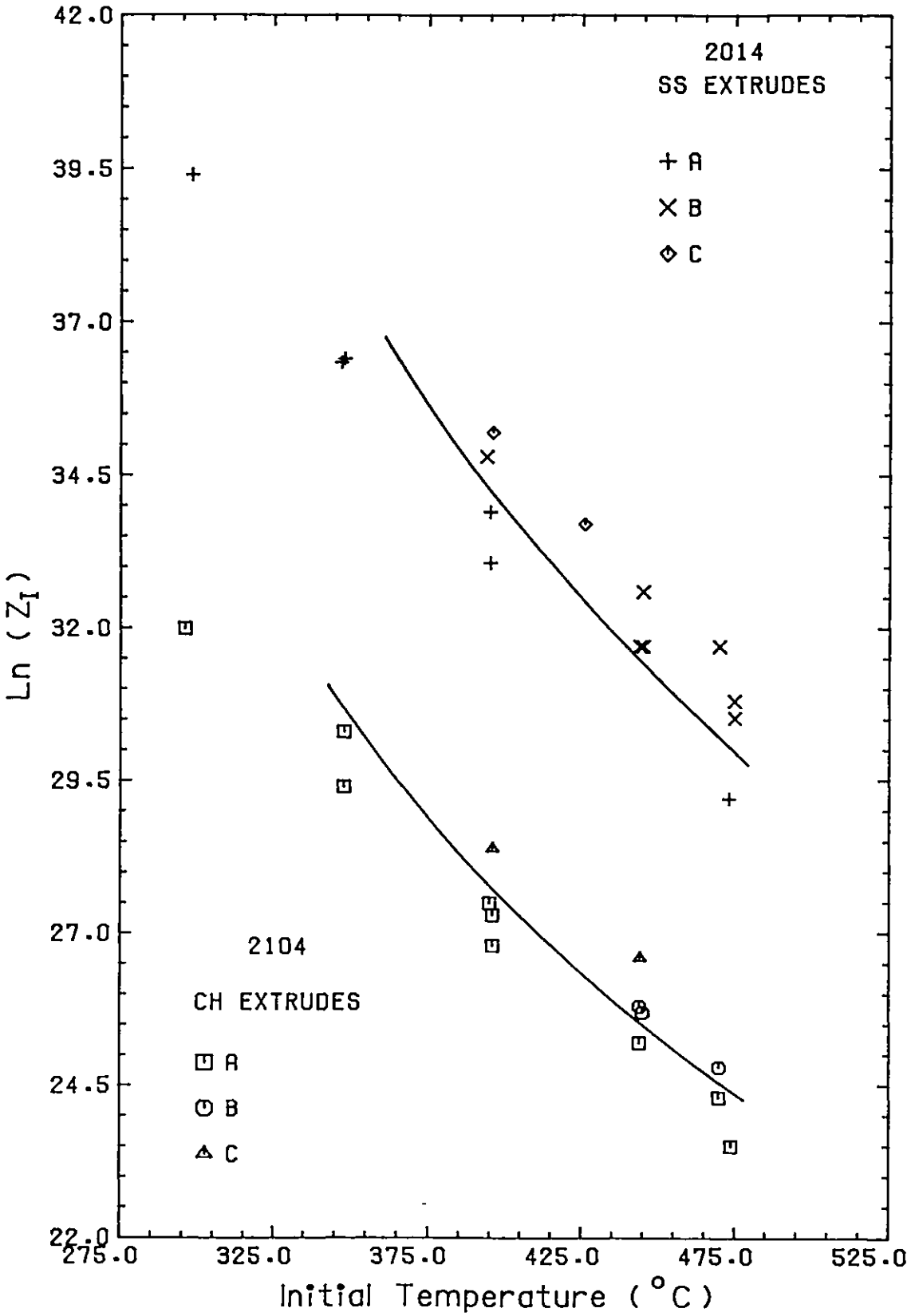


Figure 4.54 LnZ_I vs T_I - Dependence of surface cracking on the initial process conditions during direct extrusion of CH and SS 2014 alloy

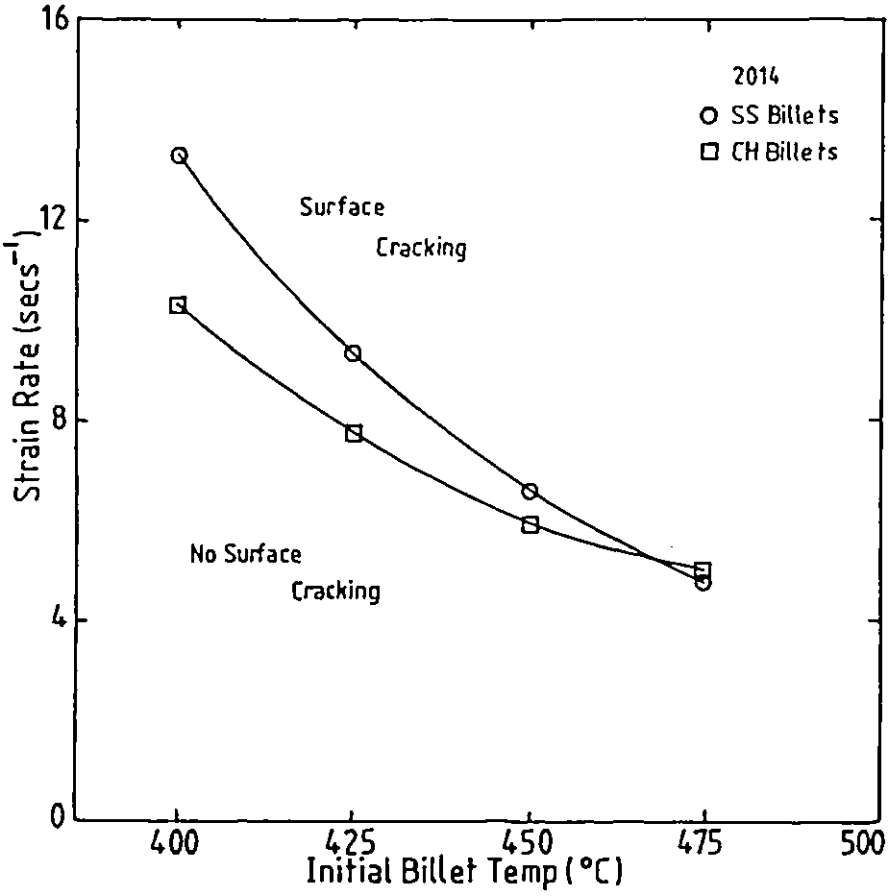


Figure 4.55 Strain rate required for surface cracking vs T_I for direct extrusion of CH and SS 2014 alloy

Conventionally Heated Extrudes

Extn Code	T_I °C	ER	v mm/s	l_c	T_c °C	T_F °C
D4462A	444	20	12	0.05	474	547
D4443A	445	30	8	0.03	470	541
D4365A	396	50	12	0.30	480	536
D4465A	445	50	12	0.03	490	573

Presolution Soak Extrudes

Extn Code	T_I °C	ER	v mm/s	l_c	T_c °C	T_F °C
D4562AS	475	20	12	0.48	537	567
D4462AS	445	20	12	0.63	525	547
D4443AS	445	30	8	0.49	518	546
D4465AS	445	50	12	0.44	540	583
D4365AS	394	50	12	0.50	530	574

l_c fraction of the distance along the extrude length cracking commences
T_c mean temperature at position l_c
T_F mean final temperature

Table 4.21 The mean temperatures evaluated by the integral profile model at which cracking occurs during CH and SS direct extrusion of 2014 alloy.

indicates that even at the high extrusion temperatures the presolution soak can retard the onset of surface cracking. The predicted temperatures at which cracking commences of 470 deg.C to 490 deg.C for the conventially heated billets agree with the temperature of 490 deg.C reported by Paterson[29] for 2014 and to some extent confirms the validity of the modification made to the temperature rise model discussed in section 2.2.2. with regards to the change in container temperature. A mean temperature of 480 deg.C and a final temperature greater than 530 deg.C indicates that surface cracking in all these extrudes may well be associated with incipient melting as shown in plate III b), since assuming a temperature gradient exists across the extrude, the temperature at the periphery may be close to or in excess of the eutectic temperature of 517 deg.C. The variation in temperature across and along the extrude will be discussed in further detail in section 4.3.6.3. However it should be noted that a final temperature in excess of 480 deg.C is not a prerequisite for surface cracking since run D4522A (T_I = 480 deg.C, ER = 20:1, v = 3.3 mm/s) exhibits of final temperature T_f = 530 deg.C but showed no signs of surface cracking due to the low ram speed used. The occurrence of surface cracking is therefore very much dependent on the strain rate and stresses generated in the die land area a phenomena which is shown more clearly in the limit diagrams in section 4.4.10.

The predicted temperatures from the SS extrudes in table 4.21. show that surface cracking commences at exceptionally high mean temperatures of 540 to 520 deg.C i.e. temperatures well above the eutectic temperature. If a large percentage of the eutectic phase remains in solution prior to testing and during extrusion then surface cracking associated with the melting of the eutectic phase will be further reduced. However the sudden appearance of surface cracking at these positions along the extrude was so severe

in most cases that cracking soon extended to the centre of the extrude. Therefore although the presolution soak treatment can be considered to retard the onset of surface cracking at high extrusion temperatures, the combination of a high initial billet temperature and the temperature rise associated with the incremental increase in load results in severe cracking towards the rear of the extrude.

In conclusion therefore it has been shown that a presolution soak treatment is effective in retarding surface cracking at all temperatures, although the large increase in load at low temperatures shown in figure 4.52. and the temperature rises at high billet temperatures reduce the effectiveness of such a preheat treatment for a given press capacity of 1130 MN/m^2 to a temperature range of approximately 350 deg.C to 450 deg.C, the temperature range in which most commercial aluminium alloy extrusions are carried out[33,35,136].

4.3 STRUCTURAL INVESTIGATION

4.3.1. INTRODUCTION

The structures have been investigated at all stages of processing from the as cast state to the fully heat treated extrudes. The effect of Cu content on the structural characteristics has been established using the 1% Cu, 3% Cu and 5% Cu alloys, whilst the effect of heat treatment has been investigated using the commercial 4% Cu 2014 alloy. The experimental techniques used for optical and transmission electron microscopy are outlined in sections 3.6.4 and 3.6.5.

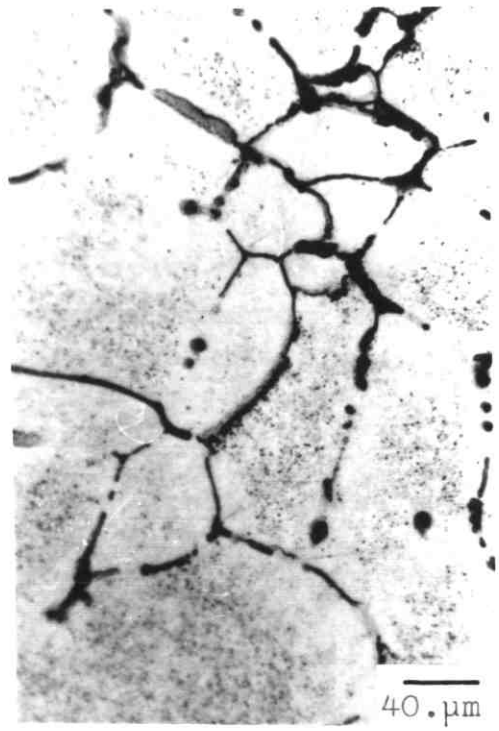
4.3.2. AS CAST STRUCTURE

The effect of decreasing copper content on the as cast structures is shown in plate IV . At high Cu contents micrographs c), d) show the structure consists of dendrites of aluminium solid solution surrounded by a eutectic which has etched up black. At the higher magnification micrograph d) shows the presence of more than one segregated constituent shown by the light and dark phases. The larger percentage of the light phase indicates this to be $CuAl_2$ which is lightly attached by the Kellers reagent. The darker constituent has been identified by previous workers[33,135,162] to consist of two separate eutectics in 2014 of compositions α + (FeMnCuSi)Al and $\alpha + \theta + Q$. However, the compositions are based upon quantitative X-ray microanalysis data, which can be thickness dependent in Al-Cu alloys due to deposition of a Cu rich film on the surface of the foil during thin foil precipitation[163] which can only be effectively removed by ion thinning in an instrument of low residual partial pressure[163], which was not available for the present work.

a) 1% Cu



b) 1% Cu



c) 5% Cu



d) 5% Cu

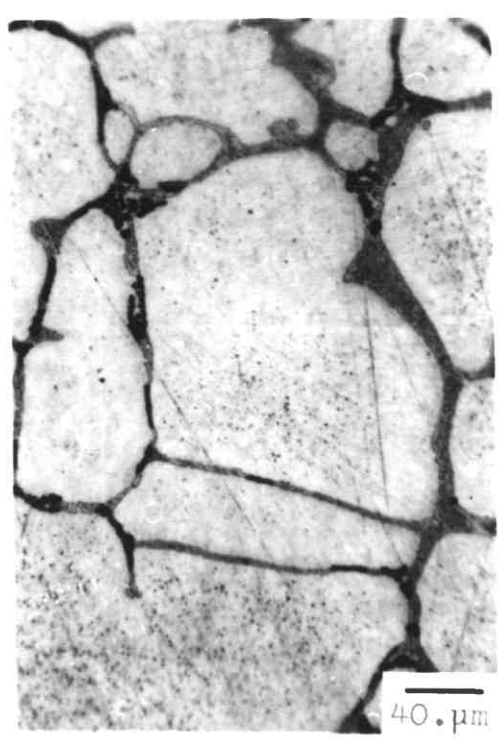


Plate IV. As Cast Microstructures of the 1% Cu and 5% Cu Alloys.

An example of the structure in the low Cu alloys is shown in micrographs a) and b) and is typical of the 1% Cu and 2% Cu alloys. The fast cooling rates and low Cu content promotes the formation of a more divorced eutectic which is shown in micrograph b) at a higher magnification. A greater amount of the aluminium is precipitated out in the primary and dendrites, removing the aluminium component for the eutectic reaction. The composition of the eutectic phase can therefore be expected to change with copper content, decreasing in Al with decreasing weight percent copper. This is also reflected in the slightly larger inter dendritic arm spacing shown in micrograph a). Although it should be noted that the dendrite cell size is also directly related to the solidification rate, the faster the solidification rate, the smaller the dendrite cell size[164].

Senary phase diagrams for the present alloy system do exist[38], but tend to be extremely complicated and applicable to equilibrium conditions which are unlikely to be achieved during the rapid cooling associated with D.C casting. A review of the literature[33,35,38] suggests the solvus and solidus lines will be similar to those of the binary system as shown in figure 4.56. where the eutectic temperature is lowered to 517 deg.C. However, the exact phase fields are likely to be more complicated than this as shown by the quaternary isothermal section in figure 4.57. for an Al-Cu-Mg-Si alloy with 0.8% silicon[36].

The as cast structures shown in plate IV are generally considered to be undesirable due to the brittle nature of the eutectic phases and the reduction in ageing caused by the segregation of Cu in the Cu rich eutectics. The modification of these structures by a subsequent homogenization heat treatment will be discussed in the next section.

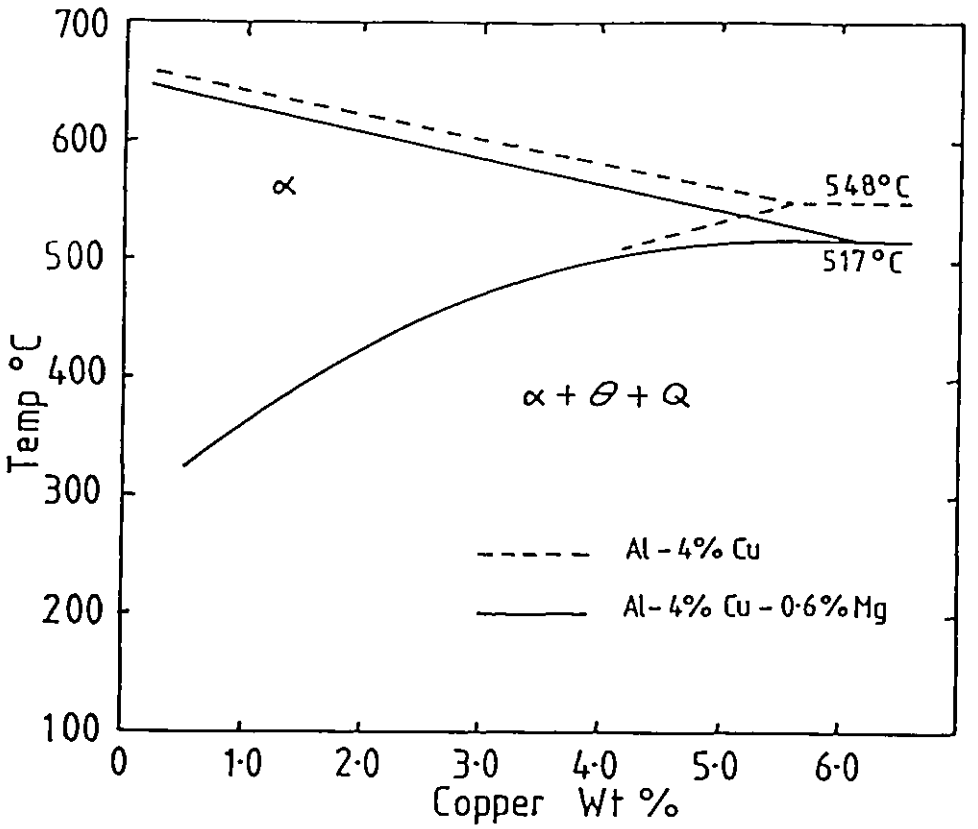


Figure 4.56 Al - 4Cu and Al - 4Cu - 0.6Mg binary phase diagrams ref. 33,35,38

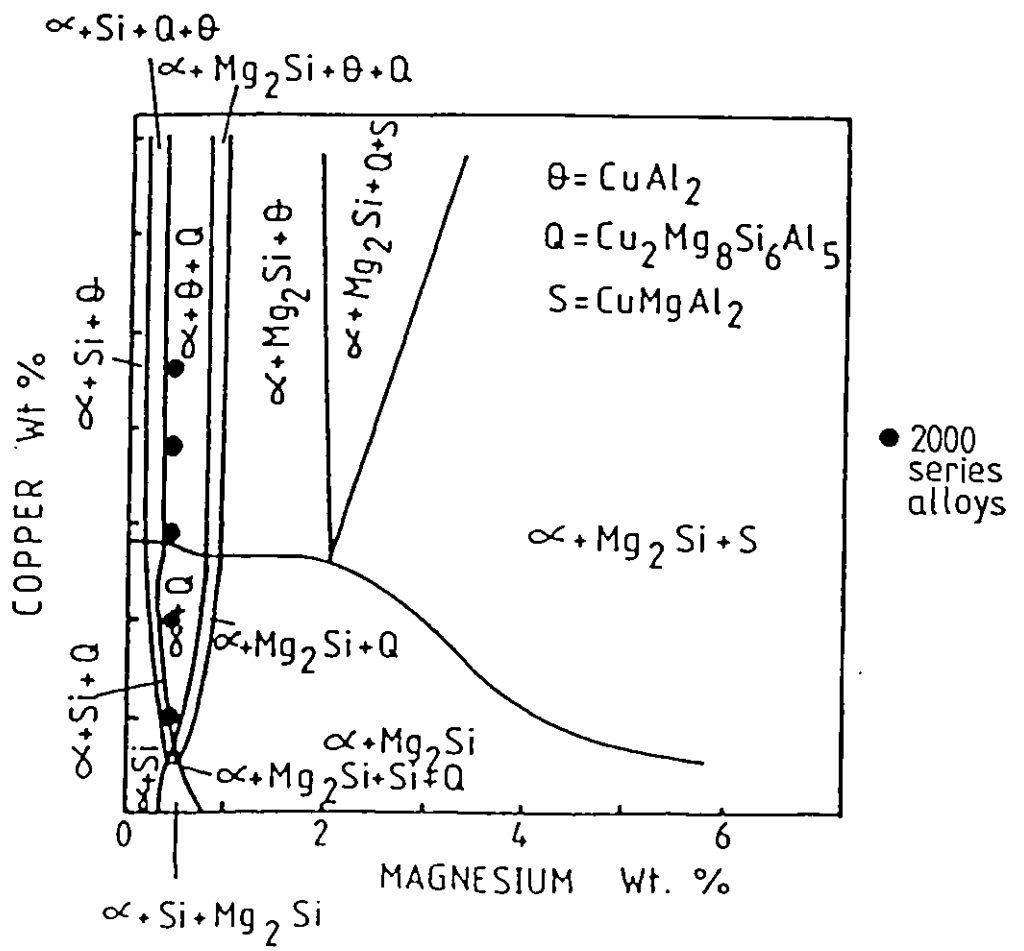


Figure 4.57 Quaternary phase diagram of Al - Cu - Mg for 0.6% Si at 460°C isothermal ref. 36

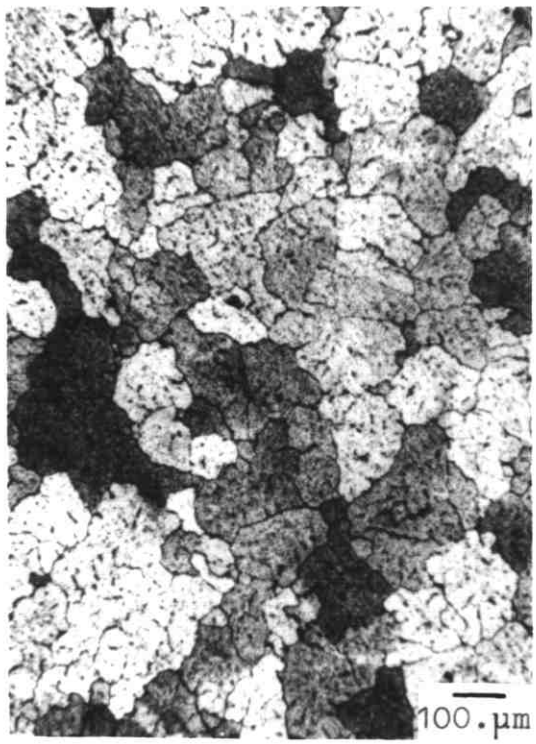
4.3.3. HOMOGENIZED STRUCTURES

Previous workers[33] have shown that a standard homogenization treatment of 24 hours at 500 deg.C is suitable for most commercial D-C cast Al-Cu Alloys. Heating at a higher temperature risks the onset of eutectic melting which can severely reduce the properties of the product[165], whilst prolonged heating has been reported[29,33] to produce no real significant change in the overall structure. The effects of the homogenization heat treatment are shown in plate V. The billets were all furnace cooled at a rate of 80 deg.C per hour.

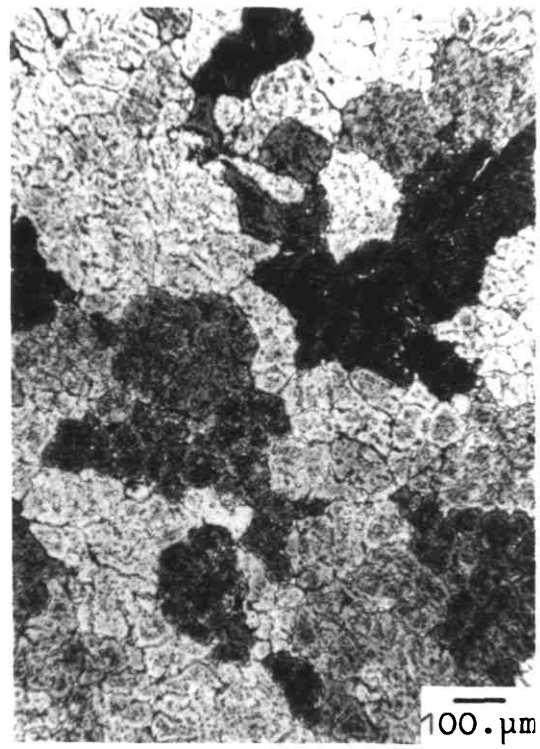
At low magnification micrographs a) and b) show that no substantial grain growth has occurred, where the average grain size ranges from 120 μm in the 1% Cu alloy to 90 μm in the 5% Cu alloy. Small amounts of the dendrite structure still remain , which is consistent with structures found by previous workers using similar alloys[25,26,29].

Examples of the structures at higher magnification are shown in micrographs c) to e). The structures are typical of those found in all the alloys extruded and consist of a uniform dispersion of second phase particles ranging in size from 0.05 μm to 1 μm, with a number of larger particles of 3-6 μm in size situated mainly at the grain boundaries as shown in micrographs a), b) and e). Micrograph e) also shows the existence of a precipitate free zone at the grain boundary, which were present in all the alloys and in some cases associated with the larger second phase particles within the matrix. The grain boundaries can act as vacancy sinks reducing the sites for precipitation adjacent to the grain boundary, whilst the larger particles may also act as sites for preferential precipitation depleting the surrounding matrix of solute.

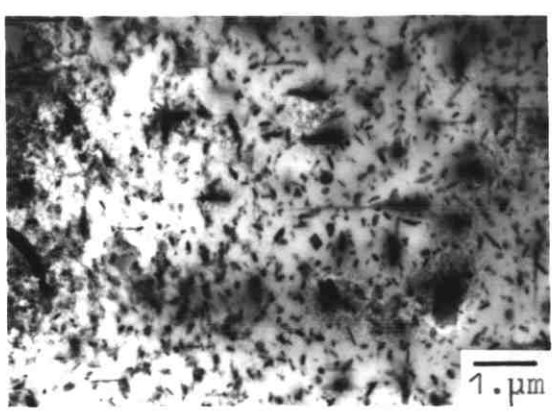
a) 1% Cu



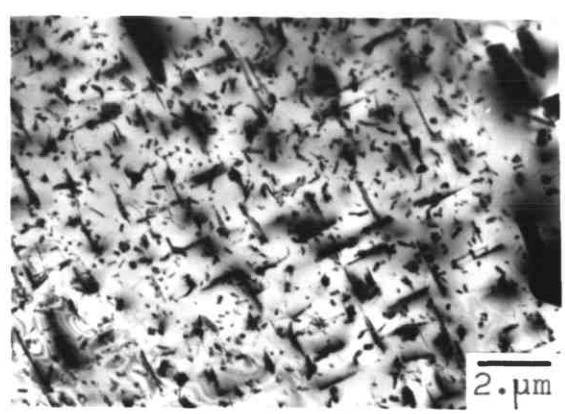
b) 5% Cu



c) 1% Cu



d) 3% Cu



e) 2% Cu

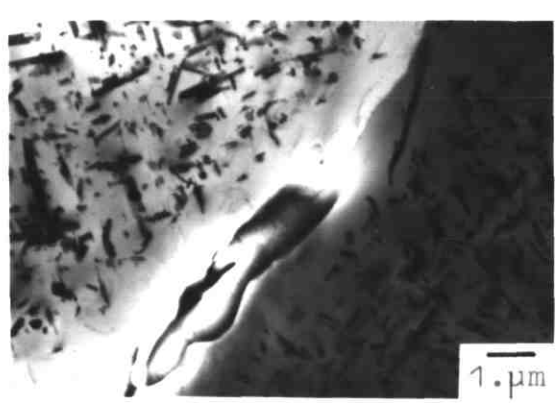


Plate V. Homogenized Microstructures.

The fine 0.05 - 0.075 μm particles have been identified[29,33] in 2014 as (Fe Mn)Al_6 and Mn Al_6 which are thought to precipitate out of solution during homogenization. The overall distribution of the particles was approximately the same in all the alloys confirming the above analysis.

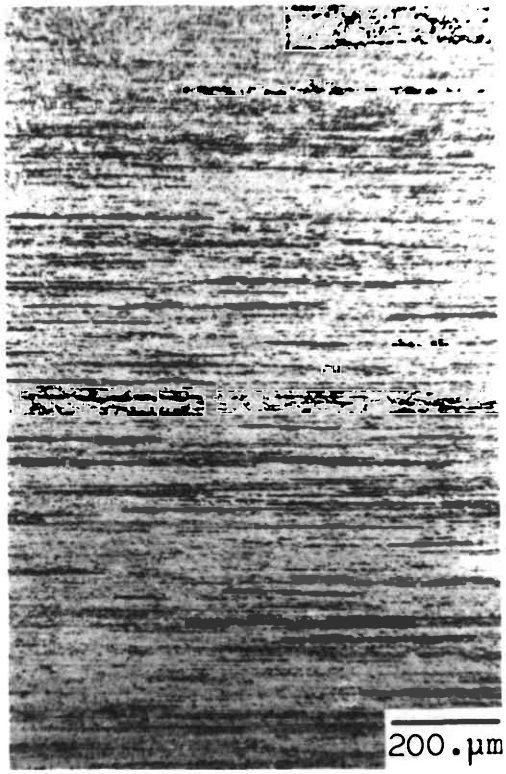
The distribution of the larger 1 μm particles lying on the cube planes of the matrix, tended to decrease with decreasing Cu content as shown in micrographs c) and d). These are therefore likely to be θ or Q phase which precipitates out of solution during cooling from the homogenization temperature. The proportion of the Q phase is likely to increase with increase in the Mg:Cu ratio as indicated by the quaternary phase diagram shown in figure 4.57.

The large 3-6 μm particles were found in all the alloys and are normally associated with insoluble as cast Fe and Si rich inclusions, but may also contain Cu due to the non-equilibrium microsegregates formed during solidification[61]. More recent works[29,33,61] have shown the particles in 2014 to be either Q phase, Al_{12} (FeMn)Si or Mg_2Si particles.

4.3.4. EXTRUSION STRUCTURES

For the present work the as quenched microstructures can be classified into one of two types. The first consist of a core of fibrous grains surrounded by a more dislocated structure at the periphery, examples of which are shown in plate VI a) and b). The fibrous structure b) consists of the original homogenised grains elongated in the extrusion direction, whilst the periphery a) originates from the heavily sheared regions outlining the deformation zone. The

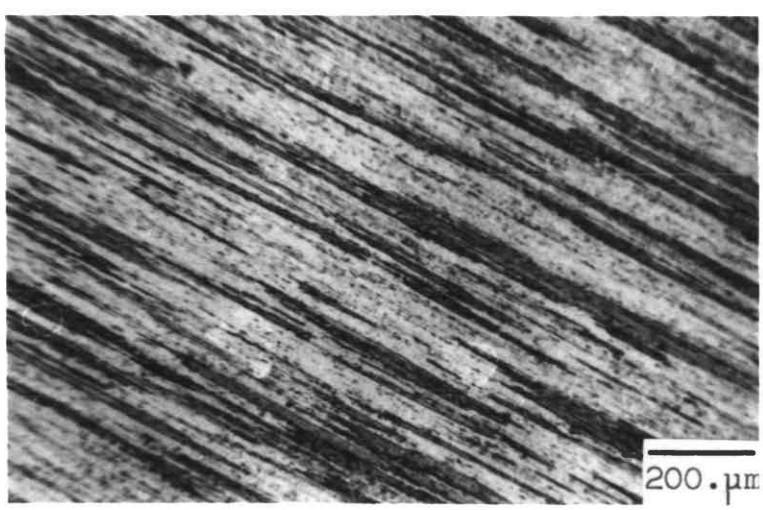
a)



Edge

D2155
T_I = 300°C
ER = 50:1

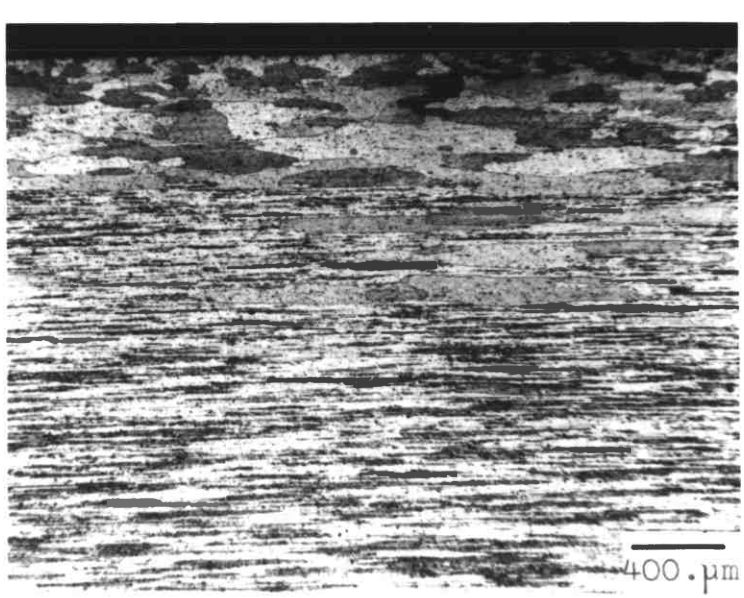
b)



D2345
T_I = 400°C
ER = 50:1

Centre

c)



Edge

D24610
T_I = 450°C
ER = 100:1

Plate VI. Typical Microstructures of the Press Quenched Extrudes - 2% Cu.

structure is typical of the low temperature extrudes below 350 deg.C and persisted to higher temperatures in the lower copper alloys. The second type of structure is shown in micrograph c) and consists of an inner core of fibrous grains surrounded by a peripheral zone of recrystallized grains. The structure is typical of the high temperature extrudes and forms as a result of the inhomogeneous deformation occurring during extrusion, where the surface elements of the outgoing extrude suffer a greater degree of deformation than elements at any other position. The increased dislocation density and resultant internal energy, increase the driving force for static recrystallization in this region before the extrude is quenched. Both the structures were observed in the direct and indirect extrudes.

Figure 4.58. shows the effect of ram speed and extrusion ratio on the volume percent of material recrystallized per unit length calculated using equation 4.20. at various extrusion temperatures in the 2% Cu and 3% Cu alloys the measurements being taken at a constant distance along the extrude corresponding to 0.3L. At low extrusion ratios the size of the recrystallized grains were normally limited to the size of the recrystallized depth, whilst at higher extrusion ratios finer less elongated grains were found, as shown in micrograph c). The increase in extrusion ratio and hence strain increases the driving force for recrystallization nucleation whilst the high ram speeds reduce the quench delay but increase the temperature rise due to the reduction in heat losses and increase in extrusion load. A combination of these factors help increase the fraction of recrystallized material with increase in extrusion ratio and ram speed, where as the recrystallized grain size decreases. The increase in alloy content increases the flow stress and temperature rise during extrusion, both of which promote primary

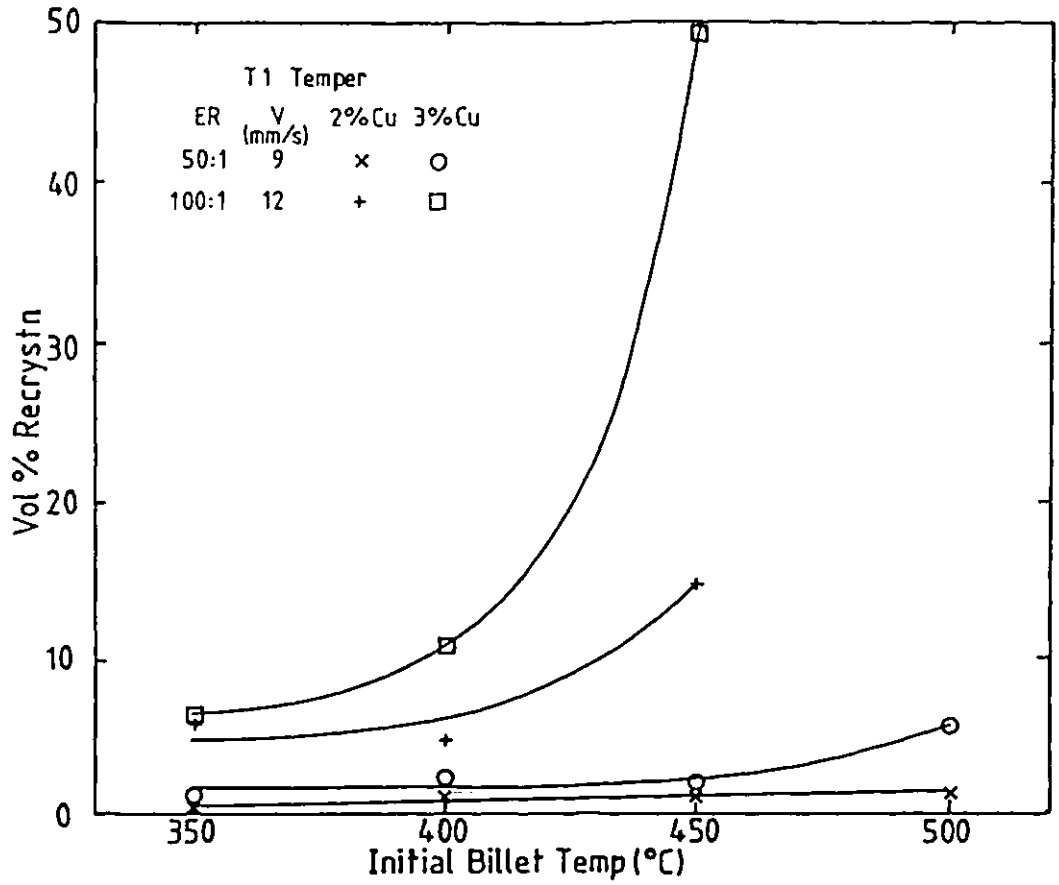


Figure 4.58 Volume % recryn vs initial billet temperature in the T1 temper for 2% Cu and 3% Cu alloys

Volume Percent Recrystallization

2014 - T1

ER = 20:1

T_I °C	CH Direct	CH Indirect	SS Direct
480	3.4	2.6	5.1
450	1.7	1.9	1.1
400	1.0	0.8	0.5

Vol% recystn = a LnZ_I + b

2014-T1

	a	b	cc
CH Direct	-0.58	16.84	0.950
CH Indirect	-0.47	13.89	0.981
SS Direct	-1.22	41.31	0.840

Table 4.22 The variation in % recrystallization during direct and indirect extrusion of CH and SS 2014 alloy in the T1 temper.

recrystallization at a specific temperature and strain rate.

$$\text{Vol\%} = \left(1 - \left[\frac{R-d}{R}\right]^2\right).100 \qquad 4.20.$$

R = Extrude Radius
d = Recrystallized depth

A slight increase in the size of the peripheral zone was found at the rear of the extrudes which can be associated with the temperature rise as extrusion proceeds. However the increase is not as significant as that reported by other workers[1,28] for aluminium alloys, which demonstrates the effectiveness with which the intermediate second phase articles inhibit grain growth during primary recrystallization.

The effect of indirect extrusion and the presolution soak treatment on percentage recrystallization at 0.3L in the 2014 alloy is shown in table 4.22. The reduction in recrystallization during indirect extrusion has been observed by previous workers[28,166-168] and attributed to the uniform nature of flow and lower temperature rise during extrusion. The SS extrudes show the highest percentage recrystallization consistent with the increased temperature rise during extrusion. Although the results in table 4.22. show that the percentage recrystallization measurements from 20:1 and 30:1 extrudes may be related to LnZ_I, such relationships can only be regarded as approximate due to the variation in quench delay with strain rate, whilst the quench delay is virtually doubled during indirect extrusion due to the arrangement of the tooling discussed in section 3.2.5., such that the percentage recrystallization in equivalent indirect extrudes may even be smaller than shown by the results in table 4.22. Since a duplex structure is reported[169] to be deleterious to both fracture toughness and corrosion

resistance the reduction in peripheral recrystallization is an important feature of the indirect process.

The effect of Cu content on the optical structures was only significant with respect to the size of the recrystallized periphery which as shown in figure 4.58. increased with Cu content, consistent with an increase in the load and temperature rise during extrusion.

4.3.5. THE VARIATION IN STEADY STATE SUBSTRUCTURE IN EXTRUSION AND TORSION

4.3.5.1. EXTRUDATE SUBSTRUCTURES

Specimens for electron microscopy were taken at equivalent positions along the length of each extrude coinciding with steady state extrusion. Examples of the extrusion substructures from the centre of the extrudes at high Z and low Z conditions in the 1% Cu, 3% Cu and 5% Cu alloys are shown in plate VII.

The steady state structures in all the alloys were characterised by a subgrain structure of low misorientation consistent with the operation of dynamic recovery and repolygonization during extrusion. The lack of contrast between the grains gives an indication of the low misorientation which exists between then, which is confirmed by the measurements shown in table 4.23. These were determined using standard diffraction techniques, by measuring the movement of kikuchi lines as the subboundaries were traversed. The results show that the misorientations are all lower than 2^{o} which agrees with the values determined by previous workers for similar alloys[25,27,29]. No consistent trend could be found with either alloy content or process conditions although the small variation shown in

table 4.23. indicates a large number of measurements would be required to show a variation in the mean value.

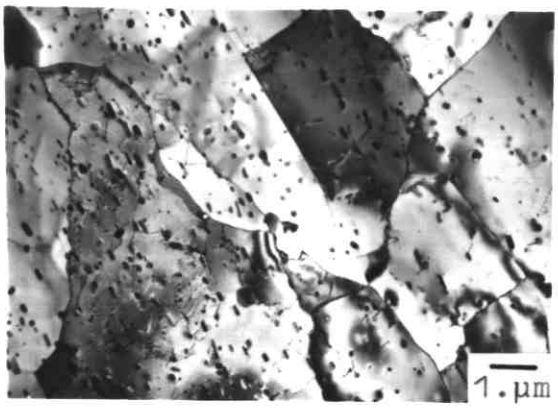
Evidence of dynamic recrystallization was not observed in any of the alloys although high angled boundaries were often detected lying parallel to the extrusion direction, their presence being associated with the grain boundaries of the original homogenized material, which give rise to the fibrous structures seen in plate VI. However evidence of static recrystallization at groups of larger particles was seen in all the alloys an example of which is shown in plate XII b), which is from the 2014 alloy extruded at 300 deg.C. Recrystallization nucleation at groups of particles $\geqslant 1\mu m$ has been observed in a number of alloy systems[142]. Humphreys[107] has shown that a deformation zone characterized by a high dislocation density and lattice misorientation exists in the vicinity of such particles and hence nucleation is thought to occur by a rapid polygonization process involving subboundary migration of the subgrains within this deformation zone. Once the nucleus has consumed the deformation zone it experiences a barrier to further growth due to the decreased driving force in the surrounding matrix. Static recrystallization and the mechanisms involved will be discussed in further detail in section 4.3.7.

Examples of the substructures in the 1% Cu, 3% Cu and 5% Cu alloys at low extrusion temperatures ie high Z are shown in micrographs b), d) and f). The subgrains are elongated in the extrusion direction and have a relatively high internal dislocation density indicating that recovery is not complete at low temperatures. It should be noted at this point that the observed structure depends on the orientation of the foil in the microscope and therefore not all the dislocations present may be observed in any one micrograph. All the second phase particles are elongated in

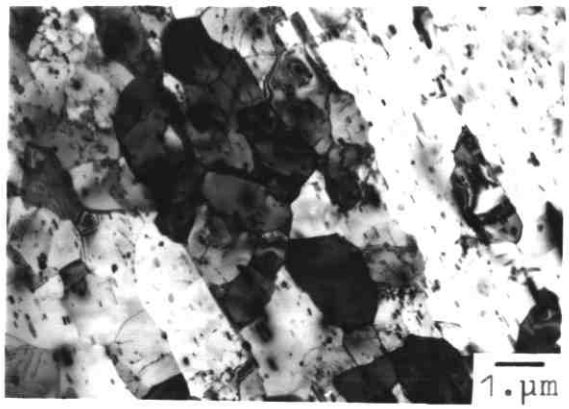
EXTRUDES

D1534 1% Cu D1143

a) T_I = 475°C LnZ_c = 25.45

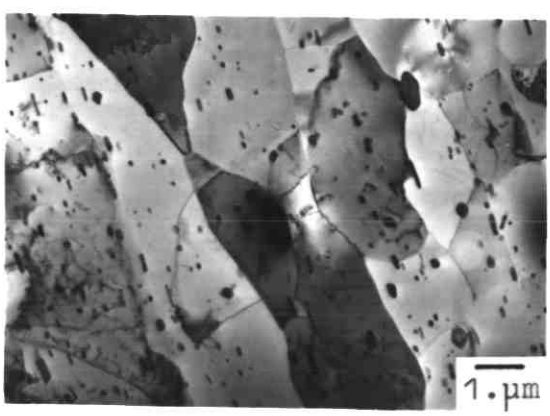


b) T_I = 300°C LnZ_c = 31.46

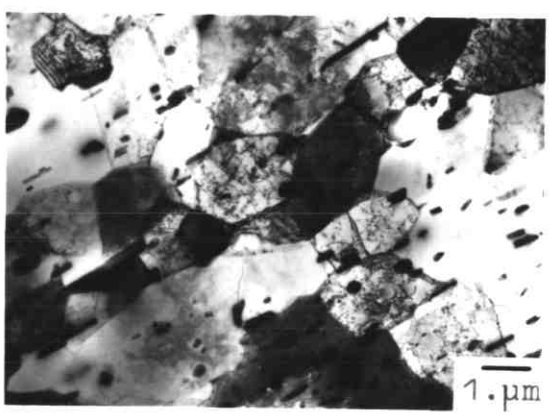


D3455 3% Cu D3255

c) T_I = 450°C LnZ_c = 25.84

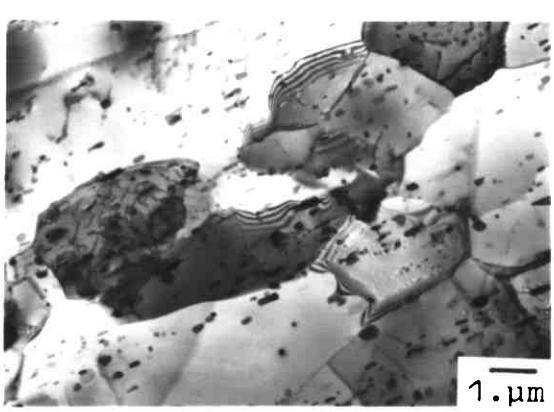


d) T_I = 350°C LnZ_c = 28.99



D543L4 5% Cu D523L4

e) T_I = 450°C LnZ_c = 23.58



f) T_I = 350°C LnZ_c = 26.56

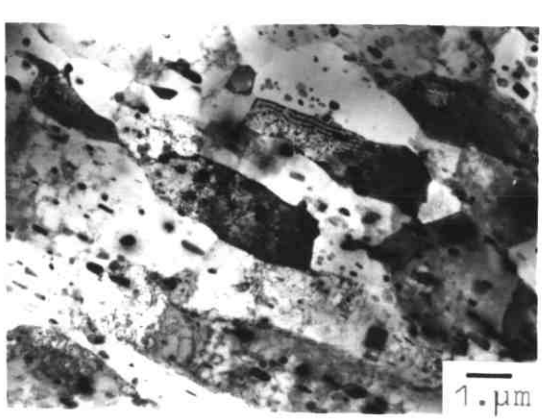


Plate VII. Substructures Observed in the Longitudinal Plane of the Press Quenched Direct Extrudes of the 1% Cu, 3% Cu and 5% Cu Alloys.

the extrusion direction and uniformly distributed throughout the matrix. Pinning of the subboundaries by both the larger as cast and intermediate size particles can be clearly seen in all the alloys although the subgrain diameter is not directly related to the interparticle spacing. This implies that the action of the applied stress is sufficient to overcome some of the interaction between the subboundary dislocations and particles which are present during steady state extrusion.

The substructures from low Z extrudes in micrographs a), c) and e) show that an increase in extrusion temperature results in a steady state substructure of larger subgrains with lower internal dislocation densities and narrower subboundary walls. The increase in thermal activation permitting easier cross slip and climb of dislocations. The subgrains are generally more equiaxed in nature which can be associated with the need to reduce the grain boundary area and thus reduce the free energy of the structure, which is further enhanced by the increased mobility of the subboundary dislocations. Pinning by the intermediate sized particles is clearly less pronounced than at low temperatures although the larger as cast particles still act as effective barriers to dislocation motion. The similarity between the substructures in micrographs a), c) and e) indicates that although an increase in solid solution content with temperature and initial copper content is predicted by the microhardness data in figure 4.14. this has little effect on the degree of recovery. Since the diffusivity of the solute species also increases with temperature the interaction of the solute atom atmospheres with the slower moving dislocation is less effective. Previous workers[28,29,172] have suggested the decrease in ΔH may be associated with an increase in vacancy concentration due to the atomic mismatch between the solute and solvent atoms, however whether this results in any appreciable increase in the available vacancies for dislocation climb

will depend on the solute atom vacancy binding energies which for Cu and Mg are considered to be high[57]. Associated with the increase in solid solution there will also be a decrease in the second phase particle distribution and hence dispersion hardening. Although there is no quantitative data to show this effect previous workers[28,29] have also observed a decrease in particle distribution with increase in temperature during hot working of heat treatable aluminium alloys.

An important feature at high extrusion temperatures, which should not be confused with the recovered microstructure is the presence of helical dislocations seen in the higher copper alloys, examples of which are shown in plate XIIa). Their formation occurs during quenching of the extrude and is caused by the interaction of quenched vacancies with screw or mixed dislocations. The vacancies condense onto the screw dislocations so that the dislocation line becomes curved to form one turn of a spiral. The helical dislocation forms when further groups of vacancies are attracted at difference points along the dislocation line. Helical dislocations were observed in the 3% Cu - 5% Cu alloys with preferred orientations in the [200] directions and tended to be locked by precipitates which prevented them from straightening out. Their presence has been reported to be beneficial during ageing since they act as sites for precipitate nucleation.[145,146]

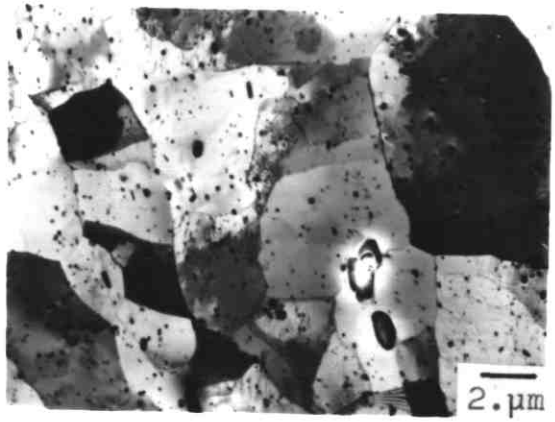
4.3.5.2. TORSION SUBSTRUCTURES

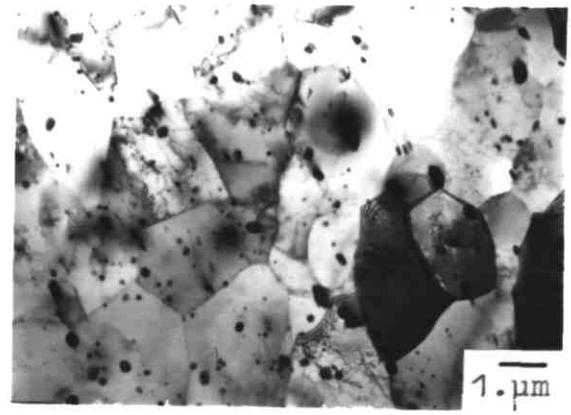
The variation in substructure with process conditions during torsion testing at high and low Z conditions in the 1% Cu, 3% Cu and 5% Cu alloys are shown in plate VIII. The radial variation in strain and strain rate in the torsion specimen means that only the structure in the outer radial elements will be representative of the nominal flow

TORSION SPECIMENS

14-3 1% Cu 12-31

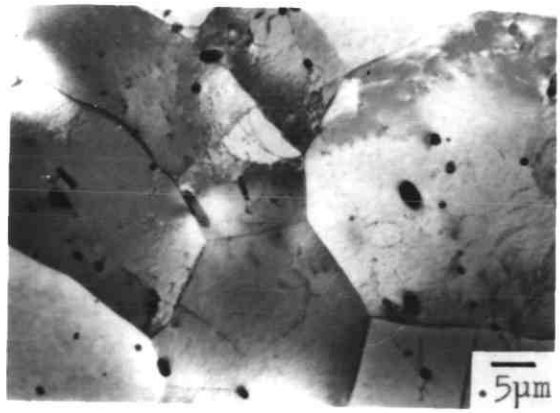
a) $T_I = 475^oC$ $LnZ_p = 24.75$ b) $T_I = 355^oC$ $LnZ_p = 29.11$

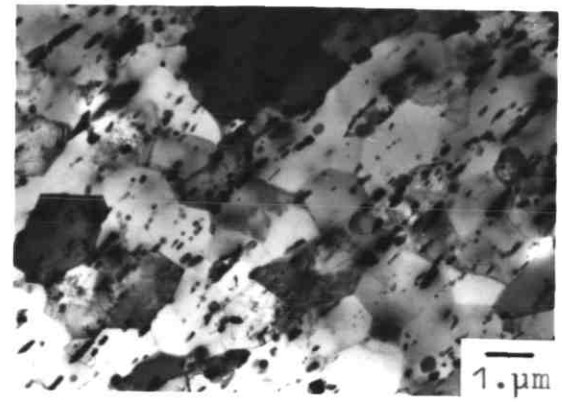




34-4 3% Cu 32-4

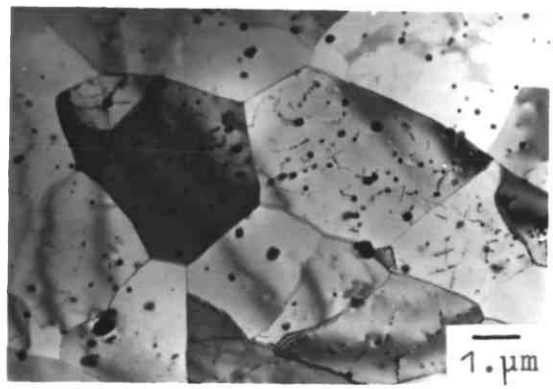
c) $T_I = 458^oC$ $LnZ_p = 26.00$ d) $T_I = 339^oC$ $LnZ_p = 30.53$





54-4 5% Cu 52-31

e) $T_I = 475^oC$ $LnZ_p = 23.91$ f) $T_I = 355^oC$ $LnZ_p = 26.85$



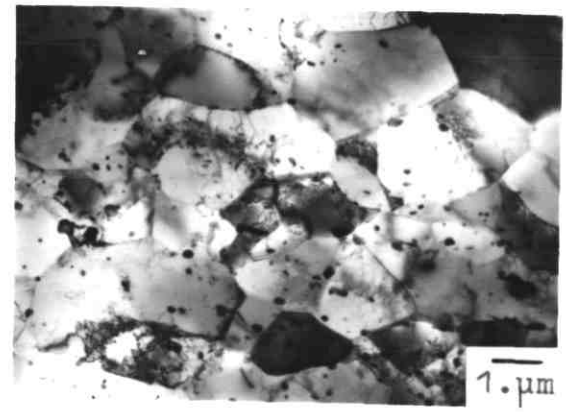


Plate VIII. Substructures Observed in the Longitudinal Plane in the Periphery of the as Quenched Torsion Specimens - 1% Cu, 3% Cu and 5% Cu.

conditions. Examination of the as quenched structures has therefore been concentrated on sections parallel to the axis in the centre of the gauge and at a constant position close to the surface of the specimen. The torsion tests were stopped and automatically quenched at peak torque which coincided the attainment of steady state flow.

No evidence of a recrystallized annuli equivalent to the duplex structures seen in extrusion was found, indicative of the smaller temperature rise predicted during testing and the almost instantaneous quench which further reduces static recrystallization after testing. Plate VII shows that a subgrain structure exist at high and low Z conditions in all the alloys, similar in characteristics to those found in extrusion at equivalent values of Z. The measured misorientation relationships were of the same order of magnitude as those found in the extrudes and again no consistent variation was found. The relatively small strains to peak torque shown in appendix I do not produce the same degree of particle alignment as in extrusion, particularly in the low Z structures shown in micrographs a), c) and e). However the reduction in strain is unlikely to have any effect on the subsubstructural characteristics since once steady state is achieved, the substructure is effectively strain independent.

It is interesting to note that the presence of GP zones in the low Z extrudes which give rise to the increase in hardness during natural ageing shown in figure 4.14 were not detected in the diffraction patterns, whilst the etching effects associated with jet thinning and window thinning prevented positive identification of a zone structure at high magnification. The absence of the characteristic [100] streaking associated with the formation of GP1 zones indicates that the increase in hardness may be associated with

GPB type zones since these produce only small lattice strains[57] and hence very little distortion of the diffraction pattern.

4.3.5.3. THE EFFECT OF PROCESS CONDITIONS ON THE STEADY STATE SUBSTRUCTURE

The dependence of the subgrain size on the process parameters in both torsion and extrusion has been established by relating the subgrain size d to Z the temperature compensated strain rate. Due to the elongated nature of the subgrain structure the dimensions have been measured in the longitudinal and transverse plane, the results are listed in table 4.24. which represent in most cases the mean values of at least 100 individual readings. The results show a greater increase in the longitudinal dimensions in all the alloys at low temperatures indicative of the decrease in recovery and repolygonization. As noted in section 1.5. the subgrain size can be related to the temperature compensated strain rate Z and hence the process condition by:

$$d^{-m} = a + bLnZ \qquad 1.10.$$

where a, b and m are constants. A value of m = 1 is normally used since it has been found to give the best overall correlation[68]. However recent work[112] has shown that equally good correlations can be achieved with $0.3 < m < 1.25$ as the variation in subgrain size is small in comparison to the range of LnZ values normally considered. In the present work a value of m = 1 was found to give the best correlation in all the alloys. The transverse dimensions have been regressed using the above expression and are shown plotted in figures 4.59. to 4.61., the regression data is shown in table 4.24., where LnZ_c corresponds to the temperature corrected values in torsion

Alloy	Extrusion Code	Misorientation		
1% Cu	D1553	0.31	0.11	0.56
	D1143	1.01	0.21	0.76
3% Cu	D3545	0.96	0.17	0.35
	D3155	0.98	0.88	0.66
5% Cu	D543IA	0.42	0.83	0.36
	D513IA	0.51	0.71	1.31

Table 4.23 Misorientation measurements between subgrains 1% Cu, 3% Cu and 5% Cu extrudes.

EXTRUDES

Code	T_I °C	$\dot{\varepsilon}$ s^{-1}	d(1) μm	±	d(t) μm	±
			1% Cu			
D1553	500	10.43	4.36	0.70	3.35	0.50
D1443	450	7.68	3.32	0.55	2.34	0.40
D1343	400	7.40	2.70	0.31	1.52	0.20
D1243	350	7.50	2.27	0.41	1.41	0.20
D1143	300	7.20	1.70	0.29	1.13	0.22
			3% Cu			
D3545	500	11.37	4.65	0.79	3.71	0.73
D3455	450	14.62	3.68	0.60	2.19	0.25
D3345	400	14.17	3.34	0.45	2.22	0.33
D3255	350	15.06	2.13	0.31	1.42	0.21
D3155	300	15.94	1.45	0.31	0.96	0.24
			5% Cu			
D543IA	450	6.00	3.52	0.35	2.25	0.17
D533IA	400	5.70	2.67	0.72	2.05	0.20
D523IA	350	5.50	2.21	0.70	1.40	0.21
D513IA	300	5.70	1.91	0.23	1.10	0.17

TORSION SPECIMENS

Code	T_I °C	$\dot{\varepsilon}$ s^{-1}	d(1) μm	±	d(t) μm	±
			1% Cu			
14-12	475	0.03	9.92	1.10	5.90	0.53
14-2	475	0.31	8.86	1.00	4.64	0.81
14-3	475	2.80	5.31	0.58	3.14	0.50
12-1	355	0.03	4.23	0.87	2.57	0.74
13-4	415	8.70	3.05	0.21	2.24	0.15
12-31	355	2.90	2.62	0.42	1.78	0.25
			3% Cu			
35-1	483	0.03	8.95	0.77	6.32	1.10
34-11	458	0.03	6.01	1.05	3.33	1.10
34-3	458	2.70	6.03	0.71	4.00	0.51
33-41	398	8.50	2.48	0.25	1.82	0.23
32-31	339	2.70	2.28	0.57	1.34	0.14
32-4	339	8.40	1.69	0.28	1.14	0.18
31-42	280	8.10	1.33	0.25	0.85	0.11
			5% Cu			
54-11	475	0.03	6.90	0.90	3.97	0.45
53-1	415	0.03	6.50	1.00	3.15	0.20
54-3	475	2.90	4.45	0.35	2.45	0.25
53-4	415	8.70	3.50	0.10	2.20	0.30
52-32	355	2.90	2.39	0.18	1.33	0.11

$$d^{-1} = aLnZ_c - b$$

1% Cu

Data	a	b	cc
Torsion	0.044	0.736	0.974
Extrusion	0.086	1.804	0.933
Combined	0.072	1.433	0.917

3% Cu

Data	a	b	cc
Torsion	0.106	2.439	0.920
Extrusion	0.125	2.854	0.946
Combined	0.103	2.288	0.912

5% Cu

Data	a	b	cc
Torsion	0.052	0.712	0.891
Extrusion	0.106	1.988	0.983
Combined	0.066	1.005	0.910

$$d^{-1} = aLnZ_I - b$$

5% Cu

Data	a	b	cc
Torsion	0.050	0.660	0.886
Extrusion	0.087	1.639	0.977

Table 4.24 Subgrain size measurements and relationships derived from extrusion and torsion specimens for the 1% Cu, 3% Cu and 5% Cu alloys.

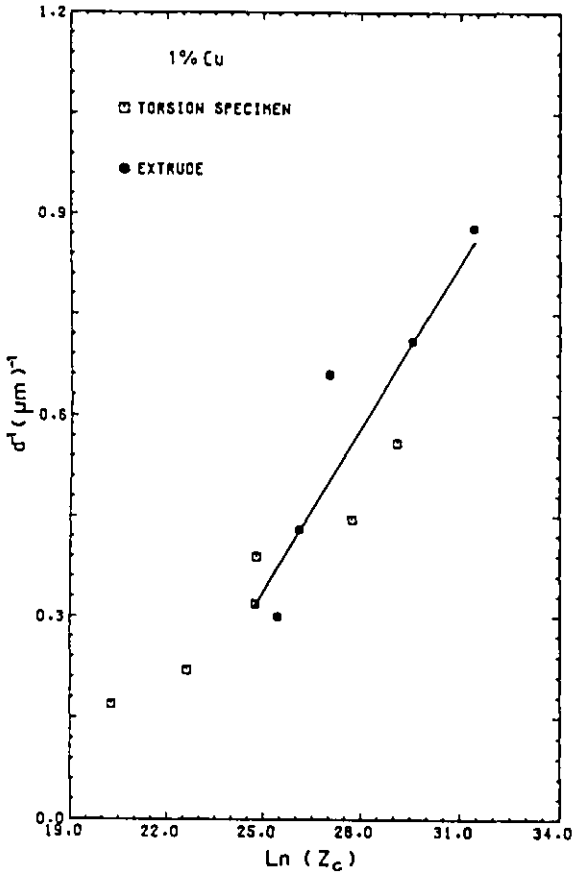


Figure 4.59 1% Cu

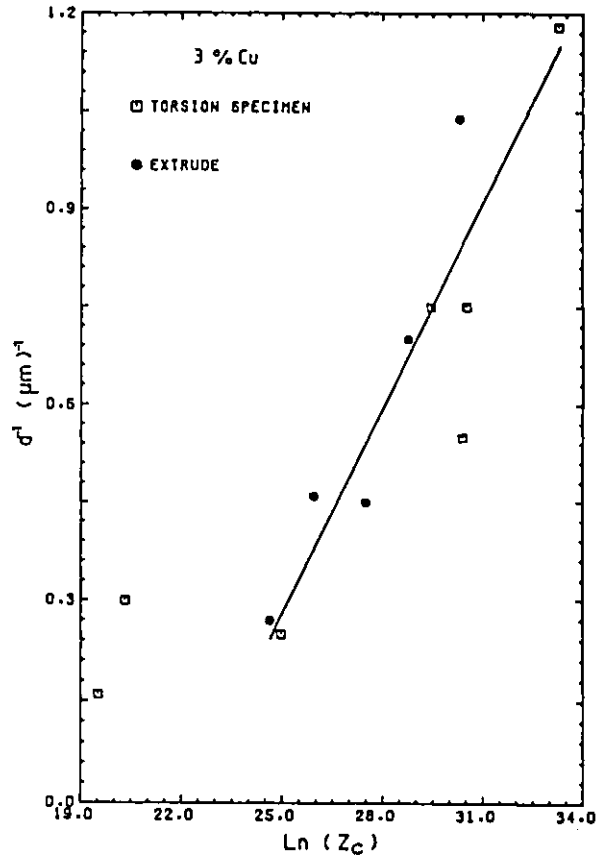


Figure 4.60 3% Cu

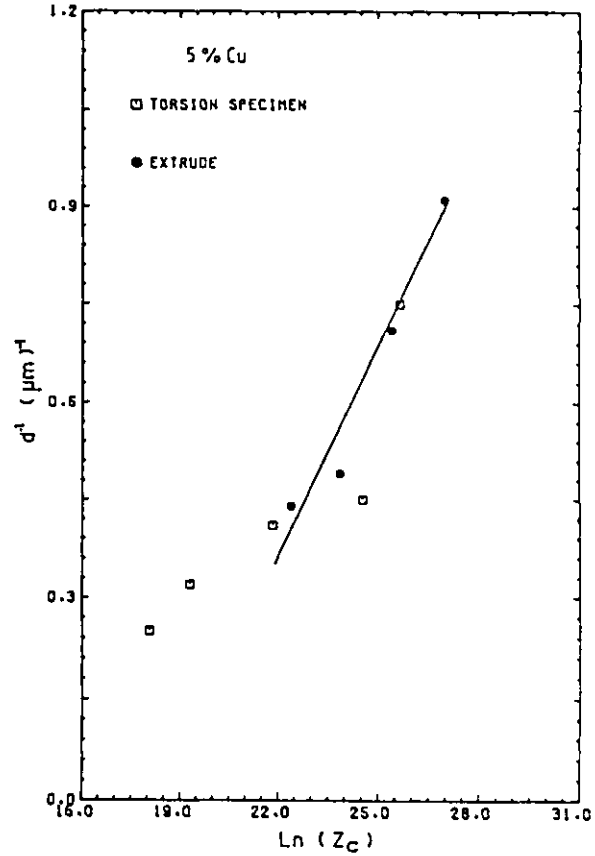


Figure 4.61 5% Cu

(Subgrain size d)$^{-1}$ vs Ln(Z_c) relationships

and extrusion. The justification for using LnZ_C can be seen by the decrease in correlation shown by the d^{-1} vs LnZ_I regression data for the 5% Cu alloy in table 4.24., a similar but smaller decrease can be established in the 1% Cu and 3% Cu alloys due to the lower temperature rises involved.

The higher than average values of d^{-1} in the low Z torsion specimens can be related to the fact that the larger subgrains are inherently difficult to measure from T.E.M. micrographs due to the limited number that can be recorded in any one plate, which is reflected in the relatively large standard deviations in table 4.24 . Therefore the true mean value may well be slightly lower since a larger proportion of the small subgrains have been measured.

The similarity between the torsion and extrusion substructures over a similar range of Z conditions confirms the use of the hot torsion test to model the flow stress characteristics during extrusion and demonstrates the possibility of using reference sets of torsion substructures obtained for a particular alloy, to predict the final substructures in extrusion with the aid of the hot working constants established from the torque twist data. It is often noted that since solution treating and ageing removes all traces of the hot worked substructure in heat treatable alloys, such information may be of academic interest only. However the nature of the substructure or more precisely the stored energy represented by the dislocation structures provides the driving force for static recrystallization and therefore plays an important role in determining the recrystallization kinetics, and hence the final structure and properties of the heat treated extrudate. The effects of subsequent heat treatment on the hot worked substructure will be considered in the following sections.

The results in table 4.24. and figures 4.59. to 4.61. show that for all the alloys the subgrain size decreases with LnZ. The decrease in strain rate reduces the dislocation generation rate whilst an increase in temperature increases the recovery rate. It is evident that neither a or b in table 4.24. show a consistent variation with copper content which implies that equation 1.10 has no real physical interpretation apart from describing the strain rate and temperature dependency of the substructure, since ΔH relates to the rate controlling mechanism and not the flow stress characteristics which are dependent on all the hot working constants.

In the room temperature region most theories of work hardening lead to an expression of the form[118]:

$$\sigma_y = \sigma_o + \alpha' G b \rho^{1/2} \qquad 4.21.$$

which relates the yield stress σ_y to the total dislocation density ρ, where σ_o is the friction stress, G the shear modulus, b the burgers vector and α' a geometric constant often referred to as the dislocation strengthening efficiency. However as noted in section 1.5 the most commonly used empirical relationship to relate the flow stress to the hot worked structure is in the form:

$$\sigma = \sigma_o + k d^{-m} \qquad 4.22.$$

where d is the subgrain size and σ_o, k and m constants. Numerous workers[68] have shown the applicability of this equation to creep and hot working data where m ranges in values from 1 to 1.5, whilst $\sigma_o \simeq 0$ and k increases with alloy content. The results and regression data in figures 4.62. to 4.64. show a similar correlation can be established in the present series of alloys, k increasing with alloy content whilst the absolute value of m decreases. Such

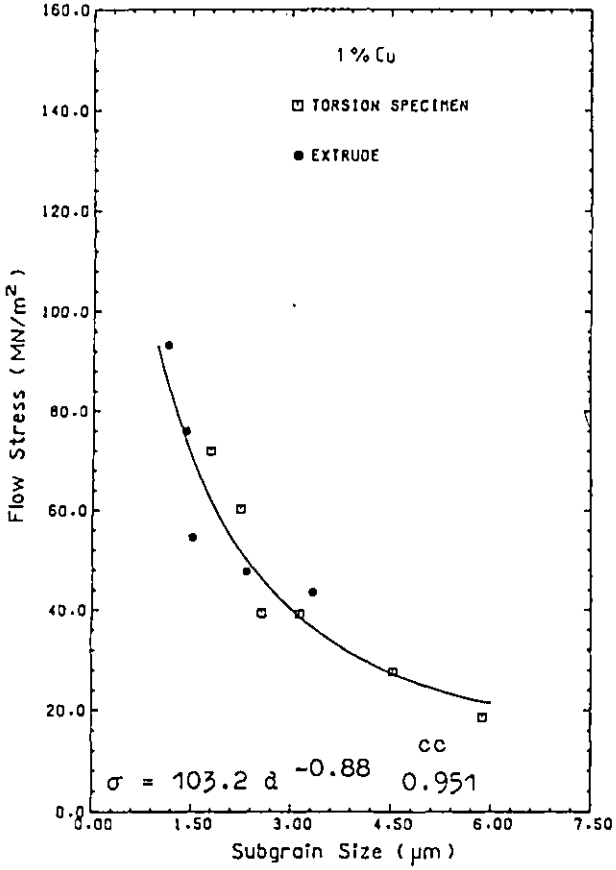


Figure 4.62 1% Cu

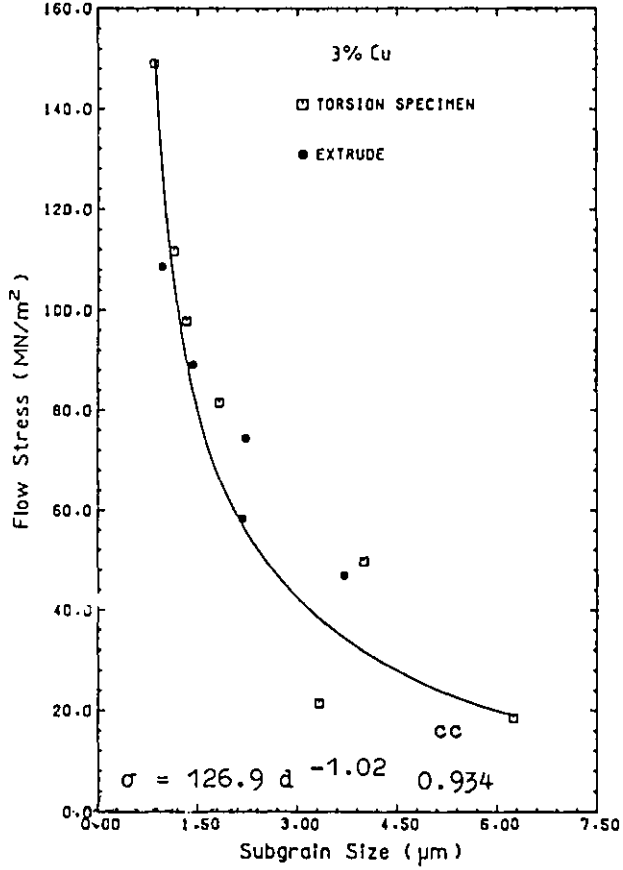


Figure 4.63 3% Cu

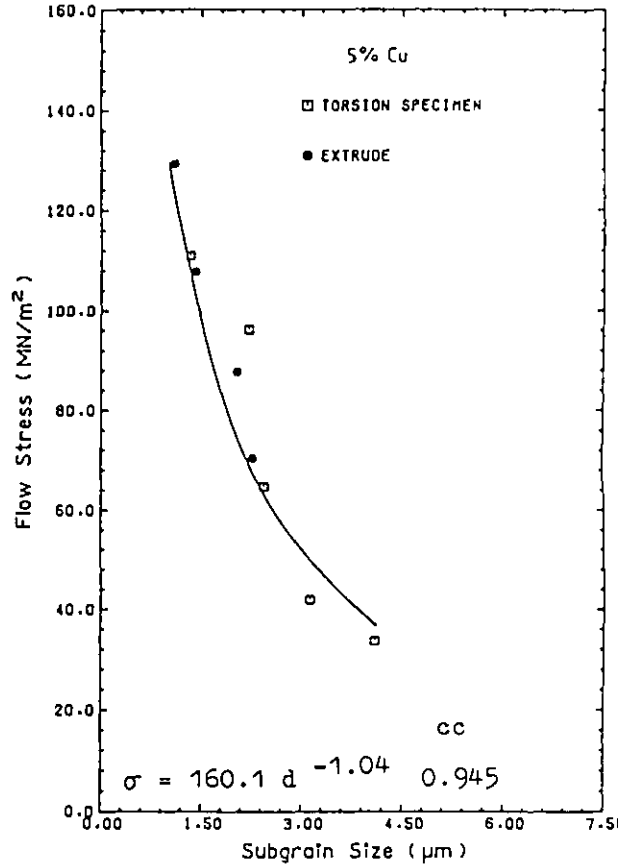


Figure 4.64 5% Cu

Flow stress vs subgrain size relationships

relationships therefore predict that the flow stress is solely a function of the subgrain size, the subboundaries acting as the principal source of internal stress, the flow stress increasing with decreasing subgrain size as the number of subboundaries increases. However it is evident from the values of k and m that the degree of substructure strengthening is alloy dependent increasing with Cu content as k increases and m decreases. This is shown more clearly in figure 4.65. which shows that the flow stress predicted by equation 4.22. increases with Cu content at equivalent subgrain sizes, the difference increasing with decreasing subgrain size.

The first point to note is that σ_o in equation 4.22 must have a positive value since it relates to the flow stress of the annealed material i.e. in the absence of substructure strenghtening, although clearly it cannot have a constant as in the case of the room temperature stress, but vary with temperature as the dislocation mobility increases. Secondly the effect of particle size and distribution has already been shown in section 4.1.3.2. to have a significant effect on the flow stress characteristics of the 2014 alloy, which implies that the second phase particle may also be regarded as a source of internal stress due to the increase in geometrically necessary dislocations required to maintain the continuity between the deforming matrix and particle. A more realistic equation relating the flow stress to the hot worked structure may therefore be written in the form:

$$\sigma = \sigma^* + A\rho^n + k_2 d^{-m} \qquad 4.23.$$

where n and m are constants, σ^* relates to the stress required to move the dislocations through the annealed material, A is a constant proportional to the burgers vector and shear modulus and k_2 may be regarded as a subboundary strengthening coefficient in a similar manner to the

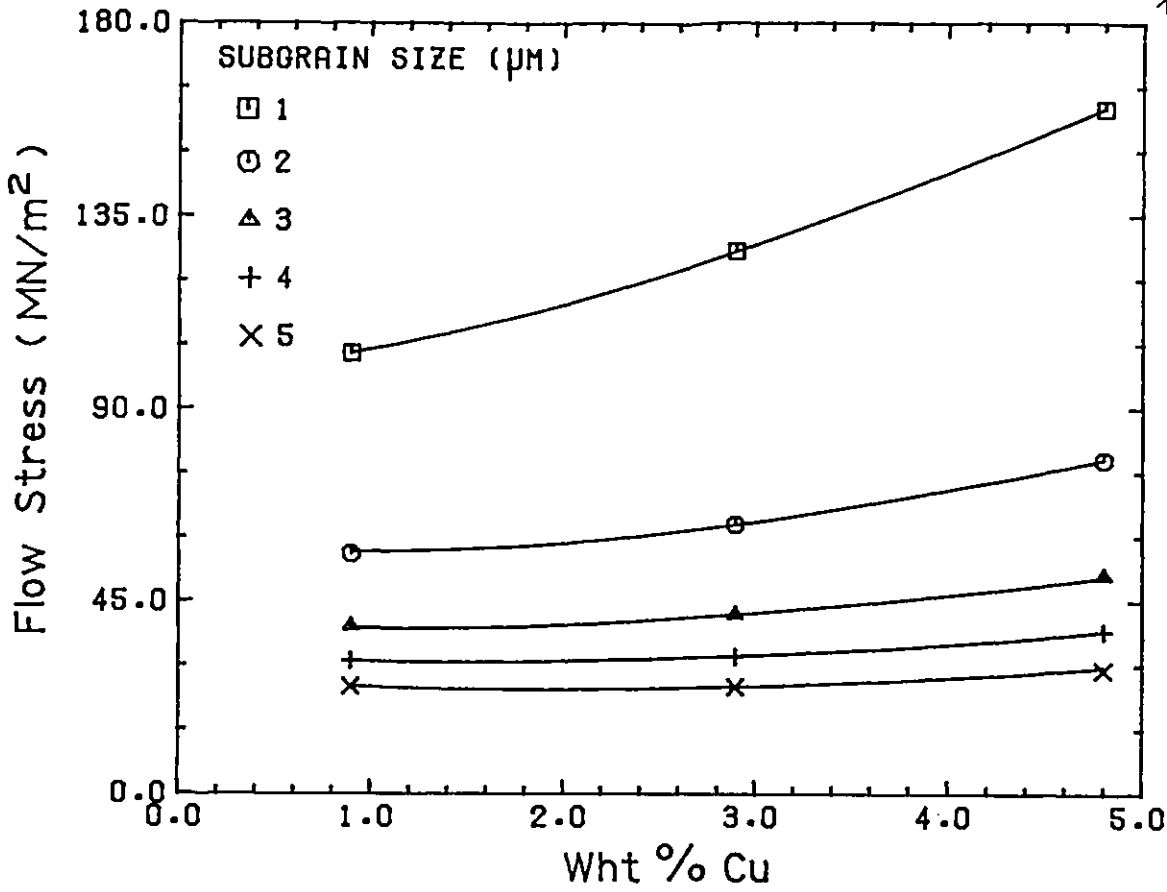


Figure 4.65 Flow stress vs wt % Cu at constant subgrain sizes

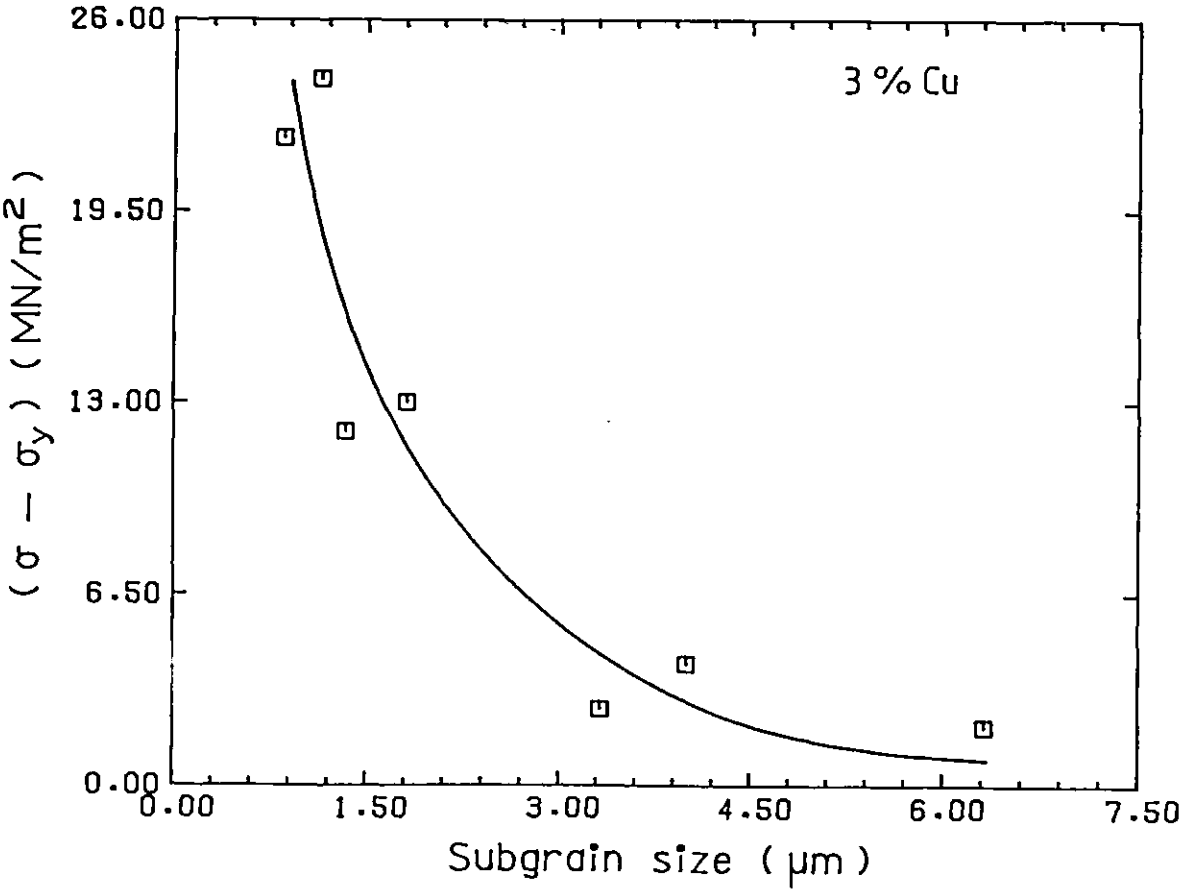


Figure 4.66 ($\sigma - \sigma_y$) vs d 3% Cu alloy

Hall-Petch equation.

Although data relating to the dislocation density is not available in the present work it is possible to regress a simplified form of equation 4.23. by assuming

$$\sigma_y \simeq \sigma^* + A\rho^n \qquad 4.24.$$

due to the absence of a well defined substructure at the yield point[69]. The yield point has been taken as the end of the linear increase in torque shown in figures 4.1. to 4.3., the torque being converted to equivalent stress from the relationship between peak torque and flow stress. The regression data for all the alloys is shown in table 4.25. and the results from the 3% Cu alloy are also plotted in figure 4.66. The relatively low correlations exhibited by all three alloys in table 4.25. can be attributed to the difficulty in measuring the true yield stress from torque twist curves derived from solid torsion specimens, due to the radial variation in strain discussed in section 4.1.4. and the assumption that the incremental increase in stress $\sigma - \sigma_y$ is directly related to the development of a subgrain structure, which is not strictly correct since the dislocation density must also increase with strain from the yield point to steady state flow. However, if one assumes that a combination of equation 4.24. and 4.23. is a more accurate physical interpretation of the dependence of flow stress on the subgrain size, then the more or less constant value of k_2 implies that the substructure strengthening coefficient is independent of alloy content, the absolute value of m decreasing with Cu content as the dependence of flow stress on the subgrain size increases due to the increase in dislocation density.

It may therefore be concluded that although the flow stress can be related to the subgrain dimensions via equation 4.22. the predicted flow stress dependency has no

$\sigma = \sigma_y + k_2 d^m$

Alloy	k_2	m	cc
1% Cu	15.71	-1.41	0.827
3% Cu	19.19	-1.26	0.930
5% Cu	14.65	-0.48	0.751

Table 4.25 $\sigma - \sigma_y$ vs subgrain size - 1% Cu, 3% Cu and 5% Cu torsion specimens

Code	Misorientation			
41-51	6.32	3.21	0.84	1.32
42-4	0.31	3.11	0.40	0.80
43-5	3.20	0.04	0.11	0.76
44-22	0.88	0.31	0.45	
45-51	0.73	2.11	0.61	0.06

Code	T_I °C	$\dot{\varepsilon}$ s^{-1}	d(1) μm	±	d(t) μm	±
41-3	275	2.51	1.02	0.17	0.59	0.64
41-51	275	25.90	0.64	0.04	0.43	0.07
42-4	330	7.99	1.83	0.09	1.24	0.02
43-5	390	28.52	1.98	0.19	1.27	0.16
44-1	430	0.03	4.89	0.54	3.83	0.45
44-22	430	0.31	6.84	0.32	5.00	0.31
45-11	450	0.03	6.60	0.43	5.74	1.53
45-51	450	27.72	2.42	0.62	1.65	0.64

Subgrain size (t) relationships

	cc
$d^{-1} = 0.142 \mathrm{Ln} Z_c - 3.92$	0.912
$\sigma = 135.6 d^{-0.67}$	0.964
$\sigma = \sigma_y + 16.5 d^{-0.92}$	0.821

Table 4.26 Presolution soak torsion subgrain misorientation and subgrain size relationships.

real significance in multiphase alloys such as the 2000 series alloys since the steady state flow stress is also dependent on the solid solution content and on the particle size and distribution which act as sources of internal stress in addition to the subboundary dislocation.

The effect of presolution soak treatment described in section 4.2.10.1. has also been considered in relation to the steady state substructures produced via torsion testing. Examples of the substructures are shown in plate VIII - b) and the subgrain size and misorientation measurements are shown in table 4.26.

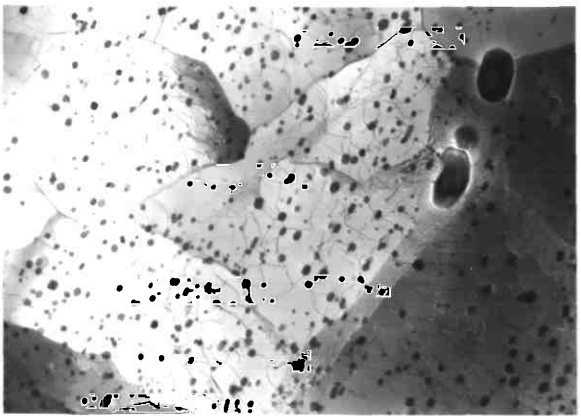
The misorientation measurements in table 4.26. confirm the existance of a subgrain structure at all test conditions although it is noticeable that a larger misorientation exists in the high Z specimens indicative of a less recovered substructure. No significant change in the distribution of the intermediate 0.05-0.3 μm particles was detected although it was noticeable that the larger as cast particles were still present within the matrix but tended to be smaller and more broken up than in the conventionally heated microstructures, which may be beneficial to the room temperature properties of the product since particle fracture and matrix decohesion at such particles plays an important role in the fracture mechanism in aluminium alloys, the presence of the larger as cast particles reducing the fracture toughness.[41,61] As in the CH material GP zones were not identified in the S.A.D.P. or microstructures of any of the specimens even though the torsion specimens were examined in the naturally aged condition, which again suggests that GPB type zones are present in the 2014 alloy.

The low Z substructures exhibit similar characteristics to those of the CH material in line with the flow stress

TORSION SPECIMENS

45-11

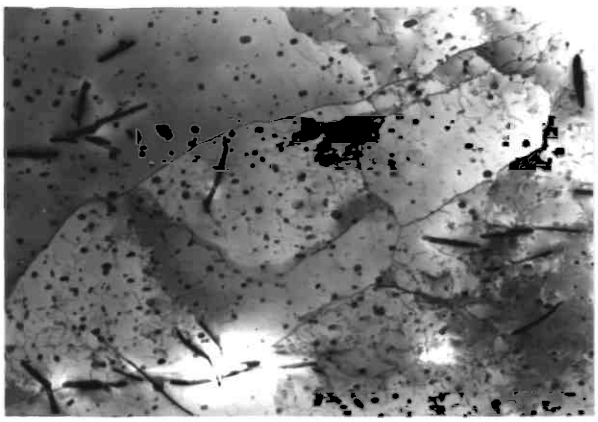
a) T_I = 450°C LnZ_c = 25.98



2.μm

44-22

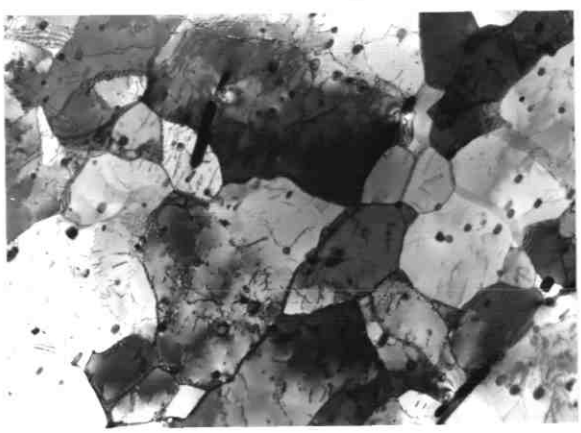
b) T_I = 430°C LnZ_c = 29.25



2.μm

45-51

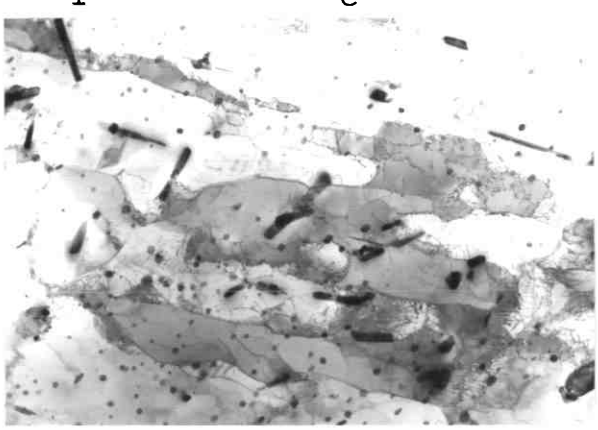
c) T_I = 450°C LnZ_c = 32.54



1.μm

43-5

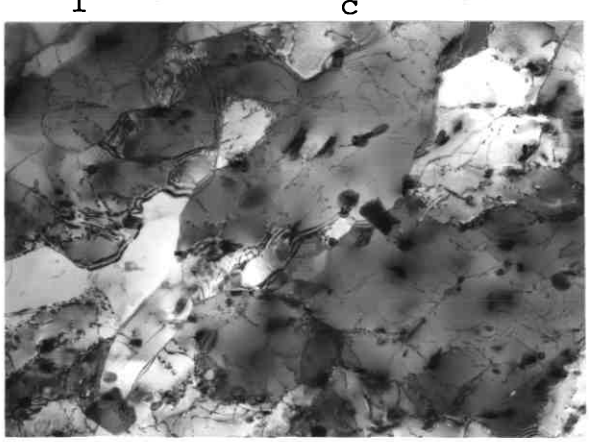
d) T_I = 390°C LnZ_c = 34.73



2.μm

42-4

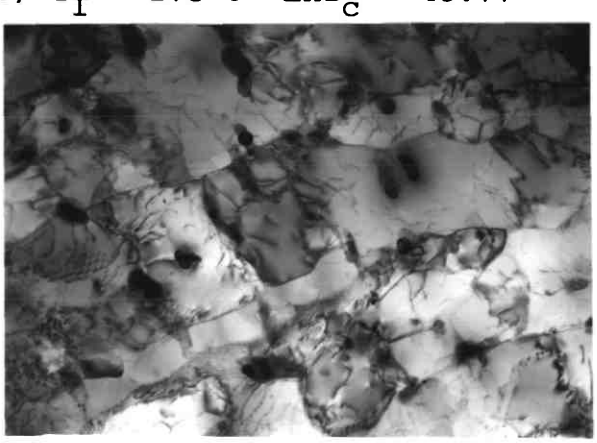
e) T_I = 330°C LnZ_c = 36.67



1.μm

41-51

f) T_I = 275°C LnZ_c = 40.77



.5μm

Plate VIII - b) Presolution soak steady state torsion substructure - 2014 alloy.

characteristics shown in figure 4.50. whilst the high Z specimens exhibit a less recovered substructure characterized by poorly defined subgrains with high internal dislocation densities. Pinning by second phase articles can be seen in all the micrographs but is clearly more prominent in the high Z structures.

The relationship between the process conditions i.e. $\mathrm{Ln}Z_C$ and the subgrain size is shown in figure 4.67. and table 4.26. as is the regression data for the dependence of flow stress on subgrain size according to equation 4.22. It is apparent that the relationships exhibit a relatively high correlation in a similar manner to the CH material although as already noted the physical interpretation of the dependencies is doubtful. It is interesting to note that if one applies equation 4.24. to the SS data, then the results in figure 4.68. and table 4.26. show that the value of k_2 and m are similar to those found in the CH material in table 4.25., which implies that the incremental increase in stress $\sigma-\sigma_y$ is unaffected by the solution soak treatment and hence the internal stress associated with the development of the subgrain structure. The increase in flow stress with Z shown in figure 4.50. may therefore be largely a function of the increase in yield stress, which implies that dislocation pinning by segregation of solute atom atmospheres at dislocations during cooling plays an important role in increasing the flow stress. Conversely the increase in flow stress associated with solid solution hardening can also as suggested in section 4.2.10.1., be explained in terms of a decrease in recovery and increase in dislocation multiplication with increasing Z which correlates with the substructural characteristics shown in plate VIIIb).

It may therefore be concluded that although a number of mechanisms are likely to be associated with the increase in flow stress shown in figure 4.50. the principal effect of

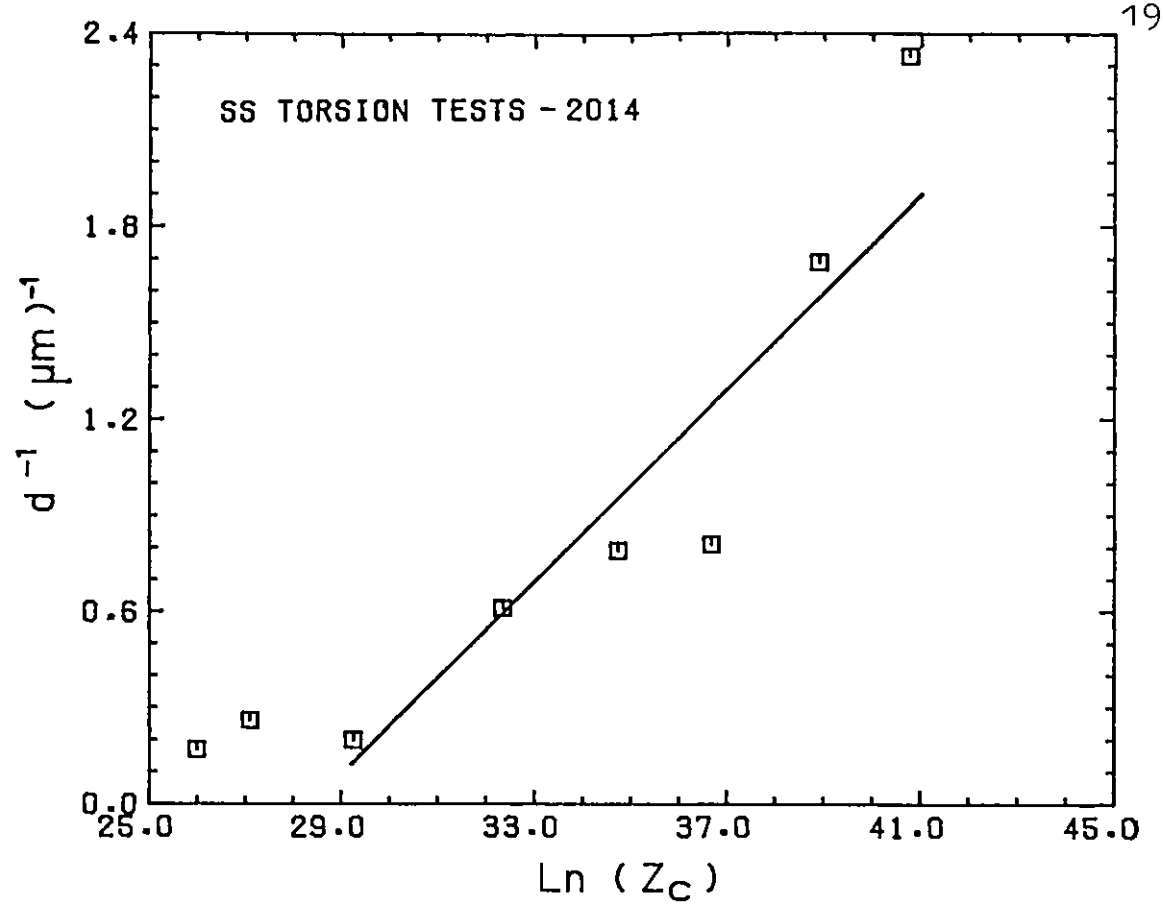


Figure 4.67 d^{-1} vs LnZ_C presolution soak torsion tests 2014 alloy

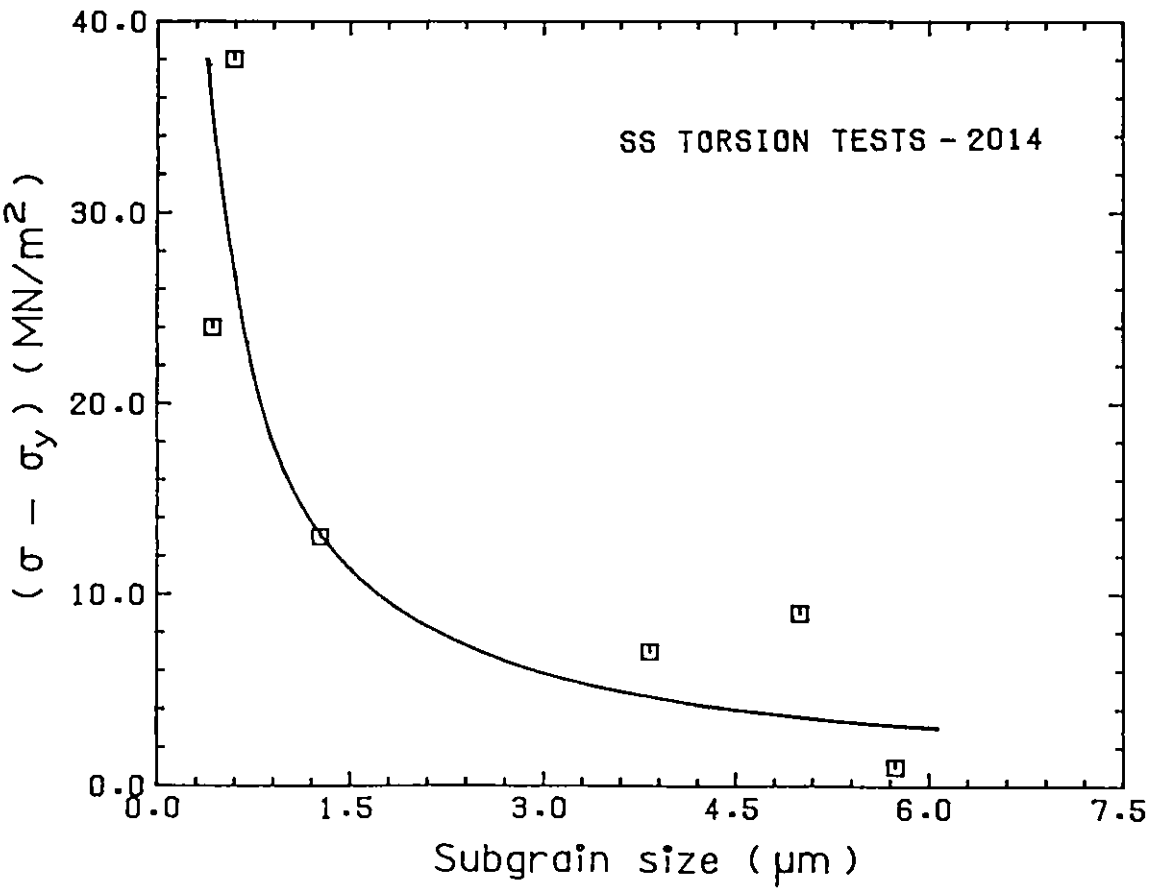


Figure 4.68 $(\sigma - \sigma_y)$ vs d presolution soak torsion tests 2014 alloy

the presolution soak treatment on the as quenched hot worked structure is to reduce the degree of recovery with Z and the second phase particle distribution associated mainly with the larger as cast particles, although this has yet to be established quantitatively.

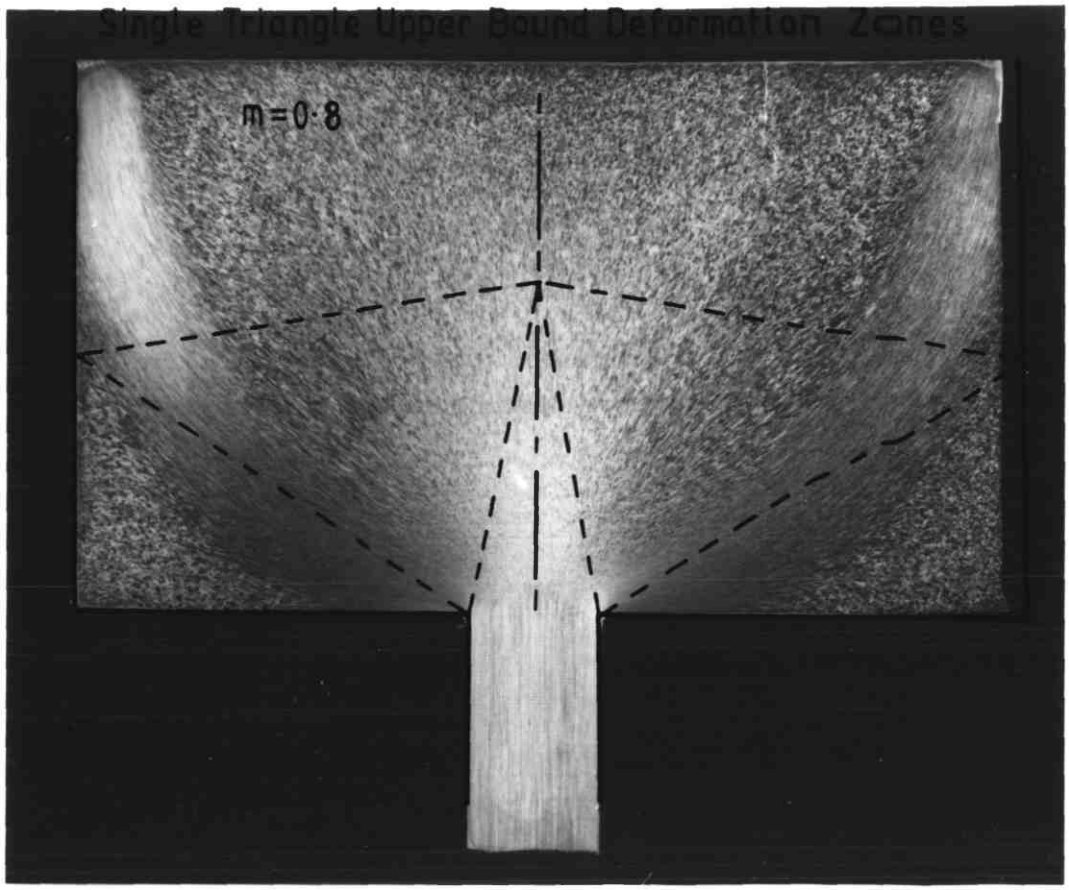
4.3.6. MATERIAL FLOW DURING STEADY STATE EXTRUSION

The development of material flow during direct and indirect extrusion has been the focus of much research in both heat treatable and non heat treatable aluminium alloys.[25,27,29] In the present work the structural variation within the steady state direct and indirect deformation zones has been established using the 1%Cu alloy extruded at 325 deg.C, with the same mean equivalent strain rates at an extrusion ratio of 40:1. The difference in flow patterns during steady state extrusion are shown in plate IX. Details of the experimental procedure are given in section 3.4.

4.3.6.1. FLOW CHARACTERISTICS DURING STEADY STATE DIRECT AND INDIRECT EXTRUSION

Plate IX a) shows that the steady state flow pattern for direct extrusion is characterised by an elliptical region of intense shear which extends from the interface between the billet and container at the rear of the billet to the die mouth. The shear zone outlines a dead metal zone in which the original homogenized material remains relatively undeformed. A second shear zone can also be seen along the central axis of the billet, bounded by regions of less pronounced deformation. The single triangular deformation zone predicted by the upper bound solution is clearly not strictly correct, although attempts at utilizing double and treble triangular arrangements have only

a) Direct Extrusion - Steady State.



b) Indirect Extrusion - Steady State.

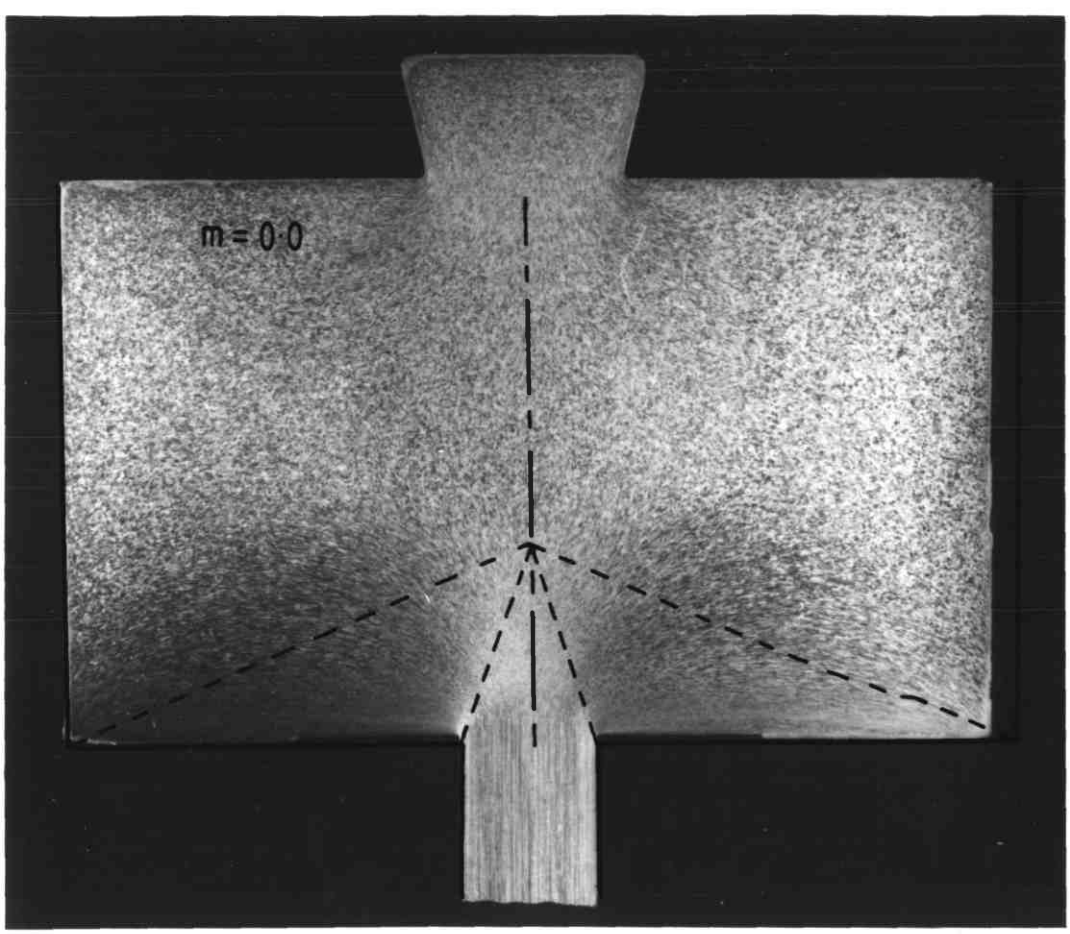
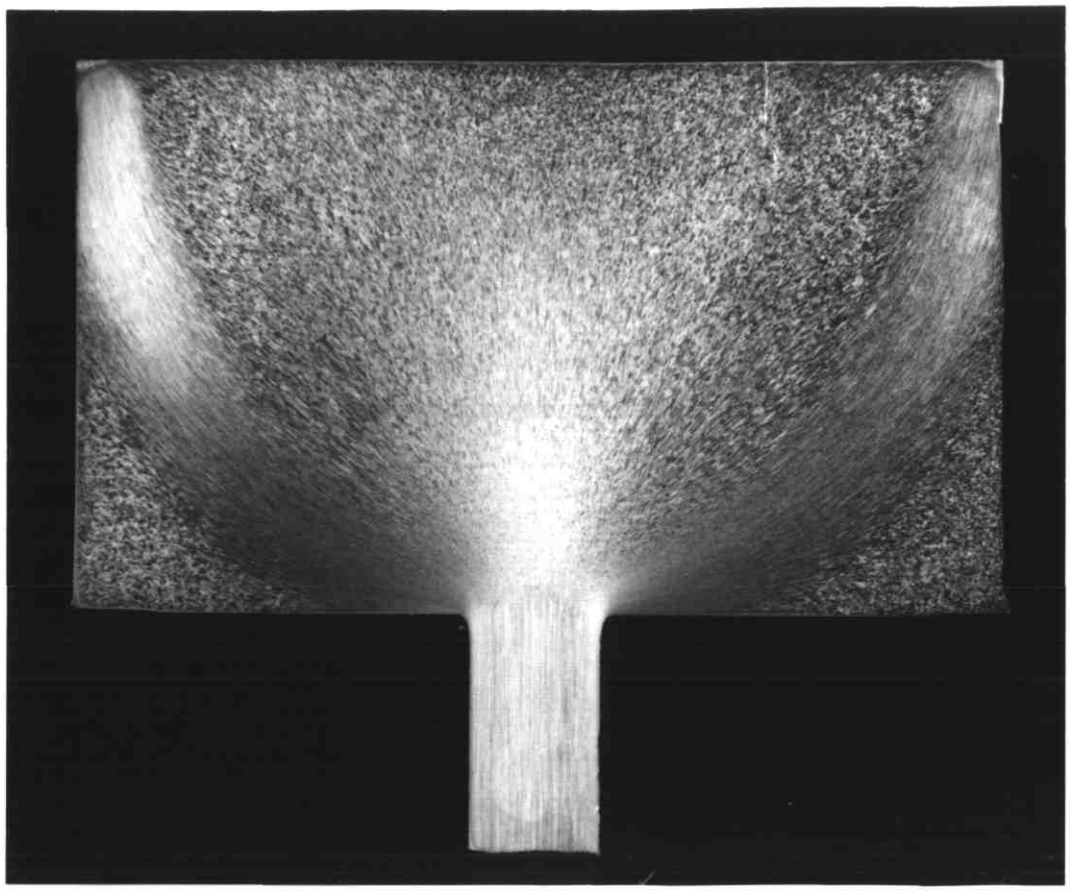


Plate IX. Macrosections of Partially Extruded Billets of the 1% Cu Alloy T_I = 325°C (x 1.64)

a) Direct Extrusion - Steady State.



b) Indirect Extrusion - Steady State.

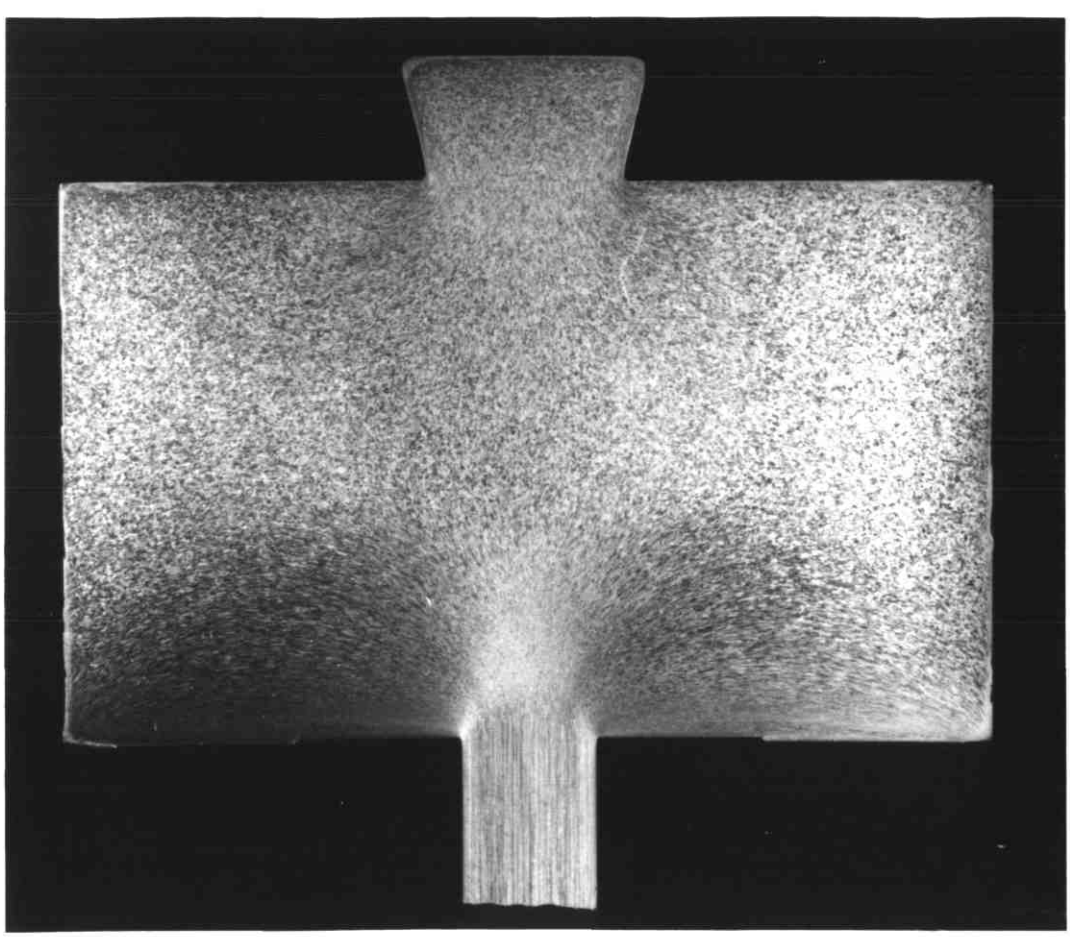


Plate IX. Macrosections of Partially Extruded Billets of the 1% Cu Alloy T_I = 325°C (x 1.64)

marginally increased the accuracy of the such solutions.[27,28] The resulting extrude is essentially fibrous, with the periphery derived from the regions of intense shear outlining the dead metal zone and the core of the extrude from the centre of the billet.

Plate IX b) shows the steady state flow pattern for indirect extrusion. The tongue at the rear of the billet is caused when the material flows back into the dummy block as the billet is upset and once established has no further influence on the material flow until the final stage of extrusion. It's presence is necessary for the removal of the discard after extrusion.

The shape of the deformation zone is radically different from that seen in the direct mode and now extends in a circular manner from die/container interface to the die mouth. The size of the deformation zone is reduced, as predicted by the upper bound zone, where a dead metal zone can only be considered to exist at the billet/die interface.

The flow of material occurs fom the sides to the centre of the billet where it is extruded through the die. A much larger percentage of the billet remains undeformed before reaching the deformation zone and there is no evidence of any billet/container friction. The absence of the heavily sheared region which existed in the direct mode and the change in flow pattern produces an extrude with a much more uniform structure across its cross section. The extrude is again essentially fibrous with the grains elongated in the extrusion direction, but a heavily sheared peripheral zone is no longer apparent.

An important feature of the indirect process is that due to the nature of the flow during extrusion, defects from the surface of the billet will be transferred to the surface

of the extrude, in contrast to the direct extrusion where the surface of the extrude originates in the regions of intense shear. However scalping of the as cast billets before extrusion removes the main source of such defects and was therefore not a serious problem in the present work.

It is evident from plate IX that there is a significant difference in the flow characteristics during steady state direct and indirect extrusion. The difference in substructure within the deformation zone and extrudate will now be considered.

4.3.6.2. SUBSTRUCTURAL VARIATION WITHIN DIRECT AND INDIRECT DEFORMATION ZONE

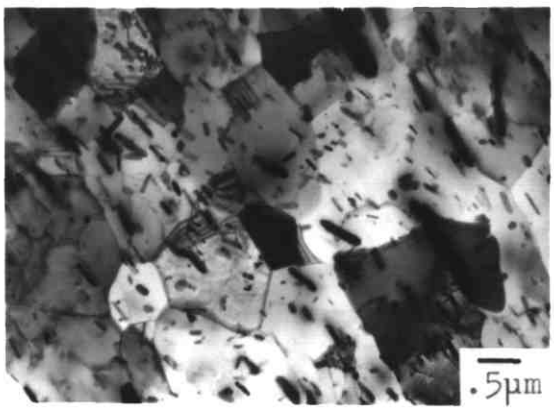
The variation of substructure within the steady state deformation zone has been investigated using the partially extruded billets of the 1% Cu alloy shown in plate IX. Disc specimens for T.E.M. were removed as described in section 3.4. from positions along the flow lines shown in figure 4.69a). The flow lines were determined from consideration of the upper bound spherical velocity field and the nature of the flow shown in plate IX.

For both modes of extrusion the quenched microstructures showed no evidence of any substantial static recrystallization due to the low extrusion temperature used and were characterised by a subgrain structure of low misorientation between 0.3° to 3° consistent with the operation of dynamic recovery. The variation in substructure during direct extrusion along the flow line shown in figure 4.69a) is shown in plate X and will now be considered.

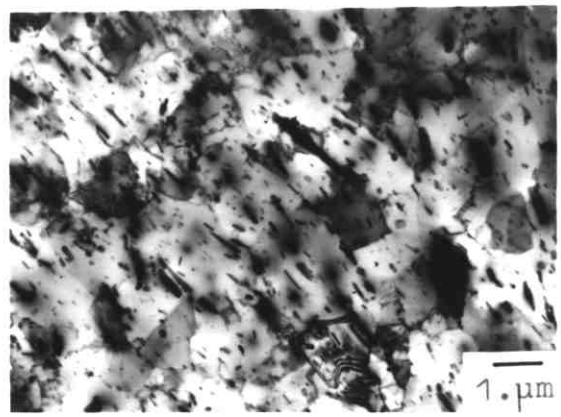
Micrograph a) shows the structure at position A in figure 4.69a) near the rear of the billet adjacent to the shear zone. The substructure is already relatively well

DIRECT EXTRUSION

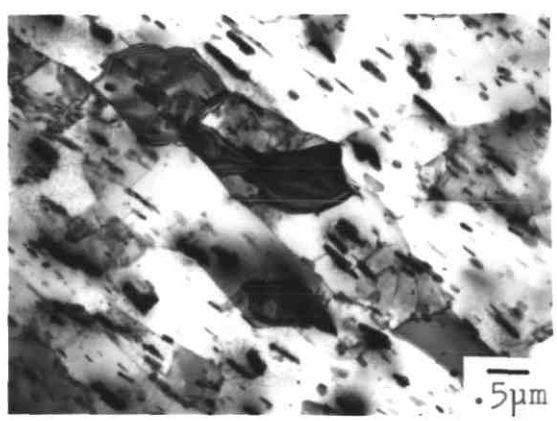
a)



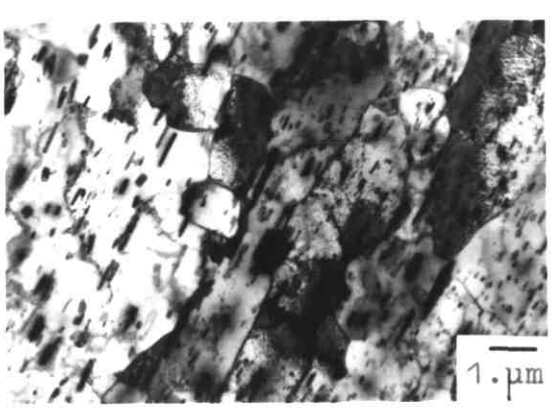
b)



c)



d)



e)

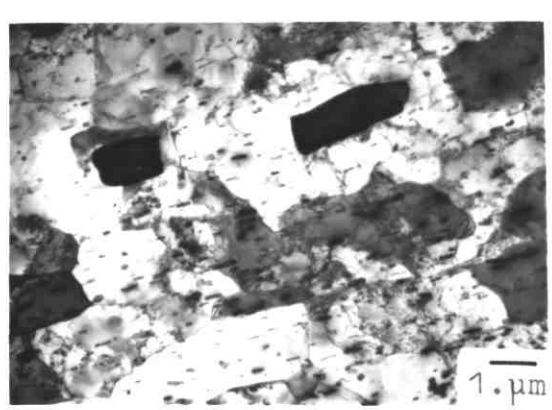
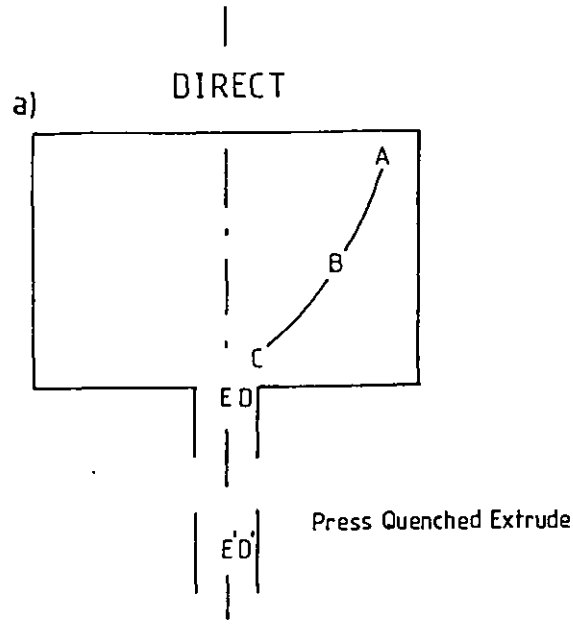


Plate X. Development of Substructure along the Flowline during Steady State Direct Extrusion of the 1% Cu Alloy.

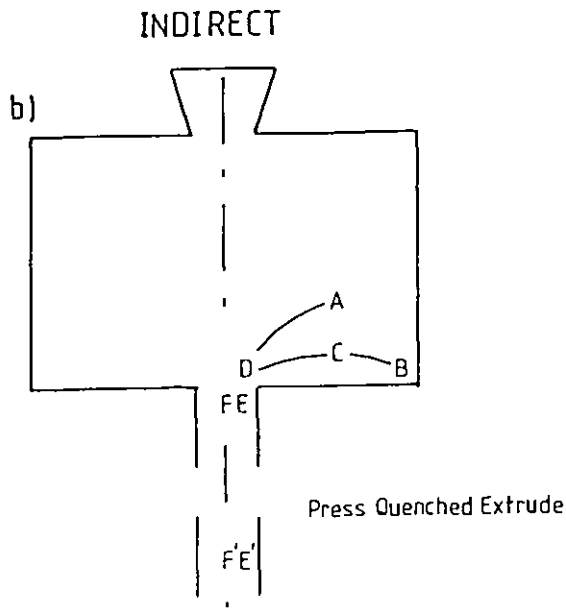
defined and equiaxed, with a fairly low internal dislocation density and the larger second phase particles are aligned in the extrusion direction. This is in contrast to the poorly defined dislocation structure reported further inside the billet in which the particles show no sign of alignment[27,28]. This would tend to indicate that the degree of substructural development varies considerably across the billet, the substructure increasing in perfection as one approaches the more highly strained material associated with the shear zone at the billet container interface.

At position B midway through the deformation zone, micrograph b) shows a subgrain structure similar to that at A, indicating that the substructure may already be fully developed between A and B, where further change in the substructure occurs by a combination of dynamic recovery and repolygonization. The increase in strain from A to B results in further alignment of the particles, although the strain is still not sufficient to align all the particles in the extrusion direction. At position C close to the die mouth micrograph c) shows a well developed substructure of low dislocation density, with all the particles aligned in the extrusion direction. The change in structure as material flows through the die is shown in micrograph d) at the centre of the emerging extrude, and is clearly similar to that at C. However the structure at the edge of the extrude in micrograph e) is characterised by a relatively high internal dislocation density and less equiaxed subgrains, consistent with the observation made in the previous section, that the material at the periphery is derived from the heavily worked shear zones. The release of the stored energy associated with the high dislocation density provides the driving force for static recrystallization after deformation[137], which promotes the development of duplex structures exhibited by the low Z extrudes discussed in section 4.3.4. The presence of the



a) DIRECT EXTRUSION

Position	Longitudinal		Transverse	
	d(μm)	±	d(μm)	±
A	1.27	0.19	0.96	0.19
B	1.38	0.11	1.11	0.13
C	1.36	0.21	1.12	0.22
D	1.88	0.12	1.25	0.17
E	1.49	0.25	1.29	0.25
D'	1.70	0.13	1.17	0.10
E'	1.57	0.26	1.23	0.25



b) INDIRECT EXTRUSION

Position	Longitudinal		Transverse	
	d(μm)	±	d(μm)	±
A	1.89	0.30	1.46	0.43
B	1.61	0.05	1.06	0.13
C	1.63	0.11	1.04	0.26
D	1.60	0.03	0.98	0.13
E	1.75	0.23	1.13	0.15
F	1.71	0.19	1.22	0.20
E'	1.73	0.13	1.02	0.20
F'	1.67	0.19	1.05	0.14

Figure 4.69

Table 4.27

Location of the T.E.M. specimens and subgrain size measurements within the steady state direct and indirect deformation zones of the 1% Cu alloy T_I = 325°C

large as cast particle which has fractured during extrusion shown in micrograph e) is indicative of the more highly strained periphery, where Humphreys[107] has shown that the lattice rotations which occur at such particles and the requirements of high dislocation densities at these sites can be beneficial to the initial stages of subgrain wall formation. The size and separation of such particles can also play a significant role in determining the recrystallization behaviour during annealing[110].

The subgrain size at each position is shown in table 4.27a), where each diameter represents the mean value of at least 100 individual measurements. The subgrain dimensions of the press quenched steady state extrudes a third of the way along the extrude are also included. The elongated nature of the subgrain at all positions within the deformation zone is indicative of the low extrusion temperature utilised to reduce static recovery and recrystallization.

The results in table 4.27a) show a sharp decrease in subgrain size at position A near the rear of the billet, which may be attributed to the combined cooling effect of the pressure pad and container, reducing the ease of recovery and hence subgrain size. The increase in strain gradient and hence strain rate from B to C to E should result in a decrease in subgrain size. The results do indeed show a slight decrease from B to C, although there is clearly a large increase in subgrain size as the material flows round and through the die, the increase being far greater in the periphery of the extrude. The sudden increase in subgrain size is perhaps to be expected due to the large increase in strain rate and associated temperature rise predicted near the die mouth, the maximum strain rate being measured closest to the die[138,139]. It is also evident from the macrosections in plate IX that for both direct and indirect extrusion there is a distinct boundary across the die mouth between the

fibrous extrudate and the structure within the deformation zone. Since the rate of internal energy dissipation $\dot{E}$ utilised in the upper bound analysis is a function of:-

$$\dot{E} = \int \sigma \dot{\bar{\varepsilon}} \, dv \qquad 4.25.$$

where σ and $\dot{\bar{\varepsilon}}$ are the mean equivalent stress and strain rate acting along the flow line and v the velocity. A large temperature rise and hence increase in subgrain size from C to E/D is not unreasonable. It is possible to estimate the magnitude of the temperature rise by correlating the increase in strain rate and subgrain size d with d^{-1} vs $\mathrm{Ln}Z_c$ relationship derived in section 4.3.5.3. If one assumes a steady state structure exists from midway through the deformation zone to the die exit then an 8 fold increase in strain rate predicted by the upper bound solution would require an absolute temperature rise of 60 deg.C in the centre of the extrude and 130 deg.C in the periphery of extrude for the increase in subgrain size shown in table 4.27a). Temperature rises which agree well with a mean temperature rise of 110 deg.C predicted by the integral profile model.

The press quenched extrude at 0.3L shows a similar variation in subgrain size across the extrudate, although the subgrains are evidently smaller due to the temperature rise as extrusion proceeds, a topic which will be considered in further detail in the following section.

The variation in structure during steady state indirect extrusion is shown in plate XI. The change in flow pattern shown in plate IX indicates that material in the deformation zone now flows parallel to the die face. With this in mind, specimens were taken from the partially extruded billets at the positions shown in figure 4.69b).

Micrograph a) corresponds to the position at the edge of the deformation zone A in figure 4.69b), and shows that the subgrain structure is fairly well defined but with a relatively high internal dislocation density. The subboundary walls formed by the coalescence of the mobile dislocations are clearly associated with larger 1.0 to 0.5 μm particles, which are beginning to be aligned in the extrusion direction.

Micrograph b) shows the structure at the edge of the deformation zone near the billet container interface corresponding to position B in figure 4.69b). The subgrains are smaller and more well developed than those at A where a similar structure was seen at the rear of the billet in the direct deformation zone shown in plate X a). However the increase in strain and strain rate is largely due to the flow of material within the deformation zone, as opposed to the strain and strain rate variation caused by the shear zones at the billet container interface during direct extrusion.

Micrograph c) corresponds to position C in figure 4.69b) midway through the deformation zone. The subgrains are well developed with a low internal dislocation density and all the particles are aligned parallel to the die face. Micrograph d) shows that a similar substructure exists adjacent to the die mouth at D in figure 4.69b).

The substructures at the centre and edge of the emerging extrude are shown in micrographs f) and e) respectively. It is evident that the subgrain structures are similar in characteristic in comparison to the direct case, although the fact that a duplex structure is seen in the low Z extrudes implies that a less recovered substructure is produced in the periphery of the extrudate

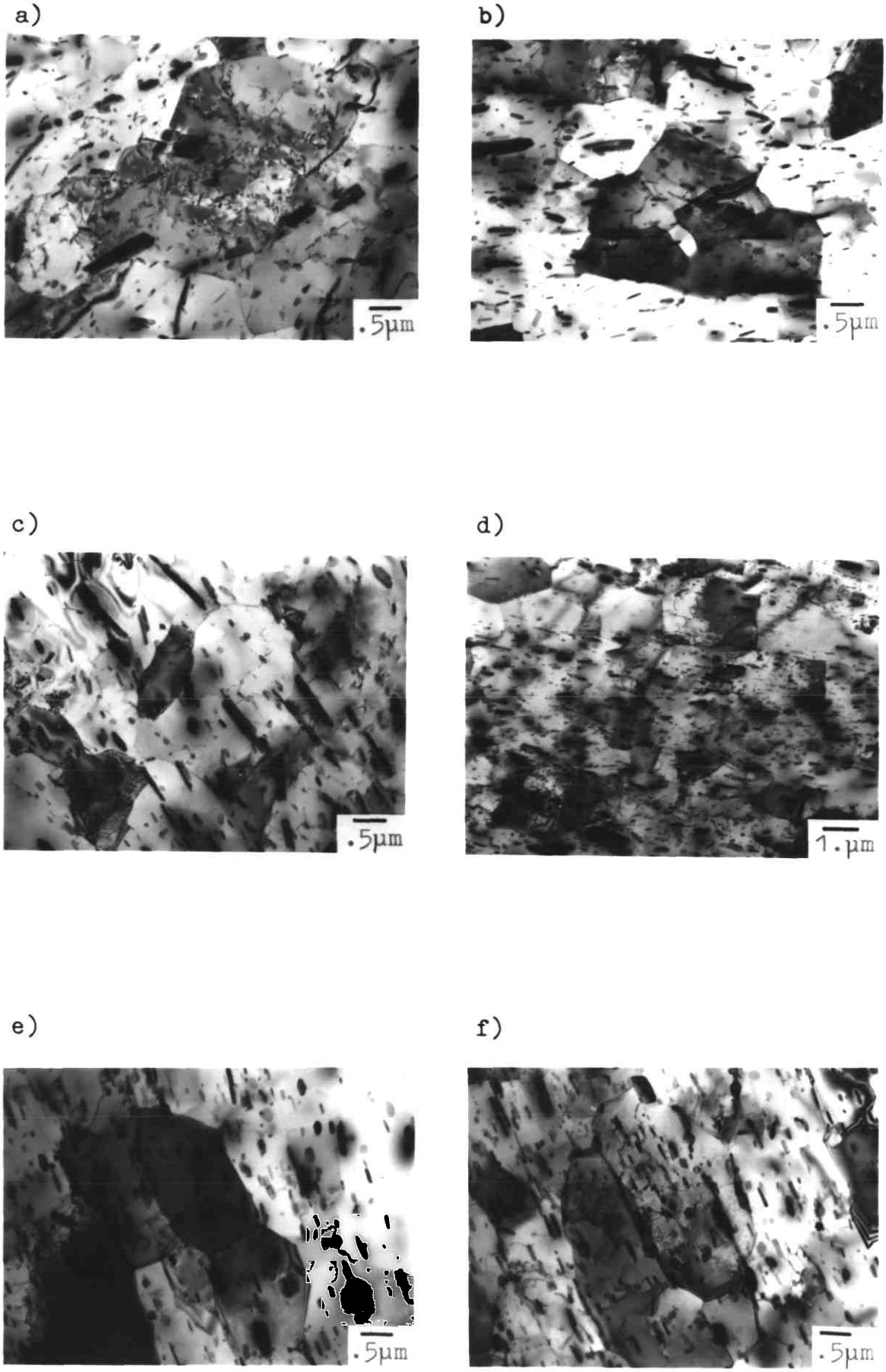


Plate XI. Development of Substructure along the Flowline during Steady State Indirect Extrusion of the 1% Cu Alloy.

due to e.g. the friction stresses generated at the die land. However the absence of any pronounced variation in substructure is a very important feature of steady state indirect extrusion since the final product can also be expected to have more uniform mechanical properties a factor which can limit the use of direct extrudes for high strength applications. The mechanical properties of the direct and indirect extrudes will be considered in section 4.4.

The subgrain sizes at each position are shown in table 4.27b). From A to C there is a large decrease in subgrain size due to the increase in strain and strain rate as material enters the deformation zone. From B to C to D there is no real change in the subgrain size indicating that only a small change in strain rate and temperature occurs along the flow line similar to direct extrusion between B and C in figure 4.69c). The increase in subgrain size from D to the extrudate substructure at positions E and F again indicates that a large temperature rise occurs as material flows round and through the die. The effect is likely to be accentuated during indirect extrusion due to the higher strain and strain rate gradient predicted adjacent to the die mouth[28,29]. The upper bound analysis predicts a 10 fold increase in strain rate from position C to the die exit, which for the increase in subgrain size shown in table would require a temperature rise of 55 deg.C and 65 deg.C at the centre of the edge of the extrude, temperature rises which are similar to the mean temperature rise derived from the intergral profile model of 50 deg.C at an equivalent position along the extrudate.

The press quenched extrudes at 0.3L show only a slight variation in subgrain size across the extrude, whilst a smaller increase in subgrain size along the length of the extrude is consistent with the lower temperature rise as extrusion proceeds.

It may be concluded that during steady state direct and indirect extrusion that the variation in substructure within the deformation zones are not significantly different considering the change in flow characteristics shown in plate IX. It is however evident from the subgrain size measurements that the final product structure and hence properties are largely dependent on the temperature and strain rate distribution adjacent to the die mouth since the steady state structure changes in accordance with the prevailing Z conditions. During direct extrusion the less recovered material in the periphery of the extrude derived from the shear zones outlining the dead metal zone results in a greater variation in substructure across the extrudate, although the predicted increase in strain rate within the deformation zone is smaller.

Clearly any conclusions which can be drawn from the present work relate to the specific alloy, flow lines and extrusion conditions considered and as such are fairly limited. To establish the affect of alloy content and process conditions on the substructure variations within the direct and indirect deformation zones would require a large number of experimental points, where at high extrusion temperatures it is unlikely that the substructure will be retained during the long quench delay involved in such experiments. The excellent correlation which exists between the temperature rises assuming steady state flow through part of the deformation zone demonstrates the possibility of predicting the variation in substructure within the zone from a knowledge of the Ln Z_c vs d relationships and the temperature and strain rate distribution within the deformation zone. Since the strain required to establish steady state flow may also be evaluated from the homologous strain analysis described in section 4.1.4. it should be possible to predict the exact size of the steady state

deformation zone and therefore the variation in substructure within the direct and indirect zone and hence the final extrudate structure for any extrusion condition and alloy. The combination of a mathematical and structural model to describe the extrusion process is of course the ultimate goal, although as already noted in section 4.2.5. the dependence of flow stress and structure on the process conditions are now fairly well established, but a realistic mathematical model for extrusion has yet to be developed.

4.3.6.3. VARIATION IN SUBSTRUCTURE ACROSS AND ALONG THE DIRECT AND INDIRECT EXTRUDES OF THE 2014 ALLOY

The variation in subgrain size across and long the extrude has been investigated in the 4% Cu 2014 alloy for direct and indirect extrudes processed at 300 and 400 deg.C, with the same mean equivalent strain rates, the results shown in table 4.28. Examples of the substructures at the centre and edge of the direct and indirect extrudes at an initial billet temperature 400 deg.C are shown in plate XII c) to d).

At a position 0.25L from the front of the extrude, corresponding to steady state extrusion, the results in table 4.28. and micrographs c) and d) show a gradual increase in subgrain size across the direct extrude consistent with the results in the previous section. The non uniform flow during extrusion results in a greater degree of deformation in the periphery of the extrude which increases the temperature rise and produces larger subgrains. A temperature rise of 100 deg.C also promotes the nucleation of the statically recrystallized grain in the vicinity of the larger particles as described in section 4.3.5.1., shown in plate XII b), which is taken from the mid radius position at 0.25L of the 300 deg.C extrude. Micrographs d) and e), and the results in table 4.28. show that a relatively small increase in subgrain size occurs

Direct (T_I = 300°C)
(D4133A) R = 30:1
v = 8 mm/s

distance along extrude		Centre (μm)	±	Mid-Radius (μm)	±	Edge (μm)	±
0.25	long	1.59	0.22	1.68	0.12	1.75	0.15
	trans	1.05	0.19	1.07	0.13	1.22	0.18
0.6	long	1.67	0.28	—	—	1.71	0.19
	trans	1.17	0.11			1.28	0.11
0.8	long	1.70	0.36	—	—	1.77	0.33
	trans	1.25	0.11			1.43	0.16

Direct (T_I = 400°C)
(D4343A) R = 30:1
v = 8 mm/s

distance along extrude		Centre (μm)	±	Mid-Radius (μm)	±	Edge (μm)	±
0.25	long	2.51	0.21	2.70	0.50	2.87	0.76
	trans	1.70	0.31	1.74	0.15	1.84	0.30

Indirect (T_I = 300°C)
(I4123A) R = 30:1
v = 6.5 mm/s

distance along extrude		Centre (μm)	±	Mid-Radius (μm)	±	Edge (μm)	±
0.25	long	1.58	0.07	1.62	0.41	1.66	0.12
	trans	0.96	0.18	0.87	0.08	1.14	0.20
0.6	long	1.62	0.15	—	—	1.71	0.31
	trans	0.89	0.15			1.12	0.30
0.8	long	1.62	0.06	—	—	1.68	0.28
	trans	1.09	0.06			1.13	0.11

Indirect (T_I = 400°C)
(I4333A) R = 30:1
v = 6.5 mm/s

distance along extrude		Centre (μm)	±	Mid-Radius (μm)	±	Edge (μm)	±
0.25	long	2.44	0.31	2.45	0.13	2.62	0.37
	trans	1.82	0.25	1.49	0.10	1.76	0.27

Table 4.28 Subgrain size measurements across and along the direct and indirect extrudes of 2014 alloy.

Direct Extrude - D4133A
T_I = 300°C

Distance along extrude	Actual Temp Tc (°C)	$d_c(t)$ (μm)	$d_a(t)$ (μm)
0.25	380	1.27	1.11
0.6	447	1.41	1.23
0.8	459	1.49	1.34

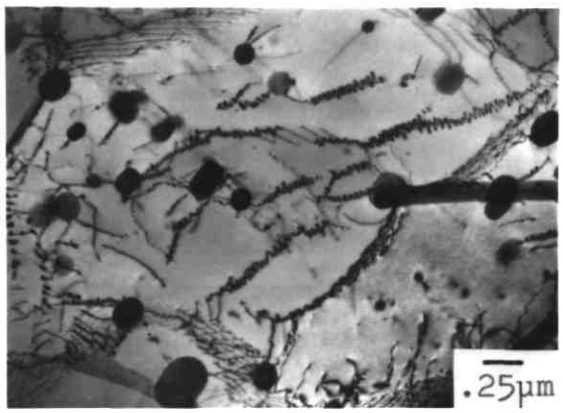
Indirect Extrude - I4123A
T_I = 300°C

Distance along extrude	Actual Temp Tc (°C)	$d_c(t)$ (μm)	$d_a(t)$ (μm)
0.25	338	1.05	0.99
0.6	376	1.23	1.01
0.8	388	1.29	1.11

Table 4.29 Predicted subgrain size and temperatures for direct and indirect extrusion of 2014 alloy.

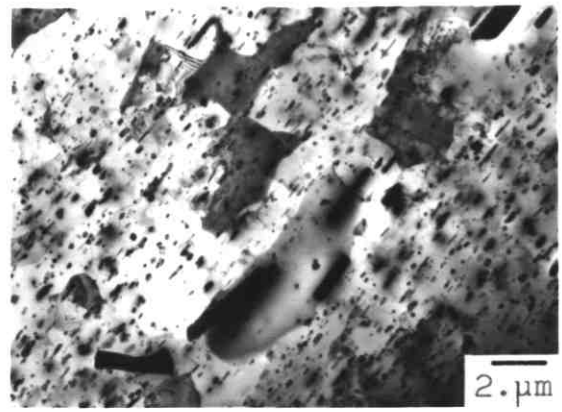
D4462AS

a) T_I = 450°C LnZ_c = 29.84



D4133A

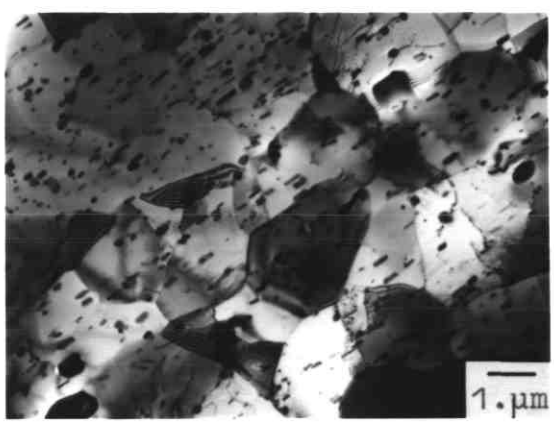
b) T_I = 300°C LnZ_c = 27.10



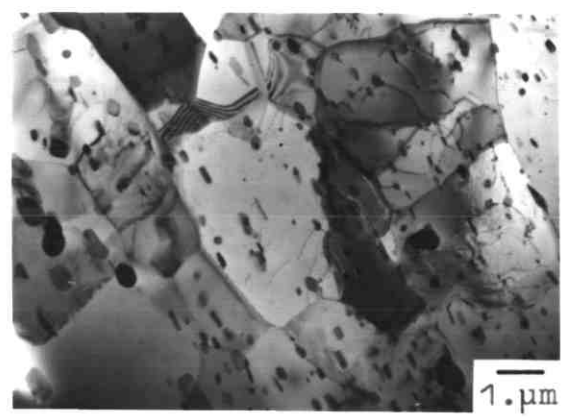
Direct - D4343A

T_I = 400°C

c) Centre LnZ_c = 25.87



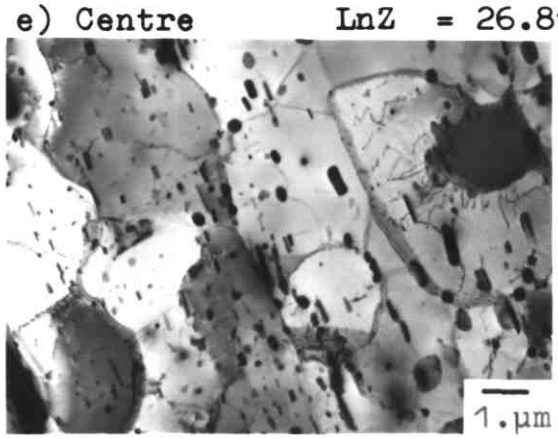
d) Edge



Indirect - I4333A

T_I = 400°C

e) Centre LnZ = 26.81



f) Edge

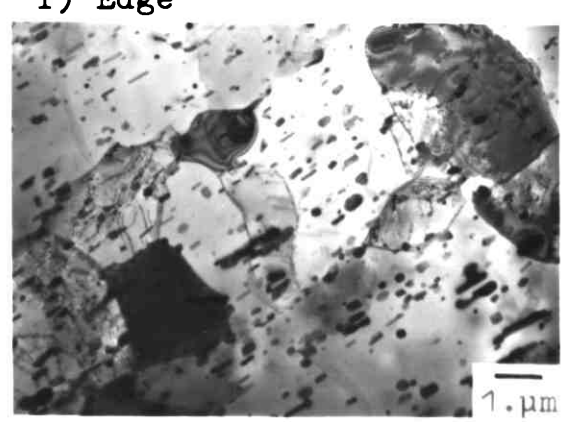


Plate XII. Substructures Observed in the Longitudinal Plane of the Press Quenched Direct and Indirect Extrudes of the 2014 Alloy.

across the indirect extrude, confirming the more homogeneous deformation described in section 4.3.6. which results in a smaller temperature gradient across the extrude, as predicted by the temperature rises evaluated in the previous section.

The variation in subgrain size along the extrude has been established at distances of 0.25L, 0.6L and 0.8L from the front of the extrudes processed at 300 deg.C, the results shown in table 4.28. For direct extrusion the subgrains at the centre of the extrude show a progressive increase in size along the extrude, where at 0.8L they are similar in size to those at the edge, which shows only a smaller increase in size. The observations are consistent with an increase in temperature as extrusion proceeds, the high thermal conductivity and hence heat flow reducing the temperature gradient across the extrude. The indirect extrude shows only a small increase in subgrain size both at the centre and edge of the extrude indicative of the lower temperature rise associated with the indirect mode.

The variation in subgrain size can be related through the change in Z as extrusion proceeds, using the relationships established by Paterson[29] for direct and indirect extrusion of the 2014 alloy.

						cc	
Direct	$d^{-1}(t)$	=	0.096 Ln Z_c	-	1.747	(0.937)	4.26.
Indirect	$d^{-1}(t)$	=	0.085 Ln Z_c	-	1.586	(0.966)	4.27.

The temperature rise at 0.25L, 0.6L and 0.8L are shown in table 4.29. along with the predicted subgrain dimensions d_c and the average subgrain size d_a from table 4.28. It is apparent that the values of d_c are consistently lower but well within the standard errors of estimate for d(t) shown in table 4.28. This therefore suggests that either the

temperature rise is too high due to e.g. the assumption of 90% work energy input, or equations 4.26. and 4.27. are incorrect. Perhaps the first point to note is that equations 4.26. and 4.27. can only be regarded as approximate relations due to the relatively low correlation which exists. Secondly, the assumption that the subgrain structure, which is continually undergoing rearrangement can change as instantaneously as equations 4.26. and 4.27. predict, will largely depend on the deformation history and the material characteristics. Since the ease of recovery decreases with alloy content and decreasing initial billet temperature, one might expect the predicted subgrain sizes established over the entire temperature range to be higher, the difference increasing as extrusion proceeds, which the results in table 4.29. do indeed show.

The fact that the 4% Cu alloy shows a similar variation in subgrain size across and along the direct and indirect extrudes to that of the 1% Cu alloy, indicates that although the substructural variation within the deformation zone may change with the flow characteristics and hence alloy content, the isotropy of the final product is largely dependent on the nature of flow and therefore extrusion process. There are clearly other factors which may influence the final product structure for a specific extrusion condition such as the initial billet structure, preheat treatment, friction conditions, liner temperature etc. The overall situation is further complicated by the fact that the extrudate is often subjected to further heat treatment after processing so that the final properties are a complex function of the as extruded structure and the effects of heat treatment. The relationships between the extrusion process, the extrusion conditions and the subsequent heat treatment will be discussed in the following sections.

4.3.7. HEAT TREATED STRUCTURES

In order to achieve the optimum mechanical properties in heat treatable aluminium alloys such as AA2014, it is usually necessary to solution heat treat and age the wrought product. The effect of this heat treatment on the as-extruded structures will now be considered.

4.3.7.1. SOLUTION TREATED STRUCTURES

The solution treatment temperature is normally chosen as close to the eutectic temperature as possible, the soaking time depending on the section thickness. In the present work a standard solution heat treatment at 500 deg.C for 30 minutes has been used for all the alloys, followed by water quenching to obtain a super saturated solid solution. In a similar manner to the as-extruded material the solution heat treated microstructures could be classified into one of two types, fully or partially recrystallized.

Fully recrystallized structures were found in all the alloys below an extrusion temperature of 350 deg.C and were characterised by relatively large grains elongated in the extrusion direction, examples of which are shown in plate XIII a) and b). Above this temperature, depending on the alloy content and extrusion mode, the extrudes exhibited a fibrous core similar to the as quenched extrudes shown in plate VI, surrounded by a recrystallized grain structure. The presence of the intermediate particles shown in plates VII and VIII restrict static recrystallization nucleation and grain growth in the more highly recovered substructures, so that the fibrous structure is retained during solution treating and ageing, a phenomena which is often referred to as the 'press effect'. The effect of alloy content, extrusion ratio and temperature on the volume percent of material recrystallized calculated using equation 4.20. is

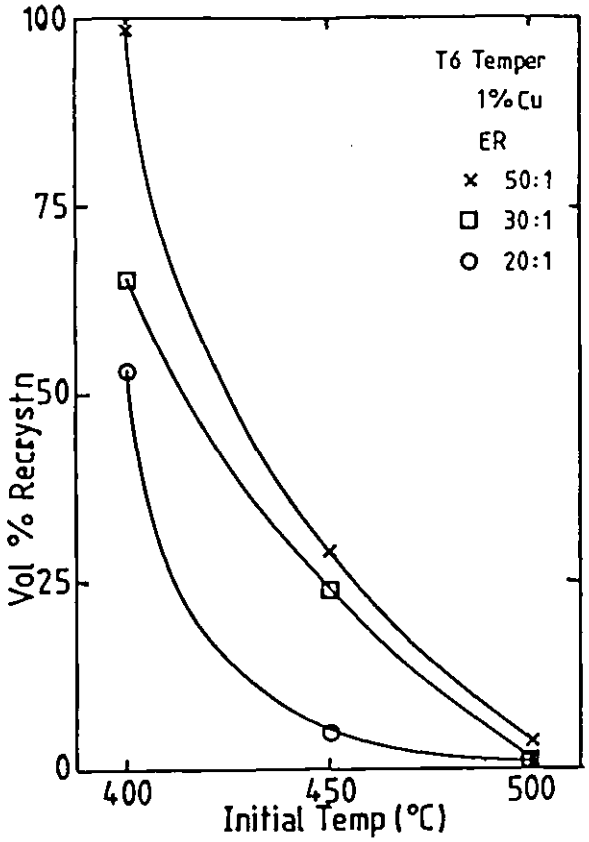


Figure 4.70

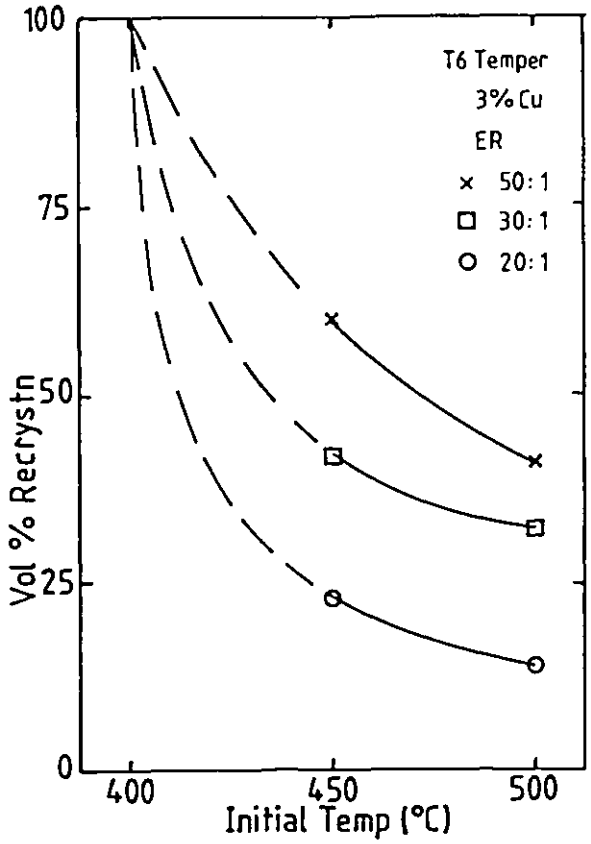


Figure 4.71

Volume % recryn vs initial billet temperature in the T6 temper – 1% Cu and 3% Cu alloys

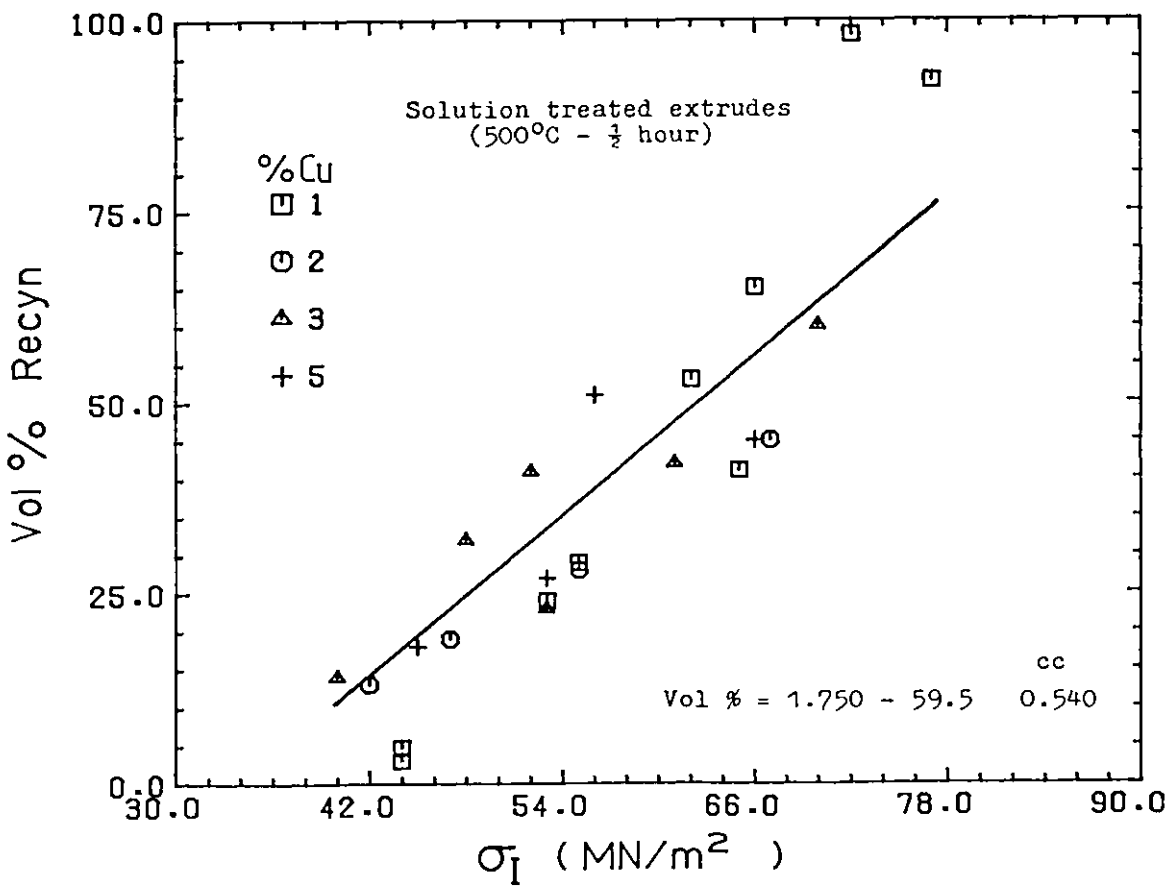


Figure 4.72 Volume % recryn vs initial flow stress for direct extrusion of the 1% Cu - 5% Cu alloys

shown in figures 4.70. and 4.71.

The figures show that the percentage recrystallization increases with increase in strain, Cu content and decreasing temperature, all of which increase the flow stress and hence driving force for static recrystallization. The relationship between the initial flow stress for each extrusion condition and the percentage recrystallization is shown more clearly in figure 4.72. for the 1, 2, 3 and 5% Cu alloys. It is evident from the figure that the driving force for recrystallization increases with the initial flow stress and would seem to be little affected by an increase in alloy content or by the increase in solute at high temperature. This is perhaps to be expected due to the high annealing temperature considered where at lower annealing temperatures the particle size and distribution have been shown to have a significant affect on the recrystallization kinetics.[104,107,142]

In order to ascertain whether a fully recrystallized structure could be obtained by solution treating for longer times at 500 deg.C, specimens from the 5%Cu alloy were solution treated in a salt bath for various times up to one hour and water quenched, the results are shown plotted in figure 4.73. The figure shows that at extrusion temperatures less than 400 deg.C a combination of the high annealing temperature and stored energy of the as-extruded substructure results in a fully recrystallized structure in less than 60 seconds. At 450 deg.C there is no evidence of a nucleation period, whilst at an initial billet temperature of 500 deg.C an incubation period of approximately 4 to 5 minutes exists followed by a slow rate of growth which shows little change after 30 minutes. It should be noted that an annealing temperature of 500 deg.C the growth kinetics

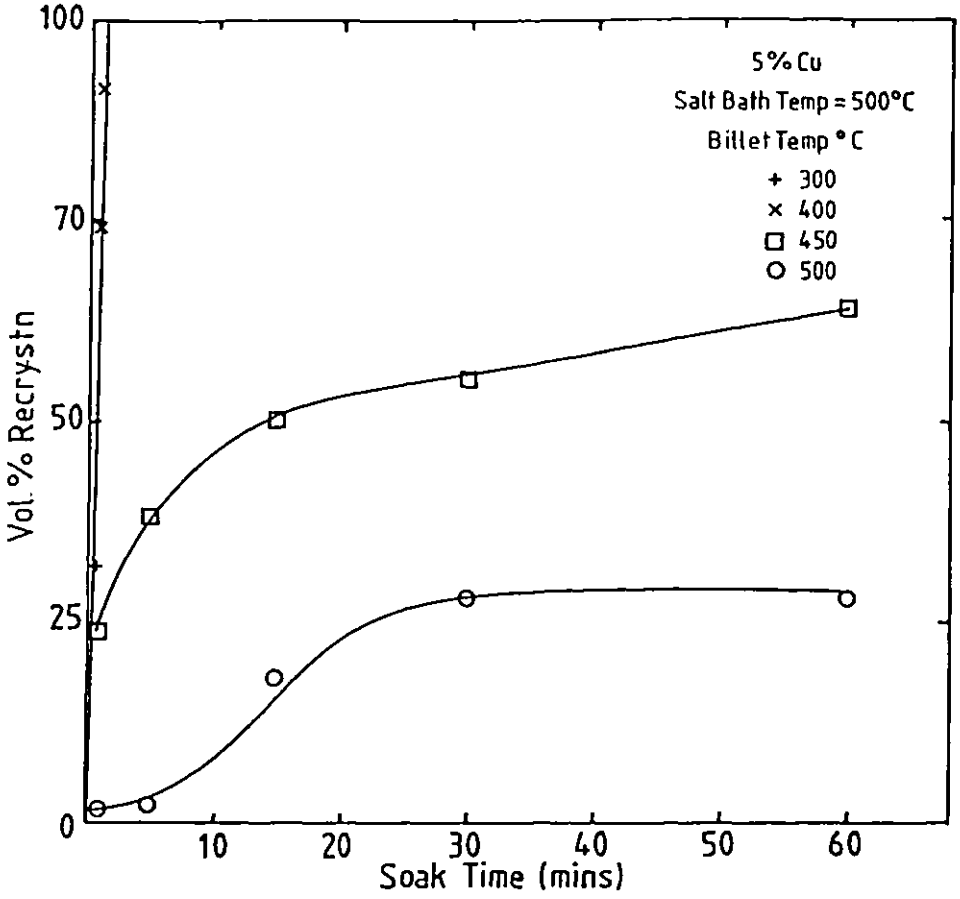


Figure 4.73 Volume % recryn vs solution soak time at 500°C-direct extrusion of the 5% Cu alloy ER = 30:1

Volume Percent Recrystallization

2014 - T6

ER = 20:1

T_I °C	CH Direct	CH Indirect	SS Direct
480	32	16	17
450	48	35	44
400	100	100	84

Vol% recystn = a LnZ_I + b

2014-T6

	a	b	cc
CH Direct	20.0	-430.0	0.995
CH Indirect	22.0	-494.0	0.994
SS Direct	14.1	-397.5	0.989

Table 4.30 The variation in % recrystallization after solution treating and ageing direct and indirect extrudes of 2014 alloy.

will also be a function of solute in solution which increases with time. It therefore seems unlikely that an extended solution treatment will have any effect on the fraction of material recrystallized at high extrusion temperatures.

The presence of a recrystallized annuli has been reported[169] to reduce the fracture toughness and corrosion properties in both high strength and medium aluminium alloy extrudes and is therefore undesirable. In the context of the present work figure 4.72. shows that by extruding at an initial flow stress below 30 MN/m^2 and above 90 MN/m^2 will result in either a fully unrecrystallized or recrystallized structure after solution treating and ageing. For 2014 extruding at a temperature of 480 deg.C, the strain rate required for an initial flow stress of 30 MN/m^2 would be $0.08s^{-1}$, which is equivalent to a ram speed of $0.1mms^{-1}$ at an extrusion ratio of 20:1. Assuming that adequate temperature and speed control could be achieved during extrusion to avoid overheating and surface cracking such production rates may not be economic and could require a longer press quench delay to avoid cooling of the extrusion billet. Therefore either a fully recrystallized structure should be aimed for or a duplex structure which may require machining away of the recrystallized annuli.

The effect of extrusion mode and presolution soak treatment on the percentage recrystallization in the 20:1 extrudes is shown in table 4.30. The results show that for the CH material the percentage recrystallization is least in the indirect extrude consistent with the results of previous workers[166-168] and is indicative of the more uniform nature of flow during extrusion. This is again a very important feature of indirect extrusion since any reduction in the size of the recrystallized annuli will be beneficial to the mechanical properties of the extrude. The increased solute in solution in the presolution soak extrudes retards primary

recrystallization to the extent that the fibrous structure is still present in the 400 deg.C extrudes. There is considerable experimental evidence[33] to show that recrystallization is retarded as the solute content of a solid solution increases where most theories explain this in terms of the boundary migration being controlled by the absorbed solute atoms at the grain boundaries. The presence of second phase particles can further affect the grain growth during recrystallization if $f/r > 0.2$ where f is the volume fraction and r the particle radius. The results in table 4.30. show that there is a linear relationship between the initial process conditions ie Ln Z_I and the percentage recrystallization, which is to be expected since Ln Z_I is directly related to the initial flow stress. It is interesting to note that for the extrusion conditions used in the previous paragraph the maximum ram speed for indirect extrusion increases to 0.3mm/s, whilst for the SS billets a ram speed 1.3mm/s may result in little or no recrystallization after solution treating and ageing.

The variation in recrystallized grain size at the centre and edge of the 2014 extrudes is shown in figures 4.74. to 4.76., the grain size measurements are listed in appendix IV. It is evident that the grain size decreases from the centre to the edge of the extrude, the more highly strained periphery providing a larger number of nucleation sites for static recrystallization, which is also reflected in the larger spread of grain sizes in the centre of the extrude. It is interesting to note that this is also a prominent feature of the indirect extrudes, where one might have expected a more uniform structure across the extrude due to the more uniform flow characteristics described in section 4.3.6. The reduction in strain energy associated with an increase in recovery with extrusion temperature reduces the driving for recrystallization so that the grain

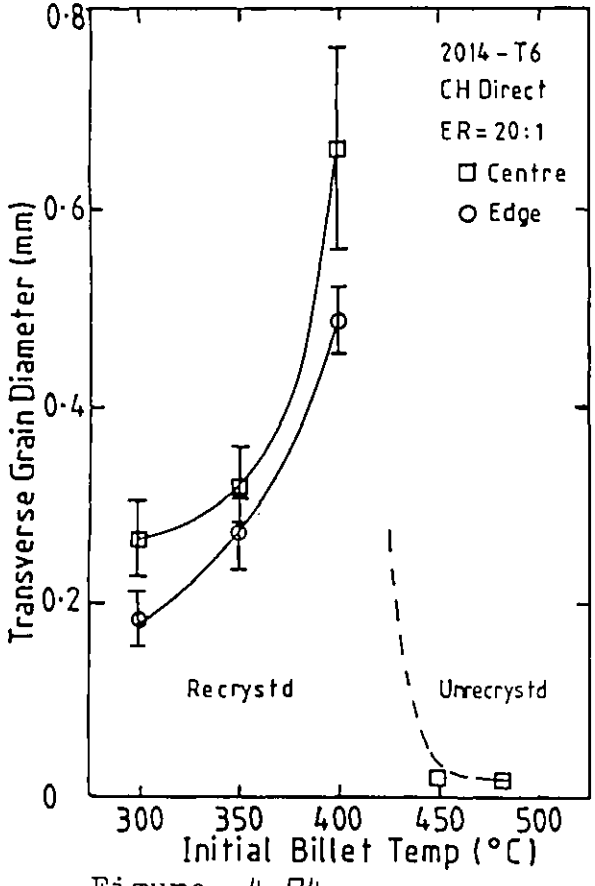


Figure 4.74

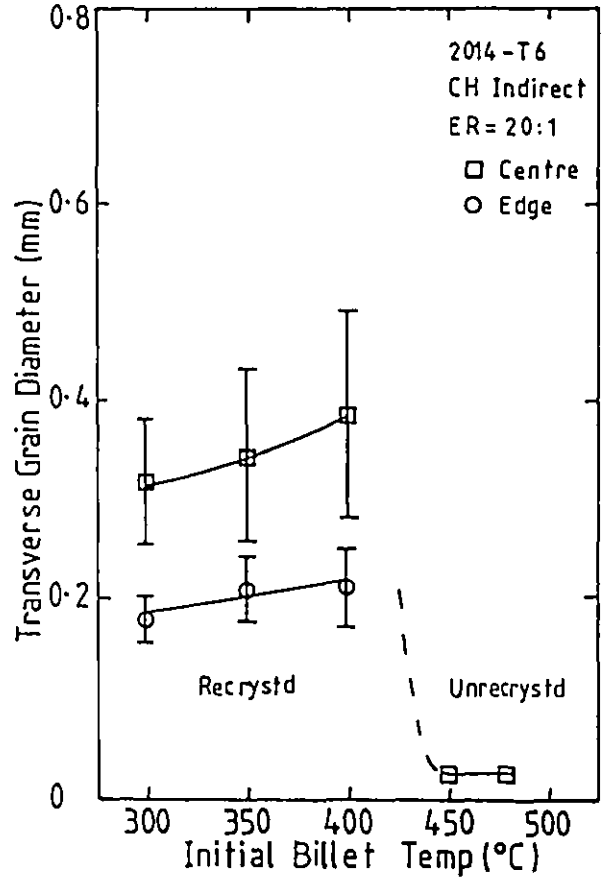


Figure 4.75

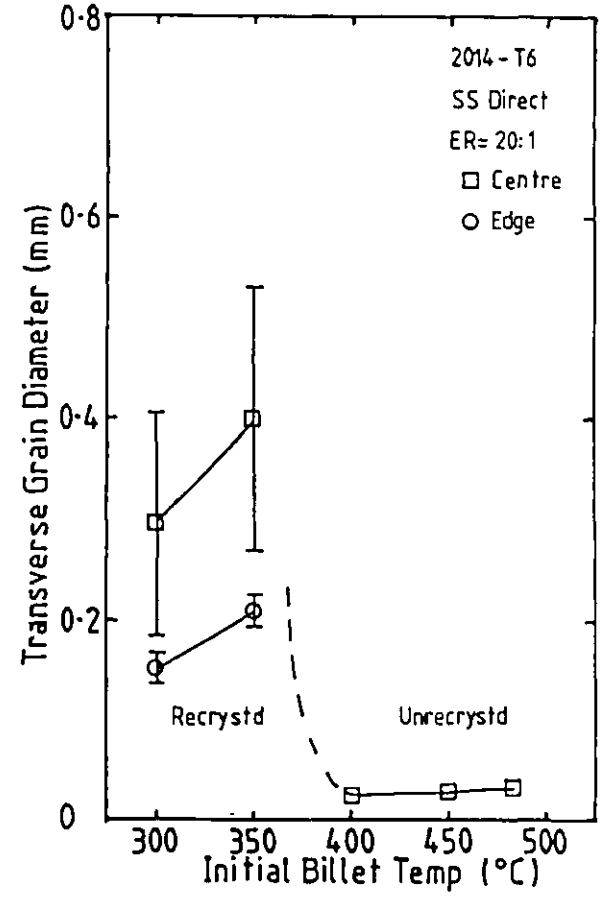


Figure 4.76

Recrystallised grain size (t) vs initial billet temperature for the CH direct, indirect and SS direct 2014 alloy

size increases with temperature as shown in figures 4.74. to 4.76.

Sheppard et al[170] have also shown that the recrystallized grain size can be directly related to the hot worked subgrain size. Using the data in tables 4.24. and 4.30. and the subgrain dimensions predicted by equations 4.26. and 4.27. the recrystallized grain size has been plotted as function of the subgrain size in figure 4.77. Also included on this figure are the results obtained by Paterson.[29] A direct correlation between the subgrain size and the recrystallized grain size has been associated[112] with subgrain coalescence as the primary recrystallization mechanism since the time per subgrain coalescence is reported[106] to decrease with the area of the subboundary walls in contact with adjacent subgrains. Assuming that a specific number of subgrain coalescences are required to form a high angled boundary and hence recrystallization nuclei, the rate of nucleation will increase with decreasing subgrain size as the area of contact decreases. Although it should be noted that the increase in subgrain size at the edge of the extrudes is also associated with an increase in grain size due to the increase in strain energy associated with the more highly strained periphery. The results in figure 4.77. clearly show that for a constant subgrain size the recrystallized grains are larger in the indirect extrudes consistent with the decrease in the peripheral recrystallization and hence strain energy. However the longer press quench delay during indirect extrusion will also result in an increase in static recovery and hence decrease in strain energy which will increase with temperature and decreasing ram speed i.e. subgrain size, which agrees with the overall trend shown in figure 4.77.

It is evident from figures 4.74. to 4.76.that the greatest difference between the T6 structures exists at an initial billet temperature of 400 deg.C. The relevant optical microstructures are shown in plate XIII.

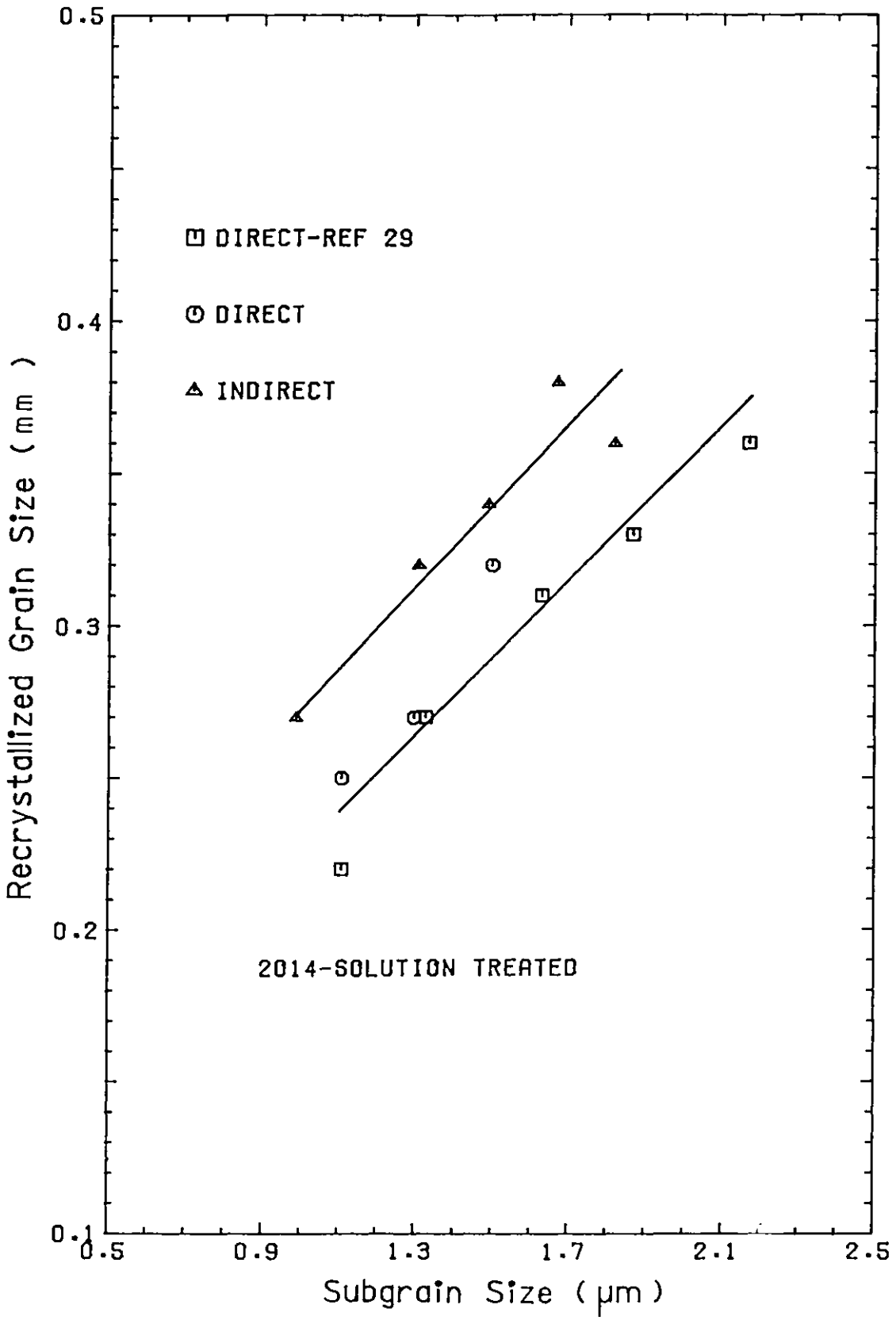
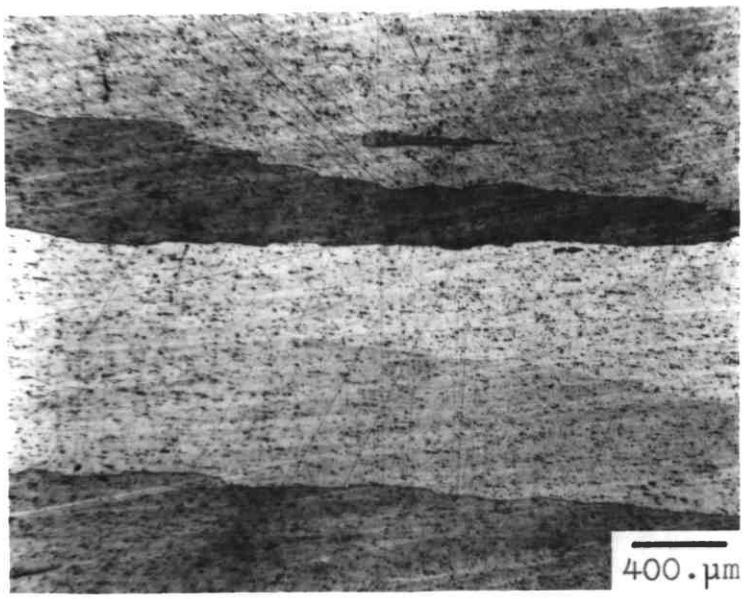


Figure 4.77 Recrystallised grain size vs subgrain size direct and indirect extrusion of 2014 alloy

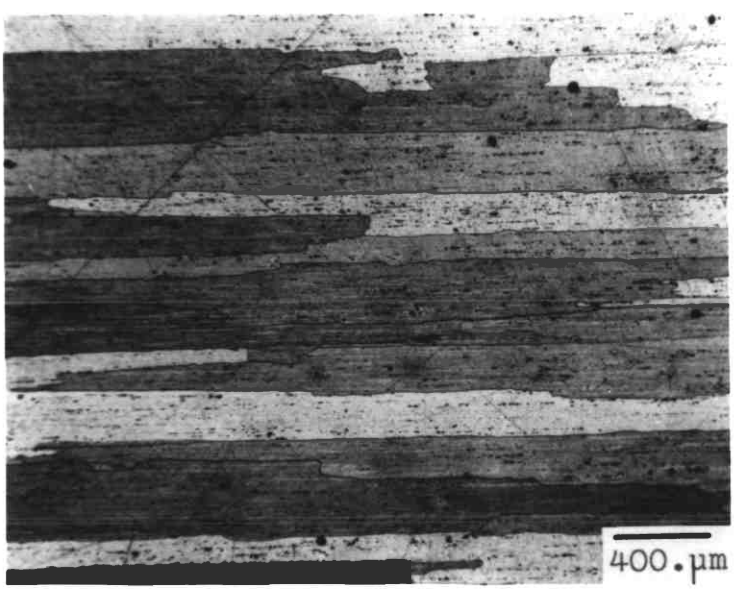
a)



Direct CH

D4362A - T6
T_I = 400°C
ER = 20:1

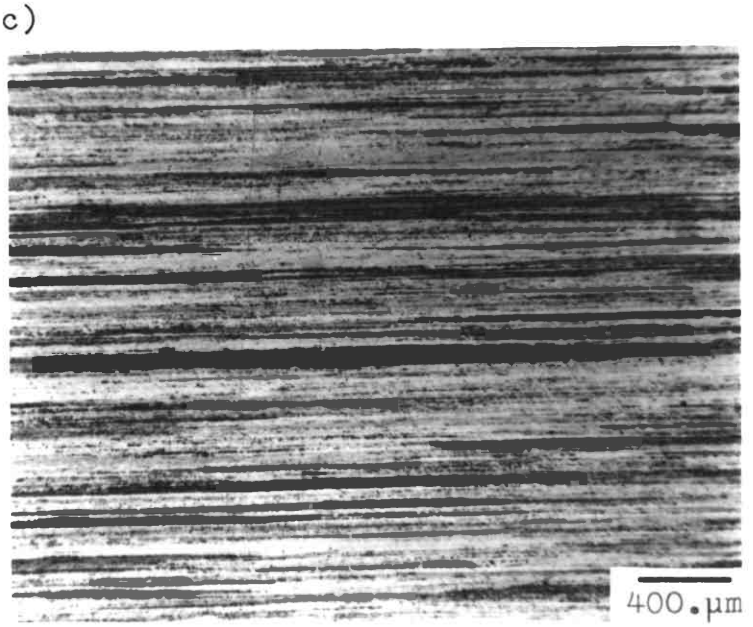
b)



Indirect CH

I4352A - T6
T_I = 400°C
ER = 20:1

c)



Direct SS

D4362AS - T6
T_I = 400°C
ER = 20:1

Plate XIII. T6 Structures 2014 Alloy

Micrographs a) and b) clearly show the large difference in recrystallized grain size between the direct (a) and indirect (b) extrudes, whilst c) shows the unrecrystallized core structure exhibited by the presolution soak extrude. The fact that the sudden increase in grain size in the CH direct extrudes is not seen in the results from reference 29 in which a constant container temperature of 300 deg.C was used, indicates that the phenomena is associated with higher container temperature used in the present work. This is to some extent confirmed by the percentage recrystallization figures in table 4.31. which show the effect of container temperature on the peripheral recrystallization in the T6 3% Cu extrudes described in section 4.2.5. The results show that above a container temperature of 400 deg.C the peripheral recrystallization decreases with container temperature and ram speed, which may be attributed to more uniform flow characteristics due to the reduction in shear stress within the peripheral shear zone. Below this temperature the grain size measurements listed in appendix IV show that the container temperature has little effect on the recrystallized grain size, although the result at 450 deg.C again shows a marked increase in grain size to approximately 0.90mm from an average grain size of approximately 0.35mm.

3% Cu - T6

ER = 50:1

Liner Temp ^{o}C	Ram Speed mm/s	
	3	13
500	16	60
450	89	100
400	100	100

Table 4.31 The variation in % recrystallization with container temperature - solution treated 3% Cu alloy.

Although it has not been possible to establish the exact recrystallization mechanism involved the recrystallization kinetics in figure 4.73. indicate that the large increase in grain size is associated with secondary recrystallization and grain growth, since it was later established from the aged microstructures in reference 29 that the low Z extrudes exhibited a retained substructure consistent with the fact that primary recrystallization is not complete. The aged microstructures of the extrudes in figures 4.74. to 4.76. will be considered in the following section.

Since an increase in grain size is reported[41,61] to reduce both the tensile and fracture toughness properties the results in the present work show that for direct extrusion of press quenched heat treatable alloys the temperature differential between the billet and container must be carefully chosen if a T6 recrystallised product is required. The relationship between the structure and properties will be considered in further detail in section 4.4.

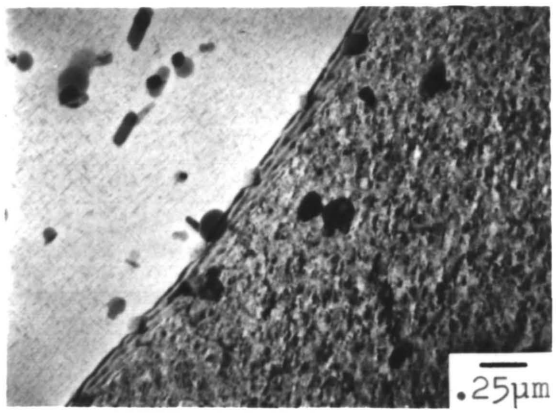
4.3.7.2. AGED MICROSTRUCTURES

The effects of ageing have been investigated using the C.H. direct, indirect and SS direct 2014 extrudes. For the following examples peak strength coincides with ageing at 160 deg.C for 18 hours in the solution treated T6 and press quenched T5 extrudes. The resulting microstructures are shown in plate XIV and XV.

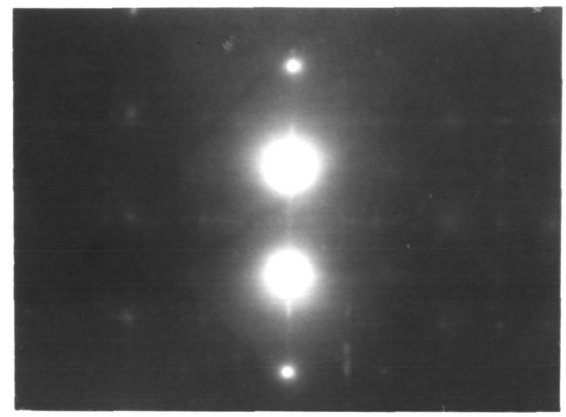
Plate XIV shows examples from the T6 CH direct and indirect extrudes where micrograph a) shows the precipitate and particle distribution either side of a grain boundary and is typical of the aged microstructure found in all the fully recrystallized extrudes. The elastic coherency

a) D4162A - T6 T_I = 300°C

Precipitate and particle distribution either side of a grain boundary.

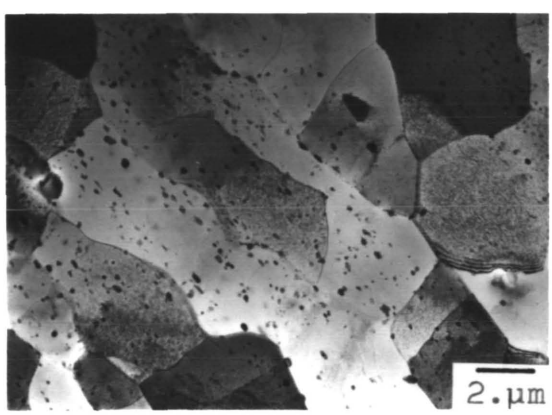


b) S.A.D.P. of the T6 matrix.



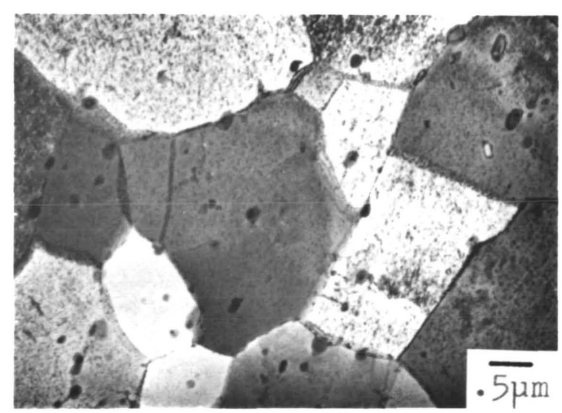
c) D4522A - T6 T_I = 475°C

Substructure retained after solution treating and ageing.



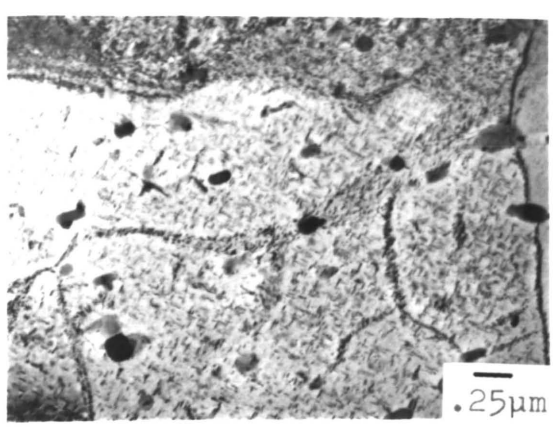
d) I4352A - T6 T_I = 400°C

Evidence of a retained substructure at the centre of the extrude.



e) I4513A - T6 T_I = 475°C

Preferential precipitation at the subgrain boundaries.



f) D4522A - T6 T_I = 475°C

Precipitate distribution either side of a subgrain boundary.

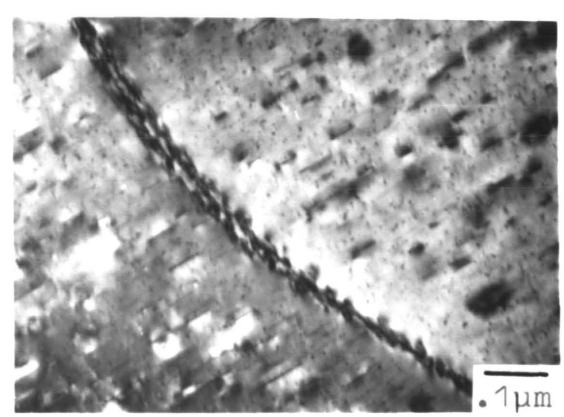


Plate XIV. T6 Solution Treated and Aged Microstructures of the Direct and Indirect 2014 Alloy - Longitudinal Plane.

strains associated with the θ" precipitates gives rise to the matrix strain field contrast shown in all the micrographs and results in the characteristic faint [100] matrix spot streaking, an example of which is shown in micrograph b). The observation of coherency strains is consistent with the theories of Mott and Nabarro[143] and Geisler[144] that precipitation hardening at peak hardness is due to the elastically strained matrix near the coherent θ" precipitates. As the precipitates grow, the strain fields become larger and at peak strength they extend from one precipitate to the next. Further ageing results in the transformation of θ' at the expense of θ" resulting in a loss of coherency and a decrease in strength. It is evident that some intermediate particles still remain aligned in the extrusion direction, their presence can be associated with the insoluble (FeMn)Al particles which inhibit recrystallization and grain growth during solution treating and ageing [110]. Micrograph a) also shows the absence of any appreciable precipitate free zone along the grain boundary. This can be attributed to the rapid quench which results in a non-equilibrium concentration of vacancies distributed uniformly throughout the matrix, where the addition of silicon helps stabilize the vacancy clusters near the grain boundaries.[145]

In the low Z_I or high temperature extrude processed at 480 deg.C micrograph c) clearly shows the presence of the subgrain structure retained after solution treating and ageing. The misorientation relationships obtained from a Kikuchi line analysis varied between 0.1° to 3° although no consistent trend was found in either the direct or indirect extrudes examined. Examples of the subgrain sizes in the T6 and T5 extrudes are shown in table 4.32. In order to establish whether any change in the substructure occurs during the heat treatment cycle the T1 transverse subgrain sizes predicted by equations 4.26. and 4.27. and the

2014 - T6

Extn Code	T_I °C	ER	d(l) µm	±	d(t) µm	±
D4522A	480	20	4.21	0.45	2.68	0.31
I4522A	480	20	3.31	0.43	2.62	0.30
I4513A	470	30	3.12	0.43	2.26	0.41
D4562AS	480	20	3.48	0.37	2.51	0.43
D4362AS	400	20	3.13	0.40	2.11	0.40

2014 - T5

Extn Code	T_I °C	ER	d(l) µm	±	d(t) µm	±
D4522A	480	20	4.03	0.33	2.56	0.22
I4522A	480	20	3.27	0.43	2.43	0.30
D4562AS	480	20	2.90	0.72	2.14	0.35
D4543AS	475	30	3.09	0.49	2.10	0.23
D4362AS	400	20	3.00	0.53	1.75	0.35
D4313AS	400	30	2.56	0.40	1.55	0.30

Table 4.32 Subgrain size measurement from T6 and T5 direct and indirect CH and SS 2014 extrudes.

2014

T_I = 480°C

ER = 20:1

Temper	CH Direct d(t)µm	CH Indirect d(t)µm
T1	2.55	2.44
T6	2.68	2.62
T5	2.56	2.43

Table 4.33 Comparison between T1 and T5, T6 subgrain dimensions 2014 alloy.

temperature corrected values of LnZ_C, have been compared with the T6 results in table 4.32. The results in table 4.33. indicate that some subgrain growth and coalescence may have occurred during the solution treatment, although clearly not enough to initiate recrystallization.

It was shown in section 4.3.7. and plate XIII b) that the indirect extrude processed at an initial billet temperature of 400 deg.C exhibited a fully recrystallized grain structure. However the aged microstructure revealed colonies of subgrains 10 to 20 subgrains in diameter within the recrystallized matrix, an example of the subgrain structure is shown in micrograph d). The existence of a retained substructure is indicative of the lower strain energy associated with the indirect substructure predicted by figure 4.77. and demonstrates the need to investigate not only the optical but also the aged microstructures. The equivalent direct extrude exhibited a fully recrystallized matrix in which no traces of a substructure were found confirming the suggestion made in the previous section that the large increase in grain size is associated with secondary recrystallization and grain growth. However why this does not occur in extrudes processed with a constant container temperature of 300 deg.C and hence higher extrusion load is still not certain. Since the extrusion billets and extrudates were subjected to as near as possible identical preheat treatments and solution treatment cycles one explanation may be associated with a change in either the hot worked or primary recrystallization texture due to a change flow characteristic associated with a higher container temperature.

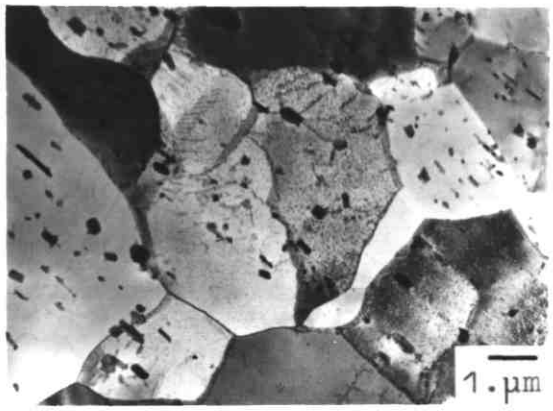
The presence of a retained substructure has been reported[135] to have little effect on the overall ageing characteristics, although as micrograph e) shows preferential precipitation does occur at the subgrain

boundaries, and as such may have a more significant effect on the corrosion and fracture properties which are very much dependent on the nature of the precipitate distribution and solute concentration at grain boundaries. At a higher magnification micrograph f) shows that a precipitate free zone $\sim$0.06 μm wide is associated with the subgrain boundary and probably forms due to the depletion of the surrounding matrix of solute caused by the preferential precipitation at the subboundary. Micrograph f) also shows a uniform distribution of fine spherical precipitates approximately 10 - 20 Å in diameter. The existence of a fine precipitate distribution tends to confirm the findings of previous workers[55-57] that GPB type zones are present in the peak aged 2014 alloy.

Examples of the aged microstructure from the press quenched and aged direct and indirect extrudes processed at 480 deg.C are shown in plate XV a) and b). An effective reduction in the solution treatment temperature to 480 deg.C and soak time to 20 minutes will reduce the solute content of the super saturated solid solution. However micrographs a) and b) clearly show that a significant ageing reaction still occurs, although it is evident that the size and distribution of the ageing precipitates is not the same as in the T6 extrudes shown in plate XIV. Micrograph b) also shows at a higher magnification the presence of helical dislocations which have acted as sites for preferential precipitation. Their presence may also account for some of the heterogeneous precipitation seen in the T6 extrudes in plate XIV. Examples of the subgrain sizes from the T5 extrudes are shown in table 4.32. and have been compared in a similar manner to the T6 extrudes with the T1 subgrain dimensions in table 4.33. The results clearly indicate that little or no subgrain growth occurs during the ageing treatment so that any strength derived from the subgrain

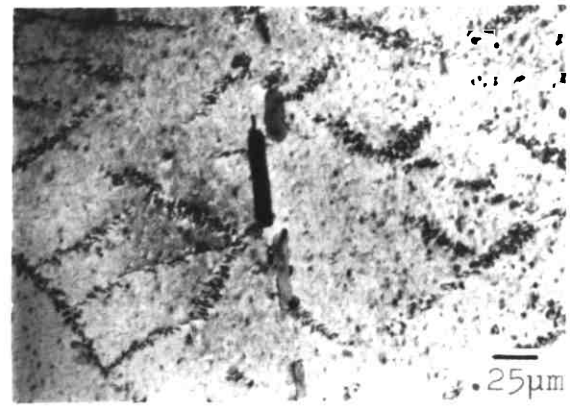
a) D4522A - T5 T_I = 475°C

Press quenched and aged.



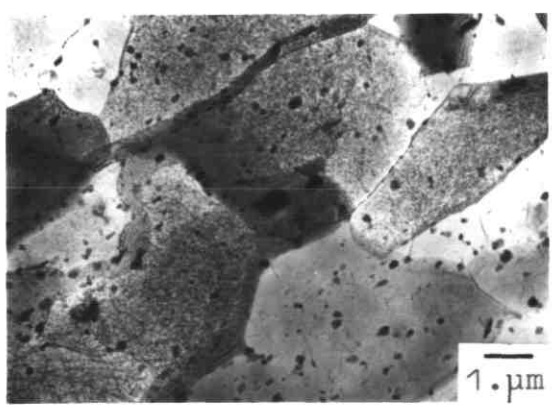
b) I4522A - T5 T_I = 475°C

Preferential precipitation at helical dislocations.



Presolution Soak Extrudes T6 + T5

c) D4562AS - T6 T_I = 475°C



d) D4362AS - T6 T_I = 400°C

Retained substructure in the centre of the extrude.



e) D4543AS - T5 T_I = 475°C

Press quenched and aged.



f) D4562AS - T5 T_I = 475°C

Press quenched and aged.

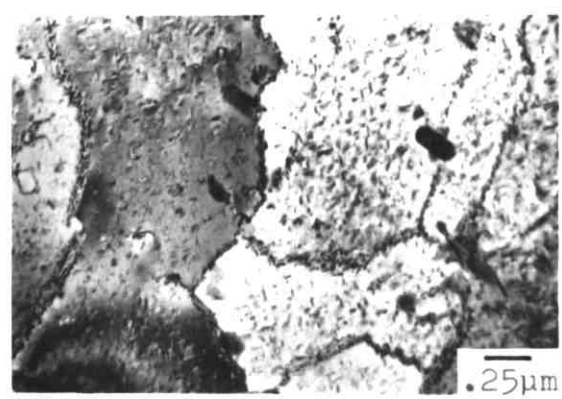


Plate XV. T5 and T6 Microstructures of the 2014 Alloy CH Direct, Indirect and SS Direct Extrudes.

structure is likely to be greater in the T5 extrudes and may effectively counter balance the possible reduction in age hardening.

Examples of the retained substructures in the T6 extrudes from the presolution soak billets processed at 475 deg.C and 400 deg.C are shown in micrographs c) and d). The intermediate particle size and distribution and precipitate morphology was found to be similar to the CH extrudes although the substructure shown in micrograph d) was characterised by a continuous subgrain structure as opposed to the recrystallized matrix and subgrain colonies seen in the CH direct and indirect extrudes. The larger as cast particles $\geqslant 2\mu m$ in size were observed in the high and low Z structures although the size and number were smaller in comparison to the CH material, consistent with the SS torsion structures discussed in section 4.3.5.3. Evidence of heterogeneous precipitation at the subboundaries and helical dislocations can be seen in both micrographs.

Examples of the T5 microstructures from extrudes extruded at 475 deg.C are shown in micrographs e) and f) at low and high magnification. The possible increase in solid solution content prior to ageing might be expected to enhance the ageing response and hence precipitate distribution, which is to some extent confirmed by comparison with the CH T5 extrudes shown in micrographs a) and b). Clearly if the age hardening can be increased in the T5 extrudes by a presolution soak treatment, then the incremental increase in strength which may be derived from the as-quenched substructure may produce an extrude with equivalent if not superior properties to those of the solution treated and aged T6 extrudes. The effect of subsequent heat treatment on the mechanical properties of the CH direct, indirect and SS direct extrudes will be considered in the following sections.

4.4 ROOM TEMPERATURE PROPERTIES OF THE EXTRUDE

4.4.1. INTRODUCTION

It is clear from the discussion in the previous sections that the choice of extrusion process and process conditions has a marked influence on the as-extruded and heat-treated structures and hence properties. In the following sections the relationship between the processing conditions and the T1, T5 and T6 properties has been investigated using the direct and indirect extrudes of the commercial 2014 alloy. The variation in hardness and tensile properties with copper content has also been considered in the T1 and T6 tempers. A full listing of the results can be found in appendix III

4.4.2. EFFECT OF EXTRUSION CONDITION ON THE HARDNESS PROPERTIES

The variation of hardness with extrusion temperature and reduction ratio is shown plotted in figure 4.78 for the 1% Cu and 5% Cu alloys. Hardness measurements were taken at the centre, mid-radius and edge positions to determine the variation in properties across the extrude. The results in figure 4.78 represent the average values from these readings since little or no variation was found for either alloy. The 1%Cu alloy shows a slight decrease in hardness with extrusion temperature below 400 deg.C, the 5%Cu alloy showing a similar trend below 350 deg.C. The decrease in strength is consistent with the increase in subgrain size with temperature shown by both alloys in section 4.3.5.3.

The increase in hardness above these temperatures is consistent with the microhardness data from the 1%Cu and 5%Cu torsion specimens in section 4.1.3.2. and indicates that the amount of solute retained in solution during

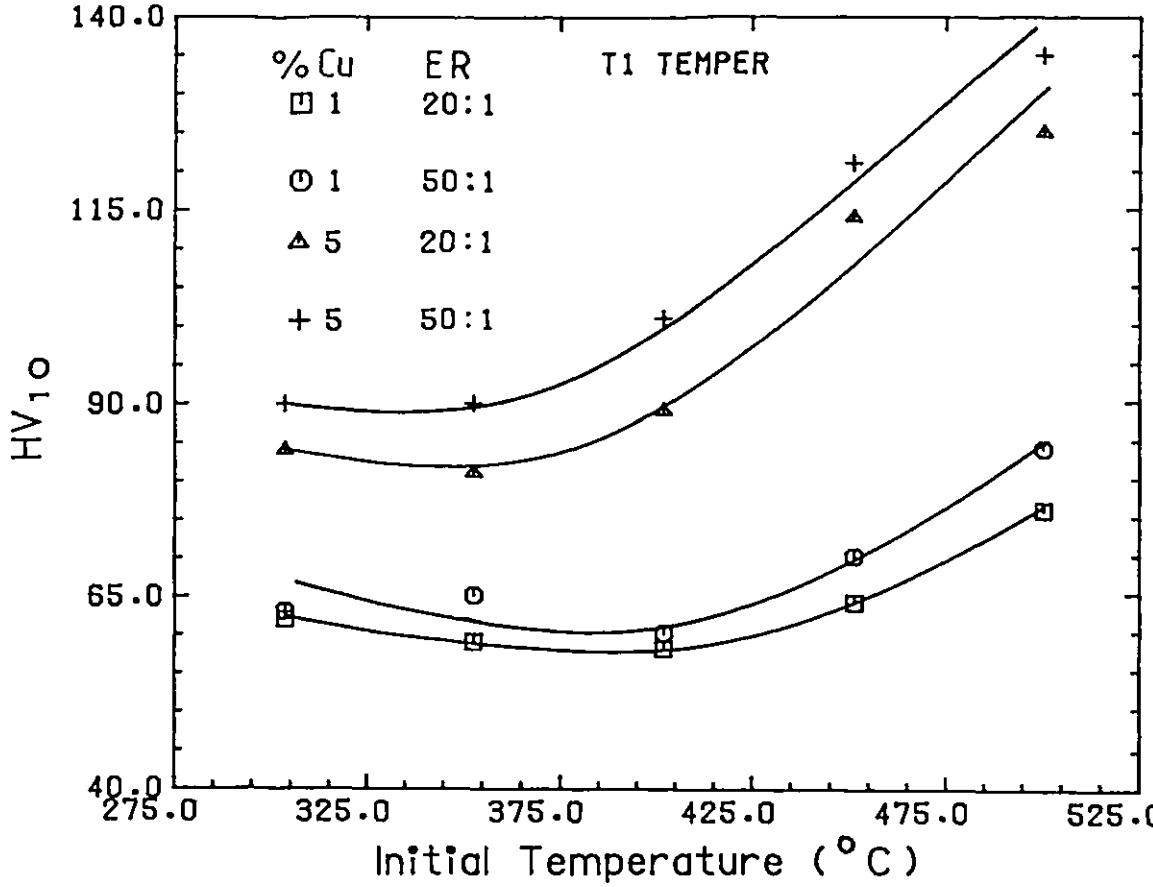


Figure 4.78 Hv_{10} vs initial billet temperature T1 temper-1% Cu and 5% Cu alloys

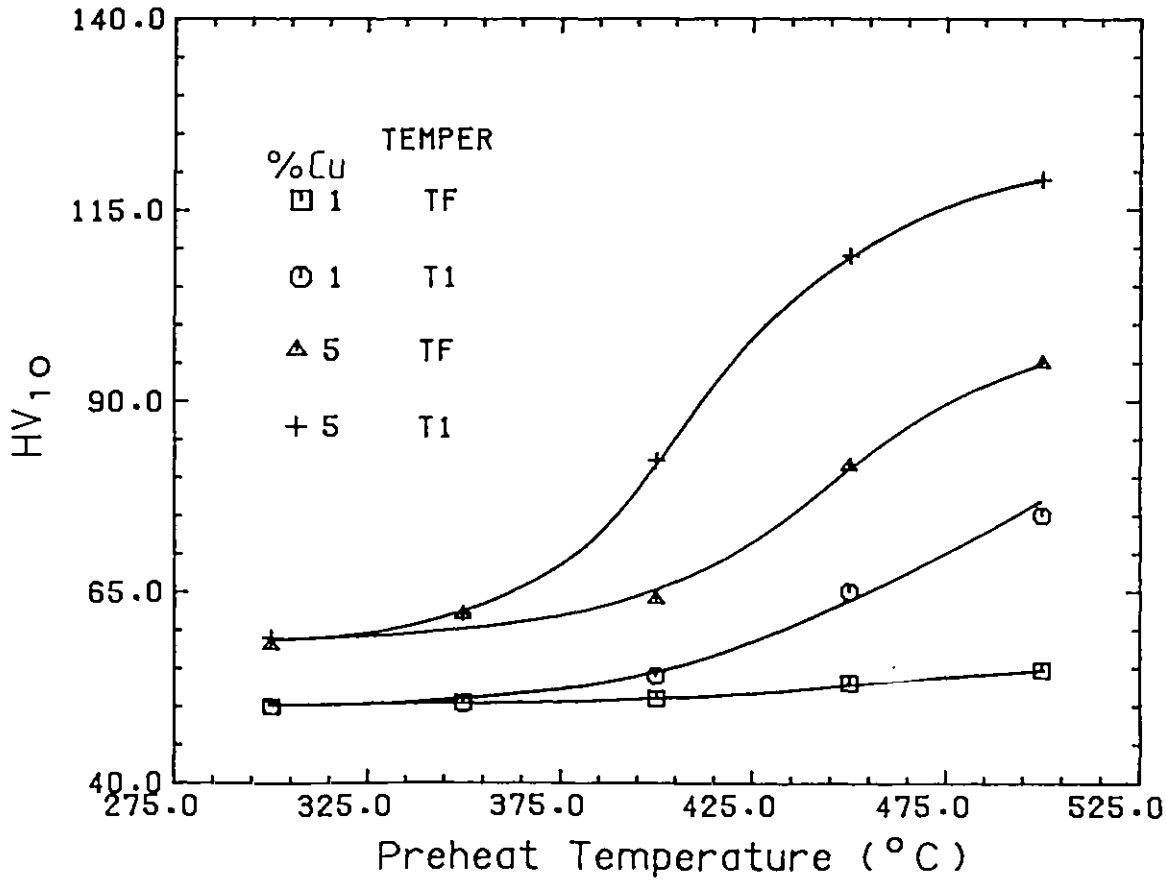


Figure 4.79 Hv_{10} vs preheat temperature TF, T1 tempers-1% Cu and 5% Cu alloys

quenching is more important than the substructure strenghtening alone. Since the extrudes were tested in the naturally aged condition, the increase in hardness is likely to be due to a combination of solid solution strengthening, and precipitation hardening associated with the formation of GPI and GPB zones at room temperature which act as obstacles to dislocation motion.[44,45] Both forms of strengthening are shown more clearly in figure 4.79 which shows the hardness properties of homogenized material subjected to identical billet pre-heat treatment cycles and tested in the as quenched and naturally aged condition, which for both alloys corresponded to ageing at room temperature for three months. Figure 4.79 shows that for the 1%Cu alloy the increase in hardness above 350 deg.C is almost entirely due to natural ageing. The 5%Cu alloy shows a large increase in hardness above 350 deg.C in the as quenched or F temper due to solid solution hardening, which further increases after natural ageing. However it should be noted that the final values of HV_{10} above 350 deg.C are $\sim$10% lower than those of the T1 extrudes in figure 4.78 indicating that the substructure still plays an important role in determining the overall mechanical properties.

The effect of extrusion ratio on the T1 hardness is also shown in figure 4.78, and shows that for all temperatures the hardness increases with extrusion ratio. This is probably due to a combination of a decrease in subgrain size associated with the higher strain rates and the greater temperature rises at higher extrusion ratios taking more solute into solution, the final temperatures in the 50:1 extrudes being approximately 30-50 deg.C higher.

4.4.3. AGEING CHARACTERISTICS

The artificial ageing characteristics of all five alloys have been determined for a constant extrusion

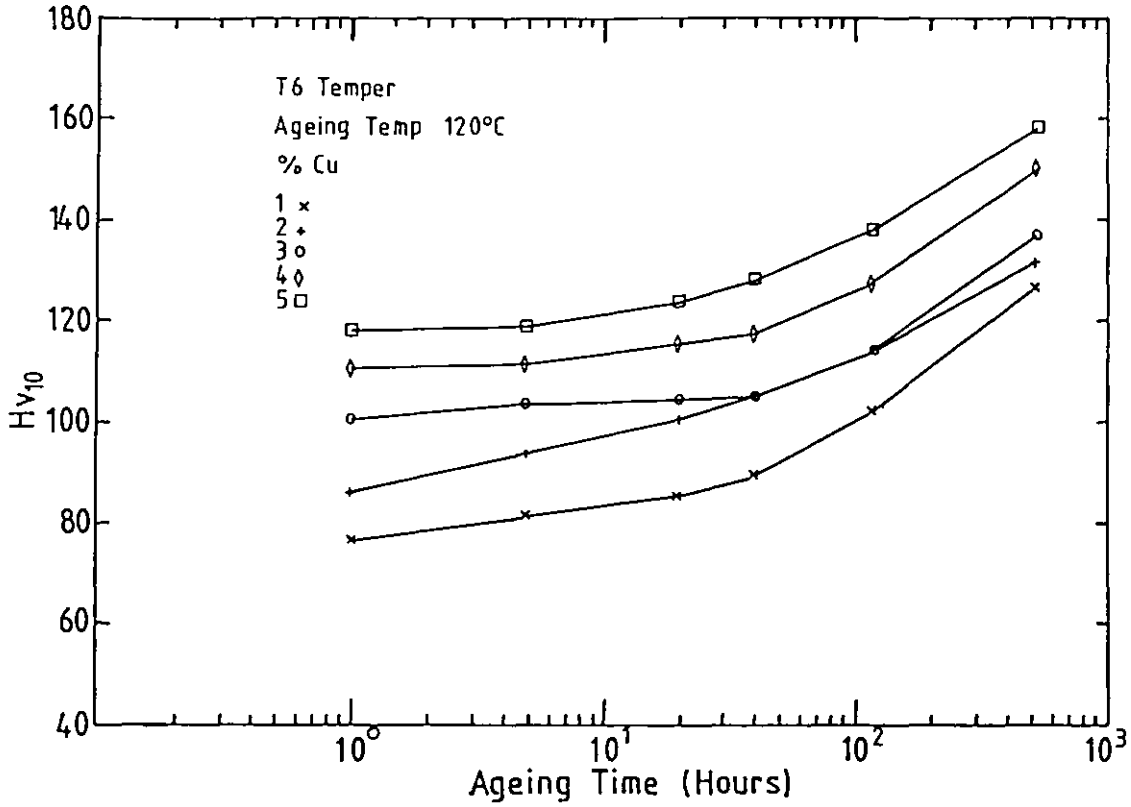


Figure 4.80 Ageing characteristics at 120°C solution treated 2000 series alloys

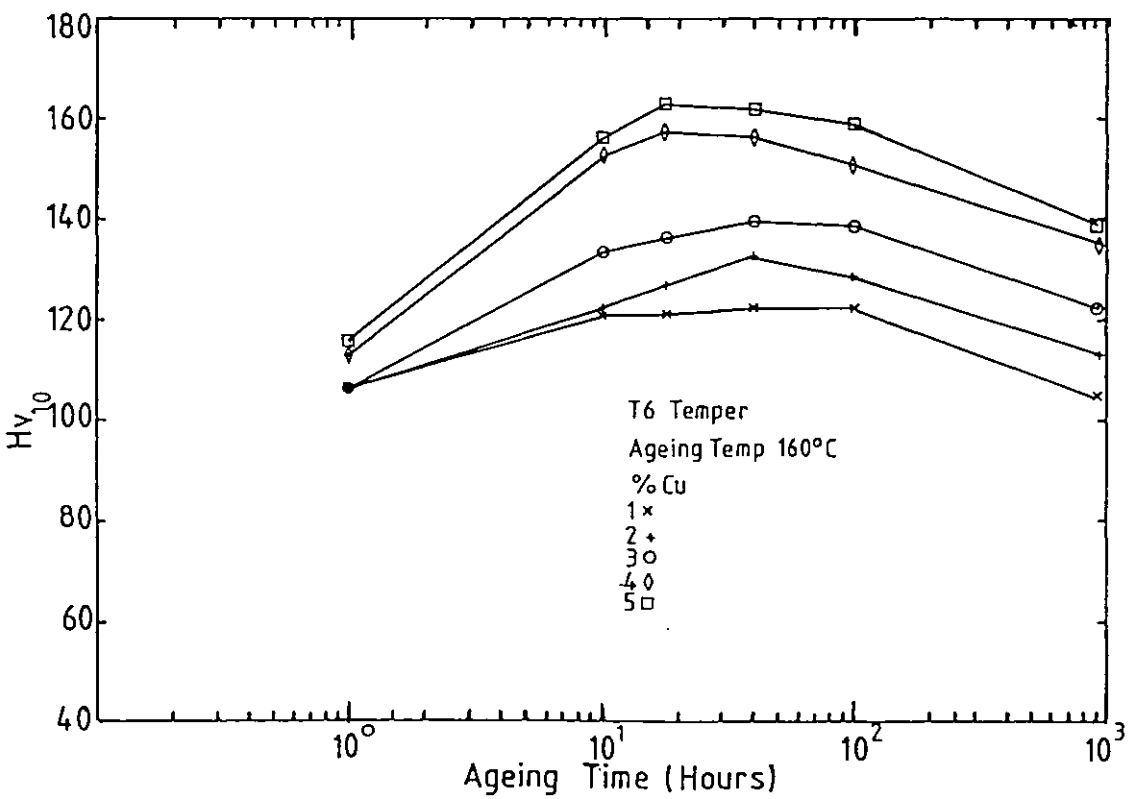


Figure 4.81 Ageing characteristics at 160°C solution treated 2000 series alloys

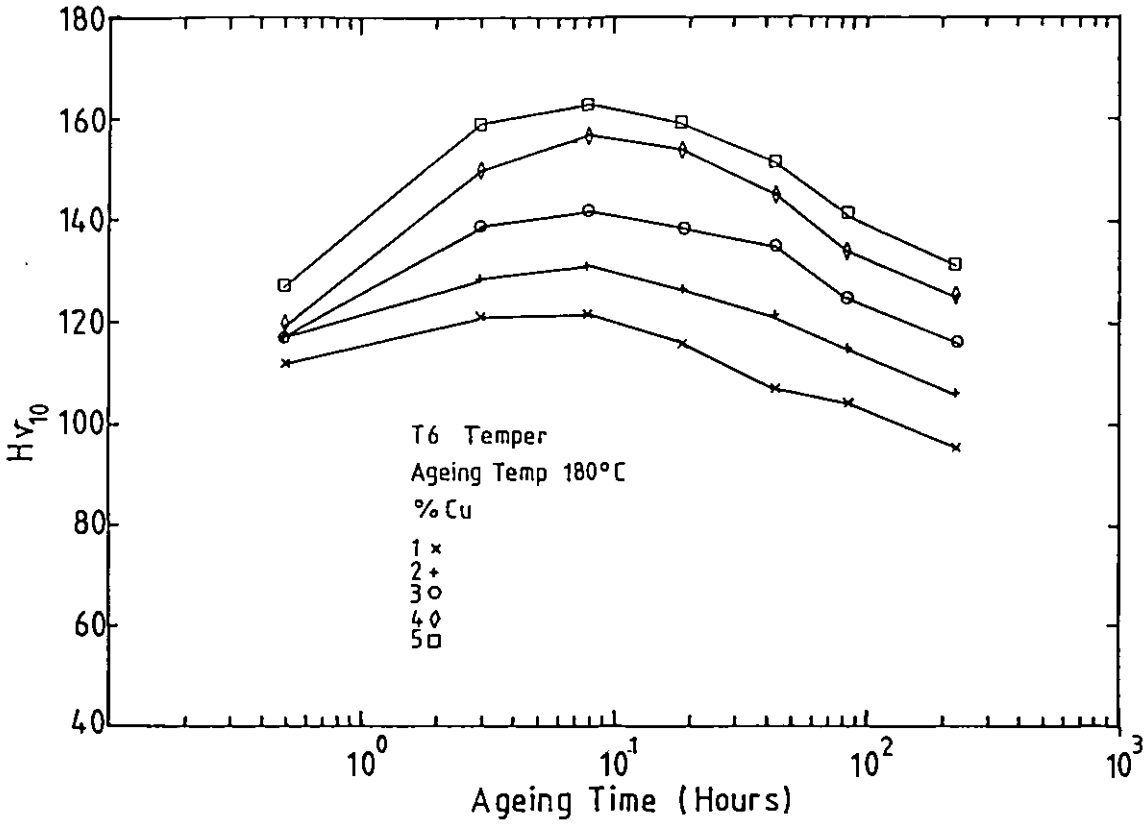


Figure 4.82 Ageing characteristics at 180°C solution treated 2000 series alloys

Strain Hardening Exponents n 2014

ER = 20:1

$\sigma = A \varepsilon^n$

T6

T_I °C	Direct(CH)	Indirect(CH)	Direct(SS)
300	0.183	0.200	0.141
475	0.095	0.113	0.113

T5

T_I °C	Direct(CH)	Indirect(CH)	Direct(SS)
300	—	—	0.215
400	—	—	0.162
475	0.121	0.135	0.128

T1

T_I °C	Direct(CH)	Direct(SS)
300	0.319	0.305
475	0.276	0.256

Table 4.34 Strain hardening exponents-2014 alloy.

temperature of 400 deg.C. Samples were solution treated at 500 deg.C for half an hour and water quenched. The ageing treatments were conducted at 120 deg.C, 160 deg.C and 180 deg.C. The specimens were removed from the ovens at set intervals of time to evaluate the hardness versus time characteristics. A full listing of the results is shown in appendix III.

At an ageing temperature of 120 deg.C figure 4.80 shows that the peak hardness is not achieved after over 500 hours ageing. Previous workers[56,135] have reported that for 2104 the peak is attained after $\sim$800 hours, whilst ageing at 100 deg.C the peak ageing time is $\sim$2000 hours[52]. The slow initial ageing response in all the alloys indicates that the early stages of ageing are dominated by the formation of GP1 or GPB zones and the nucleation of θ" or S" precipitates does not occur until the later stages. The ageing response is markedly improved at 160 deg.C as shown in figure 4.81 where peak hardness in the 4%Cu and 5%Cu alloys is achieved after 18 hours. The ageing time below 4%Cu increases with decreasing copper content, a similar trend has also been reported by Hardy[52]. At 180 deg.C figure 4.82 shows that the peak is attained after $\sim$8 hours for all the alloys, whilst overageing results in a 20% decrease in hardness after 200 hours, which in the binary system and the 2014 alloy is associated with the continuing transformation of θ" to θ' and the growth of θ'.[45,65]

It is evident from figures 4.80 to 4.82 that the ageing response and thus peak strength decreases with Cu content as the precipitation hardening effects are reduced by a reduction in the number of ageing precipitates present. However the above trends indicate that the hardening response does not dramatically change with copper content

although as discussed in section 1.3.1. a change in the nature of the ageing precipitates may occur with a change in the Cu:Mg ratio.

4.4.4. TENSILE TESTS

The ageing characteristics in section 4.4.3. clearly show that the peak hardness decreases with Cu content as the precipitation hardening is reduced. The tensile test programme has therefore been concentrated on the commercial 4%Cu 2014 alloy to establish the effect of extrusion conditions on the T1, T6 and T5 temper properties. The direct, indirect and presolution soak extrudes have been tested. Rapid ageing at room temperature prevents the F temper from being considered although the tensile properties in this condition have no real practical use.

The tensile specimens have all been machined from sections of the extrude in the steady state region corresponding to 0.3L to 0.5L which showed no signs of surface cracking. The presence of even the finest cracks can be deleterious to the tensile properties. The tests were conducted at a strain rate of 5.2×10^{-3} sec^{-1} at room temperature, as described in section 3.6.2. A full listing of the results may be found in appendix III.

4.4.5. STRESS STRAIN CHARACTERISTICS 2014

Examples of the stress strain curves from high Z and low Z extrudes in the T1 and T6 tempers are shown in figures 4.83 and 4.84. In the T1 temper figure 4.83 shows that at both extrusion temperatures the stress increases linearly with strain up to the yield point, followed by an extended plastic region in which the stress increases to a maximum value where necking commences and the stress decreases until failure at $\sim$ 22-24% strain. The curves exhibited no

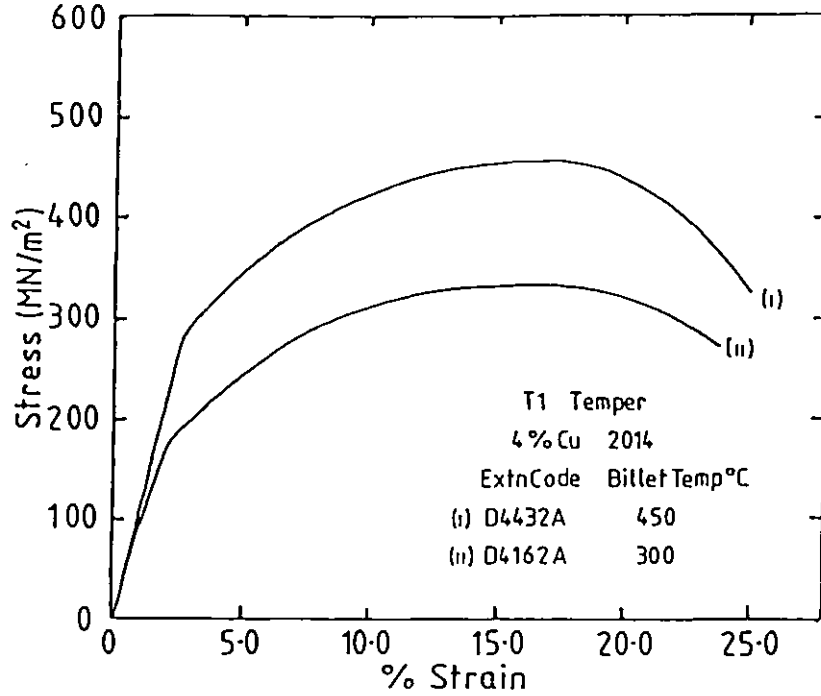
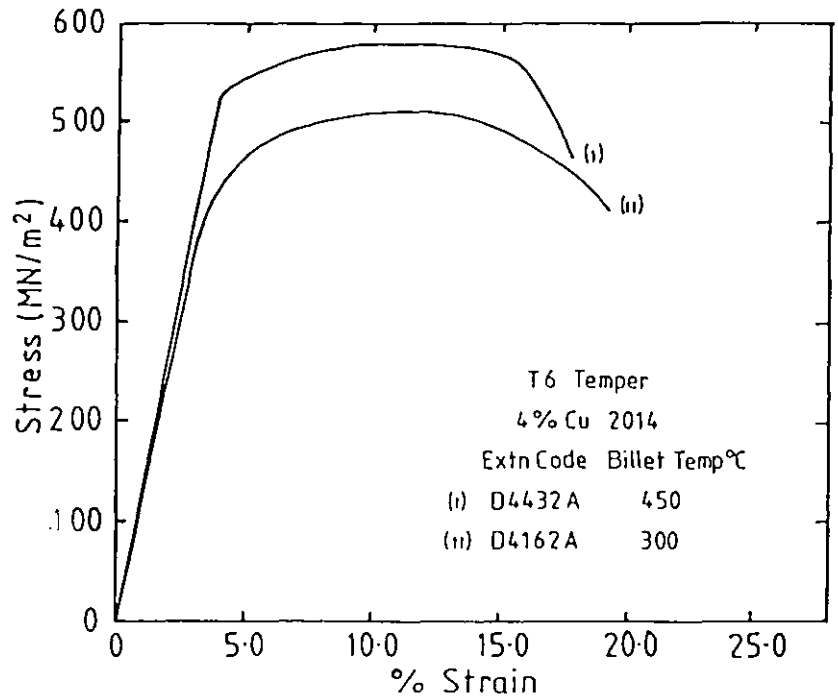


Figure 4.83 Stress strain curves - 2014 alloy T1 temper

Figure 4.84 Stress strain curves - 2014 alloy T6 temper



reduction in stress at the yield point or any signs of serrated yielding, the stress increasing in a more or less continuous manner. It is evident from the curves that the proof stress (P.S.) and ultimate tensile stress (U.T.S.) are higher in the low Z extrude ie high extrusion temperature, which is consistent with the hardness results for the 1%Cu and 5%Cu alloys in section 4.4.2.

The T6 temper extrudes in figure 4.86 show a marked increase in the P.S. and U.T.S. at both extrusion temperatures with a corresponding reduction in ductility. The low Z extrudes again show a higher P.S. and U.T.S. which is also accompanied by a reduction in the strain hardening exponent 'n' as shown in table 4.34. The effect of extrusion condition on the tensile properties will be discussed in more detail in the following sections. The T5 temper extrudes tested at low Z showed the same characteristics as the low Z T6 extrudes.

4.4.6. TENSILE PROPERTIES OF THE 2014 ALLOY

4.4.6.1. T1 TEMPER

For the T1 temper the press quenched extrudes have been aged at room temperature for three months to allow the maximum increase in strength to be achieved. Although previous workers have shown that the initial ageing characteristics are so rapid that approximately 80% of the peak strength is obtained after only one day in the solution treated 2014 alloy[57].

The effects of extrusion condition on the T1 tensile properties of the conventionally heated (C H) direct extrudes are shown plotted in figure 4.85 for reduction ratios of 20:1, 30:1 and 50:1. The extrusion conditions have been plotted as a function Ln Z_I since as shown in

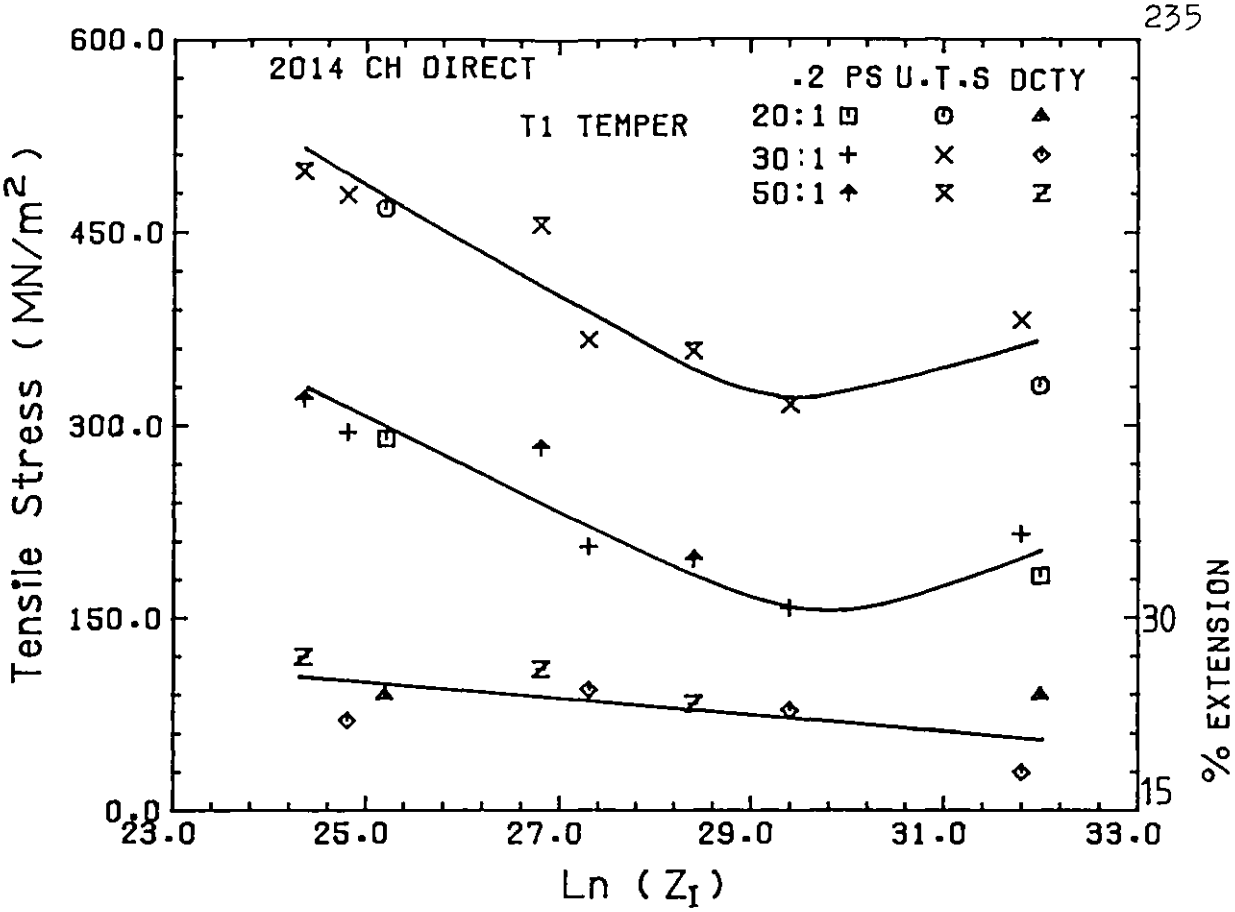


Figure 4.85 Tensile properties vs LnZ_I - T1 temper - CH direct extrusion of 2014 alloy

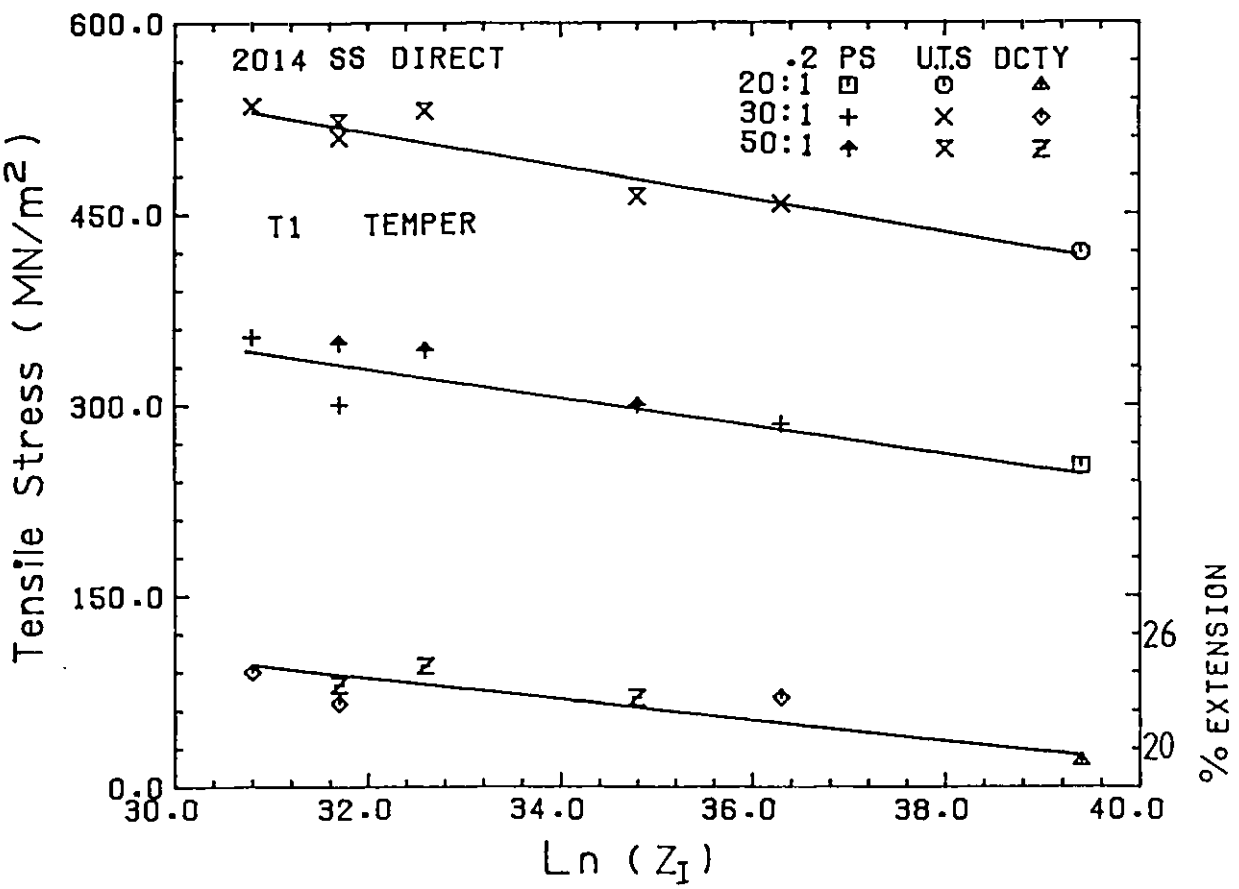


Figure 4.86 Tensile properties vs LnZ_I - T1 temper - SS direct extrusion of 2014 alloy

section 4.3.5., this parameter can be directly related to the microstructure of the extrudes and also allows for the variation in ramspeed and temperature at different extrusion ratios. The results show that the proof stress (P.S.) and ultimate tensile stress (U.T.S.) decrease at low extrusion temperatures for Ln $Z_I > 29$, whilst above this value both increase with decreasing Ln Z_I. The decrease at high Ln Z_I is consistent with the hardness results in section 4.4.2. and indicates that for these extrusion conditions the subgrain structure is the dominant strengthening mechanism, the substructure strengthening increasing with decreasing subgrain size according to the modified Hall Petch equation shown in section 1.5, increasing the extrusion temperature above 350 deg.C ie Ln $Z_I < 29$ increases the solid solubility of Cu and Mg in Al and hence the solute retained in solution after quenching, so that the P.S. and U.T.S. increase with the natural ageing and solute strengthening as indicated by the hardness results in section 4.4.2.

The effect of extrusion condition on the T1 tensile properties therefore depends on whether the extrudes are a function of the substructure strengthening at $LnZ_I > 29$ or the amount of solute in solution below this value. At high Z conditions the maximum increase in strength will be limited by the press capacity, whilst in the low Z region the increase is limited by the requirements of an adequate surface which in the present work has been associated with the onset of surface cracking. However the increase in strength shown in figure 4.85 indicates that natural ageing is a more effective strengthening mechanism and therefore extruding at the lowest Z conditions or highest temperatures will result in the highest T1 temper strength for press quenched extrudes. It should of course be noted here that the overall strength at low Z_I will still be a function of the substructure strengthening. This is shown by the values

of P.S. and U.T.S. at $Ln Z_I < 25$ which are higher than the T4 temper strength reported[32,33,35], for AA2014 shown in table 4.35, the condition which corresponds to the maximum increase in strength due to natural ageing after solution treating and quenching. Therefore control of the subgrain structure is still an important consideration even though the solute in solution is the principal source of strengthening.

Temper	P.S. MN/m^2	U.T.S. MN/m^2	% Elongation
TO	97	185	18
T4	290	425	20
T6	415	485	13

Table 4.35 Reported tensile properties of 2014 alloy from ref. 32, 33 and 35.

In section 4.2.10.1. it was shown that by solution soaking the billets at 500 deg.C for 2 hours and furnace cooling to the extrusion temperature, the flow stress and hence extrusion pressure were assumed to increase due to the increase in solute in solution. The effect of this solution treatment on the T1 temper tensile properties is shown in figure 4.86 for extrusion ratios of 20:1, 30:1 and 50:1. It is evident that the P.S. and U.T.S. now decrease with increasing Ln Z_I for all the extrusion conditions considered, there being no signs of an increase in strength at low extrusion temperatures. The P.S. and U.T.S. are higher than the CH extrudes at all extrusion temperatures which indicates that the solution treatment does indeed increase the solute in solution before extrusion even at an extrusion temperature of 300 deg.C. In fact the increase in P.S. over the CH extrudes decreases with extrusion

temperature from ~40% at 300 deg.C to 9% at 475 deg.C, which shows that in terms of the T1 strength the solution soak treatment is more beneficial to the low temperature extrudes since conventional heating does not take any solute into solution.

Both the CH and SS extrudes show a slight increase in ductility with decreasing Ln Z_I which is somewhat surprising since this also corresponds to the greatest increase in P.S. and U.T.S. This is probably due to a combination of natural ageing which is reported[33] to increase the ductility and the more perfectly recovered substructures associated with the high temperature extrudes.

The results in figures 4.85 and 4.86 indicate that in the T1 temper the extrusion conditions chosen should aim to maximise the effects of natural ageing and substructure strengthening either by extruding at high temperatures and ram speeds or at low temperatures by solution soaking and cooling as rapidly as possible to decrease the subgrain size and increase the solute in solution. However it was shown in section 4.3.4. that peripheral recrystallization also increases with decreasing Ln Z_I so that for high strength T1 extrudes some peripheral recrystallization must be tolerated.

4.4.6.2. T6 TEMPER

The T6 temper is perhaps the most commonly used heat treatment for the 2000 series alloys and has therefore been investigated in the direct, indirect and the presolution soak direct extrudes. The extrudes have been solution treated at 500 deg.C for 30 minutes and water quenched, followed by ageing at 160 deg.C for 18 hours. The tensile results are plotted in figures 4.87 to 4.89, as a function of LnZ_I for extrusion ratios of 20:1 and 30:1.

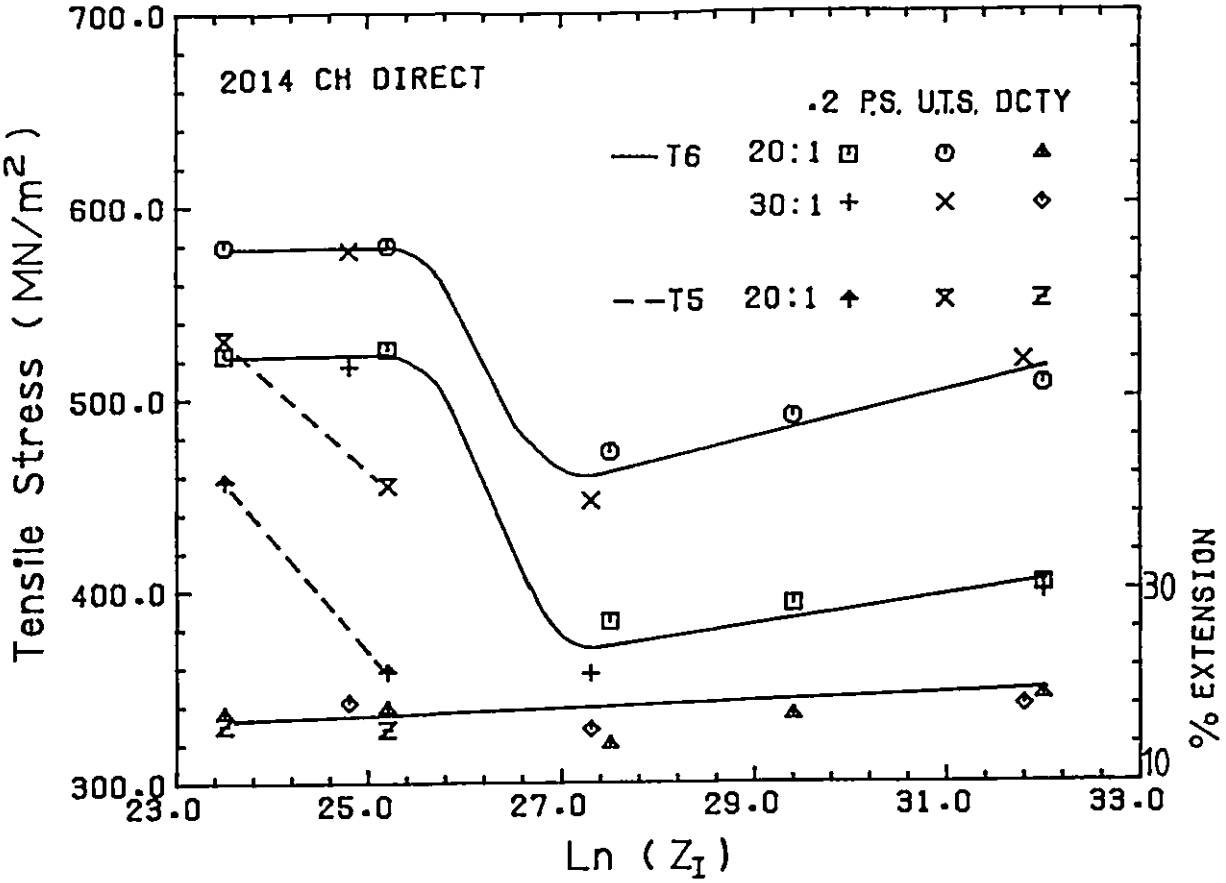


Figure 4.87 Tensile properties vs LnZ_I - T6 and T5 temper-CH direct extrusion of 2014 alloy

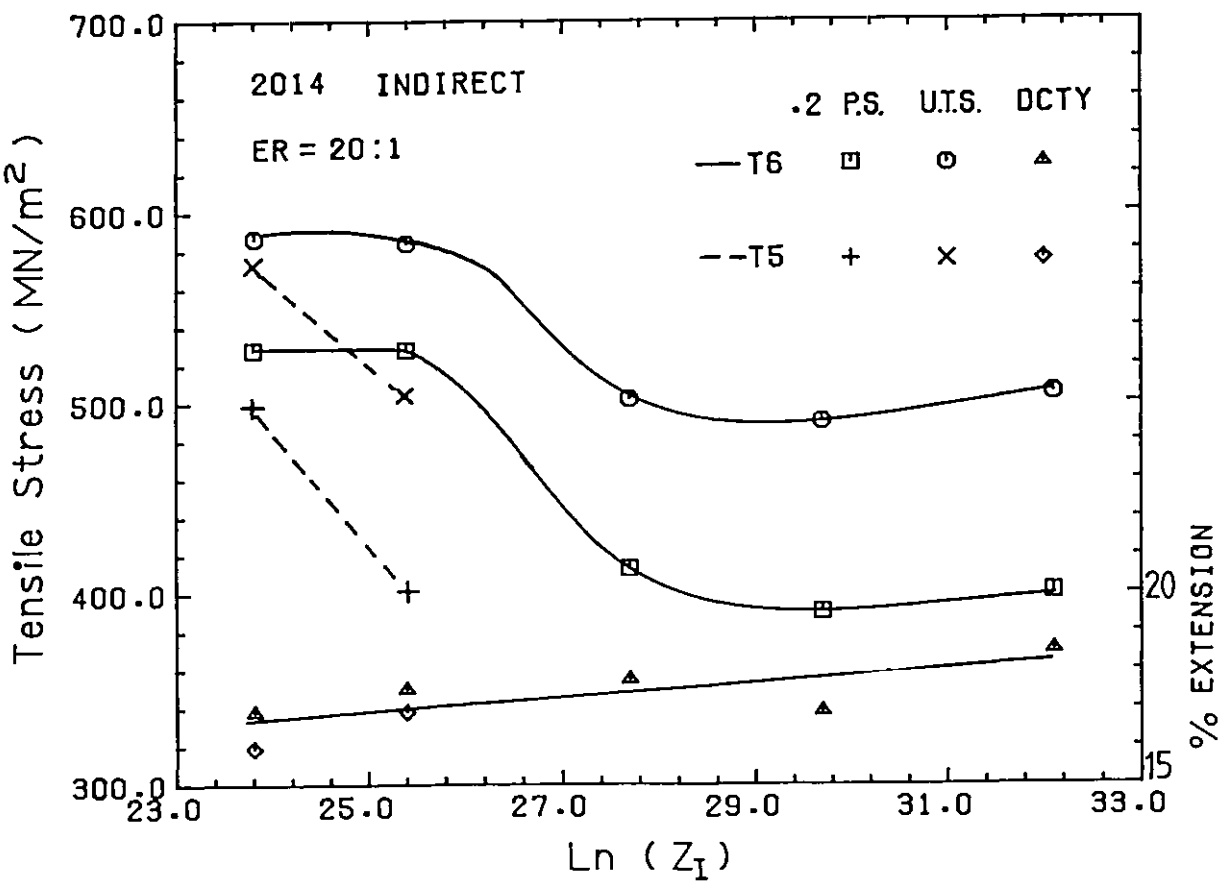


Figure 4.88 Tensile properties vs LnZ_I - T6 and T5 temper-CH indirect extrusion of 2014 alloy

The increase in P.S. and U.T.S. shown by the stress strain curves in section 4.4.5. is clearly not the result of a gradual increase with decreasing extrusion temperature, but increases suddenly below a specific value of LnZ_I for all three extrusions considered. The high strength or low Z regions correspond to the unrecrystallized substructures shown in section 4.3.7., whilst the low strength extrudes can be associated with the fully recrystallized grain structures shown in plate XIII. The question arises as to whether the increase in strength is solely due to substructure strengthening or an increase in precipitation hardening as a result of the preferential precipitation at the subgrain boundaries shown in plate XIV. Recent work[135] has shown that for the 2014 alloy, high and low temperature extrudes exhibiting a retained substructure and a fully recrystallised grain structure have identical ageing characteristics, indicating that although preferential precipitation does occur it has little effect on the attainment of peak strength due to precipitation hardening. This is perhaps to be expected since from the evidence in plates XIV and XV the amount of heterogeneous precipitation at the subgrain boundaries or helical dislocations is still not as great as the homogeneous precipitation within the subgrains. If the increase in the strength can be directly related to substructure strengthening one might expect the P.S. to increase with LnZ_I as the subgrain size decreases. Figures 4.87 to 4.89 do indeed show a slight increase with LnZ_I in the high strength region.

An estimate of the increase in strength due to substructure strengthening can be obtained by comparing the T1 temper strength at high Z_I in figure 4.85 with the reported T0 temper strength in table 4.35 since neither condition is affected by age hardening. The incremental increase in P.S. of 100 MN/m^2 is similar to that shown by

the T6 extrudes at low Z_I, which indicates that substructure strengthening is still effective even after solution treating and ageing. Therefore in the T6 temper the maximum tensile properties can be obtained by extruding in the low Z_I region, although as in the T1 temper, some peripheral recrystallization must be tolerated unless the extrusion conditions are chosen such that $LnZ_I < 22$ corresponding to an initial flow stress of 30 MN/m^2, the recrystallized depth increasing with LnZ_I above this value according to the equations shown in table 4.30.

The highest P.S. and U.T.S. in the low Z_I regions are shown by the indirect extrudes which can be associated with the smaller temperature rise and hence smaller subgrains exhibited by the indirect extrudes at equivalent values of LnZ_I.

The tensile properties of all three extrudes in the low strength region are close to those of the T6 temper shown in table 4.35. However, it is evident that both the P.S. and U.T.S. are still a function of the extrusion condition especially the CH direct extrudes in figure 4.87. Referring back to section 4.3.7.1. it was shown in figure 4.74 to 4.76. that the recrystallized grain size decreased with decreasing extrusion temperature i.e. increasing LnZ_I, the greatest increase occurring in the CH direct extrudes. The variation in P.S. and U.T.S. at high LnZ_I is therefore now related to grain boundary strengthening which increases with decreasing grain size (D) according to the standard Hall-Petch equation. The results of using this equation are shown below for all the extrusion data at high LnZ_I in figures 4.87 to 4.89.

$$\sigma_{.P.S.} = 337.5 + 0.86\ D^{-1/2} \qquad cc\ 0.975 \qquad 4.28.$$

The values of stress = 337.5 MN/m^2 is normally referred

to as the friction stress since it represents the stress required to move dislocations in a single crystal of the same composition, the value of 0.86 is a measure of the effectiveness with which the grain boundaries increase the yield stress. However the absolute values can only be considered to be approximate due to the small proof stress and grain size range considered.

It is evident from the results in figures 4.87 to 4.89. that in the fully recrystallized extrudes, extruding at highest Z_I conditions i.e. lowest temperatures and highest strain rates will result in the maximum tensile properties. Therefore for a given press capacity the indirect mode of extrusion should enable the highest T6 tensile strength extrudes to be processed in the high Z_I region.

The ductility of all the T6 extrudes are lower than in the T1 temper, although the ductility shows only a slight increase with LnZ_I, indicating that failure during tensile testing is more a function of the precipitate hardening and particle distribution than the microstructure of the extrudate.

It is interesting to note in figure 4.88. at LnZ_I = 27.6, corresponding to an initial billet temperature of 400 deg.C, the presence of only a partially retained substructure in the centre of the indirect extrude results in approximately a 10% increase in tensile strength over the fully recrystallised extrude.

The results in figure 4.89 show that the presolution soak treatment has little effect on the T6 tensile properties in the high Z region, but clearly extends the low Z_I by reducing static recrystallization during the solution treatment as shown in section 4.3.7.1.

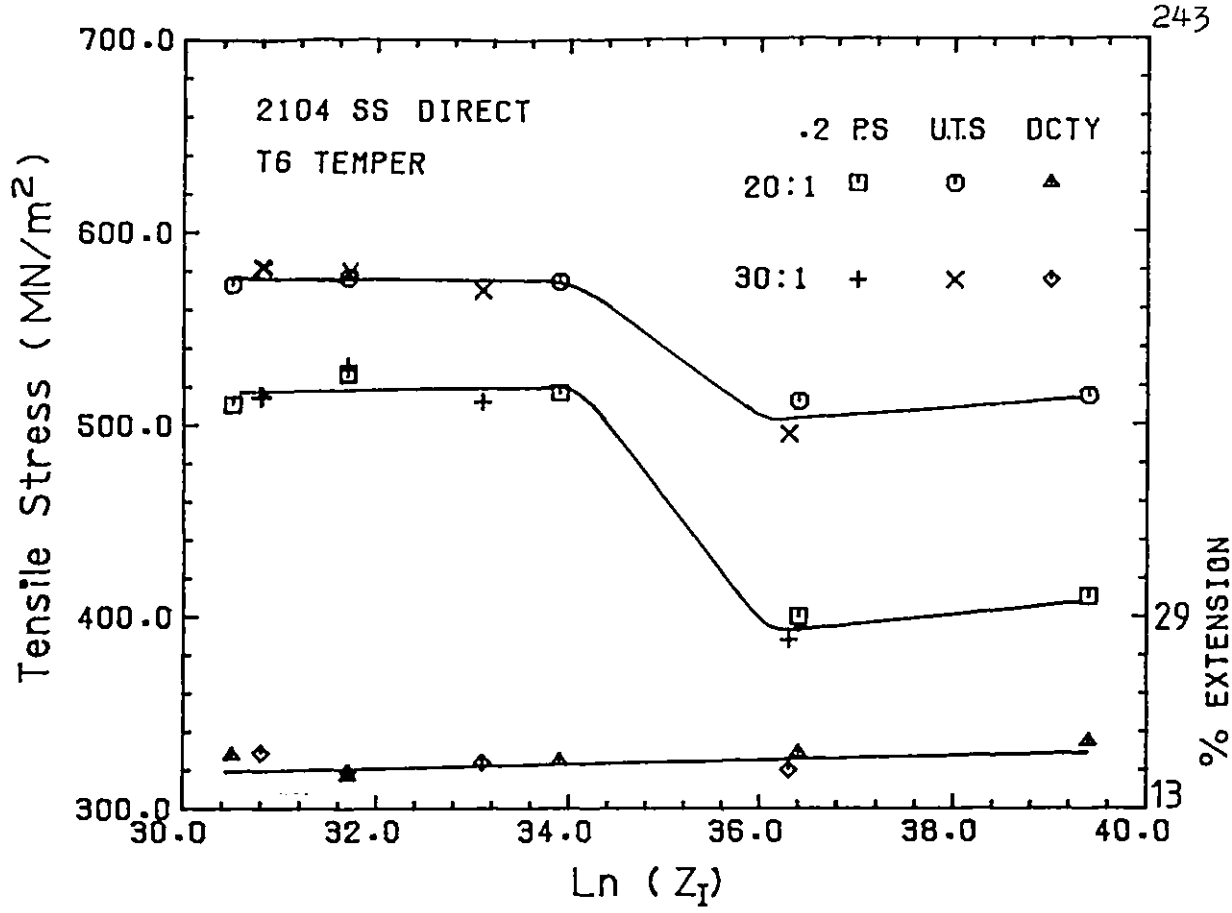


Figure 4.89 Tensile properties vs LnZ_I – T6 temper – SS direct extrusion of 2014 alloy

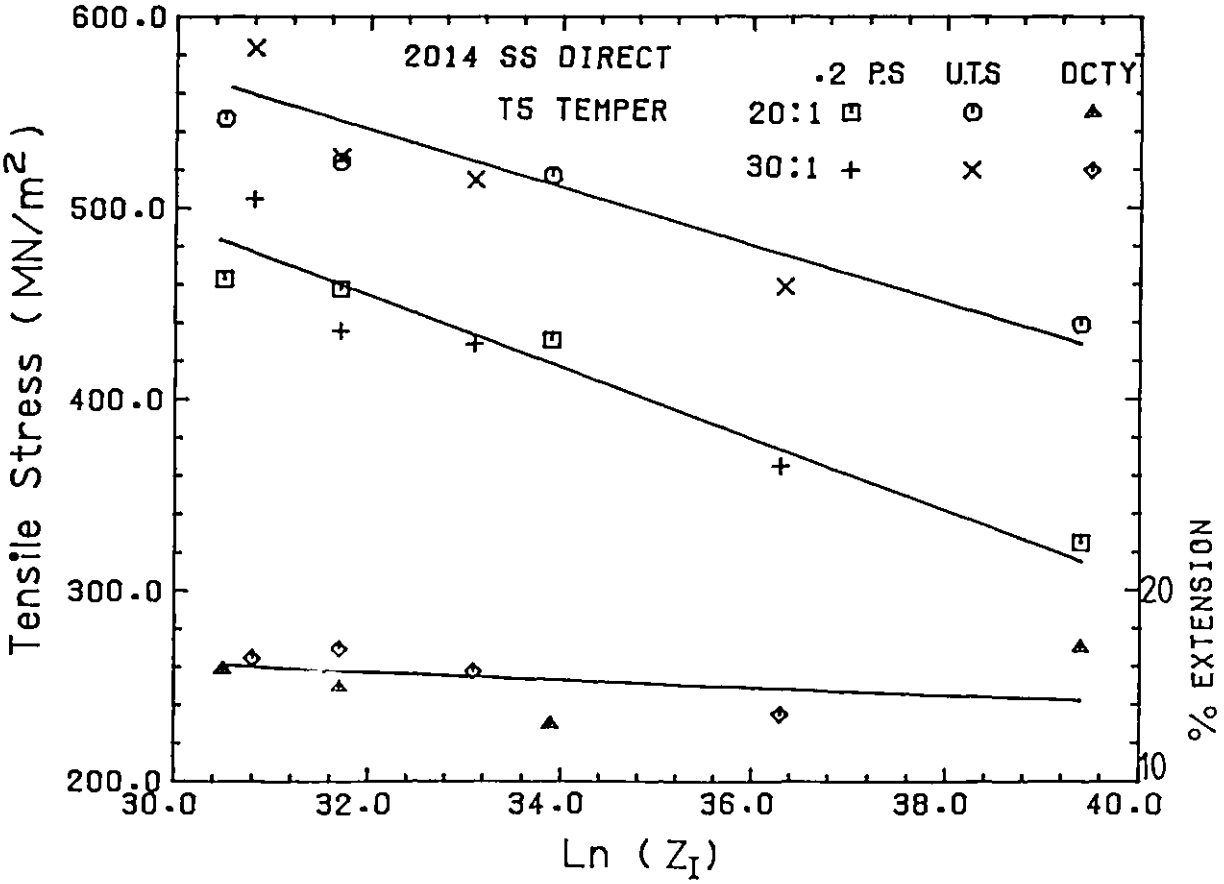


Figure 4.94 Tensile properties vs LnZ_I – T5 temper – SS direct extrusion of 2014 alloy

In conclusion the above results show that even in the solution treated and aged condition the tensile properties are still dependent on the extrusion condition, whether the extrudes are partially or fully recystallized. For either structure the indirect extrudes are likely to show the maximum tensile strength due to the increase in substructure strengthening and decrease in peripheral recrystallization at low Z_I, which may be further reduced by presolution soaking, whilst the ability to extrude at the highest Z_I conditions shown in section 4.2.6. decreases the grain size and so increases the grain boundary strengthening.

4.4.6.3. T5 TEMPER

The alternative to a full solution soak and ageing treatment is to use the billet preheat cycle as the solution treatment, the press quenched extrudes being aged immediately after extrusion. In the present work a billet presoak time of 20 minutes enables a large proportion of the hardening elements Cu and Mg to be taken into solution prior to extrusion as shown by the hardness and tensile results in the T1 temper in the previous sections. The presolution soak treatment can be expected to increase the ageing response at all extrusion temperatures if as indicated by the T1 properties, the solid solution content is increased prior to extrusion. Removing a separate heat treatment stage has an obvious economic advantage, where ageing in the presence of the as-quenched substructure may also improve the mechanical properties due to the preferential precipitation and the absence of subgrain growth noted in section 4.3.7.2.

The T5 ageing characteristics for the CH and SS extrudes extruded at 475 deg.C, 400 deg.C and 350 deg.C are shown in figures 4.90 to 4.93. The extrudes were aged immediately after extrusion at temperatures of 160 deg.C and

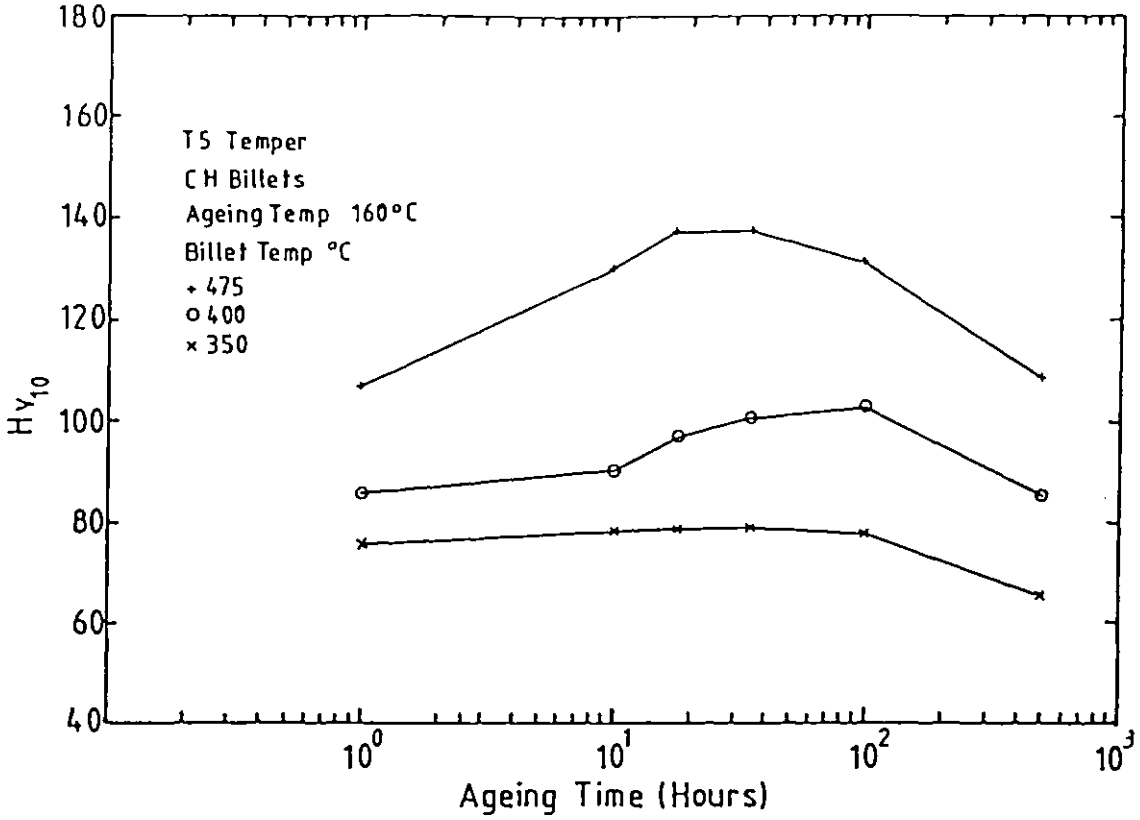
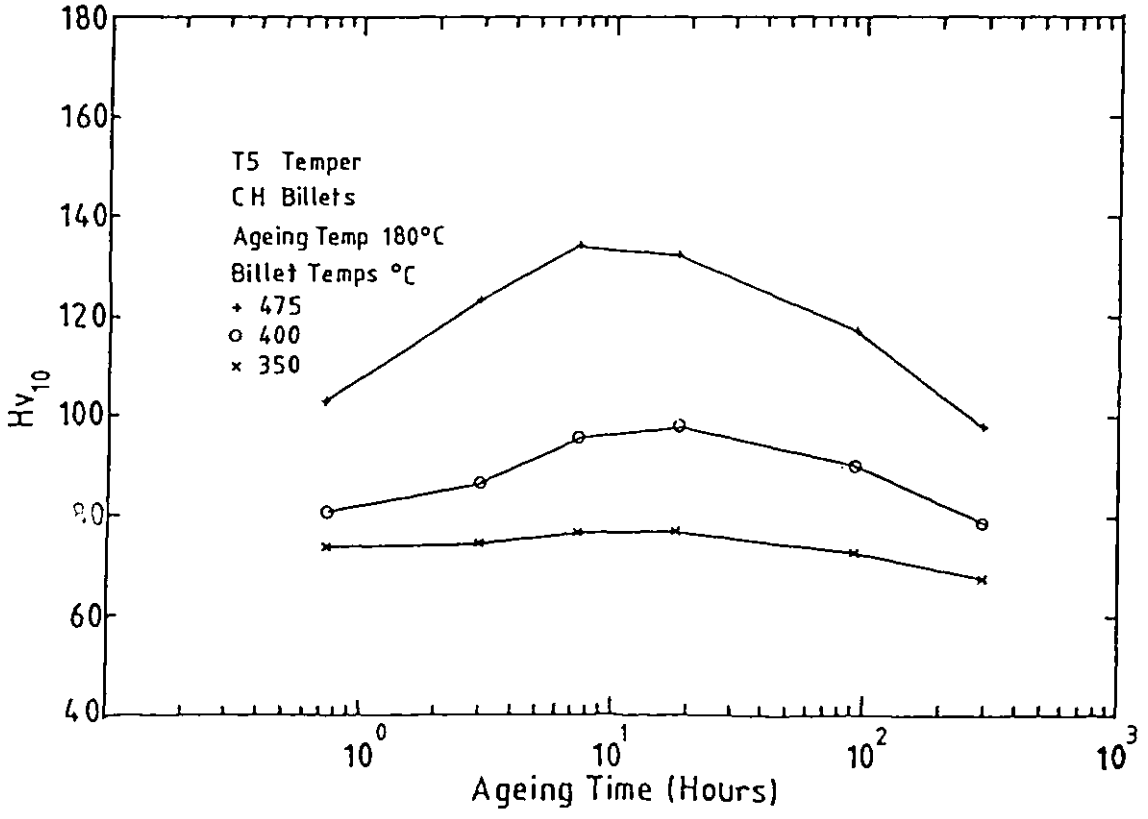


Figure 4.90 Ageing characteristics at 160°C-press quenched CH direct 2014 extrudes

Figure 4.91 Ageing characteristics at 180°C-press quenched CH direct 2014 alloy



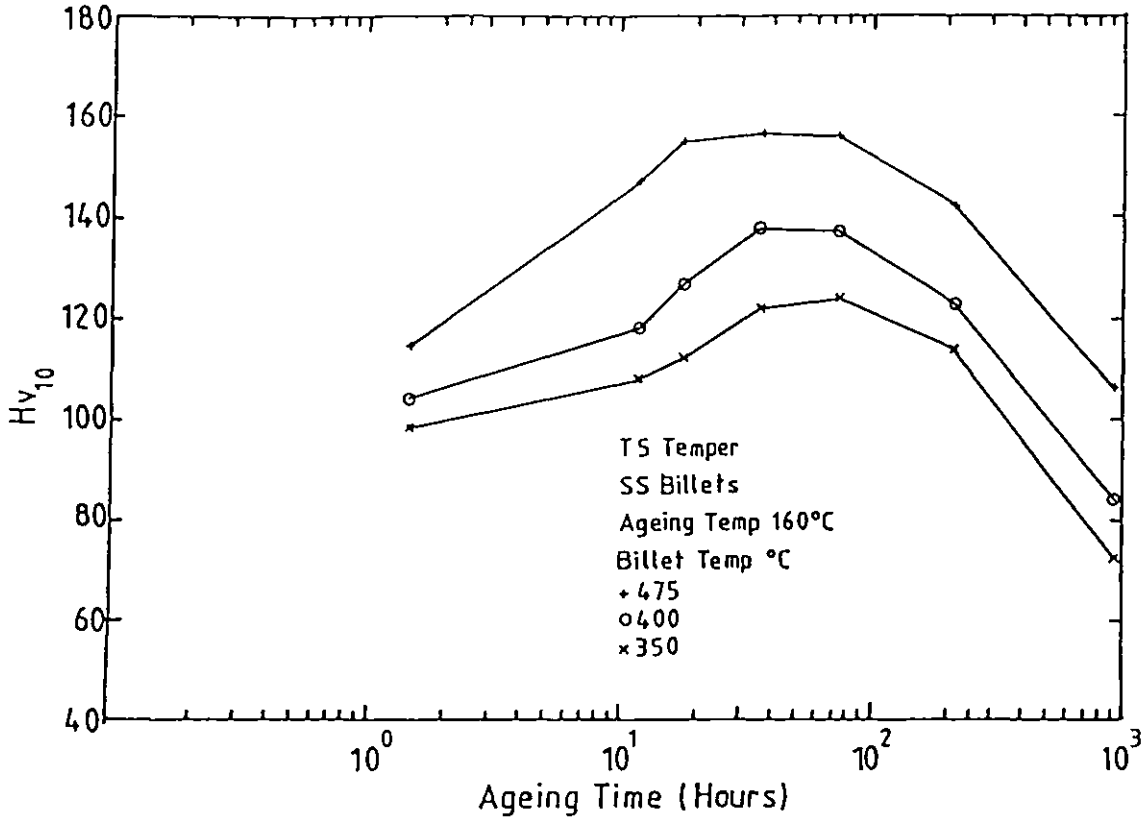
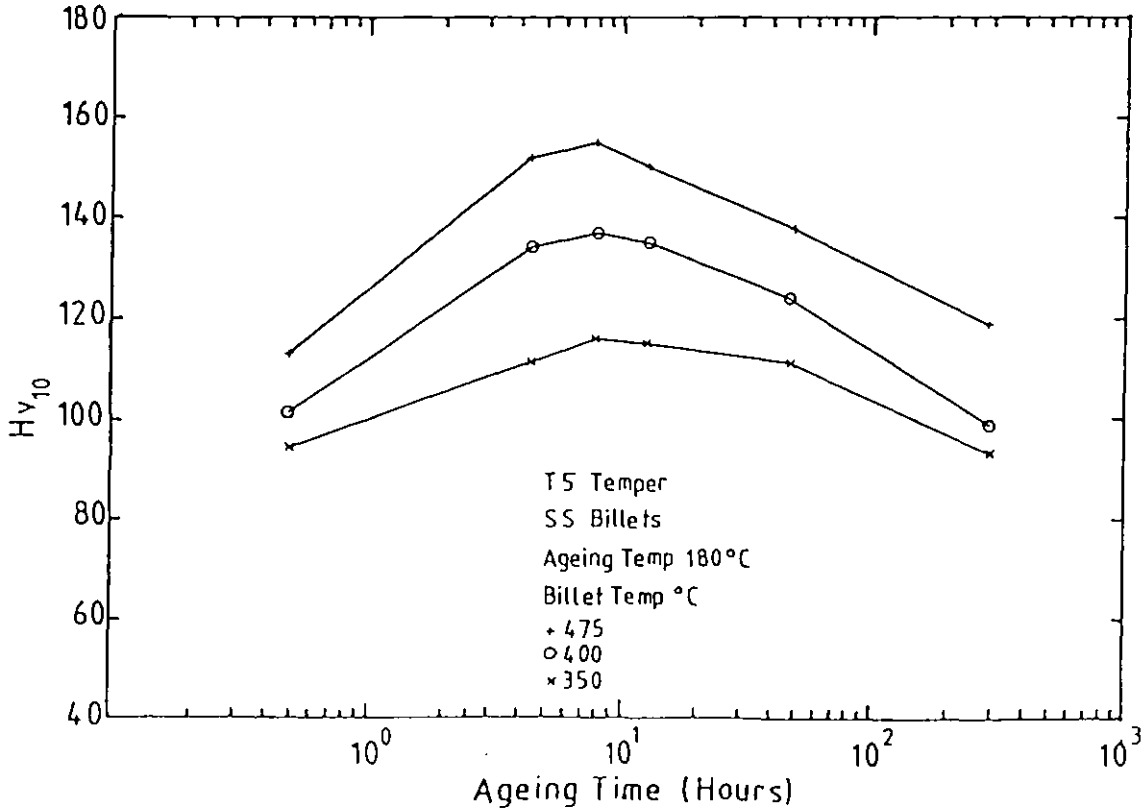


Figure 4.92 Ageing characteristics at-160°C press quenched SS direct 2014 extrudes

Figure 4.93 Ageing characteristics at-180°C press quenched SS direct 2014 extrudes



180 deg.C, the hardness results are listed in appendix III.

Figures 4.90. and 4.91. show that for the conventionally heated extrudes ageing at the highest extrusion temperature of 475 deg.C results in similar ageing characteristics to those of the T6 extrudes in figures 4.81. and 4.82. although the peak hardness is ~13% lower at both ageing temperatures. Below this temperature the ageing response and thus peak hardness decreases whilst the peak ageing time increases. A similar trend can be seen with decreasing Cu content in the T6 temper in figures 4.81. and 4.82. The ageing characteristics therefore indicate that the presence of the hot worked substructure even at the highest extrusion temperature, cannot compensate for the decrease in age hardening due to the reduction in the solid solution content, which decreases with extrusion temperature as the solid solubility of copper and magnesium in aluminium decreases.

The ageing characteristics of the SS extrudes are shown in figures 4.92. and 4.93. It is evident that the ageing response at all the extrusion temperatures is far more pronounced where a peak hardness at 475 deg.C of 156 is close to the peak of 157 in the T6 extrudes. The overall trend of decreasing hardness and increasing ageing time with decreasing billet temperature is the same as in the CH extrudes, although the peak hardness values are greater at all the extrusion temperatures considered, the difference increasing with decreasing temperature, similar to the T1 extrudes in section 4.4.6.1. Therefore as suggested in section 4.3.7.2. the T5 heat treatment is more beneficial to the SS extrudes due to the increase in solid solution content and hence ageing.

Using the ageing characteristics shown in figures 4.90 and 4.92. tensile specimens were machined from the CH peak

aged direct and indirect extrudes at extrusion temperatures of 475 deg.C and 450 deg.C. Peak aged extrudes from the SS matrix were tested at all extrusion temperatures. For comparison the tensile data for the CH direct and indirect extrudes are shown plotted with the T6 results in figures 4.87 and 4.88. The SS T5 results are shown separately in figure 4.94.

At an extrusion temperature of 475 deg.C the CH direct extrudes in figure 4.87. show a decrease in P.S. of $\sim$12% from the T6 result as predicted by the ageing characteristics in figure 4.90. However both the P.S. and U.T.S. are higher than those of the fully recrystallized extrudes at Ln $Z_I > 27$ equal to an extrusion temperature of 400 deg.C, and confirms the suggestion made in section 4.3.7.2. that a decrease in the precipitation hardening may be compensated for by the increase in strength derived from the subtructure. The indirect extrude at 475 deg.C shows only a 5% decrease in P.S. which again indicates the greater degree of strengthening associated with the indirect substructure. A similar increase in the T5 hardness for indirect extrudes has been reported by Paterson[29], which indicates that the T5 treatment may be more beneficial to the indirect extrudes. Both modes of extrusion show a large decrease in the P.S. and U.T.S. at an extrusion temperature of 450 deg.C although the tensile properties are still equivalent to the lowest T6 strength, and higher than the T1 strength at an initial billet temperature of 475 deg.C. Therefore if an adequate surface finish cannot be obtained at high extrusion temperatures, a press quenching and ageing treatment at Ln $Z_I < 29$ can produce extrudes with tensile properties equivalent to or greater than the high temperature T1 extrudes and low temperature T6 extrudes.

The tensile properties of the T5 presolution soak extrudes in figure 4.94. show that the P.S. and U.T.S.

decrease in a more or less linear fashion with Ln Z_I, as the age hardening decreases and the substructure strengthening increases. The P.S. and U.T.S. are higher than the in T1 extrudes in figure 4.86. for all the extrusion conditions considered where at 475 deg.C the P.S. is 6% higher than the C.H. T5 direct extrudes, but similar to the indirect extrudes. Below Ln Z_I = 35the tensile strength is greater than that of the fully recrystallized T6 extrudes, where at the lowest Z conditions the P.S. and U.T.S. are only 3-4% lower indicating that at the highest extrusion temperatures a solution treatment after extrusion may no longer be necessary if a small reduction in the tensile strength can be tolerated.

In conclusion the T5 tensile strength of the three extrusions considered cannot quite match the equivalent T6 extrudes at low Z_I conditions due to the greater degree of age hardening and substructure strengthening associated with these extrudes. However at the low Z_I conditions below the specific values mentioned the T5 strength is greater than the fully recrystallized T6 extrudes at high Z_I and the naturally aged T1 extrudes at the lowest Z_I conditions. As for the T1 and T6 temper the variation in peripheral recrystallization with extrusion conditions shown in the as extruded material in section 4.3.4. must also be considered when choosing the optimum process conditions, since for all three extrudes the increase in T5 strength is accompanied by an increase in the recrystallized depth, although it should be noted this did not increase during the ageing treatment.

4.4.7. THE EFFECT OF Cu CONTENT ON THE TENSILE PROPERTIES

The effect of copper content on the T1 and T6 tensile properties has been investigated using high Z and low Z extrudes. Tensile specimens were machined from extrudes extruded at 300 deg.C and 450 deg.C at an extrusion ratio of

30:1. The T1 temper coincides with ageing the press quenched extrudes for 3 months at room temperature, whilst the T6 temper extrudes were solution treated at 500 deg.C for 30 minutes and aged to peak strength at 160 deg.C, using the ageing characteristics shown in figure 4.81.

In the T1 temper figure 4.95 shows that for an extrusion temperature of 300 deg.C the P.S. and U.T.S. increase in a more or less linear fashion with Cu content, whilst the ductility decreases. The increase in strength will be a function of the decrease in subgrain size with Cu content shown in section 4.3.5. and an increase in the precipitation hardening associated with the θ precipitates in the original homogenized material. At an extrusion temperature of 450 deg.C figure 4.96. shows a marked increase in the P.S. and U.T.S. due to solute strengthening and natural ageing. The percentage increases in P.S. shown in table 4.36. indicate that solute strengthening and natural ageing are not substantially increased for Cu contents greater than 2%Cu. This coincides with the reported[123] values for the maximum solid solubility of Cu and Mg in Al at 450 deg.C of 2.4 wt %Cu and 1.1 wt % Mg. As for the 2014 results in section 4.4.6.1. there is no appreciable decrease in ductility at 450 deg.C, the ductility decreasing with Cu content.

	Wt % Cu				
Temper	1	2	3	4	5
T1	20	55	58	63	61
T6	58	48	41	32	28

Table 4.36 Percentage increase in P.S. from the high Z to low Z extrudes.

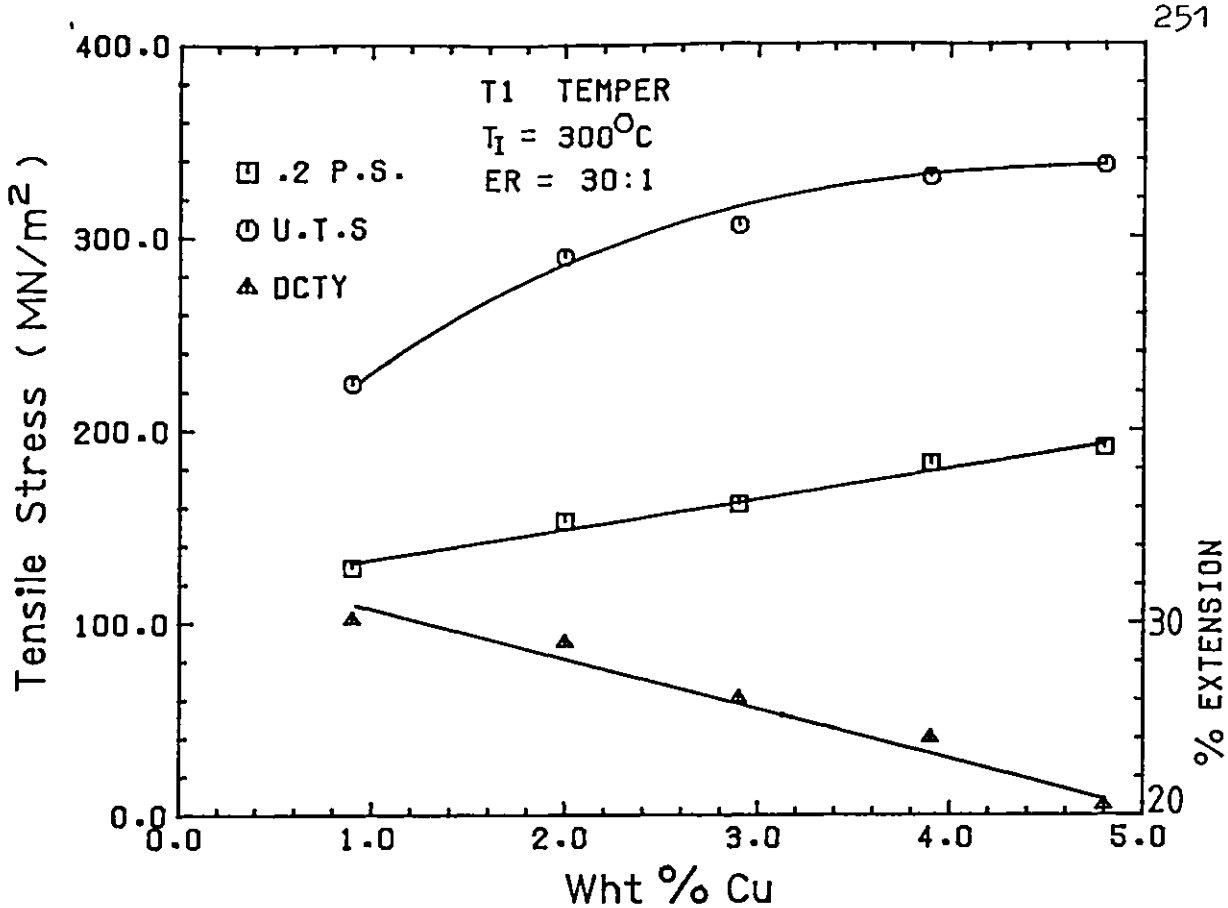


Figure 4.95 Tensile properties vs wt % Cu - T1 temper- T_I = 300°C ER = 30:1

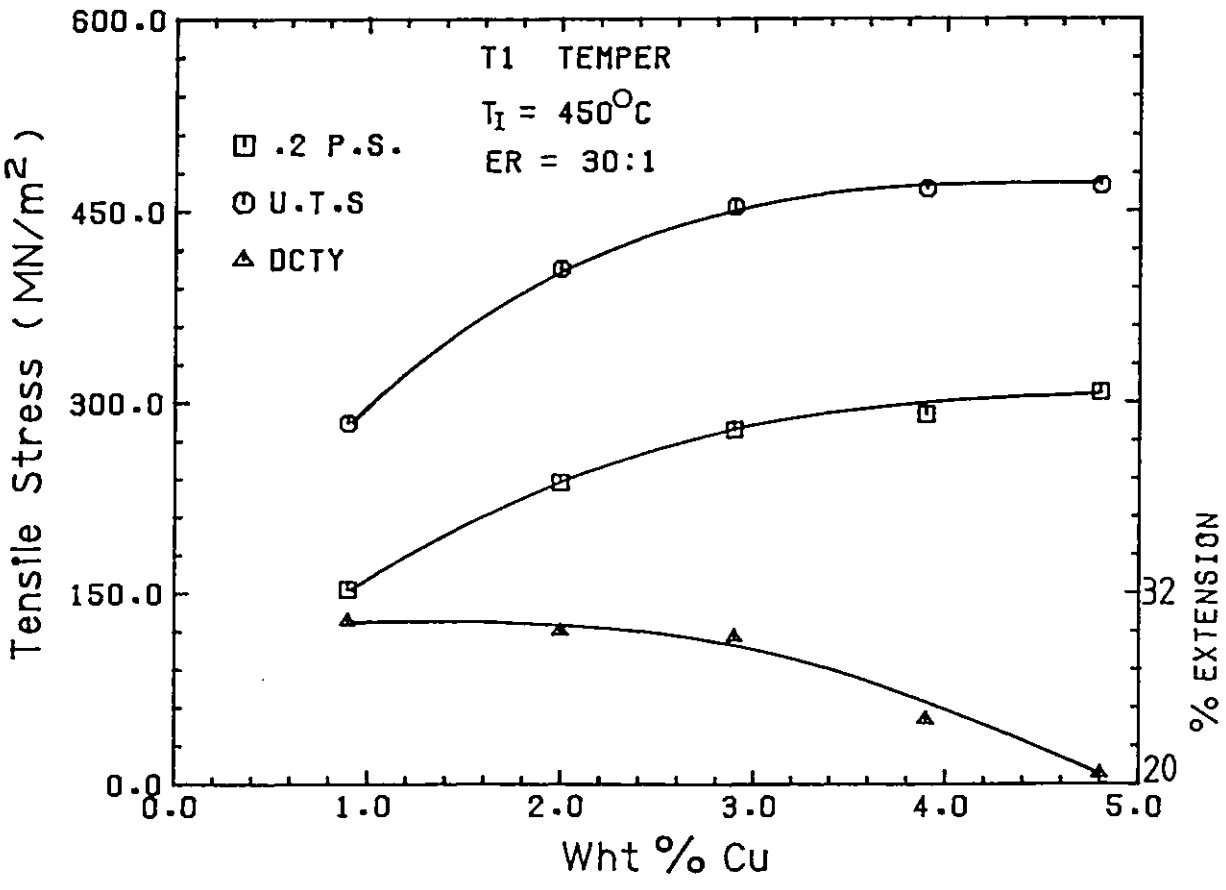


Figure 4.96 Tensile properties vs wt % Cu - T1 temper- T_I = 450°C ER = 30:1

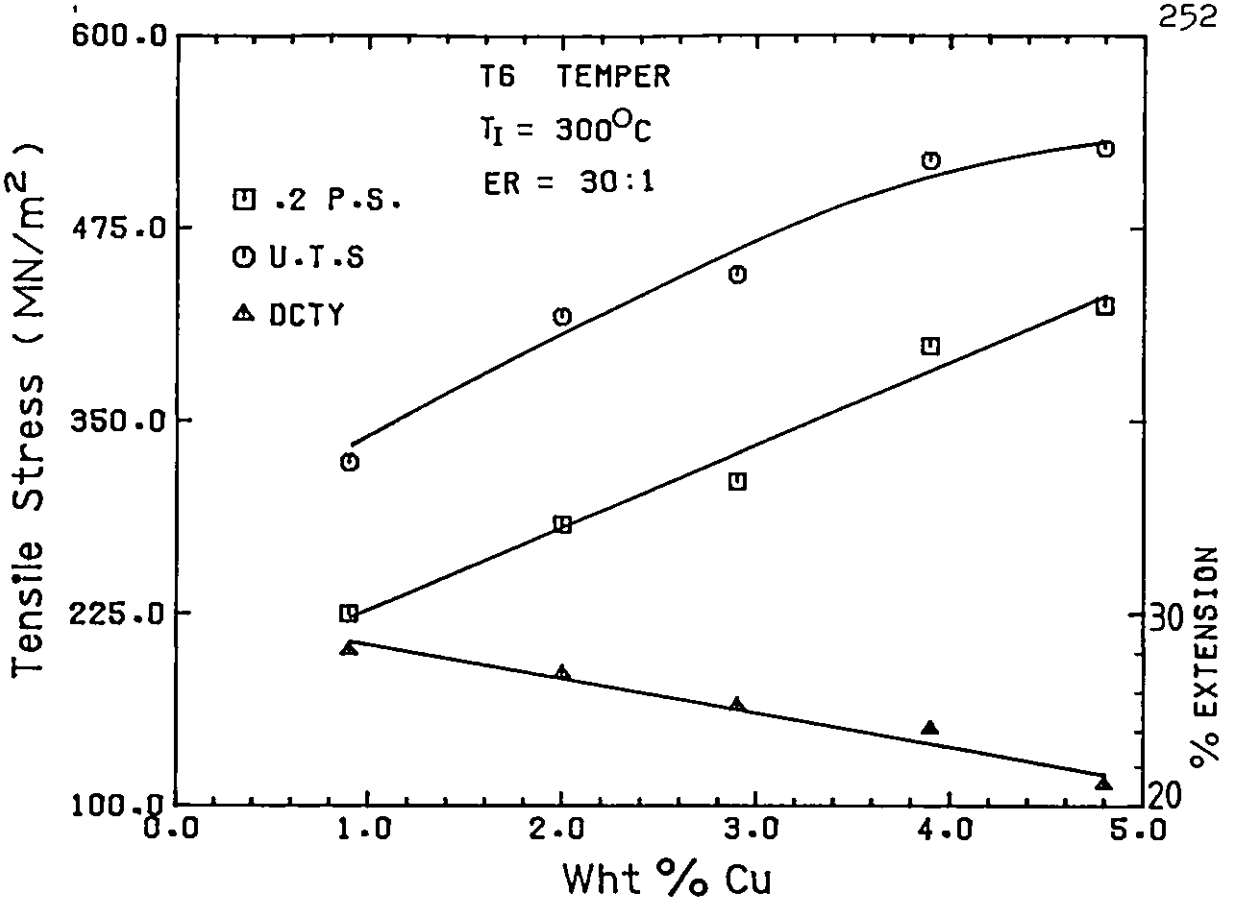


Figure 4.97 Tensile properties vs wt % Cu -T6 temper- T_I = 300°C ER = 30:1

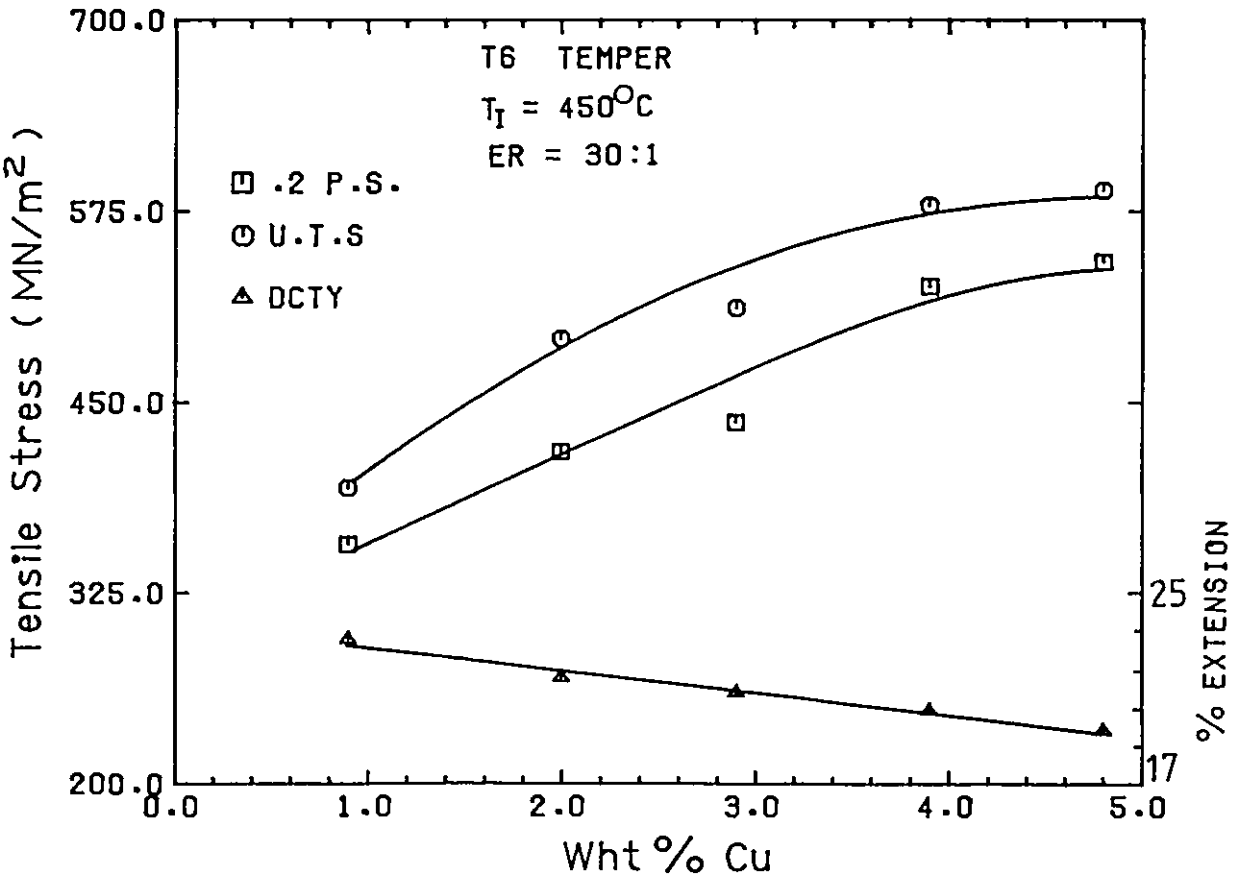


Figure 4.98 Tensile properties vs wt % Cu -T6 temper- T_I = 450°C ER = 30:1

In the T6 temper figure 4.97. shows that for the fully recrystallised extrudes extruded at 300 deg.C the P.S. and U.T.S. increase linearly with Cu content as the precipitation hardening increases, there being no significant difference found in the recrystallised grain size and hence grain boundary hardening. The low Z extrudes in figure 4.98. extruded at 450 deg.C, again show a more or less linear increase in P.S. and U.T.S. with Cu content, the ductility decreasing with Cu content. Perhaps the most interesting feature of the T6 temper are the percentage increases shown in table 4.36., for the increase in P.S. from the high Z and to low Z extrudes. The decrease in % increase with Cu content, which represents an increase in P.S. of 117 MN/m^2 in the 5% Cu alloy as opposed to 132 MN/m^2 in the 1% Cu alloy indicates that substructure strengthening after heat treating is more effective in the lower Cu alloys. It was noted in section 4.3.7.2. that subgrain growth may have occurred during solution treatment of the low Z 2014 extrudes, which effectively reduces the substructure strengthing. The decrease in peripheral recrystallization with initial flow stress and hence Cu content shown in section 4.3.7.1. indicates that subgrain growth is less likely to occur in the lower Cu alloys. Therefore in terms of the T6 temper strength of the low Z extrudes the substructure strengthing increases with decreasing Cu content, to the extent that for a Cu content as low as 1.8%Cu the P.S. is equivalent to that of the high Z 2014 T6 extrudes. The limited surface cracking exhibited by the 1% to 3% Cu alloys over the extrusion range considered also enhances the possibility of eliminating surface recrystallization in the T6 temper by extruding below an initial flow stress of 30 MN/m^2 as shown in figure 4.72.

4.4.8. FRACTURE TOUGHNESS PROPERTIES OF THE 2014 ALLOY

It is generally recognised that the fracture toughness of metals decreases as the yield strength is raised. This is particularly true of high strength aluminium alloys where the increase in strength on ageing can result in a decrease in toughness, to the extent that alloys such as 2014 are often used in the overaged condition to enhance the fracture toughness properties[63]. Several recent review papers[41,61,63] have listed the important metallurgical factors which affect the toughness in aluminium alloys, but have largely ignored the effect of process conditions. In the present work therefore the effect of process conditions on the fracture toughness of the three 2014 extrudes in the T6 and T5 tempers have been investigated.

The fracture specimens described in section 3.6.3. were machined from similar positions along the length of each 20:1 extrude, and aged to peak strength at 160 deg.C. The T6 temper was tested at all extrusion temperatures, whilst the T5 temper was tested at low Z_I conditions. Values of the maximum applied load and the plastic component of the clip gauge displacement used in the calculation of the critical cracking opening displacement δ_c are listed in appendix III. The experimental procedure and the analysis used in the evaluation of δ_c can be found in B.S. 5762:1979.

Examples of the load-clip gauge opening displacement curves in the T6 temper are shown in figure 4.99. for the high and low Z indirect extrudes. The curves are typical of all three extrudes considered and show an initial linear rise in load followed by a plastic region in which the load increases to a maximum where cracking is assumed to be initiated. The load decreases as the crack propagates

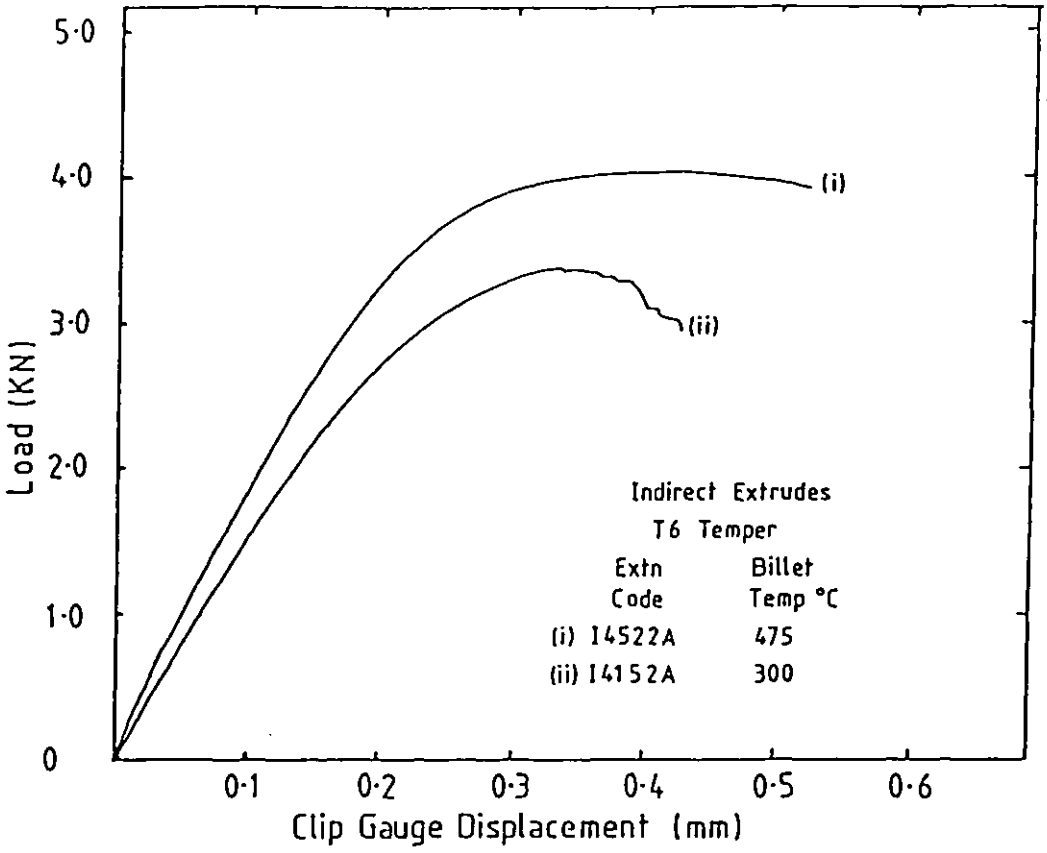


Figure 4.99 Applied load vs clip gauge displacement T6 temper - 2014 alloy

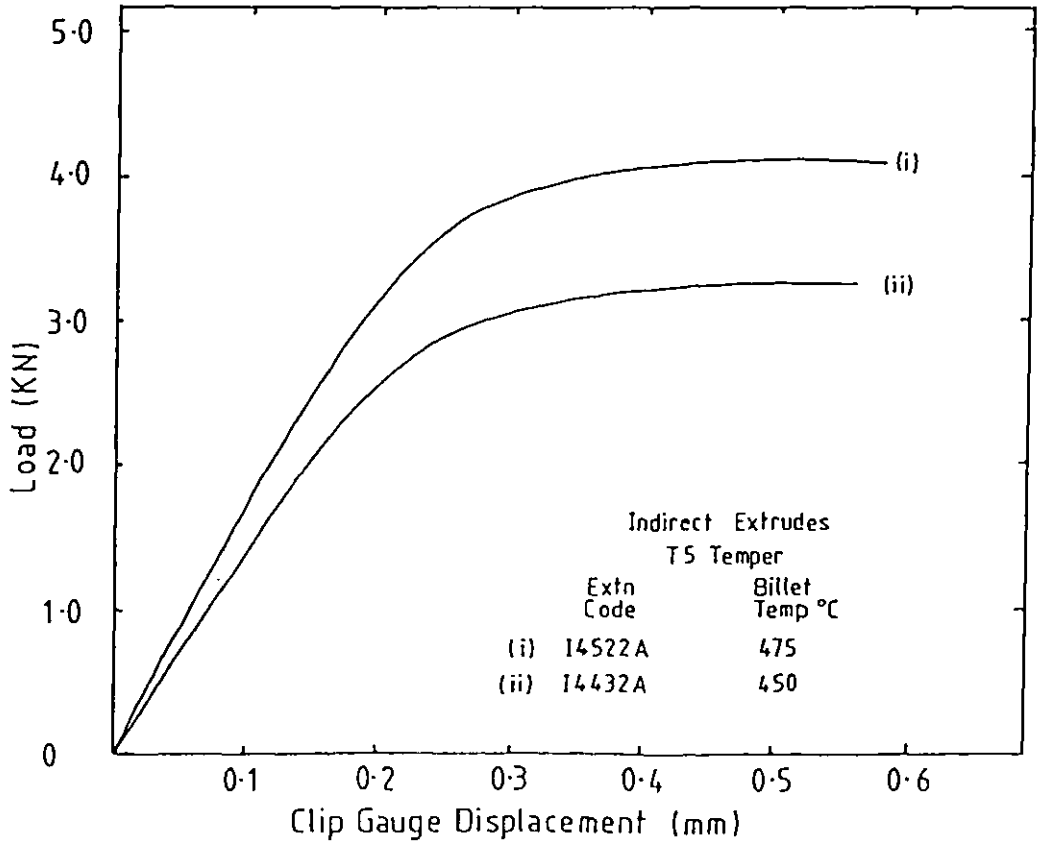


Figure 4.100 Applied load vs clip gauge displacement T5 temper - 2014 alloy

through the extrude at which point the tests were stopped. It is apparent that the maximum load and displacement are greater in the low Z extrudes, the high Z extrudes exhibiting a characteristic unstable crack growth after the attainment of the maximum load. Figure 4.100. shows typical examples from the T5 temper tests for extrusion temperatures of 475 deg.C and 450 deg.C. The curves are similar to the low Z T6 temper, where the maximum load decreases with increasing Ln Z_I. It is therefore evident that there is a change in the fracture properties due to the presence of the subgrain structure in the low Z T6 and T5 extrudes.

The fracture toughness K has been evaluated using the values of δ_c and the corresponding P.S. values shown in section 4.4.6. using the standard relationship:

$$K = (m\sigma_{p.s.} E \delta_c)^{1/2} \qquad 4.29.$$

where E is the Youngs Modulus (70 GN/m^2) and m is a geometric factor dependent on the specimen dimensions and the shape of the crack. Typical values of m range from 0.8 - 1.2, where m = 1 has been assumed in the present work which is not unreasonable for the size of specimen used[157] and since the results are intended for use on a comparative basis only. In order to establish whether the values of K listed in appendix III can be expressed in terms of K_{IC} the plane strain fracture toughness the following criteria must be satisfied.[158]

$$t_c \geqslant 2.5 \left[\frac{K_{IC}}{\sigma_y}\right]^2 \qquad 4.30.$$

where t_c is the minimum specimen thickness. The large variation in proof stress shown in section 4.4.6. and a constant specimen thickness of 10mm means that valid K_{IC}

values are only obtained in the high Z extrudes. However since only a relative index of fracture toughness is being considered the attainment of plane strain conditions is not essential for the present investigation. The fracture toughness has therefore been defined in terms of the mixed mode or plane stress fracture toughness K_c.

The effect of the initial extrusion conditions on K_c in the T6 and T5 tempers is shown in figures 4.101. to 4.103. for the CH direct, indirect and S.S. direct extrudes. It is apparent from these figures that all three extrudes in the T6 temper show a marked increase in K_c at low Z_I as indicated by the curves in figure 4.99. The results are somewhat surprising since these extrusion conditions also correspond to the highest proof stresses and lowest strain hardening coefficients, deformation characteristics which are normally associated with a decrease in the fracture toughness[63]. If the above trend is correct then extruding at low Z conditions to retain the substructure during heat treatment not only increases the tensile strength but also increases the fracture toughness in the transverse plane. Before discussing the fracture modes involved it may be useful to establish whether the method used in the evaluation of δ_c and K_c are correct. It is well known[158] that the values of the plane stress fracture toughness are thickness dependent due to the constraint of the free surfaces, which can extend through to the centre of the specimen so that crack initiation associated with K_{IC} is suppressed. Therefore in the plastic regions shown in figures 4.99. and 4.100. the exact load and displacement at which cracking is initiated may not be associated with the maximum load. A sudden increase in displacement under increasing load or 'Pop-in' is often taken as the load in plane stress conditions at which cracking commences. Pop-in was difficult to detect in the low Z extrudes and when it did occur in the high Z extrudes it was only seen

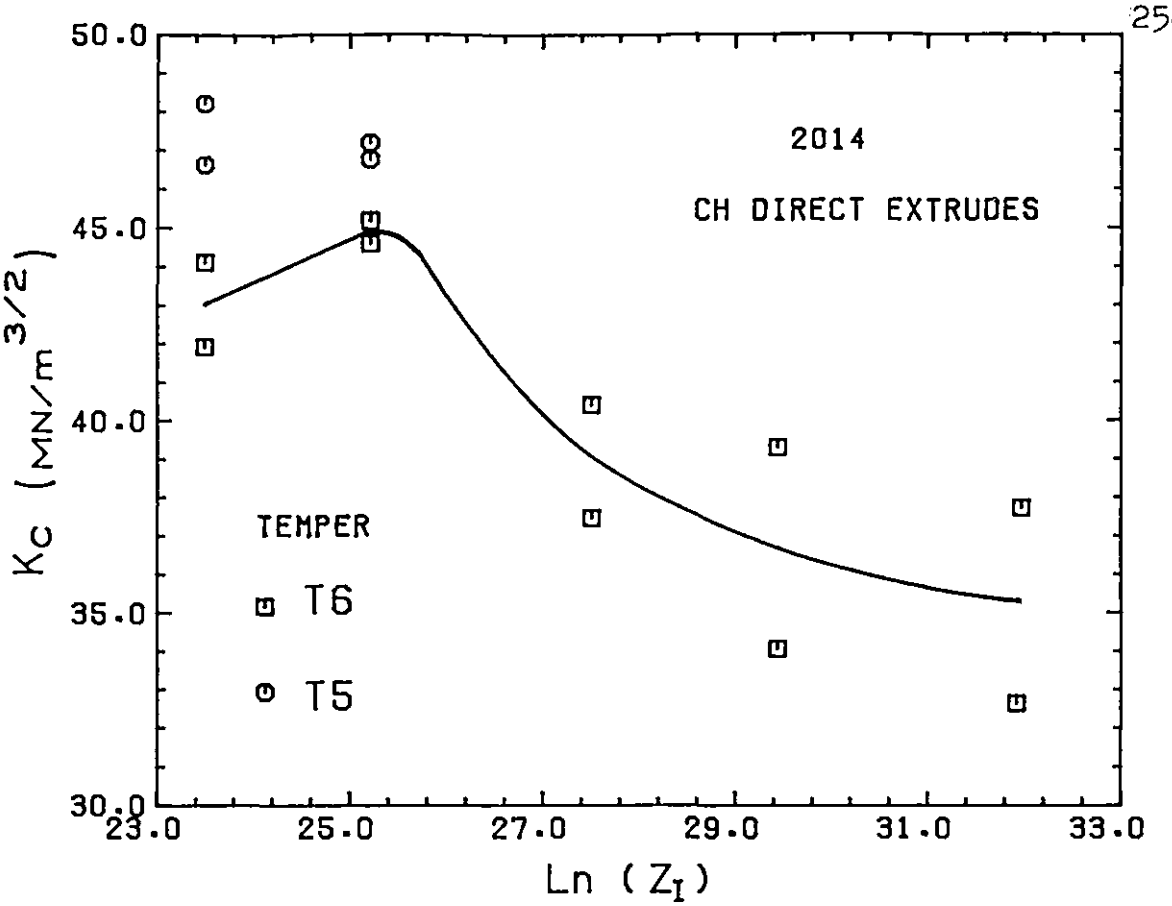


Figure 4.101 Plane stress fracture toughness K_c vs LnZ_I-T6 and T5 temper-CH direct extrusion of 2014 alloy

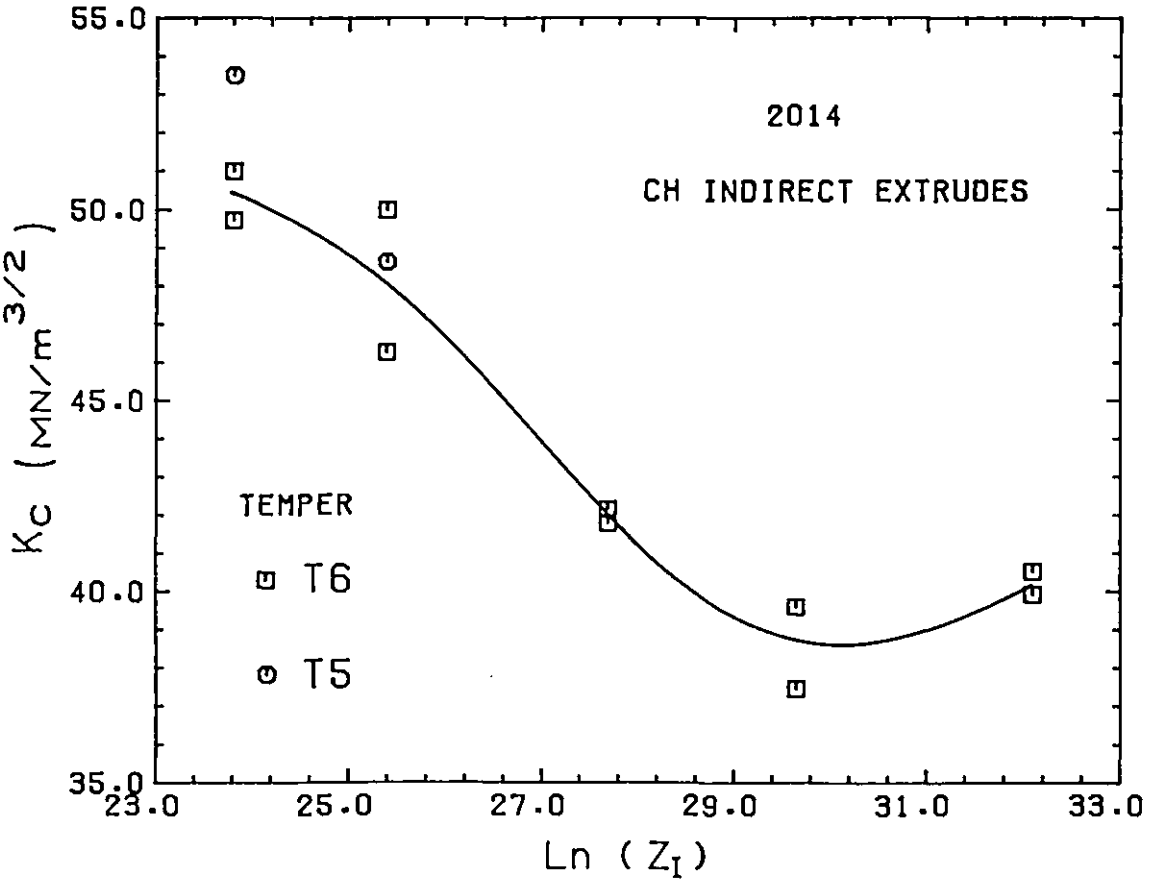


Figure 4.102 Plane stress fracture toughness K_c vs LnZ_I-T6 and T5 temper-CH indirect extrusion of 2014 alloy

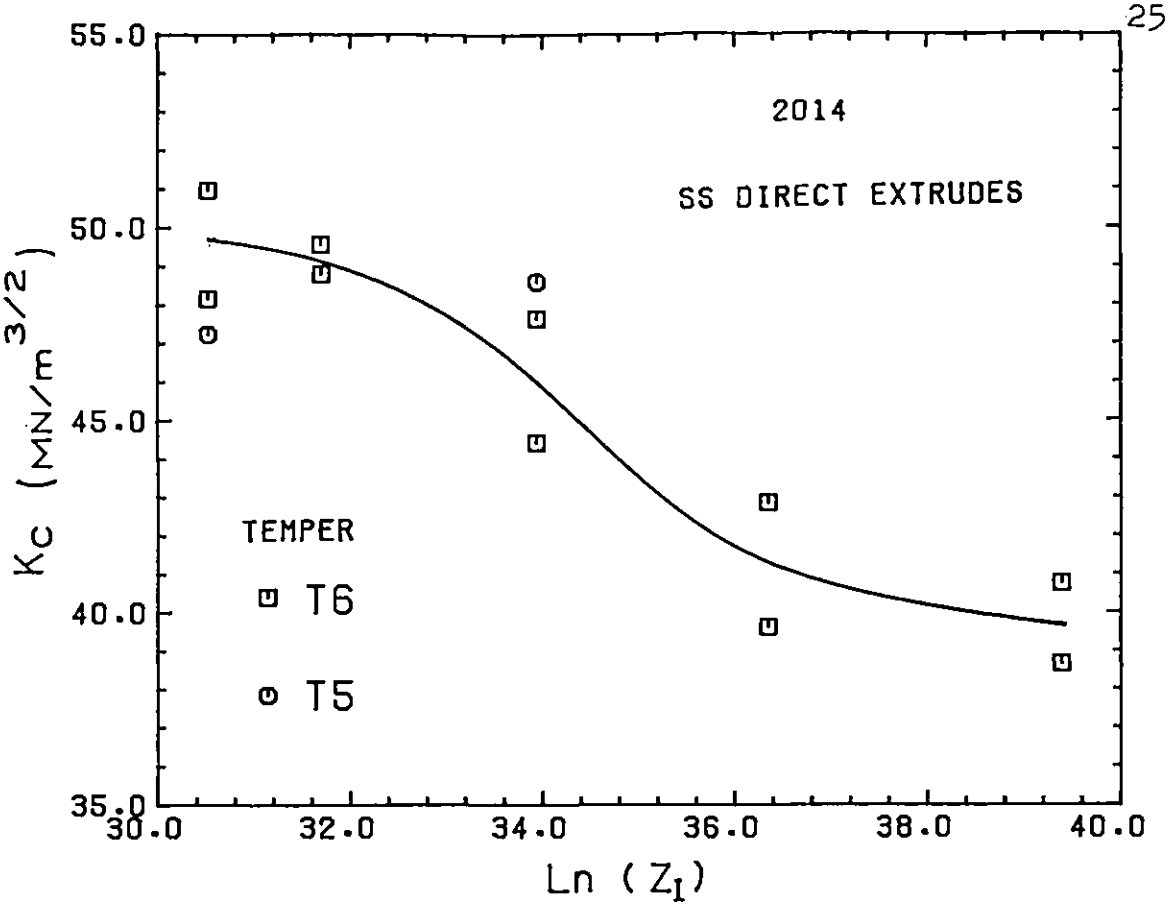


Figure 4.103 Plane stress fracture toughness vs LnZ_I-T6 and T5 temper-SS direct extrusion of 2014 alloy

INDIRECT EXTRUDES

T6

T_I(°C)	300	350	400	450	475
δ_c (mm)	0.020 0.018	0.015 0.020	0.0115 0.0179	0.0158 0.0184	0.0143 0.0149
Kc $MN/m^{3/2}$	23.72 22.68	20.23 23.37	18.22 24.77	24.17 26.05	23.02 23.43

T5

T_I(°C)	475	450
δ_c (mm)	0.0154	0.0160
Kc $MN/m^{3/2}$	23.17	21.17

Table 4.37 Values of K_c determined by the off set procedure - T6 indirect extrudes of 2014 alloy.

immediately prior to the maximum load. However the occurrence of Pop-In is still no guarantee of the correct crack initiation position[159]. The alternative method to estimate crack initiation is to use the off-set procedure described by Knott[158]. A line is drawn with a 5% decrease in slope from the linear elastic region, where the intersection with the plastic region is taken as the load and displacement at which cracking commences as opposed to the maximum load and displacement used for figures 4.101. to 4.103. The analysis therefore assumes that little or no plastic deformation occurs prior to or after crack initiation contrary to the nature of the rising load displacement curves in figures 4.99. and 4.100. However the off-set procedure has been used to evaluate new values of δ_c and K_c for the indirect extrudes the results shown in table 4.37. It is apparent that the values of K_c are now more or less constant. The results therefore do not contradict the trend shown in figures 4.101. to 4.103. the presence of the substructure at low Z_I in the T6 temper enhancing the fracture toughness at high strength levels. It should also be noted that the T6 and T5 tensile properties in figures 4.87. to 4.89. also show no significant change in ductility from the high Z to low Z regions.

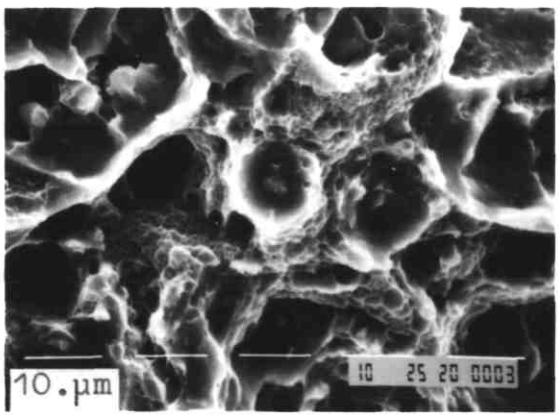
A large decrease in the plane stress fracture toughness from an unrecrystallized product to a recrystallized one has been reported[41] in a 7000 series alloy, due to a change from transgranular to intergranular fracture. In the present work the fatigue crack surface did indeed show a faceted intergranular appearance in the high Z extrudes, which changed to a smooth surface in the low Z extrudes. However the fracture surfaces were relatively flat and smooth and showed no obvious signs of intergranular cracking. This is perhaps to be expected since the fracture path in the transverse plane is normal to the grain boundaries, whilst

intergranular fracture is more likely to occur in the longitudinal plane. Indeed there are numerous experimental results[41,64] to show that wrought products of the T6 2000 and 7000 series alloys have a higher fracture toughness in the longitudinal transverse direction than in transverse longitudinal direction. Preferential precipitation at the grain boundaries and precipitate free zones are instrumental in reducing the grain boundary matrix strength and so promoting intergranular fracture. The presence of aligned weak particles or 'stringers' in the longitudinal direction also reduce the initiation fracture properties by increasing the amount of particle matrix decohesion ahead of the crack tip.

In order to establish the initiation fracture mode in the high Z and low Z extrudes, the fracture surfaces were examined directly below the fatigue cracks and in the centre of the specimens where plane strain conditions are likely to exist. The S.E.M. micrographs are shown in plate XV for the CH indirect and SS direct extrudes in the T6 and T5 tempers. Micrographs a) to d) show that in the T6 temper the fracture surfaces have a characteristic dimpled appearance associated with a ductile or fibrous mode of fracture. Micrographs a) and b) show that for the fully recrystallized high Z extrudes the large dimples have an average spacing of 18 μm and are associated with inclusions of 3-4 μm in diameter, similar in size to the as cast particles shown in section 4.3.3. The spacing of the smaller dimples of 2-3 μm is similar to the separation of the intermediate sized particles shown in plates XIV and XV. The observations are consistent with the fracture mode reported by several workers [41,61,63] for commercial age hardenable aluminium alloys. Cracking is initiated within the plastic zone ahead of the crack tip by decohesion of the particle matrix interface at the large inclusions, the voids grow to a critical size until the strain is sufficient to cause

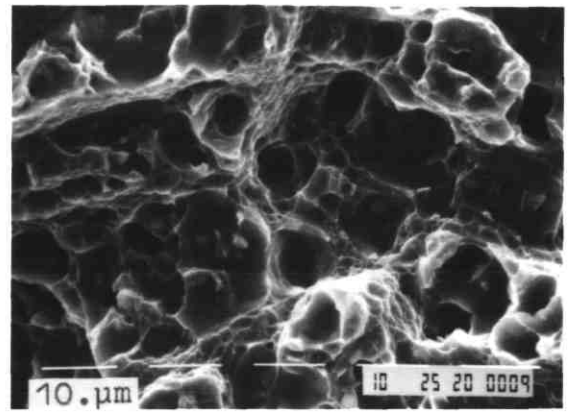
INDIRECT (CH)

a) I4152A - T6 T_I = 300°C

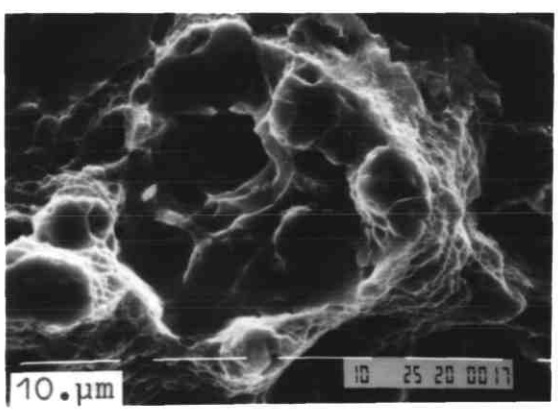


DIRECT (SS)

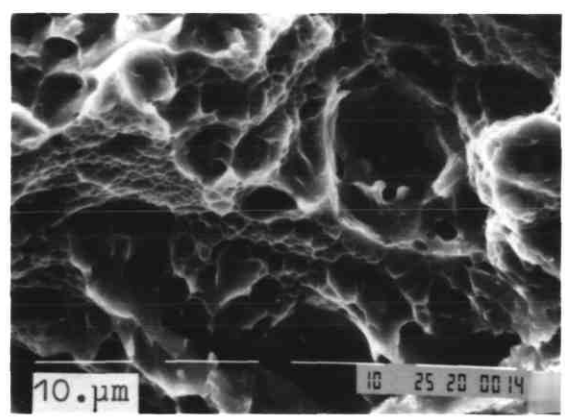
b) D4162AS - T6 T_I = 300°C



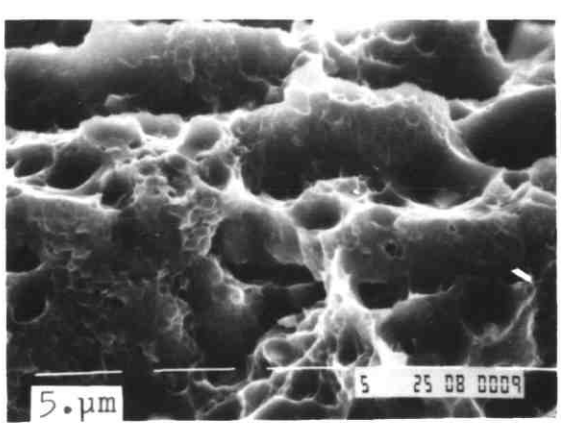
c) I4522A - T6 T_I = 475°C



d) D4562AS - T6 T_I = 475°C



e) I4522A - T5 T_I = 475°C



f) D4562AS - T5 T_I = 475°C

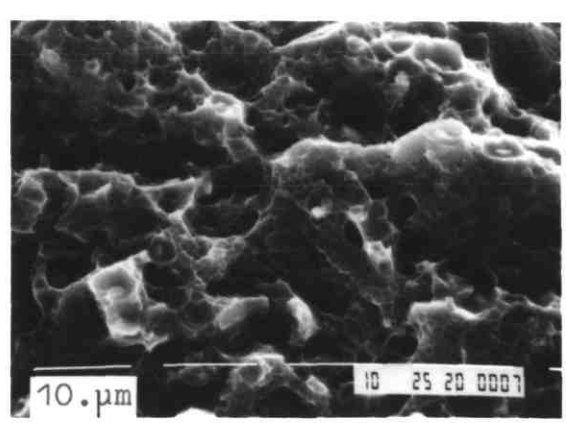


Plate XVI. Fracture Surfaces of T6 and T5 Extrudes of 2014 Alloy just below the Fatigue Crack

decohesion at the intermediate particles so that smaller secondary dimples are formed in the ligaments between the larger voids. The fracture surfaces from the low Z extrudes shown in micrographs c) and d) indicate that a similar fracture mechanism occurs in the presence of a substructure although it is noticeable that the larger dimples are larger and fewer in number. Assuming that the initiation stage in fracture of the high Z and low Z extrudes involves particle matrix decohesion at the large inclusions, the increased void size indicates that void growth continues to a higher strain and hence stress before decohesion of the ligament between the void occurs. The substructure strengthening may effectively be increasing the fracture toughness by increasing the energy required for decohesion of the ligaments. The unstable crack growth in the high Z extrudes shown in figure 4.99. is therefore due to the rapid decohesion of the inter void ligaments associated with the recrystallized matrix. Therefore although the decrease in strain hardening coefficient shown in table 4.34. may result in an increase in strain and stress localisation at the crack tip and hence increase in the particle matrix decohesion, the increase in energy required for decohesion of the substructure strengthened matrix results in an equivalent or greater fracture toughness to the high Z extrudes. Since the subgrain structure is relatively equiaxed it is likely that the fracture toughness in the transverse longitudinal direction will also be enhanced.

It is interesting to note that the values of K_C in the T6 and T5 temper for the SS extrudes are 14-11% higher than the equivalent CH direct extrudes which exhibit similar tensile properties. This may well be associated with a reduction in the size and distribution of the larger as cast particles as mentioned in section 4.3.5.3., although clearly

further results are required from plane strain tests and from particle size analysis since the CH indirect extrudes exhibit similar values of K_C to the SS extrudes.

The fracture surfaces of the T5 indirect and SS direct extrudes are shown in micrographs e) and f). The fracture surfaces show a reduction in the number of larger voids, although an increase in the number of smaller dimples indicates that decohesion of the matrix substructure plays a more prominant role in the fracture mechanism than in the low Z T6 extrudes due probably to the absence of subgrain growth during ageing. This is also reflected in the higher values of K_C at low Z_I in figures 4.101. and 4.102. for the CH direct and indirect extrudes.

The size and separation of the dimples in micrographs a) to e) indicate that the ageing precipitates play no role in the fracture mechanism but influence the fracture toughness by changing the matrix deformation characteristics.

Although the values of K_C in figures 4.101. to 4.103. are largely dependent upon whether crack initiation during plane stress testing occurs at the maximum load or some intermediate load, the off-set values of K_C and the S.E.M. micrographs indicate that the fracture toughness in the T6 and T5 tempers is enhanced by the presence of a subgrain structure produced by extruding at low Z conditions. It may be possible in future work to derive more accurate values of K_C from plain stress tests by using additional instrumentation to detect the accoustic emission at crack initiation, so that if crack initiation occurs within the plastic region prior to the maximum load the accoustic emission could be matched with the precise load and displacement at which cracking occurs.

4.4.9. STRESS CORROSION RESISTANCE OF THE 2014 ALLOY

The stress corrosion resistance of high strength aluminium alloys is often a factor which restricts their use in the aerospace industry. In certain environments and stress conditions failure can occur well below the stress required for gross yielding. It is not intended in the present work to investigate and discuss the precise mechanisms proposed for stress corrosion cracking (S.C.C.) since these have been extensively reviewed in several recent papers[64,160]. However the basic requirement for a microstructure which is susceptible to S.C.C. is the existance of a continuous zone within the material which is more susceptible to corrosion than the rest of the matrix. In aluminium copper alloys the copper constituents are cathodic with respect to aluminium so that stress corrosion resistance is influenced primarily by the copper concentration gradient in the Al-Cu solid solution in the grain boundary region. The effect of the extrusion conditions on the susceptibility to S.C.C. in the 2014 alloy has been investigated in the peak aged T6 and T5 tempers.

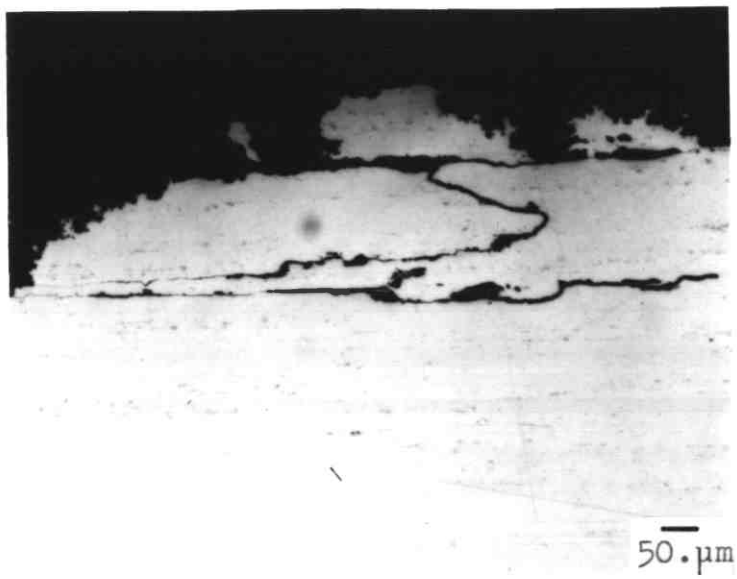
Conventionally heated direct and indirect extrudes were tested in the T6 temper at extrusion temperatures of 475 deg.C, 400 deg.C and 300 deg.C, the T5 temper at 475 deg.C. Three specimens were tested for each condition and pre-stressed to 75% of the proof stress as described in section 3.6.7. The specimens were exposed in a solution of 3% NaCl in an alternate immersion tank for a period of 3 months, after which no signs of cracking could be seen in any of the specimens. Since the object of the test is to determine whether failure occurs due to S.C.C. under a specified stress below the yield stress, the Alcoa test therefore indicates that the 2014 alloy is not susceptible to S.C.C. in either the T5 or T6 temper. The first point to note is that the grain shape and orientation especially in

the recrystallized extrudes is more or less parallel to the stress direction. If intergranular corrosion is involved in the stress corrosion mechanism then failure is least likely to occur in the longitudinal direction, since the corrosion cracks are growing parallel to the applied stress. Previous workers[64] have indeed shown that for wrought products exhibiting elongated grains in the longitudinal direction (L) then the stress corrosion resistance is alway greatest in this direction, and markedly lower in short and long transverse directions (S.T. and L.T.). In the present work a test specimen length of 51mm would have required extrudes of 2:1 or less to test the S.T. or L.T. directions.

In order to establish the extent to which corrosion has occurred during exposure, the specimens were carefully sectioned in the longitudinal plane and polished, and examined in the unetched and etched conditions. Examples of the unetched microstructures in the T6 and T5 extrudes are shown in plate XVII. It is evident from micrograph a) that intergranular corrosion has occurred in the high Z T6 extrude. Crack lengths of 0.8 - 1.0mm were measured in the direct and indirect extrudes although there was not direct correlation with extrusion mode or extrusion conditions. Micrograph b) shows an example of a low Z T6 extrude and clearly shows evidence of stress corrosion cracks developing normal to the applied stress. The grain diameters of 5-6 μm outlined by the corrosion path are similar in size to the retained substructure noted in section 4.3.7.2. It therefore seems likely that the presence of the precipitate free zone at the subgrain boundaries shown in plate XIV e) is sufficient to make the extrudes susceptible to a form of intergranular corrosion and therefore S.C.C. in the peak aged condition. However an average crack depth of 0.3 mm - 0.5mm indicates that the S.C.C. resistance may be greater in the longitudinal and L-T and S-T directions due to the equiaxed nature of the subgrain structure.

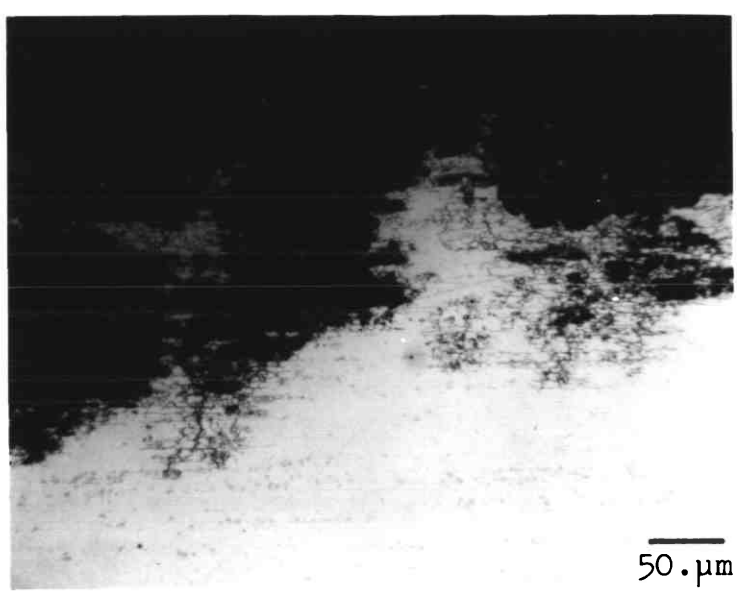
Indirect Extrudes - Longitudinal Plane

a)



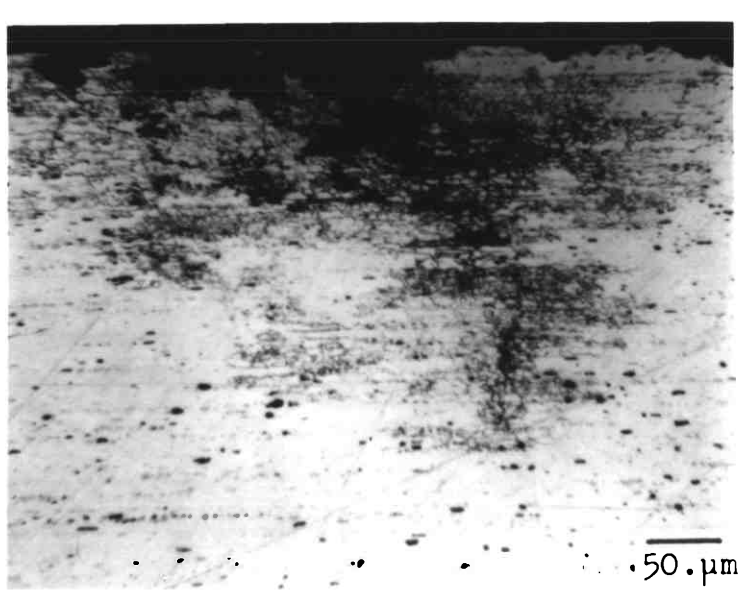
I4123A - T6
T_I = 300°C
ER = 30:1

b)



I4513A - T6
T_I = 475°C
ER = 30:1

c)



I4513A - T5
T_I = 475°C
ER = 30:1

Plate XVII. Stress Corrosion Structures of 2014 Alloy - Unetched.

The T5 extrude in micrograph c) shows a similar corrosion structure to the low Z T6 extrude where preferential corrosion along the subgrain boundaries has lead to a crack $\sim$0.5mm long normal to the stress direction.

It should be noted that all the extrudes tested showed susceptibility to pitting corrosion, the degree of attack was unaffected by either the heat treatment or extrusion mode.

The evidence presented in plate XVII indicates that in the peak aged T6 and T5 tempers the 2014 alloy is susceptible to S.C.C. at all extrusion conditions although the low Z T6 and T5 tempers are likely to have a greater stress corrosion resistance due to the presence of the subgrain structure.

Although only stress corrosions resistance has been considered in the present work, Al-Cu-Mg extrudes are also susceptible to exfoliation corrosion, which can occur in the absence of any stresses and under normal atmospheric conditions. Exfoliation corrosion is the result of selective corrosion along narrow susceptible bands within the directional grain structure which is normally associated with intergranular corrosion. The corrosion product lifts thin layers of uncorroded metal from the surface producing a characteristic layered appearance and may therefore be regarded as a form of S.C.C. due to the stresses generated by the corrosion product. The effect of microstructure on exfoliation has been studied by several workers[66,67] who have shown that in the overaged extrudes the presence of a subgrain structure prevents exfoliation since corrosion only takes place at the subgrain boundaries. The rate of

penetration of corrosion into the metal was also found to be considerably less in the presence of a subgrain structure as has been found in the present work.

4.4.10. LIMIT DIAGRAMS

Limit diagrams were originally proposed by Hirst and Ursell[111] to represent graphically the extrusion limits within which products with an adequate surface finish could be produced for a specific press capacity. This form of diagram is shown in figures 4.104. and 4.105. for the 2014 CH direct, indirect and SS direct extrudes, extruded at 3mm/s and 13 mm/s. The limiting pressure lines described by the maximum extrusion ratios and minimum billet temperatures have been established using the empirical pressure equations in section 4.2.9. for a press capacity of 1130 MN/m^2. The surface cracking lines are based on the expressions derived in section 4.2.10.2., the limiting line for indirect extrusion has been established from a combination of the results in the present work and those of Paterson[124] where the results and defining equation are shown plotted in figure 4.106. It should of course be noted here that surface cracking is only one of a number of surface defects that can appear during extrusion or after subsequent processing and therefore extrusion within these limits does not guarantee an adequate surface finish free from e.g. pick up, die lines, blistering, etc.

At specific ram speeds the limiting pressure lines in figures 4.104. and 4.105. show that as the initial billet temperature increases, the flow stress decreases so that higher extrusion ratios become possible. This continues until a critical temperature and extrusion ratio are reached, where an increase in temperature results in a decrease in the possible extrusion ratio due to the increased liklihood of surface cracking as a result of the

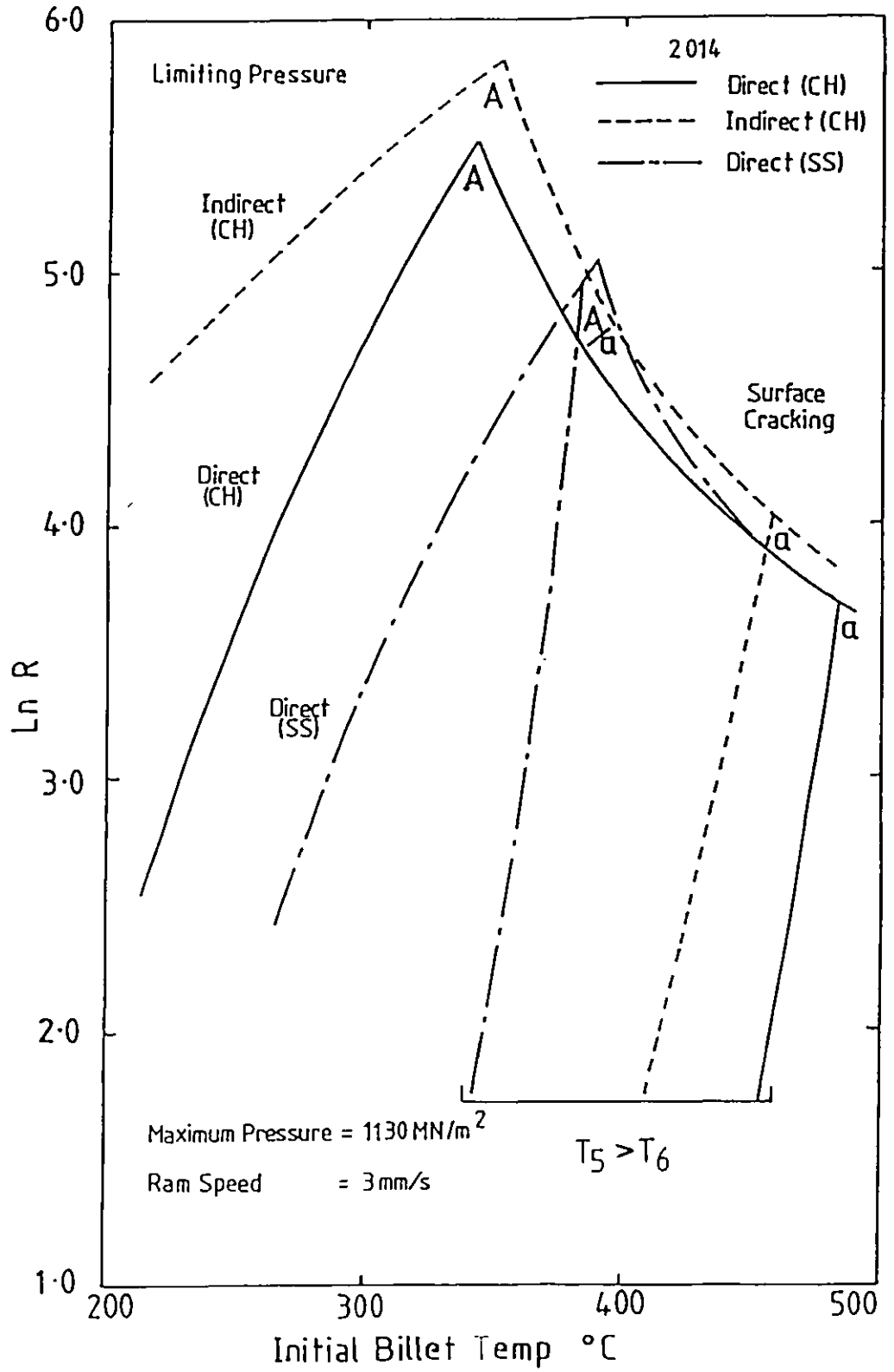


Figure 4.104 Limit diagram for CH direct, indirect and SS direct extrusion of 2014 alloy v = 3mm/s

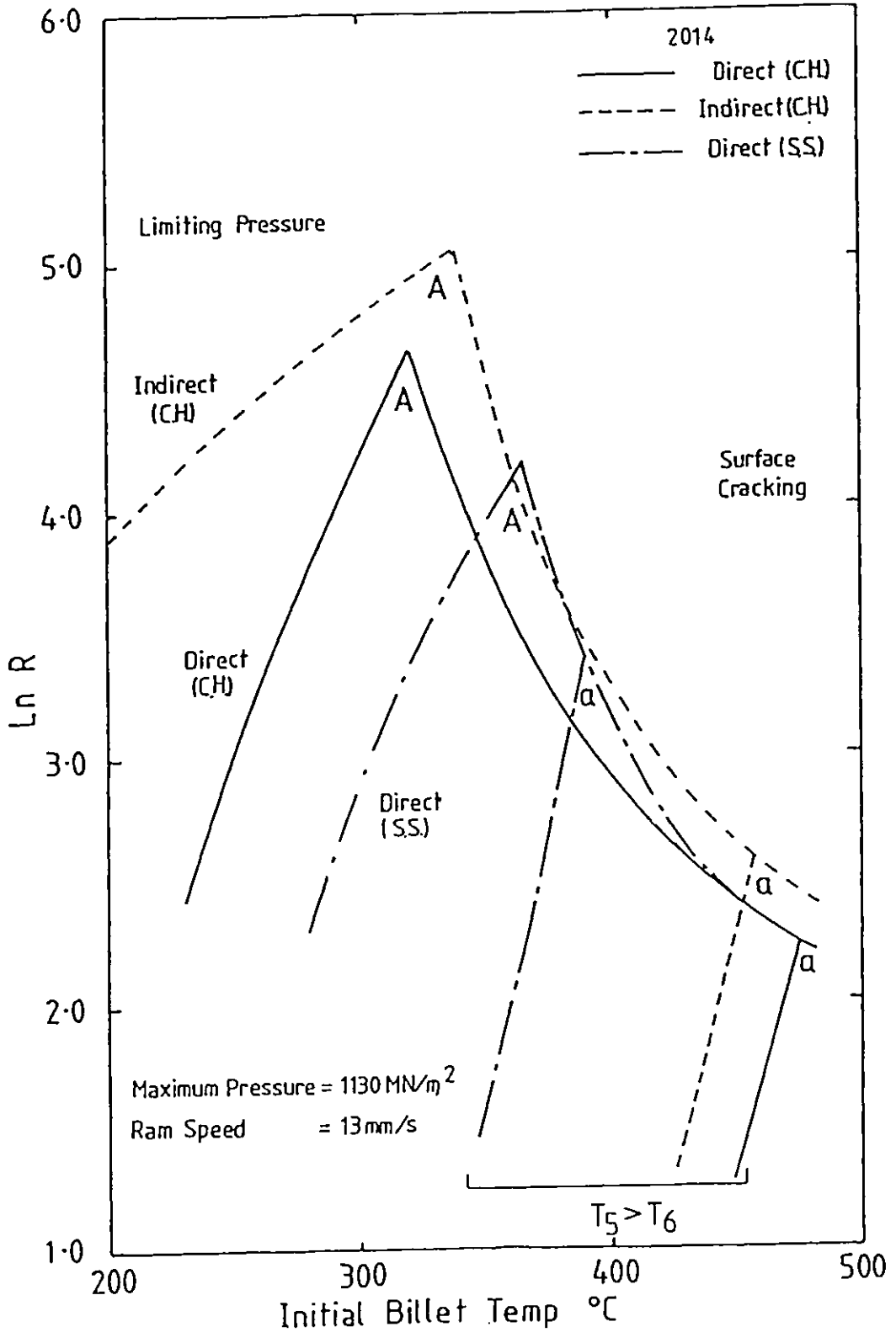


Figure 4.105 Limit diagram for CH direct, indirect and SS direct extrusion of 2014 alloy v = 13mm/s

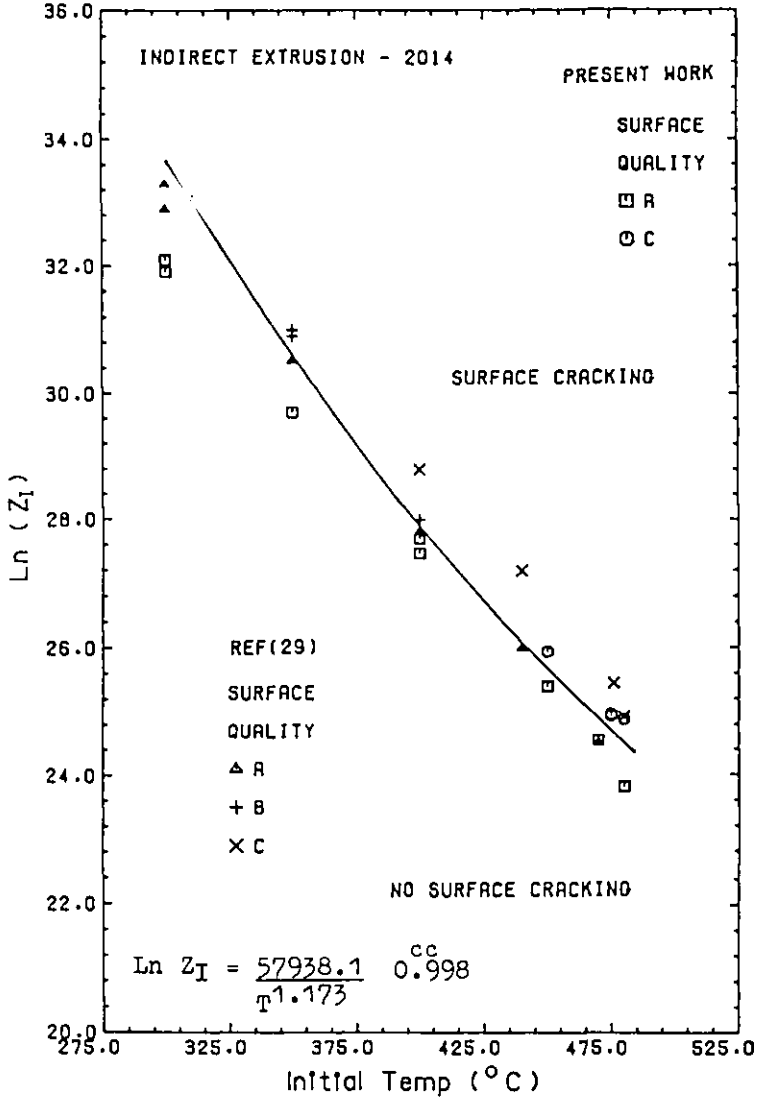


Figure 4.106 Indirect extrusion of 2014 alloy

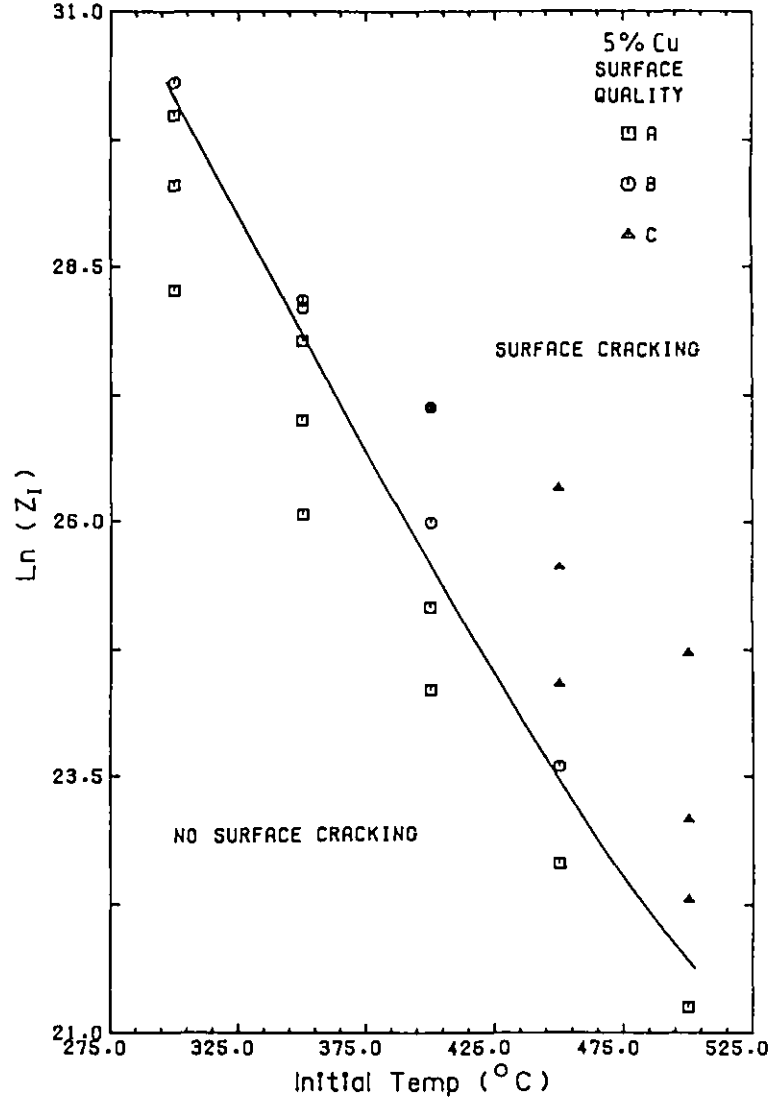


Figure 4.107 Direct extrusion of 5% Cu alloy

LnZ_I vs T_I - dependence of surface cracking on the initial process conditions.

temperature rise during extrusion. An increase in ram speed lowers the pressure limit line due to the increase in flow stress and hence load although clearly, as noted in section 4.2.10.2., ram speed has a more pronounced effect on the surface cracking limits which may be attributed to the higher temperature rise and stresses generated at the die exit.

It is evident from figures 4.104. and 4.105. that the presolution soak treatment described in section 4.2.10. is effective in extending the direct extrusion range at high and low ram speeds between $\sim$ 450 deg.C to 360 deg.C. Below this temperature the increase in extrusion pressure shown in figure 4.52. significantly reduces the extrusion range for the given press capacity. Therefore in terms of the production limits the CH billets can be extruded over a greater range of extrusion conditions in the low temperature range, whilst the SS billets have a greater extrusion range at high temperatures, which increases with ram speed as surface cracking becomes more prevalent in the CH billets. The indirect mode clearly offers the greatest range of extrusion conditions at both ram speeds due to the lower loads at low temperatures, whilst at high extrusion temperatures the more uniform nature of flow and the lower temperature rise reduce the liklihood of surface cracking. The optimum production conditions for each extrusion process correspond to the positions marked 'A' in figures 4.104. and 4.105.

Sheppard[100] has shown that limit lines may also be constructed to represent specific structures and properties which are a function of the process conditions. The results in sections 4.3. and 4.4. have shown that for heat treatable alloys such as 2014 the situation is not so simple since the process conditions structure/property relationships are also dependent on the final temper. Perhaps the most important structural features in relation to the as extruded and heat

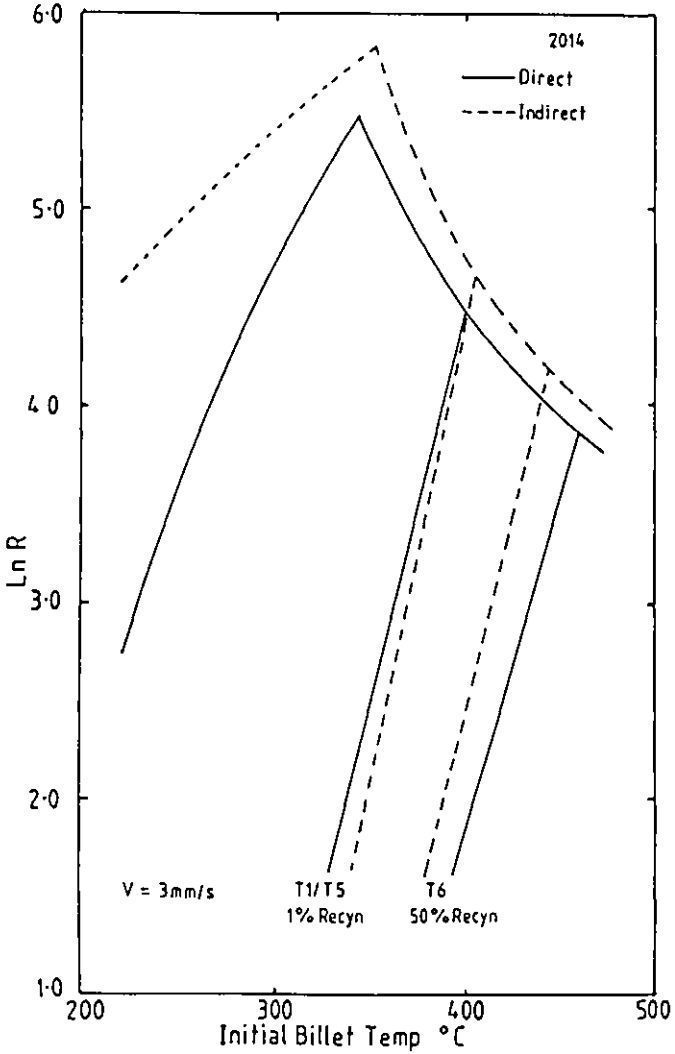


Figure 4.109 Ram speed = 13mm/s

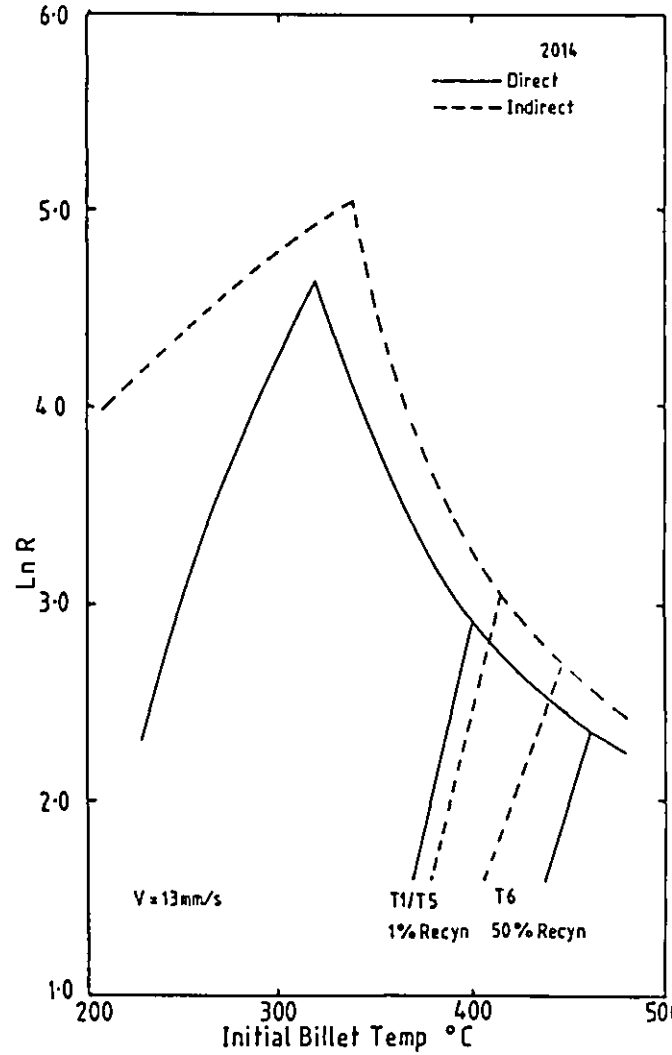


Figure 4.108 Ram speed = 3mm/s

Limit diagram showing T6 and T5 % recrystallisation lines CH direct and indirect extrusion of 2014 alloy

treated properties are the percentage recrystallization and hence substructure strengthening and the solid solution content. In section 4.3.4. and 4.3.7. it was shown that the percentage recrystallization could be related to the initial flow stress or LnZ_I and hence extrusion conditions. Using these relationships the limiting lines representing 50% recrystallization in the T6 extrudes and 1% recrystallization in the T1 and hence T5 extrudes have been drawn in figures 4.108. and 4.109. for the CH direct and indirect extrudes extruded 3 mm/s and 13 mm/s. The figures clearly show that the extrusion range is severely reduced if substructure strengthening is to be utilised in the T6 temper, the extrusion limits decreasing with increasing ram speed as the driving force for recrystallization increases with the less recovered substructure, which is also reflected in the greater extrusion range offered by the indirect mode. The limiting lines for the T1/T5 temper again show that as the percentage recrystallization increases with ram speed the extrusion range is reduced, which is accentuated by the larger temperature rises during direct extrusion. It should be noted that the arrangement of the indirect tooling described in section 3.2.5. almost doubles the quench delay time during which static recovery and recrystallization take place, so that the limiting lines for indirect extrusion may actually be at higher temperatures than those shown in figures 4.108. and 4.109.

The effect of solid solution content on the mechanical property limiting lines can be seen in figures 4.104. and 4.105. which shows the extrusion limits required to give a T5 extrude with greater than or equal tensile properties to the T6 specifications shown in table 4.35. The figures show that for this particular requirement the presolution soak treatment now offers the highest production rate shown by the positions marked 'a', followed by the CH indirect and direct extrusion. Clearly other considerations must also be

taken into account such as the fracture toughness, corrosion and fatigue properties, although inclusion of all this data on one or a number of diagrams is likely to be too complicated to be of any real practical use. One solution would be to computerize the structure/property relationships so that either the optimum extrusion conditions and heat treatment could be chosen prior to extrusion or the final properties predicted for specific extrusion conditions. However this assumes that the commercial extruder has sufficient control of the process variables such as ram speed and temperature which unfortunately is not always the case. Infact extrusion conditions are often chosen well within the limits shown in figures 4.104. and 4.105. due to the standard of error in the control of the ram speed and more especially the temperature which can be as great as ± 50 deg.C.[100]

The effect of copper content on the extrusion limits are shown plotted in figure 4.110. for a ram speed of 13 mm/s. The surface limiting line for the 5% Cu alloy has been established from the results in figures 4.107., where the surface cracking limits are defined by:-

$$\ln Z_I < \frac{42276.9}{T^{1.135}} \qquad 0.9823^{cc} \qquad 4.31.$$

where T is in deg.K. For the 2% Cu and 3% Cu alloys the surface cracking lines are only approximate since cracking did not occur below an extrusion ratio of 100:1 and the initial billet temperatures shown plotted in figure 4.110. The 1% Cu alloy showed no signs of cracking over the entire range of extrusion conditions considered.

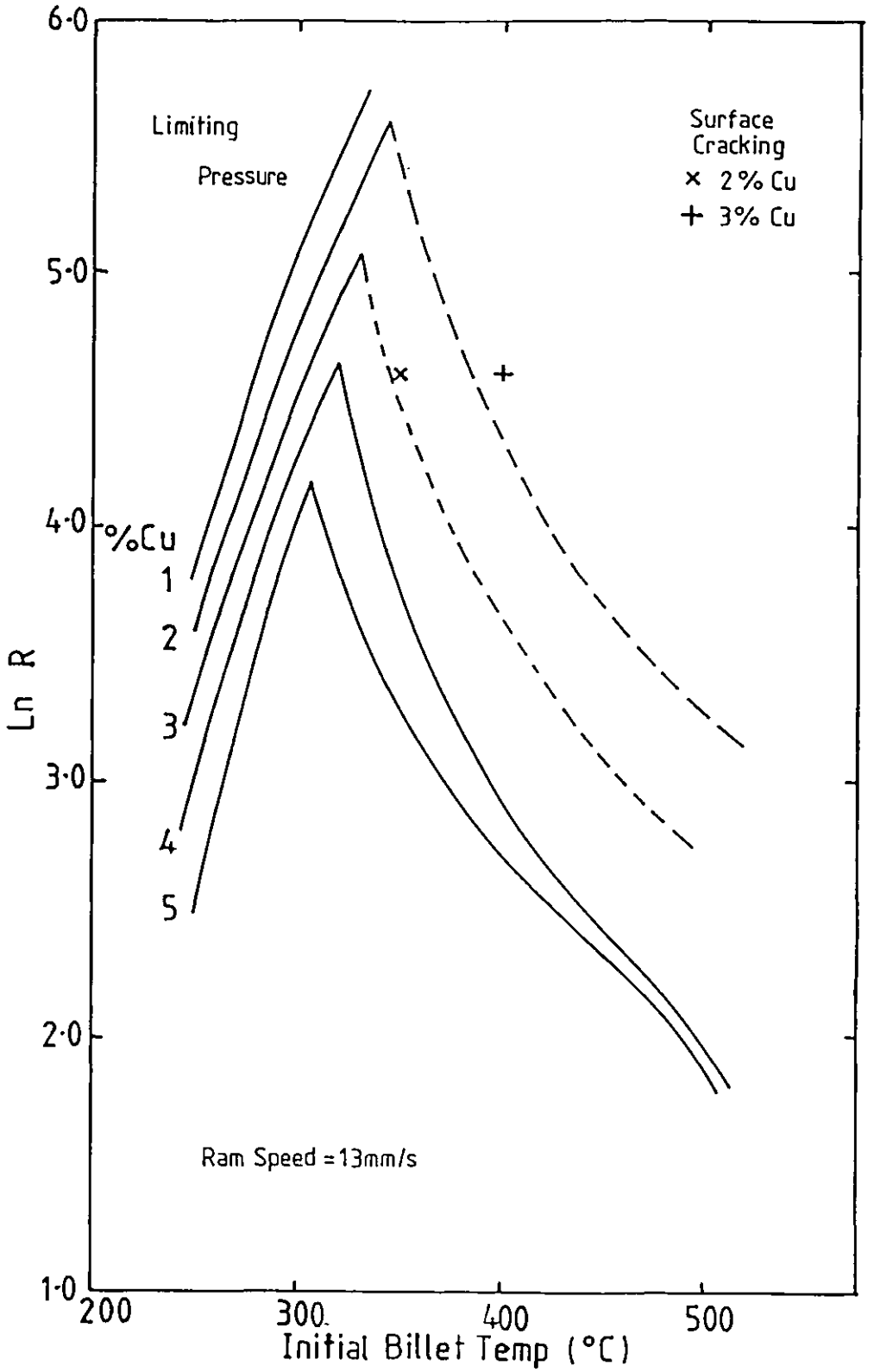


Figure 4.110 Limit diagram for direct extrusion of 1% Cu - 5% Cu alloys v = 13mm/s

It is evident from figure 4.110. that increasing the Cu content reduces the maximum possible extrusion ratio in the low temperature region as the flow stress and hence extrusion pressure increases. In the high temperature range an increase in Cu content effectively increases the temperature rise during extrusion whilst an increase in the amount of eutectic phase present increases the liklihood of surface cracking associated with incipient melting.

4.4.11. PROCESS CONDITIONS vs PROPERTIES

In order to show more clearly the relationship between the process conditions and the structure and properties of the direct and indirect 2014 T6 temper extrudes the relationships derived in sections 4.3. and 4.4. are shown plotted in figures 4.111. and 4.112. The maximum ram speeds corresponding to the initial billet temperature on the x-axis below which surface cracking does not occur are also included.

The figures show that in order to attain the highest tensile and fracture toughness properties in the T6 temper then a combination of the lowest production rates and highest billet temperatures are required to prevent surface cracking and avoid excessive recrystallization. Although indirect extrusion does offer slightly higher ram speeds and lower temperatures the difference may not be sufficient if for instance temperature control is in the region of $\pm$ 50 deg.C. Conversely higher production rates can be achieved at high Z conditions but at the expense of the mechanical properties of the extrudate, although a degree of control still remains due to the reduction in grain size with Z, which favours the indirect mode due to the reduction in load at low temperatures shown in figure 4.36.

In the T1 and T5 tempers the hardness and tensile properties in figures 4.78. and 4.85. show that again the

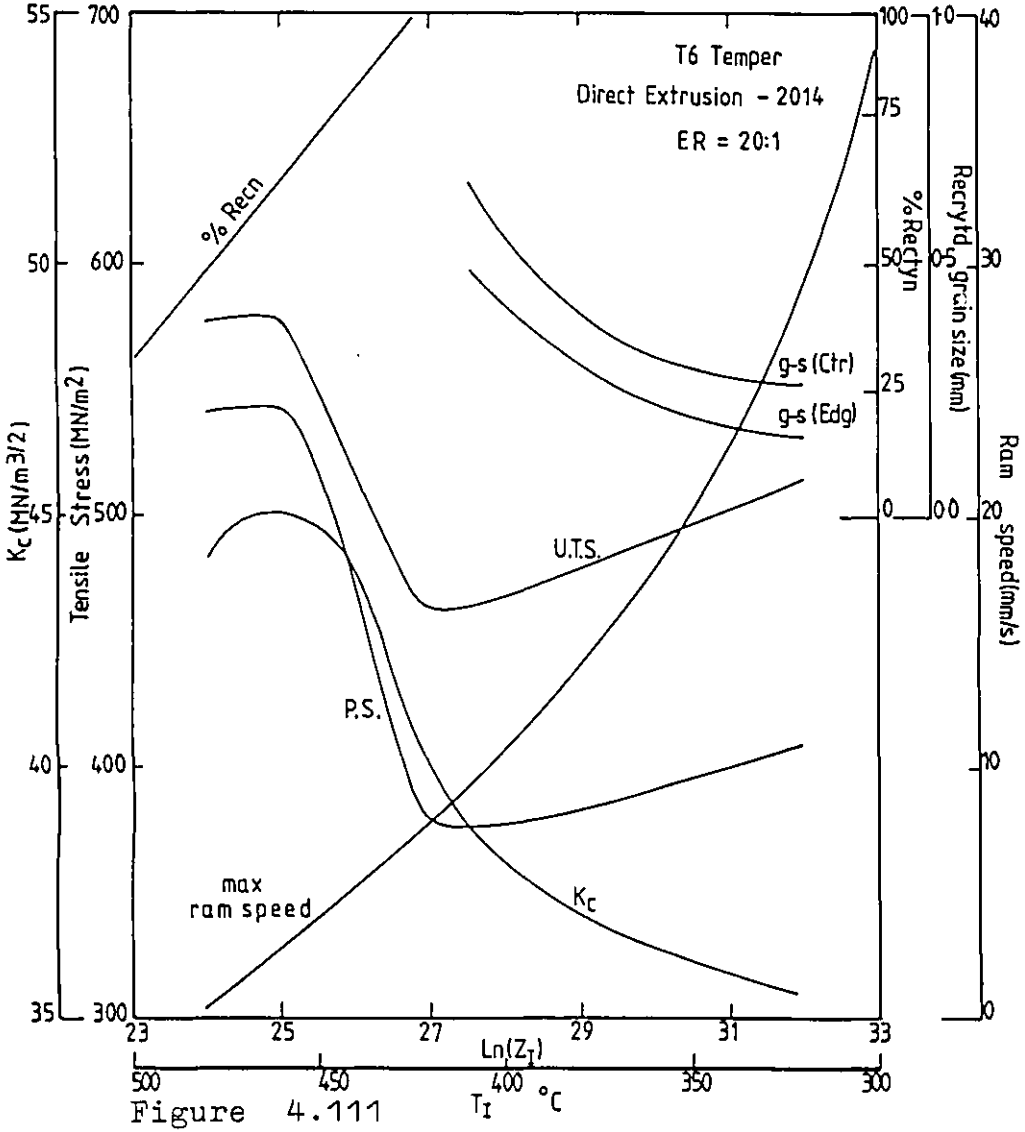


Figure 4.111

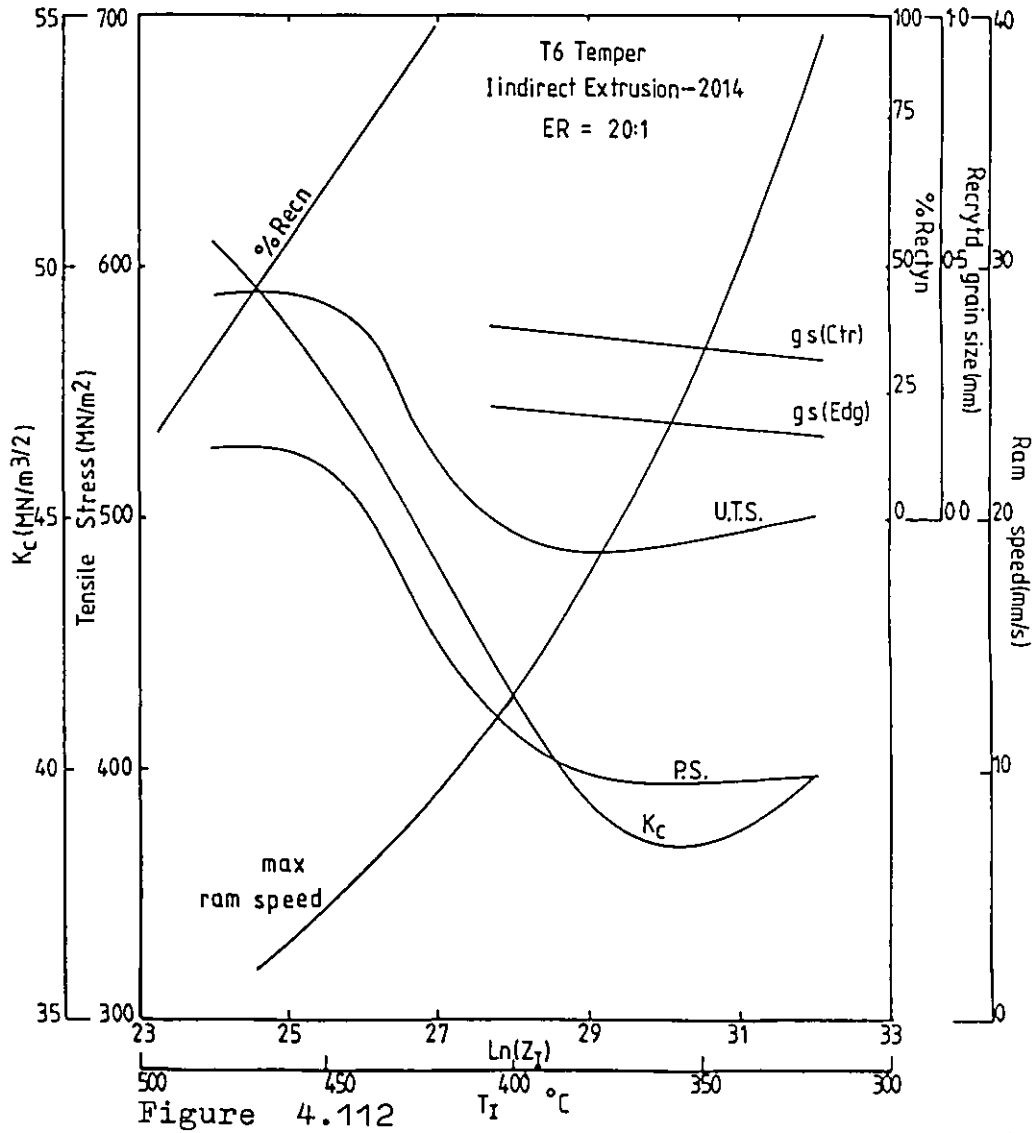


Figure 4.112

Process conditions vs properties -
direct and indirect extrusion of 2014
alloy - T6 temper extrudes ER = 20:1

mechanical properties are enhanced at low Z due to the increase in solid solution content, whilst at high Z the tensile properties are markedly lower but increase with Z due to the increase in substructure strengthening which again favours the indirect mode of extrusion.

It should of course be noted that the results in figures 4.111. and 4.112. are relevant to a specific homogenization treatment, billet preheat treatment and container temperature. Although the affect of the billet homogenization treatment and container temperature on the structure and properties of the 2014 extrudes have yet to be established, the results in section 4.2.10. and 4.4.6. to 4.4.7. indicate that a presolution soak treatment may reduce surface cracking and hence increase production rates whilst the T1 and T5 properties are enhanced by an increase in solid solution content and the T6 properties by a reduction in surface recrystallization and a possible change in the particle size and distribution. Finally, the observation that the stress corrosion resistance may be enhanced in the peak and overaged conditions in the presence of a retained substructure suggests that the optimum process conditions for 2014 T1, T5 and T6 extrudes corresponds to low Z conditions, where surface cracking and recrystallization may be reduced by indirect extrusion and a presolution soak treatment.

CHAPTER 5

Conclusions

1) All the torque twist curves exhibit a linear increase in torque with twist followed by a strain hardening region leading to a steady state torque consistent with the operation of dynamic recovery.

2) The predicted temperature rise during testing increases with strain and flow stress, the peak temperature can be described by a volume average temperature although an area average temperature may be more applicable at high strain rates.

3) The graphical analysis in section 2.2.2.2. has been shown to apply to the initial temperature high stress data.

4) The temperature corrected data obtained from torsion tests has been correlated over a range of strain rates and can be described by the hot working equation:

$$Z = A(\mathrm{Sinh}(\alpha\sigma))^{n} = \dot{\varepsilon} \exp \frac{(\Delta H)}{RT}$$

The predicted flow stress and torque increasing with Cu content in the 2000 series alloys and with the additon of Mn, Mg and Si in the 2014 alloy.

5) The constants in the above equation are alloy dependent, the absolute values changing in accordance with the flow stress range considered. The activation

energies ΔH in the low Cu alloys below 3 wt% Cu indicate that deformation is thermally activated and diffusion controlled, whilst a decrease in ΔH with Cu content and temperature in the 4% Cu and 5% Cu 2000 series and 4% Cu binary alloy imply a change in the rate controlling mechanism with an increase in solid solution content independent of the flow stress characteristics which are also dependent on second phase particle distribution.

6) A strain dependent constitutive equation can be established at increments of homologous strain using the above equation.

7) The torsion ductility decreases with flow stress below 350 deg.C independent of Cu content and decreases with Cu content above this temperature coinciding with an increase in solid solution content.

8) For all the 2000 series alloys the dependence of peak pressure on LnR is linear whilst a power relationship provides the best fit for the variation with initial billet temperature.

9) The effect of indirect extrusion is to reduce the pressure required for extrusion.

10) The peak and minimum pressure increase with decreasing container temperature below the billet temperature and decrease with an opposite temperature differential. The change in peak pressure is not a function of the predicted mean peak temperature.

11) The pressure for direct extrusion increases with billet length in the 2% Cu, 5% Cu and 5052 alloys due to friction between the billet and container. The friction conditions may be described by a friction coefficient 'μ' or friction

factor 'm' although neither method is entirely satisfactory.

12) The size of the peak height at the start of extrusion is alloy dependent increasing with Cu content and Z. The peak height during indirect extrusion is smaller. Both observations are consistent with the hypothesis that the peak is associated with the establishment of the quasi-static deformation zone, the formation of which requires an excess of dislocations.

13) A general pressure equation incorporating the hot working constants and hence flow stress characteristics has been established for constant billet length data. Inclusion of a billet dimension term has met with limited success in the 2000 series alloys due to the difficulty in defining the friction conditions.

14) Relationships describing the dependence of surface cracking on initial extrusion conditions show that surface cracking is least during indirect extrusion and may be reduced by a presolution soak treatment of 2 hours at 500 deg.C, which corresponds to the maximum increase in flow stress during torsion testing and increase in extrusion pressure.

15) The press quenched extrudes exhibit a fibrous structure at high Z and duplex structure at low Z, peripheral recrystallization increasing with copper content and extrusion temperature. Indirect extrusion of 2014 alloy reduces the percentage recrystallization the presolution soak treatment results in an increase.

16) The steady state extrusion and torsion specimens are characterized by a subgrain structure of low misorientation consistent with the operation of dynamic recovery. The

presolution soak treatment results in a less recovered substructure at high Z.

17) For all the alloys and heat treatments the subgrain size d may be related to the process conditions by:

$$d^{-1} = aLnZ_c + b$$

18) The dependence of flow stress on the subgrain size must include the influence of the solute atom atmospheres and the second phase particle distribution which also act as sources of internal stress.

19) The steady state flow pattern for indirect extrusion is noticeably different to that for direct due to the absence of billet container friction during extrusion.

20) The variation in substructure within the steady direct and indirect deformation zone results in a more uniform substructure across and along the indirect extrudate.

21) All the solution treated 2000 series alloys extruded above an initial flow stress of 90 MN/m^2 are fully recrystallized, peripheral recrystallization decreasing with flow stress. Indirect extrusion and the presolution soak treatment reduce the percentage recrystallization in the 2014 alloy. The increase in recrystallized grain size with extrusion temperature can also be directly related to the increase in subgrain size.

22) The effect of artificial ageing on the solution treated 2014 alloy is to produce transition precipitates. In the low Z partially recrystallized extrudes the presence of a retained substructure provides sites for preferential precipitation. Artificial ageing of the high extrusion temperature press quenched extrudes results in a pronounced

ageing reaction which is enhanced by the presolution soak treatment.

23) The hardness and tensile properties of the T1 extrudes are governed at low Z conditions by solute strengthening and natural ageing and at high Z by substructure strengthening.

25) The T6 tensile and fracture toughness properties of the 2014 alloy are enhanced by the presence of a retained substructure in the low Z extrudes.

26) The tensile and fracture toughness properties of the high temperature T5 2014 extrudes are superior to the high Z recrystallized T6 extrudes. The presolution soak treatment enhances the T5 temper properties.

27) The indirect process offers the highest T6 properties due to an increase in grain boundary strengthening at high Z and substructure strengthening at low Z.

28) The T6 and T5 peak aged stress corrosion resistance of the 2014 alloy is likely to be enhanced by the presence of a retained substructure.

29) Limit diagrams show that at high and low ram speeds indirect extrusion of 2014 enlarges the extrusion range, the presolution soak treatment reducing surface cracking in the mid temperature range.

30) An increase in copper content in the 2000 series alloys reduces the extrusion range.

RECOMMENDATIONS FOR FURTHER WORK

Torsion:

Experimental verification of the temperature rise during testing is required to establish the correct mean temperature. The surface temperature rise could be correlated with the temperature rise predicted at the surface and central elements by the finite difference model. The practice of using solid torsion specimens reduces the accuracy of the homologous strain analysis due to the radial variation in strain, thin walled specimens are therefore to be preferred in order to determine realistic values of ε_p.

Extrusion:

The development of a temperature rise model to predict the variation in strain rate and temperature within the deformation zone and hence extrudate is required to utilize the homologous strain constitutive equations and the structure property relationships derived in the present work. It may be possible to achieve this by the development of a thermally coupled upper bound solution or by the application of finite element techniques.

The results in the present work have shown that is possible to establish a general pressure equation incorporating the hot working constants, however further work is required to define an accurate billet dimension term either from a theoretical analysis of friction during extrusion or a comprehensive extrusion matrix including variable billet lengths and diameters at different extrusion ratios. Such an equation may be used to verify the mean temperature rise during extrusion since the decrease in pressure is a function of the increase in temperature and

decrease in friction.

The presolution soak treatment has been applied to the direct extrusion of homogenized 2014. It may be useful to establish whether this treatment is effective during indirect extrusion and to other heat treatable alloys, and for as cast billets so that a separate homogenization treatment can be eliminated.

Structures:

The variation of hot worked structure with homologous strain has yet to be established and the true dependence in of flow stress on subgrain size in relation to the total dislocation density.

The recrystallization behaviour of solution treated 2014 is clearly dependent on the process conditions, extrusion mode, billet preheat treatment and container temperature. Further work is required to establish the recrystallization mechanism and determine the optimum process conditions and billet preheat treatment to prevent recrystallization or reduce the recyrstallized grain size after solution treating and ageing.

The effect of a retained substructure on the over and under aged T6 and T5 microstructures has yet to be established to investigate the effects of preferential precipitation at the subgrain boundaries.

The effect of the presolution soak treatment on the second phase particle distribution in heat treatable alloys should be investigated to establish whether the larger as cast particles can be reduced in size to enhance the mechanical properties.

Mechanical Properties:

The effect of a retained substructure, billet preheat treatment and extrusion mode on the ageing characteristics in the T6 and T5 tempers requires further investigation in relation to the tensile, fracture toughness and corrosion properties in order to determine the effect of process conditions on the under and overaged properties.

The presolution soak treatment demonstrates the possibility of developing thermomechanical processing treatments specifically for extrusion. The mechanical properties of the 2014 alloy may also be further improved in the presence of a retained substructure by a worked and aged treatment such as the T8 temper.

The difference in properties in the longitudinal and transverse directions should be considered especially in relation to the fracture toughness and corrosion properties. The S.C.C. may also be more conveniently determined from slow strain rate stress corrosion cracking tests as described in ref. 161.

The effect of processing conditions and ageing on the fatigue properties of 2014 have yet to be established.

APPENDIX I

Torsion Results

The experimental torque, twist rate and temperature results are listed on the following pages. The mean equivalent strain rates and peak stresses evaluated from the temperature corrected hot worked constants shown in section 4.1.2. are also included. The key for the test codes is as follows:

First number:	1 to 5	-	denotes the wht%Cu
Second number:	1 to 5	-	denotes the temperature range
Third number:	1 to 5	-	denotes the strain rate range
Fourth number:	1 to 3	-	repeat test if carried out

1% Cu

CODE	INITIAL TEMP DEG.C	TWIST RATE REV/S	STRAIN RATE 1/S	PEAK STRESS MN/M2	HOMOLOGOUS STRAINS 1.00H TORQUE NM	1.00H TEMP DEG.C	0.75H TORQUE NM	0.75H TEMP DEG.C	0.50H TORQUE NM	0.50H TEMP DEG.C	STRAIN TO PEAK
11-1	295.0	.016	.029	60.86	9.15	295.0	9.04	295.0	8.81	295.0	.69
11-2	295.0	.168	.303	80.46	11.33	297.0	11.33	297.0	11.21	297.0	.47
11-3	295.0	1.540	2.778	93.41	14.62	313.0	14.56	311.0	13.50	308.0	.45
11-4	295.0	4.690	8.459	107.00	15.85	308.0	15.61	305.0	15.03	302.0	.62
11-5	295.0	14.410	25.990	115.18	17.02	314.0	16.67	309.0	15.73	306.0	.73
12-1	355.0	.016	.029	39.41	6.95	355.0	6.86	355.0	6.54	355.0	.54
12-2	355.0	.168	.303	55.41	7.18	356.0	7.03	356.0	6.89	356.0	.46
12-31	355.0	1.570	2.832	72.15	9.67	361.0	9.53	359.0	9.24	358.0	.43
12-32	355.0	1.560	2.814	71.70	9.59	362.0	9.47	360.0	9.30	359.0	.54
12-5	355.0	14.540	26.225	91.18	12.60	365.0	12.05	362.0	10.73	360.0	.46
13-1	415.0	.016	.029	26.45	3.87	415.0	3.56	415.0	3.59	415.0	.81
13-2	415.0	.168	.303	38.45	4.74	416.0	4.74	416.0	4.65	416.0	.43
13-3	415.0	1.580	2.850	52.58	7.46	420.0	7.35	419.0	7.00	418.0	.56
13-4	415.0	4.820	8.694	60.43	8.29	423.0	8.15	421.0	7.92	419.0	.81
13-5	415.0	14.940	26.946	65.04	9.99	439.0	9.62	434.0	9.24	428.0	1.72
14-11	475.0	.016	.029	18.62	2.65	475.0	2.62	475.0	2.54	475.0	.86
14-12	475.0	.016	.029	18.62	2.46	475.0	2.22	475.0	2.17	475.0	.64
14-2	475.0	.169	.305	27.58	3.73	476.0	3.70	475.0	3.67	475.0	.81
14-3	475.0	1.540	2.778	39.15	5.33	477.0	5.30	476.0	5.26	476.0	.23
14-4	475.0	4.730	8.531	45.57	7.18	481.0	7.06	480.0	6.83	478.0	.62
14-51	475.0	15.000	27.055	52.95	8.24	485.0	8.04	482.0	7.52	480.0	.80
14-52	475.0	15.230	27.469	53.30	7.98	484.0	7.92	481.0	7.52	480.0	.69

2% Cu

CODE	INITIAL TEMP DEG.C	TWIST RATE REV/S	STRAIN RATE 1/S	PEAK STRESS MN/M2	HOMOLOGOUS STRAINS 1.00H TORQUE NM	1.00H TEMP DEG.C	0.75H TORQUE NM	0.75H TEMP DEG.C	0.50H TORQUE NM	0.50H TEMP DEG.C	STRAIN TO PEAK
21-1	280.0	.014	.025	76.23	11.21	280.0	11.09	280.0	10.97	280.0	.40
21-21	280.0	.167	.301	103.59	14.64	282.0	14.52	282.0	14.14	282.0	.25
21-22	280.0	.166	.299	102.79	15.41	283.0	15.25	283.0	15.01	283.0	.87
21-2	280.0	1.440	2.597	124.73	18.69	290.0	18.50	288.0	17.82	286.0	.45
21-41	280.0	4.570	8.243	137.42	23.11	293.0	22.68	291.0	22.18	288.0	.46
21-5	280.0	14.930	26.928	147.00	22.80	301.0	22.55	296.0	21.56	292.0	.59
22-1	339.0	.014	.025	46.06	6.09	339.0	6.09	339.0	5.84	339.0	.10
22-3	339.0	.166	.299	68.02	9.59	340.0	9.41	340.0	8.89	340.0	.18
22-31	339.0	1.460	2.633	89.72	12.71	344.0	12.46	343.0	12.27	342.0	.25
22-32	339.0	1.470	2.651	89.80	13.30	344.0	12.96	343.0	12.46	342.0	.28
22-33	339.0	1.450	2.615	90.21	12.02	343.0	11.96	342.0	11.78	341.0	.24
22-4	339.0	4.700	8.477	103.11	13.96	345.0	13.71	344.0	13.21	343.0	.26
22-5	339.0	15.290	27.578	113.61	15.30	352.0	15.08	349.0	14.33	346.0	.45
23-1	398.0	.014	.025	28.54	4.47	399.0	4.38	399.0	4.16	398.0	.24
23-21	398.0	.166	.299	44.44	6.56	399.0	6.52	399.0	6.24	398.0	.12
23-22	398.0	.166	.299	44.44	6.65	399.0	6.58	399.0	6.38	399.0	.17
23-3	398.0	1.500	2.705	63.30	9.19	400.0	9.00	400.0	8.54	399.0	.16
23-41	398.0	4.730	8.531	73.38	10.62	404.0	10.56	403.0	10.28	401.0	.38
23-42	398.0	4.730	8.531	72.96	10.25	405.0	10.12	403.0	10.00	402.0	.43
23-5	398.0	15.430	27.830	81.54	11.21	415.0	11.12	411.0	10.84	408.0	.91
24-11	458.0	.014	.025	18.86	2.48	458.0	2.42	458.0	2.33	458.0	.02
24-12	458.0	.014	.025	18.86	2.64	458.0	2.42	458.0	2.36	458.0	.07
24-2	458.0	.168	.303	30.04	4.84	458.0	4.78	458.0	4.53	458.0	.03
24-3	458.0	1.510	2.723	44.18	6.43	459.0	6.37	459.0	6.09	459.0	.13
24-4	458.0	4.760	8.585	52.99	7.95	461.0	7.89	460.0	7.83	460.0	.25
24-5	458.0	15.430	27.830	63.24	9.28	463.0	9.19	463.0	8.94	461.0	.36
25-1	483.0	.014	.025	16.09	1.46	483.0	1.43	483.0	1.38	483.0	.03
25-3	483.0	1.490	2.687	38.13	5.98	484.0	5.72	484.0	5.32	483.0	.07
25-5	483.0	15.570	28.083	55.05	8.07	490.0	7.94	489.0	7.27	487.0	.52

3% Cu

CODE	INITIAL TEMP DEG.C	TWIST RATE REV/S	STRAIN RATE 1/S	PEAK STRESS MN/M2	HOMOLOGOUS STRAINS 1.00H TORQUE NM	1.00H TEMP DEG.C	0.75H TORQUE NM	0.75H TEMP DEG.C	0.50H TORQUE NM	0.50H TEMP DEG.C	STRAIN TO PEAK
31-1	280.0	.013	.023	80.27	12.58	280.0	12.21	280.0	10.96	280.0	.09
31-21	280.0	.166	.299	110.42	16.45	282.0	16.07	282.0	14.33	281.0	.14
31-22	280.0	.166	.299	110.42	17.82	282.0	17.49	282.0	16.76	282.0	.23
31-3	280.0	1.380	2.489	135.21	19.69	287.0	19.25	286.0	17.07	284.0	.29
31-41	280.0	4.460	8.044	150.02	21.56	289.0	20.81	287.0	17.44	285.0	.27
31-42	280.0	4.510	8.134	149.40	22.30	290.0	21.68	288.0	18.62	286.0	.32
31-5	280.0	14.400	25.972	154.35	24.70	305.0	23.84	299.0	21.49	295.0	.73
32-1	339.0	.014	.025	50.17	6.89	339.0	6.71	339.0	6.43	339.0	.42
32-2	339.0	.166	.299	73.44	9.66	341.0	9.36	341.0	9.16	340.0	.25
32-31	339.0	1.440	2.597	97.91	12.46	343.0	12.34	342.0	11.90	341.0	.20
32-32	339.0	1.440	2.597	98.49	11.52	342.0	11.34	341.0	10.22	341.0	.16
32-33	339.0	1.460	2.633	96.35	13.26	346.0	13.08	344.0	13.08	343.0	.38
32-4	339.0	4.640	8.369	111.81	14.58	345.0	14.20	343.0	14.20	342.0	.23
32-5	339.0	14.650	26.423	118.73	16.01	359.0	15.82	354.0	14.58	351.0	.73
33-1	398.0	.014	.025	32.09	4.88	398.0	4.72	398.0	4.56	398.0	.12
33-21	398.0	.166	.299	49.76	7.41	398.0	7.26	399.0	7.11	398.0	.23
33-22	398.0	.166	.299	49.43	6.71	399.0	6.58	399.0	5.96	399.0	.10
33-3	398.0	1.460	2.633	69.43	9.44	401.0	9.31	400.0	9.06	400.0	.23
33-41	398.0	4.690	8.459	81.56	11.36	403.0	11.23	402.0	9.99	400.0	.25
33-42	398.0	4.780	8.621	80.45	11.70	406.0	11.23	404.0	8.81	403.0	.27
34-11	458.0	.014	.025	21.50	2.55	458.0	2.51	458.0	2.44	458.0	.07
34-12	458.0	.014	.025	21.50	3.28	458.0	3.21	458.0	3.08	458.0	.10
34-2	458.0	.170	.307	34.21	5.06	458.0	4.88	458.0	4.71	458.0	.83
34-3	458.0	1.480	2.669	49.82	8.32	459.0	8.25	459.0	8.15	459.0	.13
34-4	458.0	4.750	8.567	59.17	9.70	463.0	9.44	462.0	8.81	461.0	.38
34-5	458.0	15.460	27.884	68.80	10.39	470.0	9.81	467.0	8.76	464.0	.73
35-1	483.0	.014	.025	18.50	1.70	483.0	1.65	483.0	1.64	483.0	.52
35-3	483.0	1.520	2.742	43.65	7.00	484.0	6.95	484.0	6.26	484.0	.10
35-5	483.0	16.430	29.634	62.16	9.32	493.0	9.26	491.0	9.07	489.0	.73

2% Cu

CODE	INITIAL TEMP DEG.C	TWIST RATE REV/S	STRAIN RATE 1/S	PEAK STRESS MN/M2	HOMOLOGOUS STRAINS 1.00H TORQUE NM	1.00H TEMP DEG.C	0.75H TORQUE NM	0.75H TEMP DEG.C	0.50H TORQUE NM	0.50H TEMP DEG.C	STRAIN TO PEAK
51-2	295.0	.052	.094	104.53	15.08	296.0	14.73	296.0	13.68	296.0	.46
51-3	295.0	1.500	2.705	146.17	21.19	304.0	21.01	302.0	20.54	300.0	.43
51-42	295.0	4.630	8.351	157.19	22.85	312.0	22.73	308.0	21.91	304.0	.62
51-41	295.0	4.360	7.864	159.02	23.10	308.0	22.82	306.0	20.52	302.0	.47
51-5	295.0	14.910	26.892	171.10	26.67	317.0	26.32	312.0	24.68	308.0	.64
51-1	295.0	.017	.031	90.74	13.60	295.0	13.54	295.0	12.90	295.0	.64
52-1	355.0	.017	.031	60.97	8.97	355.0	8.91	355.0	8.71	355.0	.76
52-2	355.0	.052	.094	72.32	10.50	356.0	10.41	356.0	10.24	356.0	.48
52-32	355.0	1.527	2.754	111.46	15.53	362.0	15.39	361.0	14.90	359.0	.46
52-31	355.0	1.527	2.754	110.93	14.91	363.0	14.85	363.0	14.26	360.0	.54
52-33	355.0	1.527	2.754	109.89	15.42	365.0	15.24	364.0	14.77	361.0	.73
52-4	355.0	4.670	8.423	124.75	18.13	366.0	18.01	364.0	17.43	361.0	.51
52-5	355.0	14.910	26.892	135.84	20.26	376.0	19.97	371.0	19.26	366.0	.81
53-1	415.0	.017	.031	42.02	6.53	415.0	6.48	415.0	6.33	415.0	.81
53-21	415.0	.052	.094	51.08	7.91	415.0	7.79	415.0	6.53	415.0	.13
53-22	415.0	.052	.094	51.08	7.81	415.0	7.75	415.0	7.55	415.0	.72
53-3	415.0	1.560	2.814	85.10	12.79	420.0	12.73	419.0	12.24	418.0	.43
53-42	415.0	4.710	8.495	97.31	14.31	424.0	14.17	422.0	13.39	420.0	.54
53-41	415.0	4.670	8.423	96.37	14.48	426.0	14.20	424.0	13.79	421.0	.68
53-5	415.0	15.320	27.632	110.36	15.99	430.0	15.85	427.0	15.47	423.0	.71
54-12	475.0	.016	.029	29.78	4.40	475.0	4.33	475.0	4.08	475.0	.66
54-2	475.0	.051	.092	36.86	5.47	475.0	5.40	475.0	5.04	475.0	.68
54-3	475.0	1.560	2.814	64.79	9.43	480.0	9.37	479.0	9.14	478.0	.54
54-4	475.0	4.710	8.495	76.24	11.26	482.0	10.91	481.0	10.66	479.0	.54
54-52	475.0	14.400	25.972	88.91	12.94	484.0	12.83	482.0	12.08	480.0	.51
54-51	475.0	16.060	28.966	88.91	12.78	488.0	12.67	485.0	12.54	482.0	.74
54-11	475.0	.031	.056	33.65	4.23	475.0	4.22	475.0	4.10	475.0	.73

4% Cu (Binary)

CODE	INITIAL TEMP DEG.C	TWIST RATE REV/S	STRAIN RATE 1/S	PEAK STRESS MN/M2	HOMOLOGOUS STRAINS 1.00H TORQUE NM	1.00H TEMP DEG.C	0.75H TORQUE NM	0.75H TEMP DEG.C	0.50H TORQUE NM	0.50H TEMP DEG.C	STRAIN TO PEAK
41-1	300.0	.018	.032	50.23	7.62	300.0	7.50	300.0	7.27	300.0	.74
41-12	300.0	.018	.032	50.23	6.86	300.0	6.80	300.0	6.62	300.0	.36
41-3	300.0	1.390	2.507	93.13	13.62	303.0	13.26	303.0	12.29	301.0	.58
41-51	300.0	15.950	28.768	115.85	17.07	311.0	16.24	309.0	14.33	306.0	.49
41-52	300.0	15.770	28.443	115.23	17.19	312.0	16.72	310.0	15.28	307.0	.46
42-11	350.0	.018	.032	32.69	4.55	350.0	4.18	350.0	3.94	350.0	.43
42-12	350.0	.018	.032	32.69	5.82	350.0	5.58	350.0	4.52	350.0	.27
42-3	350.0	1.460	2.633	69.46	9.51	357.0	9.30	356.0	8.88	354.0	.61
42-51	350.0	15.770	28.443	93.45	13.25	360.0	12.30	358.0	10.63	356.0	.40
42-52	350.0	15.770	28.443	93.45	13.37	360.0	12.06	358.0	10.15	356.0	.46
43-1	390.0	.018	.032	23.37	3.15	390.0	3.02	390.0	2.74	390.0	.61
43-2	390.0	.169	.305	38.05	4.87	391.0	4.75	391.0	4.57	390.0	.53
43-3	390.0	1.480	2.669	55.83	7.31	395.0	7.13	394.0	6.89	393.0	.57
43-4	390.0	4.750	8.567	66.65	10.32	397.0	9.96	395.0	9.72	394.0	.47
43-5	390.0	16.150	29.129	78.27	11.58	400.0	11.10	398.0	9.79	395.0	.46
44-1	430.0	.018	.032	17.06	2.67	430.0	2.59	430.0	2.48	430.0	.64
44-2	430.0	.169	.305	28.67	3.74	431.0	3.71	431.0	3.53	431.0	.31
44-31	430.0	1.490	2.687	44.64	5.95	433.0	5.89	433.0	5.62	432.0	.40
44-32	430.0	1.490	2.687	44.64	6.46	433.0	6.34	433.0	6.22	432.0	.38
44-4	430.0	4.750	8.567	54.28	7.25	436.0	6.89	434.0	6.10	433.0	.46
44-5	430.0	16.340	29.472	66.40	9.83	436.0	9.36	434.0	7.99	434.0	.54
45-1	475.0	.018	.032	12.34	1.73	475.0	1.69	475.0	1.63	475.0	.71
45-2	475.0	.172	.310	21.26	2.68	476.0	2.63	475.0	2.59	475.0	.63
45-3	475.0	1.530	2.760	34.64	4.83	477.0	4.71	476.0	4.59	476.0	.22
45-4	475.0	4.750	8.567	43.41	6.70	478.0	6.65	478.0	6.40	477.0	.36
45-5	475.0	16.340	29.472	54.00	8.55	480.0	8.34	479.0	7.93	478.0	.36

4% Cu-2014 SS Tests

CODE	INITIAL TEMP DEG.C	TWIST RATE REV/S	STRAIN RATE 1/S	PEAK STRESS MN/M2	HOMOLOGOUS STRAINS 1.00H TORQUE NM	1.00H TEMP DEG.C	0.75H TORQUE NM	0.75H TEMP DEG.C	0.50H TORQUE NM	0.50H TEMP DEG.C	STRAIN TO PEAK
41-12	275.0	.018	.032	132.59	19.08	275.0	19.08	275.0	18.83	275.0	.52
41-3	275.0	1.390	2.507	184.51	27.97	287.0	27.18	284.0	24.82	282.0	.35
41-51	275.0	14.360	25.900	213.24	32.38	294.0	32.06	290.0	29.82	285.0	.36
41-52	275.0	14.360	25.900	213.24	29.01	294.0	28.14	290.0	25.40	285.0	.38
42-1	330.0	.016	.029	85.27	12.04	330.0	11.80	330.0	10.73	330.0	.08
42-2	330.0	.169	.305	113.91	15.92	331.0	15.75	331.0	13.82	331.0	.08
42-4	330.0	4.430	7.990	150.97	23.71	342.0	21.50	339.0	17.90	336.0	.36
42-5	330.0	14.930	26.928	172.42	26.68	338.0	26.81	336.0	25.17	334.0	.18
43-1	390.0	.018	.032	54.65	8.60	390.0	8.38	390.0	7.88	390.0	.06
43-31	390.0	1.490	2.687	99.05	13.63	394.0	13.39	394.0	12.17	392.0	.22
43-32	390.0	1.660	2.994	99.21	14.00	396.0	13.24	394.0	12.17	393.0	.29
43-5	390.0	15.810	28.516	123.32	16.08	405.0	15.60	403.0	14.40	398.0	.52
44-1	430.0	.019	.034	42.84	5.50	425.0	5.43	425.0	5.30	425.0	.36
44-22	430.0	.169	.305	59.75	8.36	426.0	7.91	426.0	7.60	426.0	.23
44-3	430.0	1.540	2.778	81.14	11.64	428.0	11.27	427.0	8.86	427.0	.16
44-41	430.0	4.560	8.225	90.18	13.95	435.0	13.93	433.0	13.87	431.0	.54
44-42	430.0	4.580	8.261	93.31	14.18	429.0	13.93	428.0	13.29	427.0	.18
44-5	430.0	15.240	27.488	105.11	15.06	435.0	14.58	433.0	13.38	430.0	.40
45-11	450.0	.018	.032	35.84	5.41	450.0	5.42	450.0	5.33	450.0	.02
45-12	450.0	.018	.032	35.84	4.80	450.0	4.79	450.0	4.66	450.0	.03
45-3	450.0	1.500	2.705	69.77	11.17	453.0	10.78	452.0	9.51	451.0	.18
45-51	450.0	15.370	27.722	94.87	13.33	455.0	12.73	454.0	9.04	452.0	.18
45-52	450.0	14.960	26.982	93.08	12.98	458.0	12.62	457.0	11.20	455.0	.36

APPENDIX II

Extrusion Results

The experimental results and calculations for all the extrusion runs are presented on the following pages. The key for the run codes is as follows.

First letter:
- D - Direct
- I - Indirect

Second number:
- 1 to 5 - denotes the wht%Cu

Third number:
- 1 to 5 - denotes the temperature range

Fourth number:
- 1 to 5, 7, 10 or 15 - denotes the extrusion ratio

Last symbols, if any:
- L1 to L5 - billet length variation runs
- A - air circulating furnace heated
- AS - presolution soak extrudes
- CT1 to CT6 - variable liner temperature runs

1%Cu

RUN CODES	EXT RATIO	FURNACE TEMP	INITIAL TEMP	PEAK TEMP	FINAL TEMP	BILLET LENGTH	CTNR TEMP	RAM SPEED	STRAIN RATE	MAX PRESSURE	MIN PRESSURE	MAX OIL PRESSURE	MIN OIL PRESSURE	PEAK DELTAP
		DEG.C	DEG.C	DEG.C	DEG.C	MMS	DEG.C	MMS/S	SEC^{-1}	MN/M^2	MN/M^2	MN/M^2	MN/M^2	MN/M
D1522	20.0	500.0	495.0	496.2	530.5	95.0	450.0	3.7	2.33	338.64	280.97	375.88	297.73	0
D1422	20.0	450.0	445.0	448.1	500.8	95.0	400.0	3.6	2.27	436.16	390.99	491.32	392.72	4.69
D1332	20.0	400.0	397.0	401.3	485.5	95.0	360.0	7.1	4.47	522.32	444.26	566.08	462.56	11.05
D1232	20.0	350.0	348.0	354.1	442.0	95.0	300.0	7.2	4.53	604.55	441.02	649.27	448.08	35.18
D1162	20.0	300.0	298.0	309.7	458.2	95.0	260.0	13.1	8.24	854.25	637.44	890.41	649.99	41.05
D1062	20.0	250.0	246.0	259.4	435.9	95.0	200.0	13.4	8.43	1053.22	688.40	1122.20	686.65	0
D1553	30.0	500.0	495.0	497.7	562.7	95.0	440.0	11.4	10.43	354.39	398.40	485.67	404.74	5.86
D1443	30.0	450.0	445.0	447.0	524.6	95.0	390.0	8.4	7.68	488.97	398.86	514.63	402.38	0
D1343	30.0	400.0	396.0	401.3	494.7	95.0	350.0	8.1	7.41	577.45	474.84	612.30	479.30	11.73
D1243	30.0	350.0	348.0	355.8	452.3	95.0	300.0	8.2	7.50	655.74	453.30	728.55	485.67	52.78
D114[illegible]	30.0	300.0	298.0	311.6	448.9	95.0	250.0	7.9	7.23	881.35	662.46	936.73	670.73	49.84
D154[illegible]	50.0	500.0	495.0	498.5	580.5	95.0	450.0	7.8	11.52	487.35	444.26	508.78	445.20	5.86
D1445	50.0	450.0	445.0	449.6	545.1	95.0	400.0	7.9	11.66	560.08	498.00	601.31	508.78	11.73
D1345	50.0	400.0	397.0	402.7	508.0	95.0	360.0	7.8	11.52	634.66	498.00	670.73	518.63	17.59
D1245	50.0	350.0	348.0	356.2	482.9	95.0	305.0	7.8	11.52	771.79	589.26	809.48	601.31	41.05
D1145	50.0	300.0	298.0	310.1	460.1	95.0	255.0	7.9	11.66	916.09	688.86	991.57	696.72	0
D14510	100.0	450.0	445.0	451.0	568.8	95.0	400.0	10.5	31.66	673.81	523.25	716.95	526.13	64.73
D13510	100.0	400.0	396.0	402.8	538.1	95.0	350.0	10.4	31.36	759.05	592.27	793.25	597.30	64.73
D12510	100.0	350.0	298.0	306.2	473.1	95.0	300.0	10.0	30.15	858.42	660.37	948.23	685.01	70.59
D13615	150.0	400.0	395.0	406.0	563.2	95.0	350.0	12.6	56.17	867.45	676.82	924.81	687.78	11.80
D14615	150.0	450.0	442.0	451.9	599.4	95.0	400.0	12.6	56.17	776.42	676.82	818.52	651.43	11.80
D15615	150.0	500.0	491.0	497.7	613.9	95.0	450.0	12.4	55.28	613.35	549.65	690.76	551.91	0
D1134	40.0	325.0	323.0	332.9	487.6	95.0	270.0	6.7	8.01	851.93	0	921.94	0	
D1334	40.0	400.0	396.0	403.4	514.7	95.0	350.0	6.7	8.01	638.60	0	683.16	0	
D1534	40.0	480.0	475.0	479.0	563.3	95.0	430.0	6.7	8.01	495.45	0	543.28	0	
I1124A	40.0	325.0	323.0	334.2	400.3	95.0	275.0	4.8	7.90	599.45	0	705.34	0	

RUN CODES	INITIAL Z	LOG Z 1	PEAK Z	LOG Z F	FINAL Z	LOG Z F	INITIAL FLOW STRESS MN/M^2	PEAK FLOW STRESS MN/M^2	FINAL FLOW STRESS MN/M^2	EXTRUDE QUALITY
D1522	.26923E+11	24.02	.25979E+11	23.98	.96605E+10	22.99	34.85	34.65	29.53	A
D1422	.13152E+12	25.60	.11842E+12	25.50	.22036E+11	23.82	44.57	43.87	33.75	A
D1332	.15314E+13	28.06	.12918E+13	27.89	.69101E+11	24.96	63.06	61.66	40.41	A
D1232	.12628E+14	30.17	.95747E+13	29.89	.29151E+12	26.40	81.72	79.15	50.13	A
D1162	.28250E+15	33.27	.15124E+15	32.65	.30561E+12	26.45	112.09	105.80	50.47	A
D1062	.65607E+16	36.42	.27683E+16	35.56	.67239E+12	27.23	144.52	135.53	56.43	A
D1553	.12056E+12	25.52	.11115E+12	25.43	.18430E+11	23.64	43.99	43.46	32.80	A
D1443	.44602E+12	26.82	.41604E+12	26.75	.37556E+11	24.35	53.28	52.75	36.74	A
D1343	.26420E+13	28.60	.21414E+13	28.39	.86398E+11	25.18	67.67	65.88	41.82	A
D1243	.20902E+14	30.67	.14636E+14	30.31	.33974E+12	26.55	86.45	83.09	51.25	A
D1143	.24761E+15	33.14	.11996E+15	32.42	.36678E+12	26.63	110.76	103.48	51.81	A
D1545	.13314E+12	25.61	.11990E+12	25.51	.13081E+11	23.29	44.65	43.96	31.03	A
D1445	.67703E+12	27.24	.57760E+12	27.08	.32622E+11	24.21	56.48	55.25	35.93	A
D1345	.39465E+13	29.00	.31603E+13	28.78	.90546E+11	25.23	71.17	69.22	42.12	A
D1245	.32090E+14	31.10	.22067E+14	30.73	.19269E+12	25.98	90.55	86.97	47.18	A
D1145	.39964E+15	33.62	.20942E+15	32.98	.40659E+12	26.73	115.61	109.07	52.58	A
D14510	.18376E+13	28.24	.14964E+13	28.03	.47977E+11	24.59	64.59	62.87	38.18	A
D13510	.11181E+14	30.05	.85690E+13	29.78	.10596E+12	25.39	80.59	78.14	43.14	A
D12510	.10331E+16	34.57	.66488E+15	34.13	.68755E+12	27.26	125.34	120.81	56.60	A
D13615	.20843E+14	30.67	.13519E+14	30.24	.98125E+11	25.31	86.43	82.35	42.64	A
D14615	.36179E+13	28.92	.25774E+13	28.58	.40570E+11	24.43	70.40	67.46	37.19	A
D15615	.72154E+12	27.30	.58876E+12	27.10	.28605E+11	24.08	56.98	55.40	35.19	A
D1134	.74287E+14	31.94	.45632E+14	31.45	.11622E+12	25.48	98.73	93.96	43.75	A
D1334	.28574E+13	28.68	.21348E+13	28.39	.51868E+11	24.67	68.35	65.85	38.65	A
D1534	.17214E+12	25.87	.15159E+12	25.74	.13959E+11	23.36	46.40	45.53	31.36	A
I1124A	.73245E+14	31.92	.42324E+14	31.38	.23735E+13	28.50	98.60	93.23	66.76	A

2%Cu

RUN CODES	EXT RATIO	FURNACE TEMP	INITIAL TEMP	PEAK TEMP	FINAL TEMP	BILLET LENGTH	CTNR TEMP	RAM SPEED	STRAIN RATE	MAX PRESSURE	MIN PRESSURE	MAX OIL PRESSURE	MIN OIL PRESSURE	PEAK DELTAP
		DEG.C	DEG.C	DEG.C	DEG.C	MMS	DEG.C	MMS/S	SEC^{-1}	MN/M^2	MN/M^2	MN/M^2	MN/M^2	MN/M
D2321	10.0	400.0	395.0	398.0	443.7	95.0	350.0	3.1	1.52	429.44	370.61	506.52	419.32	0
D2522	20.0	500.0	487.0	489.2	536.2	95.0	450.0	3.9	2.45	365.97	349.99	455.89	402.38	8.57
D2422	20.0	450.0	442.0	445.5	492.4	95.0	400.0	3.9	2.45	411.84	338.41	506.52	391.18	11.28
D2342	20.0	400.0	395.0	401.4	481.3	95.0	350.0	6.5	4.09	550.12	447.04	661.29	484.03	38.12
D2252	20.0	350.0	345.0	353.6	460.4	95.0	300.0	9.0	5.66	679.60	511.90	754.13	551.50	49.62
D2162	20.0	300.0	295.0	305.1	439.9	95.0	250.0	12.5	7.87	797.27	582.55	928.61	630.37	64.50
D2062	20.0	250.0	247.0	258.0	436.8	95.0	200.0	13.1	8.24	1044.41	691.41	1125.59	675.36	0
D2543	30.0	500.0	493.0	495.9	560.1	95.0	450.0	7.7	7.04	420.64	353.00	453.01	360.17	17.14
D2443	30.0	450.0	442.0	447.2	528.7	95.0	400.0	7.6	6.95	523.48	428.51	557.15	427.75	21.88
D2353	30.0	400.0	395.0	405.3	507.3	95.0	350.0	10.2	9.33	648.56	500.32	725.99	506.52	0
D2253	30.0	350.0	345.0	356.8	474.9	95.0	300.0	9.9	9.06	729.63	579.07	808.04	681.00	0
D2163	30.0	300.0	294.0	309.1	464.4	95.0	250.0	11.5	10.52	929.53	691.41	1007.38	675.36	0
D2545	50.0	500.0	493.0	497.0	577.1	95.0	450.0	7.5	11.07	494.30	429.44	537.43	444.59	15.79
D2455	50.0	450.0	442.0	448.9	548.3	95.0	400.0	9.8	14.47	592.97	482.48	709.14	521.31	29.32
D2345	50.0	400.0	395.0	402.8	515.4	95.0	350.0	9.7	14.32	673.58	529.50	748.48	560.02	41.95
D2255	50.0	350.0	347.0	358.7	489.8	95.0	250.0	10.0	14.76	835.48	688.40	894.83	703.49	62.93
D2155	50.0	300.0	295.0	303.9	475.9	95.0	250.0	10.7	15.80	964.96	711.79	1035.52	771.07	87.96
D24610	100.0	450.0	441.0	451.0	580.0	95.0	400.0	12.2	36.78	712.03	600.15	768.20	610.65	57.29
D23610	100.0	400.0	395.0	403.1	550.3	95.0	350.0	11.9	35.88	817.88	617.75	877.98	6[illegible].44	45.33
D22610	100.0	350.0	347.0	359.0	519.5	95.0	300.0	11.6	34.97	900.11	706.00	984.89	731.63	68.79
D21610	100.0	300.0	295.0	305.4	489.3	95.0	250.0	11.6	34.97	988.36	776.65	1103.10	799.21	0
D23615	150.0	400.0	396.0	409.6	573.7	95.0	350.0	12.5	55.72	941.34	691.41	984.89	683.78	57.51
D24615	150.0	450.0	443.0	454.6	599.5	95.0	400.0	12.4	55.28	804.68	652.96	832.90	649.99	23.00
D214L1	30.0	300.0	296.0	310.1	426.8	60.2	250.0	8.3	7.59	811.86	664.77	906.12	699.59	0
D214L2	30.0	300.0	296.0	309.4	434.5	75.7	250.0	8.1	7.41	834.79	644.16	906.12	681.00	0
D214L3	30.0	300.0	297.0	310.4	443.9	90.5	250.0	8.4	7.68	908.91	582.55	1010.26	596.58	85.93
D214L4	30.0	300.0	297.0	310.9	449.9	105.3	250.0	7.4	6.77	947.13	594.13	1063.66	602.23	0
D214L5	30.0	300.0	295.0	309.2	456.7	120.4	250.0	8.3	7.59	999.01	553.13	1097.45	619.08	0
D234L1	30.0	400.0	395.0	408.1	483.4	60.4	350.0	7.9	7.23	580.23	529.50	641.57	571.22	0
D234L2	30.0	400.0	395.0	399.4	492.6	75.3	350.0	8.1	7.41	595.98	476.46	642.70	506.52	0
D234L3	30.0	400.0	395.0	400.2	499.3	90.2	350.0	8.0	7.32	617.75	487.11	678.13	489.57	0
D234L4	30.0	400.0	394.0	400.2	504.3	105.3	350.0	8.0	7.32	657.83	473.68	709.14	495.22	0
D234L5	30.0	400.0	395.0	400.7	508.0	120.1	350.0	8.0	7.32	688.40	444.26	745.70	504.87	0
D254L1	30.0	500.0	491.0	494.5	557.2	60.2	450.0	8.0	7.32	420.64	408.82	457.02	427.75	0
D254L2	30.0	500.0	493.0	496.9	561.5	75.0	450.0	8.0	7.32	435.46	382.42	475.60	404.12	0
D254L3	30.0	500.0	491.0	494.9	566.4	90.2	450.0	8.0	7.32	451.68	393.77	514.42	410.80	0
D254L4	30.0	500.0	491.0	494.6	573.1	105.0	450.0	8.0	7.32	488.27	391.22	531.88	410.80	0
D254L5	30.0	500.0	493.0	496.1	573.3	120.2	450.0	8.0	7.32	480.63	370.61	539.17	385.54	0

RUN CODES	INITIAL Z	LOG Z 1	PEAK Z	LOG Z P	FINAL Z	LOG Z F	INITIAL FLOW STRESS 2 MN/M	PEAK FLOW STRESS 2 MN/M	FINAL FLOW STRESS 2 MN/M	EXTRUDE QUALITY
D2321	.13539E+13	27.93	.11970E+13	27.81	.20851E+12	26.06	59.67	58.52	43.77	A
D2522	.78241E+11	25.08	.73074E+11	25.01	.17966E+11	23.61	36.84	36.40	28.19	A
D2422	.35850E+12	26.61	.31663E+12	26.48	.66010E+11	24.91	48.01	47.02	35.74	A
D2342	.36464E+13	28.92	.28101E+13	28.66	.15640E+12	25.78	69.46	66.80	41.64	A
D2252	.46777E+14	31.48	.31033E+14	31.07	.43438E+12	26.80	98.16	93.26	49.59	A
D2162	.89073E+15	34.42	.50490E+15	33.86	.12403E+13	27.85	135.25	127.91	58.85	A
D2062	.18509E+17	37.46	.89226E+16	36.73	.14540E+13	28.01	175.37	165.63	60.35	A
D2543	.18577E+12	25.95	.16947E+12	25.86	.26903E+11	24.02	42.90	42.22	30.37	A
D2443	.10154E+13	27.65	.84454E+12	27.46	.62898E+11	24.86	57.00	55.33	35.43	A
D2353	.83165E+13	29.75	.54734E+13	29.33	.15829E+12	25.79	78.24	73.71	41.73	A
D2253	.74784E+14	31.95	.42767E+14	31.39	.42714E+12	26.78	103.85	97.08	49.45	A
D2163	.12610E+16	34.77	.54457E+15	33.93	.70374E+12	27.28	139.79	128.88	53.71	A
D2545	.29204E+12	26.40	.25775E+12	26.28	.27223E+11	24.03	46.37	45.39	30.43	A
D2455	.21132E+13	28.38	.16538E+13	28.13	.75883E+11	25.05	63.96	61.58	36.64	A
D2345	.12765E+14	30.18	.92846E+13	29.86	.19101E+12	25.98	83.00	79.45	43.11	A
D2255	.11077E+15	32.34	.63991E+14	31.79	.43083E+12	26.79	108.70	101.95	49.52	A
D2155	.17886E+16	35.12	.10857E+16	34.62	.72138E+12	27.30	144.37	137.83	53.93	A
D24610	.55693E+13	29.35	.39078E+13	28.99	.83878E+11	25.15	73.90	70.17	37.30	B
D23610	.31980E+14	31.10	.23033E+14	30.77	.17832E+12	25.91	93.62	89.77	42.60	B
D22610	.26239E+15	33.20	.14929E+15	32.64	.41396E+12	26.75	119.53	112.42	49.19	A
D21610	.39598E+16	35.91	.22163E+16	35.33	.10362E+13	27.67	154.84	147.18	57.19	A
D23615	.47668E+14	31.50	.27551E+14	30.95	.14941E+12	25.73	98.38	91.86	41.31	B
D24615	.77891E+13	29.68	.51651E+13	29.27	.77852E+11	25.08	77.52	73.10	36.81	B
D214L1	.81208E+15	34.33	.37271E+15	33.55	.19369E+13	28.29	134.05	124.01	63.11	A
D214L2	.79251E+15	34.31	.37737E+15	33.56	.14234E+13	27.98	133.74	124.17	60.15	A
D214L3	.77658E+15	34.29	.37125E+15	33.55	.10466E+13	27.68	133.47	123.96	57.28	A
D214L4	.68413E+15	34.16	.31821E+15	33.39	.74539E+12	27.34	131.83	121.99	54.22	A
D214L5	.85961E+15	34.39	.39118E+15	33.60	.66040E+12	27.22	134.79	124.63	53.16	A
D234L1	.64412E+13	29.49	.38002E+13	28.97	.25871E+12	26.28	75.46	69.88	45.42	A
D234L2	.66043E+13	29.52	.55107E+13	29.34	.19766E+12	26.01	75.73	73.79	43.37	A
D234L3	.65227E+13	29.51	.52796E+13	29.29	.15862E+12	25.79	75.59	73.33	41.74	A
D234L4	.67975E+13	29.55	.52677E+13	29.29	.13629E+12	25.64	76.04	73.31	40.65	A
D234L5	.65227E+13	29.51	.51649E+13	29.27	.12172E+12	25.52	75.59	73.10	39.85	A
D254L1	.20552E+12	26.05	.18426E+12	25.94	.30148E+11	24.13	43.66	42.84	31.01	A
D254L2	.19301E+12	25.99	.17113E+12	25.87	.26921E+11	24.02	43.19	42.30	30.37	A
D254L3	.20552E+12	26.05	.18212E+12	25.93	.23699E+11	23.89	43.66	42.76	29.67	A
D254L4	.20552E+12	26.05	.18369E+12	25.94	.19889E+11	23.71	43.66	42.82	28.73	A
D254L5	.19301E+12	25.99	.17532E+12	25.89	.19799E+11	23.71	43.19	42.47	28.70	A

4%Cu

2014

RUN CODES	EXT RATIO	FURNACE TEMP	INITIAL TEMP	PEAK TEMP	FINAL TEMP	BILLET LENGTH	CTNR TEMP	RAM SPEED	STRAIN RATE	MAX PRESSURE	MIN PRESSURE	MAX OIL PRESSURE	MIN OIL PRESSURE	PEAK DELTAP
		DEG.C	DEG.C	DEG.C	DEG.C	MMS	DEG.C	MMS/S	SEC^{-1}	MN/M^2	MN/M^2	MN/M^2	MN/M^2	MN/M
D4541A	10.0	450.0	443.0	445.8	496.3	95.0	300.0	7.9	3.87	482.48	417.63	535.79	413.68	0
D4162A	20.0	300.0	296.0	315.0	452.8	95.0	250.0	12.8	8.06	911.92	600.15	973.60	596.58	82.10
D4262A	20.0	350.0	348.0	358.3	475.2	95.0	300.0	12.4	7.80	735.42	505.88	778.36	495.22	58.64
D4362A	20.0	400.0	395.0	403.2	510.1	95.0	350.0	12.4	7.80	644.85	486.42	675.36	478.38	38.34
D4432A	20.0	450.0	444.0	450.4	530.0	95.0	400.0	7.1	4.47	547.11	426.20	590.94	457.02	0
D4462A	20.0	450.0	444.0	450.6	547.6	95.0	400.0	12.4	7.80	564.71	465.57	599.36	419.32	29.32
D4522A	20.0	480.0	474.0	478.0	529.0	95.0	430.0	3.3	2.08	437.08	406.04	512.16	405.25	0
D4133A	30.0	300.0	298.0	309.1	470.8	95.0	275.0	7.9	7.23	994.61	647.17	1069.31	655.12	87.96
D4243A	30.0	350.0	348.0	357.0	480.8	95.0	300.0	7.8	7.13	773.18	596.68	838.55	590.94	52.78
D4343B	30.0	400.0	396.0	403.5	501.2	95.0	350.0	7.0	6.40	669.41	472.52	709.14	486.80	40.60
D4443A	30.0	450.0	445.0	451.0	541.6	95.0	400.0	8.2	7.50	568.42	465.57	609.52	461.53	23.91
D4543A	30.0	475.0	470.0	476.1	546.3	95.0	375.0	7.3	6.68	552.20	463.26	607.78	514.94	17.59
D4115A	50.0	300.0	297.0	312.1	335.0	95.0	275.0	.2	.30	951.07	694.89	1091.70	718.90	0
D4265A	50.0	350.0	348.0	363.6	506.4	95.0	300.0	12.0	17.72	894.32	617.75	945.46	616.82	70.37
D4315A	50.0	400.0	396.0	404.5	490.2	95.0	350.0	2.7	3.99	730.56	555.21	821.70	607.78	45.33
D4365A	50.0	400.0	396.0	405.9	536.9	95.0	350.0	12.9	19.05	779.66	547.11	830.12	540.30	61.80
D4465A	50.0	450.0	445.0	453.1	568.1	95.0	400.0	12.8	18.90	694.19	479.47	714.79	517.81	47.14
D4515A	50.0	475.0	470.0	474.9	525.1	95.0	390.0	2.9	4.28	558.22	465.57	692.20	531.88	0
I4152A	20.0	299.0	297.0	308.9	386.9	95.0	250.0	10.6	9.71	603.16	528.58	686.65	607.78	65.18
I4252A	20.0	350.0	348.0	354.3	417.4	95.0	300.0	10.5	9.61	498.00	405.35	590.94	520.59	40.15
I4352A	20.0	400.0	396.0	406.0	460.9	95.0	350.0	10.6	9.71	444.26	447.04	517.81	512.16	23.46
I4432A	20.0	450.0	445.0	451.9	484.2	95.0	400.0	6.1	5.59	352.08	370.61	440.07	450.24	0
I4452A	20.0	450.0	445.0	449.8	500.5	95.0	400.0	10.4	9.52	377.55	386.82	458.04	470.37	0
I4522A	20.0	480.0	475.0	478.1	496.7	95.0	430.0	3.2	2.93	297.18	349.99	393.96	424.87	0
I4123A	30.0	300.0	296.0	316.9	397.7	95.0	275.0	5.9	7.56	718.05	626.56	821.70	706.27	70.37
I4333A	30.0	400.0	396.0	404.6	457.5	95.0	340.0	6.1	7.82	493.37	500.32	579.64	579.64	15.11
I4513A	30.0	470.0	464.0	471.3	488.8	95.0	375.0	3.4	4.36	447.04	474.84	543.08	562.80	0
I4533A	30.0	475.0	471.0	478.5	526.4	95.0	440.0	6.2	7.95	394.23	435.46	453.01	495.22	0
I4533A	30.0	475.0	470.0	479.7	512.4	95.0	400.0	6.2	7.95	416.47	447.04	472.73	512.16	0
I4524A	40.0	480.0	473.0	480.4	522.0	95.0	430.0	4.9	8.07	425.04	0	484.03	0	

RUN CODES	INITIAL Z	LOG Z I	PEAK Z	LOG Z P	FINAL Z	LOG Z F	INITIAL FLOW STRESS 2 MN/M	PEAK FLOW STRESS 2 MN/M	FINAL FLOW STRESS 2 MN/M	EXTRUDE QUALITY
D3321	.39419E+12	26.70	.32972E+12	26.52	.65618E+11	24.91	65.91	64.09	49.16	A
D3522	.20437E+11	23.74	.18829E+11	23.66	.68449E+10	22.65	40.12	39.54	32.95	A
D3422	.11319E+12	25.45	.10431E+12	25.37	.23489E+11	23.88	53.89	53.16	41.13	A
D3342	.10873E+13	27.71	.89048E+12	27.52	.58242E+11	24.79	76.84	74.62	48.17	A
D3252	.11641E+14	30.09	.76494E+13	29.67	.14555E+12	25.70	105.65	100.27	56.18	A
D3162	.23096E+15	33.07	.10316E+15	32.27	.29684E+12	26.42	146.09	134.89	63.04	A
D3062	.40788E+16	35.94	.17047E+16	35.07	.47874E+12	26.89	186.89	174.38	67.93	A
D3543	.63335E+11	24.87	.57069E+11	24.77	.79774E+10	22.80	48.87	48.00	33.88	A
D3443	.32482E+12	26.51	.23804E+12	26.20	.19080E+11	23.67	63.94	60.86	39.64	A
D3353	.23738E+13	28.50	.15866E+13	28.09	.45790E+11	24.55	85.88	81.15	46.22	A
D3253	.19010E+14	30.58	.12808E+14	30.18	.13612E+12	25.64	112.05	106.89	55.57	A
D3163	.26889E+15	33.23	.14646E+15	32.62	.22512E+12	26.14	148.22	139.74	60.32	A
[illegible]	.10854E+12	25.41	.95569E+11	25.28	.10007E+11	23.03	53.52	52.39	35.30	A
D3455	.69762E+12	27.27	.56432E+12	27.06	.24162E+11	23.91	71.94	69.67	41.33	A
D3345	.36781E+13	28.93	.25657E+13	28.57	.47601E+11	24.59	91.15	86.80	46.53	A
D3255	.31296E+14	31.07	.19261E+14	30.59	.98225E+11	25.31	118.67	112.22	52.63	A
D3155	.40060E+15	33.62	.30266E+15	33.34	.21715E+12	26.10	153.82	149.88	59.97	A
D34610	.16685E+13	28.14	.12453E+13	27.85	.26304E+11	23.99	81.73	78.38	41.96	C
D33610	.89195E+13	29.82	.67365E+13	29.54	.63613E+11	24.88	102.23	98.67	48.90	B
D32610	.72684E+14	31.92	.44419E+14	31.42	.12355E+12	25.54	130.08	123.38	54.68	B
D34615	.24189E+13	28.51	.14969E+13	28.03	.34082E+11	24.25	86.10	80.48	43.91	B
D325CT1	.13017E+13	27.89	.78391E+12	27.39	.12516E+12	25.55	78.88	73.21	54.80	A
D365CT1	.55659E+13	29.35	.33268E+13	28.83	.77301E+11	25.07	96.27	89.93	50.55	A
D325CT2	.12941E+13	27.89	.84712E+12	27.47	.76132E+11	25.06	78.81	74.06	50.42	A
D365CT2	.52239E+13	29.28	.33296E+13	28.83	.60770E+11	24.83	95.48	89.94	48.52	A
D325CT3	.11111E+13	27.74	.87776E+12	27.50	.52568E+11	24.69	77.09	74.46	47.33	A
D365CT3	.48222E+13	29.20	.32607E+13	28.81	.40734E+11	24.43	94.49	89.69	45.29	A
D325CT4	.11877E+13	27.80	.96410E+12	27.59	.30682E+11	24.15	77.84	75.50	43.11	A
D365CT4	.47892E+13	29.20	.32243E+13	28.80	.44868E+11	24.53	94.40	89.55	46.06	A
D325CT5	.11335E+13	27.76	.92799E+12	27.56	.25720E+11	23.97	77.31	75.07	41.79	A
D365CT5	.45341E+13	29.14	.30590E+13	28.75	.40597E+11	24.43	93.72	88.92	45.26	A
D325CT6	.10812E+13	27.71	.88842E+12	27.51	.15589E+11	23.47	76.78	74.59	38.23	A
D365CT6	.40342E+13	29.03	.29176E+13	28.70	.27770E+11	24.05	92.28	88.34	42.36	A

5%Cu

RUN CODES	EXT RATIO	FURNACE TEMP	INITIAL TEMP	PEAK TEMP	FINAL TEMP	BILLET LENGTH	CTNR TEMP	RAM SPEED	STRAIN RATE	MAX PRESSURE	MIN PRESSURE	MAX OIL PRESSURE	MIN OIL PRESSURE	PEAK DELTAP
		DEG.C	DEG.C	DEG.C	DEG.C	MMS	DEG.C	MMS/S	SEC^{-1}	MN/M^2	MN/M^2	MN/M^2	MN/M^2	MN/M
D5522	20.0	500.0	494.0	496.2	543.0	95.0	450.0	3.6	2.27	419.25	333.55	464.61	343.02	0
D5422	20.0	450.0	445.0	452.0	504.4	95.0	405.0	3.6	2.27	472.29	393.77	529.62	433.29	11.73
D5322	20.0	400.0	392.0	399.3	468.4	95.0	350.0	3.5	2.20	586.02	451.68	631.91	541.64	0
D5222	20.0	350.0	347.0	355.1	446.9	95.0	300.0	3.5	2.20	730.56	550.35	757.72	586.83	67.66
D5122	20.0	300.0	298.0	307.1	419.1	95.0	260.0	3.6	2.27	850.54	587.87	938.88	630.68	79.16
D5545	50.0	500.0	494.0	497.6	596.1	95.0	450.0	9.5	14.03	568.65	462.79	616.20	477.14	0
D5445	50.0	450.0	445.0	453.9	559.8	95.0	395.0	9.0	13.29	659.21	531.59	649.99	529.62	0
D5345	50.0	400.0	396.0	406.5	531.7	95.0	365.0	8.8	12.99	775.96	545.72	749.71	559.72	64.50
D5245	50.0	350.0	348.0	356.8	507.5	95.0	300.0	8.6	12.70	890.38	667.79	878.70	662.00	0
D5145	50.0	300.0	298.0	311.4	495.0	95.0	250.0	8.6	12.70	1090.97	800.05	1150.24	794.38	94.73
D5447	70.0	450.0	445.0	452.3	572.4	95.0	410.0	8.9	17.93	705.54	537.84	740.26	550.68	0
D5347	70.0	400.0	396.0	407.6	538.0	95.0	355.0	9.0	18.13	792.86	606.64	831.87	643.93	0
D5247	70.0	350.0	348.0	350.4	529.1	95.0	310.0	8.7	17.53	953.61	711.10	974.62	740.16	73.30
D5147	70.0	300.0	298.0	307.7	507.8	95.0	265.0	8.7	17.53	1114.60	813.02	1232.40	818.52	0
D54610	100.0	450.0	444.0	453.5	594.0	95.0	400.0	13.4	40.40	808.62	567.49	907.77	600.18	108.48
D53610	100.0	400.0	396.0	407.5	584.3	95.0	350.0	13.5	40.70	975.62	716.20	1046.51	719.82	114.35
D52610	100.0	370.0	368.0	379.5	563.6	95.0	300.0	13.6	41.00	1078.00	706.93	1156.40	716.95	152.46
D553L5	30.0	500.0	494.0	497.9	589.6	104.6	455.0	7.0	6.40	572.12	437.78	589.81	481.46	0
D553L4	30.0	500.0	494.0	498.7	584.9	96.0	440.0	6.7	6.13	567.49	471.13	592.17	505.49	0
D553L2	30.0	500.0	494.0	497.2	576.5	72.3	445.0	7.1	6.49	516.53	463.26	553.66	488.65	0
D553L1	30.0	500.0	494.0	503.2	569.4	66.2	450.0	6.4	5.85	504.02	485.03	520.69	503.74	0
D543L5	30.0	450.0	444.0	449.7	554.6	106.2	397.0	6.2	5.67	646.48	547.34	676.48	559.72	20.52
D543L4	30.0	450.0	445.0	450.2	540.9	96.0	390.0	6.5	5.95	612.89	478.31	643.93	493.47	23.46
D543L3	30.0	450.0	444.0	450.6	543.8	82.5	400.0	6.3	5.76	594.13	550.35	627.09	565.67	15.83
D543L2	30.0	450.0	445.0	450.7	537.0	71.1	400.0	6.4	5.85	566.10	531.59	601.82	550.68	17.59
D543L1	30.0	450.0	445.0	450.2	531.2	63.2	405.0	6.5	5.95	554.06	494.06	578.92	505.49	44.43
D533L5	30.0	400.0	396.0	403.5	513.7	102.3	345.0	6.2	5.67	728.70	550.35	769.12	565.67	38.34
D533L4	30.0	400.0	395.0	403.1	510.5	95.6	345.0	6.2	5.67	712.26	562.86	749.30	574.71	35.18
D533L3	30.0	400.0	396.0	404.5	509.0	82.6	355.0	6.2	5.67	675.43	589.73	649.37	601.82	29.32
D533L2	30.0	400.0	396.0	403.8	503.8	72.3	350.0	6.1	5.58	665.47	597.37	692.10	620.51	0
D533L1	30.0	400.0	396.0	403.4	497.9	65.4	350.0	6.6	6.04	642.31	569.11	670.43	585.60	0
D523L5	30.0	350.0	346.0	356.3	483.9	106.4	300.0	6.1	5.58	851.23	592.97	908.79	608.50	46.91
D523L4	30.0	350.0	346.0	358.0	480.8	95.0	300.0	6.0	5.49	818.11	643.93	874.49	668.06	49.84
D523L3	30.0	350.0	346.0	356.4	476.3	82.5	303.0	6.0	5.49	810.01	625.40	865.45	650.60	35.18
D523L2	30.0	350.0	345.0	354.9	470.5	73.2	300.0	6.0	5.49	775.49	656.20	788.43	678.23	17.59
D523L1	30.0	350.0	345.0	356.4	468.0	65.6	300.0	6.4	5.85	775.49	656.67	796.23	662.00	17.59
D513L5	30.0	300.0	297.0	308.2	466.9	105.1	255.0	5.6	5.12	1050.67	680.99	1116.97	680.08	90.22
D513L4	30.0	300.0	295.0	312.7	462.7	95.3	250.0	6.2	5.67	1044.41	708.78	1102.48	711.30	83.45
D513L3	30.0	300.0	297.0	312.3	455.0	76.4	260.0	5.7	5.21	993.69	731.02	1053.19	742.01	0

RUN CODES	INITIAL Z	LOG Z I	PEAK Z	LOG Z P	FINAL Z	LOG Z F	INITIAL FLOW STRESS 2 MN/M	PEAK FLOW STRESS 2 MN/M	FINAL FLOW STRESS 2 MN/M	EXTRUDE QUALITY
D4541A	.13282E+12	25.61	.12069E+12	25.52	.24763E+11	23.93	72.00	71.05	56.32	A
D4162A	.14567E+15	32.61	.54335E+14	31.63	.19934E+12	26.02	152.09	140.08	76.10	A
D4262A	.10951E+14	30.02	.69416E+13	29.57	.94339E+11	25.27	120.88	115.50	68.63	A
D4362A	.15304E+13	28.06	.11164E+13	27.74	.33462E+11	24.23	98.08	94.55	58.97	A
D4432A	.14822E+12	25.72	.11982E+12	25.51	.11065E+11	23.13	73.09	70.98	49.63	A
D4462A	.25887E+12	26.28	.20786E+12	26.06	.12146E+11	23.22	78.79	76.52	50.37	C
D4522A	.26040E+11	23.98	.22985E+11	23.86	.52892E+10	22.39	56.76	55.68	44.00	A
D4133A	.11742E+15	32.40	.65836E+14	31.82	.10023E+12	25.33	149.45	142.41	69.22	A
D4243A	.10012E+14	29.93	.67216E+13	29.54	.72512E+11	25.01	119.81	115.12	66.10	A
D4343B	.12078E+13	27.82	.90738E+12	27.53	.35447E+11	24.29	95.42	92.25	59.48	B
D4443A	.24055E+12	26.21	.19707E+12	26.01	.13646E+11	23.34	78.03	75.98	51.31	C
D4543A	.94887E+11	25.28	.78326E+11	25.08	.10765E+11	23.10	68.69	66.84	49.41	C
[illegible]115A	.50608E+13	29.25	.23023E+13	28.46	.75491E+12	27.35	111.80	102.71	90.22	A
D4265A	.24861E+14	30.84	.12504E+14	30.16	.84441E+11	25.16	130.65	122.45	67.56	A
D4315A	.75190E+12	27.35	.54327E+12	27.02	.30474E+11	24.14	90.18	86.64	58.14	A
D4365A	.35924E+13	28.91	.24585E+13	28.53	.39194E+11	24.39	107.82	103.46	60.39	B
D4465A	.60604E+12	27.13	.46334E+12	26.86	.17580E+11	23.59	87.83	84.93	53.40	B
D4515A	.60839E+11	24.83	.52229E+11	24.68	.12128E+11	23.22	64.44	63.02	50.36	A
I4152A	.16636E+15	32.75	.89241E+14	32.12	.26170E+13	28.59	153.71	146.11	104.18	A
I4252A	.13492E+14	30.23	.10172E+14	29.95	.81239E+12	27.42	123.35	120.00	91.03	A
I4352A	.18308E+13	28.24	.12476E+13	27.85	.18422E+12	25.94	100.10	95.79	75.29	A
I4432A	.17913E+12	25.91	.14209E+12	25.68	.51166E+11	24.66	75.01	72.67	62.83	A
I4452A	.30540E+12	26.44	.26005E+12	26.28	.53774E+11	24.71	80.51	78.84	63.29	C
I4522A	.35614E+11	24.30	.32341E+11	24.20	.18494E+11	23.64	59.52	58.66	53.83	A
I4123A	.13675E+15	32.55	.46380E+14	31.47	.13332E+13	27.92	151.31	138.17	96.53	A
I4333A	.14748E+13	28.02	.10596E+13	27.69	.16591E+12	25.83	97.66	93.97	74.23	A
I4513A	.74909E+11	25.04	.59542E+11	24.81	.34745E+11	24.27	66.41	64.24	59.30	A
I4533A	.10943E+12	25.42	.86629E+11	25.18	.21687E+11	23.80	70.08	67.81	55.18	C
I4533A	.11293E+12	25.45	.83633E+11	25.15	.32005E+11	24.19	70.39	67.47	58.57	C
I4524A	.10432E+12	25.37	.82910E+11	25.14	.24862E+11	23.94	69.61	67.38	56.36	C

5052 alloy

RUN CODES	EXT RATIO	FURNACE TEMP	INITIAL TEMP	PEAK TEMP	FINAL TEMP	BILLET LENGTH	CTNR TEMP	RAM SPEED	STRAIN RATE	MAX PRESSURE	MIN PRESSURE	MAX OIL PRESSURE	MIN OIL PRESSURE	PEAK DELTAP
		DEG.C	DEG.C	DEG.C	DEG.C	MMS	DEG.C	MMS/S	SEC^{-1}	MN/M^2	MN/M^2	MN/M^2	MN/M^2	MN/M
D50-1	30.0	500.0	494.0	501.6	578.3	80.0	455.0	8.4	7.68	500.32	451.68	469.34	326.59	0
D50-2	30.0	500.0	494.0	499.6	595.5	119.5	455.0	8.3	7.59	569.81	453.99	525.82	387.18	0
D50-3	30.0	500.0	494.0	500.7	582.4	109.8	440.0	8.2	7.50	544.33	427.35	505.28	364.59	0
D50-4	30.0	500.0	494.0	501.3	580.3	89.7	455.0	8.4	7.68	521.16	423.88	466.26	364.59	0
D50-5	30.0	438.0	433.0	441.7	550.2	99.6	395.0	8.2	7.50	678.67	515.37	642.39	455.99	0
D50-6	30.0	438.0	433.0	441.3	547.5	89.7	388.0	8.3	7.59	669.41	535.06	636.74	472.42	0
D50-7	30.0	438.0	432.0	440.8	557.7	119.8	392.0	8.2	7.50	718.05	521.16	705.55	461.12	0
D50-8	30.0	438.0	433.0	442.4	555.5	110.1	383.0	8.0	7.32	706.47	555.91	690.14	478.58	0
D50-9	30.0	438.0	433.0	440.7	542.5	80.0	398.0	8.1	7.41	619.61	544.33	592.58	495.01	0
D50-10	30.0	375.0	370.0	372.1	521.6	99.5	320.0	8.0	7.32	862.82	613.82	867.82	563.82	0
D50-11	30.0	375.0	371.0	372.0	531.0	109.7	325.0	8.2	7.50	881.35	625.40	876.03	545.34	0
D50-12	30.0	375.0	371.0	373.7	529.3	119.6	325.0	8.2	7.50	906.36	579.07	911.98	527.88	0
D50-13	30.0	375.0	371.0	371.6	514.7	89.7	325.0	7.9	7.23	822.28	592.97	794.90	530.96	0
D50-14	30.0	375.0	371.0	372.4	522.2	80.1	330.0	8.1	7.41	807.92	683.30	778.47	600.80	0
D50-15	30.0	325.0	322.0	323.4	505.6	109.6	270.0	8.4	7.68	1027.97	683.30	7.19	620.31	0
D50-16	30.0	325.0	322.0	325.1	503.1	99.3	280.0	8.4	7.68	1002.95	692.57	1004.41	675.77	0
D50-17	30.0	325.0	321.0	322.5	493.8	89.7	275.0	8.4	7.68	972.84	677.51	962.30	595.66	0
D50-18	30.0	325.0	321.0	322.6	486.2	80.0	275.0	8.1	7.41	933.46	690.25	939.71	683.98	0
D50-19	30.0	550.0	545.0	549.7	612.4	99.3	495.0	8.2	7.50	414.62	377.55	376.91	333.77	0
D50-20	30.0	550.0	544.0	544.5	616.1	109.8	490.0	8.0	7.32	430.83	375.24	383.07	322.48	0
D50-21	30.0	550.0	545.0	549.5	612.9	89.9	505.0	8.1	7.41	405.35	379.87	364.59	333.77	0
D50-22	30.0	550.0	545.0	550.6	608.7	80.0	500.0	8.0	7.32	403.03	384.50	356.37	328.64	0
D50-23	30.0	550.0	545.0	549.1	626.5	119.7	505.0	8.3	7.59	437.08	422.72	400.53	306.05	0
D50-24	10.0	500.0	493.0	497.8	556.2	89.7	460.0	8.2	4.02	390.76	347.44	350.21	294.75	0
D50-25	20.0	500.0	492.0	497.2	575.4	89.9	455.0	8.0	5.04	469.05	451.68	420.04	367.67	0
D50-26	50.0	500.0	494.0	501.0	595.7	91.0	440.0	7.9	11.66	599.45	515.37	550.47	450.85	0
D50-27	80.0	500.0	494.0	502.0	605.8	90.0	450.0	8.0	18.51	646.24	525.80	614.15	462.15	0
D50-28	80.0	400.0	395.0	407.8	557.1	89.9	345.0	8.1	18.74	938.10	683.30	929.44	633.66	0
D50-29	50.0	400.0	395.0	404.9	543.9	90.0	360.0	8.0	11.81	838.50	632.35	845.22	569.99	0
D50-30	20.0	400.0	395.0	404.8	509.1	90.2	345.0	8.0	5.04	690.25	544.33	678.85	467.28	0
D50-31	10.0	400.0	395.0	395.9	492.2	90.1	345.0	8.1	3.97	584.86	460.94	564.85	347.13	0

RUN CODES	INITIAL Z	LOG Z I	PEAK Z	LOG Z P	FINAL Z	LOG Z F	INITIAL FLOW STRESS 2 MN/M	PEAK FLOW STRESS 2 MN/M	FINAL FLOW STRESS 2 MN/M	EXTRUDE QUALITY
D5522	.16979E+10	21.25	.16015E+10	21.19	.49763E+09	20.03	58.76	58.19	47.72	A
D5422	.68480E+10	22.65	.55492E+10	22.44	.12916E+10	20.98	73.33	71.00	56.15	A
D5322	.37923E+11	24.36	.29392E+11	24.10	.33400E+10	21.93	93.81	90.60	65.56	A
D5222	.20981E+12	26.07	.15125E+12	25.74	.62765E+10	22.56	116.49	112.02	72.36	A
D5122	.18889E+13	28.27	.12302E+13	27.84	.15497E+11	23.46	147.65	141.45	82.78	A
D5545	.10510E+11	23.08	.95491E+10	22.98	.95190E+09	20.67	78.21	77.10	53.34	C
D5445	.40160E+11	24.42	.30732E+11	24.15	.19808E+10	21.41	94.54	91.16	60.26	B-C
D5345	.19427E+12	25.99	.13532E+12	25.63	.37409E+10	22.04	115.43	110.51	66.75	B
D5245	.11611E+13	27.78	.81676E+12	27.43	.66733E+10	22.62	140.61	135.57	73.04	A
D5145	.10585E+14	29.99	.56519E+13	29.36	.92554E+10	22.95	173.00	163.71	76.74	A
D5447	.54202E+11	24.72	.43521E+11	24.50	.20178E+10	21.43	98.39	95.57	60.44	C
D5347	.27117E+12	26.33	.18190E+12	25.93	.44868E+10	22.22	120.03	114.53	68.69	C
D5247	.16031E+13	28.10	.14532E+13	28.00	.53751E+10	22.41	145.27	143.85	70.65	B
D5147	.14615E+14	30.31	.92193E+13	29.85	.91433E+10	22.94	177.79	170.95	76.60	B
D54610	.12588E+12	25.56	.94543E+11	25.27	.28679E+10	21.78	109.53	105.70	63.99	B-C
D53610	.60862E+12	27.13	.40991E+12	26.74	.35453E+10	21.99	131.38	125.79	66.19	B
D52610	.17061E+13	28.17	.11094E+13	27.73	.56158E+10	22.45	146.17	139.96	71.13	B
D553L5	.47983E+10	22.29	.43289E+10	22.19	.49870E+09	20.03	69.41	68.31	47.74	C
D553L4	.45927E+10	22.25	.40517E+10	22.12	.52713E+09	20.08	68.94	67.60	48.20	C
D553L2	.48668E+10	22.31	.44662E+10	22.22	.66909E+09	20.32	69.57	68.64	50.23	C
D553L1	.43870E+10	22.20	.34433E+10	21.96	.70485E+09	20.37	68.45	65.88	50.68	C
D543L5	.17671E+11	23.60	.14872E+11	23.42	.95280E+09	20.67	84.35	82.29	53.35	A-B
D543L4	.17970E+11	23.61	.15356E+11	23.45	.13740E+10	21.04	84.56	82.67	56.73	B
D543L3	.17956E+11	23.61	.14694E+11	23.41	.12409E+10	20.94	84.55	82.14	55.77	A-B
D543L2	.17694E+11	23.60	.14920E+11	23.43	.14837E+10	21.12	84.37	82.33	57.46	A-B
D543L1	.17970E+11	23.61	.15376E+11	23.46	.17323E+10	21.27	84.56	82.68	58.95	A-B
D533L5	.84803E+11	25.16	.65332E+11	24.90	.25452E+10	21.66	104.25	100.82	62.77	A
D533L4	.87830E+11	25.20	.66300E+11	24.92	.27603E+10	21.74	104.72	101.01	63.59	A
D533L3	.84803E+11	25.16	.63156E+11	24.87	.28684E+10	21.78	104.25	100.38	63.99	A
D533L2	.83435E+11	25.15	.63722E+11	24.88	.32352E+10	21.90	104.04	100.50	65.23	A
D533L1	.90274E+11	25.23	.69820E+11	24.97	.40850E+10	22.13	105.08	101.69	67.69	A
D523L5	.55363E+12	27.04	.36619E+12	26.63	.54885E+10	22.43	130.03	124.21	70.88	A
D523L4	.54455E+12	27.02	.33686E+12	26.54	.58766E+10	22.49	129.80	123.05	71.63	A
D523L3	.54455E+12	27.02	.35863E+12	26.61	.66635E+10	22.62	129.80	123.92	73.02	A
D523L2	.56732E+12	27.06	.38000E+12	26.66	.78435E+10	22.78	130.38	124.73	74.85	A
D523L1	.60515E+12	27.13	.38183E+12	26.67	.89863E+10	22.92	131.29	124.80	76.40	A
D513L5	.44812E+13	29.13	.26410E+13	28.60	.81031E+10	22.82	160.29	152.54	75.22	A
D513L4	.54657E+13	29.33	.23725E+13	28.49	.10131E+11	23.04	163.21	150.97	77.78	A
D513L3	.45612E+13	29.15	.22203E+13	28.43	.11681E+11	23.18	160.55	150.00	79.44	A

RUN CODES	INITIAL Z	LOG Z I	PEAK Z	LOG Z P	FINAL Z	LOG Z F	INITIAL FLOW STRESS MN/M^2	PEAK FLOW STRESS MN/M^2	FINAL FLOW STRESS MN/M^2	EXTRUDE QUALITY
D50-1	.25844E+12	26.28	.21286E+12	26.08	.20085E+11	23.72	70.24	68.39	47.98	A
D50-2	.25536E+12	26.27	.21434E+12	26.09	.15035E+11	23.43	70.13	68.46	45.77	A
D50-3	.25229E+12	26.25	.20474E+12	26.05	.20608E+11	23.75	70.01	68.03	48.18	A
D50-4	.25844E+12	26.28	.20740E+12	26.06	.23557E+11	23.88	70.24	68.15	49.22	A
D50-5	.20485E+13	28.35	.14840E+13	28.03	.48249E+11	24.60	91.13	87.75	55.08	A
D50-6	.20735E+13	28.36	.15245E+13	28.05	.52513E+11	24.68	91.25	88.03	55.79	A
D50-7	.21264E+13	28.39	.15388E+13	28.06	.39309E+11	24.39	91.52	88.13	53.36	A
D50-8	.19985E+13	28.32	.14139E+13	27.98	.40738E+11	24.43	90.87	87.25	53.66	A
D50-9	.20235E+13	28.34	.15218E+13	28.05	.58902E+11	24.80	91.00	88.02	56.78	A
D50-10	.26377E+14	30.90	.24012E+14	30.81	.10602E+12	25.39	118.87	117.82	61.95	A
D50-11	.25849E+14	30.88	.24750E+14	30.84	.82642E+11	25.14	118.64	118.16	59.73	A
D50-12	.25849E+14	30.88	.22866E+14	30.76	.86954E+11	25.19	118.64	117.28	60.18	A
D50-13	.24903E+14	30.85	.24293E+14	30.82	.12852E+12	25.58	118.23	117.95	63.70	A
D50-14	.25534E+14	30.87	.23998E+14	30.81	.10542E+12	25.38	118.51	117.82	61.90	A
D50-15	.28536E+15	33.28	.26495E+15	33.21	.18022E+12	25.92	145.65	144.81	66.83	A
D50-16	.28536E+15	33.28	.24331E+15	33.13	.19453E+12	25.99	145.65	143.85	67.55	A
D50-17	.30077E+15	33.34	.27811E+15	33.26	.26008E+12	26.28	146.25	145.36	70.30	A
D50-18	.29003E+15	33.30	.26659E+15	33.22	.31932E+12	26.49	145.84	144.88	72.28	A
D50-19	.55665E+11	24.74	.48930E+11	24.61	.98719E+10	23.01	56.29	55.20	42.69	A
D50-20	.55839E+11	24.75	.55007E+11	24.73	.88295E+10	22.90	56.32	56.19	41.90	A
D50-21	.54986E+11	24.73	.48563E+11	24.61	.96282E+10	22.99	56.19	55.13	42.51	A
D50-22	.54307E+11	24.72	.46491E+11	24.56	.10522E+11	23.08	56.08	54.76	43.15	A
D50-23	.56343E+11	24.75	.50331E+11	24.64	.71888E+10	22.70	56.40	55.43	40.47	A
D50-24	.13949E+12	25.66	.11978E+12	25.51	.21920E+11	23.81	64.45	63.06	48.66	A
D50-25	.18043E+12	25.92	.15312E+12	25.75	.16566E+11	23.53	66.84	65.31	46.50	A
D50-26	.39229E+12	26.70	.31541E+12	26.48	.22995E+11	23.86	74.29	72.16	49.03	A
D50-27	.62242E+12	27.16	.48424E+12	26.91	.28472E+11	24.07	78.87	76.36	50.73	A
D50-28	.22887E+14	30.76	.13580E+14	30.24	.99893E+11	25.33	117.29	111.52	61.42	A
D50-29	.14427E+14	30.30	.96275E+13	29.90	.90348E+11	25.23	112.19	107.75	60.52	A
D50-30	.61502E+13	29.45	.41084E+13	29.04	.10594E+12	25.39	102.87	98.52	61.95	A
D50-31	.48481E+13	29.21	.46714E+13	29.17	.14122E+12	25.67	100.30	99.90	64.56	A

Al	Mg	Cr	Fe	Cu	Mn	Ti	Si	B (ppm)
Rem	2.55	0.24	0.17	0.003	0.003	0.019	0.07	13

Alloy composition weight % 5052 Alloy

ΔH = 154567 J/mole α = 0.017 m^2/MN

n = 5.11 A = $3.252 \times 10^{10} sec^{-1}$

Steady state temperature corrected hot working constants from reference 122

4%Cu

2014-SS

RUN CODES	EXT RATIO	FURNACE TEMP DEG.C	INITIAL TEMP DEG.C	PEAK TEMP DEG.C	FINAL TEMP DEG.C	BILLET LENGTH MMS	CTNR TEMP DEG.C	RAM SPEED MMS/S	STRAIN RATE SEC^{-1}	MAX PRESSURE MN/M^2	MIN PRESSURE MN/M^2	MAX OIL PRESSURE MN/M^2	MIN OIL PRESSURE MN/M^2	PEAK DELTAP MN/M^2
D4162AS	20.0	300.0	298.0	316.1	477.8	95.0	250.0	13.4	8.43	1074.29	600.15	1150.34	605.52	151.79
D4262AS	20.0	350.0	348.0	364.9	500.4	95.0	300.0	12.9	8.12	908.91	553.13	968.56	557.15	137.58
D4362AS	20.0	399.0	395.0	405.6	524.1	95.0	350.0	12.9	8.12	754.18	488.27	803.63	495.22	71.04
D4462AS	20.0	450.0	445.0	452.0	547.8	95.0	400.0	12.6	7.93	606.87	411.84	640.44	430.52	49.84
D4522AS	20.0	480.0	473.0	476.1	512.8	95.0	425.0	3.1	1.95	385.43	335.40	444.59	371.47	0
D4562AS	20.0	480.0	475.0	482.3	567.4	95.0	425.0	12.7	7.99	547.11	400.02	579.64	430.52	29.77
D4243AS	30.0	350.0	347.0	359.8	488.4	95.0	300.0	8.3	7.59	915.40	511.90	999.48	594.32	21.20
D4323AS	30.0	400.0	395.0	406.5	499.4	95.0	350.0	3.7	3.38	823.67	470.21	942.68	574.09	115.25
D4443AS	30.0	450.0	444.0	450.6	545.9	95.0	400.0	8.3	7.59	633.04	438.24	695.07	467.08	29.77
D4543AS	30.0	473.0	466.0	472.0	562.7	95.0	425.0	8.1	7.41	611.27	408.82	652.86	436.17	40.15
D4365AS	50.0	398.0	394.0	407.6	573.7	95.0	350.0	12.1	17.86	996.70	662.46	1005.12	612.30	123.14
D4465AS	50.0	450.0	445.0	455.9	582.6	95.0	400.0	12.8	18.90	778.97	523.71	832.28	534.25	77.81
D4565AS	50.0	473.0	464.0	473.1	596.3	95.0	425.0	11.6	17.13	714.34	547.11	763.68	568.55	34.28
D4467AS	70.0	430.0	426.0	438.2	588.8	95.0	400.0	12.7	25.59	873.24	594.13	917.32	596.58	80.29
D4367AS	70.0	400.0	396.0	409.4	656.3	95.0	350.0	12.8	25.79	1158.14	1158.14	1058.02	669.71	0

RUN CODES	INITIAL Z	LOG Z I	PEAK Z	LOG Z P	FINAL Z	LOG Z F	INITIAL FLOW STRESS MN/M^2	PEAK FLOW STRESS MN/M^2	FINAL FLOW STRESS MN/M^2	EXTRUDE QUALITY
D4162AS	.12772E+18	39.39	.40637E+17	38.24	.17027E+14	30.47	191.78	174.34	71.42	A
D4262AS	.61233E+16	36.35	.24695E+16	35.44	.71774E+13	29.60	146.25	133.22	62.96	A
D4362AS	.54981E+15	33.94	.33505E+15	33.45	.31639E+13	28.78	112.61	106.13	55.65	A
D4462AS	.58460E+14	31.70	.43836E+14	31.41	.14277E+13	27.99	84.81	81.55	49.21	B-C
D4522AS	.47302E+13	29.18	.41996E+13	29.07	.11158E+13	27.74	59.15	58.10	47.34	A
D4562AS	.17956E+14	30.52	.13637E+14	30.24	.78716E+12	27.39	71.97	69.17	44.81	B-C
D4243AS	.60514E+16	36.34	.30215E+16	35.64	.10348E+14	29.97	146.08	136.09	66.45	A
D4323AS	.22920E+15	33.07	.13354E+15	32.53	.30986E+13	28.76	101.28	94.58	55.47	A
D4443AS	.58330E+14	31.70	.44422E+14	31.42	.14533E+13	28.00	84.78	81.70	49.35	B-C
D4543AS	.23534E+14	30.79	.18646E+14	30.56	.84261E+12	27.46	74.79	72.36	45.29	A-B
D4365AS	.12689E+16	34.78	.66997E+15	34.14	.14558E+13	28.01	123.93	115.24	49.36	B
D4465AS	.13931E+15	32.57	.89446E+14	32.12	.11857E+13	27.80	95.09	89.76	47.80	B
D4565AS	.58817E+14	31.71	.41383E+14	31.35	.72668E+12	27.31	84.88	80.91	44.24	A-B
D4467AS	.42210E+15	33.68	.25022E+15	33.15	.13447E+13	27.93	109.13	102.39	48.75	C
D4367AS	.16654E+16	35.05	.89018E+15	34.42	.22560E+12	26.14	127.69	119.08	36.66	C

APPENDIX III

Microhardness Data from the T1 Torsion Specimens

1% Cu

Initial Temp °C	Mean Twist Rate 0.016	0.17	1.56	4.7	14.75
295	54.0	52.6	52.6	51.5	55.5
355	52.0	52.5	51.2	——	53.6
415	49.8	51.0	52.6	52.6	52.6
475	72.4	74.1	75.4	77.0	——

5% Cu

Initial Temp °C	Mean Twist Rate 0.016	0.052	1.53	4.7	14.75
295	56.3	55.5	63.1	63.1	67.0
355	57.0	54.4	58.7	63.1	61.3
415	79.8	77.8	81.8	80.5	79.2
475	110.0	109.0	110.1	110.4	111.9

HARDNESS RESULTS

AS EXTRUDED

	ER	EXTRUSION TEMP DEG.C 300	350	400	450	500
1%Cu	20:1	62	59	58	64	76
	50:1	63	64	60	70	84
5%Cu	20:1	84	81	89	114	125
	50:1	90	90	101	121	135

BILLET PREHEAT MATERIAL

		TEMP DEG.C 300	350	400	450	500
1%Cu	TF	50.2	50.5	51	53	57
	T1	50	50.3	54	64.8	75.1
5%Cu	TF	58	62	63.8	81.5	95
	T1	58.9	62.2	82.2	109	119

VARIATION IN HARDNESS ACROSS THE EXTRUDE

T1 + T6

4%Cu 2014

T1 TEMPER

EXTN CODE	BILLET TEMP	CENTRE	MID-RADIUS	EDGE
I4152A	300	94.1	94.1	94.1
I4352A	400	110	110	113
I4512A	475	115	116	113
D4162A	300	93.6	91.6	93.6
D4352A	400	89.2	91.6	97.5
D4522A	475	115	115	113

T6 TEMPER

EXTN CODE	BILLET TEMP	CENTRE	MID-RADIUS	EDGE
I4152A	300	161	160	164
I4352A	400	171	176	170
I4522A	475	165	169	165
D4162A	300	159	156	159
D4362A	400	156	153	156
D4522A	475	155	153	159

T1,TF and T6 hardness measurements from torsion specimens and extrudes.

AGEING CHARACTERISTICS

1%Cu To 5%Cu

T6

INITIAL BILLET TEMP = 400 DEG.C

120 DEG.C

% Cu	Time (Hours)					
	1	5	20	40	183	528
1	76	81	86	89	102	126
2	86	93	100	105	114	132
3	100	104	105	106	115	137
4	111	112	115	117	128	150
5	118	119	124	128	138	156

160 DEG.C

% Cu	Time (Hours)					
	1	10	18	40	100	1000
1	106	120	121	122	122	103
2	106	122	126	132	128	112
3	107	134	136	140	139	122
4	113	153	157	156	151	134
5	115	155	163	162	159	138

180 DEG.C

% Cu	Time (Hours)						
	0.5	3	8	19	44	86	230
1	112	121	121	116	107	104	95
2	116	128	131	126	121	115	106
3	117	139	142	138	135	124	116
4	120	150	157	154	145	134	125
5	128	159	163	159	152	141	131

T5 TEMPER

4%Cu (C.H.)

180 DEG.C

EXTN TEMP	Time (Hours)					
	0.75	3	8	18	95	300
475	103	127	135	130	117	98
400	81	87	96	98	90	89
350	74	74	77	77	73	68

160 DEG.C

EXTN TEMP	Time (Hours)					
	1	10	18	36	100	500
475	107	130	138	137	121	104
400	86	90	97	101	103	84
350	76	78	79	79	78	65

T5 TEMPER

4%Cu (S.S.)

180 DEG.C

EXTN TEMP	Time (Hours)					
	0.5	4.5	8	13	48	300
475	113	152	155	150	138	118
400	101	134	137	135	124	98
350	94	111	116	115	111	93

160 DEG.C

EXTN TEMP	Time (Hours)						
	1.5	12	18	36	75	225	950
475	115	147	155	156	155	142	100
400	104	118	127	137	136	123	84
350	99	108	112	122	124	114	72

TENSILE RESULTS

T1 TEMPER

	EXTRUDE CODE	PROOF STRESS MN/m^2	U.T.S. MN/m^2	% STRAIN
1%Cu	D1443	153.1	284,3	31.3
	D1143	129.4	224.5	30.2
2%Cu	D2443	237.1	405.3	29.6
	D2163	153.3	290.1	29.0
3%Cu	D3443	278.4	453.8	28.9
	D3163	162.3	306.4	26.1
5%Cu	D543L4	308.7	470.3	20.5
	D513L4	191.4	337.5	20.5

T6 TEMPER

	EXTRUDE CODE	PROOF STRESS MN/m^2	U.T.S. MN/m^2	% STRAIN
1%Cu	D1443	357.0	394.3	22.6
	D1143	225.4	323.6	26.2
2%Cu	D2443	418.3	492.7	20.0
	D2163	283.7	418.6	25.3
3%Cu	D3443	437.3	512.3	19.3
	D3163	311.4	445.3	23.3
5%Cu	D543L4	542.0	589.0	16.0
	D513L4	425.3	520.2	19.1

T1 TEMPER

4% Cu - CONVENTIONALLY HEATED (C.H.)

EXTRUDE CODE	PROOF STRESS MN/m2	U.T.S. MN/m2	% STRAIN
D4162A	183.1	331.8	24.1
D4432A	290.5	468.7	24.3
D4133A	216.2	382.0	18.1
D4243A	158.1	316.1	22.9
D4343A	206.4	367.8	24.4
D4543A	295.7	479.5	22.0
D4315A	283.4	456.8	26.7
D4365A	196.3	357.9	23.3
D4515A	321.0	497.4	27.0

4% Cu - PRE SOLUTION SOAK (S.S.)

EXTRUDE CODE	PROOF STRESS MN/m2	U.T.S. MN/m2	% STRAIN
D4162AS	252.3	420.1	20.0
D4243AS	285.3	458.4	22.1
D4443AS	300.8	509.9	21.6
D4543AS	354.3	535.7	24.7
D4365AS	300.1	464.8	22.0
D4565AS	349.8	522.1	23.1

T6 TEMPER

4% Cu - (S.S.)

EXTRUDE CODE	PROOF STRESS MN/m2	U.T.S. MN/m2	% STRAIN
D4162AS	410.6	515.2	18.6
D4262AS	400.1	511.6	17.5
D4363AS	517.2	574.6	17.0
D4462AS	525.4	576.4	15.8
D4562AS	510.6	573.1	18.1
D4243AS	388.0	495.2	16.1
D4323AS	512.4	569.8	18.8
D4443AS	530.5	579.0	16.1
D4543AS	515.2	581.5	17.8
D4465AS	519.5	566.7	16.9
D4565AS	518.2	569.3	16.9

T6 TEMPER

4%Cu - (C.H.)

EXTRUDE CODE	PROOF STRESS MN/m2	U.T.S. MN/m2	% STRAIN
D4162A	402.8	507.3	19.4
D4262A	393.3	490.4	16.8
D4362A	384.2	472.3	13.9
D4432A	525.9	579.5	17.7
D4522A	522.9	579.0	17.6
D4133A	399.3	519.3	18.0
D4343A	357.4	446.7	15.4
D4543A	516.7	576.7	18.0
D4115A	403.2	518.0	18.6
D4315A	377.0	462.3	21.3
D4365A	364.4	470.2	16.8
D4465A	395.7	497.8	15.4
D4515A	515.3	575.4	16.9
I4152A	400.6	505.2	18.5
I4252A	390.2	489.7	16.7
I4352A	413.2	502.4	17.7
I4432A	528.0	584.1	17.4
I4522A	528.0	586.6	16.8

T5 TEMPER

4%Cu - (C.H.)

EXTRUDE CODE	PROOF STRESS MN/m2	U.T.S. MN/m2	% STRAIN
D4522A	456.9	531.0	16.1
D4432A	358.2	455.4	15.9
I4522A	497.6	571.6	16.8
I4432A	401.0	504.4	15.8

4%Cu - (S.S.)

EXTRUDE CODE	PROOF STRESS MN/m2	U.T.S. MN/m2	% STRAIN
D4162AS	325.0	439.3	18.8
D4362AS	431.0	516.5	13.9
D4462AS	458.0	524.5	16.2
D4562AS	462.5	546.8	17.3
D4243AS	364.7	459.1	14.2
D4323AS	428.9	514.9	16.8
D4543AS	505.0	584.1	18.5
D4443AS	436.3	525.6	18.3

FRACTURE TOUGHNESS TESTS (C.O.D.)

T6 TEMPER 4% Cu (C.H.)

EXTRUSION CODE	ā mm	Vp mm	Vc mm	Pc KN	δc mm	K MN/m3/2
D4522A	5.70	0.178	0.413	2.92	0.0531	44.11
D4522A	5.83	0.124	0.375	3.21	0.0480	41.92
D4432A	5.97	0.174	0.409	2.94	0.0540	44.58
D4432A	5.46	0.178	0.406	3.18	0.0556	45.23
D4362A	5.68	0.107	0.328	3.26	0.0522	37.46
D4362A	5.15	0.114	0.341	3.13	0.0561	40.40
D4262A	6.45	0.125	0.359	2.12	0.0422	34.06
D4262A	5.50	0.138	0.350	3.31	0.0562	39.31
D4162A	5.31	0.113	0.314	3.46	0.0505	37.73
D4162A	5.88	0.073	0.291	2.73	0.0377	32.62
I4522A	5.75	0.222	0.474	3.30	0.0699	49.73
I4522A	5.34	0.199	0.425	4.04	0.0704	51.00
I4432A	5.61	0.160	0.399	3.58	0.0580	46.28
I4432A	5.60	0.199	0.437	3.72	0.0677	50.01
I4352A	5.69	0.141	0.395	3.51	0.0615	42.15
I4352A	5.99	0.182	0.406	2.86	0.0604	41.78
I4252A	5.45	0.121	0.337	3.61	0.0574	39.59
I4252A	5.89	0.125	0.346	2.90	0.0514	37.45
I4152A	5.56	0.126	0.385	3.47	0.0568	39.92
I4152A	5.68	0.182	0.406	2.86	0.0585	40.52

T6 TEMPER 4% Cu (S.S.)

EXTRUSION CODE	ā mm	Vp mm	Vc mm	Pc KN	δc mm	K MN/m3/2
D4562AS	4.71	0.182	0.391	4.75	0.0726	50.97
D4562AS	5.13	0.192	0.437	3.73	0.0648	48.16
D4462AS	5.55	0.191	0.426	3.79	0.0668	49.56
D4462AS	5.60	0.192	0.437	3.61	0.0648	48.79
D4362AS	6.14	0.170	0.441	2.88	0.0545	44.40
D4362AS	5.56	0.166	0.404	3.81	0.0627	47.63
D4262AS	5.77	0.153	0.367	2.95	0.0546	39.62
D4262AS	5.94	0.172	0.387	3.14	0.0639	42.86
D4162AS	5.93	0.139	0.386	3.14	0.0577	40.76
D4162AS	5.89	0.131	0.369	2.95	0.0520	38.66

T5 TEMPER 4%Cu

EXTRUSION CODE	ā mm	Vp mm	Vc mm	Pc KN	δc mm	K MN/m3/2
D4522A	5.56	0.229	0.483	3.42	0.0727	48.22
D4522A	6.14	0.261	0.521	2.62	0.0680	46.63
D4432A	5.84	0.340	0.575	2.70	0.0890	47.20
D4432A	5.55	0.340	0.580	2.54	0.0873	46.77
I4522A	5.25	0.246	0.460	4.10	0.0825	53.50
I4432A	5.51	0.284	0.514	3.24	0.0843	48.65
D4562AS	5.38	0.205	0.432	3.58	0.0690	47.24
D4362AS	5.62	0.265	0.502	3.20	0.0782	48.59

T6 Temper - Recrystallized Grain Size Measurements

2014 - T6

CH Direct Extrudes

ER = 20:1

ctn. ode	T_I (°C)	Centre (mm)	±	Edge (mm)	±
162A	300	0.266	0.041	0.180	0.028
262A	350	0.321	0.040	0.266	0.040
562A	400	0.659	0.100	0.487	0.036
432A	450	0.019	0.003	0.510	0.065
522A	480	0.014	0.003	——	——
		ER = 30:1			
133A	300	0.251	0.050	0.248	0.032
343A	400	1.068	0.138	0.992	0.150

CH Indirect Extrudes

ER = 20:1

ctn. ode	T_I (°C)	Centre (mm)	±	Edge (mm)	±
152A	300	0.318	0.060	0.136	0.028
252A	350	0.340	0.090	0.208	0.300
352A	400	0.383	0.111	0.204	0.043
432A	450	0.021	0.003	0.310	0.035
522A	480	0.027	0.006	——	——
		ER = 30:1			
123A	300	0.269	0.045	0.180	0.021
323A	400	0.360	0.030	0.250	0.030

SS Direct Extrudes

ER = 20:1

Extn. Code	T_I (°C)	Centre (mm)	±	Edge (mm)	±
S4162A	300	0.297	0.110	0.152	0.013
S4262A	350	0.400	0.130	0.178	0.014
S4362A	400	0.028	0.004	0.240	0.017
S4462A	450	0.031	0.003	——	——
S4562A	480	0.037	0.004	——	——

3% Cu - T6

T_I = 400°C

ER = 50:1

Liner Temp °C	v mm/s	Centre (mm)	±	Edge (mm)	±
450	13	0.940	0.220	0.680	0.086
400	3	0.350	0.070	0.432	0.153
400	13	0.325	0.140	0.378	0.083
350	3	0.418	0.043	0.305	0.059
350	13	0.412	0.085	0.418	0.079
300	3	0.431	0.022	0.394	0.061
300	13	0.474	0.056	0.328	0.056
200	3	0.507	0.129	0.251	0.041
200	13	0.279	0.019	0.207	0.043

The Effect of Liner Temperature on the Transverse Recrystallized Grain Size.

T6 Temper

Recrystallized Depth Measurements

1% Cu Extn Code	1% Cu Depth (mm)	2% Cu Extn Code	2% Cu Depth (mm)	3% Cu Extn Code	3% Cu Depth (mm)	5% Cu Extn Code	5% Cu Depth (mm)
D1522	0	D2522	0	D3522	0.59	D5522	0.8
D1422	0.2	D2422	1.18	D3422	1.0	D5422	2.5
D1332	2.6	D2342	3.05	D3543	1.2	D553L4	0.99
D1553	0	D2543	0.46	D3443	1.6	D543L4	1.77
D1443	0.9	D2443	1.0	D3545	1.2		
D1343	2.74	D2545	0.4	D3455	1.9		
D1545	0.09	D2455	1.6				
D1445	0.8	D2345	3.58				
D1345	4.7	D24510	1.0				
D14510	0.84						
D13510	1.7						

CH Direct Extrudes

ER = 30:1

%Cu	Extn. Code	T_I (°C)	Centre (mm)	±
1	D1143A	300	0.198	0.021
2	D2163A	300	0.213	0.060
3	D3163A	300	0.220	0.040
5	D513L4	300	0.267	0.051

APPENDIX V

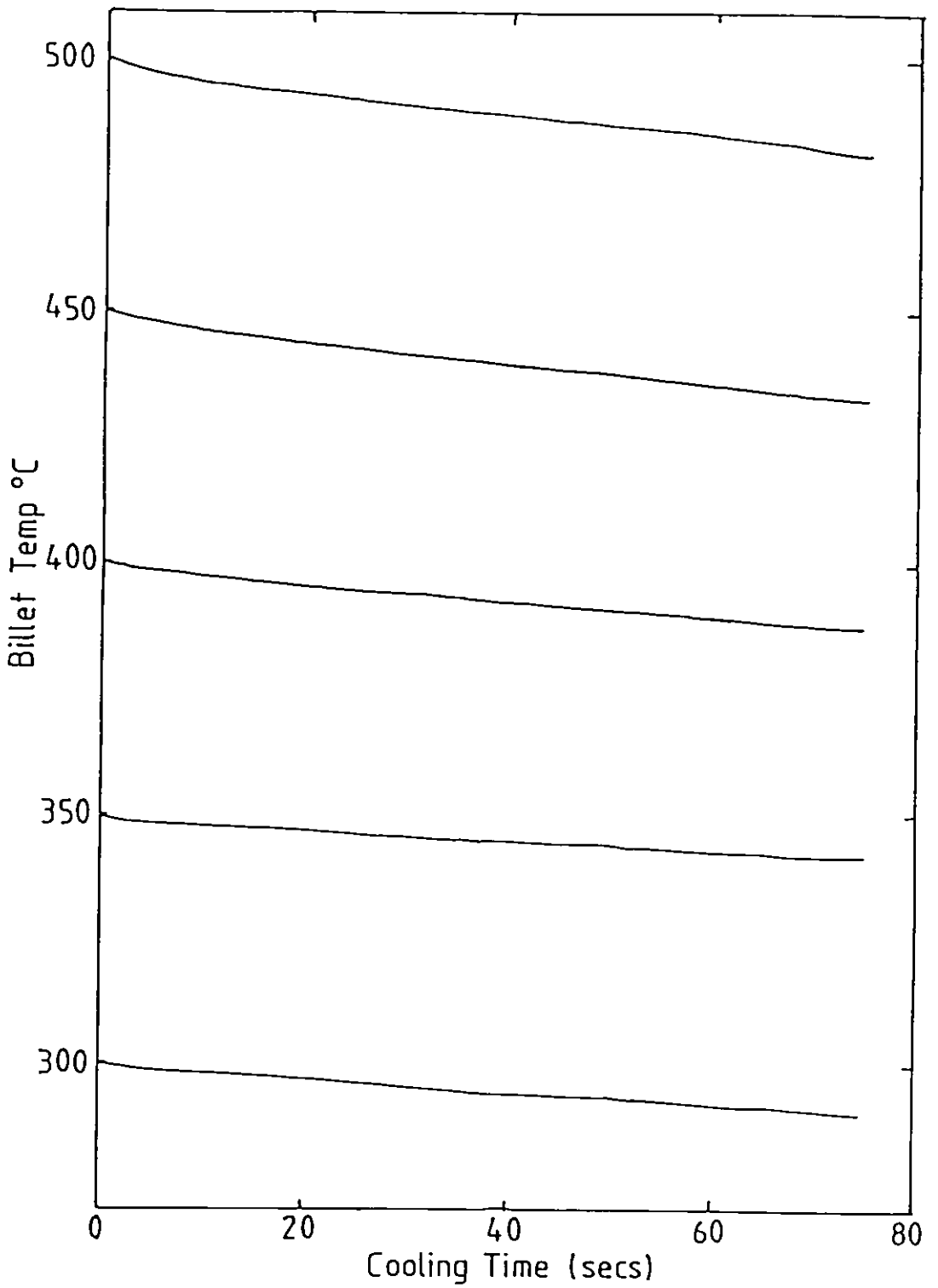
EXPERIMENTAL ERROR

During the course of the experimental work repeat tests were made where possible to estimate the accuracy of the results. Listed below are the percentage reproducibilities found from the duplicate tests:

Parameter	% Reproducibility Error
Extrusion Load	4%
Extrusion Ram Speed	4%
Torque	4%
Twist Rate	5%
Tensile Strength	3%
Elongation	8%
Fracture Toughness	14%
Hardness	8%
Microhardness	6%

The accuracy of the temperature rise during extrusion and torsion testing could not be experimentally verified but are considered to be realistic after comparison with the structure and properties of the extrudate and torsion specimens.

It should be noted that the figures quoted are for the maximum error observed, and it was generally found that percentage error was well within these limits.



Billet cooling curve

Container 50°C below billet temperature

APPENDIX VI

Programme THTEMP

Computer programme to calculate the temperature distribution and the volume average and area average temperature rise in a torsion specimen using a finite difference method which allows for heat generation, radial and axial conduction and correction heat transfer from the surface. The stress distribution and hence energy input is determined from the homologous strain analysis described in section 2.2.1. where 90% of te energy input is assumed to be converted into heat energy.

Input Data:

- Initial Temperature (^{o}C)
- Shear strain to peak
- Shear strain rate (sec^{-1})
- Hot Working Constants at 1.0, 0.75 and 0.5 homologous strain
- A Value of Modulus

The modulus value determines the time increment for the analysis. The stress as a function of strain is determined using the appropriate strain dependent hot working constants.

Internal Data:

Thermal conductivity	=	193.2	($W/m^{o}K$)
Specific heat	=	913.0	($J/Kg^{o}K$)
Density	=	2800.0	(Kg/m^{3})
Specimen radius	=	0.005	(m)
Specimen length	=	0.010	(m)

Output Data:

- Volume average and area average temperature rise (^{o}C).
- Temperature distribution on Tape 6.

```
00100 PROGRAM IHTEMP (INPUT,OUTPUT,TAPE5=INPUT,TAPE6,TAPE9,TAPE10,TAPE11)
00110C
00120C          R.P.V  4/82  VERSION   1.0
00130C      FINITE DIFFERENCE METHOD FOR CALCULATING TEMPERATURE
00140C      RISE IN A TORSION SPECIMEN, ALLOWING FOR HEAT
00150C      GENERATION AND CONVECTIVE HEAT TRANSFER FROM THE
00160C      SURFACE.
00170C
00180C      CONDUCTION CONSIDERED ALONG BOTH THE SPECIMAN AXIS
00190C      AND ITS RADIUS. ENDS OF GAUGE LENGTH ARE HELD AT INITIAL
00200C      TEMPERATURE.          I= LENGTH AXIS OF SPECIMEN
00210C                            J= RADIAL AXIS
00220C
00230C      THIS VERSION HAS BEEN ADAPTED FOR THE HOMOLOGOUS STRAIN
00240C      MODEL , VALUES OF THE HOT WORKING CONSTANTS ARE READ ONTO
00250C      TAPE9, DATA FOR INDIVIDUAL SPECIMENS ON TAPE10.
00260C
00270C*****************************************************************
00280C
00290 DIMENSION TOLD(100,50),TNEW(100,50),TRISE(50),H(100),ELVOL(21),
00300+STRESS(100),STRAN(100),AVAREAT(50),ELAREA(50),HTMP(3),ATMP(3),
00310+TART(100),DOT(100),RMAX(100),NUM(100),MSG(4),INAME(4),NNAME(4)
00320 REAL LENGTH
00330C
00340C      SET NUMBER OF STEPS ALONG THE SPECIMEN RADIUS
00350C      FRAC = FRACTION OF WORK TURNED TO HEAT
00360C
00370 R=8.314
00380 PI = 3.14159
00390 NSTEPS = 10
00400 MAX1 = NSTEPS + 1
00410 FRAC = .90
00420 RADIUS = .005
00430 LENGTH = .01
00440 VOL = PI*RADIUS*RADIUS*LENGTH
00450 AREA = PI*RADIUS*RADIUS
00460C      SET THERMAL PROPERTIES OF ALUMINIUM
00470C      ALL UNITS ARE MKS
00480 ALK = 176
00490 ALC = 913
00500 ALRHO = 2800
00510 ALPHA = ALK/(ALC*ALRHO)
00520C
00530 PRINT*,' DO YOU REQUIRE INFORMATION ON DATAFILE FORMAT '
00540 READ(5,1000) ANS
00550 1000 FORMAT(A3)
00560 IF(ANS.EQ.1HY) CALL INFO
00570C
00580C
00590 PRINT*,' ENTER THE CONSTS DATAFILE NAME '
00600 READ(5,2000) INAME(3)
00610 2000 FORMAT(A10)
00620 DATA INAME(1)/9HGET,TAPE9/,INAME(2)/1H=/,INAME(4)/1H,/
00630 CALL PFREQ(INAME,MSG,ICODE)
00640C
00650  READ(9,*) DH1,ALFA1,EN0,ACON1,DH3,ALFA3,EN3,ACON3,
00660+DH4,ALFA4,EN4,ACON4
00670C      SET AMBIENT ROOM TEMP
00680 TAMB = 20
00690C
00700C      WORK OUT DIMENSIONS OF ELEMENT
00710C
00720 DELTA = RADIUS/FLOAT(NSTEPS)
00730C DHALF = DELTA/2.0
00740 DSQUARE = DELTA*DELTA
00750 LMAX = IFIX(LENGTH/DELTA)
00760 LMAX1 = LMAX+1
00770 PRINT*,' ENTER THE DATA FILE NAME '
00780 READ (5,678)NNAME(3)
00790 678 FORMAT(A10)
00800 DATA NNAME(1)/10HGET,TAPE10/,NNAME   /1H=/,NNAME(4)/1H,/
00810 CALL PFREQ(NNAME,MSG,ICODE)
00820C
00830 READ(10,*) NPTS
00840 DO 453 L=1,NPTS
00850 453 READ(10,*)(NUM(L),TART(L),DOT(L),RMAX(L))
00860 PRINT 711
00870 711 FORMAT(*     CLACULATED PEAK TEMPERATURES:*/
00880+* SPECIMEN     T(0.5H)     T(0.75H)     T(1.0H)*/
00890+*  NUMBER*/
00900+*-------------------------------------------*/)
00910 DO 454 L=1,NPTS
00920 TSTART = TART(L)
00930 GDOT = DOT(L)
00940 GMAX = RMAX(L)
00950 DH=DH1
00960 EN=EN0
00970 ALFA=ALFA1
00980 ACON=ACON1
00990 DO 10 I=1,LMAX1
01000 DO 10 J=1,MAX1
01010   TNEW(I,J) = TSTART
01020  10 TOLD(I,J) = TSTART
01030 K=0
01040
01050C       CALCULATE HEAT TRANSFER COEFFICIENT AND BIOT NUMBER
01060
01070 H(1) = 3.79*(TSTART-TAMB)**0.25
01080 BIOT = H(1)*2.*DELTA/ALK
01090 BIGGEST = 1./(2.*(3.+BIOT))
01100 DO 15 I=1,LMAX1
01110    15 H(I) = H(1)
01120 IF (BIGGEST .GT. 0.25) BIGGEST = 0.25
01130C
01140C      READ IN MODULUS ETC
01150C
01160 AMOD=0.1667
01170 GDOT=GDOT*PI
```

```
01180 IPRINT = 5
01190C
01200 G3=3.0*GMAX/4.0
01210 IA=0
01220 GLIMIT=GMAX/2.0
01230 GM = GMAX/15.0
01240 TIME = 0.0
01250C
01260C      CALCULATE TIME INCREMENT FROM MODULUS
01270C
01280 DT = AMOD*DELTA*DELTA/ALPHA
01290C
01300C      GET STRAIN INCREMENT CORRESPONDING TO DT FOR THE GIVEN GDOT
01310C
01320 GAMINC = GDOT*DT
01330 GAMTOT = 0.0
01340 CONST = 2.0*ALPHA*DT/DSQUARE
01350C
01360C      CALCULATE TEMP RISE AS A FUNCTION OF RADIUS
01370 ZTEMP=TSTART
01380C
01390 47 RADI = DELTA/2.0
01400 ELAREA(1)= PI*RADI*RADI
01410 ELVOL(1) = PI*LENGTH*(RADI*RADI)
01420 DO 11 J=2,NSTEPS
01430       RADO = RADI + DELTA
01440 ELAREA(J) = PI*(RADO*RADO-RADI*RADI)
01450       ELVOL(J) = PI * LENGTH *(RADO*RADO-RADI*RADI)
01460    11 RADI = RADO
01470 ELVOL(MAX1) = PI*LENGTH*(RADIUS*RADIUS-RADI*RADI)
01480 ELAREA(MAX1) = PI*(RADIUS*RADIUS-RADI*RADI)
01490 RAD = 0.0
01500 DO 12 J=2,MAX1
01510 RAD = RAD + DELTA
01520 STRAIN = GAMINC*RAD/(RADIUS*SQRT(3.0))
01530C STRAN(J)=STRAIN
01540 EDOT = GDOT*RAD/(RADIUS*SQRT(3.0))
01550 EN1=1.0/EN
01560 EN2=2.0/EN
01570 ZNH=EDOT*EXP(DH/(R*(ZTEMP+273.0)))
01580 ZUPA=(ZNH)/(EXP(ACON))
01590 STRESS(J)=(1.0/ALFA)*ALOG((ZUPA**EN1)+
01600+SQRT((ZUPA**EN2)+1.0))
01610 STRES=STRESS(J)*1.E+06
01620 12 TRISE(J)=STRES*STRAIN*FRAC/(ALC*ALRHO)
01630C PRINT *,(STRESS(J),J=2,NSTEPS)
01640C PRINT *,(STRAN(J),J=2,NSTEPS)
01650C PRINT *,DH,ALFA,EN,ACON
01660 IF (IA.EQ.1) GO TO 48
01670C
01680 110  IROUND = 1
01690 GOUT = GM/FLOAT(IPRINT)
01700 KOUNT = 0
01710 KMAX = 50
01720C
01730 17 DO 35 I=2,LMAX
01740C
01750C      CALCULATE TEMPS IN BODY OF SPECIMEN.
01760 RAD = 0.0
01770 DO 20 J=2,NSTEPS
01780       RAD = RAD + DELTA
01790       CONST1 = DT*ALPHA/(2.*RAD*DELTA)
01800       T = TOLD(I,J) + AMOD*(TOLD(I,J-1)+TOLD(I,J+1)-2.*TOLD(I,J))
01810       TT = T + TRISE(J) + CONST1*(TOLD(I,J+1) TOLD(I,J-1))
01820    20 TNEW(I,J) = TT + (TOLD(I+1,J)-2.*TOLD(I,J)+TOLD(I-1,J))*AMOD
01830C     CALCULATE SURFACE TEMP
01840 T = TOLD(I,NSTEPS) + TOLD(I-1,MAX1) + TOLD(I+1,MAX1)-3.0*TOLD(I,MAX1)
01850 TT = T*ALK*(RADIUS-(DELTA/2.))/DELTA
01860 TTT = (TT-H(I)*RADIUS*(TOLD(I,MAX1)-TAMB))*2.*DT/(ALC*ALRHO*RADIUS*DELTA)
01870 TNEW(I,MAX1) = TOLD(I,MAX1) + TRISE(MAX1)*(1.-DELTA/(4.0*RADIUS)) + TTT
01880C      CALCULATE CENTRAL TEMPERATURES WITH GAUGE LENGTH ENDS AT TSTART
01890  TNEW(I,1) = TOLD(I,1) + 2.*CONST*(TOLD(I,2)-TOLD(I,1))
01900+ +ALPHA*DT*(TOLD(I+1,1)-2.*TOLD(I,1)+TOLD(I-1,1))/DELTA
01910C
01920C       RECALCULATE H FOR ACTUAL TEMP
01930 H(I) = 0.133 * (TNEW(I,MAX1)-TAMB)**0.25
01940 35 CONTINUE
01950 TIME = TIME +DT
01960 KOUNT = KOUNT + 1
01970 IF (KOUNT .LT. KMAX ) GO TO 45
01980 KOUNT = 0
01990 45 GAMTOT = GAMTOT + GAMINC
02000 IF (GAMTOT .GT. GMAX) GO TO 40
02010C
02020C      RESET OLD TEMPERATURES AND EVALUATE AGAIN
02030 DO 30 I=2,LMAX
02040 DO 30 J=1,MAX1
02050    30 TOLD(I,J) = TNEW(I,J)
02060 IF (GAMTOT.LT.GLIMIT) GO TO 48
02070 ASUM=0.0
02080 DO 66 J=1,MAX1
02090 ATOTAL=0.0
02100 DO 77 I=1,LMAX1
02110 77 ATOTAL=ATOTAL+TNEW(I,J)
02120 ATOTAL=ATOTAL*ELVOL(J)/FLOAT(LMAX1)
02130 66 ASUM=ASUM+ATOTAL
02140 ZTEMP=ASUM/VOL
02150 HOMA=GLIMIT/GMAX
02160 K=K+1.0
02170 HTMP(K)=ZTEMP
02180 PRINT *,DH,EN,ALFA,ACON
02190C PRINT 990,HOMA,ZTEMP
02200C 990 FORMAT (*HOMOLOGOUS STRAIN OF *,F6.2,*..HAS BEEN REACHED*/
02210C+*THE VOL AVERAGE TEMPERATURE=*,F6.2,*..DEG.C*)
02220       TIN  =  0.0
02230  605           DO 73 I=1,LMAX1
02240           TAREA=  0.0
02250            DO 74 J=1,MAX1
```

```
02260          74 TAREA=TAREA+TNEW(I,J)*ELAREA(J)
02270     73   AVAREAT(I) = TAREA/AREA
02280C PRINT*,' AREA AVE TEMP PROFILE '
02290C PRINT*,(AVAREAT(I),I=1,LMAX1)
02300 ATMP(K)=AVAREAT(11)
02310    IF(TIN .EQ. 1.0) GO TO 606
02320 GLIMIT = GLIMIT  + GMAX/4.0
02330 IF(GLIMIT.LE.G3) GO TO 98
02340 GO TO 99
02350 98 DH=DH3
02360 ACON=ACON3
02370 ALFA=ALFA3
02380 EN=EN3
02390 GO TO 111
02400 99 DH=DH4
02410 ACON=ACON4
02420 ALFA=ALFA4
02430 EN=EN4
02440 111 CONTINUE
02450 IA=1
02460 GO TO 47
02470 48 IF(GAMTOT .GE. GOUT) GO TO 40
02480 GO TO 17
02490C
02500C      WRITE OUT RESULTS
02510C
02520C 40 WRITE (6,600) GAMTOT,TSTART,GOUT,STRESS,EN
02530C 600 FORMAT(1HS/'1   TEMPERATURE DISTRIBUTION ACROSS A TORSION SPECIMEN'/
02540C+' TWISTED TO A SHEAR STRAIN OF ',F5.2,' FROM ',F5.1,' DEGREES C'/
02550C+'  WITH A SHEAR STRAIN RATE OF ',F5.2,' PER SEC'//
02560C+'      STRESS = ',F5.1, ' ( STRAIN RATE)**',F4.4,'     (MN/M**2)')
02570C WRITE (6,620)
02580C 620 FORMAT(/* TEMPERATURE PROFILE ALONG THE AXIS OF THE SPECIMEN*/
02590C+            * IN GROUPS FROM THE CENTRE TO THE OUTSIDE RADIUS*)
02600 40 SUM = 0.0
02610 DO 60 J=1,MAX1
02620       TOTAL = 0.0
02630       WRITE (6,630) (TNEW(I,J),I=1,LMAX1)
02640             630 FORMAT(/,20(1X,F5.1))
02650 DO 50 I=1,LMAX1
02660    50 TOTAL = TOTAL + TNEW(I,J)
02670       TOTAL = TOTAL * ELVOL(J)/FLOAT(LMAX1)
02680    60 SUM = SUM + TOTAL
02690       TAV = SUM/VOL
02700       WRITE(6,640) TAV
02710             640 FORMAT ( * VOLUME AVERAGE TEMPERATURE    *,F6.2 )
02720 IROUND = IROUND + 1
02730 GOUT = GM*FLOAT(IROUND)/FLOAT(IPRINT)
02740 IF (IROUND .LE. IPRINT) GO TO 17
02750 IF ( GM .GE. GMAX/5.) GO TO 120
02760 GM = GMAX/5.
02770 GO TO 110
02780 120 IF (GM .GE. GMAX) GO TO 130
02790 GM = GMAX
02800 GO TO 110
02810C 130 PRINT 640, TAV
02820 130    TIN=1.0
02830 K=K+1.0
02840 ATMP(K)=TAV
02850 PRINT *,DH,EN,ALFA,ACON
02860    GO TO 605
02870 606 PRINT 4000,(NUM(L),ATMP(1),ATMP(2),ATMP(3))
02880 4000 FORMAT(3X,I3,7X,F6.2,5X,F6.2,6X,F6.2)
02890 WRITE(11,5000)(NUM(L),ATMP(1),ATMP(2),ATMP(3))
02900 5000 FORMAT(3X,I3,7X,F6.2,5X,F6.2,6X,F6.2)
02910C
02920C DH=DH1
02930C ALFA=ALFA1
02940C EN=EN1
02950C ACON=ACON1
02960 454 CONTINUE
02970C*****************************************************
02980C
02990 PRINT*,' MAXIMUM AREA AVERAGE TEMPERATURES ARE ON TAPE11 '
03000C
03010C
03020 STOP
03030 END
03040 SUBROUTINE INFO
03050 PRINT 3000
03060 3000 FORMAT(*        TWO DATAFILES ARE REQUIRED, ONE CONTAINING THE*/
03070C
03080+* HOT WORKING COSTANTS IN THIS ORDER: */
03090+*     DELTAH, ALPHA, N, LOGA */
03100+* WITH 0.5H FIRST THEN 0.75 AND 1.0H .*/
03110+* A SECOND DATAFILE WITH THE NUMBER OF TESTS THEN: */
03120+* SPECIMEN NUMBER(NUMERIC), TEMP(DEG.C), SHEAR STRAIN RATE, */
03130+* AND SHEAR STRAIN TO PEAK TORQUE. */
03140+* THIS PROGRAM WILL NOW TERMINATE */
03150+*        HAVE A NICE DAY - RICK -*)
03160 STOP
03170 END
```

Programme TRQGRAF

Computer programme to calculate values of the stress-strain rate exponents and hot working constants from raw torque twist data via the graphical analysis described in section 2.2.2.2.

Input Data:

Initial test temperatures (°C)
Mean Twist rate (Rev/sec)
Peak Torque (Nm)

The date is entered in free format in the form of a matrix:-

x	y		
X(1)	X(2).....		X(x)
Y(1)	$T_{y_1x_1}$	$T_{y_1x_2}$.....	$T_{y_1x_x}$
Y(2)	$T_{y_2x_1}$	$T_{y_2x_2}$.....	$T_{y_2x_x}$
Y(y)	$T_{y_yx_1}$	$T_{y_yx_2}$.....	$T_{y_yx_x}$

x - number of twist rates considered
y - number of temperatures considered

X(1) ... X(x) the mean twist rates
Y(1) ... Y(y) the initial temperatures

Tyx are the relevant values of torque at the appropriate temperatures and twist rates. Note the matrix must be completed, if experimental points are not available these should be estimated from invididual torque - temperature or twist ratecharacteristics. The data must be on Tape 7.

Output Data:

The output data is in the form of a table listing the individual constants, standard errors and correlation coefficients. The data may be saved on Tape 6.

```
00100 PROGRAM TRAGRAF(INPUT,OUTPUT,TAPE5=INPUT,TAPE6=OUTPUT,TAPE7)
00110 COMMON RCOEF,SDEV,B,AM
00120 DIMENSION T(10),SE(10,50),SA(50),ALA(50),S(50),ALE(50)
00130+,BETA(10),AN2(10),ALPHA(10),SLH(50),ADH1(10),ADH2(10),SIH(50),TI(50)
00140+,ALZ(50),ALNA(10),AN(10),SHI(50),ALTHET(50)
00150 DATA R,PIE,RAD,EL/8.314,3.142,0.005,0.01/
00160C
00170C*****************************************************************
00180C       THIS PROGRAMME EXECUTES THE GRAPHICAL ANALYSIS
00190C       DESCRIBED IN R.P.VIEROD P.H.D THESIS - 1984
00200C
00210C*****************************************************************
00220 READ(7,*) NSA,KT
00230 READ(7,*) (SA(I),I=1,NSA)
00240 DO 10 K=1,KT
00250 READ(7,*) (T(K),(SE(K,I),I=1,NSA))
00260 10 CONTINUE
00270 SALPHA=0
00280 BETAC=(2.0*PIE*(RAD**3.0))/(3*1.732)
00290 DO 20 I=1,NSA
00300 ALA(I)=ALOG(SA(I))
00310 20 CONTINUE
00320 CALL HEAD
00330 DO 30 K=1,KT
00340 DO 40 I=1,NSA
00350 S(I)=SE(K,I)
00360 ALE(I)=ALOG(SE(K,I))
00370 40 CONTINUE
00380 CALL LINFIT(S,ALA,NSA)
00390 BETA(K)=AM*(BETAC*1.0E6)
00400 CALL LINFIT(ALE,ALA,NSA)
00410 AN2(K)=AM
00420 ALPHA(K)=BETA(K)/AN2(K)
00430 SALPHA=SALPHA+ALPHA(K)
00440 30 CONTINUE
00450 PRINT*,'   TEMP/DEG.C   BETA            N2          ALPHA
00460+       -------      -------          -----              - - -'
00470 DO 35 K=1,KT
00480 WRITE(6,*)(T(K),BETA(K),AN2(K),ALPHA(K))
00490 35 CONTINUE
00500 SBET=0
00510 SNT=0
00520 DO 200 K=1,2
00530 SBET=SBET + BETA(K)
00540 200 CONTINUE
00550 ASBET=SBET/2.0
00560 J=KT-2.0
00570 DO 300 K=J,KT
00580 300 SNT=SNT + AN2(K)
00590 ASNT=SNT/(KT-2.0)
00600 UALPHA=ASBET/ASNT
00610 PRINT*,'ALPHA CALC USING HIGH AND LOW STRESS VALUES '
00620 WRITE(6,*) UALPHA
00630 UUALPHA=BETA(1)/AN2(KT)
00640 PRINT*,' ALPHA FROM INITIAL AND FINAL TEMP DATA '
00650 WRITE(6,*) UUALPHA
00660 TALPHA=SALPHA/FLOAT(KT)
00670 PRINT*,' AVERAGE ALPHA  '
00680 WRITE(6,*) TALPHA
00690 AVADH1=0
00700 AVADH2=0
00710 CT=(2.0*PIE*RAD)/(1.732*EL)
00720 CS=(3.0*1.732)/(2.0*PIE*(RAD**3.0)*1.0E6)
00730 CALL HEAD
00740 DO 45 K=1,KT
00750 DO 55 I=1,NSA
00760 ALTHET(I)=ALOG(SA(I)*CT)
00770 SLH(I)=ALOG(SINH(UUALPHA*SE(K,I)*CS))
00780 55 CONTINUE
00790 CALL LINFIT(SLH,ALTHET,NSA)
00800 ADH1(K)=AM
00810 AVADH1=AVADH1+ADH1(K)
00820 45 CONTINUE
00830 TADH1=AVADH1/FLOAT(KT)
00840 DO 60 I=1,NSA
00850 DO 65 K=1,KT
00860 SIH(K)=ALOG(SINH(UUALPHA*SE(K,I)*CS))
00870 TI(K)=1.0/(T(K)+273.0)
00880 65 CONTINUE
00890 CALL LINFIT(TI,SIH,KT)
00900 ADH2(I)=AM
00910 AVADH2=AVADH2+ADH2(I)
00920 60 CONTINUE
00930 TADH2=AVADH2/FLOAT(NSA)
00940 PRINT*,' TEMP/DEG.C     DELTA H'
00950 PRINT*,'  -----           - - -'
00960 DO 67 K=1,KT
00970 TDELTA=ADH1(K)*TADH2*R
00980 WRITE(6,*) T(K),TDELTA
00990 67 CONTINUE
01000 DELTAH=R*TADH1*TADH2
01010 PRINT*,' AVERAGE VALUE OF DELTA H '
01020 WRITE(6,*) DELTAH
01030 AVALNA=0
01040 AVAN=0
01050 DR=DELTAH/R
01060 CA=(4.0*PIE*RAD)/(3.0*1.732*EL)
01070 CALL HEAD
01080 DO 70 I=1,NSA
01090 DO 75 K=1,KT
01100 ALZ(K)=ALOG(SA(I)*CA*EXP(DR*TI(K)))
01110 SHI(K)=ALOG(SINH(UUALPHA*SE(K,I)*CS))
01120 75 CONTINUE
01130 CALL LINFIT(SHI,ALZ,KT)
01140 AN(I)=AM
01150 ALNA(I)=0
01160 AVAN=AVAN+AN(I)
01170 AVALNA=AVALNA+ALNA(I)
```

```
01180 70 CONTINUE
01190 TAN=AVAN/FLOAT(NSA)
01200 TALNA=AVALNA/FLOAT(NSA)
01210 PRINT*,' AVERAGE VALUE OF N '
01220 WRITE(6,*) TAN
01230 PRINT*,' AVERAGE VALUE OF LOG(A) '
01240 WRITE(6,*) TALNA
01250 DO 90 K=1,KT
01260 DO 95 I=1,NSA
01270 ALZ(I)=ALOG(SA(I)*CA*EXP(DR*TI(K)))
01280 SHI(I)=ALOG(SINH(UUALPHA*CS*SE(K,I)))
01290 95 CONTINUE
01300 CALL LINFIT(SHI,ALZ,NSA)
01310 AN(K)=AM
01320 ALNA(K)=B
01330 AVAN=AVAN+AN(K)
01340 AVALNA=AVALNA+ALNA(K)
01350 90 CONTINUE
01360 PRINT*,'    TEMP       N        LNA '
01370 DO 80 K=1,KT
01380 PRINT *,(T(K),AN(K),ALNA(K))
01390 80 CONTINUE
01400 STOP
01410 END
01420C*****************************************************************
01430 SUBROUTINE LINFIT(X,Y,NTS)
01440 COMMON RCOEF,SDEV,B,AM
01450 DIMENSION X(50),Y(50)
01460 SY=0
01470 SX=0
01480 DO 12 I=1,NTS
01490   SX=X(I)+SX
01500   SY=Y(I)+SY
01510 12 CONTINUE
01520 SXM=SX/FLOAT(NTS)
01530 SYM=SY/FLOAT(NTS)
01540 AY1=0
01550 AX1=0
01560 DO 13 I=1,NTS
01570 V=(X(I)-SXM)*(Y(I)-SYM)
01580 AX1=V+AX1
01590 W=(X(I)-SXM)**2.0
01600 AY1=AY1+W
01610 13 CONTINUE
01620 AM=AX1/AY1
01630 B=SYM-(AM*SXM)
01640 AX2=0
01650 AY2=0
01660 DO 14 I=1,NTS
01670 AX12=(X(I)-SXM)**2.0
01680 AX2=AX12+AX2
01690 AY12=(Y(I)-SYM)**2.0
01700 AY2=AY12+AY2
01710 14 CONTINUE
01720 DXY=SQRT(AX2*AY2)
01730 RCOEF=AX1/DXY
01740 SDEV=SQRT(AX2)/(FLOAT(NTS)-1)
01750 WRITE(6,*) AM,B,RCOEF,SDEV
01760 RETURN
01770 END
01780C*****************************************************************
01790 SUBROUTINE HEAD
01800 PRINT*,'       M          B      CORRELATION   STANDARD
01810+                                 COEFFECIENT   DEVIATION
01820+      ---         ---     ---- ---- ---- ---- ---- ---- '
01830 RETURN
01840 END
```

Subroutine EXTEMP

Subroutine to calculate the temperature rise during direct or indirect extrusion using the theory outlined in section 2.3.2. This routine calculates the temperature rise using an integral profile calculation and is part of a simple main programme used in processing the extrusion data.

Input Data:

BL - Initial billet length (m)
BLT - Billet length at which temperature rise is required (m)
ER - Extrusion ratio
TB - Billet temperature (^{o}C)
AQ1 - Energy input evaluated from the load displacement locus (J)
DB - Billet diameter
v - Ram speed (mm/S)
X1 - Extent of the deformation zone esimated from the single triangle upper bound solutions[100,129]
RANGLE - Angle of the direct deformation zone (radians)
IFLAG - Denotes: 1 - direct extrusion
2 - indirect extrusion
TEMPCON - Liner Temperature (^{o}C)
TEMPAD - Pressure Pad Temperature (^{o}C)

Internal Data:

Extrusion Billet

Aluminium density	=	2800 (Kg/m^3)
Aluminium specific heat	=	1063.9 ($J/Kg^{o}K$)
Aluminium thermal conductivity	=	201.0 ($W/m^{o}K$)

Tooling

Steel density	=	7860 (Kg/m^3)
Steel specific heat	=	489.76 ($J/Kg^{o}K$)
Steel thermal conductivity	=	32.65 ($W/m^{o}K$)

Die land length = 0.00508 (m)

Output Data:

TEMPD - Temperature of billet after temperature rise (^{o}C)

```
03080 SUBROUTINE EXTEMP(BL,ER,BLT,TB,AQ1,DB,V,X1,TEMPD,TEMPCON,RANGLE,IFLAG)
03090C
03100C
03110C         THIS SUB-ROUTINE CALCULATES THE TEMPERATURE RISE
03120C         DURING EXTRUSION AND IS INCLUDED IN A PROGRAMME
03130C         WHICH PROCESSES ALL THE EXTRUSION DATA
03140C         THE VARIABLES WHICH SHOULD BE PASSED TO THIS
03150C         ROUTINE ARE AS INDICATED, FURTHER DETAILS MAY
03160C         BE OBTAINED FROM S.J.PATERSON-PH.D.THESIS
03170C         THE FOLLOWING ARE ASSUMED TO BE CONSTANT:-
03180C         DENSITIES OF ALUMINIUM ALLOY AND STEEL,RHOAL,RHOST;
03190C         HEAT CAPACITIES OF ALUMINIUM ALLOY AND STEEL,CAL,CST;
03200C         THERMAL CONDUCTIVITIES OF ALUMINIUM ALLOY AND STEEL,AKAL,AKST;
03210C         LAND LENGTH-ALL
03220C
03230C
03240 TEMPAD=TEMPCON-80.0
03250 ALL = 0.00508
03260 RHOAL = 2800.0
03270 RHOST = 7860.0
03280 CAL = 1063.9
03290 CST = 489.762
03300 AKAL = 201.0
03310 AKST = 32.6508
03320C
03330C
03340C          SETS UP DIMENSIONS OF DEFORMATION ZONE AND
03350C          CALCULATES VALUE OF WORK CONSTANT
03360C
03370C
03380 RANGLE= (90./57.29578)-RANGLE
03390 TANANG = SIN(RANGLE)/COS(RANGLE)
03400 DB2 = DB*DB
03410 DE = SQRT(DB2/ER)
03420C
03430C         DIRECT EXTRUSION
03440C
03450 IF (IFLAG.EQ.2) GO TO 90
03460 COSRAN = COS(RANGLE)
03470 ALD = X1-(((DB-DE)/2.0)*TANANG)
03480 GO TO 91
03490C
03500C          INDIRECT EXTRUSION
03510C
03520 90 COSRAN = 1.0
03530 ALD = X1
03540 91 ALT = BL-X1
03550C
03560C
03570 ALFAST = AKST/(CST*RHOST)
03580 ALFAAL = AKAL/(CAL*RHOAL)
03590 ALFA = SQRT(ALFAST/ALFAAL)
03600C
03610C
03620C          CALCULATION OF CONSTANTS IN THE HEAT BALANCE EQUATION.
03630C
03640C
03650 AK1 = (3.142*((DB2)-(DE*DE))/COSRAN)*SQRT(AKST*CST*RHOST/12.0)
03660 AK2 = 3.142 *ALD/6.0*(18.0*AKST*DB*SQRT(RHOST*CST))**(2.0/3.0)
03670 AK3 = 3.142 *ALD/6.0*DB*(18.0*AKST*DB*((RHOST*CST)**2))**(1.0/3.0)
03680 AK4 = 3.142*ALL/6.0*(18.0*AKST*DE*SQRT(RHOST*CST))**(2.0/3.0)
03690 AK5 = 3.142*ALL/6.0*DE*(18.0*AKST*DE*((RHOST*CST)**2))**(1.0/3.0)
03700 AK7 = 3.142/6.0*ALT*(18.0*AKST*DB*SQRT(CST*RHOST))**(2.0/3.0)
03710 AK9 = 3.142/6.0*(18.0*AKST*(DB**4)*(ALT**3)*(RHOST*CST)**2)**(1.0/3.0)
03720 AK11 = 3.142 *DB2*SQRT(RHOST*AKST*CST/12.0)
03730C
03740C
03750C          EVALUATION OF THE TEMPERATURE RISE
03760C
03770C
03780 AK6  = 3.142*DE*BE/4.0*RHOAL*CAL*ER*V
03790 AK8  = -AK7*3.0*V /(5.0*ALT)
03800 AK10  = -AK9*3.0*V /(4.0*ALT)
03810 TIME  = BLT/V
03820 CTOT2  = (AK1*SQRT(TIME ))+((AK2+AK4)*TIME **(2.0/3.0))+((AK3+
03830+AK5)*TIME **(1.0/3.0))
03840 CTOT1  = (AK6 *TIME )+CTOT2
03850 CTOT3  = CTOT2 +(AK7*TIME **(2.0/3.0))+(AK8 *TIME **(5.0/3.0))
03860++(AK9*TIME **(1.0/3.0))+(AK10 *TIME **(4.0/3.0))
03870 CTOT4=(AK11*SQRT(TIME))
03880 TB =TB +273.
03890 TEMPI  = (TB +(ALFA*TEMPCON))/(1.0+ALFA)
03900 TMPRISE  = 0.9*(AQ1-(TEMPI -TEMPCON)*CTOT3-(TEMPI-TEMPAD)*CTOT4)/CTOT1
03910 TEMPD  = TB +TMPRISE-273.0
03920 TB=TB-273.0
03930 RANGLE=(90./57.29578)-RANGLE
03940C
03950 RETURN
03960 END
```

NOMENCLATURE

A	Area
	Hot working constant
A_1, A_2	Constants in hot working theory
a	Constant
$\bar{a}$	Mean fatigue crack length
a"	Constant in flow stress equation
b	Burgers vector
	Constant
b"	Constant in flow stress equation
C_A	Specific heat of aluminium
C_t	Container temperature
C_S	Specific heat of steel
CH	Conventionally heated material
D	Recrystallized grain size
DCTY	% elongation in tensile tests
D_B	Billet diameter
D_E	Extrude diameter
ER	Extrusion ratio
d	Mean subgrain size
d_p	Displacement to peak
$\dot{E}$	Rate of energy dissipation
G	Shear Modulus
ΔH	Activation energy
J_1, J_2, J_3	Integrals in torsion data analysis
K_C	Plane stress fracture toughness
K_{IC}	Plane strain fracture toughness
$\bar{k}$	Mean shear flow stress
k	Shear flow stress
	Boltzman constant
	Constant in modified Hall Petch equation
k_A	Thermal conductivity of aluminium
k_S	Thermal conductivity of steel
L_p	Peak extrusion load
L_B	Billet length
L	Gauge length of torsion specimen
	Extrude length
M	Torque
m	Exponent relating subgrain size to z
	Constant friction factor
n	Strain hardening exponent
	Strain rate exponent
	Hot working constant
n'	Strain rate exponent
P	Extrusion pressure
Pc	Maximum load in C.O.D. tests
ΔP	Peak pressure increment
PS	0.2% proof stress
R	Gas constant
	Extrusion ratio
R_B	Billet radius
R_E	Extrude radius
r	Radius
r_1, r_2	Inner and outer radius of torsion specimen
SS	Presolution soak material
T	Temperature
T_c	Actual temperature
T_F	Final temperature

T_V	Volume average temperature rise - torsion
T_{AV}	Area average temperature rise - torsion
t	Time
UTS	Ultimate tensile stress
V	Volume
V_B	Billet volume
V_p	Elastic component of clip gauge displacement
V_c	Plastic component of clip gauge displacement
v	Ram speed
	Velocity
x	Constant
$\bar{Y}$	Mean yield stress
y	Constant
Z	Zener-Holloman parameter
Z_I	Z calculated using initial temperature
Z_p	Z calculated using peak temperature
Z_c	Z calculated using actual temperature
Z_f	Z calculated using final temperature
α	Hot working constant
α'	Dislocation strengthening efficiency
β	Constant in hot working theory
γ	Shear strain
$\dot{\gamma}$	Shear strain rate
δ_c	Critical crack opening displacement
ε	Equivalent strain
ε_P	Strain to peak
ε_H	Homologous strain
	Strain rate
	Mean strain rate

ρ_A	Density of aluminium
ρ_S	Density of steel
ρ	Dislocation density
σ	Flow stress
$\bar{\sigma}$	Mean flow stress
σ_I	Initial flow stress
σ_p	Flow stress at peak
σ_o	Constant in modified Hall Petch equation
θ	Twist
θ_p	Twist to peak
θ_H	Homologous twist
$\dot{\theta}$	Twist rate
τ	Shear stress
μ	Friction coefficient
σ_y	Yield stress
σ^*	Constant in stress equations

REFERENCES

1 C.E. Pearson & R.N. Parkins. The Extrusion of Metals. 1961. Chapman & Hall Ltd.. London.
2 R. Hill. The Mathematical Theory of Plasticity. 1950. Oxford Univ. Press.
3 W. Johnson & H. Kudo. The Mechanics of Metal Extrusion. 1962. Manchester Univ. Press.
4 L.E. Farmer & P.L.B. Oxley. J.Mech.Phys.Solids. 1971. 19. 369.
5 P.L.B. Oxley. Proc.Conf.Mech.Props. of Materials at High Rates of Strain. Inst. of Phys. 1973.
6 A.H. Shabaik. Application of Numerical Methods to Forming Processes. A.S.M.E. San Fransisco. 1978.
7 J.F.W. Bishop. Quart.J.Mech.Appl.Math. 1956. 9. 236.
8 R.I. Tanner & W. Johnson. Int.J.Mech.Sci. 1960. 1. 28.
9 M.T. Watkins, K. Ashcroft & J. McKenzie. Mech.Eng.Res. Lab.(Plasticity Div). Rep. 1954. (102). 1956 (111).
10 K. Ashcroft & G.S. Lawson. J.I.M. 1960-61. 89. 369.
11 A.R.E. Singer & S.H.K. Al-Sammarai. IBID. 1960. 89. 225.
12 A.R.E. Singer & J.W. Coakham. IBID. 1960. 89. 177.
13 R. Akeret. IBID. 1967. 95. 204.
14 T. Sheppard & D. Raybould. IBID. 1973. 101. 33 & 73.
15 F.W. Sharman. Metals.Tech. 1977. 4. 91.
16 P.M. Reynolds. J.I.M. 1966. 94. 379.
17 A.F. Castle & T. Sheppard. Metals.Tech. 1976. 3. 454.
18 G.D. Lahoti & T. Altan. 21st Sagamore Army Mat.Res. Conf.Proc.
19 C.P. Hinesley & H. Conrad. Mat.Sci. & Eng. 1973. 12. 47.
20 C. Gagnon & J.J. Jonas. Trans.Met.Soc. A.I.M.E. 1969. 245. 2581.
21 D. Raybould & T. Sheppard. J.I.M. 1973. 101. 65.
22 M. Farag & C.M. Sellars. IBID. 1973. 101. 137.
23 W.A. Wong & J.J. Jonas. Trans.Met.Soc. A.I.M.E. 1968. 242. 2271.
24 A.F. Castle & T. Sheppard. IBID. 1976. 3. 465.
25 A.F. Castle P.H.D. Thesis. Univ. of London. 1974.
26 E.P. Wood P.H.D. Thesis. Univ. of London. 1978.
27 M.G. Tutcher P.H.D. Thesis. Univ. of London.1979.
28 P.A. Tunnicliffe P.H.D. Thesis. Univ. of London.1979.
29 S.J. Paterson P.H.D. Thesis. Univ. of London. 1981.
30 A. Wilm Metallurgie. 1911. 8. 223. (Translation. Metal Progress. 1939. 36. 259): Aluminium. 1936. 18. 336.
31 P.D. Merica Et Al. Sci.Paper (U.S. Bureau of Standards). 1919. 347.
32 Properties of Alcan Aluminium. Alcan Booth Ltd..
33 L.F. Mondolfo Aluminium Alloys. Vol1. 1976. Butterworth. London.
34 K.R. Van Horn Aluminium Vol1. 1967. A.S.M. Metals Park. Ohio.
35 M.V. Lancker Metallurgy of Aluminium Alloys. 1967. Chapman Hall. London.
36 H.J. Axon J.I.M. 1952-53. 81. 449.
37 R.B. Ross Metallic Materials Specification Handbook. 1972. Spon. London.
38 G. Phragmen J.Inst. Metals. 1950.
39 F.C. Lea Et Al. IBID. 28. 583.
40 M.V. Hyatt Allumino. 1977. 46. (2). 81.
41 D.S. Thompson Met.Trans. 1975. Vol6A. April. 671.
42 H. Westengen et al. Proc. 1st Riso Int. Symposium Met. & Mat. Sci.. 1980. Riso.
43 A.J. Bryant Allumino. 1977. 46. 5. 228-243.
44 R. Nicholson & J. Nutting Phil.Mag.. 1958. 3.8.531.
45 J.W. Martin Precipitation Hardening. 1968. Pergamon Press.
46 E. Hornbogen Aluminium. 1967. 43. pp 41.115.163.
47 A. Guinier Compt.Rend.. 1938. 206.1641.
48 V.A. Phillips Acta Met.. 1973. 21.219.
49 J.M. Silcock et al. J.I.M.. 1953. 83.239.
50 C. Laird & H. Aaronson Acta Met.. 1966. 14.171.
51 J.W. Martin Micromechanisms in Particle Hardened Alloys. 1980. Cambridge Univ. Press.
52 H.K. Hardy J.I.M.. 1954. 83.17.
53 J.M. Silcock J.I.N.. 1960. 89.203.
54 N. Sen & D.R.F. West Proc.Int. Symp. The Mechanism of Phase Transformations in Crystalline Solids. Inst.Met.Rep. 33. 1968. p 49.
55 R.N. Wilson Ibid. p 80.
56 W. Bonfield & P.K. Datta J.Mat.Sci.. 1977. 12.1050.
57 W. Bonfield & P.K. Datta J.Mat.Sci.. 1976. 11.1661.
58 D.S. Thompson & S.A. Levy Aluminium Alloys In the Aircraft Industry. Symp. Turin. 1-2 Oct. 1976.
59 J.D. Cook & J. Nutting Ref. 54. p 54.
60 F.W. Sharman Metals Tech.. 1977. 4.91.
61 G. Hahn & A. Rosenfield Met.Trans.. 1975. Vol6A. 653.
62 E.A. Starke J.Met.. 1970. 22.1.p54.
63 G.G. Garret et al. Met.Trans.. 1978. 9A.1187.
64 M.O. Spiedel Met.Trans.. 1975. Vol6A.631.
65 K. Sugimoto et al. Corrosion Science. 1975. 15.709.
66 W. Bell & H. Cambell J.I.M.. 1960-61. 89.464.
67 E. Liddiard & J. Whittaker J.I.M.. 1960-61. 89.p423+377.
68 J.J. Jonas C.M. Sellars & W.J.McG Tegart Met.Rev.. 1969. 14.1.
69 H. McQueen & J. Jonas Treatise on Mat.Sci.. Vol6. p393. Academic Press. 1975.
70 J.F. Alder & V.A. Philips J.I.M.. 1954-55. 83.80.
71 C. Rossard & P. Blain Rev.Met.. 1958. 55.573.
72 R.R. Arnold & B.J. Parker J.I.M.. 1959-60. 88.225.
73 J.A. Bailey & A.R. Singer J.I.M.. 1960-61. 89.94.
74 H.J. McQueen & J.J. Jonas Hot Workability Testing Techniques.
75 C.M. Sellars & W.J. McG Tegart Int.Met.Rev..1972. 17.1.
76 A. Castle & T. Sheppard Metals Tech.. 1976.3.465.
77 F. Garafalo Trans.Met.Soc.. A.I.M.E.. 1963. 227.351.
78 T. Sheppard & D. Raybould J.I.M.. 1973. 101.65.
79 W.A. Wong & J.J. Jonas Trans.Met.Soc.. A.I.M.E.. 1968. 242.2271.
80 C.M. Sellars & W.J. McG Tegart Mem.Sci.Rev.Met.. 1966. 63.731.
81 C. Zener & J. Holloman J.Appl.Physics. 1944. 15.22.
82 T. Sheppard & D. Raybould J.I.M.. 1973. 101.33.
83 J.A. Bailey Int.J.Mech.Sci.. 1972. 14.375
84 P.R. Swann Electron Microscopy & Strength of Metals. 1963. Interscience.
85 J. Cotner & W.J. McG Tegart J.I.M.. 1969. 97.73.

86 M. Luton & J.J. Jonas Proc.2nd Conf. Strength of Metals and Alloys. A.S.M. Metals Park. Ohio. 1970. pp1100.
87 D. Hull Introduction to Dislocations. 1975. Pergamon Press.
88 D. Sastry M. Luton & J.Jonas Phil.Mag.. 1974. 30.115
89 T. Sheppard & M.G. Tutcher Metal Science J.. 1980. 14.579.
90 N.F. Foire & C.L. Bauer Prog.Mat.Sci.. 1968. 13.87.
91 H. Ormerod & W.J. McG Tegart J.I.M.. 1960-61. 89.94.
92 W. Wong H.McQueen & J.J. Jonas J.I.M.. 1967. 95.129.
93 H. McQueen Met.Trans.. 1977. Vol8A.807.
94 A. Korbel & K. Swiatkowski Metal Science J.. 1972. 6.60.
95 R. Sandstrom Acta Met.. 1977. 25.p897 + 905.
96 H.J. McQueen J.Metals. 1968. 3.31.
97 H. McQueen W. Wong & J. Jonas Acta Met.. 1967. 15.586.
98 H. McQueen t al. Can.J.Phys.. 1967. 45.1225.
99 K.J. Gardner & R. Grimes Metal Science J.. 1979. 13.216.
100 T. Sheppard Modern Extrusion Symposium. 1980. Birmingham Met.Assoc..
101 E.C.W. Perryman Creep and Recovery. A.S.M.. 1956. p111.
102 R.A. Petkovic et al. Can.Met.Quart.. 1975. 14.
103 H.J. McQueen Trans.Jap.Inst.Met.. 1968. 9.170.
104 J. Byrne Recovery. Recrystn. and Grain Growth. 1956. McMillan. N.Y..
105 H. Hu Trans. A.I.M.E.. 1962. 224.75.
106 J.C.M. Li J.Appl.Phys.. 1962. 33.2958.
107 F.J. Humphreys Acta Met.. 1977. 25.1323.
108 J.A. Bailey & P.B. Hirsch Proc. Royal Soc.. 1962. (A).267.11.
109 P. Beck & P.R. Sperry J.Appl.Phys.. 1950. 21.150.
110 F.J. Humphreys Metal Science J.. 1979. 13.131.
111 S. Hirst & D. Ursell Metal Treatment. 1958. 25.409.
112 M. Zaidi Ph.D. Thesis. Univ. of London. 1980.
113 W.A. Wong Ph.D. Thesis. McGill Univ. Canada. 1967.
114 L.J. Cuddy Met.Trans.. 1970. 1.395.
115 T. Sheppard et al. Mat Sci.J.. 1979. 6.473.
116 D. Raybould & T. Sheppard 4th Int.Conf. Strength of Metals.and Alloys. 1976. Nancy. France. p664.
117 A.F. Castle & T. Sheppard Metals Tech.. 1976. 2.483.
118 R.J. McElroy & Z.C. Sckopiak Int.Met.Rev.. 1972. 17.175.
119 A.W. Thompson Met.Trans.. 1977. Vol8A. 833.
120 H.A. Lipsitt & C.M. Sargent 2nd Int.Conf. on the Strength of Metal and Alloy. 1970. 3.937-40.
121 H.A. Lipsitt & C.M. Sargent. Electron Microscopy and Structure of Materials. 1972. Univ. of California Press.
122 D.S. Wright Ph.D. Thesis. Univ. of London. 1978.
123 A.S.M. Handbook Vol1.
124 T. Sheppard & S.J. Paterson Met.Tech.. 1982. 9.274.
125 W.S. Faren & G.I. Taylor Proc.Royal Soc.. 1925. 107.422.
126 D.S. Fields & W.A. Backofen Proc. A.S.T.M.. 1957. 57.1529.
127 G. Canova et al. A.S.T.M. Symposium 'Formability-2000'. 1980. Chicago.
128 T. Sheppard & E.P. Wood Proc. 17th M.T.D.R.. 1976. McMillan. London. p411.
129 T. Sheppard et al. J.Mech. Work Tech.. 1982. 6.p313-31.
130 T. Sheppard & D. Wright Met.Tech.. 1979. 6.215.
131 D. Wright & T. Sheppard IBID. 1979. 7.224.
132 D.O. Sprowls Alcoa Research Laborateries. Sp.Rep.1967.
133 W.H. Ailor Handbook on Corrosion Testing and Evaluation. John Willey & Sons. New York. 1971.
134 J.F.W. Bishop Met.Rev.. 1957. 2.8.p361.
135 S.J. Paterson & T. Sheppard Met.Tech.. 1982. 9.389.
136 R. Chadwick Int.Met.Rev. 1980.3.94..
137 Clareborough et al. Recovery and Recrystallisation of Metals. L. Himinel edit. N.Y.Int.Sci..1963. p63.
138 L. Farmer & P. Oxley J.Strain Analysis. 1976. 11.1.
139 T.H.C. Childs Metals Tech.. 1974. 1.305.
140 J.G. Tweedale M.Sc. Thesis. Univ. of London. 1974
141 K.E. Hughes et al. Met.Tech. 1974 April 161.
142 F.J. Humphreys Proc.1st Riso Int.Symposium on Met. & Mat.Sci. 1980. p35.
143 N. Mott & F. Nabarro Conf.on "Strength of Solids". 1948. Phys.Soc. London. p1.
144 A.H. Geisler Phase Transformations in Solids. 1951. Chapman & Hall. London. p287
145 R.E. Smallman "Modern Physical Metallurgy". 1970. Butterworths. London.
146 R. Nicholson. G. Thomas & J. Nutting J.I.M. 1958-59. 87.429..
147 T. Sheppard & D. Raybould J.I.M. 1973. 101.45..
148 A.M. Reti & M.C. Flemings Met.Trans. July 1972. 3.1869..
149 T. Sheppard & M.G. Tutcher Met.Tech. December 1980. 488..
150 H. McShane Ph.D. Thesis. Univ. of London. 1978.
151 B. Chin, W. Nix & G. Pound Met.Trans.. 1977. Vol8A p1523.
152 R.W. Honeycombe 'The Plastic Deformation of Metals' 1968. p172. Arnold. London.
153 P. Haasen Dislocations in Solids. North Holland Pub. 1979. 4. 156.
154 J.M. Alexander J.I.M.. 1961-62. 90. 193.
155 C.G. Schmidt & A.K. Miller Acta Met. 1982. 30.615.
156 ISIS, Interactive Statistic Instructional System, ICCC.
157 C. Chen & J.F. Knott Met.Sci. 1981. 15.357.
158 J.F. Knott Fundamentals of Fracture Mechanics.1973. Butterworths, London.
159 J.F. Knott Mater Sci.Eng. 1971. 7.1.
160 J. Yahalom Stress Corrosion Cracking. 1980. Freund Publishing House.
161 G.M. Ugiansky Stress Corrosion Cracking - The Slow Strain Rate Technique. 1977. ASTM. STP665.
162 A. Munitz Met.Trans.A. 1980. 11.1863.
163 P.L. Morris Inst.Phys.Cont.Ser. No.36. 1977. 9.377.
164 T.F. Bower Trans. A.I.M.E.. 1966. 236.624.
165 A.J. Bryant Aluminium. 1974. 50.10.639.
166 J. Eulitz & G. Scharf Aluminium. 1975. 51.3.214.
167 Hiroaki Yokobayashi Proc 2nd Int. Extrusion Tech. Seminar. 1977 Vol1.115.
168 Hiromasa Hayashi Light Metal Age. 1975. Feb.p8.
169 A.J. Bryant Metals Tech. 1975. 2.21.
170 T.Sheppard & M.Zaidi,Met Tech,1982,9,368
171 M.Molitor,Factors contributing to surface finish of aluminium extrusions,Proc 2nd Int Extn Tech Sem,1977,1,99
172 D.Raybould,P.H.D.Thesis.Univ.of London,1978

ACKNOWLEDGEMENTS

The author is indebted to the Science and Engineering Research Council for financial support and to Alcan International for sponsorship under the Case award scheme. I would like to personally thank the following people who, without their help, this thesis would never have been written.

Dr T. Sheppard

For the initiation of this project and for the supervision and constructive criticism, discussion and advice throughout the duration of the research work.

Alcan International Ltd.

For the provision of materials and experimental facilities, and useful discussions and technical advice from Dr A.J. Bryant, Dr R. Elkington and D. Fletcher.

Technical Assistance

From A. Neve and R. Baxter and their colleagues especially M. Andrews and A. Willis.

John Percy Group

For useful discussion and help from past and present members especially Dr S.J. Paterson, Dr H. McShane, Dr M. Zaidi, R. Parkinson, Eric, J. Norley, N. Parsons and P. Cooper.

Finally I would like to thank my parents for moral support and invaluable help in preparing this thesis and N. Johnston for her prompt and efficient typing.